Technologies-Based Advanced Machine Learning Models: Applications in Civil Engineering

Lead Guest Editor: Haitham Abdulmohsin Afan
Guest Editors: Chongchong Qi and Mostafa Al-Emran

Technologies-Based Advanced Machine Learning Models: Applications in Civil Engineering

Technologies-Based Advanced Machine Learning Models: Applications in Civil Engineering

Lead Guest Editor: Haitham Abdulmohsin Afan
Guest Editors: Chongchong Qi and Mostafa Al-Emran

Contents

WILEY | Hindawi

Research Article

Fusion-Learning-Based Optimization: A Modified Metaheuristic Method for Lightweight High-Performance Concrete Design

Ghodrat Rahchamani [ID],[1] **Seyed Mojtaba Movahedifar** [ID],[1,2] **and Amin Honarbakhsh** [ID][1,2]

[1]Department of Civil Engineering, Neyshabur Branch, Islamic Azad University, Neyshabur, Iran
[2]New Materials Technology and Processing Research Center, Department of Civil Engineering, Neyshabur Branch, Islamic Azad University, Neyshabur, Iran

Correspondence should be addressed to Amin Honarbakhsh; amin_honarbakhsh@yahoo.com

In order to build high-quality concrete, it is imperative to know the raw materials in advance. It is possible to accurately predict the quality of concrete and the amount of raw materials used using machine learning-enhanced methods. An automated process based on machine learning strategies is proposed in this paper for predicting the compressive strength of concrete. Fusion-learning-based optimization is used in the proposed approach to generate a strong learner by pooling support vector regression models. The SVR technique proposes an optimization method for finding the kernel radial basis function (RBF) parameters based on improving the innovative gunner algorithm (AIG). As a result of AIG's diverse solutions, local optima are effectively avoided. Therefore, the novelty of our research is that, in solving the uncertainty of predicted outputs based on integrated models, we use fusion-learning-based optimization to improve regression discrimination. We also collected a standard dataset to analyze the proposed algorithm, and subsequently, the dataset was designed from concrete laboratory tests on 244 samples, seven features, and three outputs. Different regression intensities are determined by correlation analysis of responses. Regression fusion is sufficiently accurate to estimate the number of desired outcomes examined based on the appropriate input data sample. The best quality concrete can be achieved with an error rate of less than 5%.

1. Introduction

The structural materials of concrete and the reaction between these materials play a critical and decisive role in explaining high-strength concrete's mechanical properties. Therefore, concrete designers and engineers seek to gain an accurate and thorough understanding of the relationship between the appropriate choice of type and amount of materials for concrete construction [1]. Concrete is a mixture of water, cement, and other materials, and from a chemical perspective, the strength of this material depends more than anything on cement and water [2]. High-strength concrete must exhibit resistance and flexibility against various forces and environmental factors. Hence, the proper mixture of raw materials can enhance the strength and quality of the concrete. The compressive strength of concrete depends on various factors, including mixing properties, mixing methods, mixing conditions, transport, and concrete [3]. Sometimes the concrete design engineer knows the initial composition and the estimated percentage of material mixing; however, the importance of an accurate estimate cannot be overestimated. Therefore, the concrete quality can only be assessed after making efficient concrete, and the elapse of a specific period, often a long interval (usually one month) using special tests [4]. Consequently, making quality concrete is conducted based on resembles a trial and error approach and may lead to extensive raw materials loss. By observing the falling slope in concrete, helpful information about the concrete performance can be obtained [5].

In addition, due to the great importance of concrete in structures and the significant growth of urbanization, the increase in demand for high-quality concrete is substantial

[6]. In many developing countries, such as China, the ready-mixed concrete, prepared by mixing concrete, dominates the entire concrete market [7]. As an advanced industry, the ready-mixed concrete trade is of utmost importance in significant sectors of industry and construction, transportation, and after-sales service. However, the current concrete industry management is still at the fundamental information management level because the knowledge generated during the management process is too complex to be used [8]. A goal-oriented and efficient way to address this problem is knowledge management and the adoption of artificial intelligence technology [9].

In recent decades, due to the proliferation of construction globally, a significant body of research has attempted to optimize the quality of concrete. Therefore, artificial intelligence (AI) has received growing attention as an analyzer of information in this field. The main application of soft computing-based methods is to determine concrete strength [10–18]. Most researchers focus on accurate estimation of raw materials based on artificial neural networks (ANNs) ability to estimate correct regression outputs [19–21]. Some researchers have also used ANN and clustering methods such as adaptive neuro-fuzzy inference system (ANFIS) [22]. In other studies, rapid learning and its combination with Cascade-forward neural network (CfNN) have been highlighted, which has led to the decreased processing time of concrete ingredients and achievement of the desired output [23]. Some investigations have utilized a combination of neural networks and evolutionary algorithms or metaheuristic (MH) to improve the precision of obtaining desired outcome [24, 25]. Combination with evolutionary algorithms (EA) is typically intended to amend inherent defects of ANN or other regression-based estimation methods. These algorithms are extensively used in ANN training for accurate error estimation. These include the genetic algorithm (GA) [26, 27], particle swarm optimization (PSO) [28], or simulated annealing (SA) [29]. The genetic algorithm can find global and local optimums and may be even trapped in local optimums, but it has rapid convergence [26, 27]. A growing number of studies have recently adopted ANN [27, 28, 30] and SVR [29] as a model for regression network estimation. The utilization of methods such as deep learning to estimate the quality of concrete has drawn considerable attention, urging researchers to adopt different deep learning models to improve the quality of concrete [31–33]. Sadrossadat and others. [34] have developed an evolutionary-based prediction model of the 28-day compressive strength of high-performance concrete containing cementitious materials.

Estimating the concrete performance is an essential process in ensuring the quality of various concrete components. Concrete testing is a method that measures near-performance parameters and provides valuable information about these parameters. The methods currently used in the world measure the stability of concrete in the laboratory or on-site. In some experiments, a kind of failure is estimated by measuring the reduction in the upper surface of freshly crushed concrete. Low accuracy, uncertainty, computational complexity, and the lack of a generalized method in the

automatic determination of concrete raw materials in previous strategies have led us to look for more appropriate and accurate solutions.

Given that specific percentages of materials need to be combined to produce concrete of varying grades, this process is usually based on personal experience, and trial and error deems necessary to avoid wasting materials. For this to happen, an automated method is required for the analysis of raw materials. The importance of research becomes more apparent, knowing that a significant portion of its constituents include water, cement, and sand and are among finite resources that are rapidly depleted. Therefore, either one must possess exceptional skills and expertise, or a solution must be found to estimate the precise percentage of ingredients. Thus, the previous automated models are highly dependent on the optimized regression-learning model and the input components selection. Concrete design decisions on the component level must be correlated to operational cost and emissions on the supply chain level to evaluate commercial and environmental influence [35]. The main difficulty is finding a qualified approach to produce proper outputs on concrete designing in the real world. Fitting outputs are achieved by relying on appropriate learning methods. Recently, the relevant studies have considered optimization algorithms based on support vector models for high-quality concrete design [36–40].

Although both SVR and ANN models can map input data to a higher dimensional space to determine the decision boundary, NNs require numerous data input than SVR to better training. In addition, SVRs need minimal or more negligible processing of input data, which saves a lot of time. Besides, the ANN model usually necessitates much more modification, cleaning, data processing, etc. Typically the ANNs involve batch conversion to numbers, feature scaling, etc.

In the current study, we present an effective prediction design of concrete structure based on the proper fusion model of Support Vector Regression (SVR) learner and innovative gunner algorithm (AIG). Also, the AIG algorithm is described by a significant search space exploration, owing to solution vectors, typical for swarming techniques. Thus, the AIG algorithm achieves diverse solutions, which provides it high efficiency in avoiding local optima [41]. Besides, it can be utilized successfully to determine target functions of different shapes and with multiple optima and multidimensional functions.

The proposed method can remarkably reduce the classification error in regression mode to design lightweight and high-performance concrete. Our model has produced desirable results for predicting 28-day compressive strength and helps save the raw materials for concrete production. The method has been applied to a set of laboratory data collected by the authors. Similarly, attempts have been made for innovation to generate actual data in the laboratory within three months and fabricate different concrete types with varying qualities.

The remainder of this paper is organized as follows: the method components are described in Section 3. Section 4 introduces the proposed model, including the used

optimization algorithm and the regression learner. Section 5 presents the results and interpretations of the classification under various conditions. Finally, the paper is concluded by summarizing the key points in Section 6.

2. Contribution and Learning Structure

In this section, the components we utilized to optimize the concrete quality prediction based on learning process are described. As shown in Figure 1, the significant contributions of designing lightweight and high-performance concrete have been related to data development, automated analysis of outputs (i.e., effective design), and best learning to discriminate concrete quality.

2.1. Regression Learning. Assuming that one training data is available, if each input has D attributes (i.e., belongs to the D-dimensional space), and each point is assumed to have Y corresponding special, a function can be found that relates the input to the output [42]:

$$f(x, w) = w^T x + b. \tag{1}$$

To obtain the function f, the values of w and b in the following equation must be minimized:

$$R = \frac{1}{2}\|w\|^2 + C_1 \frac{1}{l} \sum_{i=1}^{l} L_\varepsilon (y_i, f_i(x, w)), \tag{2}$$

where C_1 is a constant value, the value of which is set by the user. The C_1 value is intended to create balance and change the weights of the penalty due to the omission of the variable ε and, at the same time, maximize the margin for discrimination. Accordingly, function L_ε is introduced according to

$$|y - f(x, w)|_\varepsilon = \begin{cases} 0, & |y - f(x, w)| \le \varepsilon, \\ |y - f(x, w)| - \varepsilon, & \text{otherwise.} \end{cases} \tag{3}$$

The equation is rewritten as a maximum of the following equation [43]:

$$L_P (a_i, a_i^*) = -\frac{1}{2} \sum_{j=1}^{l} (a_i - a_i^*)(a_j - a_j^*) x_i^T x_j - \varepsilon \sum_{i=1}^{l} (a_i + a_i^*)$$

$$+ \sum_{i=1}^{l} (a_i - a_i^*) y_i, \tag{4}$$

where conditions are defined based on

$$\text{Condition:} \begin{cases} \sum_{j=1}^{l} (a_i - a_i^*) = 0, \\ 0 \le a_i \le C, \quad i = 1, \ldots, l, \\ 0 \le a_i^* \le C, \quad i = 1, \ldots, l. \end{cases} \tag{5}$$

By solving the above equations, the SVR function, i.e., f in (1), can be obtained using the kernel function:

$$f(x, w) = w_0^T x + b = \sum_{j=1}^{l} (a_i - a_i^*) x_i^T x + b. \tag{6}$$

2.2. Innovative Gunner Algorithm (AIG). According to Newton's law, a projectile's motion can be directed vertically in a homogeneous gravitational field where the initial velocity in the horizontal direction is not zero [41]. A projectile is thrown with the initial velocity v_0 at an angle δ, and its horizontal surface is assumed to be perpendicular to the direction of gravity. It has a parabolic motion in a frame with dimensions d and h. This equation is defined according to (7), where g denotes the acceleration caused by the gravitational force:

$$h = \tan \delta . d - \frac{g . d^2}{2 . v_0^2 . \cos^2 \delta}. \tag{7}$$

Computations will be more complicated if drag forces are involved. For the simplest model, where the tensile force is assumed to be proportional to the velocity of the projectile, (7) will be significantly complicated because [41]

$$h = \left(\tan \delta + \frac{g}{k . v_0 . \cos \delta} \right) . d + \frac{g}{k^2} . \ln \left(1 - \frac{d . k}{v_0 . \cos \delta} \right), \tag{8}$$

where k is defined as drag coefficient (unit 1/s), and its value depends on weight and air resistance. Several analytical and experimental methods have been proposed to ensure the accuracy of the projectiles equations based on ballistics. Figure 2 shows the bullet motion curve for three different angles.

However, it should be noted that the actual projectile curve can be expressed as

$$h = \left(\tan \delta + \frac{g}{k . v_0 . \cos \delta} \right) . d + \frac{g}{k^2} . \ln \left(1 - \frac{d . k}{v_0 . \cos \delta} \right) + f_h(\xi), \tag{9}$$

where $f_h(\xi)$ is a function influenced by interfering factors, including changes in air resistance, temperature, wind, shape, and motion of the Earth. In this case, the angle δ can be assumed as a decision variable for the optimization process, whose objective function is as follows:

$$F_{obj}(\delta) = |h(\delta)| \mapsto \min. \tag{10}$$

Given the complex form of equation (10) and the uncertainty of the function $f_h(\xi)$, a metaheuristic method could be used to calculate the value of angle and firing.

3. Proposed Method

Figure 3 shows the overall steps for the suggested implementation of concrete designing.
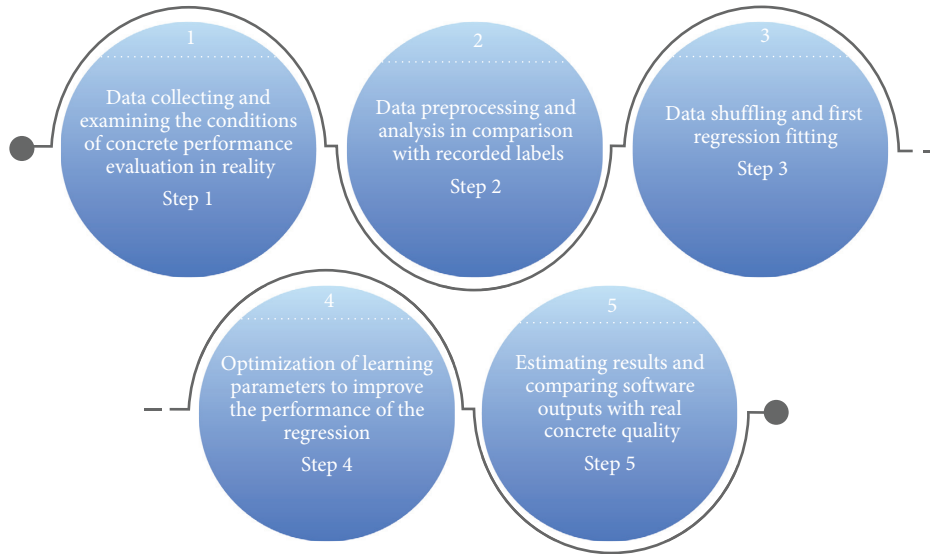
FIGURE 1: A general schematic of the main contributions in concrete quality prediction.
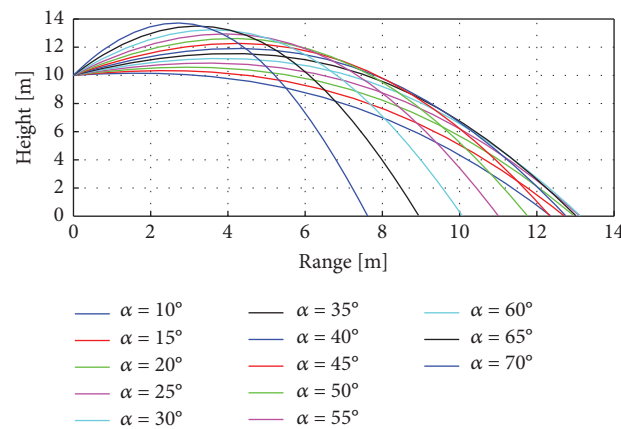
FIGURE 2: Bullet motion curve for three different angles.
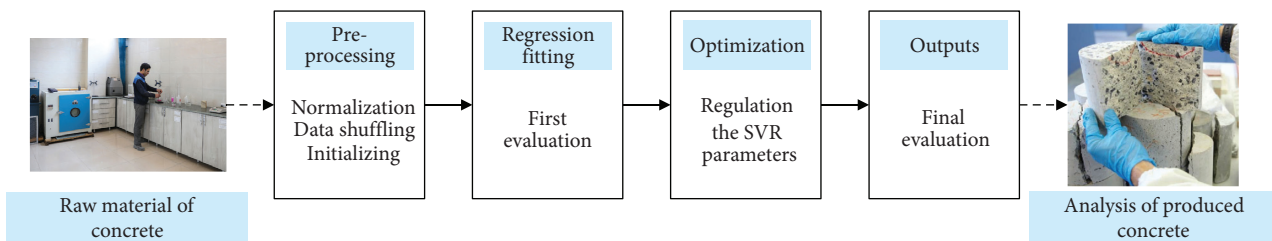
FIGURE 3: This diagram shows the overall design for the proposed implementation method.

3.1. Preprocessing. First, as shown in Figure 4, we shuffled the data in the preprocessing step to prevent overtraining of the automatic classification procedure. Although the samples are randomly mixed, the label's position changes regularly according to the classes of each received sample. We are applying such a method to prevent overfitting, leading to a considerable increase in classification accuracy. Because each data's concrete is intrinsically highly distributed and uses numerous diverse samples in a wide range, they must be normalized in the next step of the preprocessing step. Normalization of samples reduces the processing cost and positively affects the optimization of concrete quality prediction [44].

$$Y_{\text{norm}} = \frac{Y_s - Y_{s_{\min}}}{Y_{s_{\max}} - Y_{s_{\min}}}. \tag{11}$$
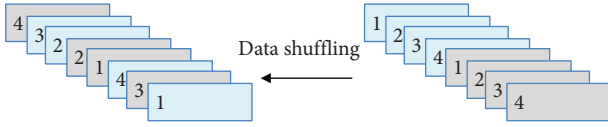
FIGURE 4: Data shuffling in preprocessing step.

Y_{norm} is considered the normalized value, and the variables Y_{smin} and $Y_{S_{max}}$ are the minimum and maximum values, respectively. Besides, Y_s is the current value of the concrete sample under study.

3.2. Fusion Regression. In the first step, data normalization is performed. This process is conducted using the Min-Max method to reduce excessive dispersion of data. The main goal of support vector machines is to find an optimal hyper-plane as a decision-making level that maximizes the margin between two classes. The data are moved to a considerably larger space by the Φ kernel function to classify highly complex data. The kernel function maps data from the input space on a space with higher dimensions, so that it is possible to separate the data in that space linearly. In the first part, the SVR regression learning pool as regression fusion model is used by applying training data. The general diagram is shown in Figure 5 and depicts the general learning framework. The initialization of γ and s for each regression classifier is initially randomized. The change interval for these two parameters varies from zero to 20. By applying the training data, the structure with the lowest mean square error (MSE) is selected, and its parameters ? and s are given to input to the AIG algorithm. In this way, convergence towards the optimal response is faster and more accurate. The regression fusion of pool structure is evaluated by five repetitions, averaging accuracy, and finding the best corresponding parameters. The best matching parameter is a grid with the highest accuracy rate. In addition, finding the best RBF kernel values facilitates the search for the global optimum in the modified AIG algorithm.

3.3. Improving the Best Model. In order to optimize the model parameters, various methods can be used. The space networked with RBF kernel was identified as the best kernel for the data [45, 46]. This kernel can be expressed for two variables and b:

$$K(a, b) = \exp\left(-\gamma \|a - b\|^2\right) = \exp\left(-\frac{\|a - b\|^2}{2\sigma^2}\right), \quad (12)$$

where the parameter γ corresponds to the square of the width of Gaussian kernel. By finding the initial values γ and C in the classification pool, the modified AIG algorithm is used by accounting for air resistant. This constraint is considered more than other constraints for $f_h(\xi)$ because other constraints do not always exist in real conditions, but air resistance is present under almost any condition.

The most typical case of air resistance, for Reynolds numbers above 1000, is Newton drag with a drag force proportional to the speed squared, $F_{air} = -kv^2$. In air, which

has a kinematic viscosity around $0.15\,\mathrm{cm}^2/\mathrm{s}$, this means that the product of speed and diameter must be greater than about $0.015\,\mathrm{m}^2/\mathrm{s}$. Unfortunately, the equations of motion cannot be easily solved analytically for this case. Therefore, a numerical solution will be examined.

$$F_D = -\frac{1}{2} c \rho A v V, \quad (13)$$

where F_D, c, ρ and A are defined as drag force, drag coefficient, air density, and cross sectional area of the projectile, respectively, and μ is defined according to

$$\mu = \frac{k}{m} = \frac{c\rho A}{(2m)}. \quad (14)$$

In light of these limitations and initialization in the previous step, the fitness function is defined in the meta-heuristic algorithm, according to MSE. The termination condition of the algorithm is based on calculating the minimum error of MSE. Suppose that the algorithm is not realized in a certain number of iterations. In that case, the parameters matching the best regression network are selected, which produce a more significant effect on regression learning than other SVR structures do. On the other hand, considering the drag conditions and air resistance, the shot angle widens, and the best angle is set between 30 and 80°. According to the calculations, the best shot angle is 45°, but in changing the initial velocity of the bullet, the optimal angle is altered considering air resistance.

4. Experimental Results

The proposed method was implemented by MATLAB R2019b in Windows 10 operating system. The hardware platform used for simulation was an Intel® Core ™ i5-8500 system with 8 GB of RAM, plus 16 GB of SSD RAM. Other complementary software such as SPSS was also used. The input data were incorporated into an integrated algorithm, and the inputs were normalized in the first step. Mean square error (MSE) and mean absolute percentage error (MAPE) are expressed in (15) and (16), respectively. They were tested using adaptive algorithms in input analysis.

$$\text{MAPE} = \frac{1}{N} \sum_{i=1}^{N} \frac{|T_i - P_i|}{T_i}. \quad (15)$$

$$\text{MSE} = \frac{1}{N} \sum_{i=1}^{N} (T_i - P)^2. \quad (16)$$

In these equations, T_i, P_i, and N are the actual output values, the values predicted by the algorithm, and all specimens. In addition to the MSE and MAPE calculation, the maximum and minimum errors were also estimated, and the results of the K-fold cross-validation were calculated for each test.

4.1. Dataset. Data were obtained from the concrete testing laboratory at Imam Khomeini University of Sabzevar, Iran, over six months. The data consists of seven inputs and three
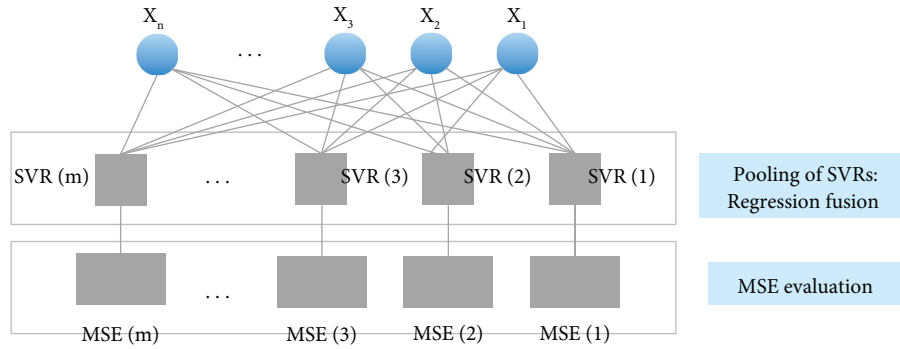
FIGURE 5: Regression fusion based on pooling the SVRs models.

TABLE 1: Practical data collected from the concrete laboratory of Imam Khomeini University of Sabzevar.

Data	Components	Max	Min	Average	Standard deviation	Variance ($\times 10^{-3}$)
	Cement	383	142	240.40	79.02	6.24
	Water	199	0	73.14	60.52	3.66
	Fly ash	287	3.5	152.47	85.55	7.32
Input (Kg in M^3)	Fine aggregate	244.35	176	200.83	20.35	0.423
	Coarse aggregate	25	3.12	12.92	3.73	0.134
	Superplasticizers	1118	631	887.13	88.37	7.839
	Slag	943	543.12	744.08	63.98	4.12
	FLOW (cm)	34.87	0	22.43	9.124	0.0831
Output	SLUMP (cm)	96	21	54.514	17.82	0.317
	28-day compressive (Mpa)	66.34	18.56	40.82	8.233	0.678

TABLE 2: Calculation of MSE, MAPE average, minimum, and maximum error for predicting high-strength lightweight concrete by the proposed regression fusion based on pool of SVRs and modified AIG algorithm. In this table, the K value in K-fold CV is considered to be equal to 5.

K-fold	Minimum error			Maximum error			MSE			MAPE		
	Output 1	Output 2	Output 3	Output 1	Output 2	Output 3	Output 1	Output 2	Output 3	Output 1	Output 2	Output 3
5-Fold (1)	0.273	0.383	0.317	14.31	21.18	9.53	1.73	4.59	1.24	0.965	1.53	0.894
5-Fold (2)	0.206	0.412	0.237	12.73	14.31	13.12	1.39	5.03	1.08	0.524	0.823	0.776
5-Fold (3)	0.229	0.374	0.365	10.33	28.73	14.43	1.58	4.87	1.44	0.947	1.34	0.739
5-Fold (4)	0.441	0.480	0.594	16.43	19.17	11.29	2.65	6.27	1.57	0.731	1.13	0.947
5-Fold (5)	0.202	0.711	0.254	15.45	29.83	16.56	2.61	9.07	0.794	0.575	0.767	0.722
5-Fold (6)	0.503	0.308	0.408	15.32	11.43	0.08	1.14	8.24	0.647	0.995	1.42	18.1
5-Fold (7)	0.153	0.494	0.211	17.40	15.87	9.86	1.09	9.01	0.733	0.673	0.865	0.712
5-Fold (8)	0.328	0.487	0.264	17.73	28.65	7.22	1.76	7.11	0.851	0.801	0.915	0.834
5-Fold (9)	0.162	0.374	0.183	16.56	26.73	13.25	2.11	8.14	0.578	0.787	1.27	0.912
5-Fold (10)	0.258	0.448	0.379	16.30	34.19	9.45	1.39	8.76	0.476	0.413	0.873	0.748
Avg.		0.347			16.248			3.262			1.4576	

outputs, including cement, slag, fly ash, water, super-plasticizers, coarse aggregate, and fine aggregate. All of these inputs are in component kg in one M^3 concrete. Besides, the outputs of this dataset are SLUMP (cm), FLOW (cm), and 28-day Compressive Strength (Mpa). The number of constructed specimens is higher than the first data samples (243 specimens), and the number of feature inputs and outputs is equal. The necessary information of this dataset is shown in Table 1.

4.2. Assessments. As presented in Table 2, regression predictions for datasets are a combination of different algorithms at the time of testing by selection K value equal to 5. Changing the values of RBF parameters and preventing overfitting in many repetitions, the SVRs pool as regression fusion was used to find the lowest amount of MSE among the five structures in each pool.

If the MSE is less than 5% of the total error in the sample data in this structure, the corresponding SVR is selected as the base network. Otherwise, the minimum MSE and the corresponding network structure should be chosen. Figure 6 shows the results of the RMSE convergence and corresponding Loss function of the algorithm set to reach the minimum value. When the algorithm tries to achieve the optimal value in the training step, more satisfactory outputs
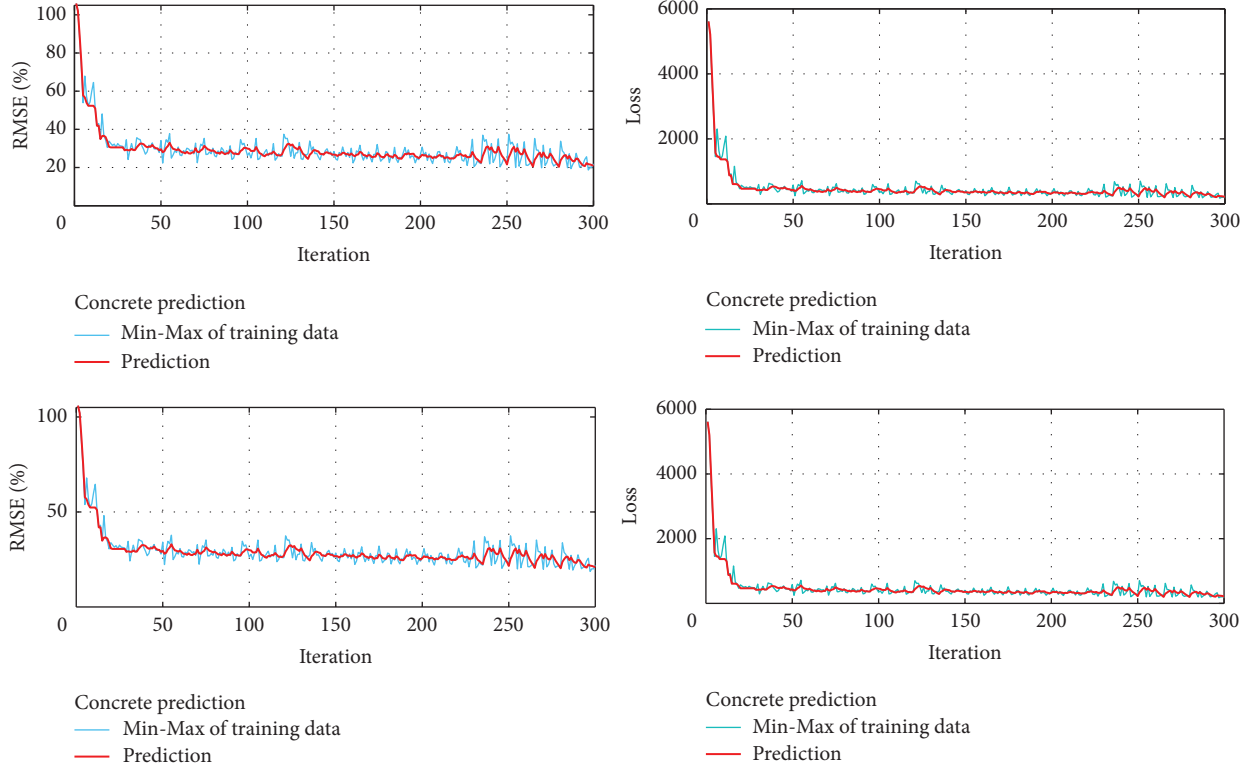
FIGURE 6: RMSE convergence and corresponding Loss function in training step.

TABLE 3: Calculation of MSE, MAPE average, minimum, and maximum error for predicting high-strength lightweight concrete by the proposed regression fusion based on pool of SVRs and modified AIG algorithm. In this table, the K value in K-fold CV is considered to be equal to 10.

K-fold	Minimum error			Maximum error			MSE			MAPE		
	Output 1	Output 2	Output 3	Output 1	Output 2	Output 3	Output 1	Output 2	Output 3	Output 1	Output 2	Output 3
10-Fold (1)	0.254	0.418	0.339	13.74	20.23	10.65	1.80	4.53	1.28	0.932	1.41	0.844
10-Fold (2)	0.211	0.467	0.166	11.53	13.56	7.83	1.64	5.17	1.12	0.556	0.794	0.760
10-Fold (3)	0.287	0.456	0.373	11.76	27.31	5.22	1.48	4.75	0.98	0.971	1.11	0.734
10-Fold (4)	0.411	0.434	0.622	16.05	17.37	10.09	2.23	6.31	1.01	0.754	1.32	0.978
10-Fold (5)	0.228	0.773	0.267	14.37	24.13	5.76	2.42	8.94	0.765	0.543	0.732	0.651
10-Fold (6)	0.537	0.491	0.418	16.29	19.29	8.53	1.06	8.07	0.678	0.986	1.20	1.12
10-Fold (7)	0.243	0.565	0.467	15.81	13.91	11.51	1.12	9.12	0.743	0.640	0.876	0.793
10-Fold (8)	0.375	0.437	0.241	16.29	26.44	8.97	1.43	6.88	0.876	0.813	0.967	0.867
10-Fold (9)	0.291	0.414	0.212	18.16	29.23	6.13	2.08	7.95	0.561	0.804	1.13	0.946
10-Fold (10)	0.243	0.473	0.356	15.27	30.89	7.38	1.51	8.37	0.441	0.587	0.663	0.331
Avg.	0.382	12.387	3.148	0.8637								

can be obtained in the experimental section by increasing the number of search alterations of the AIG algorithm or increasing the number of SVRs.

The change in evaluation criteria is not significant due to the change in K, and thus, Table 3 shows that a slight improvement in K accompanies the experiment.

However, although the training phase results are done offline, due to the numerous repetitions in finding the best SVR structure of the learning pool and the time-consuming AIG optimization algorithm, computational complexity is observed, especially in the training step. A similar

implementation for random data in convergence to the optimal value for four validation data is shown in Figure 7. In these plots, a limited number of repetitions are seen, and the level of error originates from the training stage.

On average, for each run of the algorithm, the average value of correlation is greater than 0.9 and, in some cases, reaches as high as 0.98. Assuming that, in the prediction of concrete quality regression, y_t and x_t are static variables in the detection or estimation of parameters and T and F tests, the results were used by increasing the sample size, and sample variance to population variance was used to
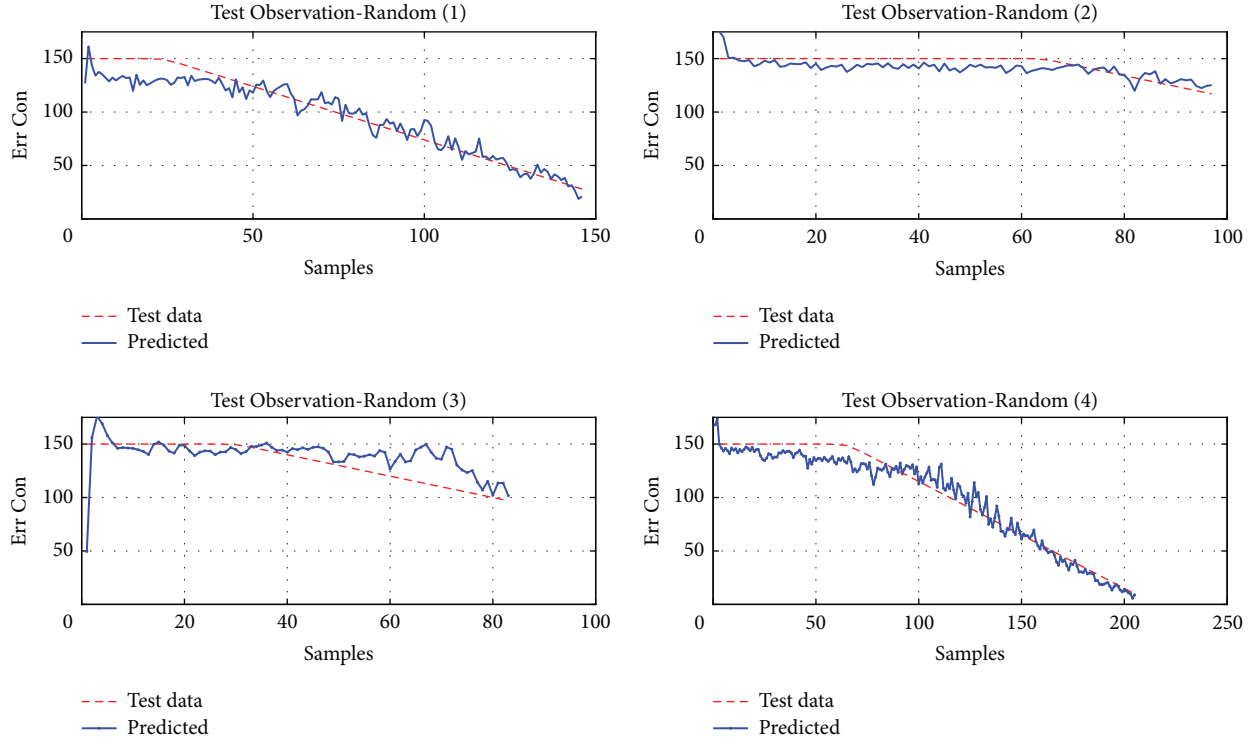
FIGURE 7: Algorithm convergence to minimum error for four random validation data with limited number of iterations.

demonstrate minimal normal consistency. Estimating the MES for an estimate of the predicted time sequence with dynamic properties may suggest that the variance has not been well defined. Therefore, this value will not fluctuate around a specific mean. To further explain the variables y_t and x_t, it was assumed that the regression trend was defined as the quality prediction trend in a random step:

$$
\begin{aligned}
y_t &= y_{t-1} + \varepsilon_1 t \quad (t = 1, \dots, N), \\
x_t &= x_{t-1} + \varepsilon_2 t \quad (t = 1, \dots, N),
\end{aligned} \tag{17}
$$

where $\varepsilon_1 t$ and $\varepsilon_2 t$ had independent distribution functions, and the relationship between the variables y_t and x_t was not justifiable.

To perform a regression analysis, we first assumed a relationship between the two variables selected from the seven input variables. Based on the assumption that there is a linear relationship between the two variables, quantitative data was collected from both variables, and the data were plotted as points on a two-dimensional map. As shown in Figure 8, the difference between the main and predicted outputs is small, and the variances between them are negligible. Table 4 shows the calculated variances of ten experiments. Variances indicate great independence of the features selected by SPSS software. Therefore, using the output quality, a small portion of the low-impact features can be distinguished from the others.

As noted earlier, concrete strength is defined in terms of its ingredients, weight, and specific properties. Data were obtained under laboratory conditions based on real conditions. Other factors such as data collection, mixing, and other parameters affecting concrete strength are also included in this section. Although the laboratory data presented in some studies offer valuable information on this subject, there were essential details, the absence of which could significantly predict performance in many cases.

5. Discussion

In concrete preparation by learning-based methods, the most crucial design issue is the lack of significant differences between the predicted outputs and the actual output. Hence, the R-Squared is considered as one of the most specific criteria for comparison between methods, where y, $\hat{y}$, and $\overline{y}$ are the main, mean, and predicted values, respectively. The R-Squared is expressed as (19):

$$
R^2(y, \hat{y}) = 1 - \frac{\sum_{i=1}^{n} (y_i - \hat{y})^2}{\sum_{i=1}^{n} (y_i - \overline{y})^2}. \tag{18}
$$

In these experiments, different test conditions are investigated:

(1) When SVR is used alone in estimating outputs (Model 1).

(2) When fusion between SVRs is used in estimation (Model 2).

(3) When the fusion between SVRs is combined with the genetic algorithm in the analysis (Model 3).

(4) When the fusion between SVRs is combined with the PSO algorithm in the estimation (Model 4).

(5) When the fusion between SVRs is combined with the AIG algorithm in the estimate (Model 5).
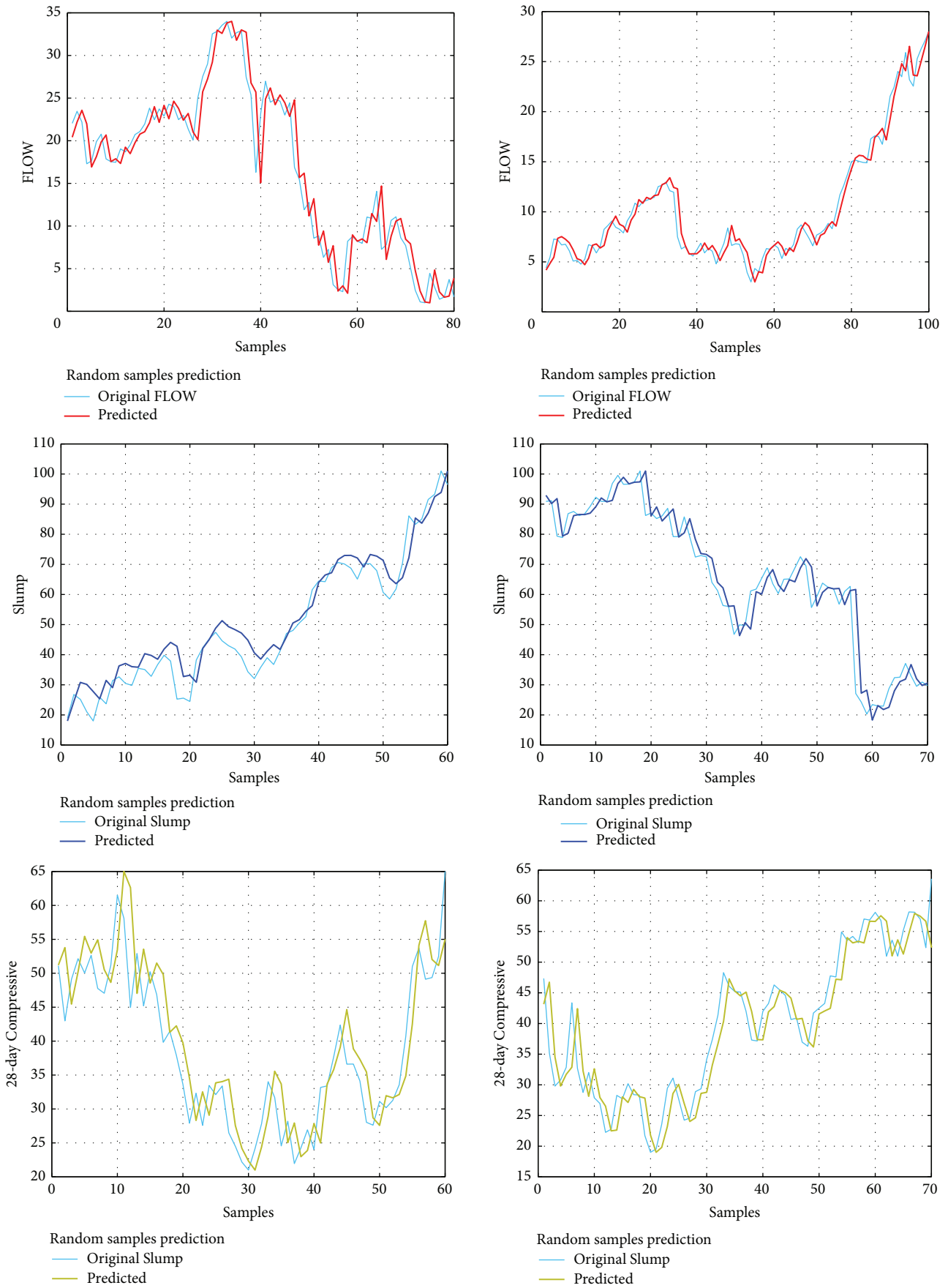
FIGURE 8: Difference between the main and predicted outputs of test step is small, and the variances between them are negligible.

TABLE 4: Computed variances in 10 experiments: blue arrows indicate that the final variance between the main outputs and the forecast is small compared to experts' opinions. Red arrows also denote higher variance compared to experts' opinions.

Experiments	Expert 1	Expert 2	Simple SVR	Fusion-SVRs (linear)	Fusion- SVRs (RBF)	Fusion- SVRs (RBF)-AIG	Fusion-SVRs-(RBF)-mAIG
1	±1.18	±1.67	±3.03	±2.27	±2.04	±1.29	±0.96 ↑
2	±1.43	±1.28	±4.17	±3.83	±2.46	±1.13	±0.85 ↑
3	±1.83	±1.65	±4.22	±3.47	±2.72	±2.57	±1.39 ↑
4	±2.11	±1.68	±5.84	±3.13	±2.51	±1.21	±0.75 ↑
5	±1.78	±2.07	±5.12	±4.73	±3.62	±3.16	±2.11 ↓
6	±1.91	±1.69	±3.19	±2.48	±2.92	±1.94	±1.06 ↑
7	±1.44	±1.73	±4.41	±2.36	±2.08	±1.37	±0.84 ↑
8	±2.33	±2.27	±5.93	±4.27	±3.63	±2.71	±1.48 ↑
9	±1.76	±2.44	±5.51	±3.26	±2.71	±1.28	±1.02 ↑
10	±1.45	±1.61	±4.31	±3.44	±2.59	±2.42	±1.76 ↓

(6) When the fusion between SVRs is combined with the modified AIG algorithm in the estimation (Model 6).

Experimental representations for five different and random types of data are shown in Figure 9 separately for each of the six models. The p-value in the proposed algorithm indicated a significant relationship between the proposed algorithm's output and regression values. For this reason, we rounded the outputs ($p < 0.05$), which manifest the significance of outputs. The comparison with other similar outputs and methods provides a valid justification for rejecting the null hypothesis (H_0). This is because the test result was not in the acceptable range of H_0 and thus H_0 was not confirmed ($\alpha = 0.05$) and therefore -$Z_{\alpha-1}$ is equal to -1.65. This meant that the confidence interval was greater than 95% and the outputs more accurately resembled reality, as indicated by the studied samples and K-equal validation. To test the claims regarding the correlation of concrete properties, aside from selection by the genetic algorithms, SPSS software was used to analyze the correlation factor between the measured properties. The results were significantly identical and except for the fifth feature (which had a lower correlation compared to other coefficients), features with 100% correlation were selected correctly.

However, as noted in Abrams' law, in real weather conditions, other factors may also affect the mixture of substances. This rule, which predicts concrete performance based on a combination of water-cement mixture, indicated a slight error for the coefficient of determination. This could be attributed to water interference in the hydration process of cement, which can cause changes in the molecular structure of cement material and thus affect the process of achieving optimal concrete performance.

We know that concreting at a temperature of less than 5 °C slows down the hydration process, and the process of obtaining concrete strength practically stops. As the temperature of concrete decreases, its hardening and achieving strength decreases, and at the temperature below freezing point, the chemical process of hardening of concrete stops. In general, at low temperatures, the rate of gain of concrete strength decreases. Experiments were performed after producing the concrete, which was considered for the built

concretes according to the regional conditions and the occurrence of frost.

In the experiments, the decrease of temperature and change of each of the outputs is considered noise, and the algorithm's resistance to change of each of the concrete components is investigated. The effect of freezing is measured, and the temperature drop is considered as the fourth output. It was found that, among the primary materials, changes in some of them can significantly prevent concrete from freezing. In general, for a given degree of hydration, the higher the water-to-cement ratio, or for an offered water-to-cement rate, the lower the degree of hydration, and the larger the pore volume in the hydrated cement paste. Since freezing water settles quickly in large pores, it can be hypothesized that the amount of freezing water for water-to-cement ratios is higher and, in the early processing times at a given freezing temperature, will be more. By performing the above software tests on typical weight concretes exposed to freezing and thawing in wet conditions, the maximum water-to-cement ratio should be considered for tabulations, water ducts, and guardrails, or parts thereof equal to 0.45 and equal to 0.5 for the remaining pieces. It is clear that these water limits to cement ratio are based on the assumption of sufficient hydration of cement. In other words, the amount of water that can freeze in concrete with a specific rate of water to cement increases with decreasing temperature, and the amount of water that freezes at a particular temperature increases with an increasing ratio of water to cement. Based on this, it was concluded that as the temperature decreases, the water-to-cement rate should be considered, and the combination of some slags should be used more sensitively.

High error, computational complexity, and uncertainty challenges in algorithms are common problems in quality recognition optimization methods. Table 5 presents the analytical comparison between the former techniques and the proposed approach. They also tried to predict the compressive strength of lightweight structural concrete.

Future designs should incorporate deep learning models that are transferable, such as transfer learning structures [55, 56]. Optimization algorithms as well as deep learning based on neural networks have a major impact on the classification process. Except for the optimization method
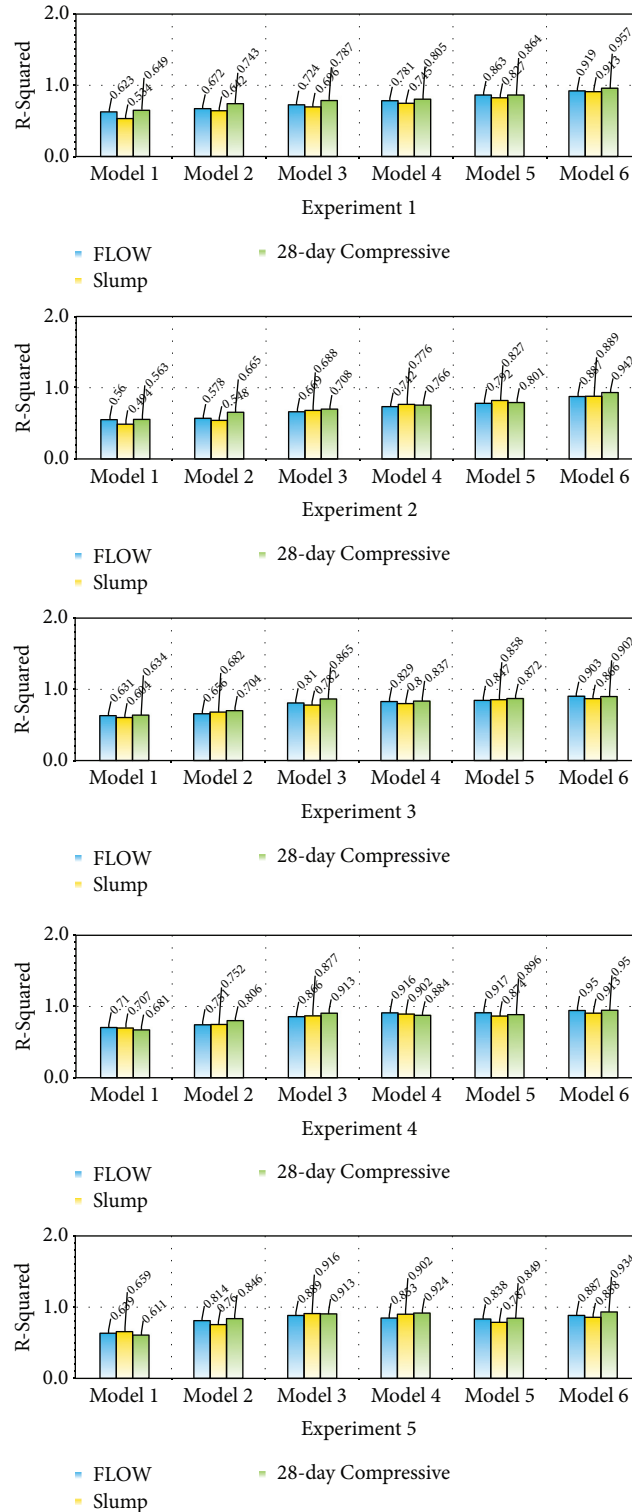
FIGURE 9: R-Squared estimation in six different models for all three outputs in concrete production and display of experiments for 5 random types of data.

employed in the paper, some of the most representative computational intelligence algorithms can be utilized to solve the challenges of high-quality concrete prediction. Some recent optimization algorithms include monarch butterfly optimization (MBO) [57], earthworm optimization algorithm (EWA) [58], elephant herding optimization (EHO) [59], moth search (MS) algorithm [60], Slime mould algorithm (SMA) [61], and Harris hawks optimization (HHO) [62].

TABLE 5: Comparison of the proposed algorithm to similar approaches based on used assessments.

Method	Optimization technique	Learning model	Dataset	Results
Atici [11]	-	Multivariate regression analysis and artificial neural network	Collected data	Optimal accuracy in regression analysis (90%)
Rahchamani et al. [14]	GBMO	ANFIS regression learner	UCI and collected data	MSEs for testing step were 1.065 to 3.16 respectively
Sadowski et al. [21]	CCA	Neural networks regression analysis	Collected data	MSE in the training and testing were 0.157 and 0.024 respectively
Zarandi et al [22]	-	Fuzzy neural network regression analysis	Collected data	Correlation factor in training and testing steps was 90% and 96% respectively
Chandwani et al. [26]	GA	Regression analysis of neural network	Collected data	MAPE for training and testing was 4% to 19% respectively
Nikoo et al. [27]	GA	Multilayer neural networks regression analysis	Collected data	MSE for training and testing was 0.09 to 0.813 respectively
Sadowski et al. [47]	PCA and GA	Neural Networks/Self-Organizing maps (SOM)	Collected data	MSE in the training and testing were 0.006 and 0.007 respectively
Behnood et al. [48]	Multi-objective grey wolves	Neural networks regression analysis	Collected data	Correlation coefficient is 0.96
Yaman et al [49]	-	Self-compacting concrete using artificial neural network	Collected data	R^2 is 0.65 to 1
Alshihri et al. [50]	-	Neural network regression analysis	Collected data	MAE for training and testing was 1% and 3% respectively.
Tsai et al. [51]	PSO	Cascaded neural network regression analysis	Collected data	Index values were not computed
Madandoust et al. [52]	GA	Regression analysis of neural network	Collected data	Maximum error in the training and testing was 9% to 13% respectively
Yeh et al. [53]	-	Second-order neural network regression analysis	UCI database [54] (103 samples)	RMSE for training and testing was 5% to 10% respectively
Proposed	Modified AIG	Regression fusion based on pool of SVRs	Collected data	MSEs for testing step were 0.7 to 3.2

6. Conclusion

Predicting the quality of high-strength concrete is a critical issue in the concrete industry. Our investigations in this paper showed that using an improved model, including the fusion of multiple SVR networks and the modified AIG algorithm, can produce satisfactory outcomes in predicting 28-day compressive strength. Unlike previous methods, which only work in fabricating concrete compositions, the estimator model utilizes a fast yet efficient model and facilitates the regression classification process. The research results suggest that the degree of complexity in the sample data can be reduced to establish a correlation in a standard pattern between the features. Accordingly, it can be concluded that employing the proposed method as an automated method can facilitate the analysis of concrete data and, therefore, offers an accurate estimation of the quality of high-strength concrete. In the future, the authors will use several statistical criteria and various machine learning models for further and more extensive investigation. Furthermore, the use of fusion between neural networks (considering the challenge of uncertainty) and support vectors can be effective in mapping input data and extracting the appropriate pattern.

Data Availability

All the data and codes are available from the corresponding authors.

Ethical Approval

The research meets all applicable standards with regard to the ethics of experimentation and research integrity, and the following is being certified/declared true. As an expert scientist and along with co-authors of concerned field, the paper has been submitted with full responsibility, following due ethical procedure, and there is no duplicate publication, fraud, plagiarism, or concerns about animal or human experimentation.

Conflicts of Interest

The authors have no conflicts of interest to declare.

Authors' Contributions

Gh. Rahchamani and S. M. Movahedifar conceived and planned the experiments. A. Honarbakhsh and Gh. Rahchamani planned and carried out the simulations. A. Honarbakhsh and Gh. Rahchamani contributed to the interpretation of the results. Gh. Rahchamani, S. M. Movahedifar, and A. Honarbakhsh took the lead in writing the manuscript. All authors provided critical feedback and helped shape the research, analysis, and manuscript.

Acknowledgments

References

[1] K. Samrajyam, B. Sobha, T. G. Rao, and R. S. Prasad, "Plastic optic fiber (POF) based phase difference measurement method for estimation of crack mouth opening displacement (CMOD) in concrete," *i-manager's Journal on Civil Engineering*, vol. 4, no. 2, pp. 2231–1068, 2014.

[2] N. Makul, "Modern sustainable cement and concrete composites: review of current status, challenges and guidelines," *Sustainable Materials and Technologies*, vol. 25, Article ID e00155, 2020.

[3] Z. Leng, Z. Tan, H. Yu, and J. Guo, "Improvement of storage stability of SBS-modified asphalt with nanoclay using a new mixing method," *Road Materials and Pavement Design*, vol. 20, no. 7, pp. 1601–1614, 2019.

[4] J. Opon and M. Henry, "An indicator framework for quantifying the sustainability of concrete materials from the perspectives of global sustainable development," *Journal of Cleaner Production*, vol. 218, pp. 718–737, 2019.

[5] M. K. Haridharan, S. Matheswaran, G. Murali et al., "Impact response of two-layered grouted aggregate fibrous concrete composite under falling mass impact," *Construction and Building Materials*, vol. 263, Article ID 120628, 2020.

[6] D. Darwin, C. W. Dolan, and A. H. Nilson, *Design of concrete Structures*, McGraw-Hill Education, New York, 2016.

[7] D. Sobhani, S. Zarei, H. Savoj, and M. Shayanfar, "Investigation on corrosion effects of reinforcement on the moment-curvature diagram of reinforced concrete sections," *Mapta Journal of Architecture, Urbanism and Civil Engineering (MJAUCE)*, vol. 1, no. 3, pp. 11–22, 2018.

[8] C. Zhou, Y. Feng, and Z. Yin, "Maintaining complex formations and avoiding obstacles for multi-agents," *Computers, Materials & Continua*, vol. 62, no. 2, pp. 877–891, 2020.

[9] S. Lee, Y. Ahn, and H. Young Kim, "Predicting concrete compressive strength using deep convolutional neural network based on image characteristics," *Computers, Materials & Continua*, vol. 65, no. 1, pp. 1–17, 2020.

[10] P. G. Asteris and V. G. Mokos, "Concrete compressive strength using artificial neural networks," *Neural Computing & Applications*, vol. 32, no. 15, pp. 11807–11826, 2020.

[11] U. Atici, "Prediction of the strength of mineral admixture concrete using multivariable regression analysis and an artificial neural network," *Expert Systems with Applications*, vol. 38, no. 8, pp. 9609–9618, 2011.

[12] D. Dao, H.-B. Ly, S. Trinh, T.-T. Le, and B. Pham, "Artificial intelligence approaches for prediction of compressive strength of geopolymer concrete," *Materials*, vol. 12, no. 6, p. 983, 2019.

[13] A. Shiuly, N. Roy, and R. B. Sahu, "Prediction of peak ground acceleration for Himalayan region using artificial neural network and genetic algorithm," *Arabian Journal of Geosciences*, vol. 13, no. 5, pp. 1–10, 2020.

[14] G. Rahchamani, S. M. Movahedifar, and A. Honarbakhsh, "A hybrid optimized learning-based compressive performance of concrete prediction using GBMO-ANFIS classifier and genetic algorithm reduction," *Structural Concrete*, vol. 22, p. E779, 2021.

[15] N. D. Hoang, Q. L. Nguyen, and X. L. Tran, "Automatic detection of concrete spalling using piecewise linear stochastic gradient descent logistic regression and image texture analysis," *Complexity*, vol. 2019, Article ID 5910625, 14 pages, 2019.

[16] V. Chandwani, V. Agrawal, and R. Nagar, "Modeling slump of ready mix concrete using genetically evolved artificial neural networks," *Advances in Artificial Neural Systems*, vol. 2014, Article ID 629137, 9 pages, 2014.

[17] J. A. Bogas, M. G. Gomes, and A. Gomes, "Compressive strength evaluation of structural lightweight concrete by non-destructive ultrasonic pulse velocity method," *Ultrasonics*, vol. 53, no. 5, pp. 962–972, 2013.

[18] T. T. Nguyen, H. Pham Duy, T. Pham Thanh, and H. H. Vu, "Compressive strength evaluation of fiber-reinforced high-strength self-compacting concrete with artificial intelligence," *Advances in Civil Engineering*, vol. 2020, Article ID 3012139, 12 pages, 2020.

[19] J.-S. Chou, C.-K. Chiu, M. Farfoura, and I. Al-Taharwa, "Optimizing the prediction accuracy of concrete compressive strength based on a comparison of data-mining techniques," *Journal of Computing in Civil Engineering*, vol. 25, no. 3, pp. 242–253, 2011.

[20] Q. B. Pham, H. A. Afan, B. Mohammadi et al., "Hybrid model to improve the river streamflow forecasting utilizing multi-layer perceptron-based intelligent water drop optimization algorithm," *Soft Computing*, vol. 24, pp. 18039–18056, 2020.

[21] L. Sadowski and M. Nikoo, "Corrosion current density prediction in reinforced concrete by imperialist competitive algorithm," *Neural Computing & Applications*, vol. 25, no. 7-8, pp. 1627–1638, 2014.

[22] M. F. Zarandi, I. B. Türksen, J. Sobhani, and A. A. Ramezanianpour, "Fuzzy polynomial neural networks for approximation of the compressive strength of concrete," *Applied Soft Computing*, vol. 8, no. 1, pp. 488–498, 2008.

[23] M. Nikoo, P. Zarfam, and H. Sayahpour, "Determination of compressive strength of concrete using self organization feature map (SOFM)," *Engineering with Computers*, vol. 31, no. 1, pp. 113–121, 2015.

[24] A. Johari, A. A. Javadi, and G. Habibagahi, "Modelling the mechanical behaviour of unsaturated soils using a genetic algorithm-based neural network," *Computers and Geotechnics*, vol. 38, no. 1, pp. 2–13, 2011.

[25] A. R. Ghanizadeh, H. Abbaslou, A. T. Amlashi, and P. Alidoust, "Modeling of bentonite/sepiolite plastic concrete compressive strength using artificial neural network and support vector machine," *Frontiers of Structural and Civil Engineering*, vol. 13, no. 1, pp. 215–239, 2019.

[26] V. Chandwani, V. Agrawal, and R. Nagar, "Modeling slump of ready mix concrete using genetic algorithms assisted training of Artificial Neural Networks," *Expert Systems with Applications*, vol. 42, no. 2, pp. 885–893, 2015.

[27] M. Nikoo, F. Torabian Moghadam, and Ł. Sadowski, "Prediction of concrete compressive strength by evolutionary artificial neural networks," *Advances in Materials Science and Engineering*, vol. 2015, Article ID 849126, 8 pages, 2015.

[28] M. Shariati, M. S. Mafipour, P. Mehrabi et al., "Application of a hybrid artificial neural network-particle swarm optimization (ANN-PSO) model in behavior prediction of channel shear connectors embedded in normal and high-strength concrete," *Applied Sciences*, vol. 9, no. 24, p. 5534, 2019.

[29] M. Ayubi Rad and M. S. Ayubirad, "Comparison of artificial neural network and coupled simulated annealing based least square support vector regression models for prediction of compressive strength of high-performance concrete," *Scientia Iranica*, vol. 24, no. 2, pp. 487–496, 2017.

[30] T. A. Nguyen, H. B. Ly, H. V. T. Mai, and V. Q. Tran, "Prediction of later-age concrete compressive strength using feedforward neural network," *Advances in Materials Science and Engineering*, vol. 2020, Article ID 9682740, 8 pages, 2020.

[31] T. Nguyen, A. Kashani, T. Ngo, and S. Bordas, "Deep neural network with high-order neuron for the prediction of foamed concrete strength," *Computer-Aided Civil and Infrastructure Engineering*, vol. 34, no. 4, pp. 316–332, 2019.

[32] J. Guo, M. Li, L. Wang et al., "Estimating cement compressive strength using three-dimensional microstructure images and deep belief network," *Engineering Applications of Artificial Intelligence*, vol. 88, Article ID 103378, 2020.

[33] Y. Jang, Y. Ahn, and H. Y. Kim, "Estimating compressive strength of concrete using deep convolutional neural networks with digital microscope images," *Journal of Computing in Civil Engineering*, vol. 33, no. 3, Article ID 04019018, 2019.

[34] E. Sadrossadat and H. Basarir, "An evolutionary-based prediction model of the 28-day compressive strength of high-performance concrete containing cementitious materials," *Advances in Civil Engineering Materials*, vol. 8, no. 3, pp. 484–497, 2019.

[35] M. Lieder, F. M. Asif, A. Rashid, A. Mihelič, and S. Kotnik, "Towards circular economy implementation in manufacturing systems using a multi-method simulation approach to link design and business strategy," *International Journal of Advanced Manufacturing Technology*, vol. 93, no. 5, pp. 1953–1970, 2017.

[36] Y. Yu, W. Li, J. Li, and T. N. Nguyen, "A novel optimised self-learning method for compressive strength prediction of high performance concrete," *Construction and Building Materials*, vol. 184, pp. 229–247, 2018.

[37] Y. Yu, T. N. Nguyen, J. Li, L. F. Sanchez, and A. Nguyen, "Predicting elastic modulus degradation of alkali silica reaction affected concrete using soft computing techniques: a comparative study," *Construction and Building Materials*, vol. 274, Article ID 122024, 2021.

[38] Y. Yu, C. Zhang, X. Gu, and Y. Cui, "Expansion prediction of alkali aggregate reactivity-affected concrete structures using a hybrid soft computing method," *Neural Computing & Applications*, vol. 31, no. 12, pp. 8641–8660, 2019.

[39] K. Shaswat, "Concrete slump prediction modeling with a fine-tuned convolutional neural network: hybridizing sea lion and dragonfly algorithms," *Environmental Science and Pollution Research*, vol. 2021, pp. 1–12, 2021.

[40] T. N. Nguyen, Y. Yu, J. Li, N. Gowripalan, and V. Sirivivatnanon, "Elastic modulus of ASR-affected concrete: an evaluation using artificial neural network," *Computers and Concrete*, vol. 24, 2019.

[41] P. Pijarski and P. Kacejko, "A new metaheuristic optimization method: the algorithm of the innovative gunner (AIG)," *Engineering Optimization*, vol. 51, pp. 2049–2068, 2019.

[42] C. Cortes and V. Vapnik, "Support-vector networks," *Machine Learning*, vol. 20, no. 3, pp. 273–297, 1995.

[43] K. Rezaee and S. Zolfaghari, "A Direct Classification Approach to Recognize Stress Levels in Virtual Reality Therapy for Patients with Multiple Sclerosis," *Computational Intelligence*, vol. 38, 2021.

[44] N. Tavasoli, K. Rezaee, M. Momenzadeh, and M. Sehhati, "An ensemble soft weighted gene selection-based approach and

[45] R. Li, Y. Liu, Y. Qiao, T. Ma, B. Wang, and X. Luo, "Street-level landmarks acquisition based on SVM classifiers," *CMC-Computers Materlals & Continua*, vol. 59, no. 2, pp. 591–606, 2019.

[46] K. Rezaee, J. Haddadnia, and M. Rasegh Ghezelbash, "A novel algorithm for accurate diagnosis of hepatitis B and its severity," *International Journal of Hospital Research*, vol. 3, no. 1, pp. 1–10, 2014.

[47] Ł. Sadowski, M. Nikoo, and M. Nikoo, "Principal component analysis combined with a self organization feature map to determine the pull-off adhesion between concrete layers," *Construction and Building Materials*, vol. 78, pp. 386–396, 2015.

[48] A. Behnood and E. M. Golafshani, "Predicting the compressive strength of silica fume concrete using hybrid artificial neural network with multi-objective grey wolves," *Journal of Cleaner Production*, vol. 202, pp. 54–64, 2018.

[49] M. A. Yaman, M. Abd Elaty, and M. Taman, "Predicting the ingredients of self compacting concrete using artificial neural network," *Alexandria Engineering Journal*, vol. 56, no. 4, pp. 523–532, 2017.

[50] M. M. Alshihri, A. M. Azmy, and M. S. El-Bisy, "Neural networks for predicting compressive strength of structural light weight concrete," *Construction and Building Materials*, vol. 23, no. 6, pp. 2214–2219, 2009.

[51] H. C. Tsai, "Predicting strengths of concrete-type specimens using hybrid multilayer perceptrons with center-unified particle swarm optimization," *Expert Systems with Applications*, vol. 37, no. 2, pp. 1104–1112, 2010.

[52] R. Madandoust, R. Ghavidel, and N. Nariman-Zadeh, "Evolutionary design of generalized GMDH-type neural network for prediction of concrete compressive strength using UPV," *Computational Materials Science*, vol. 49, no. 3, pp. 556–567, 2010.

[53] I. Yeh, "Modeling slump of concrete with fly ash and superplasticizer," *Computers and Concrete*, vol. 5, no. 6, pp. 559–572, 2008.

[54] I. C. Yeh, "Exploring concrete slump model using artificial neural networks," *Journal of Computing in Civil Engineering*, vol. 20, no. 3, pp. 217–221, 2006.

[55] K. Rezaee, S. Savarkar, X. Yu, and J. Zhang, "A hybrid deep transfer learning-based approach for Parkinson's disease classification in surface electromyography signals," *Biomedical Signal Processing and Control*, vol. 71, Article ID 103161, 2022.

[56] K. Rezaee, S. M. Rezakhani, M. R. Khosravi, and M. K. Moghimi, "A survey on deep learning-based real-time crowd anomaly detection for secure distributed video surveillance," *Personal and Ubiquitous Computing*, vol. 2021, pp. 1–17, 2021.

[57] G. G. Wang, S. Deb, and Z. Cui, "Monarch butterfly optimization," *Neural Computing and Applications*, vol. 31, no. 7, pp. 1995–2014, 2019.

[58] G. G. Wang, S. Deb, and L. D. S. Coelho, "Earthworm optimisation algorithm: a bio-inspired metaheuristic algorithm for global optimisation problems," *International Journal of Bio-Inspired Computation*, vol. 12, no. 1, pp. 1–22, 2018.

[59] G. G. Wang, S. Deb, and L. D. S. Coelho, "Elephant herding optimization," in *Proceedings of the 2015 3rd International Symposium on Computational and Business Intelligence (ISCBI)*, pp. 1–5, IEEE, Bali, Indonesia, 2015, December.

[60] G. G. Wang, "Moth search algorithm: a bio-inspired meta-heuristic algorithm for global optimization problems," *Memetic Computing*, vol. 10, no. 2, pp. 151–164, 2018.

[61] S. Li, H. Chen, M. Wang, A. A. Heidari, and S. Mirjalili, "Slime mould algorithm: a new method for stochastic optimization," *Future Generation Computer Systems*, vol. 111, pp. 300–323, 2020.

[62] A. A. Heidari, S. Mirjalili, H. Faris, I. Aljarah, M. Mafarja, and H. Chen, "Harris hawks optimization: algorithm and applications," *Future Generation Computer Systems*, vol. 97, pp. 849–872, 2019.

Research Article

Application of Soft Computing Paradigm to Large Deformation Analysis of Cantilever Beam under Point Load

Yanmei Cui,[1] Yong Hong ®,[1] Naveed Ahmad Khan ®,[2] and Muhammad Sulaiman ®[2]

[1]*School of Mechanical Engineering, Shanghai Dianji University, Shanghai 201306, China*
[2]*Department of Mathematics, Abdul Wali Khan University, Mardan, Khyber Pakhtunkhwa, Pakistan*

Correspondence should be addressed to Yong Hong; hongyong83@126.com

In this paper, a mathematical model for large deformation of a cantilever beam subjected to tip-concentrated load is presented. The model is governed by nonlinear differential equations. Large deformation of a cantilever beam has number of applications is structural engineering. Since finding an exact solution to such nonlinear models is difficult task, this paper focuses on developing soft computing technique based on artificial neural networks (ANNs), generalized normal distribution optimization (GNDO) algorithm, and sequential quadratic programming (SQP). The strength of ANN modeling for governing the equation of cantilever beam is exploited by the global search ability of GNDO and further explored by the local search mechanism of SQP. Design scheme is evaluated for different cases depending on variations in dimensionless end-point load (ρ). Furthermore, to validate the effectiveness and convergence of algorithm proposed technique, the results of the differential transformation method (DTM) and exact solutions are compared. The statistical analysis of performance indicators in terms of mean, median, and standard deviations further establishes the worth of ANN-GNDO-SQP algorithm.

1. Introduction

Mechanical systems, which involve nonlinearity due to large deflection of compliant mechanism, continue to be an interesting problem. Since large deformation phenomena occur often in various geotechnical practices [1]. Therefore, this topic is of practical interest and has been widely studied by many researchers. In past decades, a number of numerical methods have been developed to solve large deformation problems. The large deflection of cantilever beams was studied by Wang [2]. They developed nonlinear differential equations for postbuckling loads on the basis of Eringen's nonlocal constitutive relation. Shooting method was used to obtain postbuckling load and the buckled shape of the beam. Framework of arbitrary Lagrangian–Eulerian (ALE) is commonly used approach to study large deformation in geotechnical engineering [3]. Based on ALE three different approaches named as the efficient ALE approach (EALE) [4, 5], interpolation technique by small strain (RITSS) [6, 7] and the Abaqus built-in coupled Eulerian–Lagrangian (CEL)

method [8]. Modified Chebyshev's polynomial is used by Schmidt and Dadeppo [9] to study large deflection of beam. Large deformation of a spring-hinged beam was investigated by Nageswara Rao [10, 11] subjected to a tip rotational concentrated and distributed load.

Ludwick's large deformation was studied by Lee [12] to made cantilever beams with a combined loading effect of a focused load at the tip and a uniformly dispersed load over the beam length. Phungpaigram and Chucheepsakul [13, 14] used elliptic integrals to calculate exact solutions for large deflection in elastic beams with variations in arc length and inclined force. Dado and Al-Sadder [15, 16] investigated the behaviour of large deformation of prismatic and nonprismatic cantilever beams under various type of loadings. Wang [17, 18] used homotopy perturbation method (HPM) to obtain analytical solution for large deformation of beam under point load with free tip. References [19, 20] studied the longitudinal vibration analysis for microbars based on strain gradient elasticity theory. Feasibility of Adomian decomposition method for such complex nonlinear problems was

studied by Tolou and Herder [21]. Mutyalarao [22] studied large deflections of a uniform cantilever beam with concentrated load at tip and having normal inclination to the deflected axis of the beam. All these recently introduced techniques have their own grains and limitations in terms of accuracy, robustness, convergence, and applicability, but they are based on well-established deterministic procedures. Complex nonlinear differential equation of large deformation of beams subjected to a concentrated load is of great interest in scientific and engineering field. The quest of finding analytical solution for the problem motivates the author to develop a soft computing technique based on feed forward artificial neural networks (ANNs).

Stochastic solvers based on computational intelligence methods using artificial neural networks (ANNs) are considered to be fundamental in pattern recognition and machine learning. In general, neural networks are widely used to solve fractional differential equations, integro-differential equations (IDEs), partial differential equations (PDEs), and ordinary differential equations (ODEs). In ANN modeling, the optimization procedure is carried by using combination of global and local search algorithms. Some recent application of stochastic algorithm are multiphase flow through porous media for imbibition phenomena [23], eye model [24], wire coating dynamics [25, 26], optimal design and temperature distribution of heat fin [27, 28], beam-column design [29], and hybrid feature analysis for diabetic retinopathy classification using fundus images [30].

In the present study, a novel soft computing technique is applied to find analytical series solution for large deformation of cantilever beam subjected to point load by using ANN models optimized globally with generalized normal distribution optimization (GNDO) algorithm hybrid with sequential quadratic programming (SQP) for rapid local convergence. The prominent features of the present study are given as follows.

(i) Mathematical model for large deformation of cantilever beam under end point load is formulated and analyzed to study the influence of variations in dimensionless end point load (ρ).

(ii) A novel soft computing paradigm is developed to model series solutions based on artificial neural networks with the generalized normal distribution optimization algorithm and the sequential quadratic programming. Our approach is named as ANN-GNDO-SQP algorithm.

(iii) To validate the efficiency of the proposed technique, four cases of large deformation cantilever beam are considered. The statistical results are compared with differential transformation method (DTM) and analytical solutions.

(iv) Statistical analysis of absolute errors (AE), fitness evaluation (Fit), mean absolute deviation (MAD), Theil's inequality coefficient (TIC), root mean square error (RMSE), Nash–Sutcliffe efficiency (NSE), and error in Nash–Sutcliffe efficiency

(ENSE) are presented in terms of minimum, mean, median, and standard deviation.

(v) Provision of continuous solutions, computational complexity, convergence, and easy execution of the proposed methodology show the robustness and correctness of the ANN-GNDO-SQP algorithm.

2. Problem Formulation

Consider a cantilever beam with a large deformation due to end point load as shown is Figure 1. By Euler–Bernoulli beam theory, the curvature (κ) of the beam can be given as

$$\kappa = \frac{d\theta}{ds} = \frac{M}{EI}, \tag{1}$$

where θ represents the slope or rotation of a beam, s is the natural distance from the fixed end, E is Young's modulus, M is bending moment, I is moment of inertia, and EI is the bending stiffness of cantilever beam. From Figure 1, moment (M) for the deflected beam under end point load is given as

$$M = F(L - \delta_h - x), \tag{2}$$

where concentrated load at end point is denoted by F, δ_h is the horizontal deflection, and L is the distance of deflected beam from fixed point. Hence, bending equation of uniform cross sectional beam for large deformation is written as

$$\frac{d\theta}{ds} = \frac{F}{EI}(L - \delta_h - x), \quad \theta(0) = 0, \theta'(L) = 0. \tag{3}$$

If $F = 0$, then concentrated force is a dead force such as gravity, and if $F = 1$, then the concentrated force is perpendicular to the deflected beam at the end [31] (Figure 1).

Differentiation of (1) with respect to s is given as

$$\frac{d^2\theta}{ds^2} = \frac{dM/ds}{EI}, \tag{4}$$

considering a dimensionless parameter $\xi = s/L$. Differentiating (2) with respect to s and substituting $\cos(\theta) = dx/ds$ in (4) will result in governing second-order differential equation for large deformation of continuer beam with end point load as

$$\frac{d^2\theta}{d\xi^2} + \rho\cos\theta = 0, \tag{5}$$

with boundary conditions

$$\text{at} \quad \xi = 0, \ \theta = 0, \tag{6}$$

$$\text{at} \quad \xi = 1, \ \frac{d\theta}{d\xi} = 0, \tag{7}$$

where $\rho = FL^2/EI$, and it represents the dimensionless load at end point. Angle of rotation of the beam at free end is denoted by $\theta_{tip}(1) = 1$. Furthermore, dimensionless horizontal displacement (δ_h) of the free end is given by [17, 32, 33] as
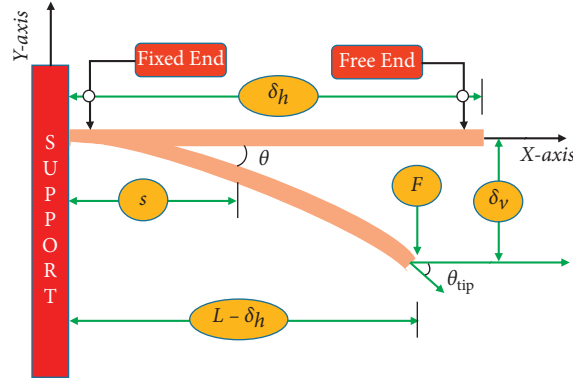
FIGURE 1: Large deformation of a cantilever beam under end point loading.

$$\frac{L - \delta_h}{L} = \sqrt{\frac{2EI\left(\sin \theta_{\text{tip}}\right)}{FL^2}} = \sqrt{\frac{2 \sin \theta_{\text{tip}}}{\rho}}, \tag{8}$$

then, the dimensionless horizontal displacement of the free tip is

$$\frac{\delta_h}{L} = 1 - \frac{1}{\sqrt{\rho}} \sqrt{2 \sin \theta_{\text{tip}}}. \tag{9}$$

For large deformation equation (5) along with boundary conditions, (6) and (7) are given as

$$\frac{d^2\theta}{d\xi^2} + \rho = 0,$$

$$\text{at} \quad \xi = 0, \ \theta = 0, \tag{10}$$

$$\text{at} \quad \xi = 1, \ \frac{d\theta}{d\xi} = 0.$$

The analytical solution for the problem is given as

$$\theta(\xi) = \frac{\rho}{2} (2 - \xi)\xi, \tag{11}$$

at the tip $\xi = 1$.

$$\theta(\xi) = \frac{\rho}{2}. \tag{12}$$

3. Proposed Methodology

The proposed soft computing paradigm for calculating approximate solutions for mathematical model of large deformation of cantilever beam consists of two parts. In the first part, an unsupervised ANNs model is constructed in terms of input, hidden, and output layers for governing differential equation. In the second part, neurons in ANN structure are trained or tuned by hybridizing generalized normal distribution optimization (GNDO) algorithm and sequential quadratic programming (SQP).

3.1. Construction of ANN Model.
Feedforward artificial neural networks (ANNs) are used to model series solutions for governing equation of large deformation of

cantilever beam with end point loading. Neural network model for (5)–(7) are formulated using continuous mapping approach for the solution $\theta(\xi)$ and its respective derivatives in terms of input, hidden, and output layer are given as follows:

$$\widehat{\theta}(\xi) = \sum_{i=1}^{k} \phi_i f\left(\omega_i \xi + \beta_i\right), \tag{13}$$

$$\widehat{\theta}'(\xi) = \sum_{i=1}^{k} \phi_i f'\left(\omega_i \xi + \beta_i\right), \tag{14}$$

$$\widehat{\theta}''(\xi) = \sum_{i=1}^{k} \phi_i f''\left(\omega_i \xi + \beta_i\right), \tag{15}$$

where $\phi = [\phi_1, \phi_2, \phi_3, \ldots, \phi_m]$, $\omega = [\omega_1, \omega_2, \omega_3, \ldots, \omega_m]$, and $\beta = [\beta_1, \beta_2, \beta_3, \ldots, \beta_m]$ are real-valued vectors and are bounded, f is the activation function, and i represents the number of neurons in ANN structure. In the hidden layer, (13)–(15) used log sigmoid as an activation function, and then, the updated form of solution and its derivatives is given as

$$\widehat{\theta}(\xi) = \sum_{i=1}^{k} \phi_i \omega_i \left(\frac{1}{1 + e^{-\left(\omega_i \xi + \beta_i\right)}}\right),$$

$$\widehat{\theta}'(\xi) = \sum_{i=1}^{k} \phi_i \omega_i \left(\frac{e^{-\left(\omega_i \xi + \beta_i\right)}}{\left(1 + e^{-\left(\omega_i \xi + \beta_i\right)}\right)^2}\right),$$

$$\widehat{\theta}''(\xi) = \sum_{i=1}^{k} \phi_i \omega_i^2 \left(\frac{2e^{-\left(\omega_i \xi + \beta_i\right)}}{\left(1 + e^{-\left(\omega_i \xi + \beta_i\right)}\right)^3} - \frac{e^{-\left(\omega_i \xi + \beta_i\right)}}{\left(1 + e^{-\left(\omega_i \xi + \beta_i\right)}\right)^2}\right). \tag{16}$$

3.2. Formulation of Fitness Function.
Fitness function or objective function for mathematical model of large deformation in cantilever beam is developed as a sum of two mean square error (MSE):

$$\text{Minimize } E = E_1 + E_2, \qquad (17)$$

where E_1 and E_2 are MSE of (5) and (6) and (7), respectively, which are defined as

$$E_1 = \frac{1}{N} \sum_{m=1}^{N} \left(\frac{d^2 \widehat{\theta}}{d\xi^2} + \rho \right)^2,$$

$$\qquad (18)$$

$$E_2 = \frac{1}{2} \left((\widehat{\theta}(0) - 0)^2 + \left(\frac{d\widehat{\theta}(1)}{d\xi} - 0 \right)^2 \right).$$

For the approximate solution of (5), fitness function equation (17) is optimized by training neurons in such a way that MSEs, E_1 and E_2, should approach to zero, and consequently, the approximate solution by proposed method will converge to exact solution.

3.3. Training of Neurons.
Methodologies adopted for training of unknown neurons in ANNs structure for optimization of fitness function equation (17) are presented, which is based on hybridization of unsupervised and supervised learning of GNDO and SQP, respectively. The working mechanism of the proposed algorithm is provided in Figure 2.

3.4. Generalized Normal Distribution Optimization.
Generalized normal distribution optimization (GNDO) algorithm is a novel metaheuristic technique presented by Zhang et al. [34], inspired by generalized normal distribution theory. GNDO algorithm is widely used for parameter extraction of model, unlike other metaheuristic algorithms; GNDO is easy to implement, and it only requires the essential population size and termination criteria. GNDO has a simple structure, where the position of each individual is updated by using normal distribution curve. The working strategy of GNDO algorithm is subdivided into two phases, exploitation and exploration.

3.4.1. Exploitation.
Exploitation is a process of finding best solution around the search space consisting of the current positions of all individuals. Initially, model for optimization by generalized distribution model is given as

$$v_i^t = \widehat{\mu}_i + \widehat{\delta}_i \times \widehat{\eta}, \quad i = 1, 2, 3, \ldots, N, \qquad (19)$$

where v_i^t, $\widehat{\mu}_i$, $\widehat{\delta}_i$, and $\widehat{\eta}$, are trial vector, generalized mean position, generalized standard variance, and penalty factor, respectively. Moreover, $\widehat{\eta}$, $\widehat{\delta}_i$, and $\widehat{\mu}_i$ are formulated as

$$\widehat{\eta} = \begin{cases} \sqrt{-\log(\zeta_1)} \times \cos(2\pi\zeta_2), & \text{if } a \le b, \\[2mm] \sqrt{-\log(\zeta_1)} \times \cos(2\pi\zeta_2 + \pi), & \text{otherwise,} \end{cases}$$

$$\widehat{\delta}_i = \sqrt{\frac{1}{3}\left[\left(x_i^t - \widehat{\mu}\right)^2 + \left(x_{\text{Best}}^t - \widehat{\mu}\right)^2 + (M - \widehat{\mu})^2 \right]}, \qquad (20)$$

$$\widehat{\mu}_i = \frac{1}{3}\left(x_i^t + x_{\text{Best}}^t + M \right),$$

$$M = \frac{\sum_{i=1}^{N} x_i^t}{N},$$

where M is the mean position, x_{Best}^t is the current best so far, and a, b, ζ_1, and ζ_2 are the random numbers between 0 and 1. Furthermore, $\widehat{\eta}$, $\widehat{\delta}_i$, and $\widehat{\mu}_i$ are discussed in the exploration phase.

3.4.2. Exploration.
Exploration refers to the searching of population space to get best solution. Exploration of GNDO is based on three randomly selected individuals as follows:

$$v_i^t = x_i^t + \underbrace{\beta \times \left(|\zeta_3| \times v_1\right)}_{\text{Local information sharing}} + \underbrace{(1 - \beta) \times \left(|\zeta_4| \times v_2\right)}_{\text{Global information sharing}}, \qquad (21)$$

where v_1 and v_2 are the trail vectors, β is the adjustment parameter, and ζ_3 and ζ_4 are the random numbers between 0 and 1, which are subjected to the standard normal distribution. Trail vectors are computed as follows:

$$v_1 = \begin{cases} x_i^t - x_{p1}^t, & \text{if } f\left(x_i^t\right) < f\left(x_{p1}^t\right), \\[2mm] x_{pl}^t - x_i^t, & \text{otherwise,} \end{cases}$$

$$\qquad (22)$$

$$v_2 = \begin{cases} x_{p2}^t - x_{p3}^t, & \text{if } f\left(x_{p2}^t\right) < f\left(x_{p3}^t\right), \\[2mm] x_{p3}^t - x_{p2}^t, & \text{otherwise,} \end{cases}$$

where $p1$, $p2$, and $p3$ are integers. It is worth mentioning that GNDO algorithm is inspired by the relationship between normal distribution law and traditional teaching phenomena, search process of metaheuristics, and group teaching phenomena, respectively. GNDO has been applied to study the parameter extraction of photovoltaic models [34].

3.5. Sequential Quadratic Programming.
The best performance (weights) obtained by GNDO algorithm is refined by the process of hybridization with efficient local search technique known as sequential quadratic programming using MATLAB toolbox setting. SQP is one of the powerful methods for numerical solution of constrained
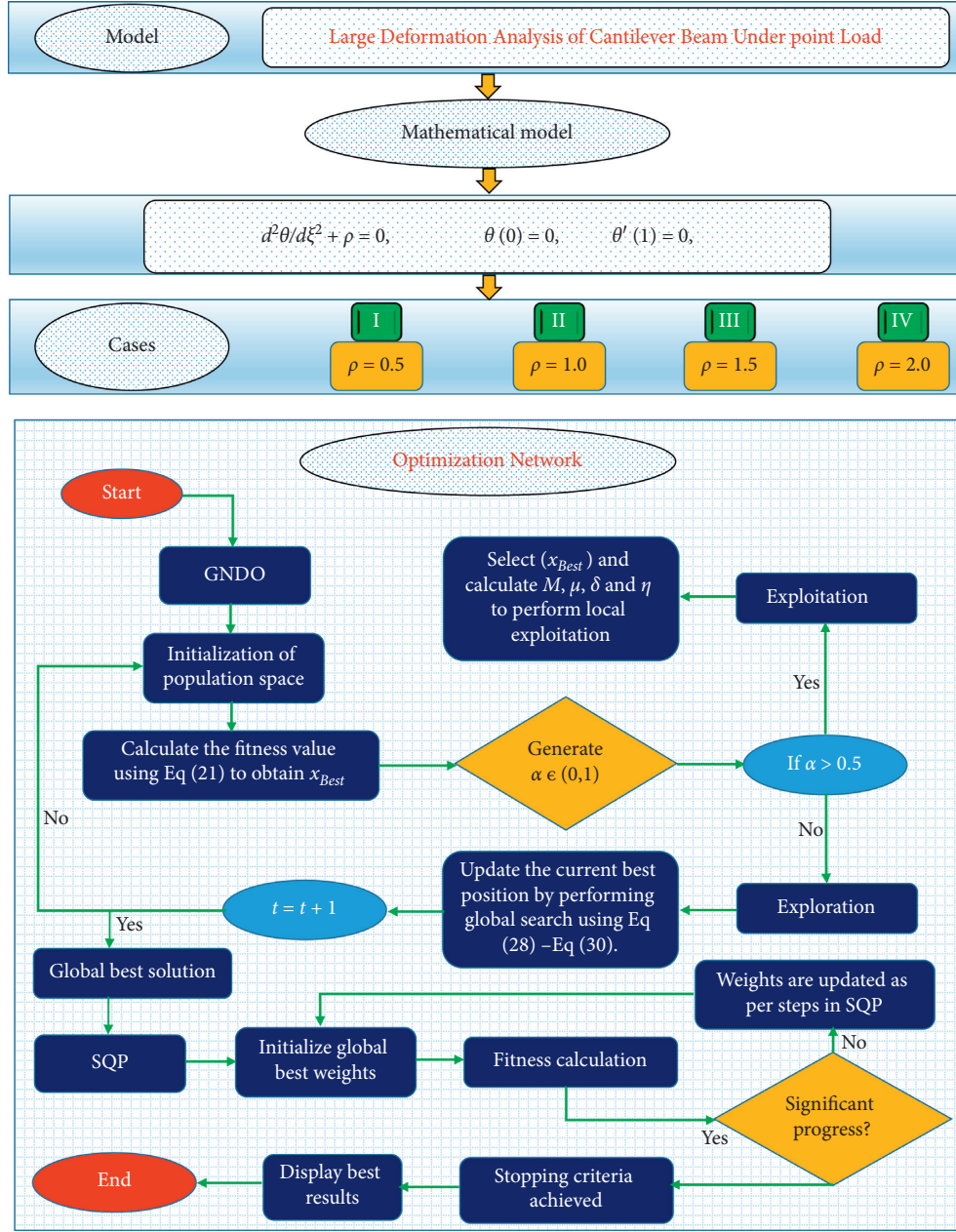
FIGURE 2: Graphical overview of the model, cases studies, and flow chart of the ANN-GNDO-SQP algorithm.

nonlinear optimization problems. It was developed in 1963 and further refined in 1970 [35]. SQP has been applied to a number of problems, which proves its power, accuracy, and efficiency. Nocedal and Wright [35] discuss SQP in detail and also give a mathematical formulation for various large-scale numerical optimization problems. Some recent applications of SQP are numerical solution for transient heat conduction problem [36], profile error evaluation of free-form surface [37], nonlinear model predictive control [38], OPF problem in DC grids [39], Bagley–Torvik systems arising in fluid mechanics [40], and optimal design of heating system in rapid thermal cycling blow mold [41].

3.6. Hybrid ANN-GNDO-SQP Algorithm.
Necessary details of the procedural steps for proposed algorithm are given as follows.

Step 1. Initialization of GNDO: Initial weights are created randomly from population space with number of entries equal to number of neurons in ANN structure. Mathematical formulation is given as

$$C = [(\phi, \omega, \beta)]^T = \begin{bmatrix} \phi_1 & \omega_1 & \beta_1 \\ \phi_2 & \omega_2 & \beta_2 \\ \vdots & \vdots & \vdots \\ \phi_m & \omega_m & \beta_m \end{bmatrix}, \quad (23)$$

where ϕ, ω, and β are the real values of unknown neurons in ANN model. Parameter setting for GNDO algorithm is given in Table 1.

Step 2. Fitness evaluation: Objective function equation (17) is evaluated to calculate the fitness value for the problem using the weights generated in the previous step.

Step 3. Criteria for termination: Execution of GNDO is stopped when any of the following criteria is satisfied.

Objective value ie $\varepsilon \longrightarrow 10^{-15}$
Function tolerance ie $\prime$Fun$\prime$TOL $\longrightarrow 10^{-15}$
Predefined number of iterations is achieved

If stopping criteria are fulfilled, then go to step V otherwise continue.

Step 4. Storage: Store the global best weight corresponding to minimum fitness value and time taken for the execution.

Step 5. Hybridization: Global best weights obtained by GNDO for minimization of (21) are considered as an initial guess for SQP to start the procedure.

Step 6. Fitness evaluation: SQP starts the supervised learning, update the weights, and evaluate the fitness function until the following terminations conditions are satisfied.

Objective value, i.e., $\varepsilon \longrightarrow 10^{-15}$.

Predefined number of iterations is achieved.

Step 7. Storage: Store the best weight, minimum fitness value, and time taken for the execution by SQP and the total time by GNDO-SQP in seconds.

Repeat the procedure from steps I–VII for a sufficient large number of independent runs to generate a large dataset for reliable statistical analysis.

4. Performance Indices

In this section, the performance of design scheme for solving mathematical model of large deformation of cantilever beam is examined by incorporating performance indicators in terms of mean absolute deviation (MAD), Theil's inequality coefficient (TIC), root mean square error (RMSE), and Nash–Sutcliffe efficiency (NSE). Mathematical formulations of these indicators are given as follows [23].

$$\text{MAD} = \frac{1}{N} \sum_{m=1}^{N} \left| \theta_m(\xi) - \widehat{\theta}_m(\xi) \right|,$$

$$\text{TIC} = \frac{\sqrt{(1/N) \sum_{n=1}^{N} \left(\theta_m(\xi) - \widehat{\theta}_m(\xi) \right)^2}}{\left(\sqrt{(1/N) \sum_{m=1}^{N} \left(\theta_m(\xi) \right)^2} + \sqrt{(1/N) \sum_{m=1}^{N} \left(\widehat{\theta}_m(\xi) \right)^2} \right)},$$

$$\text{RMSE} = \frac{1}{N} \sqrt{\sum_{m=1}^{N} \left(\theta_m(\xi) - \widehat{\theta}_m(\xi) \right)^2},$$

$$\text{NSE} = \left\{ 1 - \frac{\sum_{m=1}^{N} \left(\theta_m(\xi) - \widehat{\theta}_m(\xi) \right)^2}{\sum_{m=1}^{N} \left(\left(\theta_m(\xi) - \underline{\widehat{\theta}}_m(\xi) \right)^2 \right)}, \quad \underline{\widehat{\theta}}_m(\xi) = \frac{1}{N} \sum_{m=1}^{N} \widehat{\theta}(\xi), \right.$$

$$\text{ENSE} = (1 - \text{NSE}),$$

(24)

where θ_m is the analytical solution and $\widehat{\theta}_m$ represents the approximate solution by proposed algorithm. N denotes the grid points.

5. Numerical Simulation and Discussion

In this section, different cases of (5) are considered to study the effect of variations in dimensionless end point load (ρ) on large deflection of cantilever beam. The following cases are considered. Case I: $\rho = 0.5$, Case II: $\rho = 1.0$, Case III: $\rho = 1.5$, and Case IV: $\rho = 2.0$. The formulation of fitness functions for each case is given as follows:

$$\text{Minimize } E = \frac{1}{N} \sum_{m=1}^{N} \left(\frac{d^2 \widehat{\theta}}{d\xi^2} + 0.5 \right)^2 + \frac{1}{2} \left((\widehat{\theta}(0) - 0)^2 + (\widehat{\theta}'(1) - 0)^2 \right),$$

(25)

$$\text{Minimize } E = \frac{1}{N} \sum_{m=1}^{N} \left(\frac{d^2 \widehat{\theta}}{d\xi^2} + 1.0 \right)^2 + \frac{1}{2} \left((\widehat{\theta}(0) - 0)^2 + (\widehat{\theta}'(1) - 0)^2 \right),$$

(26)

$$\text{Minimize } E = \frac{1}{N} \sum_{m=1}^{N} \left(\frac{d^2 \widehat{\theta}}{d\xi^2} + 1.5 \right)^2 + \frac{1}{2} \left((\widehat{\theta}(0) - 0)^2 + (\widehat{\theta}'(1) - 0)^2 \right),$$

(27)

TABLE 1: Setting of parameters for GNDO and SQP algorithm.

Method	Parameters	Settings	Parameters	Settings
GNDO	Initialization	Random search	Bounds (Lb, Ub)	[−1, 1]
	Search agents	70	Max. iterations	2000
	Function tolerance	10^{-15}	Fitness limit	10^{-15}
SQP	Initiation	Global best of GNDO	Bounds (Lb, Ub)	[−1, 1]
	Max. iterations	1500	X-tolerance	10^{-15}
	Function tolerance	10^{-15}	Fitness limit	10^{-15}
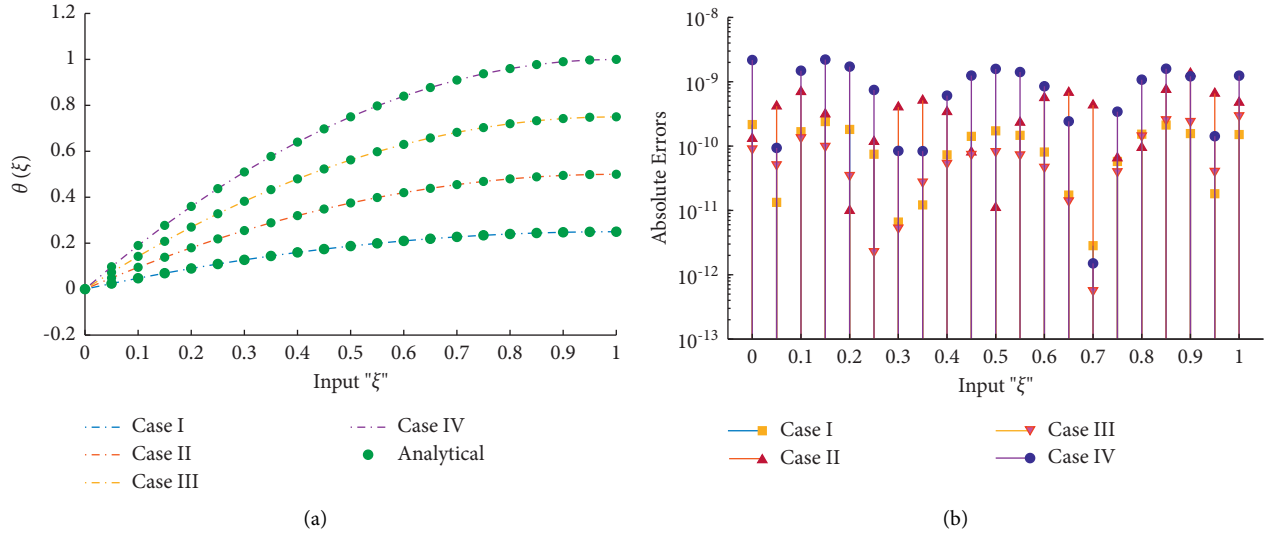
FIGURE 3: (a) Comparison of approximate solutions obtained by ANN-GNDO-SQP algorithm with analytical solution for each case. (b) Absolute errors in solutions of proposed algorithm for different cases.

$$\text{Minimize } E = \frac{1}{N} \sum_{m=1}^{N} \left(\frac{d^2\widehat{\theta}}{d\xi^2} + 2.0 \right)^2 + \frac{1}{2} \left((\widehat{\theta}(0) - 0)^2 + (\widehat{\theta}'(1) - 0)^2 \right). \tag{28}$$

In this paper, the mathematical model of large deflected cantilever beam under end point load is investigated by developing soft computing technique. ANNs-based fitness function is constructed to model approximate solutions, which are further optimized by using hybridization of GNDO and SQP algorithms. To briefly study the efficiency and behaviour of proposed technique, it is executed for 100 times. Results obtained by ANN-GDDO-SQP algorithm are compared with exact solution and differential transformation method [33]. Approximate solutions along with absolute errors obtained by the proposed algorithm for different cases of deflected cantilever beam are shown in Figure 3. Figures 4(a) and 4(b) illustrate the influence of variations in dimensionless end point load (ρ) on horizontal distance (δ_h/L) and rotational angle (θ_{tip}) of the beam at the tip or free end, respectively. Convergence of fitness values, MAD, TIC, RMSE, and ENSE for each case of large deflected cantilever beam during 100 independent runs is shown in Figures 5 and 6. Figure 7 represents the boxplots analysis for each case of deflected cantilever beam. The graphical illustration of mean absolute values, global values for fitness function, and performance indicators for each case study are presented in Figure 8.

It can be seen that the approximate solutions overlap the exact solution with minimum errors that show the accuracy of proposed technique. Table 2 dictates the comparison of approximate solutions and analytical solutions for different cases depending on variations in dimensionless point load at free end. Tables 3 and 4 show that absolute errors in best solutions for case I-IV lie around $1.51E - 10$ to $2.83E - 12$, $1.36E - 10$ to $5.72E - 13$, $1.35E - 09$ to $9.89E - 12$ and $1.08E - 09$ to $1.50E - 12$ with standard deviations 10^{-9} to 10^{-10}, 10^{-9} to 10^{-11}, 10^{-8} to 10^{-10} and 10^{-8} to 10^{-9}, respectively. Table 5 dictates that mean or global values of fitness function for each case study are $1.80E - 08$, $5.18E - 08$, $1.10E - 07$, and $1.60E - 07$. Also, minimum values of MAD, TIC, RMSE, and ENSE lie around 10^{-6}, 10^{-7}, 10^{-6}, and 10^{-10} with standard deviations around $1.80E - 05$ to $4.94E - 06$, $4.27E - 06$ to $1.59E - 06$, $1.50E - 05$ to $4.13E - 06$ and $2.35E - 08$ to $7.74E - 09$, respectively. Analyses based on the computational complexity of the design scheme for obtaining solution to equations (25)–(28) are dictated in Table 6. Weights in ANN structure for best solution of each case obtained by proposed algorithm are presented in Table 7 and graphically shown in Figure 9.

(a)

(b)
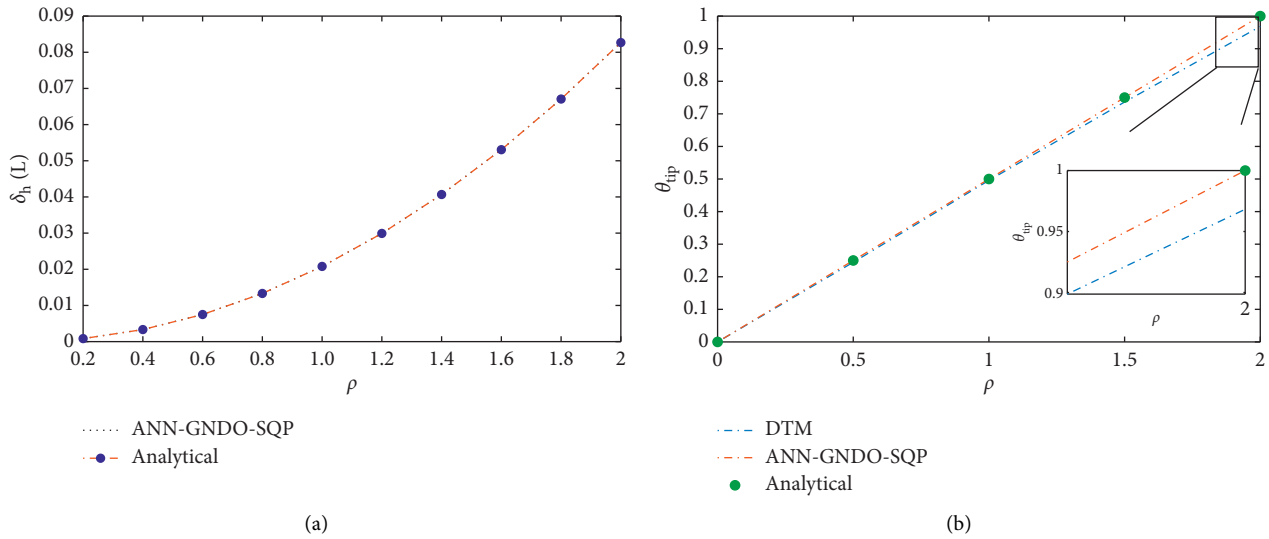
FIGURE 4: Comparison between the (a) dimensionless horizontal distance and (b) rotational angle of the beam obtained by analytical method, DTM, and proposed algorithm for variations in dimensionless end-point load.

(a)

(b)
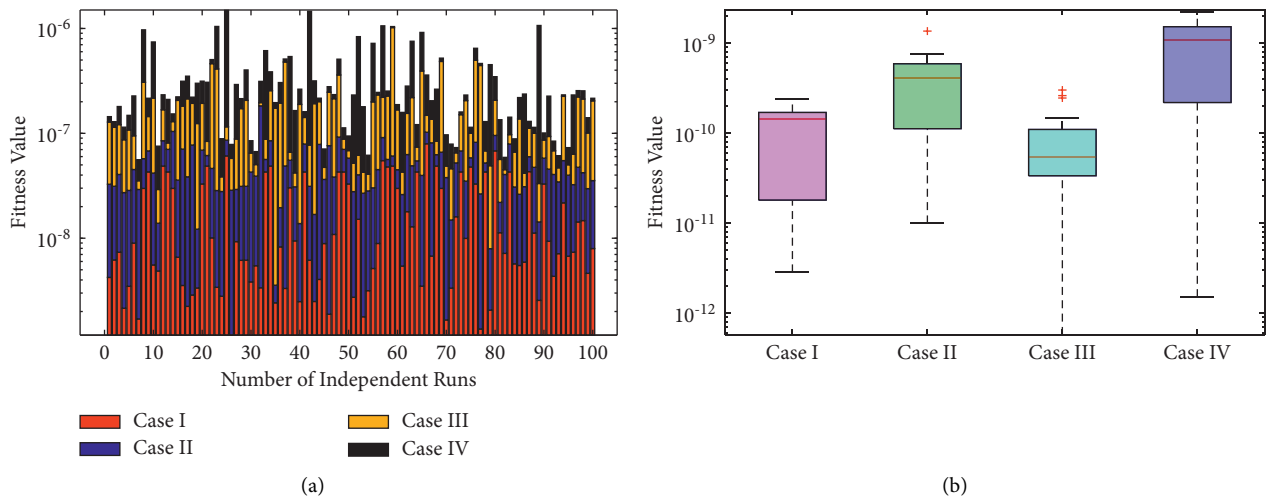
FIGURE 5: (a) Convergence of fitness value. (b) Box plot analysis for each case during 100 independent runs of ANN-GNDO-SQP algorithm.

(a)

(b)

FIGURE 6: Continued.

(c)
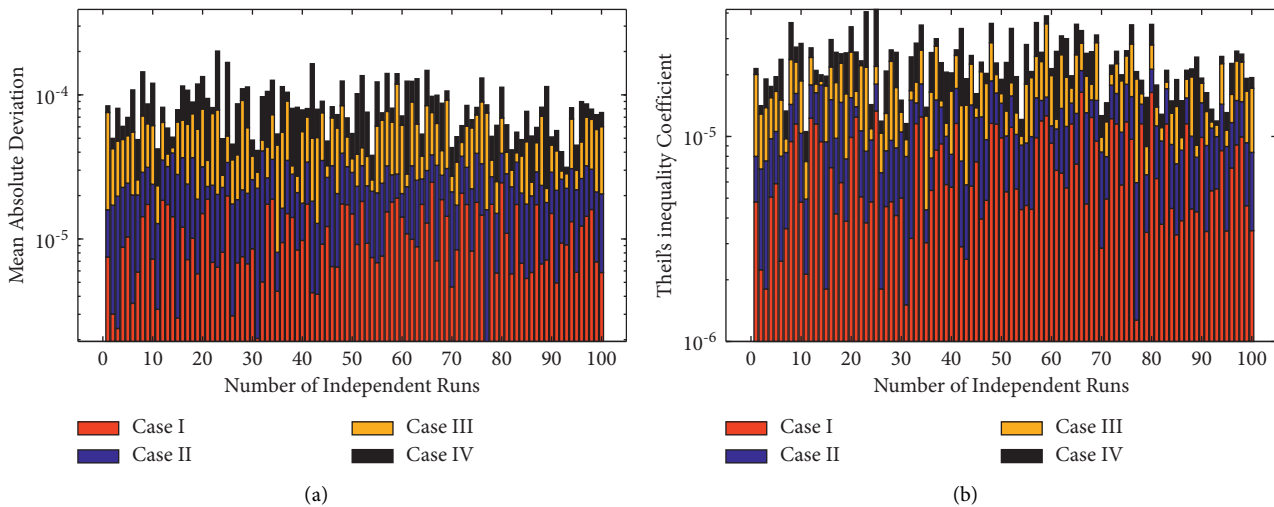
(d)
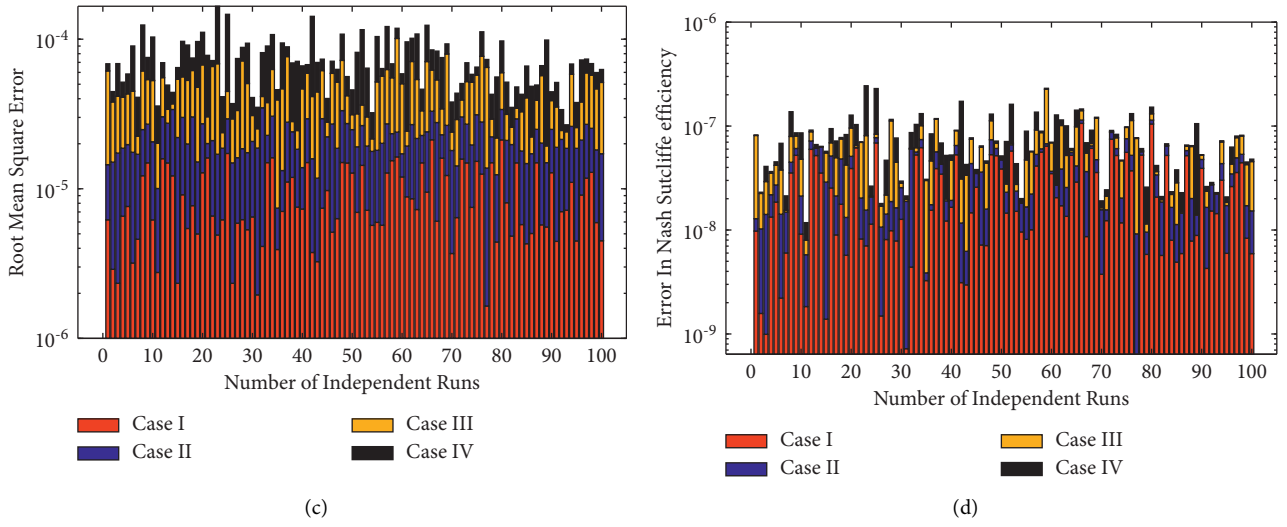
FIGURE 6: Convergence analysis of (a) MAD, (b) TIC, (c) RMSE, and (d) ENSE during 100 independent runs for each case of large deflected beam.

(a)

(b)

(c)

(d)
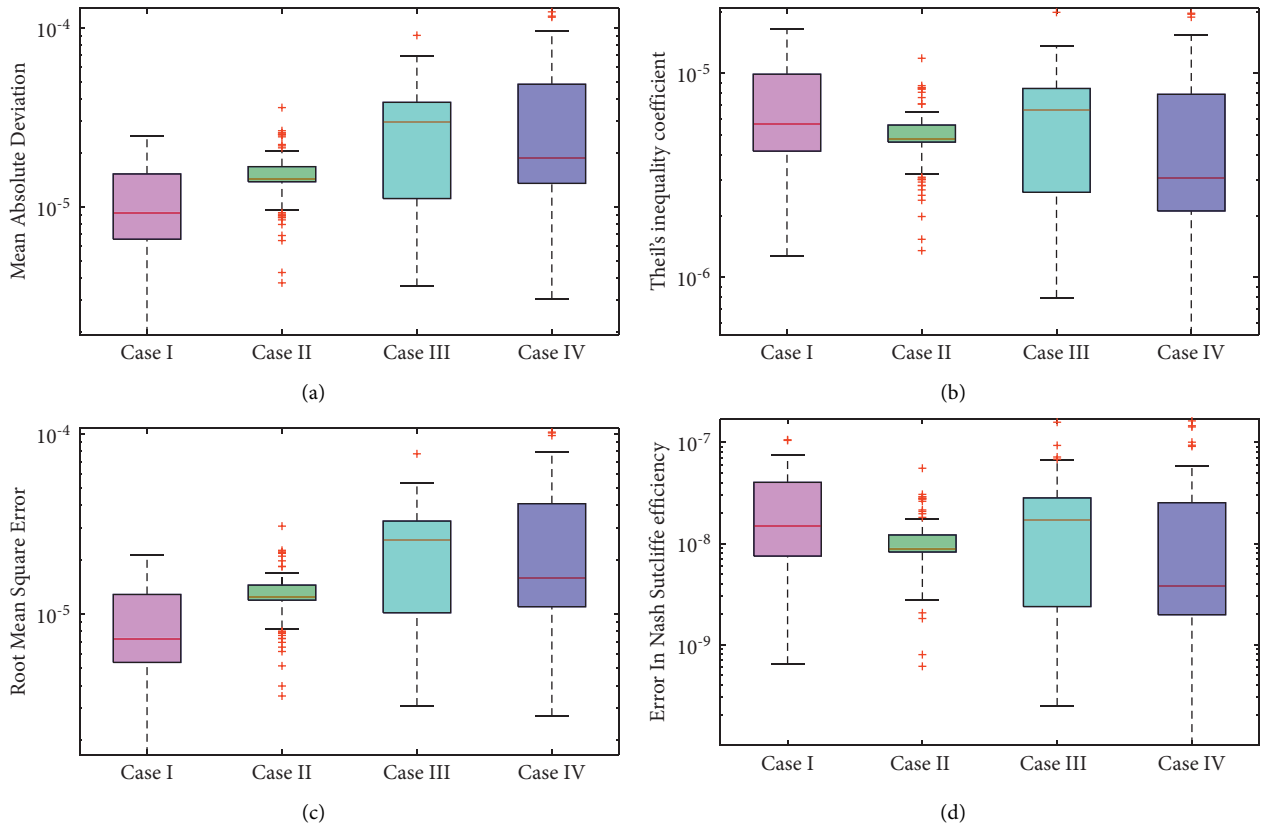
FIGURE 7: (a–d) represents the boxplot analysis for each case of large deflected cantilever beam under end-point load during 100 independent executions. (a) MAD, (b) TIC, (c) RMSE, and (d) ENSE.

(a)

(b)
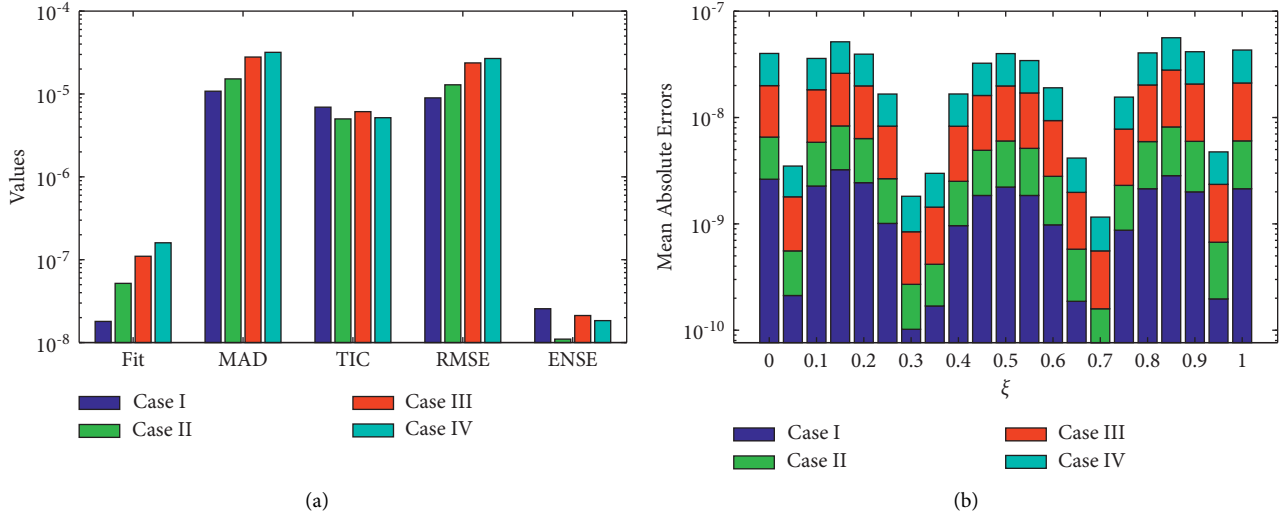
FIGURE 8: (a) The global values of fitness function and performance indicators obtained during multiple execution of ANN-GNDO-SQP algorithm. (b) Mean absolute errors in the solutions of proposed algorithm for different cases of large deflected cantilever beam.

TABLE 2: Comparison of the approximate solution obtained by ANN-GNDO-SQP algorithm with analytical solution for different variations is dimensionless end point load of large deflected cantilever beam.

ξ	$\rho = 0.5$		$\rho = 1.0$		$\rho = 1.5$		$\rho = 2.0$	
	Exact	ANN-GNDO-SQP	Exact	ANN-GNDO-SQP	Exact	ANN-GNDO-SQP	Exact	ANN-GNDO-SQP
0.0	0	$2.02E-09$	0	$-5.11E-08$	0	$-5.70E-09$	0	$6.07E-07$
0.1	0.0475	0.04750000	0.0950	0.09500000	0.1425	0.14250000	0.1900	0.19000004
0.2	0.0900	0.09000000	0.1800	0.18000000	0.2700	0.27000000	0.3600	0.36000005
0.3	0.1275	0.12750000	0.2550	0.25500000	0.3825	0.38250000	0.5100	0.51000000
0.4	0.1600	0.16000000	0.3200	0.32000000	0.4800	0.48000000	0.6400	0.64000000
0.5	0.1875	0.18750000	0.3750	0.37500000	0.5625	0.56250000	0.7500	0.75000008
0.6	0.2100	0.21000000	0.4200	0.42000000	0.6300	0.63000364	0.8400	0.84000000
0.7	0.2275	0.22750000	0.4550	0.45500000	0.6825	0.68250000	0.9100	0.91000000
0.8	0.2400	0.24000188	0.4800	0.48000000	0.7200	0.72000000	0.9600	0.96000004
0.9	0.2475	0.24750207	0.4950	0.49500000	0.7425	0.74250001	0.9900	0.99000006
1.0	0.2500	0.25000192	0.5000	0.50000000	0.7500	0.75000000	1.0000	1.00000001

TABLE 3: Maximum and minimum absolute errors obtained in ANN-GNDO-SQP solutions for different cases of large deflection of cantilever beam.

ξ	$\rho = 0.5$		$\rho = 1.0$		$\rho = 1.5$		$\rho = 2.0$	
	Maximum AE	Minimum AE	Maximum AE	Minimum AE	Maximum AE	Minimum AE	Maximum AE	Minimum AE
0.0	$1.07E-08$	$2.16E-10$	$2.54E-08$	$9.14E-11$	$1.28E-07$	$1.30E-10$	$1.24E-07$	$2.18E-09$
0.1	$1.03E-08$	$1.67E-10$	$2.18E-08$	$1.36E-10$	$1.06E-07$	$6.97E-10$	$1.46E-07$	$1.48E-09$
0.2	$1.02E-08$	$1.82E-10$	$2.46E-08$	$3.53E-11$	$1.27E-07$	$9.89E-12$	$1.41E-07$	$1.72E-09$
0.3	$2.23E-10$	$6.59E-12$	$1.20E-09$	$5.38E-12$	$7.64E-09$	$4.03E-10$	$2.14E-09$	$8.42E-11$
0.4	$4.76E-09$	$7.30E-11$	$8.77E-09$	$5.44E-11$	$4.32E-08$	$3.40E-10$	$8.23E-08$	$6.09E-10$
0.5	$9.86E-09$	$1.73E-10$	$2.25E-08$	$8.30E-11$	$1.20E-07$	$1.10E-11$	$1.75E-07$	$1.58E-09$
0.6	$3.79E-09$	$8.09E-11$	$1.11E-08$	$4.73E-11$	$6.36E-08$	$5.62E-10$	$7.28E-08$	$8.51E-10$
0.7	$5.26E-10$	$2.83E-12$	$3.14E-10$	$5.72E-13$	$1.06E-09$	$4.32E-10$	$8.63E-09$	$1.50E-12$
0.8	$1.02E-08$	$1.53E-10$	$2.09E-08$	$1.46E-10$	$1.14E-07$	$9.45E-11$	$2.06E-07$	$1.08E-09$
0.9	$8.53E-09$	$1.56E-10$	$2.22E-08$	$2.44E-10$	$1.28E-07$	$1.35E-09$	$1.93E-07$	$1.22E-09$
1.0	$1.04E-08$	$1.51E-10$	$2.07E-08$	$2.99E-10$	$1.20E-07$	$4.76E-10$	$2.30E-07$	$1.24E-09$

TABLE 4: Statistical analysis of absolute errors in term of minimum, mean, and standard deviation for different cases of large deformation of cantilever beam.

ξ	Case I			Case II			Case III			Case IV		
	Min	Mean	Std.	Min	Mean	Std.	Min	Mean	Std.	Min	Mean	Std.
0.00	$1.59E-10$	$2.63E-09$	$2.69E-09$	$9.14E-11$	$3.92E-09$	$2.78E-09$	$1.30E-10$	$1.34E-08$	$1.71E-08$	$3.18E-10$	$2.01E-08$	$3.07E-08$
0.05	$1.22E-11$	$2.12E-10$	$2.32E-10$	$1.55E-11$	$3.45E-10$	$2.42E-10$	$4.50E-13$	$1.24E-09$	$1.37E-09$	$3.30E-13$	$1.70E-09$	$3.06E-09$
0.10	$1.48E-10$	$2.27E-09$	$2.38E-09$	$1.36E-10$	$3.58E-09$	$2.52E-09$	$6.97E-10$	$1.24E-08$	$1.52E-08$	$2.20E-10$	$1.77E-08$	$2.86E-08$
0.15	$2.00E-10$	$3.23E-09$	$3.39E-09$	$1.00E-10$	$5.11E-09$	$3.61E-09$	$3.13E-10$	$1.77E-08$	$2.22E-08$	$7.32E-10$	$2.55E-08$	$4.07E-08$
0.20	$1.43E-10$	$2.44E-09$	$2.57E-09$	$3.53E-11$	$3.90E-09$	$2.76E-09$	$9.89E-12$	$1.35E-08$	$1.73E-08$	$7.91E-11$	$1.96E-08$	$3.11E-08$
0.25	$5.35E-11$	$1.01E-09$	$1.09E-09$	$2.31E-12$	$1.65E-09$	$1.18E-09$	$1.17E-10$	$5.64E-09$	$7.56E-09$	$1.03E-10$	$8.33E-09$	$1.32E-08$
0.40	$4.70E-14$	$1.02E-10$	$1.23E-10$	$6.30E-13$	$1.68E-10$	$1.34E-10$	$1.39E-13$	$5.73E-10$	$9.06E-10$	$6.13E-17$	$9.75E-10$	$1.70E-09$
0.35	$1.22E-11$	$1.69E-10$	$1.93E-10$	$1.18E-13$	$2.48E-10$	$1.73E-10$	$1.91E-14$	$1.02E-09$	$1.05E-09$	$2.33E-12$	$1.55E-09$	$2.98E-09$
0.40	$7.24E-11$	$9.62E-10$	$1.01E-09$	$5.44E-11$	$1.55E-09$	$1.08E-09$	$1.50E-10$	$5.77E-09$	$6.72E-09$	$1.40E-10$	$8.37E-09$	$1.44E-08$
0.45	$1.30E-10$	$1.85E-09$	$1.93E-09$	$7.50E-11$	$3.07E-09$	$2.15E-09$	$8.02E-11$	$1.12E-08$	$1.36E-08$	$2.68E-11$	$1.63E-08$	$2.73E-08$
0.50	$1.50E-10$	$2.22E-09$	$2.32E-09$	$8.30E-11$	$3.80E-09$	$2.66E-09$	$1.10E-11$	$1.38E-08$	$1.72E-08$	$3.66E-13$	$2.01E-08$	$3.32E-08$
0.55	$1.21E-10$	$1.85E-09$	$1.94E-09$	$7.38E-11$	$3.28E-09$	$2.29E-09$	$2.33E-10$	$1.19E-08$	$1.51E-08$	$2.94E-10$	$1.73E-08$	$2.83E-08$
0.60	$6.08E-11$	$9.79E-10$	$1.03E-09$	$4.73E-11$	$1.82E-09$	$1.28E-09$	$2.64E-10$	$6.56E-09$	$8.58E-09$	$3.36E-10$	$9.68E-09$	$1.55E-08$
0.65	$5.74E-13$	$1.87E-10$	$2.03E-10$	$1.42E-11$	$3.91E-10$	$2.79E-10$	$2.37E-11$	$1.40E-09$	$1.99E-09$	$3.65E-11$	$2.18E-09$	$3.39E-09$
0.70	$5.20E-17$	$7.64E-11$	$1.09E-10$	$7.67E-14$	$8.27E-11$	$6.02E-11$	$4.19E-15$	$3.98E-10$	$4.11E-10$	$2.46E-15$	$6.01E-10$	$1.38E-09$
0.75	$5.77E-11$	$8.72E-10$	$9.63E-10$	$4.03E-\nu11$	$1.43E-09$	$9.91E-10$	$3.41E-13$	$5.48E-09$	$6.37E-09$	$2.81E-13$	$7.78E-09$	$1.46E-08$
0.80	$1.49E-10$	$2.14E-09$	$2.30E-09$	$1.46E-10$	$3.80E-09$	$2.62E-09$	$9.45E-11$	$1.43E-08$	$1.72E-08$	$9.41E-11$	$2.03E-08$	$3.64E-08$
0.85	$1.94E-10$	$2.84E-09$	$3.02E-09$	$2.60E-10$	$5.32E-09$	$3.65E-09$	$7.53E-10$	$1.98E-08$	$2.44E-08$	$3.27E-10$	$2.83E-08$	$4.97E-08$
0.90	$1.32E-10$	$2.00E-09$	$2.11E-09$	$2.44E-10$	$3.97E-09$	$2.72E-09$	$8.33E-10$	$1.47E-08$	$1.83E-08$	$6.37E-12$	$2.09E-08$	$3.62E-08$
0.95	$8.48E-12$	$1.97E-10$	$2.05E-10$	$4.10E-11$	$4.75E-10$	$3.23E-10$	$6.60E-11$	$1.68E-09$	$2.23E-09$	$2.93E-11$	$2.40E-09$	$4.00E-09$
0.10	$1.51E-10$	$2.14E-09$	$2.34E-09$	$2.99E-10$	$3.89E-09$	$2.67E-09$	$1.35E-10$	$1.51E-08$	$1.81E-08$	$2.40E-10$	$2.20E-08$	$3.97E-08$

TABLE 5: Analysis of fitness value and performance indicators obtained by the proposed algorithm during 100 independent runs for different cases of dimensionless end-point load.

	Case I			Case II			Case III			Case IV		
	Min	Mean	Std.	Min	Mean	Std.	Min	Mean	Std.	Min	Mean	Std.
Fit	$1.19E-09$	$1.80E-08$	$1.88E-08$	$1.83E-09$	$5.18E-08$	$3.59E-08$	$4.51E-09$	$1.10E-07$	$1.36E-07$	$7.39E-09$	$1.60E-07$	$2.64E-07$
MAD	$1.92E-06$	$1.08E-05$	$5.53E-06$	$3.75E-06$	$1.52E-05$	$4.94E-06$	$3.58E-06$	$2.79E-05$	$1.80E-05$	$3.05E-06$	$3.18E-05$	$2.64E-05$
TIC	$1.27E-06$	$6.93E-06$	$3.66E-06$	$1.35E-06$	$5.00E-06$	$1.59E-06$	$7.94E-07$	$6.12E-06$	$3.86E-06$	$5.23E-07$	$5.17E-06$	$4.27E-06$
RMSE	$1.65E-06$	$8.97E-06$	$4.73E-06$	$3.50E-06$	$1.29E-05$	$4.13E-06$	$3.08E-06$	$2.37E-05$	$1.50E-05$	$2.71E-06$	$2.68E-05$	$2.21E-05$
ENSE	$6.39E-10$	$2.56E-08$	$2.35E-08$	$6.10E-10$	$1.10E-08$	$7.74E-09$	$2.47E-10$	$2.12E-08$	$2.42E-08$	$1.01E-10$	$1.84E-08$	$3.09E-08$

TABLE 6: Computational complexity analysis of each case of deflected cantilever beam.

Cases	GNDO		SQP		GNDO-SQP		Fitness evaluations	
	Mean	Std.	Mean	Std.	Mean	Std.	Mean	Std.
I	11.1057s	1.7891s	3.8720s	0.0026s	17.8550s	2.9866s	85003	9995.5
II	14.5593s	2.7746s	5.156s	0.2764s	21.1397s	3.278s	90134	10003
III	16.3445s	1.5448s	5.723s	0.2682s	23.2314s	4.4431s	91022	8948.3
IV	17.2363s	2.1532s	5.9681s	1.0352s	24.5428s	4.8774s	91539	9323.1

TABLE 7: Unknown parameters in ANN model for finding best solution for each case of large deflected beam with cantilever beam under end-point load using ANN-GNDO-SQP algorithm.

i	Case I			Case II			Case III			Case IV		
	α	ω	β	α	ω	β	α	ω	β	α	ω	β
1	−2.9962626	−0.65813310	−1.9949390	1.48586354	−0.7044589	2.44833643	−2.0618838	−0.2837740	2.30806094	−6.06573860	0.86825787	−2.33438240
2	−2.8313012	0.59715086	−2.4652621	−2.29465530	−0.9937027	−1.48608260	1.4326512	1.2909630	0.41306818	−8.68057533	−0.61741762	−1.96299418
3	−2.8313010	0.59715056	−2.4652635	2.40794827	−1.1209820	3.41884685	−5.1431940	−0.9214788	−2.53963320	−6.06575258	0.86882569	−2.33421836
4	0.2424393	0.81624788	0.9989734	−2.29465550	−0.9937063	−1.48608340	−5.1431899	−0.9214561	−2.53962473	−8.68058082	−0.61739784	−1.96303574
5	−2.9962567	−0.65820220	−1.9949300	−2.29465580	−0.9937174	−1.48607800	0.9991961	0.5095847	3.05528986	1.88766152	−1.93692688	5.66526002
6	0.6959822	0.58787992	1.768609	−2.29465660	−0.9937021	−1.48608350	0.9883707	0.5164401	3.07199558	−8.68057978	−0.61743654	−1.96298424
7	0.6315080	−0.39080880	2.1960290	2.40797982	−1.1206391	3.41897235	−5.1431949	−0.9214901	−2.53962702	−8.68057609	−0.61744398	−1.96300933
8	1.2045178	0.65966357	−0.7020318	−1.14915000	1.5518567	1.25665993	−8.4468052	1.1202166	−3.24654750	2.29100504	−0.70151323	4.57057840
9	−2.8312966	0.59714525	−2.4652530	−3.73471870	0.2862061	1.44003308	0.9883813	0.5164715	3.07202476	2.29100362	−0.70152426	4.57058216
10	−2.9962649	−0.65808110	−1.9949521	−2.29465600	−0.9936976	−1.48608900	−5.1431979	−0.9214801	−2.53963468	−8.68057385	−0.61743850	−1.96300282
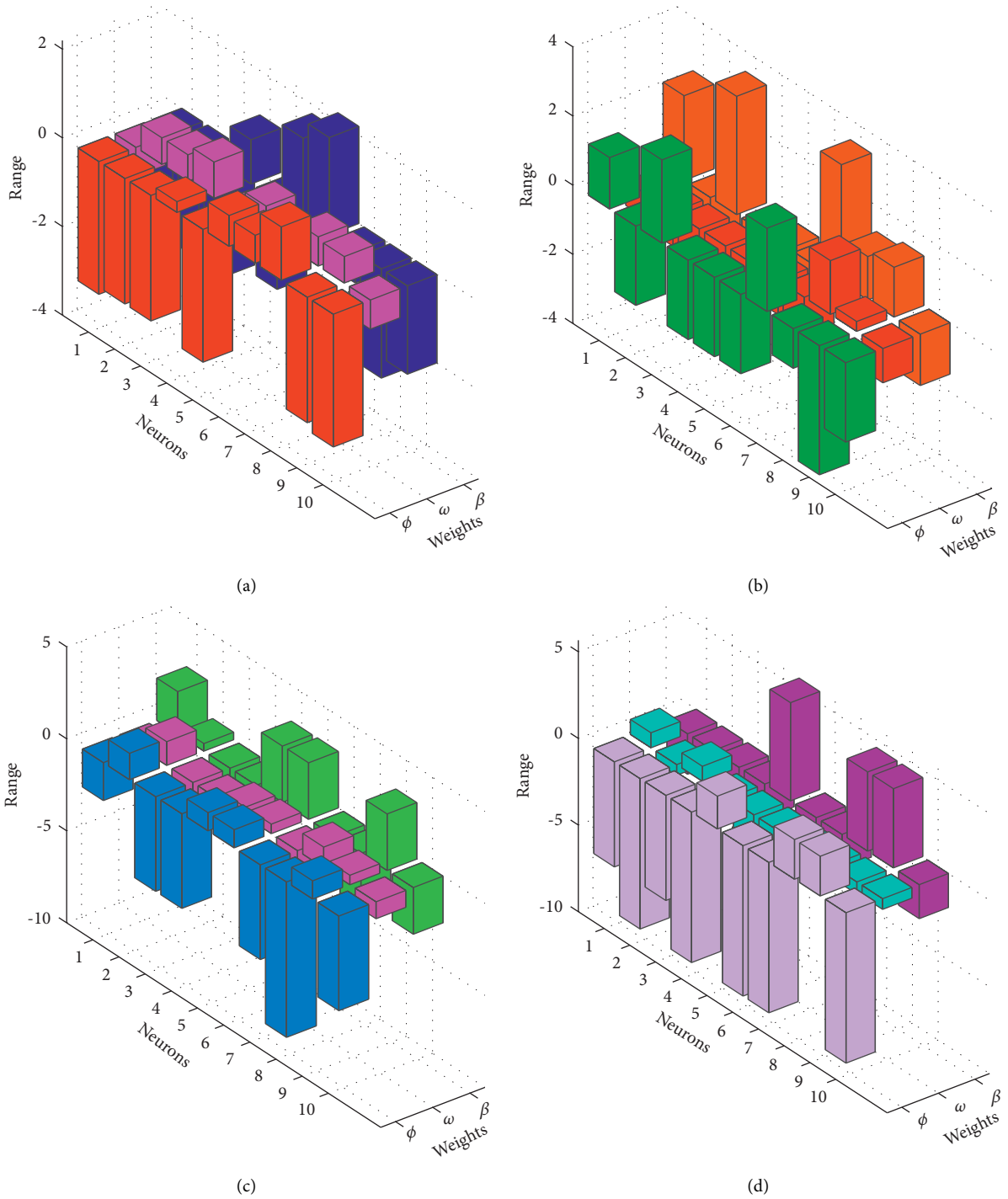
Figure 9: Unknown neurons in ANN structure corresponding to best solutions for each case large deflected cantilever beam. (a) Case I. (b) Case II. (c) Case III. (d) Case IV.

6. Conclusion

In this paper, we have analyzed the mathematical model of large deflected beam under variational point load and the free end. Furthermore, we present a new soft computing technique to calculate approximate solution for different cases depending on variations in end point load. We conclude our finding as follows.

(i) A new soft computing evolutionary algorithm is developed in which the strength of artificial neural networks are utilized to model an approximate series solution and combined with hybridization of generalized normal distribution optimization algorithm and sequential quadratic programming. The proposed algorithm is named as ANN-GNDO-SQP algorithm.

(ii) ANNs-based fitness functions are constructed and optimize with the ANN-GNDO-SQP algorithm to obtain an overlapping solutions with minimum absolute errors as shown in Figure 3.

(iii) It can be seen that increasing end-point load increases the angle of deflection, horizontal distance, and rotational angle of the cantilever beam.

(iv) Convergence graphs and boxplots of 100 independent executions for fitness evaluation, MAD,

TIC, RMSE, and ENSE show the stability of proposed algorithm.

(v) Extensive graphical and statistical analysis along with complexity analysis of the proposed algorithm for solving large deflected cantilever beam shows the correctness and robustness of ANN-GNDO-SQP algorithm.

Approximate solutions for cases I–IV are as follows:

$$\widehat{\theta}(\xi) \begin{cases} \dfrac{-2.9962626}{1+e^{-(-0.65813310t-1.9949390)}} + \dfrac{-2.8313012}{1+e^{-(0.59715086t-2.4652621)}}, \\[3mm] +\dfrac{-2.8313010}{1+e^{-(0.59715056-2.4652635)}} + \dfrac{0.2424393}{1+e^{(0.81624788t+0.9989734)}}, \\[3mm] +\dfrac{-2.9962567}{1+e^{-(-0.65820220t-1.9949300)}} + \dfrac{0.6959822}{1+e^{-(0.58787992t+1.7968609)}}, \\[3mm] +\dfrac{0.6315080}{1+e^{-(-0.39080880t+2.1960290)}} + \dfrac{1.2045178}{1+e^{(0.65966357t-0.7020318)}}, \\[3mm] +\dfrac{-2.8312966}{1+e^{-(0.59714525t-2.4652530)}} + \dfrac{-2.9962649}{1+e^{-(-0.65808110t-1.9949521)}}, \end{cases}$$

$$\widehat{\theta}(\xi) \begin{cases} \dfrac{1.48586354}{1+e^{-(-0.7044589t+2.44833643)}} + \dfrac{-2.29465530}{1+e^{-(-0.9937027t-1.48608260)}} \\[3mm] +\dfrac{2.40794827}{1+e^{-(-1.1209820+3.41884685)}} + \dfrac{-2.29465550}{1+e^{(-0.9937063t-1.48608340)}} \\[3mm] +\dfrac{-2.29465580}{1+e^{-(-0.9937174t-1.48607800)}} + \dfrac{-1.48607800}{1+e^{-(-0.9937021t-1.48608350)}} \\[3mm] +\dfrac{2.40797982}{1+e^{-(-1.1206391t+3.41897235)}} + \dfrac{-1.14915000}{1+e^{(1.5518567t+1.25665993)}} \\[3mm] +\dfrac{-3.73471870}{1+e^{-(0.2862061t+1.44003308)}} + \dfrac{-2.29465600}{1+e^{-(-0.9936976t-1.48608900)}}, \end{cases}$$

$$\widehat{\theta}(\xi)\begin{cases}\dfrac{-2.0618838}{1+e^{-(-0.2837740t+2.30806094)}}+\dfrac{1.4326512}{1+e^{-(1.2909630t+0.41306818)}},\\[3mm]+\dfrac{-5.1431940}{1+e^{-(-0.9214788-2.53963320)}}+\dfrac{-5.1431899}{1+e^{-(-0.9214561t-2.53962473)}},\\[3mm]+\dfrac{0.9891961}{1+e^{-(0.5095847t+3.05528986)}}+\dfrac{0.9883707}{1+e^{-(0.5164401t+3.07199558)}},\\[3mm]+\dfrac{-5.1431949}{1+e^{-(-0.9214901t-2.53962702)}}+\dfrac{-8.4468052}{1+e^{(1.1202166t-3.24654750)}},\\[3mm]+\dfrac{0.9883813}{1+e^{-(0.5164715t+3.07202476)}}+\dfrac{-5.1431979}{1+e^{-(-0.9214801t-2.53963468)}},\end{cases}$$

$$\widehat{\theta}(\xi)\begin{cases}\dfrac{-6.06573860}{1+e^{-(0.86825787t-2.33438240)}}+\dfrac{-8.68057533}{1+e^{-(-0.61741762t-1.96299418)}},\\[3mm]+\dfrac{-6.06575258}{1+e^{-(0.86882569-2.33421836)}}+\dfrac{-8.68058082}{1+e^{(-0.61739784t-1.96303574)}},\\[3mm]+\dfrac{1.88766152}{1+e^{-(-1.93692688t+5.66526002)}}+\dfrac{-8.68057978}{1+e^{-(-0.61743654t-1.96298424)}},\\[3mm]+\dfrac{-8.68057609}{1+e^{-(-0.61744398t-1.96300933)}}+\dfrac{2.29100504}{1+e^{(-0.70151323t+4.57057840)}},\\[3mm]+\dfrac{2.29100362}{1+e^{-(-0.70152426t+4.57058216)}}+\dfrac{-8.68057385}{1+e^{-(-0.61743850t-1.96300282)}}.\end{cases}$$

$$(29)$$

Abbreviations

ANNs:	Artificial neural networks
GNDO:	Generalized normal distribution optimization
MAD:	Mean absolute deviation
TIC:	Theil's inequality coefficient
NSE:	Nash–Sutcliffe efficiency
ENSE:	Error in Nash–Sutcliffe efficiency
SQP:	Sequential quadratic programming
RMSE:	Root mean square error
DTM:	Differential transform method
L:	Distance of deflected beam
F:	Concentrated load
$\phi_n, \omega_n, \beta_n$:	Unknown real valued neurons in ANNs
ρ:	End-point load
κ:	Curvature
θ:	Rotation of beam
s:	Distance from fix point
I:	Inertia
M:	Bending moment
EL:	Bending stiffness
δ_h:	Horizontal deflection of beam
ξ:	Dimensionless parameter
v_i^t:	Trail vector
$\widehat{\mu}_i$:	Mean position
$\widehat{\delta}_i$:	Standard variance
v_i^t:	Trail vector
$\widehat{\mu}_i$:	Mean position
δ_i:	Standard variance.

Data Availability

The data used to support the findings of this study are available from the corresponding author upon request.

Conflicts of Interest

The authors declare that they have no conflicts of interest.

Acknowledgments

References

[1] M. A. Maneshi, E. Ghavanloo, and S. Ahmad Fazelzadeh, "Closed-form expression for geometrically nonlinear large deformation of nano-beams subjected to end force," *The European Physical Journal Plus*, vol. 133, no. 7, p. 256, 2018.

[2] C. M. Wang, Y. Xiang, and S. Kitipornchai, "Postbuckling of nano rods/tubes based on nonlocal beam theory," *International Journal of Applied Mechanics*, vol. 1, no. 2, pp. 259–266, 2009.

[3] D. Wang, B. Bienen, M. Nazem et al., "Large deformation finite element analyses in geotechnical engineering," *Computers and Geotechnics*, vol. 65, pp. 104–114, 2015.

[4] L. Monforte, M. Arroyo, J. M. Carbonell, and A. Gens, "Numerical simulation of undrained insertion problems in geotechnical engineering with the Particle Finite Element

Method (PFEM)," *Computers and Geotechnics*, vol. 82, pp. 144–156, 2017.

[5] L. Monforte, M. Arroyo, J. M. Carbonell, and A. Gens, "Coupled effective stress analysis of insertion problems in geotechnics with the Particle Finite Element Method," *Computers and Geotechnics*, vol. 101, pp. 114–129, 2018.

[6] Y. Hu and M. F. Randolph, "H-adaptive FE analysis of elasto-plastic non-homogeneous soil with large deformation," *Computers and Geotechnics*, vol. 23, no. 1-2, pp. 61–83, 1998.

[7] Y. Hu and M. F. Randolph, "A practical numerical approach for large deformation problems in soil," *International Journal for Numerical and Analytical Methods in Geomechanics*, vol. 22, no. 5, pp. 327–350, 1998.

[8] G. Qiu, S. Henke, and J. Grabe, "Application of a Coupled Eulerian-Lagrangian approach on geomechanical problems involving large deformations," *Computers and Geotechnics*, vol. 38, no. 1, pp. 30–39, 2011.

[9] R. Schmidt and D. A. Dadeppo, "Approximate analysis of large deflections of beams," *ZAMM-Zeitschrift für Angewandte Mathematik und Mechanik*, vol. 51, no. 3, pp. 233-234, 1971.

[10] B. N. Rao and G. V. Rao, "On the large deflection of cantilever beams with end rotational load," *ZAMM - Journal of Applied Mathematics and Mechanics/Zeitschrift für Angewandte Mathematik und Mechanik*, vol. 66, no. 10, pp. 507–509, 1986.

[11] B. N. Rao and G. V. Rao, "Large deflections of a cantilever beam subjected to a rotational distributed loading," *Forschung im Ingenieurwesen*, vol. 55, no. 4, pp. 116–120, 1989.

[12] K. Lee, "Large deflections of cantilever beams of non-linear elastic material under a combined loading," *International Journal of Non-Linear Mechanics*, vol. 37, no. 3, pp. 439–443, 2002.

[13] S. Chucheepsakul and B. Phungpaigram, "Elliptic integral solutions of variable-arc-length elastica under an inclined follower force," *Zamm*, vol. 84, no. 1, pp. 29–38, 2004.

[14] L. Li, H. Tang, and Y. Hu, "The effect of thickness on the mechanics of nanobeams," *International Journal of Engineering Science*, vol. 123, pp. 81–91, 2018.

[15] M. Dado and S. Al-Sadder, "A new technique for large deflection analysis of non-prismatic cantilever beams," *Mechanics research communications*, vol. 32, no. 6, pp. 692–703, 2005.

[16] S. D. Akbas, "Forced vibration analysis of cracked functionally graded microbeams," *Advances in Nano Research*, vol. 6, p. 39, 2018.

[17] J. Wang, J.-K. Chen, and S. Liao, "An explicit solution of the large deformation of a cantilever beam under point load at the free tip," *Journal of computational and applied mathematics*, vol. 212, no. 2, pp. 320–330, 2008.

[18] M. Khorasani, H. Elahi, M. Eugeni, L. Lampani, and O. Civalek, "Vibration of FG porous three-layered beams equipped by agglomerated nanocomposite patches resting on Vlasov's foundation," *Transport in Porous Media*, pp. 1–30, 2021.

[19] L. Li, Y. Hu, and X. Li, "Longitudinal vibration of size-dependent rods via nonlocal strain gradient theory," *International Journal of Mechanical Sciences*, vol. 115-116, pp. 135–144, 2016.

[20] R. Barretta, R. Luciano, F. Marotti de Sciarra, and G. Ruta, "Stress-driven nonlocal integral model for Timoshenko elastic nano-beams," *European Journal of Mechanics-A/Solids*, vol. 72, pp. 275–286, 2018.

[21] N. Tolou and J. Herder, "A seminalytical approach to large deflections in compliant beams under point load," *Mathematical Problems in Engineering*, vol. 2009, Article ID 910896, 13 pages, 2009.

[22] M. Mutyalarao, D. Bharathi, and B. N. Rao, "Large deflections of a cantilever beam under an inclined end load," *Applied Mathematics and Computation*, vol. 217, no. 7, pp. 3607–3613, 2010.

[23] N. A. Khan, M. Sulaiman, A. J. Aljohani, P. Kumam, and H. Alrabaiah, "Analysis of multi-phase flow through porous media for imbibition phenomena by using the LeNN-WOA-NM Algorithm," *IEEE Access*, vol. 8, pp. 196425–196458, 2020.

[24] W. Waseem, M. Sulaiman, A. Alhindi, and H. Alhakami, "A soft computing approach based on fractional order DPSO algorithm designed to solve the corneal model for eye surgery," *IEEE Access*, vol. 8, pp. 61576–61592, 2020.

[25] N. A. Khan, M. Sulaiman, P. Kumam, and A. J. Aljohani, "A new soft computing approach for studying the wire coating dynamics with oldroyd 8-constant fluid," *Physics of Fluids*, vol. 33, no. 3, p. 036117, 2021.

[26] Y. Zhang, J. Lin, Z. Hu, N. A. Khan, and M. Sulaiman, "Analysis of third-order nonlinear multi-singular emden-fowler equation by using the LeNN-WOA-NM Algorithm," *IEEE Access*, vol. 9, pp. 72111–72138, 2021.

[27] A. Ahmad, M. Sulaiman, A. Alhindi, and A. J. Aljohani, "Analysis of temperature profiles in longitudinal fin designs by a novel neuroevolutionary approach," *IEEE Access*, vol. 8, pp. 113285–113308, 2020.

[28] N. A. Khan, O. I. Khalaf, C. A. T. Romero, M. Sulaiman, and M. A. Bakar, "Application of euler neural networks with soft computing paradigm to solve nonlinear problems arising in heat transfer," *Entropy*, vol. 23, no. 8, p. 1053, 2021.

[29] W. Huang, T. Jiang, X. Zhang, N. A. Khan, and M. Sulaiman, "Analysis of beam-column designs by varying axial load with internal forces and bending rigidity using a new soft computing technique," *Complexity*, vol. 2021, Article ID 6639032, 19 pages, 2021.

[30] A. Ali, S. Qadri, W. Khan Mashwani et al., "Machine learning based automated segmentation and hybrid feature analysis for diabetic retinopathy classification using fundus image," *Entropy*, vol. 22, no. 5, p. 567, 2020.

[31] H. Wei, Q. X. Pan, O. B. Adetoro, E. Avital, Y. Yuan, and P. H. Wen, "Dynamic large deformation analysis of a cantilever beam," *Mathematics and Computers in Simulation*, vol. 174, pp. 183–204, 2020.

[32] P. Salehi, H. Yaghoobi, and M. Torabi, "Application of the differential transformation method and variational iteration method to large deformation of cantilever beams under point load," *Journal of Mechanical Science and Technology*, vol. 26, no. 9, pp. 2879–2887, 2012.

[33] H. Abbasi and A. Javed, "Implementation of differential transform method (DTM) for large deformation analysis of cantilever beam," *IOP Conference Series: Materials Science and Engineering*, vol. 899, Article ID 012003, 2020.

[34] Y. Zhang, Z. Jin, and S. Mirjalili, "Generalized normal distribution optimization and its applications in parameter extraction of photovoltaic models," *Energy Conversion and Management*, vol. 224, Article ID 113301, 2020.

[35] J. Nocedal and S. Wright, *Numerical optimization*, Springer Science & Business Media, Berlin, Germany, 2006.

[36] K. Long, X. Wang, and X. Gu, "Multi-material topology optimization for the transient heat conduction problem using a sequential quadratic programming algorithm," *Engineering optimization*, vol. 50, no. 12, pp. 2091–2107, 2018.

[37] A. Lang, Z. Song, G. He, and Y. Sang, "Profile error evaluation of free-form surface using sequential quadratic programming algorithm," *Precision Engineering*, vol. 47, pp. 344–352, 2017.

[38] Z. B. Sun, Y. Y. Sun, Y. Li, and K. P. Liu, "A new trust region-sequential quadratic programming approach for nonlinear systems based on nonlinear model predictive control," *Engineering Optimization*, vol. 51, no. 6, pp. 1071–1096, 2019.

[39] O. D. Montoya, W. Gil-González, and A. Garces, "Sequential quadratic programming models for solving the OPF problem in DC grids," *Electric Power Systems Research*, vol. 169, pp. 18–23, 2019.

[40] M. A. Z. Raja, M. A. Manzar, S. M. Shah, and Y. Chen, "Integrated intelligence of fractional neural networks and sequential quadratic programming for Bagley–Torvik systems arising in fluid mechanics," *Journal of Computational and Nonlinear Dynamics*, vol. 15, 2020.

[41] C.-L. Xiao and H.-X. Huang, "Optimal design of heating system in rapid thermal cycling blow mold by a two-step method based on sequential quadratic programming," *International Communications in Heat and Mass Transfer*, vol. 96, pp. 114–121, 2018.

Research Article

An Improved Lattice Hydrodynamic Model by considering the Effect of "Backward-Looking" and Anticipation Behavior

Jin Wan , **Xin Huang** , **Wenzhi Qin** , **Xiuge Gu** , **and Min Zhao**

School of Science, Nantong University, Nantong, Jiangsu 226019, China

Correspondence should be addressed to Min Zhao; zhao.m@ntu.edu.cn

In order to prevent the occurrence of traffic accidents, drivers always focus on the running conditions of the preceding and rear vehicles to change their driving behavior. By taking into the "backward-looking" effect and the driver's anticipation effect of flux difference consideration at the same time, a novel two-lane lattice hydrodynamic model is proposed to reveal driving characteristics. The corresponding stability conditions are derived through a linear stability analysis. Then, the nonlinear theory is also applied to derive the mKdV equation describing traffic congestion near the critical point. Linear and nonlinear analyses of the proposed model show that how the "backward-looking" effect and the driver's anticipation behavior comprehensively affect the traffic flow stability. The results show that the positive constant γ, the driver's anticipation time τ, and the sensitivity coefficient p play significant roles in the improvement of traffic flow stability and the alleviation of the traffic congestion. Furthermore, the effectiveness of linear stability analysis and nonlinear analysis results is demonstrated by numerical simulations.

1. Introduction

With the rapid development of wireless technologies and intelligent vehicles in the past years, the vehicle-to-vehicle (V2V) communication [1, 2] can not only alleviate the congested traffic flow but also provide pleasurable driving experiences. To reveal the realistic traffic phenomena, there have emerged various traffic models such as car-following models [3–10], cellular automation models [11, 12], macrotraffic models [13–15], lattice hydrodynamic models [16–21], continuum models [22–24], and gas kinetic models [25].

By incorporating the ideas of car-following as well as continuum models, the first lattice hydrodynamic model [26] with a conservation equation (1) and a flow equation (2) was proposed in 1998.

$$\partial_t \rho_j + \rho_0 \left(\rho_j v_j - \rho_{j-1} v_{j-1} \right) = 0, \tag{1}$$

$$\partial_t \left(\rho_j v_j \right) = a \left[\rho_0 V \left(\rho_{j+1} \right) - \rho_j v_j \right], \tag{2}$$

where $\rho_0 V(\rho_{j+1})$ and $\rho_j v_j$ denote the optimal flow and the actual flow, respectively. ρ_0 is the average density, and a refers to the driver's sensitivity. Then, the stability condition and mKdV equation can be, respectively, obtained with the linear analysis and nonlinear analysis methods. Subsequently, many extended works have been developed by taking different factors into accounts, such as driver's memory [27–31], driver's anticipation effect [32–34], density difference [35], traffic interruption probability [36–38], and "backward-looking" effect [39–41].

In addition to the information from the preceding vehicle, drivers always focus on the running conditions of the rear vehicles from the rear-view mirror to change their driving behavior. By considering the "backward-looking" effect, Ge and Cheng [39] presented the BL-LV model as follows:

$$\rho_j (t + \tau) v_j (t + \tau) = \rho_0 V_F \left(\rho_{j+1} (t) \right) \\ + H \left(\bar{\rho} - \rho_{j-1} (t) \right) \cdot H \left(\rho_{j-1} (t) - \rho_c \right) \rho_0 V_B \left(\rho_{j-1} (t) \right), \tag{3}$$

where $H(\cdot)$ and ρ_c represent the Heaviside function and the safety density, respectively. $\overline{\rho}$ denotes a parameter close to 1. $V_F(\cdot)$ is the optimal velocity function for "forward-looking." While $V_B(\cdot)$ is the optimal velocity function for "backward-looking," which works if and only if $\rho_c \le \rho_{j-1}(t) \le \overline{\rho}$ holds. Functions $V_F(\cdot)$ and $V_B(\cdot)$ have exactly the opposite effects and are defined as

$$
V_F\left(\rho_{j+1}\right) = \tanh\left(\frac{2}{\rho_0} - \frac{\rho_{j+1}}{\rho_0^2} - \frac{1}{\rho_c}\right) + \tanh\left(\frac{1}{\rho_c}\right),
$$

$$
V_B\left(\rho_{j-1}\right) = \gamma\left[-\tanh\left(\frac{2}{\rho_0} - \frac{\rho_{j-1}}{\rho_0^2} - \frac{1}{\rho_c}\right) + \tanh\left(\frac{1}{\rho_c}\right)\right],
$$

(4)

where γ is a positive constant that represents the relative role of the "backward-looking."

For the sake of safe and comfortable driving, drivers always predict the velocity of the preceding vehicles so that they can adjust their driving velocity at the next moment. This driving behavior is known as the anticipation effect [42] or predictive effect [43, 44]. Wang et al. [43] added the driver's anticipation effect into the optimal velocity (OV) function in a single-lane lattice model. Later, Kaur and Sharma [44] extended the single-lane model [43] to the two-lane case along with the optimal current difference (OCD) effect. By considering the anticipation effects in the OCD term as well as the OV function, Sharma [45] constructed a new lattice hydrodynamic model with an anticipation coefficient α, where the positive α represents the anticipation effect while the negative α represents the delay effect. Then, Li et al. [32] adopted this anticipation effect to the multiple optimal current differences' anticipation version. Meanwhile, numerical results indicated that only the information of three preceding lattices [46] was enough for the improvement of traffic stability. In view of the anticipation effect of flux difference, Chang and Cheng [47] proposed a new lattice model as follows:

$$
\partial_t\left(\rho_j v_j\right) = a\rho_0 V\left(\rho_{j+1}\right) - a\left(1 + k_1\right)\rho_j v_j \\
+ k_2\left[\rho_{j+1}(t+\tau)v_{j+1}(t+\tau) - \rho_j v_j\right],
$$

(5)

where p is the sensitivity coefficient of the anticipation flux difference. The greater p is, the stronger the driver's anticipation effect is. τ means the anticipation time, and $\rho_{j+1}(t+\tau)v_{j+1}(t+\tau) - \rho_j v_j$ represents the anticipation flux difference between the preceding lattice $j+1$ and the

where τ represents the driver's anticipation time and k_1 and k_2 denote the deviation degree of speed v_j and the feedback gain, respectively. Some previous studies have considered the "backward-looking" effect and the anticipation effect of flux difference separately. In a real traffic system, the velocity of the current vehicles is not only affected by the preceding vehicles but also affected by the rear vehicles. Generally, the information of the rear vehicles could be received by the rear-view mirror. According to the information, drivers could change their driving behavior to avoid the traffic accidents. Meanwhile, the velocity of the preceding vehicles could be predicted by drivers on the basis of the vehicle distance information, so that they can adjust their driving velocity in a period of anticipation time. However, the above two factors have never been considered simultaneously in the existing lattice models. This motivates us to develop a new lattice model by incorporating the "backward-looking" effect with the anticipation effect of flux difference.

The outline of this paper is organized as follows. In Section 2, we introduce a new lattice hydrodynamic model considering the flux anticipation difference effect and the "backward-looking" effect and use the linear stability theory to derive the stability condition of the traffic flow. In Section 3, the propagation behavior of traffic density waves is presented by means of the nonlinear analysis method. In Section 4, numerical simulations are carried out to validate the results of linear and nonlinear stability analyses. At last, the conclusions are drawn in Section 5.

2. The Extended Lattice Hydrodynamic Model and Linear Stability Analysis

In light of the aforementioned facts, a novel lattice model is presented by taking the flux anticipation difference effect and the "backward-looking" effect (FADBE) into account as follows:

$$
\partial_t\left(\rho_j v_j\right) = a\left[\rho_0 V_F\left(\rho_{j+1}(t)\right) + H\left(\overline{\rho} - \rho_{j-1}(t)\right) \cdot H\left(\rho_{j-1}(t) - \rho_c\right)\rho_0 V_B\left(\rho_{j-1}(t)\right)\right] \\
- a\rho_j v_j + ap\left(\rho_{j+1}(t+\tau)v_{j+1}(t+\tau) - \rho_j v_j\right),
$$

(6)

current lattice j. The optimal velocity functions and the function $H(\cdot)$ are the same as those in Ge and Cheng's model [39].

After eliminating the velocity term v_j in equations (1) and (6), the following density equation can be derived:

$$\partial_t^2 \rho_j(t) + a\rho_0^2 \left[V\big(\rho_{j+1}(t)\big) - V_F\big(\rho_j(t)\big) + V_B\big(\rho_{j-1}(t)\big) - V_B\big(\rho_{j-2}(t)\big) \right]$$
$$+ a\partial_t \rho_j + ap\big(\partial_t \rho_j - \partial_t \rho_{j+1}(t+\tau)\big) = 0. \tag{7}$$

When $p = 0$, the model reduces to Ge and Cheng's model [39]. In addition, the lattice model coincides with Nagatani's model [26] when $p = 0$ and $\tau = 0$.

The influence of the "backward-looking" effect and the anticipation effect has been studied by linear stability analysis. The uniform traffic stream with the fixed density ρ_0 and the optimal velocity $V(\rho_0)$ is defined as the stable state. One can obtain the solution of the steady-state vehicular system as follows:

$$\rho_j(t) = \rho_0,$$
$$v(j) = V_F(\rho) + V_B(\rho). \tag{8}$$

Then, y_j is supposed as a small perturbation added into the steady-state solution at lattice j, and the perturbed solution is

$$\rho_j(t) = \rho_0 + y_i(t). \tag{9}$$

Equation (9) is substituted into equation (7), and the derived equation is linearized. The equation is obtained as

$$\partial_t^2 y_j(t) + a\rho_0^2 V_F'(\rho_0)\big(y_{j+1}(t) - y_j(t)\big)$$
$$+ a\rho_0^2 V_B'(\rho_0)\big(y_{j-1}(t) - y_{j-2}(t)\big) \tag{10}$$
$$- ap\partial_t y_{j+1}(t+\tau) + (ap+a)\partial_t y_j = 0.$$

Let the small perturbation $y_j(t) = \exp(ikj + zt)$, and inserting it into equation (10), we gain

$$z^2 + a\rho_0^2\left[V_F'(\rho_0)\big(e^{ik} - 1\big) + V_B'(\rho_0)\big(e^{ik} - e^{-2ik}\big)\right]$$
$$- apze^{z\tau+ik} + (ap+a)z = 0. \tag{11}$$

Assuming $z = z_1(ik) + z_2(ik)^2 + \cdots$ and putting it into equation (11), we reserve the first-order and second-order terms of ik by neglecting higher-order terms. Then, one can get

$$z_1 = -\rho_0^2\big(V_F'(\rho_0) + V_B'(\rho_0)\big),$$

$$z_2 = \frac{2apz_1 - 2z_1^2 + 2apz_1^2\tau - aV_F'(\rho_0)\rho_0^2 + 3aV_B'(\rho_0)\rho_0^2}{2a}. \tag{12}$$

The uniform steady-state flow remains stable as z_2 is positive. On the contrary, the uniform flow tends to be unstable if the value of z_2 is negative. When z_2 is equal to zero, the formula of the neutral stability condition is acquired as

$$a = \frac{2\big(V_F'(\rho_0) + V_B'(\rho_0)\big)^2 \rho_0^2}{M}, \tag{13}$$

where $M = -V_F'(\rho_0) + 3V_B'(\rho_0) - 2\big(V_F'(\rho_0) + V_B'(\rho_0)\big)p + 2\big(V_F'(\rho_0) + V_B'(\rho_0)\big)^2 p\tau\rho_0^2$. The stability condition for the uniform traffic flow is obtained as

$$a > \frac{2\big(V_F'(\rho_0) + V_B'(\rho_0)\big)^2 \rho_0^2}{M}. \tag{14}$$

It is obvious that the stable condition (14) is reduced to that of Ge and Cheng's model [39] when $p = 0$. Equation (14) shows that the parameters p, τ, and γ play important roles in the performance of the traffic system.

The phase diagram of (ρ, a) is shown in Figure 1, where ρ is density and a denotes sensitivity. Note that γ denotes a positive constant considering the "backward-looking" effect [40, 41]. Three solid curves in each pattern of Figure 1 represent the neutral stability curves under $\gamma = 0.1$. The phase diagram is divided into two regions: the stable and unstable regions are above and below the solid neutral stability curve, respectively. In the stable region, the traffic flow will remain stable with a perturbation. In the unstable region, the congested traffic will happen even with a small perturbation. Figure 1 depicts the neutral stability curves of the FADBE model for different values of driver's anticipation time τ and the sensitivity coefficient p of the anticipation flux difference when $\gamma = 0.1$. As shown in Figure 1, the corresponding stable region expands gradually with the increasing values of τ and p, which means that the driver's anticipation effect can contribute to the stabilization of traffic flow obviously.

Figure 2 demonstrates the neutral stability curves of the FADBE model for different values of τ and γ when $p = 0.1$. As shown in Figure 2, the corresponding neutral stability curves and critical points decrease gradually with the increasing values of τ and γ. When the value of γ is fixed in each pattern of Figure 2, the stability of the traffic flow can be improved efficiently with the increasing value of anticipation time τ.

Figure 3 exhibits that the phase diagram of (ρ, a) of the FADBE model for different values of the positive constant γ ($\gamma = 0.05, 0.1, 0.15, 0.2$) and the sensitivity coefficient p ($p = 0.1, 0.2, 0.3$) when $\tau = 1.5$. With the increasing value of the positive constant γ in each pattern of Figure 3, the amplitudes of neutral stability curves all fall down gradually when the value of the parameter p is fixed. For different values of γ, it can be seen from each pattern of Figure 3 that the corresponding peak value of solid curves lowers down with the increasing value of p. These phenomena demonstrate that when the value of γ or p increases, the area of the stable region becomes larger. Thus, it can be concluded that the traffic flow stability can be improved by incorporating the positive constant γ and the sensitivity coefficient p.

3. Nonlinear Stability Analysis

To investigate the influence of the "backward-looking" effect and the anticipation effect of flux difference, we carried out the reduction perturbation method to obtain the mKdV equation. The slow variables X and T are defined as follows:
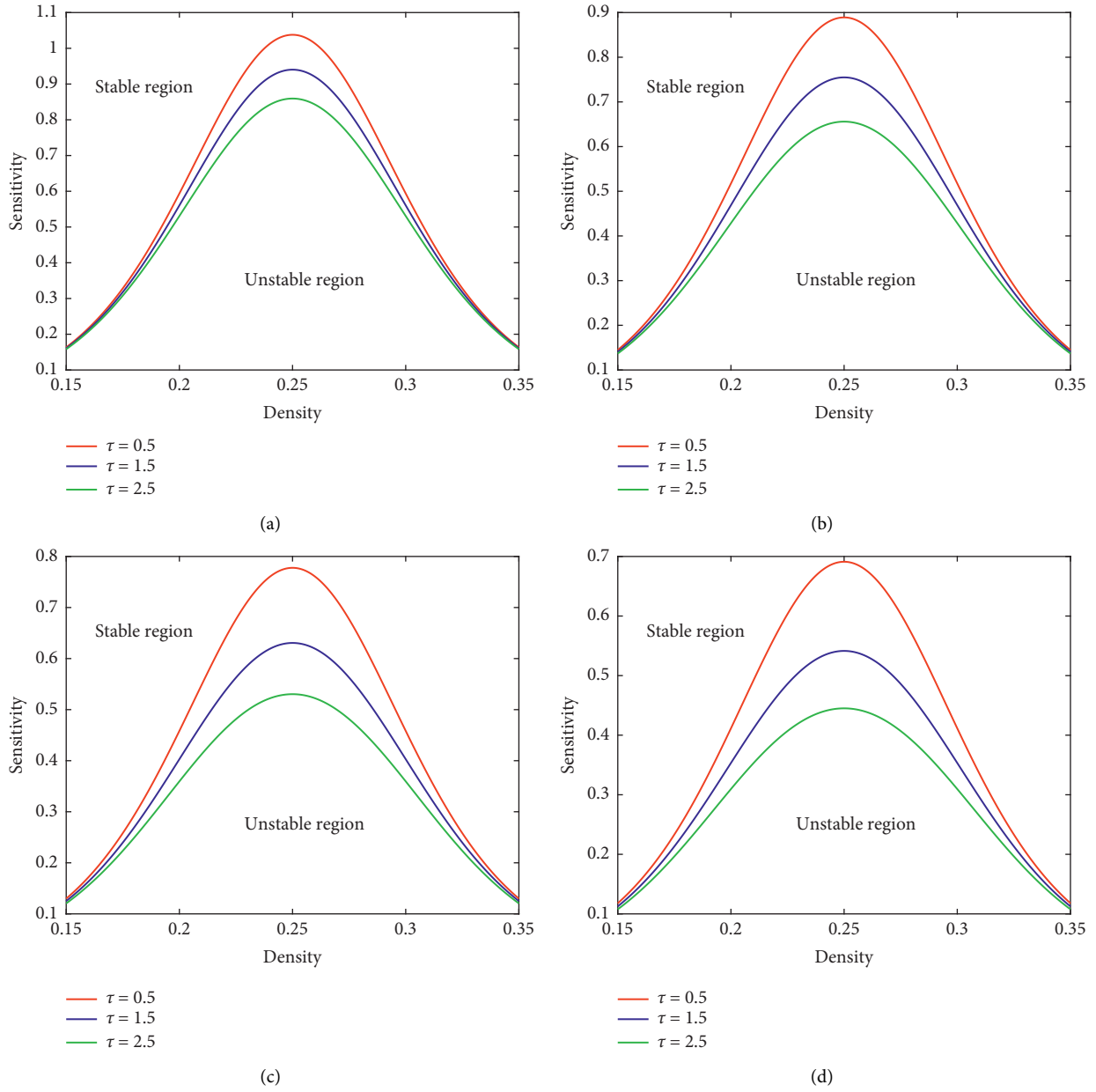
Figure 1: The neutral stability curves for $\gamma = 0.1$ for different values of p and τ: (a) $p = 0.1$; (b) $p = 0.2$; (c) $p = 0.3$; (d) $p = 0.4$.

$$X = \varepsilon(j + bt),$$
$$T = \varepsilon^3 t, \qquad\qquad (15)$$
$$\rho_j = \rho_c + \varepsilon R(X, T),$$

where ε $(0 < \varepsilon \ll 1)$ is a small positive scaling parameter.

Substituting equation (15) into equation (7), each term of equation (7) is expanded up to the fifth-order of ε with the Taylor expansion technique as follows:
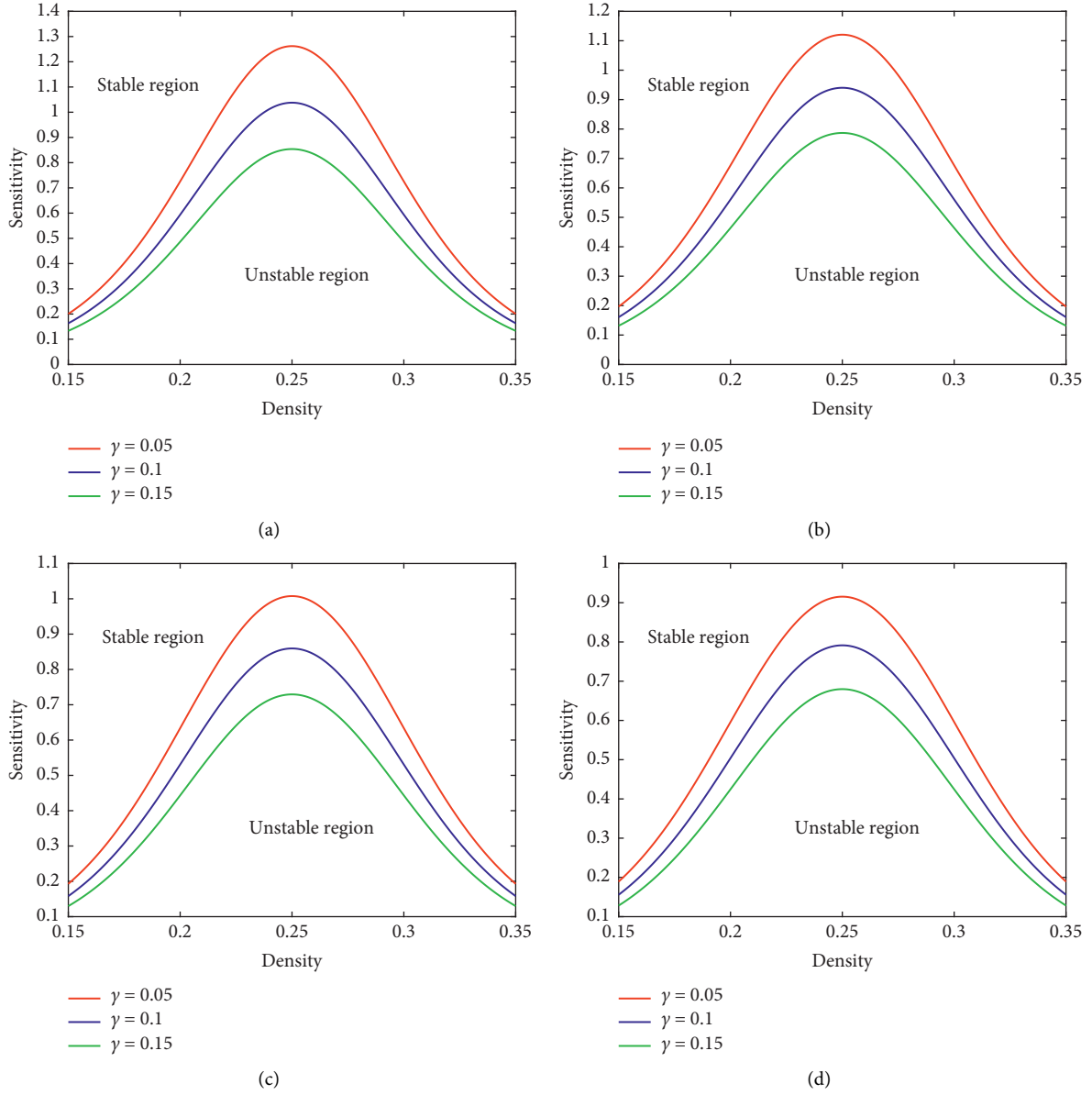
FIGURE 2: The neutral stability curves for $p = 0.1$ for different values of τ and γ: (a) $\tau = 0.5$; (b) $\tau = 1.5$; (c) $\tau = 2.5$; (d) $\tau = 3.5$.

$$\varepsilon^2 \left[b + \rho_c^2 \left(V_F' + V_B' \right) \right] \partial_X R$$

$$+ \varepsilon^3 \left(\frac{b^2}{a} - b^2 p\tau - \frac{3}{2}\rho_c^2 V_B' + \frac{1}{2}\rho_c^2 V_F' \right) \partial_X^2 R$$

$$+ \varepsilon^4 \left[\partial_T R - \left(\frac{1}{2}b^3 p\tau^2 - \frac{7}{6}\rho_c^2 V_B' - \frac{1}{6}\rho_c^2 V_F' \right) \partial_X^3 R + \left(\frac{1}{6}\rho_c^2 V_B'' + \frac{1}{6}\rho_c^2 V_f^{x2032''} \right) \partial_X R^3 \right]$$

$$+ \varepsilon^5 \left[\left(\frac{2b}{a} - 2bp\tau \right) \partial_X \partial_T R + \left(-\frac{1}{6}b^4 p\tau^3 - \frac{5}{8}\rho_c^2 V_B' + \frac{1}{24}\rho_c^2 V_F' \right) \partial_X^4 R + \left(\frac{1}{12}\rho_c^2 V_f'' - \frac{1}{4}\rho_c^2 V_B'' \right) \partial_X^2 R^3 \right] = 0,$$

(16)

(a)

(b)

(c)

(d)
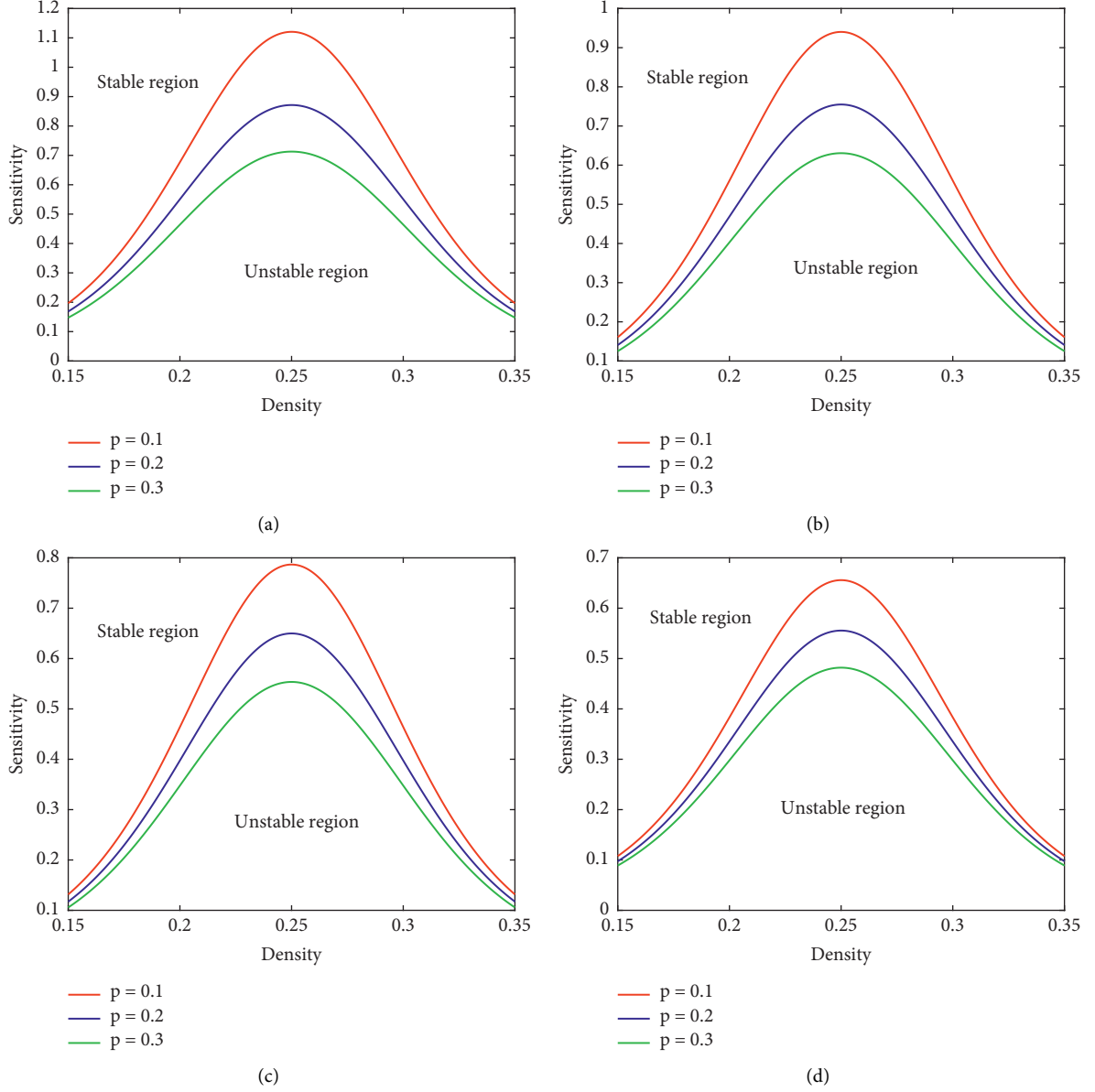
Figure 3: The neutral stability curves for $\tau = 1.5$ for different values of γ and p: (a) $\gamma = 0.05$; (b) $\gamma = 0.1$; (c) $\gamma = 0.15$; (d) $\gamma = 0.2$.

where
$$\begin{cases} V_F' = (dV(\rho)/d\rho)|_{\rho=\rho_c} \\ V_F'' = (d^3V(\rho)/d\rho^3)|_{\rho=\rho_c} \end{cases} \quad \text{and}$$
$\begin{cases} V_B' = (dV(\rho)/d\rho)|_{\rho=\rho_c} \\ V_B'' = (d^3V(\rho)/d\rho^3)|_{\rho=\rho_c} \end{cases}$. Near the critical point (ρ_c, a_c),
the value of a_c is defined as $a_c = a(1 + \varepsilon^2)$. The squared and cubic terms of ε are eliminated in equation (16) with the

consideration of $b = -\rho_c^2(V_F' + V_B')$. One can get the simplified equation as follows:

$$\begin{aligned} \varepsilon^4 &\left[\partial_T R - g_1 \partial_X^3 R + g_2 \partial_X R^3 \right] \\ &+ \varepsilon^5 \left[g_3 \partial_X^2 R + g_4 \partial_X^4 R + g_5 \partial_X^2 R^3 \right] = 0, \end{aligned} \quad (17)$$

where

$$g_1 = -\frac{1}{6}\rho_c^2\left(7V_B' + V_F' + 3p\rho_c^4\tau^2(V_B' + V_F')^3\right),$$

$$g_2 = \rho_c^2\left(V_F'' + V_B''\right),$$

$$g_3 = \frac{1}{2}\rho_c^2\left(3V_B' - V_F' - 2p(V_B' + V_F') + 2p\rho_c^2\tau(V_B' + V_F')^2\right),$$

$$g_4 = -\frac{1}{24}\rho_c^2\left(15V_B' - V_F' + 4p\rho_c^6\tau^3(V_B' + V_F')^4\right) - \frac{1}{3a}\rho_c^4(ap\tau - 1)(V_B' + V_F')\left(3p\rho_c^4\tau^2(V_B')^3 + V_F'\right)$$

$$- \frac{1}{3a}\rho_c^4(ap\tau - 1)(V_B' + V_F')\left(3p\rho_c^4\tau^2(V_F')^3 + V_B'\left(7 + 9p\rho_c^4\tau^2(V_F')^2\right)\right),$$

$$g_5 = -\frac{1}{12}\rho_c^2\left(3V_B'' - V_F''\right) - \frac{1}{3a}\rho_c^4(ap\tau - 1)(V_B' + V_F')\left(V_B'' + V_F''\right).$$

$$(18)$$

To derive the standard mKdV equation, the following transformations are applied:

$$T = \frac{1}{g_1}T',$$

$$R = \sqrt{\frac{g_1}{g_2}}R'.$$

$$(19)$$

Thus, equation (17) is converted into the standard mKdV equation as follows:

$$\partial_{T'}R' = \partial_X^3 R' - \partial_X R'^3 + \varepsilon\left[\frac{g_3}{g_1}\partial_X^2 R' + \frac{g_4}{g_1}\partial_X^4 R' + \frac{g_5}{g_2}\partial_X^2 R'^3\right].$$

$$(20)$$

When the term $O(\varepsilon)$ is ignored, the kink-antikink soliton solution of the mKdV equation can be rewritten as

$$R_0'(X, T') = \sqrt{c}\tanh\left(\sqrt{\frac{c}{2}}(X - cT')\right),$$

$$(21)$$

where c represents the propagation velocity. The specific value of c can be provided only when the following solvability condition is satisfied:

$$(R_0', M[R_0']) \equiv \int_{-\infty}^{\infty} dX R_0' M[R_0'] = 0,$$

$$(22)$$

where $M[R_0'] = (1/g_1)[g_3\partial_X^2 R' + g_4\partial_X^4 R' + (g_1 g_5/g_2)\partial_X^2 R'^3]$. By solving equation (22), the general solution of propagation velocity c can be calculated as

$$c = \frac{5g_2 g_3}{2g_2 g_4 - 3g_1 g_5}.$$

$$(23)$$

Hence, the corresponding kink-antikink solution is derived as

$$\rho_j = \rho_c + \varepsilon\sqrt{\frac{g_1 c}{g_2}}\tanh\left(\sqrt{\frac{c}{2}}(X - cg_1 T)\right),$$

$$(24)$$

where $\varepsilon^2 = ((a_c/a) - 1)$, and the amplitude of the density wave A is defined as $\sqrt{(g_1\varepsilon^2 C/g_2)}$. According to the kink-antikink solution equation (24), one can get the coexisting phases which include the freely moving phase with low density $(\rho_j = \rho_c - A)$ and the congested phase with high density $(\rho_j = \rho_c + A)$.

Based on the linear and nonlinear theory analyses, numerical simulations are carried out with the comprehensive consideration of the anticipation effect of flux difference and the "backward-looking" effect.

4. Numerical Simulations

As a positive constant γ considering the "backward-looking" effect has been studied fully in some previous studies [36, 40, 41], this paper will focus on the effects of parameters p and τ in this part. Periodic boundary conditions are adopted by a step function as follows:

$$\rho_j(0) = \rho_0 = 0.25, \quad j \in [1, N],$$

$$\rho_j(1) = \begin{cases} \rho_0; & j \neq \frac{N}{2}, \frac{N}{2} - 1, \\ \rho_0 + \Delta\rho; & j = \frac{N}{2} - 1, \\ \rho_0 - \Delta\rho; & j = \frac{N}{2}, \end{cases}$$

$$(25)$$

where $\Delta\rho = 0.01$ is the initial perturbation and other parameters are set as $N = 200$, $a = 1.2$, and $\rho_0 = \rho_c = 0.25$.

4.1. The Effect of Anticipation Time τ.

In order to analyze the anticipation time's influence on the stability of the traffic system, the temporal and spatial evolution of density waves between time $t = 10000 - 10200$ s is depicted in Figure 4 for different anticipation time τ with fixed parameters $p = 0.1$ and $\gamma = 0.05$. Since the given parameters in Figures 4(a)–4(c) do not satisfy the linear stable condition equation (14), kink-antikink density waves appear and the initial stable traffic flow evolves into nonuniform traffic flow with the added perturbation. To reveal the amplitude of the density wave more clearly, Figure 5 describes the density profile of each
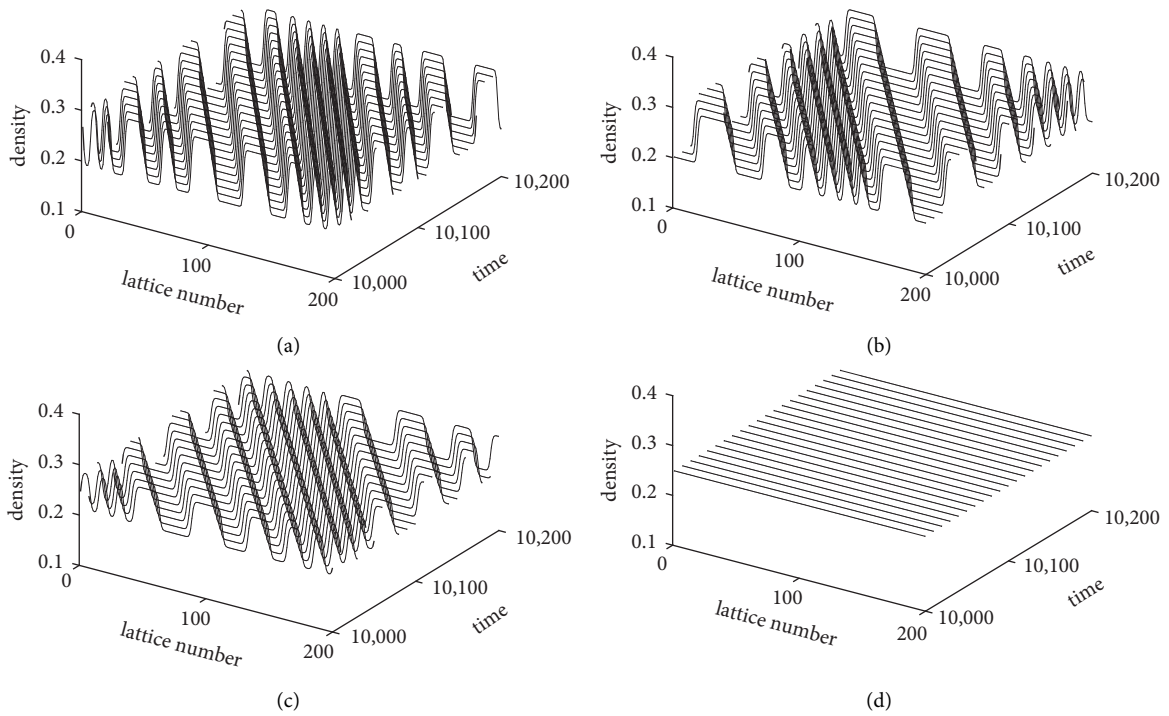
FIGURE 4: The evolution of the traffic densities for different values of parameter τ: (a) $\tau = 1.0$; (b) $\tau = 1.5$; (c) $\tau = 2.0$; (d) $\tau = 2.5$.
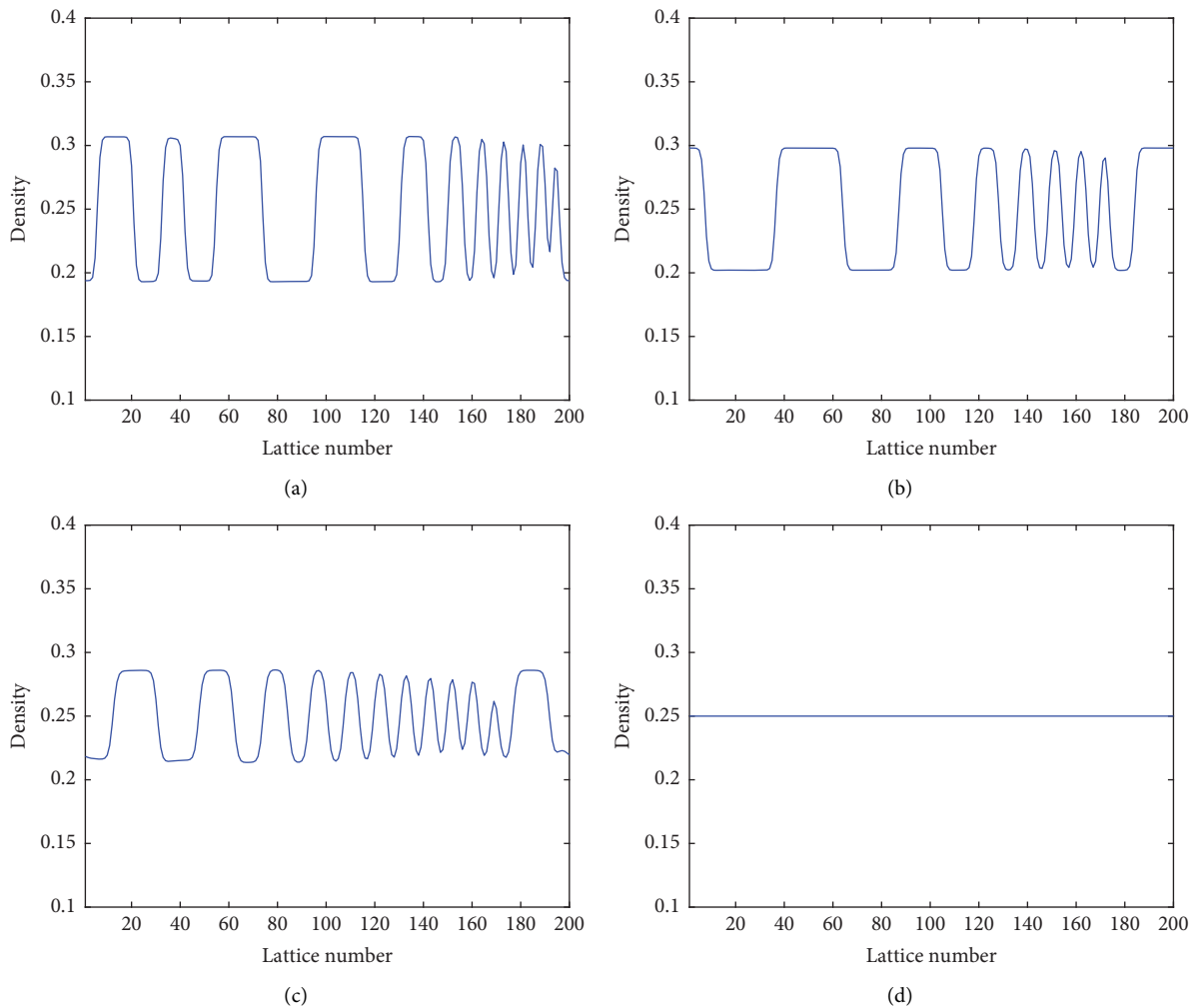
FIGURE 5: The density profile at $t = 10200$ with different values of τ: (a) $\tau = 1.0$; (b) $\tau = 1.5$; (c) $\tau = 2.0$; (d) $\tau = 2.5$.
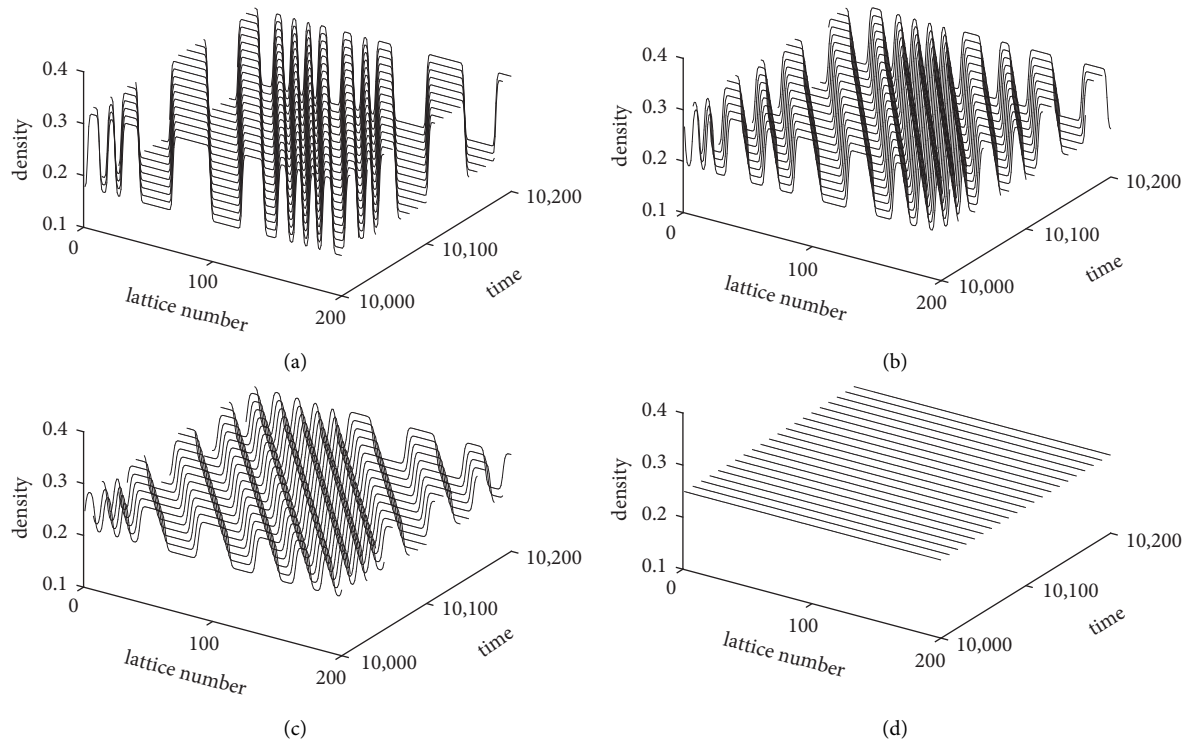
FIGURE 6: The evolution of the traffic densities for different values of parameter p: (a) $p = 0$; (b) $p = 0.05$; (c) $p = 0.1$; (d) $p = 0.15$.

(a)

(b)

FIGURE 7: Continued.

(c)
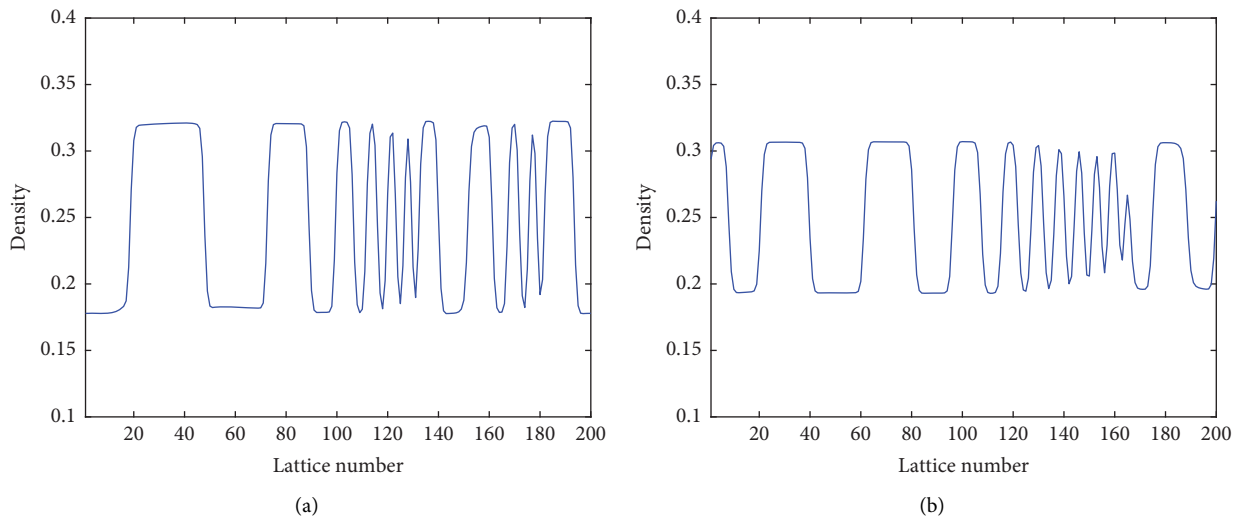
(d)

FIGURE 7: The density profile at $t = 10200$ with different values of p: (a) $p = 0$; (b) $p = 0.05$; (c) $p = 0.1$; (d) $p = 0.15$.
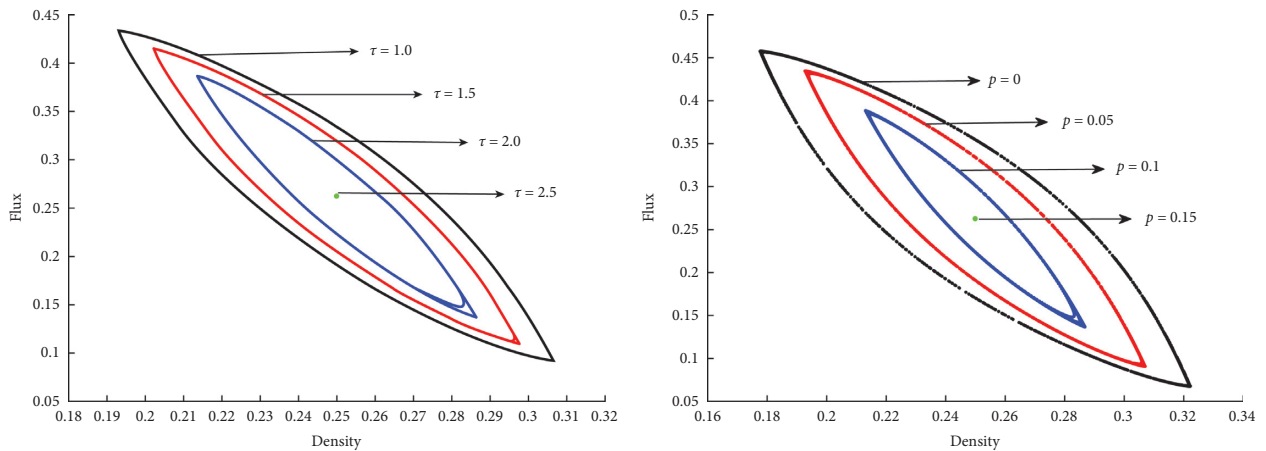
FIGURE 8: Hysteresis loops of traffic flux and density for (a) $\tau = 1$, 1.5, 2, and 2.5 with fixed $\gamma = 0.05$ and (b) $p = 0$, 0.05, 0.1, and 0.15 with fixed $\gamma = 0.05$.

subfigure shown in Figure 4 at $t = 10200$. Moreover, Figures 5(a)–5(c) reveal that the amplitudes of density waves corresponding to Figures 4(a)–4(c) weaken as the anticipation time τ increases. When $\tau = 2.5$, i.e., the parameters in Figure 4(d) satisfy the linear stability condition, the added perturbation will disappear, and the traffic flow will eventually return to a uniform state. Figure 5(d) can get results similar to Figure 4(d). This phenomenon indicates that driver's anticipation effect of flux difference could significantly promote the stabilization of traffic flow.

4.2. The Effect of Sensitivity Coefficient p. To expose the sensitivity coefficient's influence on the stability of the traffic system, the temporal and spatial evolution of density waves between time $t = 10000 - 10200$ s is exhibited in Figure 6 for different values of p with fixed $\gamma = 0.05$ and $\tau = 2$. When $p = 0$, the FADBE model degrades into Ge and Cheng's model [39]. Note that the parameters in Figures 6(a)–6(c) do

not satisfy the linear stable condition equation (14). Therefore, the stop-go traffic density waves occur with the small added perturbation in Figures 6(a)–6(c). Meanwhile, the amplitude of the density wave decreases gradually as the value of p increases. Especially in Figure 6(d), the congested state entirely disappears when $p = 0.15$. The relationship between Figures 6 and 7 is similar to the relationship between Figures 4 and 5. Figure 7 describes the density profile of each subfigure shown in Figure 6 at $t = 10200$. As parameter p increases, the traffic flow becomes more gentle and stable. This indicates that the sensitivity coefficient p contributes to suppressing the traffic congestion.

Figures 8(a) and 8(b) describe the flux against the density with different parameters corresponding to the traffic flow in Figures 4 and 6, respectively. In Figure 8, the amplitude of the hysteresis loops reduced with the increasing value of τ or p. When the corresponding parameter $\tau \geq 2.5$ or $p \geq 0.15$, the hysteresis loop turns into a stable point, which means that the traffic flow eventually becomes stable even with the

added small perturbation. To sum up, as the anticipation time τ or the sensitivity coefficient p increases, the stability of the system can be enhanced by incorporating the driver's anticipation effect and the "backward-looking" effect.

5. Conclusion

In this paper, a novel lattice hydrodynamic model with the anticipation effect of flux difference and the "backward-looking" effect is constructed to explore the traffic driving behavior for a single-lane traffic system. The stability conditions and the solution of the mKdV equation are deduced, respectively, based on the linear stability analysis and nonlinear theory. The results of the theoretical analysis display that the increasing values of both the driver's anticipation time and the sensitivity coefficient of the anticipation flux difference can contribute to enlarging the stable region. Numerical simulations reveal that the FADBE model is effective in stabilizing traffic flow even with perturbations. By considering the anticipation effect of flux difference and the "backward-looking" effect simultaneously, the traffic congestion can be alleviated effectively, which is in accordance with the conclusions of the theoretical analysis. Future work will focus on solving the traffic congestion on multilane road problem, the automation for longitudinal driving, and the vehicular emergency warning system.

Data Availability

The data used to support the findings of this study are available from the corresponding author upon request.

Conflicts of Interest

The authors declare that there are no conflicts of interest regarding the publication of this paper.

Acknowledgments

References

[1] H. Zhao, H. Yue, T. Gu, and W. Li, "Cps-based reliability enhancement mechanism for vehicular emergency warning system," *International Journal of Intelligent Transportation Systems Research*, vol. 17, no. 3, pp. 232–241, 2019.

[2] H. Zhao, H. Yue, T. Gu, C. Li, and D. Zhou, "Low delay and seamless connectivity-based message propagation mechanism for VANET of VCPS," *Wireless Personal Communications*, vol. 118, no. 4, pp. 3385–3402, 2021.

[3] T. Tang, H. Huang, S. C. Wong, and R. Jiang, "A car-following model with the anticipation effect of potential lane changing," *Acta Mechanica Sinica*, vol. 24, no. 4, pp. 399–407, 2008.

[4] T. Tang, W. Shi, H. Shang, and Y. Wang, "A new car-following model with consideration of inter-vehicle communication," *Nonlinear Dynamics*, vol. 76, no. 4, pp. 2017–2023, 2014.

[5] W.-X. Zhu and L.-D. Zhang, "A new car-following model for autonomous vehicles flow with mean expected velocity field," *Physica A: Statistical Mechanics and Its Applications*, vol. 492, pp. 2154–2165, 2018.

[6] H. Kuang, Z.-P. Xu, X.-L. Li, and S.-M. Lo, "An extended car-following model accounting for the average headway effect in intelligent transportation system," *Physica A: Statistical Mechanics and Its Applications*, vol. 471, pp. 778–787, 2017.

[7] H. Kuang, Z. P. Xu, X. L. Li, and S. M. Lo, "An extended car-following model accounting for the honk effect and numerical tests," *Nonlinear Dynamics*, vol. 87, 2017.

[8] W.-X. Zhu and L.-D. Zhang, "Analysis of car-following model with cascade compensation strategy," *Physica A: Statistical Mechanics and Its Applications*, vol. 449, pp. 265–274, 2016.

[9] M. Ma, G. Ma, and S. Liang, "Density waves in car-following model for autonomous vehicles with backward looking effect," *Applied Mathematical Modelling*, vol. 94, 2021.

[10] H. Zhao, Q. Chen, W. Shi, T. Gu, and W. Li, "Stability analysis of an improved car-following model accounting for the driver's characteristics and automation," *Physica A: Statistical Mechanics and Its Applications*, vol. 526, Article ID 120990, 2019.

[11] T.-Q. Tang, Y.-X. Rui, J. Zhang, and H.-Y. Shang, "A cellular automation model accounting for bicycle's group behavior," *Physica A: Statistical Mechanics and Its Applications*, vol. 492, pp. 1782–1797, 2018.

[12] M. Zamith, R. C. P. Leal-Toledo, E. Clua, E. M. Toledo, and G. V. P. d. Magalhães, "A new stochastic cellular automata model for traffic flow simulation with drivers' behavior prediction," *Journal of Computational Science*, vol. 9, pp. 51–56, 2015.

[13] R. Cheng, H. Ge, and J. Wang, "An extended macro traffic flow model accounting for multiple optimal velocity functions with different probabilities," *Physics Letters A*, vol. 381, no. 32, pp. 2608–2620, 2017.

[14] R. Cheng, H. Ge, and J. Wang, "KdV-Burgers equation in a new continuum model based on full velocity difference model considering anticipation effect," *Physica A: Statistical Mechanics and Its Applications*, vol. 481, 2017.

[15] H. Liu, P. Zheng, K. Zhu, and H. Ge, "KdV-Burgers equation in the modified continuum model considering anticipation effect," *Physica A: Statistical Mechanics and Its Applications*, vol. 438, pp. 26–31, 2015.

[16] G. Zhang, D.-H. Sun, H. Liu, and D. Chen, "Stability analysis of a new lattice hydrodynamic model by considering lattice's self-anticipative density effect," *Physica A: Statistical Mechanics and Its Applications*, vol. 486, pp. 806–813, 2017.

[17] G. Zhang, "The self-stabilization effect of lattice's historical flow in a new lattice hydrodynamic model," *Nonlinear Dynamics*, vol. 91, no. 2, pp. 809–817, 2018.

[18] G. Peng, "A new lattice model of traffic flow with the consideration of individual difference of anticipation driving behavior," *Communications in Nonlinear Science and Numerical Simulation*, vol. 18, no. 10, pp. 2801–2806, 2013.

[19] Y. Zhang, M. Zhao, D. Sun, Z. Zhou, and C. Dong, "A new feedback control scheme for the lattice hydrodynamic model with drivers' sensory memory," *International Journal of Modern Physics C*, vol. 32, 2021.

[20] Z. Li, X. Li, and F. Liu, "Stabilization analysis and modified KdV equation of lattice models with consideration of relative current," *International Journal of Modern Physics C*, vol. 19, no. 8, pp. 1163–1173, 2008.

[21] H. Zhao, D. Xia, S. Yang, and G. Peng, "The delayed-time effect of traffic flux on traffic stability for two-lane freeway,"

Physica A: Statistical Mechanics and Its Applications, vol. 540, Article ID 123066, 2020.

[22] C. Zhai and W. Wu, "Designing continuous delay feedback control for lattice hydrodynamic model under cyber-attacks and connected vehicle environment," *Communications in Nonlinear Science and Numerical Simulation*, vol. 95, Article ID 105667, 2021.

[23] G. Zhang and G.-H. Peng, "Research on the stabilization effect of continuous self-delayed traffic flux in macro traffic modeling," *Physica A: Statistical Mechanics and Its Applications*, vol. 526, Article ID 121012, 2019.

[24] G. Zhang, Y. Zhang, D.-B. Pan, and R.-J. Huang, "Study on the continuous delayed optimal flow on traffic stability in a new macro traffic model," *Physica A: Statistical Mechanics and Its Applications*, vol. 534, Article ID 122029, 2019.

[25] D. Helbing and M. Treiber, "Gas-kinetic-based traffic model explaining observed hysteretic phase transition," *Physical Review Letters*, vol. 81, pp. 3042–3045, 1999.

[26] T. Nagatani, "Modified KdV equation for jamming transition in the continuum models of traffic," *Physica A: Statistical Mechanics and Its Applications*, vol. 261, no. 3-4, pp. 599–607, 1998.

[27] G. Peng, F. Nie, B. Cao, and C. Liu, "A driver's memory lattice model of traffic flow and its numerical simulation," *Nonlinear Dynamics*, vol. 67, no. 3, pp. 1811–1815, 2012.

[28] Q. Zhai, H. Ge, and R. Cheng, "An extended continuum model considering optimal velocity change with memory and numerical tests," *Physica A: Statistical Mechanics and its Applications*, vol. 490, pp. 774–785, 2018.

[29] S. Qin, Z. He, and R. Cheng, "An extended lattice hydrodynamic model based on control theory considering the memory effect of flux difference," *Physica A: Statistical Mechanics and Its Applications*, vol. 509, pp. 809–816, 2018.

[30] C. Liu, Y. He, and G. Peng, "The impact of the density difference memory integral on traffic stability in two-lane lattice hydrodynamic model," *Physica A: Statistical Mechanics and Its Applications*, vol. 532, Article ID 121750, 2019.

[31] Q. Wang, R. Cheng, and H. Ge, "A novel lattice hydrodynamic model accounting for driver's memory effect and the difference of optimal velocity on curved road," *Physica A: Statistical Mechanics and Its Applications*, vol. 559, Article ID 125023, 2020.

[32] X. Li, K. Fang, and G. Peng, "A new lattice model accounting for multiple optimal current differences' anticipation effect in two-lane system," *Physica A: Statistical Mechanics and Its Applications*, vol. 486, pp. 814–826, 2017.

[33] A. K. Gupta and P. Redhu, "Analyses of driver's anticipation effect in sensing relative flux in a new lattice model for two-lane traffic system," *Physica A: Statistical Mechanics and Its Applications*, vol. 392, no. 22, pp. 5622–5632, 2013.

[34] D.-H. Sun, G. Zhang, M. Zhao, S.-L. Cheng, and J.-D. Cao, "Stability analysis of feedforward anticipation optimal flux difference in traffic lattice hydrodynamic theory," *Communications in Nonlinear Science and Numerical Simulation*, vol. 56, pp. 287–295, 2018.

[35] T. Wang, Z. Gao, J. Zhang, and X. Zhao, "A new lattice hydrodynamic model for two-lane traffic with the consideration of density difference effect," *Nonlinear Dynamics*, vol. 75, 2014.

[36] C. Jiang, R. Cheng, and H. Ge, "An improved lattice hydrodynamic model considering the "backward looking" effect and the traffic interruption probability," *Nonlinear Dynamics*, vol. 91, no. 2, pp. 777–784, 2018.

[37] G. Peng, W. Lu, and H. He, "Impact of the traffic interruption probability of optimal current on traffic congestion in lattice model," *Physica A: Statistical Mechanics and Its Applications*, vol. 425, pp. 27–33, 2015.

[38] D.-H. Sun, G. Zhang, W.-N. Liu, M. Zhao, S.-L. Cheng, and T. Zhou, "Effect of explicit lane changing in traffic lattice hydrodynamic model with interruption," *Nonlinear Dynamics*, vol. 86, pp. 269–282, 2016.

[39] H.-X. Ge and R.-J. Cheng, "The "backward looking" effect in the lattice hydrodynamic model," *Physica A: Statistical Mechanics and Its Applications*, vol. 387, no. 28, pp. 6952–6958, 2008.

[40] Q. Wang and H. Ge, "An improved lattice hydrodynamic model accounting for the effect of "backward looking" and flow integral," *Physica A: Statistical Mechanics and Its Applications*, vol. 513, pp. 438–446, 2019.

[41] X. Qi, H. Ge, and R. Cheng, "Analysis of a novel lattice hydrodynamic model considering density integral and "backward looking" effect," *Physica A: Statistical Mechanics and Its Applications*, vol. 525, pp. 714–723, 2019.

[42] A. K. Gupta and P. Redhu, "Analyses of the driver's anticipation effect in a new lattice hydrodynamic traffic flow model with passing," *Nonlinear Dynamics*, vol. 76, no. 2, pp. 1001–1011, 2014.

[43] T. Wang, R. Zang, K. Xu, and J. Zhang, "Analysis of predictive effect on lattice hydrodynamic traffic flow model," *Physica A: Statistical Mechanics and Its Applications*, vol. 526, Article ID 120711, 2019.

[44] D. Kaur and S. Sharma, "A new two-lane lattice model by considering predictive effect in traffic flow," *Physica A: Statistical Mechanics and Its Applications*, vol. 539, Article ID 122913, 2020.

[45] S. Sharma, "Effect of driver's anticipation in a new two-lane lattice model with the consideration of optimal current difference," *Nonlinear Dynamics*, vol. 81, no. 1-2, pp. 991–1003, 2015.

[46] P. Redhu and A. K. Gupta, "Effect of forward looking sites on a multi-phase lattice hydrodynamic model," *Physica A: Statistical Mechanics and Its Applications*, vol. 445, pp. 150–160, 2016.

[47] Y. Chang and R. Cheng, "Effect of speed deviation and anticipation effect of flux difference in the lattice hydrodynamic model," *Physica A: Statistical Mechanics and Its Applications*, vol. 531, Article ID 121751, 2019.

WILEY | Hindawi

Research Article

Corrosion Predictive Model in Hot-Dip Galvanized Steel Buried in Soil

Lorena-De Arriba-Rodríguez, Francisco Ortega-Fernández, Joaquín M. Villanueva-Balsera [ID], and Vicente Rodríguez-Montequín [ID]

Project Engineering Area, University of Oviedo, C/Independencia 13, 33004 Oviedo, Spain

Correspondence should be addressed to Vicente Rodríguez-Montequín; montequi@uniovi.es

Corrosion is one of the main concerns in the field of structural engineering due to its effect on steel buried in soil. Currently, there is no clearly established method that allows its calculation with precision and ensures the durability of this type of structures. Qualitative methods are commonly used rather than quantitative methods. The objective of this research is the development of a multivariate quantitative predictive model for estimating the loss of thickness that will occur in buried hot-dip galvanized steel as a function of time. The technique used in the modelling is the Adaptive Regression of Multivariate Splines (MARS). The main drawback of this kind of studies is the lack of data since it is not possible to have a priori the corrosive behaviour that the buried material will have as a function of time. To solve this issue, a solid and reliable database was built from the analysis and treatment of the existing literature and with the results obtained from a predictive model to estimate the thickness loss of ungalvanized steel. The input variables of the model are 5 characteristics of the soil, the useful life of the structure, and the loss of corroded ungalvanized steel in the soil. This last data is the output variable of another previous predictive model to estimate the loss of thickness of bare steel in a soil. The objective variable of the model is the loss of thickness that hot-dip galvanized steel will experience buried in the ground and expressed in g/m^2. To evaluate the performance and applicability of the proposed model, the statistical metrics RMSE, R^2, MAE, and RAE and the graphs of standardized residuals were used. The results indicated that the model offers a very high prediction performance. Specifically, the mean square error was $290.6\,g/m^2$ (range of the objective variable is from $51.787\,g/m^2$ to $5950.5\,g/m^2$), R^2 was 0.96, and from a relative error of 0.14, the success of the estimate was 100%. Therefore, the use of the proposed predictive model optimizes the relationship between the amount of hot-dip galvanized steel and the useful life of the buried metal structure.

1. Introduction

Soil is a complex and highly heterogeneous environment whose local characteristics damage buried or semiburied steel structures [1]. The main cause of failure of this type of structure is the corrosion [2, 3]. Corrosion is a mechanism of steel degradation that deteriorates the metal until it ends up causing the failure of the infrastructure [4, 5]. Throughout history, there have been numerous environmental disasters and risks to human health derived from this type of structural failure [6, 7]. In addition to its consequences on the resistance of structures, it also has an economic impact

[8]. The corrosion that occurs in buried steel represents a serious economic and environmental problem [9]. In 2016, the National Association of Corrosion Engineers International revealed that the global cost triggered by corrosion in 2013 represented 3.4 of world Gross Domestic Product [10].

In the design of buried steel structures, it is intended to define the appropriate amount of steel in accordance with the required guarantees that ensure its useful life. Currently, many infrastructure projects are being undertaken that require a buried structure for which a long-term guarantee is required, such as solar plants. These kinds of projects are usually performed under the form of EPC (engineering,

procurement, and construction) contracts. The contractor usually has to offer a long-life guaranty of the facility (e.g., solar plants could be more than 25 years). Under this context, it is not enough following the existing standards for the design of the structure, but they need to determine the thickness of coating to have enough chance of accomplishing the guaranty avoiding the expensive penalties. To achieve the optimal trade-off between safety and cost of buried steel structures, it is vital to provide designers with the optimal tools [11]. The problem is that there is no clearly established method that provides quantitative values for the loss of thickness that galvanized steel will experience over time [12, 13]. The engineer/designer has to study in depth the effect of soil corrosion to size this type of infrastructure and then look at the reference guides published by lobby of the relevant industry sector and select the option that best fits the calculation.

The most accepted methodology for the evaluation of the corrosive nature consists of using qualitative guidelines to predict the aggressiveness of the soil on the metal and using extrathicknesses to ensure the durability and safety of the structure [14]. These methodologies are tables that relate the fundamental variables that intervene in the loss of thickness of the material with points. Depending on the result obtained, they classify the soils according to their aggressiveness into generic groups, without distinguishing the specific characteristics of each place or determining quantitative data that facilitate the design. Based on these guidelines, the responsible engineer must decide the thickness that will guarantee the useful life of the infrastructure and that will not cause its collapse and its serious consequences for humans, the environment, and the economy.

The most widespread qualitative techniques are the standards developed by the American Society for Testing and Materials (ASTM G187-18), the National Association of Corrosion Engineers (NACE), and the American Association of Works of Water (ANSI/AWWA C105) [15–17]. The NACE and ASTM methods are tables that relate soil resistivity with the severity of corrosion. Depending on the values presented by the soil, five corrosive degrees are differentiated: negligible, mild, moderate, severe, and extreme. Their main drawback is that they only consider one parameter. Therefore, its applicability is very limited since the final corrosion is due to the combined effect of several factors [18, 19]. The AWWA standard is the most widely used method to predict the corrosive behaviour of buried galvanized steel [20]. It consists of a point system that qualitatively classifies corrosive behaviour. Each type of soil is obtaining different qualifications depending on the resistivity, the pH, and the redox power. Total amount of these variables is classified into four corrosive categories: mild, moderate, appreciable, and severe. Although it considers more soil characteristics than the NACE and ASTM methods, they are still few compared to the variables involved in corrosion.

Although the most widely used methodologies are those cited above, there are more studies that develop this qualitative approach of classifying the degree of soil corrosion based on the factors that they consider to be the most influential in corrosion [21–23]. The main advantage of all of them is that they are generally simple formatting and handling tables or diagrams. This simplicity that allows an agile use of the tool is also associated with its main disadvantage since it does not provide a numerical value. Therefore, the engineer who uses this type of technique obtains information on the rate of corrosivity of the soil that will affect the buried metallic structure, but it is the designer who decides the thickness of the galvanized steel. They are methods strongly subject to interpretation and do not help to decide optimal galvanized steel thicknesses based on the lifetime of the structure.

The work developed by Romanoff for the United States National Standards Office (NBS) is one of the most outstanding studies in the field of quantifying the loss of thickness experienced by metals buried in the soil. In 1910, this revolutionary scientist led the most comprehensive and exemplary quantitative study on the corrosion experienced by galvanized steel buried in the soil. The project consisted of burying thousands of galvanized steel strips in soils with different corrosive characteristics and analysing their evolution over approximately 20 years. As a result, in 1957 Romanoff published a series of tables detailing the characteristics of the soils and the evolution of the thickness loss that had occurred in metals [24]. Later, he carried out another series of works that supplemented his initial research [25]. The reason that it is considered the most important study in the field of engineering related to corrosion is due to the duration of the tests, the large number of samples, the number of soils with different characteristics, and that it was an experiment carried out in a real environment. However, the project had the drawback that it focused especially on bare steel and the number of samples dedicated to galvanized steel being much smaller.

Subsequent quantitative studies have been carried out based on burying galvanized steel samples in the soil and periodically digging them up to calculate their mass loss [26, 27]. The main disadvantages that they present in comparison to Romanoff tables are short duration of the test, use of simulated environments in the laboratory, small number of samples, small number of soils, or study of few corrosive factors.

In recent years, a new quantitative approach has been initiated in the field of soil corrosion, which consists of modelling the results obtained in real or laboratory tests of the evolution of corrosion over time. Several methods have been used for modelling, mainly neural networks, genetic algorithms, and fuzzy adaptive systems [28–32]. The problem is that these methods require very large databases, and in most studies, the raw data tend to respond to tests of short duration, with few soils or in simulated environments that do not allow its use to be extrapolated to other locations. In this study, the Multivariate Adaptive Regression Splines (MARS) method has been used. It is a nonparametric regression technique that provides optimal results when there is a limited number of cases.

When comparing quantitative and qualitative methods, it is evident that the first are a more precise tool in the design

of buried steel structures. However, the use of the qualitative approach is much more extended. The main reason is that there is no clearly established quantitative method and those that do exist are complex and require more time to use. In addition, the most important quantitative research led by Romanoff are data tables published in 1952 that describe the effect of corrosion over time of steels and steel alloys that were used at that time in the construction of buried metal structures.

In this sense, the predictive model developed in this research allows to automatically obtain the loss of thickness of the buried material. It is a model fed by a database created from the tests that Romanoff carried out in a real environment and for more than 20 years with galvanized steel. The database includes the physical, chemical, granulometric, and climatological characteristics of the soil that influence the rate of corrosion and the real effect that they caused on the metal. To complete this information, the output variable of another predictive model on the loss of thickness of bare steel in the soil due to corrosion has been introduced as an input variable, for which there is a more extensive database [33]. Once these data have been processed, the duration and number of soils analysed allows the results to be extrapolated to any type of soil.

The material used in the development of this work is a reference steel in construction models: hot galvanized steel. Currently, it is used in partially or fully buried in soil in power transmission and distribution structures, solar projects, or storage of different chemicals [34–36]. Metallic coatings of zinc and their alloys are widely used to protect the base steel against corrosion phenomena that can take place in the steel/environment interaction [37, 38]. In 2003, the International Lead Zinc Research Organization led a project that concluded that zinc coatings reduce corrosion rates, promote uniform attack, and ultimately increase the life of structures in the ground [39]. The hot galvanizing technique consists of immersing a suitably conditioned steel strip in a bath of molten zinc [40]. Thus, a rapid reaction is generated between the molten zinc and the steel, producing an intimate union (intermetallic layer) between both materials. Control of the thickness of the intermetallic layer is done by adding aluminium to the bath.

A fact that Romanoff himself was able to conclude in his research was the existence of similar behaviours in terms of corrosion experienced by galvanized steel in the different groups of soils (reducing, oxidizing, alkaline, acidic, etc.), being the behaviours between groups much more diverse than in the case of bare steel, while within each group they are more homogeneous. For instance, on acid-oxidizing inorganic soils, the galvanized coating remained virtually intact even after 13 years of exposure. On the contrary, acid-reducing organic soils presented a more heterogeneous behaviour in terms of their corrosion rate, although in all cases, the galvanized coating used in the tests (with a thickness of 3 oz/ft^2, which is equivalent to about 915 g/m^2) ends up being consumed at the end of the tests.

These behaviours show that the oxidizing or reducing, acidic to alkaline, and organic or inorganic nature of the soil where the structure is buried plays a very important role.

Therefore, it is possible to draw conclusions by classifying soils based on three main variables: if the soil was organic or inorganic, if the soil was acidic or alkaline, and if the environment was oxidizing or reducing. Based on these three characteristics, the soils have been classified as follows: Cinders (Cin), Acid Oxidizing Inorganic (AOI) soils, Inorganic Oxidizing Alkaline (IOA) soils, Acid Reducing Inorganic (ARI) soils, Inorganic Alkaline Reducing (IAR) soils, and Acid Reducing Organic (ARO) soils. It should be noted that, for the rest of the possible combinations of values of these variables, there was no soil among those studied by Romanoff that fulfilled them. To determine the group to which the case under study belongs, the factors, degree of soil aeration, organic or inorganic nature, pH value (acidic or basic nature), and whether the water table is reached must be studied.

The objective of this study is the construction of a quantitative predictive model that estimates the thickness of hot-dip galvanized steel buried in the soil that will be lost over time due to the effect of corrosion. In this way, the engineer in charge of the design of this type of the structure will have a quantitative value of the loss of the material that the buried galvanized steel will experience as a function of time.

The paper is organized as follows. First, the composition of the studied galvanized steel is presented. Then, the steps for the construction of the database were described and how the model was built using the MARS technique. Finally, the results are presented and discussed, and the conclusions obtained in the investigation are detailed.

2. Materials and Methods

Starting from the data collected in the literature, a solid and robust database of hot-dip galvanized steel samples has been analysed, transformed, and prepared. Finally, a model has been developed to quantitatively estimate the loss of thickness that will occur in buried galvanized steel. The process is detailed below.

2.1. Hot-Dip Galvanized Steel. The material studied in this research is hot-dip galvanized steel. The approximate composition of steel (wt. %) is 0.09% carbon, 0.39% manganese, 0.08% phosphorus, and 0.04% sulphur, and its density is greater than that attributed to iron, reaching 7850 kg/m^3. The galvanized coating used has a thickness of 3 oz/ft^2 equivalent to about 915 g/m^2 and consists of a continuous zinc coating with a density of 7140 kg/m^3.

2.2. Database. The database that feeds the models has been constituted from two different sources: on the one hand, from the values compiled in the tables prepared by Romanoff and Denison [24, 25]; on the other hand, from the results of a predictive model that estimates the corrosion of buried bare steel. To continue, it is detailed how the data collected in the literature has been analysed and refined. Then, the introduction of the output variable of the other model in the database is explained.

Romanoff led a project that studied the corrosion of galvanized steel in 62 different soils. In 47 of them, only a point value of the loss of thickness of galvanized steel is available, which was taken around 10 years after burial. In the remaining 15 soils, various corrosion measurements are available at different times between the start of the experiment and its completion. The collection of these data provides much information on the evolution of corrosion over time and provides a detailed characterization of the soil variables involved in corrosion.

Once the raw data was configured, the next step was to assess the quality of the information contained in that set. After an exhaustive analysis, it was determined that there were deficiencies in the set that had to be solved for the database to be solid and reliable. These limitations had already been previously detected in other publications [41]. All of them are summarized in two groups: lack of data for some variables in the original trials and identification of unusual values.

To detect unusual values, the dispersion of each variable in each soil was studied. For instance, Figure 1 shows the scatter plot of the total acidity variable where the 62 soils studied by Romanoff are located on the x-axis and the y-axis showing its total acidity value. As can be seen, there is a value that is far to the rest of the values that the variable usually takes. These results that come out of the range of usual values of the variables have been defined as outliers.

After its identification, each specific outlier was studied, grouping its causes into two types: on the one hand, strange values due to errors in measurement, annotation, or transcription in the original tests; on the other hand, rare data due to real measurements in soils with special characteristics and, therefore, not caused by measurement or transcription errors.

The solution that has been adopted for the problem of the absence of data is not to fill in empty values by cases. The reason is that entering new data would distort the initial information. For unusual values, only cases where they have been shown with certainty to be errors have been removed. The selection of the MARS algorithm as a prediction technique has allowed working with a limited set of samples since this technique adjusts to this type of dataset better than other modelling techniques that require a more abundant dataset.

In summary, the treatment of the Romanoff data that has been carried out to achieve a reliable and representative database is described in Table 1.

Once the limitations of Romanoff's research were resolved, the way to solve the problem of data scarcity was studied. After multiple tests, it was concluded that the only possible way to generate a reliable model to predict the corrosion of galvanized steel was to add to the database the parameter thickness loss in g/m^2 experienced by bare steel buried in the ground. The problem is that when a soil is to be studied to bury a galvanized steel structure, the loss of thickness that bare steel will experience in that same soil is not available. The decision taken to compensate for the lack of information was to enter into the database the information on the estimate of the loss of thickness of bare steel
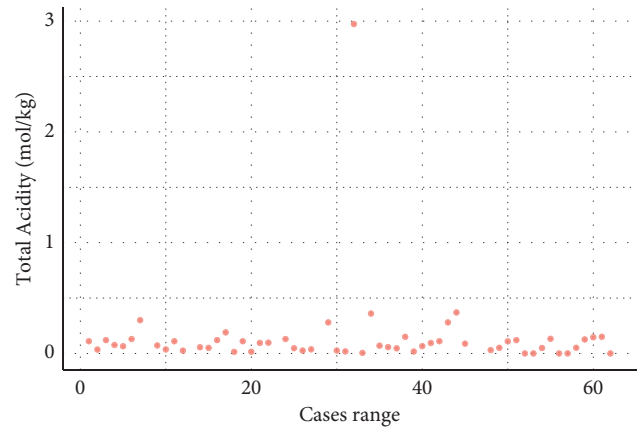
Figure 1: Scatter plot of the total acidity variable.

Table 1: Treatment of the database.

Database problems	Solution
Empty values	Not to falsify data
Outliers:	
Errors	Elimination
Soil with special characteristics	Not worked

provided by the basic predictive model of a previous study [33].

Once the modifications explained have been made, a reliable dataset is available which constitutes a firm foundation to feed the predictive models.

2.3. Predictive Model. The technique used for the development of the predictive corrosion estimation model is the MARS algorithm. This algorithm was designed by Friedman in 1991 to solve difficult, multivariate regression problems with complex nonlinear relationships. Regression problems are those in which a model must predict a numerical value. Its selection is based on its predictive capacity, its multidimensional adjustment, its robustness, and that once trained, it can be easily implemented in an application [42].

The MARS algorithm consists of finding a set of simple linear functions (splines) that characterize the data and uses them together to obtain the best predictive performance. The procedure consists of partitioning the definition domain of the function into different regions and adjusting each of them to a spline-type function. The MARS algorithm generates many of these simple linear functions, called base functions for one or more input variables.

The construction of the MARS model to fit the data is carried out in two phases [43]. In the first, an algorithm is used to select the base functions and the nodes. In the second, an algorithm is used to eliminate base functions, until the best set of these is found. At each step, the base function is suppressed, the elimination of which improves the degree of fit or causes the least loss of information. The purpose of this last stage is to reduce the degree of complexity of the model and significantly reduce the high dimensionality of the problem.

MARS is a multidimensional fitting method, and its objective is to approximate an unknown function f defined in a domain D contained in the vector space R^n, to a domain D' defined in R, from the projection of a sample of data from the input space onto the space of exit. For this, the algorithm looks for the approximation function $f''(x_1, x_2, \ldots, x_n)$, by means of the linear combination of a set of base functions $B_i(x)$ parameterized by the position of the nodes.

The final approximation provided by MARS is in the form of the following equation:

$$f'(x_1, x_2, \ldots, x_n) = \sum_{i=1}^{M} a_i B_i(x), \tag{1}$$

where x belongs to D' contained in Rm and $1 \le m \le n$ is the number of variables involved in the construction of the base function B_i.

The coefficients of the base functions B_i are a_i variables, and M is the number of base functions of the model.

The base functions used by MARS are built as products of base functions:

$$b_k(x) = (x - t_k)_+ = \mathrm{Max}(0, x - t_k), \tag{2}$$

where t_k is the position of node k and the subscript "+" denotes the positive part of the affected parentheses.

The maximum number of base functions involved in the construction (number of products) is called the number of interactions between the variables. The value of this parameter is set by the user, and it remains fixed during algorithm training.

Thus, the base functions used by the MARS algorithm have the following form:

$$B_i(x) = \begin{cases} 1, & i = 1, \\ \prod_{j=1}^{J_i} \left[S_{ji} \cdot \left(x_{v(j,i)} - t_{ji} \right) \right]_+, & i = 2, 3, \ldots, \end{cases} \tag{3}$$

where J_i is the degree of interaction of the Bi functions, S_{ji} is the sign indicator (± 1), $v(j, i)$ is the index of the independent variable that is being divided, and t_{ji} the position of the division and is called the node.

In this paper, the input variables of the algorithm are 7, and they are detailed in Table 2. The output of the model is the loss of mass due to corrosion that galvanized steel will experience on the soil, expressed in g/cm^2.

The performance of this tool for the design of a galvanized steel structure on a soil consists in introducing in the model the 7 input variables of Table 2. Then, the developed model provides a quantitative value in g/m^2 of the loss of thickness that the material will experience.

3. Results and Discussion

A key phase in the development of a predictive model is the evaluation of the reliability of its predictions. The aim is to compare the estimates proposed by the model with the real corrosion values in the training and test phases of the model.

Table 2: Input variables for the predictive model of galvanized steel.

Input variables	Unit
Resistivity	Ohm m
Temperature	°C
Precipitation	mm/year
Soil moisture	%
pH	—
Time	years
Loss of mass due to corrosion of bare steel	g/m²

The problem is that it is not possible to have a priori the corrosive behaviour that galvanized steel buried in soil will suffer over time. Therefore, the only way to evaluate the accuracy of the model is by dividing the database created with the actual values of thickness loss of galvanized steel due to corrosion in training and test patterns.

It was decided to allocate 90% of the cases to training patterns and 10% to test patterns. The reason for choosing a 90/10 ratio is based on the fact that removing more than 10% of the information that feeds the model in the training phase could distort the results due to the loss of relevant information.

The model has been trained with the degree of interaction between variables equal to 2 and maximum number of model terms before pruning, i.e., the maximum number of terms created by the forward pass equal to 35.

The following sections detail the evaluation of the predictive model. In addition, an analysis of the results according to the type of soil has been carried out to study the homogeneity of the corrosive behaviour in soils with the same typology.

3.1. Predictive Model. The statistical metrics used to evaluate the goodness of the model are Root Mean Square Error (RMSE), Coefficient of Determination (R^2), Mean Absolute Error (MAE), and Relate Absolute Error (RAE).

In addition, a graphic study of standardized residuals has been carried out. The residual concept refers to the difference between the real value and the result predicted by the model and is therefore the estimation error. The graphs that have been used in this paper were regression error characteristic curve (REC), observed vs predicted, density of residuals, normal Q-Q, and scale location.

3.1.1. RMSE and R^2. It is important to highlight that the object variable has a variation interval between 51.87 and 5950.5 g/m^2. The RMSE and R^2 results obtained in the training and the model test are shown in Table 3.

An RMSE (train) = 280.43 and RMSE (test) = 290.60 have been obtained. As the variation range of the object variable is from 51.87 to 5950.5, the errors generated by the model in both cases are low for the slack experienced by the variable. The behaviour in both phases is very similar, so we can conclude that the model is stable.

The R^2 value is very close to 1 in the model in the training phase and in the test phase. In the latter case, the result is slightly higher due to the smaller number of cases.

TABLE 3: RMSE and R^2 of the model in the training and analysis phase.

Phase	RMSE (g/m^2)	R^2
Train analysis	280.43	0.93
Test analysis	290.60	0.96

3.1.2. REC. The purpose of Regression Error Characteristic curves is to compare different regression models. To do this, they plot the tolerance for error on the *x*-axis versus the precision of a regression model on the *y*-axis [44]. This accuracy value is calculated as the percentage of cases that fit each relative error tolerance.

Figure 2 shows the REC curve that results from comparing the training model (green line) and the test model (blue line). In addition, a control model (red line) has been considered that corresponds to the mean value of the corroded thickness. The quick rising of the curve to the top entails that the model provides correct predictions.

Table 4 shows the relationship between the RAE and the precision of the estimate in a quantitative way. In addition, it adds the MAE metric that expresses the loss of thickness in g/m^2 that each percentage of relative error supposes.

As we can see in Table 4, the test phase and the training have a similar behaviour, which makes the model stable. Furthermore, for a relative error of 0.1, a precision of 0.95 over 1 is reached, and from a relative error of 0.14, the precision is maximum. In addition, it provides a significant improvement over the defined control.

3.1.3. Predicted vs Predicted Plot. Figure 3 reflects the results obtained when comparing the real corrosion values of galvanized steel with the values estimated by the model. In Figure 3(a), we can see the result of the training model, and in 3(b), the behaviour in the test phase. The blue line corresponds to the theoretical evolution of the model, and the points are the estimates it provides. The further the predictions are from the blue reference line, the points are represented by colours ranging from green (optimal) to red (maximum error).

The only difference between the behaviour in the training phase and in the test phase is the amount of data. In both cases, the points are adjusted to the theoretical evolution of the model, indicating an optimal behaviour of the predictive model.

3.1.4. Density of Residuals' Plot. The density plot detects the incorrect behaviour of the residuals and shows us the shape of the distribution of the relative error of the model. The peaks of the function reflect where the error values are concentrated.

Figure 4 shows the density plot of the predictive model in the training phase and in the test phase. As we can see, in both cases, the model of the relative error distribution is adjusted to the normal distribution.

The curves are highly centred on the mean errors, indicating that there are few modelling failures.
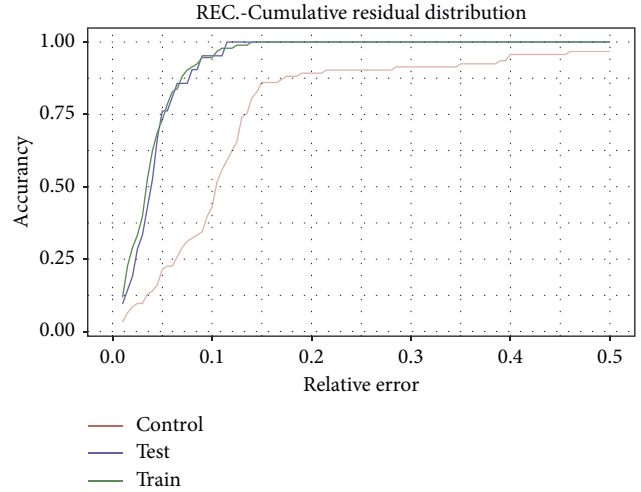
FIGURE 2: REC plot of the predictive model.

TABLE 4: RAE, MAE, and model accuracy training results.

RAE (%)	MAE (g/m^2)	Accuracy
0.01	59	0.11
0.05	295	0.75
0.10	590	0.95
0.14	826	1
0.20	1180	1
0.25	1475	1

3.1.5. Normal Q-Q. A Q-Q graph has been made to know the distribution of the error in the model. As we can see in Figure 5, both in the case of training and in the test, the points fall on the diagonal. This means that the model error follows a normal distribution.

The training phase and the test phase indicate that the predictive model follows a normal error distribution. Therefore, for errors that are associated with randomness, there is no cause of failure in the model.

3.1.6. Scale-Location Plot. Scale location plot is used to assess the independence of the model residuals. For a correct functioning of the model, they must respond to a cloud of points without any pattern. In Figure 6 we see that, in both the training and test models, there is no pattern in the placement of the points.

In this graph, the model in the training phase and the test phase do not follow any pattern; therefore, no anomalies are detected.

The statistical values RMSE, R^2, MAE, and RAE that have been obtained in the training and test models are very similar and reflect a stable and precise behaviour of the model. The standardized residual plots confirm that there are no anomalies in the performance and that the distribution of the errors adjusts to the normal distribution, which show the success of the estimates.

Therefore, according to the comparative evaluation of the training and testing phase carried out in this study, the results obtained show that the predictive model developed in
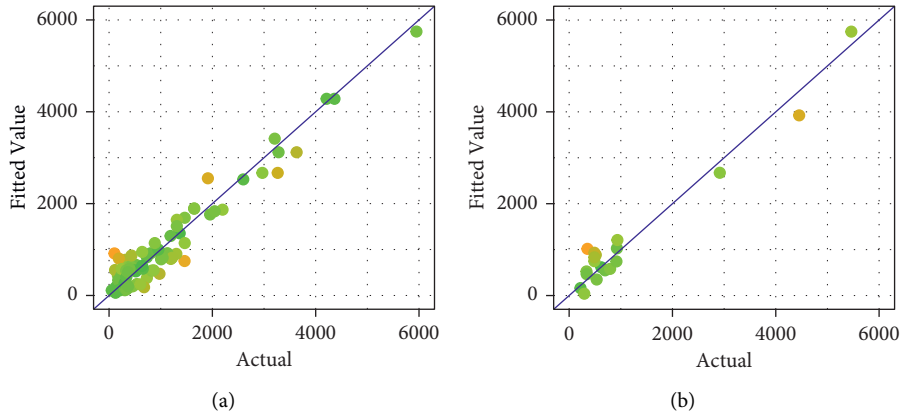
Figure 3: Real value vs estimate in the training phase (a) and in the test phase (b).
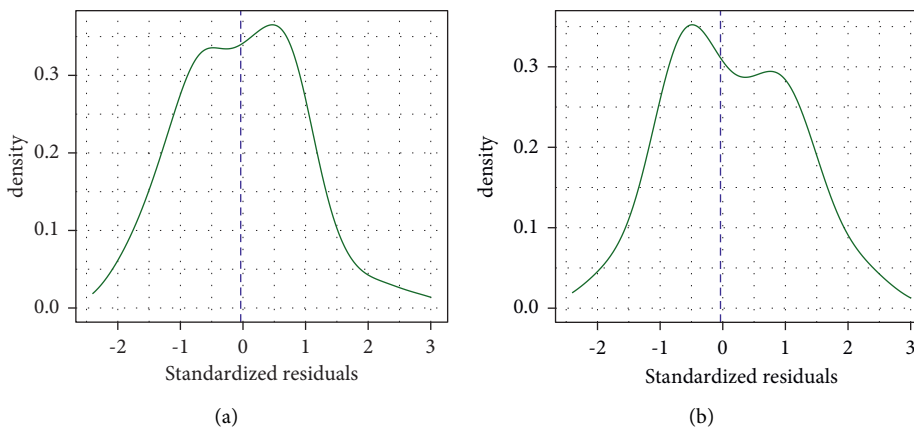
Figure 4: Density plot of the model in the training phase (a) and in the test phase (b).
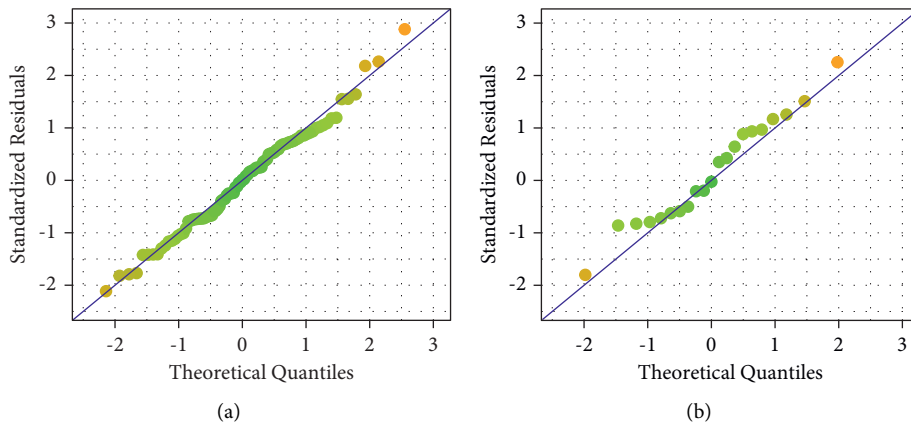
Figure 5: Normal Q-Q plot of the predictive model in training (a) and in test (b).

this paper allows to successfully estimate the loss of thickness of hot-dip galvanized steel buried in a soil. The main advantage of the developed model is that it provides the quantitative value of the thickness that will be lost due to the corrosion of the steel in the useful life of the structure. In this way, the quantity of the material is optimized with its service time. In addition, it eliminates the subjectivity in the

dimensioning of the structure, avoiding an excess of thickness that increases the cost of the structures.

3.2. Study of the Influence of the Type of Soil. As already mentioned in this paper, the existing literature in the field of corrosion corroborates similar behaviours of galvanized

(a)

(b)
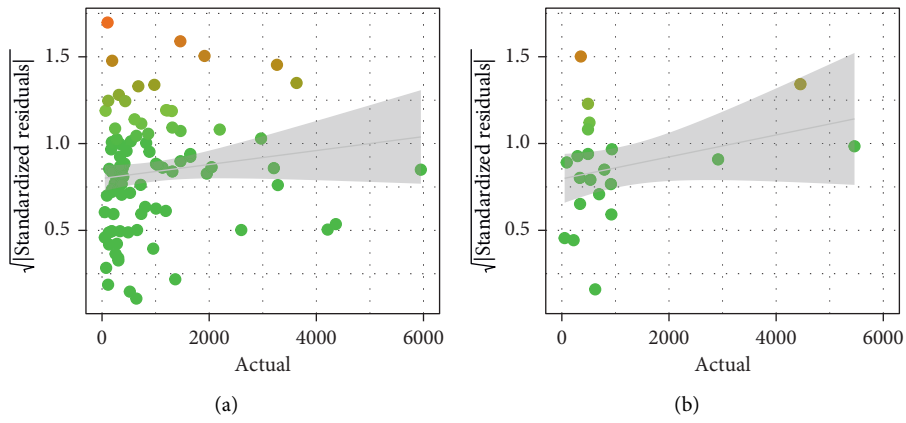
FIGURE 6: Scale-location plot in the training phase (a) and in the test (b).

TABLE 5: Analysis of the number of cases and the average thickness loss by soil type.

Soil group	Number of cases (%)	Average thickness loss
Cin	4.39	2704.31
AOI	28.95	247.07
IOA	9.65	469.66
ARI	18.42	664.98
IAR	18.42	1114.37
ARO	20.17	1918.90
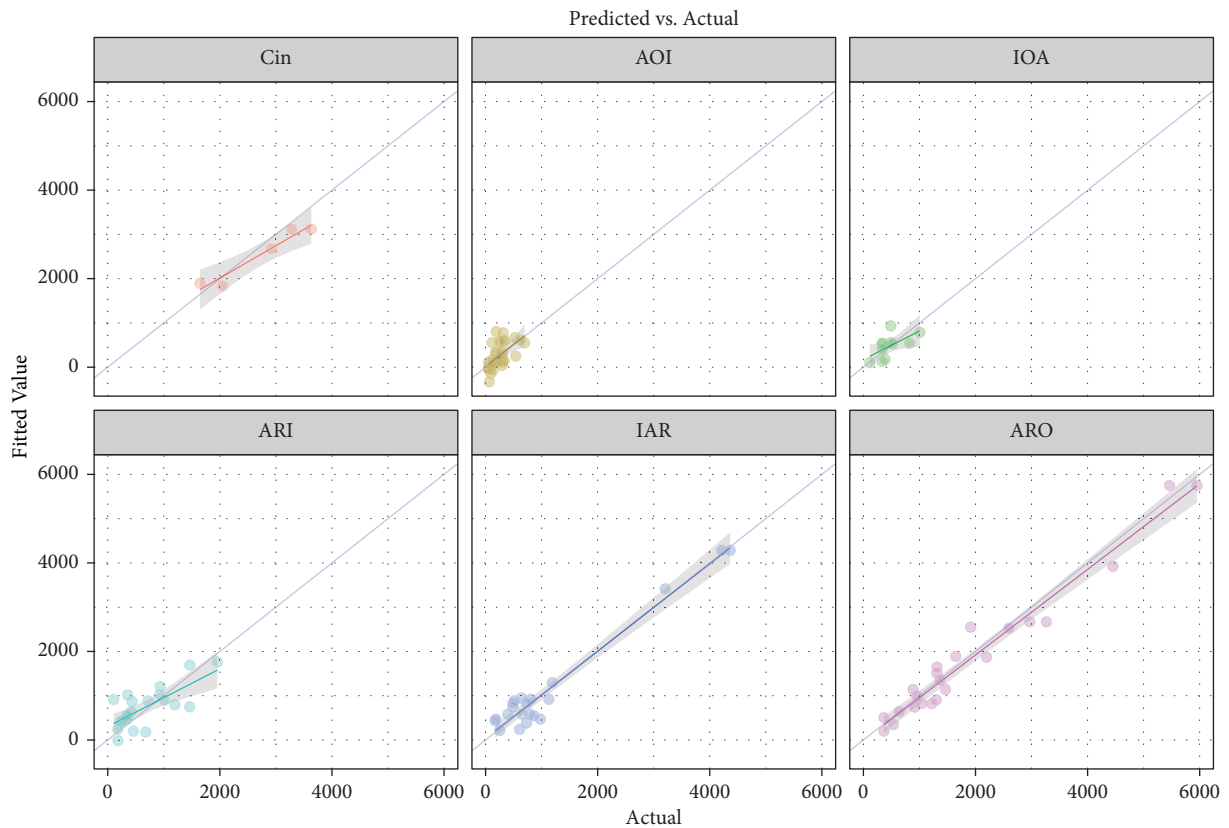
FIGURE 7: Predicted vs actual plot for each soil type.
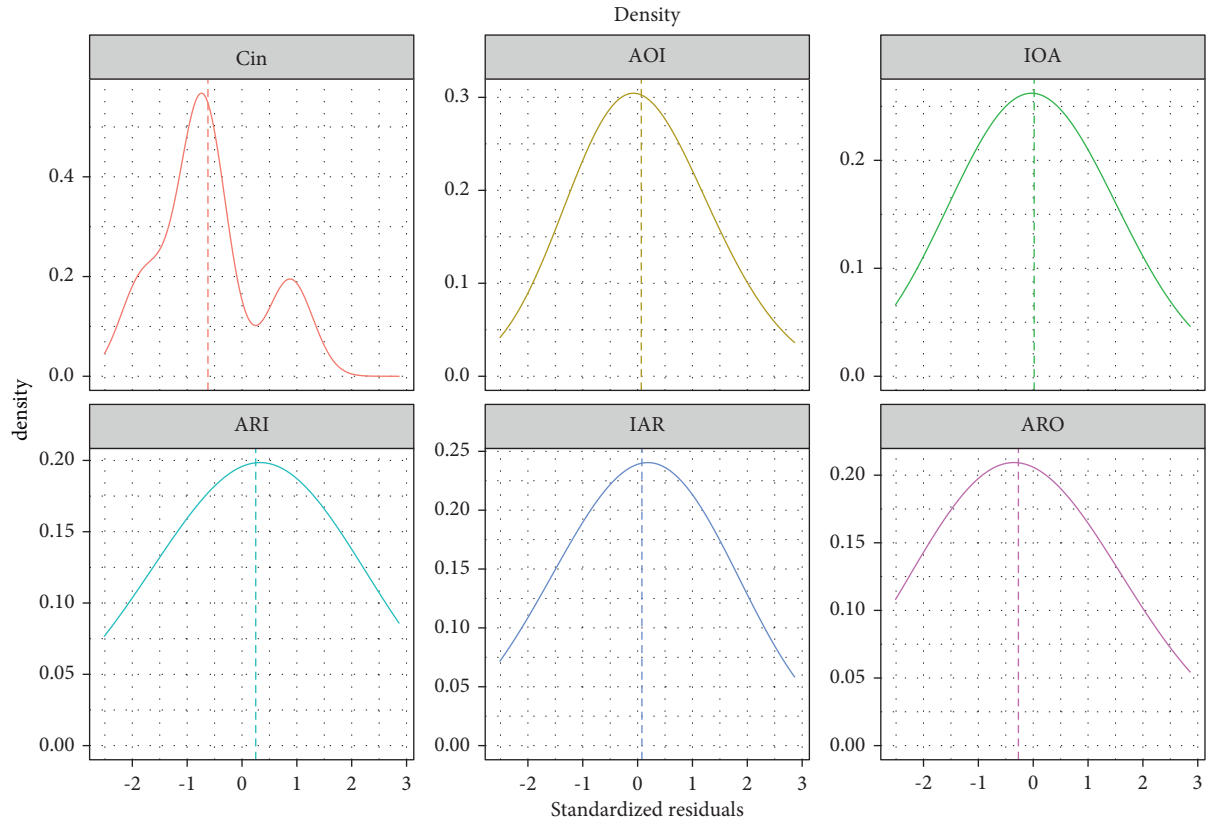
FIGURE 8: Density plot for each type of soil.

steel buried in soils of the same typology. For this reason, the study of the object variable, metal thickness loss, has been considered relevant, depending on the soil groups. Remember that the soils collected in the database are divided into Cin, AOI, IOA, ARI, IAR, and ARO.

Table 5 shows the amount of data available for each of them and the average loss of thickness of galvanized steel buried in each type of soil.

Figure 7 shows the progression of the model results in the optimal case (blue line) and the predictions made by the model for each of the soil types (points).

In all types of soil, the trend of the points is close to the main diagonal that represents the theoretical behaviour of the model; therefore, the behaviour is stable.

The distribution of the results for each type of soil is grouped in different areas of the main diagonal; accordingly, it is evident that the loss of thickness is similar to each type of soil.

The density graph has been constructed for each one of the soils to detect if there is any anomalous behaviour of the errors (Figure 8).

The functions are highly centred on the mean of the errors, which indicates the goodness of the model. There is an anomalous behaviour in the case of the Cin soil type, and the reason is that, of this soil, we have very few cases in the database (less than 5%).

The analysis of results by type of soil shows similar behaviours for soils belonging to the same typology, as shown in the existing bibliography.

4. Conclusions

The most widely used methods to estimate the thickness loss suffered by steel buried in a soil are qualitative guidelines that provide information on the aggressiveness of the corrosion. Therefore, the dimensioning of the structure depends on the responsible engineer. The predictive model developed in this paper consists of a multivariate quantitative model that provides the loss of thickness in g/m^2 as a function of the useful life of the structure. The model is fed from a database consisting of real tests that Romanoff carried out for more than 20 years and is completed with the results of a multivariate predictive model that estimates the loss of ungalvanized steel in the soil due to corrosion.

One of the most remarkable points of the model is that we are introducing as input of the model the output given by other model that predicts the loss of thickness that a bare steel will experience in the same conditions. So, with this information, the model is able to learn the inherent relations and extrapolate all this information to forecast the loss of thickness of the galvanized steel.

The use of the model makes the dimensioning of the structure independent of the engineer, and an efficient relationship between the amount of material and durability is achieved. The results were evaluated through a comparative statistical analysis between the model in the training and testing phase, which confirmed the reliability of the estimates and the good performance of the model. In addition, it

shows the homogeneity of the corrosion behaviour in soils of similar typologies.

The major limitation of this study is the lack of data. Accordingly, the recommendations for future research are to carry out new tests in the areas of the multidimensional space that present lower density of points in order to achieve a more representative dataset. Due to the large time frames required to carry out representative tests on the evolution of corrosion over time, the database can be supplemented with accelerated corrosion tests to study the effect of specific conditions on the metal. Furthermore, a limitation of the research is that it responds to a single construction material. Therefore, the introduction of other reference materials in the field of structural engineering is proposed as a future line of research.

Data Availability

The data supporting this research are from previously reported studies and datasets, which have been cited.

Conflicts of Interest

The authors declare that they have no conflicts of interest.

References

[1] O. Oudbashi, "A methodological approach to estimate soil corrosivity for archaeological copper alloy artefacts," *Heritage Science*, vol. 6, no. 1, p. 2, 2018.

[2] K. M. Usher, A. H. Kaksonen, I. Cole, and D. Marney, "Critical review: microbially influenced corrosion of buried carbon steel pipes," *International Biodeterioration & Biodegradation*, vol. 93, pp. 84–106, 2014.

[3] A. Chen, X. Ruan, and D. M. Frangopol, "Life-cycle civil engineering: innovation, theory and practice," in *Proceedings of the 7th International Symposium on Life-Cycle Civil Engineering*, CRC Press, Shangai, China, February 2021.

[4] O. V. Hembara and O. E. Andreikiv, "Effect of hydrogenation of the walls of oil-and-gas pipelines on their soil corrosion and service life," *Materials Science*, vol. 47, no. 5, pp. 598–607, 2012.

[5] R. Pierre and P. D. Roberge, *Handbook of Corrosion Engineering*, ISBN 978-260-7, McGraw-Hill Education, New York, NY, USA, Third edition, 2019.

[6] K. Siler-Evans, A. Hanson, C. Sunday, N. Leonard, and M. Tumminello, "Analysis of pipeline accidents in the United States from 1968 to 2009," *International Journal of Critical Infrastructure Protection*, vol. 7, no. 4, pp. 257–269, 2014.

[7] G. A. Papadakis, "Major hazard pipelines: a comparative study of onshore transmission accidents," *Journal of Loss Prevention in the Process Industries*, vol. 12, no. 1, pp. 91–107, 1999.

[8] B. Hou, X. Li, X. Ma et al., "The cost of corrosion in China," *Npj Materials Degradation*, vol. 1, no. 1, pp. 1–10, 2017.

[9] G. H. Koch, M. P. H. Brongers, N. G. Thompson, Y. P. Virmani, and J. H. Payer, "Corrosion Cost and Preventive Strategies in the United States (No. FHWA-RD-01-156)," *CC Technologies Laboratories*, U.S. Federal Highway Administration, Washington, DC, USA, 2002.

[10] G. Koch, J. Varney, N. Thompson, O. Moghissi, M. Gould, and J. Payer, "International measures of prevention, application, and economics of corrosion technologies study," *NACE International*, vol. 216, 2016.

[11] A. Yajima, H. Wang, R. Y. Liang, and H. Castaneda, "A clustering based method to evaluate soil corrosivity for pipeline external integrity management," *International Journal of Pressure Vessels and Piping*, vol. 126-127, pp. 37–47, 2015.

[12] L.-d. Arriba-Rodriguez, J. Villanueva-Balsera, F. Ortega-Fernandez, and F. Rodriguez-Perez, "Methods to evaluate corrosion in buried steel structures: a review," *Metals*, vol. 8, no. 5, p. 334, 2018.

[13] Y. Beauregard and A. Mah, "Assessing soil corrosivity for buried structural steel," in *Proceedings of the International Pipeline Conference, American Society of Mechanical Engineers Digital Collection*, vol. 84447, p. V001T03A005, Virtual conference, 2021.

[14] A. Poudel, K. Prasad Dahal, K. C. Dinesh, and J. Bhattarai, "A classification approach for corrosion rating of soil to buried water pipelines: a case study in budhanilkantha-maharajganj roadway areas of Nepal," *World Journal of Applied Chemistry*, vol. 5, no. 3, p. 47, 2020.

[15] ASTM G187 - 18, Standard Test Method for Measurement of Soil Resistivity Using the Two-Electrode Soil Box Method, 2005.

[16] American Water Works Association ANSI/AWWA C105, *Ductil-Iron Pipe Standard*, American Water Works Association, Denver, CO, USA, 2012.

[17] P. R. Roberge, *Corrosion Basics: An Introduction*, NACE international, Houston, TX, USA, 2006.

[18] M. N. Norhazilan, Y. Nordin, K. S. Lim, R. O. Siti, A. R. A. Safuan, and M. H. Norhamimi, "Relationship between soil properties and corrosion of carbon steel," *Journal of Applied Sciences Research*, vol. 8, pp. 1739–1747, 2012.

[19] R. Amaya-Gómez, E. Bastidas-Arteaga, F. Muñoz, and M. Sánchez-Silva, "Statistical soil characterization of an underground corroded pipeline using in-line inspections," *Metals*, vol. 11, no. 2, p. 292, 2021.

[20] H. Najjaran, R. Sadiq, and B. Rajani, "Modeling pipe deteriorarion using soil properties - an application of fuzzy logic expert system," *Pipeline Engineering and Construction*, vol. 2004, Article ID 14673, 10 pages, 2004.

[21] M. Taghipour, G. R. Lashkaripour, M. Ghafoori, and N. Hafezimoghaddas, "Evaluating the soil corrosion of bushehr, Iran, based on a new classification system for corrosive soils," *Anti-corrosion Methods & Materials*, vol. 63, no. 5, pp. 347–354, 2016.

[22] European Standard Store EN 12501-2, *Protection of Metallic Materials against Corrosion*, European Standard Store, Pilsen, Czech Republic, 2003.

[23] German Technical and Scientific Association for Gas and Water DVGW GW 9, Evaluation of Soils in View of Their Corrosion Behaviour towards Buried Pipelines and Vessels of Non-alloyed Iron Materials, 2011.

[24] M. Romanoff, *Underground Corrosion*, US Government Printing Office, Washington, DC, USA, 1957.

[25] I. A. Denison and M. Romanoff, "Corrosion of galvanized steel in soils," *Journal of Research of the National Bureau of Standards*, vol. 49, no. 5, pp. 299–316, 1952.

[26] D. Nguyen Dang, L. Lanarde, M. Jeannin, R. Sabot, and P. Refait, "Influence of soil moisture on the residual corrosion rates of buried carbon steel structures under cathodic protection," *Electrochimica Acta*, vol. 176, pp. 1410–1419, 2015.

[27] T. Wu, J. Xu, M. Yan, C. Sun, C. Yu, and W. Ke, "Synergistic effect of sulfate-reducing bacteria and elastic stress on

corrosion of X80 steel in soil solution," *Corrosion Science*, vol. 83, pp. 38–47, 2014.

[28] J. L. Alamilla, M. A. Espinosa-Medina, and E. Sosa, "Modelling steel corrosion damage in soil environment," *Corrosion Science*, vol. 51, no. 11, pp. 2628–2638, 2009.

[29] F. A. V. Bazán and A. T. Beck, "Stochastic process corrosion growth models for pipeline reliability," *Corrosion Science*, vol. 74, pp. 50–58, 2013.

[30] C. Yang, "Parallel-series multiobjective genetic algorithm for optimal tests selection with multiple constraints," *IEEE Transactions on Instrumentation and Measurement*, vol. 67, no. 8, pp. 1859–1876, 2018.

[31] J. Zhang, H. Sun, Z. Sun, W. Dong, and Y. Dong, "Fault diagnosis of wind turbine power converter considering wavelet transform, feature analysis, judgment and BP neural network," *IEEE Access*, vol. 7, pp. 179799–179809, 2019.

[32] A. Pourdaryaei, H. Mokhlis, H. A. Illias, S. H. A. Kaboli, and S. Ahmad, "Short-term electricity price forecasting via hybrid backtracking search algorithm and ANFIS approach," *IEEE Access*, vol. 7, pp. 77674–77691, 2019.

[33] L.-D. Arriba-Rodríguez, V. Rodríguez-Montequín, J. Villanueva-Balsera, and F. Ortega-Fernández, "Design of predictive models to estimate corrosion in buried steel structures," *Sustainability*, vol. 12, no. 23, p. 9879, 2020.

[34] D. Nakhaie, A. Kosari, J. M. C. Mol, and E. Asselin, "Corrosion resistance of hot-dip galvanized steel in simulated soil solution: a factorial design and pit chemistry study," *Corrosion Science*, vol. 164, Article ID 108310, 2020.

[35] L. Hanson, "Increase stell service life using hot-dip galvanizing," *Building blocks*, vol. 11, 2015.

[36] American Galvanizers Association, *Performance of Hot-Dip Galvanized Steel Products*, American Galvanizers Association, Centennial, CO, USA, 2010.

[37] Robinson, J; Ltd, P., *Predicting the In-Ground Performance of Galvanized Steel*, Robinson, J; Ltd, P, Rock Hill, South Carolina, 2005.

[38] R. F. D. C. Pereira, E. S. D. D. Oliveira, M. A. G. D. A. Lima, and S. L. D. C. Brasil, "Corrosion of galvanized steel under different soil moisture contents," *Materials Research*, vol. 18, no. 3, pp. 563–568, 2015.

[39] International Lead Zinc Research Organization Review of Data Available on the Corrosion Rate of Galvanized Steel in Soil, 2003.

[40] J. Bian, Y. Zhu, X.-H. Liu, and G.-D. Wang, "Development of hot dip galvanized steel strip and its application in automobile industry," *Journal of Iron and Steel Research International*, vol. 13, no. 3, pp. 47–50, 2006.

[41] R. E. Ricker, "Analysis of pipeline steel corrosion data from NBS (NIST) studies conducted between 1922-1940 and relevance to pipeline management," *Journal of research of the National Institute of Standards and Technology*, vol. 115, no. 5, p. 373, 2010.

[42] J. H. Friedman, "Multivariate adaptive regression splines," *Annals of Statistics*, vol. 19, pp. 1–67, 1991.

[43] M. Kuhn and K. Johnson, *Applied Predictive Modelling*, vol. 26, Springer, Berlin, Germany, 2003.

[44] B. Aşıkgil and A. Erar, "Regression error characteristic curves based on the choice of best estimation method," *Selçuk Journal of Applied Mathematics*, vol. 14, pp. 1–9, 2013.

WILEY | Hindawi

Research Article

Evaluation of Several Machine Learning Models for Field Canal Improvement Project Cost Prediction

Saadi Shartooh Sharqi [iD] [1] **and Aayush Bhattarai** [iD] [2]

[1]*Civil Engineering Department, Engineering College, University Of Anbar, Ramadi, Iraq*
[2]*Department of Mechanical and Aerospace Engineering, Pulchowk Campus, Institute of Engineering, Tribhuvan University, Kathmandu, Nepal*

Correspondence should be addressed to Aayush Bhattarai; aayush@pcampus.edu.np

Project cost prediction is one of the key elements in the civil engineering activities development. Project cost is a highly sensitive component to diverse parameters and hence it is associated with complex trends that make it difficult to be predicted and fully understood. Due to the massive advancement of soft computing (SC) and Internet of things (IoT), the main research objective of the current study was initiative. Several machine learning (ML) models including extreme learning machine (ELM), multivariate adaptive regression spline (MARS), and partial least square regression (PLS) were adopted to predict field canal cost. Several essential predictors were used to develop the prediction network "the learning process" including the total length of the PVC pipeline, served area, geographical zone, construction year, and cost and duration of field canal improvement projects (FCIP) construction. Data were collected from the open source published literature. The modeling results evidenced the potential of the applied SC models in predicting the FCIP cost. In numerical magnitude evaluation, MARS model indicated the least value for the root mean square error (RMSE = 27422.7), mean absolute error (MAE = 19761.8), and mean absolute percentage error (MAPE = 0.05454) with Nash–Sutcliffe efficiency (NSE = 0.94), agreement index (MD = 0.89), and coefficient of determination ($R^2 = 0.94$), with best precision of prediction using all predictors, except geographical zone parameter in which less influence on the cost construction is presented. In general, the research outcome gave an informative primary cost initiative for cost civil engineering project.

1. Introduction

The scarcity of freshwater has been a global problem recently and expected to worsen in the future due to the increasing human population and decline in annual water allocation per capita [1, 2]. The present scenario portrays water unsustainability due to the drastic increase in water utilization (>6 folds) in the 20th century [3]. It is presently estimated that about 1.2 billion people globally have no access to a clean water supply [4]. Hence, several policies and projects are being implemented globally to ensure water sustainability. One of such projects aimed at water sustainability is the FCIP which aims at increasing the conveyance efficiency of field canals by about 25% via improvement of the field canals during irrigation

processes in farmlands [5]. The project requires the construction of a burden PVC pipeline rather than relying on earthen field canals for the reduction of water seepage or losses during field operations [6]. FCIP is comprised of several simple components and structures which include concrete pain intakes for water collection from the source; water is channelled through the suction pipes to a plain concrete sump [7]. Water is first accumulated in the sump before being pumped by the pumping sets through the PVC pipelines by the irrigation valves. The FCIPs are comprised of civil works, mechanical components, and electrical components as the major components. The components of the civil works are the pump house, pipelines, suction pipes, intake, and sump structure while the mechanical components are the

irrigation valves, pump sets, and mechanical connections. The electrical boards and connections make up the electrical components of FCIPs [8].

The most interesting part of FCIPs is the cost estimation aspect that must be performed; manual cost estimation processes are time-consuming [9]. However, in some cases, scan be attained based on personal engineering and decision-makers' expertise. Cost estimation is highly associated with bias and inaccuracy and to overcome these issues of bias and inaccuracy during cost estimation [10]. Therefore, SC models have been proposed as the potential solution. In line with this, the aim of this work is to come up with a robust ML-based SC model for FCIP cost estimation. The proposed models are expected to help decision-makers and management engineers in making decisions from the perspective of the stockholders.

Literature review studies suggested that numerous researches have focused on the development of reliable regression and mathematical techniques that can be used for cost estimation in civil engineering projects [11–16]. The nagging problem in this domain still relates to the performance accuracy of these models as the predicted cost is required to be highly accurate before the conception of the project. The weighted ANN has been developed for unit cost prediction in highway projects by [16], while a parametric cost model was developed based on a questionnaire survey for the estimation of the final cost of pump stations by [17]. A fuzzy logic- (FL-) based parametric cost estimate model has been presented by [18], for the prediction of the cost of building projects in the Gaza Strip. The study by [19] presented a hybrid ANN-FL model for cost prediction of water infrastructure. The prediction of the unit cost of the highway project in Libya using the ANN model has been presented by [20] and the performance of the ANN model was excellent. A conceptual cost model for the German residential building project was developed by [21] using historical data for 75 residential projects sourced from the building cost information center. The use of ANN to determine the relevant parameters for cost prediction during tunnel construction in Greece was reported by [22] based on survey questionnaires. The survey was based on expert opinions and interviews in relation to the key cost drivers.

The reviewed literature suggests the need for intelligence models that are robust and capable of understanding the civil engineering complexity in more realistic manners. Several ML models have been reported recently, such as ANN [23], SVM [24], ANFIS [25], genetic programming [26], decision tree [27], and gradient boosting [28], and several others were reported in the latest review [29]. However, the fact remains that each of these models behaves differently in terms of prediction accuracy. Some existing models are also capable of providing accurate results interpretation; for instance, the variable coefficients of the regression models can explain the influence of each variable on the response of the model.

Numerous studies have focused on building projects without giving much attention to the conceptual cost of FCIPs. Hence, the attention of this study is on the pipeline construction projects which have not attracted appropriate research attention, especially on the provision of detailed model development

steps in terms of sample size, multicollinearity, outliers, and singularity. For instance, the study by [16] only applied 14 and 4 cases for the training and validation of their neural network model. This may have elicited concerns about the sample size in this study as stated by [30]. The motivation of the current study was inspired from the exhibited literature on the prediction of the FCIP cost using newly explored machine learning models including ELM, MARS, and PLS. These models are proven to be advantageous as they have very quick learning speeds with good performances and are useful in capturing complicated data mapping in very high set of predictors which produces interpretative results [31–34]. Modeling structure was adopted based on the correlation statistic to identify the input predictors for the built ML models. Based on the reported modeling results, comprehensive comparative analytical aspects were reported and discussed.

2. Soft Computing Models

2.1. Extreme Learning Machine. ELM model is one of the new methods of training recently developed single-layer feedforward neural networks [35]. The traditional ELM, as shown in Figure 1, has one input layer, one hidden layer, and one output layer; each of these layers has a specific number of neurons. The linear function is generally selected as the activation function of the input and output layers of ELM while the sigmoid function is selected for the hidden layer [36]. The first step of the standard ELM is a random input weight and hidden biases determination, followed by the determination of the hidden weights using the Moore–Penrose generalized inverse method to achieve the optimal solution of the linear system [37]. The advantages of the ELM over the other gradient-based methods are its strong generalization capability, no parameter tuning, and fast learning; these have made ELM more popular in numerous engineering tasks [38–40]. Consider a training dataset with N samples; the first process is to linearly map the input vectors into an L-dimensional feature space via nonlinear transformation; the expression of the simulated values of the ELM model is as follows:

$$\widetilde{t}_i = \sum_{l=1}^{L} \beta_l \cdot g\left(w_l \cdot x_i + b_l\right), \quad i = 1, 2, \ldots, N, \tag{1}$$

where N represents the number of samples for training, $\widetilde{t}_i$ represents the output vectors that are associated with the input vector x_i; β_l stands for the weight vectors that connect the hidden neuron to the output layer; w_l is the weight vectors that connect the hidden neuron with the input layer; b_l is the bias; and g is the activation function.

In the ELM, the idea is that the classical single-layer ANN can approach all the samples with zero deviation as mathematically expressed in the relation:

$$\sum_{i=1}^{N} t_i - \widetilde{t}_t = \sum_{i=1}^{N} \left\| t_i - \sum_{l=1}^{L} \beta_l \cdot g\left(w_l \cdot x_i + b_l\right) \right\| = 0, \tag{2}$$

where t_i is the target output vector that is related to the input vector x_i. The reconstruction of the above expression gives the following:

$$\tilde{t}_i = \sum_{i=1}^{L} \beta_i \cdot g(w_l \cdot x_i + b_l)$$
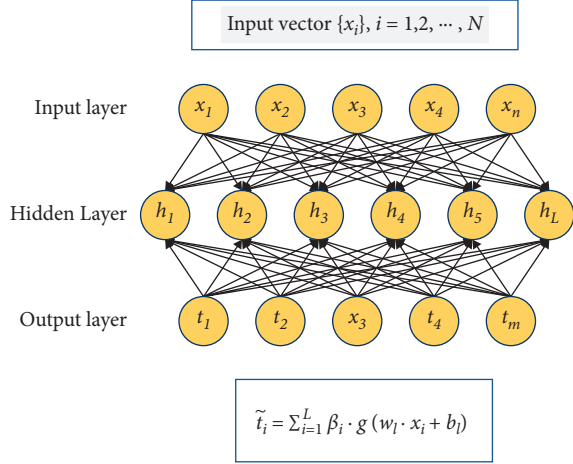
FIGURE 1: The extreme learning machine model paradigm.

$$H\beta = T, \tag{3}$$

where

$$H = \begin{bmatrix} g(w_1 \cdot x_1 + b_1) & \cdots & g(w_L \cdot x_1 + b_L) \\ \vdots & \ddots & \vdots \\ g(w_1 \cdot x_N + b_1) & \cdots & g(w_L \cdot x_N + b_L) \end{bmatrix}_{N \times L},$$

$$\beta = \begin{bmatrix} \beta_{1,1} & \cdots & \beta_{1,m} \\ \vdots & \ddots & \vdots \\ \beta_{L,1} & \cdots & \beta_{L,m} \end{bmatrix}_{L \times m}, \tag{4}$$

$$T = \begin{bmatrix} t_{1,1} & \cdots & t_{1,m} \\ \vdots & \ddots & \vdots \\ t_{N,1} & \cdots & t_{N,m} \end{bmatrix}_{N \times m},$$

where β is the weight of the matrix that connects the hidden and output layers; H is the hidden layer output matrix based on N samples; and T is the target output matrix based on N samples.

Assume that the hidden biases and input weights are constant; it implies that the model may be considered a special linear system in which H and T are equal to the matrixes of the known dependent and independent parameters, while β is considered the coefficient matrix that should be optimized. Hence, the least-squares solution of the represented linear system mentioned above can be derived as

$$\tilde{\beta} = H^{\dagger}T, \tag{5}$$

where $H^{\dagger}$ is the Moore–Penrose generalized inverse matrix of H.

2.2. Multivariate Adaptive Regression Spline Model.

MARS algorithms are nonlinear-nonparametric flexible regression models that were first developed by [41] and have found application in many fields of engineering due to their robustness [42]. This model is built with three major components, which are the basis functions (BFs), the knots, and the spline function [43]. The role of the BFs is to capture

the relationship between the predictands and the predicted variables, amounting max $(0, c - x)$ or max $(0, x - c)$, where x is the threshold value, while c is the input variable value. The knots also represent the function of the base and base endpoints. A regression model is developed for each node by applying a spline function that consists of 1 or more BFs, followed by the substitution of the principal predictors [44]. In the MARS model, the predicted value is based mainly on linear BF elements combination. The MARS model can be reviewed as follows: consider Y as the target variable and $X = (X1, X2, \ldots, XP)$ as the P input variable matrix; then, the equation of the MARS model can be as follows:

$$Y = f(X) = \beta_0 + \sum_{m=1}^{M} \beta_0 BF_m(X), \tag{6}$$

where β_0 is the initial fixed value; BF_m is the applied BF for the fitting of the MARS model; and M is the total number of BFs [45]. The two major phases of the MARS model are the selection phase (or forward search) and the reversal pruning phase, as seen in Figure 2. The forward phase or selection phase can be regarded as a set of optimum input parameters. A complicated over fitted model normally results from an excessive forward stepwise selection process due to a series of splits and such models cannot perform well predictively despite fitting the data perfectly. Hence, the backward procedure is normally applied to improve the predictive performance of the model by removing the unwanted variables that have been selected in the selection phase. The generalized cross-validation (GCV) is calculated as the deletion criterion as it is the basis for the backward pruning process [46, 47].

$$GCV(M) = \frac{(1/N) \sum_{i=1}^{N} (O_i - f(x_i))^2}{(1 - (C(M)/N))^2},$$

$$C(M) = (d + 1) \times M, \tag{7}$$

where O_i is the observed values; N is the number of data; $f(x_i)$ is the predicted values for pattern i; M is the number of BFs; and $C(M)$ is the penalty factor. In equation (7), the quantity of parameter d significantly impacts the procedure as it is the optimization cost of each BF; its range is $2 \le d \le 4$. The inclusion of several BFs can result in overfitting; therefore, it is important to omit some BFs during the pruning phase to enable the emergence of a well-fitted model with the least GCV value [48].

2.3. Partial Least Square Regression (PLS) Model.

The first application of the PLS regression model was introduced over the literature by [49], and since then the model has been widely considered a new multivariate analysis technique in many fields [50, 51]. It combined the features of principal components, typical multiple regression, and linear regression analyses; hence, it is suitable for finding the solution to numerous problems, especially problems that cannot be solved using the conventional multiple regression methods and problems with multiple correlations [52]. The efficiency of PLS in such cases is based on its ability to decompose and
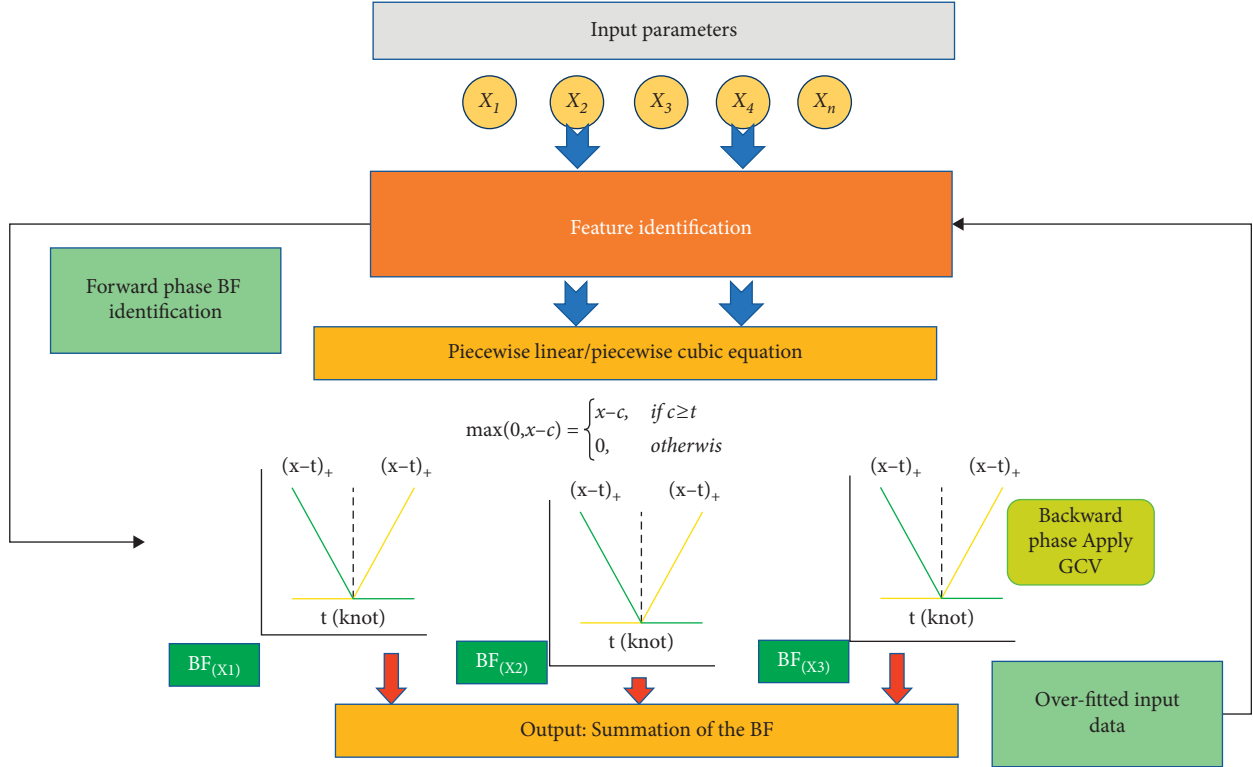
FIGURE 2: The systematic structure of the MARS model.

screen the variables that mostly explain the dependent variables [53]. The first step of the PLS method is to extract the new variable called the component which serves as the independent variable, followed by the determination and establishment of the linear relationship between the dependent and independent variables [54]. After calculating the coefficient using PLS, the next step is the construction of the regression equation of the dependent variable. The regression model developed by using the PLS method is represented as

$$y_m = a_{0m} + a_{1m}x_1 + \cdots + a_{Pm}x_p, \quad (m = 1, 2, \ldots, p),$$

(8)

where $x_1, \ldots, x_p$ represents the linear combinations of the remote sensing variables and $a_{0m}, a_{1m}, \ldots, a_{Pm}$ are the PLS-computed regression model parameters. A higher number of principal components in the established model by PLS translates to better model accuracy; however, an excessive number of principal components results in overfitting and higher error. Thus, the optimal number of principal components must be determined to achieve a balanced PLS model. The cross-validation method was used to calculate the sum of squared residuals in this study. The prediction ability of the resulting model is a function of the extent of predictive residual errors sum of square (PRESS) value. So, the optimal number of principal components can be determined based on the minimum PRESS value and this PRESS value can be calculated as

$$\text{PRESS} = \sum_{i=1}^{k} \left(y_i - y_{i,-1} \right)^2,$$

(9)

where y_i, $y_{i,-i}$ represent the measured value of the ith sample and the estimated value upon exclusion of the ith sample and k is the number of iterations for validation.

3. Case Study and Data Explanation

For the modeling purpose, datasets were collected from the open source of literature [7]. The datasets are explained the key cost derived from the FCIPs. The data were including $P1$, the served area; $P2$, the total length of the PVC pipeline; $P3$, irrigation valve number; $P4$, construction year; $P5$, geographical zone; and cost and duration of field canal improvement projects (FCIP) construction. The significance of the dataset is contributing to the best knowledge of irrigation authorities and decision makers to have a prior understanding on the FCIP cost. The biodata of the current research were collected from the survey conducted for Soltani Canal, Egypt. The quantitative costs are related to construction sites recorded between 2011 and 2018. The polyvinyl chloride (PVC) pipeline system is explained in Figure 3 with diameter ranging between 22.5 and 35 cm. The statistical properties of the dataset over the training and testing phases are reported in Tables 1 and 2. It is seen that all together of 228 data were taken for both training and testing phase. In Tables 1 and 2, the parameters that are collected for training and test phase are mean, standard error, median, mode, standard deviation, sample variance, kurtosis,
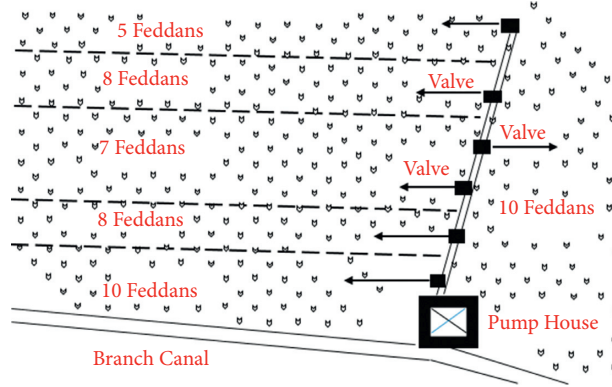
FIGURE 3: The Soltani Canal FCIP planning.

TABLE 1: The statistical properties of the dataset selected for the training modeling phase.

Parameter	C	D	P1	P2	P3	P4	P5
Parameter name	Cost of FCIP	Duration of FCIP construction	Area served	Total length of PVC pipeline	Number of irrigation values	Construction year	Geographical zone
Unit	LE/FCIP	Day	Hectare	Meter	Number	Year	Zone
Mean	353463.30	76.34	49.41	813.83	8.18	2013.20	0.00
Standard error	7539.45	0.78	1.28	26.10	0.23	0.10	0.00
Median	320292.58	75.00	45.90	753.75	8.00	2014.00	0.00
Mode	514778.00	64.00	51.00	530.00	5.00	2014.00	0.00
Standard deviation	113843.24	11.71	19.31	394.03	3.52	1.48	0.00
Sample variance	12960283390.67	137.20	372.83	155258.84	12.36	2.18	0.00
Kurtosis	−0.22	1.90	−0.07	−0.24	2.72	−0.13	−1.18
Skewness	0.77	1.04	0.75	0.60	0.94	−1.05	−0.58
Range	518824.50	69.00	85.00	1956.45	26.00	5.00	0.00
Minimum	186825.98	58.00	19.00	119.00	1.00	2010.00	0.00
Maximum	705650.48	127.00	104.00	2075.45	27.00	2015.00	0.00
Sum	80589633.51	17405.00	11265.43	185554.07	1866.02	459010.00	0.00
Count	228.00	228.00	228.00	228.00	228.00	228.00	228.00
Confidence level (95.0%)	14856.26	1.53	2.52	51.42	0.46	0.19	0.00

skewness, range, minimum and maximum, sum, count, and confidence interval from C to $P5$. The mean value of FCIP cost is 353463.0 for training modeling phase whilst a mean cost of 352714.35 was taken for testing phase. From Tables 1 and 2, it can be seen that the duration for FCIP construction ranges from 58 days to 127 days in the training model dataset while it ranges from 59 days to 126 days in the testing model dataset. The datasets in both training model and testing model are well distributed and almost resemble a normal distribution, as for most of the datasets, the mean and median are very close to each other.

4. Application Results and Analysis

The feasibility of three machine learning models (ELM, MARS, and PLS) was evaluated to predict cost of FCIP construction. The models were built based on different input combinations, as reported in Table 3. Based on the correlation statistics, the input combinations were constructed as shown in Figure 4.

Based on the tabulated input parameters, it can be recognized that the total length of the PVC pipeline has the substantial correlation to the construction cost followed by the time duration, served area, irrigation valve number, and geographical zone.

Different statistical performance metrics including determination coefficient (R^2), root mean square error (RMSE), mean absolute error (MAE), mean absolute percentage error (MAPE), Nash–Sutcliffe efficiency (NSE), and agreement index (MD) were calculated to validate the applied models statistically [55, 56].

$$R^2 = \left(\frac{\sum_{i=1}^{N}\left(y_p - \overline{y_p}\right) \cdot \left(y_o - \overline{y_o}\right)}{\sqrt{\sum_{i=1}^{N}\left(y_p - \overline{y_p}\right)^2 \sum_{i=1}^{N}\left(y_o - \overline{y_o}\right)^2}} \right)^2, \quad (10)$$

$$\text{RMSE} = \sqrt{\frac{1}{N}\sum_{i=1}^{N}\left(y_p - y_o\right)^2}, \quad (11)$$

TABLE 2: The statistical properties of the dataset selected for the testing modeling phase.

Parameter	C	D	P1	P2	P3	P4	P5
Parameter name	Cost of FCIP	Duration of FCIP construction	Area served	Total length of PVC pipeline	Number of irrigation values	Construction year	Geographical zone
Unit	LE/FCIP	Day	Hectare	Meter	Number	Year	Zone
Mean	352714.35	77.00	48.46	807.57	8.41	2013.23	1.29
Standard error	7469.77	0.81	1.24	27.65	0.26	0.09	0.05
Median	318652.92	76.00	45.68	720.82	7.46	2014.00	2.00
Mode	201587.44	66.00	51.00	630.00	5.00	2014.00	2.00
Standard deviation	112791.09	12.19	18.79	417.58	3.96	1.41	0.79
Sample variance	12721830134.86	148.62	352.92	174372.83	15.71	1.99	0.63
Kurtosis	0.05	2.09	0.21	0.06	6.34	0.12	−1.18
Skewness	0.88	1.22	0.84	0.76	1.72	−1.14	−0.58
Range	503217.10	67.00	86.00	1916.15	27.87	5.00	2.00
Minimum	198035.54	59.00	19.00	119.00	1.02	2010.00	0.00
Maximum	701252.64	126.00	105.00	2035.15	28.89	2015.00	2.00
Sum	80418872.53	17556.00	11049.13	184125.65	1917.50	459016.00	295.00
Count	228.00	228.00	228.00	228.00	228.00	228.00	228.00
Confidence level (95.0%)	14718.96	1.59	2.45	54.49	0.52	0.18	0.10

TABLE 3: The modeling input combinations for the adopted dataset.

M1	P2					
M2	P2	D				
M3	P2	D	P1			
M4	P2	D	P1	P3		
M5	P2	D	P1	P3	P4	
M6	P2	D	P1	P3	P4	P5

$$MAE = \frac{\sum_{i=1}^{N} |y_p - y_0|}{N}, \tag{12}$$

$$MAPE = \frac{1}{n} \sum_{i=1}^{n} \frac{|y_o - y_p|}{y_p} \times 100, \tag{13}$$

$$NSE = 1 - \frac{\sum_{i=1}^{N} (y_p - y_o)^2}{\sum_{i=1}^{N} (y_p - \overline{y_p})^2}, \tag{14}$$

$$MD = 1 - \frac{\sum_{i=1}^{N} (y_o - y_p)^j}{\sum_{i=1}^{N} (|y_p - \overline{y_o}| + |y_o - \overline{y_o}|)^j}, \tag{15}$$

where y_o and y_p are the observed and predicted values of the FCIP cost; $\overline{y_o}$ and $\overline{y_p}$ are the mean values of the observed and predicted values of the FCIP cost; N is the number of observations; and j is the exponent term.

Tables 4 and 5 report the statistical measures over the training and testing phases, respectively. In general, prediction performance of the models indicated less accuracy by using few predictors. However, MARS model exhibited better predictability performance over both the training and testing phases. It has been noticed that the maximum determination coefficient was achieved for model M6 ($R^2 = 0.94$) with a minimum RMSE of 28458.17 in the training phase while 27422.7 in the testing phase using all the
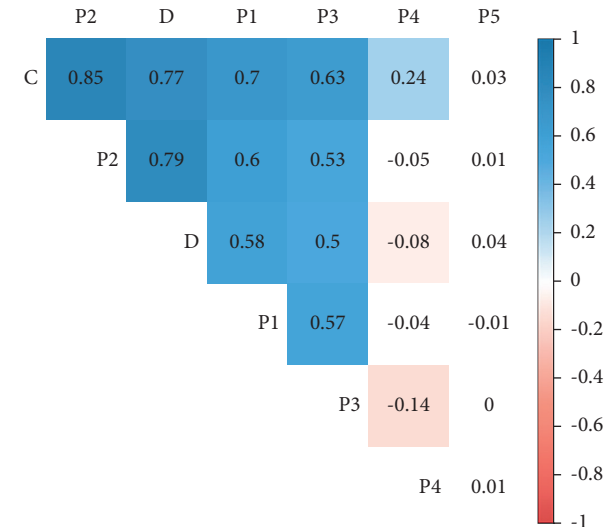
FIGURE 4: The correlation matrix between the predictors and the FCIP cost.

predictor parameters, excluding the geographical zone in which less influence on the cost phenomena was revealed when compared to ELM and PLS whose coefficient of determination (R^2) maxed out at 0.90 with RMSE of 36011.43 and 36013.16, respectively, for model M6 in the training phase. Similarly, in testing phase ELM and PLS, coefficient of determination (R^2) maxed out at 0.89 with RMSE of 37141.8 and 37140.3 for model M6. In addition, it is seen that the ratio of the MSE and the potential error which is denoted by MD is 0.89 for MARS M6 model on both cases, i.e., training and testing phases.

The model performances were assessed using graphical presentations such as scatter plots and Taylor diagram. Figure 5 shows the scatter plots between the actual observations and the predicted values. Among the three applied prediction models, MARS model is indicated as the best

TABLE 4: Prediction performance results over the training phase.

	R^2	RMSE	MAE	MAPE	Nash	MD
MARS model						
M1	0.76	57097.21	40090.04	0.11	0.76	0.78
M2	0.79	52443.11	35922.94	0.10	0.79	0.80
M3	0.83	46957.45	35377.61	0.10	0.83	0.81
M4	0.87	41427.33	31383.75	0.09	0.87	0.83
M5	0.94	28458.17	20444.55	0.06	0.94	0.89
M6	0.94	28458.17	20444.55	0.06	0.94	0.89
ELM model						
M1	0.72	61144.00	42644.28	0.12	0.72	0.76
M2	0.75	58309.91	40861.50	0.12	0.75	0.77
M3	0.79	52776.65	40372.48	0.11	0.79	0.78
M4	0.81	50951.98	39296.32	0.11	0.81	0.79
M5	0.90	36019.94	24352.69	0.07	0.90	0.87
M6	0.90	36011.43	24362.29	0.07	0.90	0.87
PLS model						
M1	0.72	61182.31	43650.76	0.12	0.72	0.75
M2	0.73	59634.10	42063.22	0.12	0.73	0.76
M3	0.79	52816.73	40059.10	0.11	0.79	0.78
M4	0.81	50951.98	39297.60	0.11	0.81	0.79
M5	0.90	36026.97	24406.13	0.07	0.90	0.87
M6	0.90	36013.16	24393.67	0.07	0.90	0.87

TABLE 5: Prediction performance results over the testing phase.

	R^2	RMSE	MAE	MAPE	Nash	MD
MARS model						
M1	0.75562	55636.4	39175.3	0.11317	0.75561	0.77964
M2	0.78542	52169	36042.4	0.10461	0.78513	0.79856
M3	0.81853	47949.3	36928.8	0.10698	0.81848	0.79537
M4	0.86669	41152.6	32861.1	0.09655	0.86629	0.82096
M5	0.94125	27422.7	19761.8	0.05454	0.94063	0.89374
M6	0.94125	27422.7	19761.8	0.05454	0.94063	0.89374
ELM model						
M1	0.70389	61662	43434.8	0.12204	0.69981	0.75368
M2	0.72687	59271.2	41879.9	0.11948	0.72264	0.76358
M3	0.77521	53666.1	41776.6	0.11991	0.77262	0.76784
M4	0.80047	50554.1	40050.8	0.11642	0.79822	0.77885
M5	0.894	37239.8	25507.3	0.06922	0.89051	0.86168
M6	0.89463	37141.8	25376.6	0.06887	0.89109	0.86241
PLS model						
M1	0.6997	62852.2	45250.3	0.12747	0.68811	0.74448
M2	0.71411	60628.3	43182.2	0.12358	0.70979	0.75411
M3	0.77381	53854.1	41631.9	0.11941	0.77102	0.76864
M4	0.80047	50554.3	40051.8	0.11643	0.79822	0.77884
M5	0.8941	37229.5	25541	0.06928	0.89057	0.86148
M6	0.89464	37140.3	25418.7	0.06898	0.89109	0.86217

identical match with high correlation value. On the other hand, Figure 6 shows the Taylor diagram map in which the prediction models were evaluated based on the distance coordination in accordance with multiple statistical metrics (i.e., standard deviation, RMSE, and correlation value).

5. Discussion

Various studies have been conducted to estimate a reliable parametric cost model, but there is no available study carried out for FCIP [5]. However, prediction of cost is not new; a simplex optimization of ANN weights was used to create a model for estimating the unit cost of highway projects with a mean absolute percentage error (MAPE) of 1% [16]. Another study used a combination of ANN and fuzzy logic to create a high-precision cost prediction model for water infrastructure based on the sum of squares of mistakes. During the validation phase, the researchers produced multiple prediction models with perceptions ranging from 4.6 percent to 0.6 percent
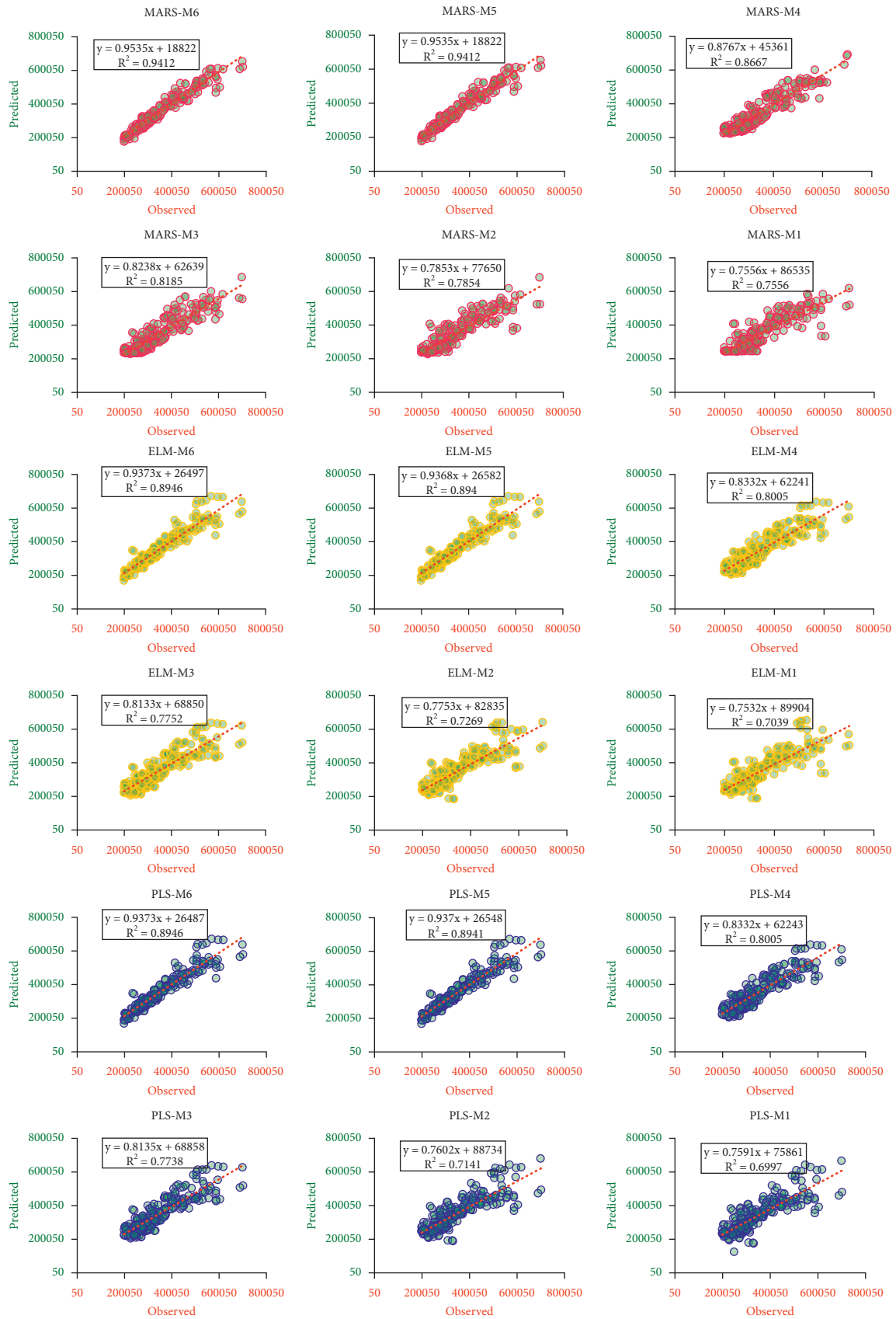
FIGURE 5: The scatter plots between the observed and predicted values of the cost over the testing phase for all tested input combinations and applied predictive models.
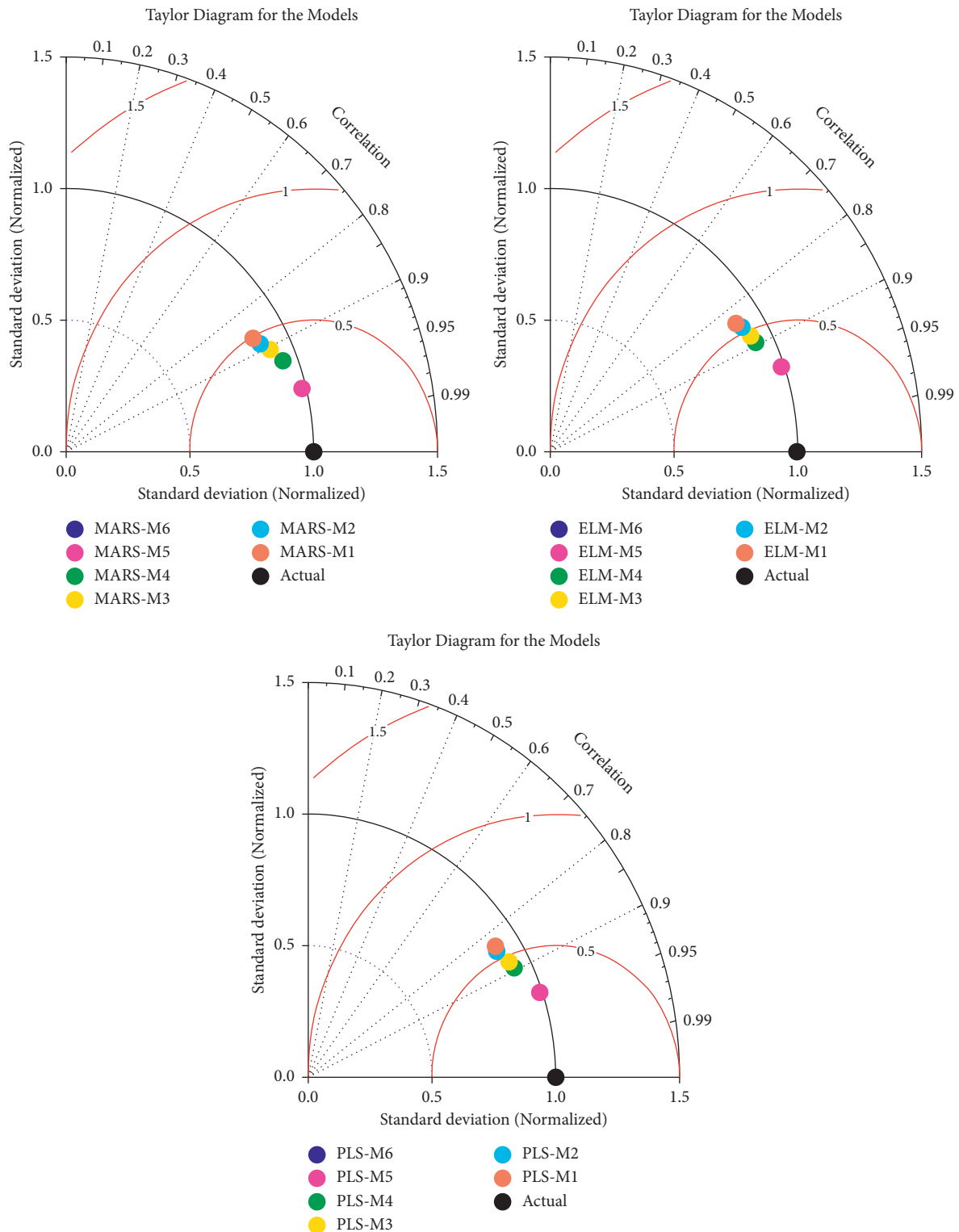
Figure 6: The Taylor diagram for the adopted modeling scenarios and the established machine learning models over the testing phase.

[19]. Furthermore, by varying the ANN structure, training function, and training algorithm until an optimum model was found, a researcher built a prediction model with a MAPE of 1.4 percent for the unit cost of the highway project in Libya [20]. It is seen that, in this study, the value of MAPE for MARS model M6 in both training and testing phases ranges from 5% to 6% when compared with other models.

6. Conclusion and Remarks

The prediction of cost related to civil engineering project is considered as vital topic to be studied comprehensively. In this study, couple of machine learning models including extreme learning machine (ELM), multivariate adaptive regression spline (MARS), and partial least square regression (PLS) were developed to predict field canal improvement project (FCIP) cost. For the purpose of the modeling development, datasets related to irrigation projects were collected from the open source published literature. Input combinations were initiated based on the total length of the PVC pipeline, served area, geographical zone, construction year, and cost and duration of FCIP construction. The prediction results showed that MARS and ELM models were presented positively in comparison with the PLS model. However, MARS model reported the superior results. Also, the research finding exhibited that all the predictors are substantial toward the cost calculation with almost no influence for the geographical zone of the pipeline network.

Nomenclature

ANFIS: Adaptive neuro-fuzzy inference system
MD: Agreement index
ANN: Artificial neural network
BF: Basic function
R^2:   Determination coefficient
ELM: Extreme learning machine
FCIP: Field canal improvement project
FL: Fuzzy logic
GCV: Generalized cross validation
IoT: Internet of things
NSE: Nash–Sutcliffe efficiency
ML: Machine learning
MAE: Mean absolute error
MAPE: Mean absolute percentage error
MARS: Multivariate adaptive regression spline
PLS: Partial least square regression
PVC: Polyvinyl chloride
PRESS: Predictive residual errors sum of square
RMSE: Root mean square error
SC: Soft computing
SVM: Support vector machine.

Data Availability

The data used in this study can be provided upon request from the authors.

Conflicts of Interest

The authors report no conflicts of interest.

References

[1] M. T. Rock, "Freshwater use, freshwater scarcity, and socioeconomic development," *The Journal of Environment & Development*, vol. 7, no. 3, pp. 278–301, 1998.

[2] J. Awange, "Global freshwater resources," *Lake Victoria Monitored from Space*, Springer, Berlin, Germany, pp. 3–19, 2021.

[3] H. S. Salem, Y. Yihdego, and H. H. Muhammed, "The status of freshwater and reused treated wastewater for agricultural irrigation in the Occupied Palestinian Territories," *Journal of Water and Health*, vol. 19, no. 1, pp. 120–158, 2021.

[4] D. P. Loucks and E. Van Beek, *Water Resource Systems Planning and Management: An Introduction to Methods, Models, and Applications*, Springer, Berlin, Germany, 2017.

[5] H. H. ElMousalami, A. H. Elyamany, and A. H. Ibrahim, "Predicting conceptual cost for field canal improvement projects," *Journal of Construction Engineering and Management*, vol. 144, Article ID 4018102, 2018.

[6] H. H. Elmousalami, "Artificial intelligence and parametric construction cost estimate modeling: State-of-the-art review," *Journal of Construction Engineering and Management*, vol. 146, no. 1, 2020.

[7] H. H. Elmousalami, "Data on field canals improvement projects for cost prediction using artificial intelligence," *Data in Brief*, vol. 31, Article ID 105688, 2020.

[8] H. G. Radwan, "Sensitivity analysis of head loss equations on the design of improved irrigation on-farm system in Egypt," *International Journal of Advanced Research in Science*, vol. 2, pp. 1–9, 2013.

[9] L. Sabol, "Challenges in cost estimating with building information modeling," *IFMA World Work*, pp. 1–16, 2008.

[10] H. D. S. Budiono, G. Kiswanto, and T. P. Soemardi, "Method and model development for manufacturing cost estimation during the early design phase related to the complexity of the machining processes," *International Journal of Technology*, vol. 5, no. 2, pp. 183–192, 2014.

[11] R. Sonmez and B. Ontepeli, "Predesign cost estimation of urban railway projects with parametric modeling," *Journal of Civil Engineering and Management*, vol. 15, no. 4, pp. 405–409, 2009.

[12] S.-H. Ji, M. Park, and H.-S. Lee, "Cost estimation model for building projects using case-based reasoning," *Canadian Journal of Civil Engineering*, vol. 38, no. 5, pp. 570–581, 2011.

[13] T. Hegazy and O. Moselhi, "Elements of cost estimation: a survey in Canada and the unit," *Cost Engineering*, vol. 37, p. 27, 1995.

[14] F. M. S. Al-Zwainy and T. H. Neran, "Investigation and evaluation of the cost estimation methods of Iraqi communication projects," *International Journal of Engineering and Management Research*, vol. 5, pp. 41–48, 2015.

[15] D. A. Hollar, W. Rasdorf, M. Liu, J. E. Hummer, I. Arocho, and S. M. Hsiang, "Preliminary engineering cost estimation model for bridge projects," *Journal of Construction Engineering and Management*, vol. 139, no. 9, pp. 1259–1267, 2013.

[16] T. Hegazy and A. Ayed, "Neural network model for parametric cost estimation of highway projects," *Journal of Construction Engineering and Management*, vol. 124, no. 3, pp. 210–218, 1998.

[17] M. M. Marzouk and R. M. Ahmed, "A case-based reasoning approach for estimating the costs of pump station projects," *Journal of Advanced Research*, vol. 2, no. 4, pp. 289–295, 2011.

[18] N. I. El-Sawalhi, "Modelling the parametric construction project cost estimate using fuzzy logic," *International Journal of Emerging Technology and Advanced Engineering*, vol. 2, no. 4, p. 2, 2012.

[19] D. D. Ahiaga-Dagbui, O. Tokede, S. D. Smith, and S. Wamuziri, "A neuro-fuzzy hybrid model for predicting final cost of water infrastructure projects," in *Proceedings of*

the 29th Annual ARCOM Conference, pp. 181–190, SD Smith DD Ahiaga-Dagbui, Cambridge, UK, September 2013.

[20] E. Elbeltagi, O. Hosny, R. Abdel-Razek, and A. El-Fitory, "Conceptual cost estimate of Libyan highway projects using artificial neural network," International Journal of Engineering Research in Africa, vol. 4, pp. 56–66, 2014.

[21] C. Stoy, S. Pollalis, and O. Dursun, "A concept for developing construction element cost models for German residential building projects," International Journal of Project Organisation and Management, vol. 4, no. 1, pp. 38–53, 2012.

[22] K. Petroutsatou, E. Georgopoulos, S. Lambropoulos, and J. P. Pantouvakis, "Early cost estimating of road tunnel construction using neural networks," Journal of Construction Engineering and Management, vol. 138, no. 6, pp. 679–687, 2012.

[23] C. L. C. Roxas and J. M. C. Ongpeng, "An artificial neural network approach to structural cost estimation of building projects in the Philippines," in Proceedings of the DLSU Research Congress, Manila, Philippines, February 2014.

[24] I. Peško, V. Mučenski, M. Šešlija et al., "Estimation of costs and durations of construction of urban roads using ANN and SVM," Complexity, vol. 2017, Article ID 2450370, 2017.

[25] D. Jumas, F. A. Mohd-Rahim, N. Zainon, and W. P. Utama, "Improving accuracy of conceptual cost estimation using MRA and ANFIS in Indonesian building projects," Built Environment Project and Asset Management, vol. 8, no. 4, 2018.

[26] K. J. Kim and K. Kim, "Preliminary cost estimation model using case-based reasoning and genetic algorithms," Journal of Computing in Civil Engineering, vol. 24, no. 6, pp. 499–505, 2010.

[27] A. Mahmoodzadeh, M. Mohammadi, A. Daraei, H. Farid Hama Ali, A. Ismail Abdullah, and N. Kameran Al-Salihi, "Forecasting tunnel geology, construction time and costs using machine learning methods," Neural Computing & Applications, vol. 33, no. 1, pp. 321–348, 2021.

[28] H. H. Elmousalami, "Comparison of artificial intelligence techniques for project conceptual cost prediction: a case study and comparative analysis," IEEE Transactions on Engineering Management, vol. 68, pp. 183–196, 2020.

[29] S. T. Hashemi, O. M. Ebadati, and H. Kaur, "Cost estimation and prediction in construction projects: a systematic review on machine learning techniques," SN Applied Sciences, vol. 2, pp. 1–27, 2020.

[30] S. B. Green, "How many subjects does it take to do a regression analysis," Multivariate Behavioral Research, vol. 26, no. 3, pp. 499–510, 1991.

[31] G.-B. Huang, D. H. Wang, and Y. Lan, "Extreme learning machines: a survey," International Journal of Machine Learning and Cybernetics, vol. 2, no. 2, pp. 107–122, 2011.

[32] G.-B. Guang-Bin Huang, H. Hongming Zhou, X. Xiaojian Ding, and R. Rui Zhang, "Extreme learning machine for regression and multiclass classification," IEEE Transactions on Systems, Man, and Cybernetics, Part B (Cybernetics), vol. 42, no. 2, pp. 513–529, 2012.

[33] Y. Miche, M. Van Heeswijk, P. Bas, O. Simula, and A. Lendasse, "TROP-ELM: A double-regularized ELM using LARS and Tikhonov regularization," Neurocomputing, vol. 74, no. 16, pp. 2413–2421, 2011.

[34] W. Zhang and A. T. C. Goh, "Multivariate adaptive regression splines and neural network models for prediction of pile drivability," Geoscience Frontiers, vol. 7, no. 1, pp. 45–52, 2016.

[35] N.-Y. Nan-Ying Liang, G.-B. Guang-Bin Huang, P. Saratchandran, and N. Sundararajan, "A fast and accurate online sequential learning algorithm for feedforward networks," IEEE Transactions on Neural Networks, vol. 17, no. 6, pp. 1411–1423, 2006.

[36] M. Hou, T. Zhang, F. Weng, M. Ali, N. Al-Ansari, and Z. Yaseen, "Global solar radiation prediction using hybrid online sequential extreme learning machine model," Energies, vol. 11, no. 12, p. 3415, 2018.

[37] L. Zhang and D. Zhang, "Evolutionary cost-sensitive extreme learning machine," IEEE Transactions on Neural Networks and Learning Systems, vol. 28, no. 12, pp. 3045–3060, 2017.

[38] G. Huang, G.-B. Huang, S. Song, and K. You, "Trends in extreme learning machines: a review," Neural Networks, vol. 61, pp. 32–48, 2015.

[39] S. Sekhar Roy, R. Roy, and V. E. Balas, "Estimating heating load in buildings using multivariate adaptive regression splines, extreme learning machine, a hybrid model of MARS and ELM," Renewable and Sustainable Energy Reviews, vol. 82, pp. 4256–4268, 2018.

[40] M. Ali and R. Prasad, "Significant wave height forecasting via an extreme learning machine model integrated with improved complete ensemble empirical mode decomposition," Renewable and Sustainable Energy Reviews, vol. 104, pp. 281–295, 2019.

[41] J. H. Friedman, "Multivariate adaptive regression splines," Annals of Statistics, vol. 19, no. 1, pp. 1–67, 1991.

[42] F. Yerlikaya-Özkurt, İ. Batmaz, and G.-W. Weber, "A review and new contribution on conic multivariate adaptive regression splines (CMARS): A powerful tool for predictive data mining," Springer Proceedings in Mathematics & Statistics, vol. I, pp. 695–722, 2014.

[43] M. A. Sahraei, H. Duman, M. Y. Çodur, and E. Eyduran, "Prediction of transportation energy demand: Multivariate adaptive regression splines," Energy, vol. 224, Article ID 120090, 2021.

[44] G. Zheng, W. Zhang, H. Zhou, and P. Yang, "Multivariate adaptive regression splines model for prediction of the liquefaction-induced settlement of shallow foundations," Soil Dynamics and Earthquake Engineering, vol. 132, Article ID 106097, 2020.

[45] Q.-S. Xu, M. Daszykowski, B. Walczak et al., "Multivariate adaptive regression splines-studies of HIV reverse transcriptase inhibitors," Chemometrics and Intelligent Laboratory Systems, vol. 72, no. 1, pp. 27–34, 2004.

[46] A. A. H. Alwanas, A. A. Al-Musawi, S. Q. Salih, H. Tao, M. Ali, and Z. M. Yaseen, "Load-carrying capacity and mode failure simulation of beam-column joint connection: Application of self-tuning machine learning model," Engineering Structures, vol. 194, pp. 220–229, 2019.

[47] L. Wang, C. Wu, X. Gu, H. Liu, G. Mei, and W. Zhang, "Probabilistic stability analysis of earth dam slope under transient seepage using multivariate adaptive regression splines," Bulletin of Engineering Geology and the Environment, vol. 79, no. 6, pp. 2763–2775, 2020.

[48] R. C. Deo, O. Kisi, and V. P. Singh, "Drought forecasting in eastern Australia using multivariate adaptive regression spline, least square support vector machine and M5 tree model," Atmospheric Research, vol. 184, pp. 149–175, 2017.

[49] H. Abdi, "Partial least square regression (PLS regression)," Encyclopedia of Social Science Research Methods, vol. 6, pp. 792–795, 2003.

[50] H. Abdi and L. J. Williams, "Partial least squares methods: partial least squares correlation and partial least square regression," Methods in Molecular Biology, vol. 930, pp. 549–579, 2013.

[51] J. Hulland, "Use of partial least squares (PLS) in strategic management research: a review of four recent studies," *Strategic Management Journal*, vol. 20, no. 2, pp. 195–204, 1999.

[52] L. Kaufmann and J. Gaeckler, "A structured review of partial least squares in supply chain management research," *Journal of Purchasing and Supply Management*, vol. 21, no. 4, pp. 259–272, 2015.

[53] B. D. Liengaard, P. N. Sharma, G. T. M. Hult et al., "Prediction: coveted, yet forsaken? Introducing a cross-validated predictive ability test in partial least squares path modeling," *Decision Sciences*, vol. 52, no. 2, pp. 362–392, 2021.

[54] H. M. Lin, M. H. Lee, J. C. Liang, H. Y. Chang, P. Huang, and C. C. Tsai, "A review of using partial least square structural equation modeling in e-learning research," *British Journal of Educational Technology*, vol. 51, no. 4, pp. 1354–1372, 2020.

[55] R. Walpole, R. Myers, S. Myers, and K. Ye, "Probability and Statistics for Engineers and Scientist," *Pearson*, Boston, MA, USA, 2011.

[56] H. V. Gupta, H. Kling, K. K. Yilmaz, and G. F. Martinez, "Decomposition of the mean squared error and NSE performance criteria: Implications for improving hydrological modelling," *Journal of Hydrology*, vol. 377, no. 1-2, pp. 80–91, 2009.

WILEY | Hindawi

Research Article

Study on an Intelligent Prediction Method of Ticket Price in a Subway System with Public-Private Partnership

Shengmin Wang [iD],[1,2] **Jun Fang** [iD],[1] **Lanjun Liu** [iD],[1] **and Han Wu** [iD][1]

[1]*School of Civil Engineering and Architecture, Wuhan University of Technology, Wuhan 430070, China*
[2]*School of Safety Science and Emergency Management, Wuhan University of Technology, Wuhan 430070, China*

Correspondence should be addressed to Han Wu; wuhan20170620@163.com

The accurate and rapid prediction of ticket prices for a public-private partnership (PPP) subway system, which is an important research topic in the field of civil engineering management, is of critical importance to ensure its smooth operation. To effectively cope with the effects of multiple influencing factors and strong nonlinearity among them, the mean impact value (MIV) method and the back-propagation (BP) feed-forward neural network improved by the sparrow search algorithm (SSA) are used in this study to develop an intelligent prediction model. First, we considered the relationship of the supply and the subway system service, which is a typical quasi-public product, and analyzed the relevant factors affecting its price adjustment. Then, we developed an intelligent method for the prediction of ticket prices based on the SSA-BP. This model not only makes full use of the powerful nonlinear modeling ability of the BP algorithm, but also takes advantage of the strong optimization ability and fast convergence speed of the SSA. Finally, this study screened out the key input factors by adopting the MIV method to simplify the structure of the BP algorithm and achieve a high prediction accuracy. In this study, Beijing Subway Line 4, Wuhan Metro Line 2, and Chengdu Metro Line 1 were selected as case study sites. The results showed that the linear correlations between influencing factors and ticket price for the PPP subway system service were weak, which indicated the need for using nonlinear analysis methods such as the BP algorithm. Compared with other prediction methods (the price adjustment method based on PPP contract, the traditional BP algorithm, the BP neural network improved by the genetic algorithm, the BP algorithm improved by the particle swarm optimization, and the support vector machine), the model proposed in this paper showed better prediction accuracy and calculation stability.

1. Introduction

Currently, numerous subway systems are being built around the world to meet the needs of rapid urban development [1]. As an important infrastructure, a subway system has the characteristics of large initial investment, high operating cost, and long payback period, which drive decision-makers to often use the public-private partnership (PPP) to build subway systems [2, 3]. Under the PPP mode, the private sector cooperates with the government to participate in the construction and operation of subway systems. The private sector is mainly responsible for the financing, construction, operation, and maintenance of subway systems. Government departments mainly provide policy support, land, and operating subsidies. For the government, the goal is the construction of a subway system that is compatible with the sustainable development of the country, and the charging price for the subway system service needs to maintain its public welfare attribute. For the private sector, investing in the construction of PPP subway system projects can generate considerable investment income during the operation period. For the public (customers), the charging price for the subway system service needs to meet their ability to pay. If the price is too high, it will be unbearable for the customers, which will lead them to choose other means of transport for competitive services. If the price is too low, the return on the private sector investment will not be sufficient to grow their assets. Therefore, predicting the ticket price rapidly and

accurately is of critical importance to ensure an acceptable return on the funds invested by the private sector and the welfare level of the public, which decide whether the subway system could be implemented smoothly.

At present, subway systems mainly adopt either a single fare system or a mileage-based pricing system, of which the latter is the most common, and this is adopted by this study. The ticket price in this study is the price per kilometre and is also the price for the cooperation game between the government agencies and the private sector during the operation period of the PPP subway system. If the traditional financial calculation method is adopted, the ticket price studied in this paper is the ticket price per kilometre in order to achieve the predetermined revenue target. With this price, which is the research object of this paper, the subway operating company is able to further put forward the actual selling price for the public. In addition, the determination of the final price for the customer is a more complicated issue, which is not the content of this paper.

In terms of research objects, relevant scholars have conducted some research on the PPP subway systems, but the related research results mainly focused on the concept of PPP, risk sharing, performance management, and driving force [4]. Chang [5] analyzed the driving force and feasibility of adopting the PPP mode in Beijing Metro Line 4 (Beijing, China). Sturup [6] took Copenhagen's Metro System (Copenhagen, Denmark) and Melbourne City Link (Melbourne, Australia) as examples and analyzed the problems that might arise in the implementation of the PPP subway system projects. Gordon et al. [7] studied the performance management of the PPP subway system in the Sydney Metro (Sydney, Australia). Li and Love [8] evaluated the impact of land appreciation on the economic feasibility of the Delhi Airport Metro Express Line (New Delhi, India). Cohen and Boast [9] studied the game between social capital and government of Milan Metro Line 4 (Milan, Italy). However, it was not difficult to find that most of this research was focused on the field of public administration or sociology, and there was almost no research on the operation and management contents, such as price prediction of PPP subway systems. The main reasons for this situation might be as follows: (1) The research on PPP subway systems is still at a theoretical stage, and the pertaining research has not yet reached the stage of operation management. (2) The PPP subway system is too complicated, which requires a lot of effort and time to obtain enough engineering data to support the related research on price adjustment.

In terms of research methods, the PPP subway system has many participants, many years of operation, and complex management; as a result, there are many factors that affect the price of PPP subway system service [10]. Therefore, in engineering practice and scientific research, there is no universal and unified PPP subway system service price adjustment or prediction mechanism. Currently, in the practice of the PPP subway system management, the price of the subway ticket is often adjusted according to the price adjustment conditions agreed on in the PPP contract. This method has the disadvantages of slow prediction speed and unstable prediction results, which easily leads to the instability of the subway operating income and ultimately results in bad consequences, such as the failure of the PPP subway system cooperation [11]. In addition, the multiple regression method is also a commonly used mathematical method [12, 13], but it has the shortcomings of low prediction accuracy and narrow application range. The main reason for these deficiencies is that these methods cannot capture the possible and complex nonlinear relationships between multiple factors.

The artificial neural network (ANN) is a common artificial intelligence prediction model. In recent years, it has gradually replaced the linear modeling method in the fields of financial time series prediction [14], machine failure prediction [15], and rainfall prediction [16]. An ANN model can determine the complex nonlinear mapping relationship between different variables through data training and then complete the prediction work. When an ANN model is applied to the subway ticket price prediction, a prediction model can be established using the factors influencing ticket price as the input and the fare as the output. The back-propagation (BP) feed-forward neural network can approximate any nonlinear function, so it is the most commonly used ANN algorithm [17]. However, in the process of using the BP neural network, there are often some problems, such as slow convergence speed, ease of falling into local minima, and poor robustness [18, 19].

At present, with the aim of addressing the above shortcomings of the BP algorithm, the genetic algorithm (GA), the particle swarm optimization (PSO), and other metaheuristic algorithms are often used to optimize the weights and thresholds of the BP neural network. Zou et al. [20] used the BP algorithm, optimized by the GA, to effectively identify the shear parameters of lunar rock mass. However, such study did not compare the calculation results of the GA with other optimization algorithms and did not conduct further research and analysis on the shortcomings of the GA, such as complex programming, complex parameter setting, and slow convergence speed [21]. Nasimi et al. [22] predicted the bottomhole pressure of drilling facilities by using the BP algorithm optimized by the PSO algorithm. Another study did not analyze the premature convergence and convergence to the local optimal solution of the PSO algorithm [23]. In 2020, Xu and Shen [24] proposed the sparrow search algorithm (SSA) referring to the biological phenomenon of the sparrow population foraging. The SSA can achieve higher global exploration ability and local development ability with the help of a flexible foraging and antipredation mechanism in the sparrow population.

As the SSA is quite new, there are few reports on its application in engineering problems and theoretical analysis. Xue and Shen [24] used the SSA, grey wolf optimizer (GWO), gravitational search algorithm (GSA), and PSO algorithms to calculate and analyze 19 typical optimization functions and two engineering problems. The calculation results showed that the SSA had the advantages of good stability, strong global search ability, and few parameters compared with other optimization algorithms. Lv et al. [25] solved the image segmentation problem by using the SSA

method. Their case study showed that the SSA method had better definition than the classical image segmentation methods. Tang et al. [26] used the improved SSA algorithm to study the path planning of an unmanned aerial vehicle (UAV). Their study showed that the improved SSA algorithm was superior to the PSO algorithm, the beetle antennae search (BA), the whale optimization algorithm (WOA), and the GWO. According to the no-free-lunch (NFL) theory [27], the expected performance of each algorithm is the same for solving all optimization problems. In other words, the computing performance of the same optimization algorithm in different optimization problems may be quite different. Therefore, this study will use the SSA to optimize the BP model to test the optimization performance of the SSA in the BP model. To the best of our knowledge, there has been no study published on the optimization of the BP model using the SSA.

Besides the optimization of model parameters, the selection of the input characteristic variables is also a key factor to determine the prediction accuracy of the BP neural network model [28, 29]. In order to reduce the number of input variables of the BP neural network, Mao et al. [30] used principal component analysis (PCA) to screen 10 key factors affecting magnesite grade. The PCA is used to integrate the original influencing factors into a small number of irrelevant variables by linear combination. Xu et al. [31] used a regression model to select the variables with high correlation as the input variables to predict the snow surface reflectance spectra at different depths during snow melting. Xu et al. [32] obtained the key input variables for the BP prediction model of chlorophyll in water by the multiple linear regression method. Their research results were based on the correlation between variables and screening of the key input variables of the BP neural network prediction model, and there were the following drawbacks. (1) The variable screening results of these methods might not be ideal. When choosing input variables, the researchers often chose independent variables to avoid the correlation of variables, which made the screening effect of multivariate regression analysis and PCA with the correlation of variables as the core likely not good. (2) The variable screening results of these methods were not easily interpretable. They studied the data relationship of variables, which could well explain the linear or nonlinear relationship between variables but could not clearly evaluate the influence of the linear or nonlinear relationship between variables on the prediction results.

In view of the above shortcomings, the mean impact value (MIV) has been increasingly widely used in input variable screening in recent years. The MIV is used to screen the key input variables by evaluating the extent of the influence of each input variable relative to the output variable, which has a great influence on the output variable. Li et al. [33] used the MIV to effectively identify the key factors affecting the soil corrosion of carbon steel in China. Their case study showed that the key factors identified based on MIV were consistent with the actual situation of soil corrosion of carbon steel in China, and the prediction of soil corrosion of carbon steel based on MIV-BP had a good accuracy. However, this study did not compare the

calculation results of the BP algorithm with those of other intelligent algorithms. Considering the numerous evaluation indexes of pollutants in bus stations, Xu et al. [34] screened the indexes by the MIV method to reduce the number of input variables for the subsequent BP neural network. Dai et al. [35] developed a MIV-GA-BP model to calculate the optimal values of coal pillars. In their model, the MIV was used to identify the key factors affecting the optimal solution of the coal pillar. Their case study showed that the prediction error of this model was less than 5%, and the calculation accuracy was higher than that of other common artificial intelligence algorithms.

By summarizing the existing research, in this paper we put forward the following key issues that need to be studied. (1) To date, most of the research results on PPP subway systems have been in the field of public management, and there has been almost no research on the prediction of the price for the PPP subway service, which is a typical operation and management problem. Rapid and accurate price prediction is crucial for the smooth operation of the PPP subway system. (2) In the study to determine the key input variables of the BP model, researchers often used multiple regression analysis or PCA methods to obtain the key input variables by analyzing the correlation between input variables. These selection methods are subjective, and the calculation results are not easily interpretable. Choosing quantitative analysis methods, such as the MIV method, might be a reasonable approach to effectively deal with the deficiency that there are many factors affecting the prediction of the fare for the PPP subway system service. (3) At present, the commonly used prediction methods based on contract price adjustment, regression analysis and BP, GA-BP, and PSO-BP models have many shortcomings, such as low prediction accuracy and being time-consuming. Using the SSA method to optimize the BP model provides a new idea for accurately and rapidly predicting the ticket price for the PPP subway system service.

Based on the above literature, this paper used the MIV method, the SSA, and the BP model to develop an intelligent prediction method of the ticket price for the PPP subway system, which had the following literature contributions. (1) Previous related studies rarely predicted the ticket price for the PPP subway system. In this paper, the conducted in-depth theoretical and case studies provided new insights into the operation and management of the PPP subway system. (2) Starting from the relationship between the subway ticket price and the supply and demand of the subway service, this study analyzed the related factors affecting its price adjustment and produced the data acquisition and processing methods of each input variable. The MIV method was used to determine the key factors affecting the ticket prices for Beijing Subway Line 4, Wuhan Metro Line 2, and Chengdu Metro Line 1. The investment return rate, the local GDP, the number of similar vehicles, the financial subsidies, and the loan interest rates were key factors for these three systems. This processing method also reduced the number of input variables for subsequent BP models. (3) Considering the shortcomings of BP neural network model, such as its slow convergence speed and ease of falling into local optimum,

this study, for the first time, used the SSA to optimize initial weights and thresholds and effectively solved these problems. (4) The case study showed that, compared with the traditional prediction method (the price adjustment method based on the PPP contract, the multiple regression analysis, the traditional BP, the GA-BP, and the PSO-BP), the calculation results of the model proposed in this paper had better prediction accuracy and stability.

The remainder of this paper is arranged as follows. In Section 2, the input variable system and the prediction model of the ticket price for the PPP subway system service are studied in detail. In Section 3, the prediction model is applied to Beijing Subway Line 4, Wuhan Metro Line 2, and Chengdu Metro Line 1. In addition, Section 3 describes the analysis of the nonlinear relationship between the variables to highlight the need to use the BP model. In Section 4, the calculation results of the different prediction models are compared, and the analysis of the key parameters of the MIV method is described. Section 5 summarizes the study and gives the research directions that warrant further study.

2. Materials and Methods

2.1. Input Variable System for Price Prediction of the PPP Subway System

2.1.1. Analysis of Factors Influencing the Ticket Price for the PPP Subway System.
According to the definition and classification of public goods in economics, subway service belongs to quasi-public goods [36]. Under the PPP mode, the public (customer) can be regarded as the demand side of the subway service, while the supply side is the government departments and private investors who partnered with each other through concession contracts. Discussing the factors that affect the ticket price for the PPP subway service from the perspective of supply and demand can comprehensively consider the interests of the public, government departments, and private investors, which is more conducive to the smooth operation of the PPP subway system [37].

The greater the demand by the public for the subway service, the greater the transportation volume of the subway system, and the lower the ticket price. From the perspective of the demand of the subway service, there are three main factors that may affect the ticket price for the PPP subway service. (1) The number of potential subway passengers is determined by the number of urban residents and the local gross domestic product (GDP), and its size change has a great impact on subway service demand. The greater the number of urban residents, the greater the local GDP and the greater the subway demand. (2) The existence of similar means of transportation will divert to a certain extent the number of subway passengers, who will choose according to the change of the transportation price. Generally speaking, the lower the price of subway tickets, the fewer the similar means of transportation and the greater the demand for the subway service. (3) The satisfaction of the public with the subway service quality will also affect the demand for the subway service, such as subway congestion, on-time departure, on-time arrival, and safety.

From the perspective of the supply side, the ticket price for the PPP subway service is the result of the cooperation and game between government agencies and private investors [38]. This study does not delve into the complex game process between the two sides but rather analyzes the factors that may affect the ticket price for the PPP subway service from the following three perspectives. (1) Due to the public welfare aspect of the subway service, the government has strict supervision over subway service prices, and it is impossible for private investors to recover their investment through ticket revenue, thus subsidies have a great impact on the revenue of private investors [39]. In general, the greater the government subsidy, the lower the fare of the PPP subway system. (2) The construction and operation costs of the subway project have a direct impact on the revenue of the system. As the cooperation period of the PPP subway system is often as long as 30 years, the loan interest rate of construction loans [40] and inflation during the operation period [41] have a great impact on the cost of PPP subway systems. When the project cost increases, the private capital will increase the price of the ticket to ensure the revenue of system. (3) The expectation of investment revenue from the PPP subway system by the private investors also has great influence on ticket price. The higher the expected return on the investment, the higher the price of the ticket. Moreover, from the macro environment, due to the long operation period of the PPP subway system, the introduction of relevant national policies and laws will cause changes in the demand or supply of the PPP subway service during the operation period [41]. Therefore, it will cause fluctuations in subway ticket prices.

2.1.2. Selection and Quantification Method of Input Variables for the Prediction of Prices for the PPP Subway Service.
According to the research results of Section 2.1.2, based on the scientificity, representativeness, and independence provisions and taking into account the availability and operability data of the PPP subway system, the following eight variables are selected as the input variables for the prediction of the ticket price for the PPP subway service, as shown in Table 1.

The value of $X8$ was obtained through a questionnaire survey. In the questionnaire for $X8$, $[0, 25)$ indicated dissatisfaction, $[25, 50)$ indicated dissatisfaction, $[50, 75)$ indicated basic satisfaction, and $[75, 100)$ indicated satisfaction. The $X2$, $X4$, and the output variable can be in the same currency unit, such as RMB, USD, or EUR.

Each input variable in Table 1 is normalized based on (1) to ensure the calculation accuracy of the subsequent prediction model, as reported in [31].

$$x_i^* = \frac{x_i - x_{\min}}{x_{\max} - x_{\min}}, \tag{1}$$

where x_i^* is the normalized value, x_i is the i-th value of input variable x, $x_{\max}$ is the maximum value of input variable x, and $x_{\min}$ is the minimum value of input variable x.

TABLE 1: Input variables for the prediction of the ticket for the PPP subway systems.

Input variable	No.	Unit	Data acquisition method
Number of local people	X1	Million	Access to government notices
Total local GDP	X2	Billion	Access to government notices
Number of similar vehicles	X3	—	On-site investigation or access to government announcements
Financial subsidy	X4	Million	Access to government notices
Loan interest rate	X5	%	Check on the project management data
Inflation rate	X6	%	Access to statistical data
Rate of return on investment	X7	%	Check on the project management data
Public satisfaction	X8	RMB/km	Questionnaire survey

2.2. Intelligent Prediction Method of Ticket Price for the PPP Subway Service

2.2.1. Introduction to the BP Model.

As a typical feed-forward neural network, the BP neural network is mainly used in nonlinear learning, pattern recognition and classification, system control, and other fields [15]. The BP neural network takes the input data as learning samples, adjusts the weights and thresholds of the whole network by the back-propagation algorithm, constructs a mapping relationship between input and output that is closest to the sample, and uses this mapping relationship to predict the output value. Based on the black box theory, this method simulates the structure and function of a neural network in the human brain and can solve any nonlinear mapping process without constructing a specific mathematical formula, which has the characteristics of good adaptability, high fault tolerance, and strong nonlinear processing ability [15, 16].

MLP is a multilayer fully connected feed-forward network, which is only an algorithm structure. After the samples are input, the samples are fed forward layer by layer in the MLP network (from the input layer to the hidden layer and to the output layer, the results are calculated layer by layer, that is, the so-called feed-forward), and the final output value is obtained. However, the connection coefficients and offsets of neurons in each layer of MLP need training and optimization, and the BP is often used to get the coefficients and offsets in the model. Strictly from the field of algorithm research, the reviewer's statement is more accurate. The neural network is MLP, and the BP neural network (BP-MLP) is an MLP network optimized by BP algorithm.

A complete BP neural network model usually includes three basic network structures, namely, the input layer, hidden layer, and output layer [15]. Taking the process of ticket price prediction for the PPP subway service as an example, the basic structure of the BP neural network model is shown in Figure 1.

Combined with the diagram shown in Figure 1, the construction process of the BP neural network in this paper is as follows.

The input vector $X = (x_1, x_2, \ldots, x_n)$ and the output variable $Y = (y)$ are brought into the BP neural network, and the output values of each unit in the hidden layer [15] are

$$Z_j = F\left(\sum_{i=1}^{n}(w_{ij}x_i - b_j)\right), \quad (2)$$

where Z_j is the input value of the hidden layer; w_{ij} and b_j are, respectively, the connection weights and thresholds of input layer and hidden layer; i is the dimension of the input layer, $i = 1, 2, \ldots, n$; and j is the dimension of hidden layer, $j = 1, 2, \ldots, n$. F is the activation function of the hidden layer.

The output value of each unit in the output layer is calculated by using the connection weight w_{ij} and threshold b_j of the hidden layer and the output layer as reported in [15]:

$$O_t = G\left(\sum_{j=1}^{m}\left(w_{tj}F\left(\sum_{i=1}^{n}(w_{ij}x_i - b_j)\right) - b_t\right)\right), \quad (3)$$

where O_t is the output value of the output layer, t is the dimension of the output layer, $j = 1, 2, \ldots, l$, and G are the activation functions of the output layer.

Therefore, the sum of the error squares of the output vector O and the actual value Y of the ticket price is as previously reported [15, 16]:

$$E = \frac{1}{2}\sum_{t=1}^{l}(y_t - O_t)^2. \quad (4)$$

Gradually extending backward to the hidden layer and the input layer, we can further calculate and obtain (5) as reported in [14, 15]:

$$E = \frac{1}{2}\sum_{t=1}^{l}\left(y_t - G'\left(\sum_{j=1}^{m}\left(w_{jt}F'\left(\sum_{i=1}^{n}(w_{ij}x_i - b_j)\right) - b_t\right)\right)\right)^2, \quad (5)$$

where F' and G' are the inverse functions of activation functions F and G, respectively.

According to the principle of minimum error, the gradient descent method is adopted, and through iterative solution, connection weights, and thresholds of the input layer and hidden layer, the hidden layer and output layer are corrected item by item, so that the final output result of the neural network approaches the expected output value, thus reaching the preset value of the error square sum E.
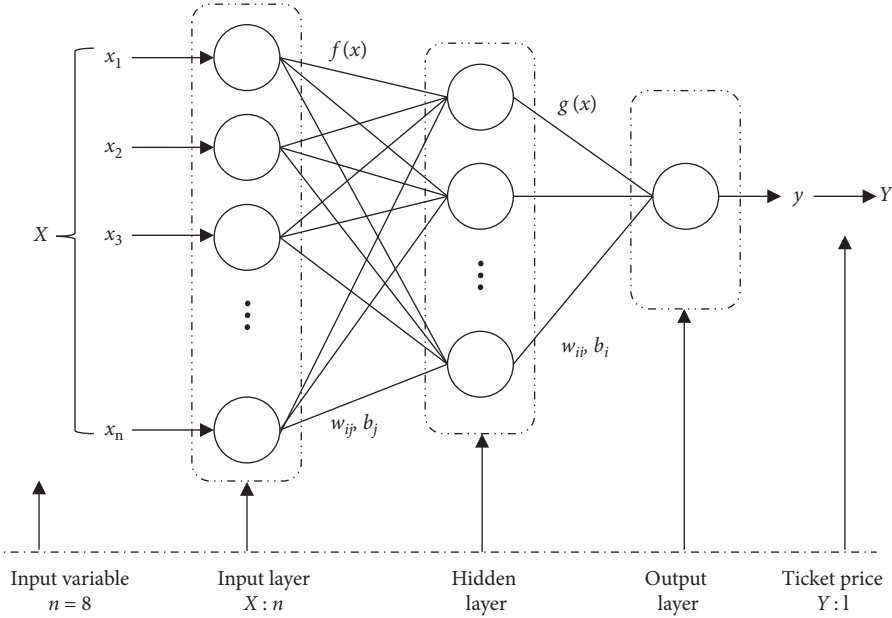
FIGURE 1: Structure diagram of the neural network.

2.2.2. Introduction to SSA. The SSA was proposed in 2020. SSA is mainly inspired by the sparrows' foraging behavior and antipredation behavior. This is a novel algorithm that has the advantages of strong optimization ability and fast convergence speed. The SSA is used to optimize the initial weights of the BP neural network and develop the SSA-BP model, which not only makes full use of the mapping ability of the BP neural network, but also has the rapid global convergence and learning ability of the SSA.

Considering that the SSA is quite new, this paper introduces the main rules of the SSA in detail as reported in [24], so that the readers can better understand the research content of this paper:

Rule (1). The discoverer usually has a high energy reserve and is responsible for searching for areas rich in food in the whole environment, providing foraging areas and directions for all participants. In the development of the model, the level of energy reserve depends on the fitness value of sparrows.

Rule (2). Once sparrows find predators, individuals start to sing as alarm signals. When the alarm value is greater than the safe value, the discoverer will take the participants to other safe areas for foraging.

Rule (3). The identities of the discoverers and entrants are dynamically changing. As long as we can find a better food source, every sparrow can become a discoverer, but the proportion of discoverers and entrants in the total population remains unchanged.

Rule (4). The lower the energy of the participants, the worse their foraging position in the whole population. Some hungry entrants are more likely to fly to other places to find food for more energy.

Rule (5). In the process of foraging, participants can always search for the discoverer that provides the best food and then get food from the best food source or forage around the discoverer. At the same time, in order to increase their predation rate, some participants may constantly monitor the discoverers and compete for food resources.

Rule (6). When being aware of the danger, sparrows at the edge of the population will quickly move to a safe area to get a better position, while sparrows in the middle of the population will fly randomly to get close to other sparrows.

According to the above rules, when using virtual sparrows to search for food, the population composed of n sparrows can be expressed [24] as follows:

$$\mathbf{X} = \begin{bmatrix} x_{11} & x_{12} & \cdots & x_{1d} \\ x_{21} & x_{22} & \cdots & x_{2d} \\ \cdots & \cdots & \cdots & \cdots \\ x_{n1} & x_{n2} & \cdots & x_{nd} \end{bmatrix}, \tag{6}$$

where d denotes the dimension of the problem variable to be optimized and n is the number of sparrows.

The fitness values of all sparrows can be expressed [24] as follows:

$$\mathbf{F}_x = \begin{bmatrix} f([x_{11} \quad x_{12} \quad \cdots \quad x_{1d}]) \\ f([x_{21} \quad x_{22} \quad \cdots \quad x_{2d}]) \\ \cdots \\ f([x_{n1} \quad x_{n2} \quad \cdots \quad x_{nd}]) \end{bmatrix}, \tag{7}$$

where f denotes fitness.

In the SSA, the discoverer with better fitness value will get food first during the search process. In addition, the discoverer is responsible for finding food for the whole sparrow population and providing foraging directions for all

participants. Therefore, the discoverer can obtain a larger foraging search range than the entrant. According to Rule (1) and Rule (2), $R_2 < ST$ means that there are no predators around the foraging environment at that time and the discoverer can perform extensive search operations. $R_2 \geq ST$ means that some sparrows in the population have found predators and sent an alarm to other sparrows in the population. At this time, all sparrows need to rapidly fly to other safe places for foraging.

During each iteration, the location update of the discoverer is described [25] as follows:

$$
\mathbf{X}_{i,j}^{t+1} = \begin{cases} \exp\left(-\dfrac{1}{\alpha * \text{item}_{\max}}\right) * \mathbf{X}_{i,j}^{t}, & \text{if } R_2 < ST, \\ \\ \mathbf{X}_{i,j}^{t} + Q * \mathbf{L}, & \text{if } R_2 \geq ST, \end{cases} \tag{8}
$$

where t represents the current iteration number, $j = 1, 2, 3, \ldots, d$, and $\text{item}_{\max}$ denotes the maximum iteration number. $\mathbf{X}_{i,j}^{t}$ indicates the position information of the i-th sparrow in the j-th dimension in the t-th iteration, and α represents a random number less than or equal to 1 but greater than 0. R_2 ($R_2 \in [0,1]$) and ST ($ST \in [0.5,1]$) represent the warning value and the safety value, respectively. Q is a random number that obeys normal distribution. $\mathbf{L}$ denotes a $1 \times d$ matrix, in which every element in the matrix is 1.

For the participants, they need to execute Rule (3) and Rule (4). As described above, during the foraging process, some participants will keep an eye on the discoverer. Once they perceive that the discoverer has found better food, they will immediately leave their present position to compete for food. If they win, they can get the food of the discoverer immediately; otherwise, they need to continue to execute Rule (4). When $i > 0.5n$, this indicates that the i-th participant with low fitness value does not have food and is in a very hungry state. At this time, it is necessary to fly to other places for food to get more energy. The location update of the enrolee is described [24, 25] as follows:

$$
\mathbf{X}_{i,j}^{t+1} = \begin{cases} Q * \exp\left(\dfrac{\mathbf{X}_{\text{worst}} - \mathbf{X}_{i,j}^{t}}{i^2}\right), & \text{if } i > 0.5n, \\ \\ \mathbf{X}_P^{t+1} + \left|\mathbf{X}_{i,j} - \mathbf{X}_P^{t+1}\right| \cdot \mathbf{A}^+ \cdot \mathbf{L}, & \text{otherwise,} \end{cases} \tag{9}
$$

where $\mathbf{X}_P$ is the best position occupied by the discoverer at the moment and $\mathbf{X}_{\text{worst}}$ represents the worst position in the world at the moment. $\mathbf{A}$ represents a $1 \times d$ matrix, in which each element is randomly assigned 1 or -1, and $\mathbf{A}^+ = \mathbf{A}^T(\mathbf{A}\mathbf{A}^T)^{-1}$.

In the simulation experiment, we assume that the sparrows aware of danger account for 10% to 20% of the total population. The initial positions of these sparrows are randomly generated in the population. According to Rule (5), $f_i > f_g$ means that the sparrows are at the edge of the population at that time and are extremely vulnerable to predators. $\mathbf{X}_{\text{best}}$ indicates that the sparrow at that position is

at the best position in the population and is very safe. When $f_i = f_g$, it shows that sparrows in the middle of the population are aware of the danger and need to approach other sparrows to minimize the risk of predation.

The specific mathematical expression can be written [24, 26] as follows:

$$
\mathbf{X}_{i,j}^{t+1} = \begin{cases} \mathbf{X}_{\text{best}}^{t} + \beta * \left|\mathbf{X}_{i,j}^{t} - \mathbf{X}_{\text{best}}^{t}\right|, & \text{if } f_i > f_g, \\ \\ \mathbf{X}_{i,j}^{t} + K * \left(\dfrac{\left|\mathbf{X}_{i,j}^{t} - \mathbf{X}_{\text{worst}}^{t}\right|}{(f_i - f_w) + \varepsilon}\right), & \text{if } f_i = f_g, \end{cases} \tag{10}
$$

where $\mathbf{X}_{\text{best}}^{t}$ is the current global optimal position. β, as a step control parameter, is a random number that obeys the standard normal distribution. $K \in [0,1]$ is a random number, which indicates the moving direction of sparrows and is also a step control parameter. f_i is the fitness value of individual sparrows. f_g and f_w are the best and worst fitness values, in the world, respectively. ε is used to avoid having zero in the denominator.

2.2.3. Introduction to the MIV Method.
The MIV method proposed by Dombi et al. [42] is considered as one of the best indexes to evaluate the correlation of variables in neural networks. The basic idea of applying the MIV method to the model developed in this study is to take the variables with a significant impact on the price of the ticket for the PPP subway system as the input parameters of the prediction model and to eliminate the variables that have less impact.

The specific implementation method of the MIV method is as follows:

Step 1. The training samples to train the SSA-BP neural network are selected, and the prediction model Ptrain is obtained .

Step 2. Each characteristic variable in sample $\mathbf{T}$ is increased or decreased by 10%, and the new samples $\mathbf{T}_1$ and $\mathbf{T}_2$ are obtained. Samples $\mathbf{T}_1$ and $\mathbf{T}_2$ are then regressed with the aid of the model Ptrain, and the regression results $\mathbf{A}_1$ and $\mathbf{A}_2$ are obtained.

Step 3. $\mathbf{E} = \mathbf{A}_1 - \mathbf{A}_2$ is taken as the change value that influences the output result after the characteristic variable changes, and the MIV is obtained by averaging $\mathbf{E}$ according to the number of samples. According to the MIV value, the extent of the influence of each characteristic variable on ticket price is obtained.

Step 4. The relative contribution rate of each variable α_i is calculated [24] as follows:

$$
\alpha_i = \frac{|\text{MIV}_i|}{\sum_{i=1}^{n} |\text{MIV}_i|}, \tag{11}
$$

where MIV_i is the MIV value of the i-th index.

Step 5. Input variables with relative contribution rate greater than 10% are selected as key input variables.

2.2.4. Prediction Model Based on the MIV-SSA-BP. The basic flow chart of the SSA-BP model is shown in Figure 2, and the input variable screening method based on the MIV is shown in Figure 3. The prediction model proposed in this paper is mainly divided into three parts. (1) All input variables are brought into the fare prediction model based on the SSA-BP. (2) The MIV method is used to obtain the key variables. (3) The key variables are brought into the SSA-BP to predict the ticket price again.

It should be emphasized that the mathematical model constructed in this paper can be applied to the study of complex and nonlinear data prediction. If the input and output variable system constructed in this paper is adopted, the model proposed in this paper can quickly and accurately predict the price of subway PPP project.

The calculation steps of the intelligent prediction method proposed in this paper are as follows:

Step 1. The input data is normalized by (1).

Step 2. The learning parameters of the SSA and BP algorithm are determined according to the size and characteristics of the learning samples. Equation (6) is used to initialize the predator and joiner. Then, (2)–(5) are used to initialize the BP neural network. The detailed construction process of the BP neural network is shown in Section 2.2.1.

Step 3. The fitness value of each virtual sparrow is calculated by (7) and then sorted. The positions of the discoverer, joiner, and watcher are updated with (8)–(10), respectively.

Step 4. The fitness value is calculated and the sparrow position is updated.

Step 5. Whether the stop condition is met is determined; if yes, then exit and output the result. Otherwise, Steps 3–4 are repeated.

Step 6. The MIV method described in Section 2.2.3 is used to calculate and obtain the key input variables.

Step 7. Finally, Steps 2–5 are reexecuted, and the obtained key input variables are brought into the SSA-BP model to obtain the final output result.

3. Case Study

3.1. Data Sources. In this paper, Beijing Subway Line 4, Wuhan Metro Line 2, and Chengdu Metro Line 1, three typical PPP subway systems, were selected as case studies. Beijing Metro Line 4 was put into trial operation on September 28, 2009. As of October 1, 2020, the private capital investors and government agency have adjusted the price 10 times. Wuhan Metro Line 2 was put into operation on December 28, 2012. As of October 1, 2020, Wuhan Metro Line 2 has a total length of 60.8 kilometres, with an average daily passenger flow of more than 150,000 passengers. During the operation period, the private capital investors and government agency have adjusted the price six times. Chengdu Metro Line 1 was put into operation on September 27, 2010. As of October 1, 2020, Chengdu Metro Line 1 has a total length of 41 kilometres, with a total of 35 stations, with

the highest single-day passenger traffic of 1,091,900 passengers on February 19, 2019. During the operation of Chengdu Metro Line 1, the private capital investors and the government agency adjusted the price nine times.

Using the index acquisition method of each input variable shown in Table 1, the 25 price adjustment data sets of the three PPP subway systems are obtained as shown in Table 2.

In Table 2, the monetary unit of $X1$, $X2$, and $X4$ is RMB. The $X5$ loan interest rate is the five-year national debt interest rate issued by the Chinese government. The $X6$ is expressed by the consumer price index (CPI) published by the Chinese government. The $X8$ data is directly derived from the questionnaire survey results provided by the PPP Project Company of Metro.

3.2. Correlation Analysis of Various Variables. In order to study the linear correlation between the input variables and the output variable (the ticket price), the Pearson correlation analysis method is used to quantitatively describe the degree of linear correlation between the parameters [43]. The detailed calculation principle and method used have been previously reported [43]. The closer the Pearson correlation coefficient (r) is to 1, the stronger the linear correlation between the two indicators. When the r is equal to 0, there is no linear correlation between the two indicators. When the r is positive, the indicators are positively correlated, and when r is negative, they are negatively correlated; r is defined as

$$r = \frac{\sum_{i=1}^{n} (x_i - \overline{x})(y_i - \overline{y})}{\sqrt{\sum_{i=1}^{n} (x_i - \overline{x})^2 (y_i - \overline{y})^2}}, \tag{12}$$

where x_i is the value of an input variable, $\overline{x}$ is the average value of an input variable, y_i is the value of another input variable, and $\overline{y}$ is the average value of another input variable.

Substituting the data in Table 2 into (12), the obtained calculation results are shown in Table 3. In Table 3, the absolute value of the values in bold is greater than 0.8, which indicates that there is a significant correlation between these two indicators.

According to the calculation results listed in Table 3, among the 8 input variables of the ticket price prediction of the PPP subway system, the linear relationship between the indexes is mostly weak. However, $X2$ and $X4$ have a correlation coefficient of 0.812, $X4$ and $X7$ have a correlation coefficient of 0.857, and $X5$ and $X6$ have a correlation coefficient of 0.894, which indicates that these variables have a certain positive linear correlation between them. The correlation coefficient between $X5$ and $X7$ is −0.840, and the correlation coefficient between $X6$ and $X7$ is −0.913, which indicates that there is a certain negative linear correlation between these variables. The absolute values of other correlation coefficients are all lower than 0.8, indicating that their linear correlation is quite weak. Therefore, when using the input variables constructed in Section 2.1 of this paper to predict the PPP subway tickets, the nonlinear modeling method should be favored [28].
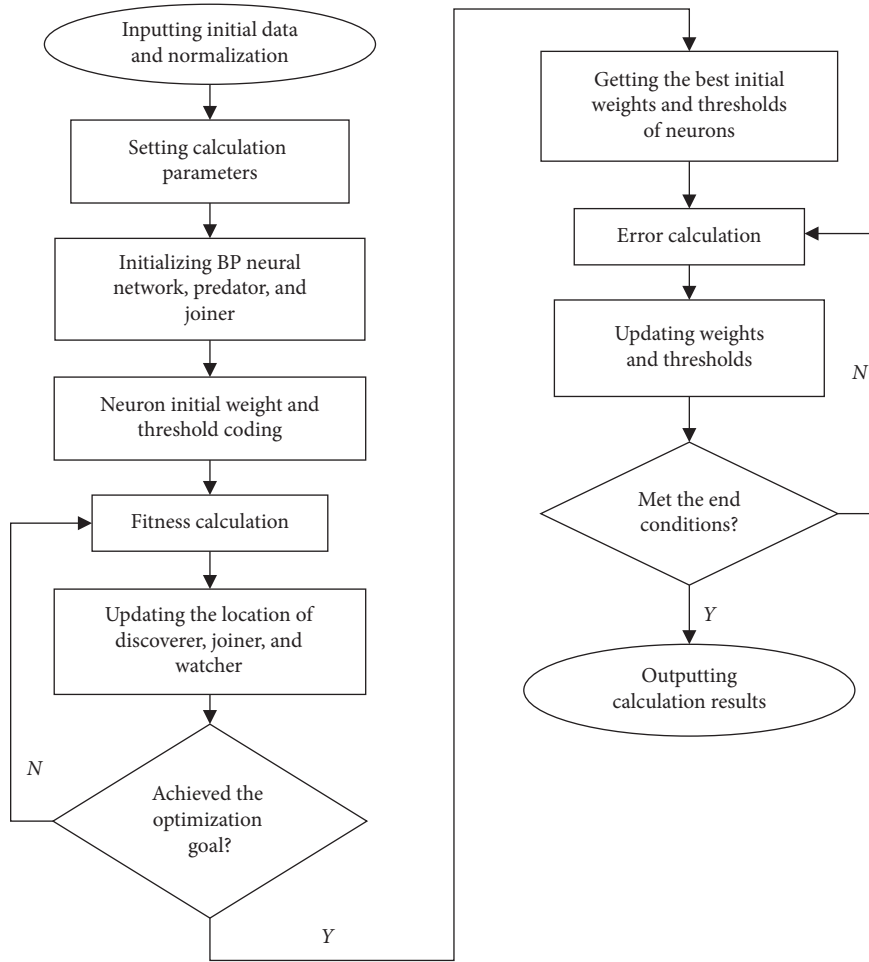
Figure 2: Flow chart of the SSA-BP model.
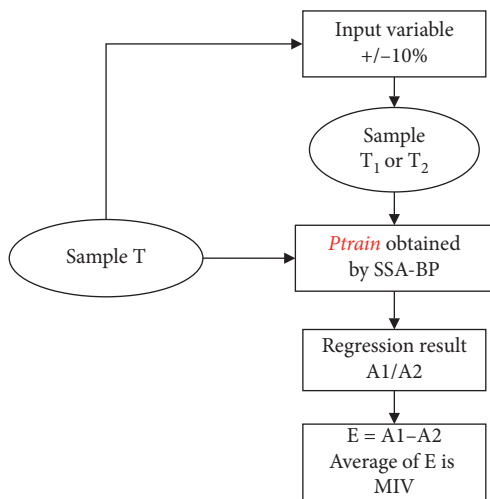
Figure 3: Flow chart of the MIV method.

3.3. Ticket Price Forecast Based on SSA-BP. In the modeling process of the SSA-BP, data sets can be divided into training sets and test sets. Among them, the training data set is used to train the model, while the test data set is used to evaluate the model. The ratio between the common training data set and test set is 90 : 10%, 80 : 20%, or 70 : 30% [44]. Considering that there are 25 data sets in this paper, the first 20 samples are set as the training data set, and the last 5 samples are set as the test data set. In other words, the ratio between training data set and test data set in this paper is 75 : 25%.

In this study, three indexes, namely, the mean absolute percentage error (MAPE), the root mean square error (RMSE), and the coefficient of determination (R^2), are used to evaluate the calculation accuracy of the prediction model.

The value of the MAPE is 0%, indicating that the prediction result is perfect [45]. If the MAPE is greater than 100%, it is generally considered that the prediction result is unavailable. MAPE is defined as follows:

$$\text{MAPE} = \frac{1}{n} \sum_{i=1}^{n} |y_i - \dot{y}_i|, \tag{13}$$

where n is the number of sample points, y_i is the predicted value of the ticket price of the PPP subway system, and $\dot{y}_i$ is the actual value.

The RMSE [46] can directly reveal the average error between the predicted value and the true value, and when the predicted value is completely consistent with the true value,

TABLE 2: Engineering data.

No. (unit)	X1 (million)	X2 (billion)	X3	X4 (million)	X5 (%)	X6 (%)	X7 (%)	X8	Y (RMB/km)
1	19.612	1411.360	4	138.800	4.39	2.9	8	77	0.37
2	20.186	1625.190	5	156.000	4.40	1.3	7	60	0.37
3	20.693	1780.102	5	173.200	4.42	1.4	6.8	82	0.38
4	20.693	1780.102	6	178.800	4.42	1.7	7	83	0.42
…	…	…	…	…	…	…	…	…	…
24	16.330	1534.277	7	217.000	4.40	4.5	5.5	87	0.48
25	16.581	1701.265	9	223.500	4.42	4.9	6.5	80	0.50

TABLE 3: Pearson correlation coefficient between indexes.

Factor	X1	X2	X3	X4	X5	X6	X7	X8
X1	1.000	0.514	0.231	0.423	0.123	−0.362	0.378	0.271
X2	—	1.000	0.482	**0.812**	−0.381	−0.575	0.432	0.154
X3	—	—	1.000	**−0.834**	0.041	0.234	0.340	0.299
X4	—	—	—	1.000	0.104	0.246	**0.857**	0.430
X5	—	—	—	—	1.000	**0.894**	**−0.840**	0.255
X6	—	—	—	—	—	1.000	**−0.913**	0.129
X7	—	—	—	—	—	—	1.000	−0.311
X8	—	—	—	—	—	—	—	1.000

Bold values mean that the absolute value is greater than 0.8.

it is equal to 0, that is, the perfect model. The larger the error, the larger the value. The RMSE is defined as shown in (14), which can be used to calculate it, as follows:

$$\text{RMSE} = \sqrt{\frac{1}{n} \sum_{i=1}^{n} (y_i - \dot{y}_i)^2}. \tag{14}$$

The closer the value of R^2 [47] is to 1, the better the prediction result is. The result obtained here is 0, indicating that the model fitting effect is very poor.

$$R^2 = 1 - \frac{\sum_{i=1}^{n} (y_i - \dot{y}_i)^2}{\sum_{i=1}^{n} (y_i - \overline{y}_i)^2}, \tag{15}$$

where $\overline{y}_i$ is the average value of the predicted values.

In the SSA proposed in this paper, the population size is set to $n = 50$, the maximum number of iterations is 200, the safety threshold ST = 0.8, discoverers account for 20% of the population size, and the number of sparrows aware of danger SD = 5. The experimental environment is as follows: the simulation experiment was performed in the Matlab 2016a on a 3.40 GHz Intel i7 processor and a computer with 16 GB memory.

In this study, the BP neural network is trained by the Levenberg–Marquardt algorithm. The maximum training times are 200, the coefficient of motion vector is 0.3, and the minimum mean square error is 10^{-5}.

The activation functions of the hidden layer and output layer, respectively, adopt the logsin function $F(x)$ and purelin linear function $G(x)$, shown as follows:

$$F(x) = \frac{1}{1 + e^{-x}},$$
$$G(x) = x. \tag{16}$$

The number of nodes in different hidden layers may have an impact on the BP prediction results. Therefore, this study calculates the calculation error of the prediction model under different hidden layer nodes. According to past research studies [20, 22], the number m of hidden layer nodes is selected according to the following empirical equation:

$$m = \sqrt{n + l} + \delta, \tag{17}$$

where δ is a constant in the range of 1–10, n is the dimension of hidden layer, and l is the dimension of the output layer.

Substituting $n = 8$ and $l = 1$ into (17), we can obtain $m = 4, 5, \ldots, 13$. In order to find the optimal value of the hidden layer node m, the SSA-BP neural network is trained with $m = 4, 5, \ldots, 13$, and the training results are compared. The calculation results are shown in Table 4. In Table 4, the values in bold indicate the calculation results with the highest calculation accuracy.

The data in Table 4 reveal that when the number of hidden layer neuron nodes is $m = 6$, the MAPE and RMSE are the smallest and R^2 is the largest, and the BP neural network is the most accurate algorithm to predict the ticket price for the PPP subway service. Therefore, the number of hidden layer nodes in the SSA-BP model is ultimately determined to be 6.

The data in Table 4 show that when all variables affecting the prediction of the ticket price for the PPP subway service are taken as the input parameters of the SSA-BP neural network model, the calculation accuracy reaches 95.59%, which still does not meet the practical application requirements. Considering that the input variables may have influence on the prediction accuracy of the BP neural network model, the key variables are screened out by this method, and the calculation results are shown in Table 5.

The data in Table 5 reveal that 8 input variables have different effects on the prediction of ticket price for the

TABLE 4: Effect of the number of nodes in different hidden layers on the prediction.

Number of hidden layer nodes	MAPE (%)	RMSE	R^2 (%)
4	4.213	0.029	93.23
5	3.487	0.022	94.31
6	**2.912**	**0.018**	**95.59**
7	4.781	0.027	92.65
8	6.573	0.029	90.46
9	7.378	0.023	88.10
10	9.958	0.030	86.02
11	8.260	0.0300	88.35
12	6.317	0.026	91.13
13	4.098	0.023	93.49

The numerical value in bold represents the calculation result with the highest calculation accuracy.

TABLE 5: Calculation results of the input variables based on MIV.

Variables	MIV	Order	Relative contribution rate (%)	Cumulative contribution rate (%)
$X7$	0.071	1	28.63	28.63
$X2$	−0.053	2	21.37	50.00
$X3$	0.046	3	18.55	68.55
$X4$	0.032	4	12.90	81.45
$X5$	−0.027	5	10.89	92.34
$X6$	0.014	6	5.65	97.98
$X1$	−0.003	7	1.21	99.19
$X8$	0.002	8	0.81	100.00

PPP subway service. The MIV values of $X2$, $X5$, and $X1$ are all negative, which indicates that these three input variables are negatively correlated with the ticket price. Other indicators are positively correlated with the ticket price. The relative contribution rates of $X7$, $X2$, $X3$, $X4$, and $X5$ are all higher than 10%, while the relative contribution rates of the remaining input variables are lower than 10%. Therefore, in this case study, $X7$, $X2$, $X3$, $X4$, and $X5$ are selected as the key input variables for the prediction of the ticket price for the PPP subway service.

The $X7$, $X2$, $X3$, $X4$, and $X5$ are brought back into the prediction model based on the SSA-BP model, and some parameter settings are almost unchanged. However, since the input variables have changed, the number of hidden layer nodes needs to be redetermined. According to empirical equation (17), when the number of hidden layer neuron nodes is $m = 5$, the MAPE (2.381%) and RMSE (1.4780) are the smallest and R^2 (97.31) is the largest, and the BP neural network is the most accurate to predict the ticket price for the PPP subway service. The chart of the error loss function is shown in Figure 4.

To further clarify the optimization calculation process of SSA, detailed optimization calculation process is shown in Table 6.

According to the calculation results shown in Figure 4 and Table 6, the fitness of the SSA rapidly decreases in the initial stage (about 20–55 generations). Then, with the increase of the number of iterations, the fitness eventually converges to 45.31411. This shows that the SSA effectively optimizes the BP model. Comparison with the convergence curves of the GA and PSO algorithm indicates that the SSA has faster convergence speed. The analysis of the calculation results of the different algorithms will be shown in detail in Section 4.1.
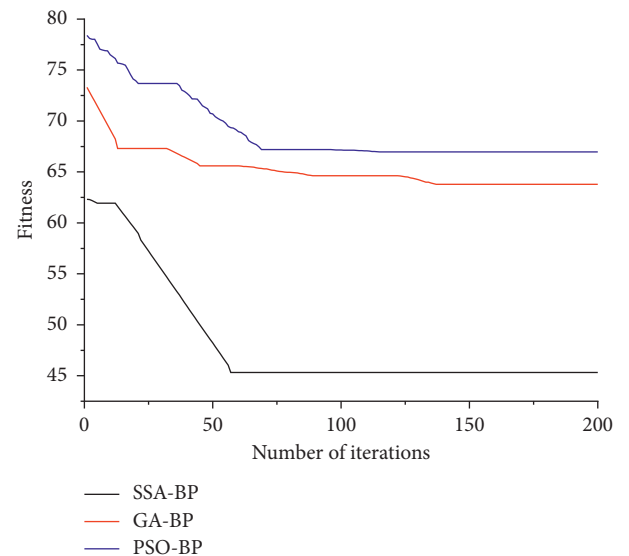
FIGURE 4: Chart of the fitness.

The Bland–Altman analysis of the predicted and measured ticket prices [48], shown in Figure 5, reveals that the predicted values of five groups of ticket prices are within (−1.96SD, +1.96SD). Thus, according to the Bland–Altman analysis method, 95% of the predicted points are within the consistent range. Therefore, considering the application of ticket price prediction, the prediction method developed in this study is feasible.

The 10-fold cross-validation method is often used to test the accuracy of algorithms. The basic idea is to divide the data set into ten parts, and take turns to take 9 parts as

TABLE 6: Detailed optimization calculation process.

Iteration (n)	Fitness ($n-1$)	Fitness (n)	Fitness (n)–fitness ($n-1$)	Result
56	46.39730	46.03623	0 < 0.00001	Continue
57	46.03623	45.31411	0.361063611 > 0.0001	Continue
58	45.31411	45.31411	0 < 0.0001	Continue
200	45.31411	45.31411	0 < 0.0001	Stop
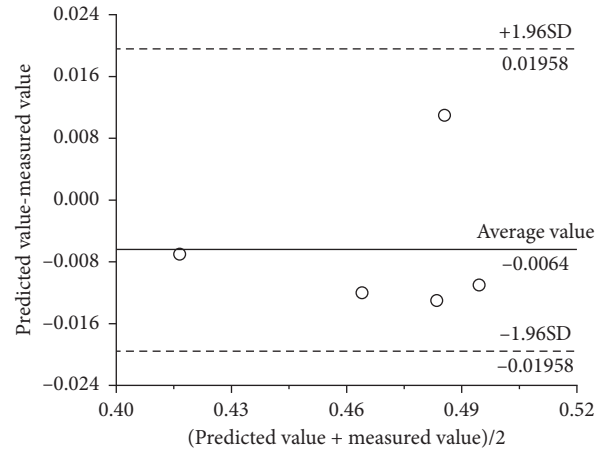
FIGURE 5: Bland–Altman analysis of the predicted values and actual values.

TABLE 7: Calculation results of the 10-fold cross-validation.

No.	1	2	3	4	5	6	7	8	9	10
MAPE (%)	2.38	2.45	2.94	2.57	2.01	2.50	1.95	2.48	3.14	2.63
RMSE	0.014	0.015	0.015	0.015	0.014	0.015	0.014	0.014	0.015	0.015
R^2 (%)	97.31	96.45	97.58	96.85	95.97	96.79	97.30	96.43	97.52	97.93

training data and 1 part as test data for experiments. In this paper, the 10-fold cross-validation method is used to test the accuracy of the proposed model, and the calculation results are shown in Table 7.

The calculation data in Table 7 indicate that the ten prediction results have good prediction accuracy and calculation stability. These findings show that the calculation results of the case analysis are accurate and no overfitting phenomenon occurs.

4. Discussion

Based on the MIV method, the SSA, and the BP algorithm, this study developed an intelligent prediction method of the ticket price for a PPP subway system. However, this study has the following three limitations: (1) The definition of the ticket price for the PPP subway system in the introduction of this paper is the ticket price when the government and private capital investors play a game, not the actual ticket price for the customers. Different definitions of the ticket price may influence the research results of this study. (2) More novel algorithms, such as chaotic local search-based differential evolution algorithm (CLSDEA) [49], can be used to optimize the BP model. (3) The calculation parameter

setting of optimization algorithm has obvious influence on the calculation efficiency of optimization algorithm [50, 51], but this paper has not completed the relevant analysis.

4.1. Analysis of the Calculation Accuracy of Different Prediction Models.
The research results in the third section of this paper show that the prediction model proposed in this paper has high accuracy and stability. However, these research results can only confirm the validity of the model proposed in this paper. In order to further analyze the advancement of the model proposed in this paper, in this section we compare various prediction methods, including price adjustment method based on PPP contract, multiple regression, BP, GA-BP, PSO-BP, and support vector machine (SVM).

According to the historical data of three subway station projects, the price adjustment results based on the PPP contract were obtained and are shown in Table 8. In engineering practice, every price adjustment based on contract took about 1-2 months.

When multiple regression analysis was adopted, the first 20 groups of data of 8 input variables were all brought in. According to the calculation of Excel 2016 software, the relationship between 8 input variables and output variable was

TABLE 8: Comparison of calculation results of different models with 8 input variables.

Error representations	MAPE (%)	RMSE	R^2 (%)
Price adjustment method based on PPP contract	49.375	0.052	65.12
Multiple regression	37.421	0.091	46.43
BP	12.684	0.043	80.92
GA-BP	7.471	0.029	88.39
PSO-BP	3.070	0.018	92.50
SVM	3.467	0.016	93.45
SSA-BP	2.912	0.015	95.59

TABLE 9: Comparison of the results of different models after processing by the MIV method.

Error representations	Number of input variables	MAPE (%)	RMSE	R^2 (%)
BP	6	13.403	0.042	82.50
GA-BP	5	7.849	0.024	84.62
PSO-BP	5	3.345	0.019	93.36
SVM	5	2.762	0.016	94.93
SSA-BP	5	2.380	0.014	97.31

$$Y = -0.000265 * X2 + 0.043352 * X3 - 0.026143 * X5$$
$$+ 0.002107 * X7.$$

(18)

The last five groups of data were brought into (18), and the calculation results are shown in Table 8. In addition, according to (18), it was not difficult to find that the output variable only had linear relationships with $X2$, $X3$, $X5$, and $X7$. This was basically similar to the analysis results in Section 3.2.

The calculation parameters of BP model were the same as those in Section 3.3. In the GA [20], the learning step was 0.1, the number of genetic iterations was 200, the initial population number was 20, and the classification error was 0.00001. In the PSO [22], inertia weight was 0.6, learning factors $C1$ and $C2$ were 2, initial population number was 20, and maximum iteration number was 200. In the SVM [52], the range of penalty variable was [1, 1000], and the range of width parameter was [0.1, 10]. The related calculation results are shown in Table 8.

From the convergence curves of the GA and the PSO in Figure 4, it is not difficult to find that GA converges in 120–150 generations, while the PSO converges in 80–100 generations. However, the SSA had faster convergence speed than the GA or the PSO.

In this paper, the MIV method was used to screen the input variables of the SSA-BP model, which might affect the calculation results. Therefore, the MIV method was used to screen the input variables of the BP, GA-BP, PSO-BP, and SVM, and the key input variables with relative contribution rate greater than 10% were selected. The calculation results are shown in Table 9.

4.2. Stability Analysis of Different Prediction Models. In addition to the calculation accuracy, the stability of the calculation results of the model is another factor that affects its application and popularization. In this paper, the BP, the

GA-BP, the PSO-BP, the SVM, and the SSA-BP were used for repeated calculation 100 times, and the standard deviations of R^2 are shown in Table 10.

It can be seen from the calculation results in Table 10 that the standard deviation of R^2 of SSA-BP model is the smallest (0.001398) and its calculation result is the most stable. The stabilities of the PSO-BP, the GA-BP, and the BP decreased in turn. This showed that the computational stabilities of these metaheuristic algorithms were SSA (0.001398) > PSO (0.008376) > GA (0.023339), which was the same as the previous results [24, 25, 53]. In addition, the standard deviation of R^2 of BP was obviously larger than SSA-BP, PSO-BP, and GA-BP. This indicates that the optimization algorithm is reasonable and effective in improving the BP model. It is worth mentioning that Wu [53] used the SSA to find the optimal parameters of the Least Squares Support Vector Machine (LSSVM) and achieved good results. This further proves the superiority of the SSA, which is a novel metaheuristic optimization algorithm.

4.3. Comparison of the Prediction Results of Different Relative Contribution Rates. Relative contribution rate is an important concept in the MIV model, which is the threshold for selecting key input variables. At present, the selection of this threshold is artificial and subjective [33, 34]. In Section 3, the variables whose relative contribution rates were greater than 10% were selected as the key variables. In order to discuss the rationality of this approach, this paper made a parametric analysis of the relative contribution rate in the MIV. When the relative contribution rate was 5%, 15%, and 20%, the prediction results of the model were calculated and are shown in Table 11.

In this section, the relative contribution rate was analyzed by parameters, and the influence of different input variables on the calculation results was actually analyzed. According to the calculation results in Table 11, when $\alpha_i = 10\%$, the model has the best calculation accuracy and calculation time. This shows that the artificial

TABLE 10: Stability analysis of different calculation methods.

Calculation method	BP	GA-BP	PSO-BP	SVM	SSA-BP
Number of input variables	6	5	5	5	5
Standard deviation of R^2	0.029487	0.023339	0.008376	0.002843	0.001398

TABLE 11: Analysis of prediction results under different relative contribution rates.

α_i (%)	Selected input variables	MAPE (%)	RMSE	R^2	Computing time
5	$X7, X2, X3, X4, X5, X6$	3.047	0.016	95.64	15 min 18 s
10	$X7, X2, X3, X4, X5$	2.381	0.014	97.31	13 min 42 s
15	$X7, X2, X3$	3.515	0.016	92.58	7 min 29 s
20	$X7, X2$	5.487	0.018	87.63	5 min 37 s

selection of 10% in most studies using MIV is reasonable. With the increase of the value of α_i, the number of input variables becomes less and less, the calculation error becomes larger and larger, and the calculation time becomes shorter.

When $\alpha_i = 25\%$, only one input variable, $X7$, is selected. At this time, the problem degenerates into studying the mapping relationship between an input variable ($X7$) and an output variable (Y). Therefore, this paper did not discuss the calculation accuracy and time when the value of α_i was larger.

5. Conclusions

It is critically important to rapidly and accurately predict the ticket price to protect the interests of the customer, the private capital investors, and the government. In order to deal with the complexity and nonlinear relationship of the PPP subway system ticket prediction, a new intelligent prediction method is proposed in this paper. The model combines the global convergence of the SSA and the nonlinear analysis ability of a neural network algorithm and improves the accuracy and stability of the neural network training. This study shows that, for Beijing Subway Line 4, Wuhan Metro Line 2, and Chengdu Metro Line 1, the linear relationship between most input variables is not adequate. Among all pairwise correspondences, only three groups of correspondences have significant linear correlation. A nonlinear modeling method should be given priority in the prediction of ticket price for PPP subway system. The MIV method is used to screen the characteristic variables of the ticket price prediction for the PPP subway system, and it is found that the rate of return on investment, total local GDP, number of similar vehicles $X3$, financial subordinate $X4$, and loan interest rate $X5$ can be used as key input variables. Compared with other prediction methods (the price adjustment method based on PPP contract, the traditional BP, the BP improved by the GA, the BP improved by the PSO algorithm, and the SVM), the model proposed in this paper had better prediction accuracy and calculation stability. How to predict the actual fare of subway according to the results of this study is the direction of further research in the future.

Data Availability

The case analysis data used to support the findings of this study are available from the corresponding author upon request.

Conflicts of Interest

The authors declare that there are no conflicts of interest regarding the publication of this paper.

Acknowledgments

References

[1] X. J. Li and P. E. D. Love, "State-of-the-art review of urban rail transit public-private partnerships," *Journal of Infrastructure Systems*, vol. 26, no. 3, Article ID 03120002, 2020.

[2] L. E. Brandão, C. Bastian-Pinto, and L. L. Gomes, "Government supports in public-private partnership contracts: metro line 4 of the sao paulo subway system," *Journal of Infrastructure Systems*, vol. 18, no. 3, pp. 218–225, 2012.

[3] M. De Jong, R. Mu, D. Stead et al., "Introducing public-private partnerships for metropolitan subways in China: what is the evidence?" *Journal of Transport Geography*, vol. 18, no. 2, pp. 301–313, 2010.

[4] H. M. Wang, W. Xiong, G. D. Wu et al., "Public-private partnership in public administration discipline: a literature review," *Public Management Review*, vol. 20, no. 2, pp. 293–316, 2018.

[5] Z. Chang, "Public-private partnerships in China: a case of the Beijing no. 4 Metro line," *Transport Policy*, vol. 30, no. 2013, pp. 153–160, 2013.

[6] S. Sturup, "Swimming or drowning in the depths of partnership," *Australian Journal of Public Administration*, vol. 76, no. 3, pp. 288–300, 2017.

[7] C. Gordon, C. Mulley, N. Stevens et al., "Public-private contracting and incentives for public transport: can anything be learned from the Sydney Metro experience?" *Transport Policy*, vol. 27, no. 2013, pp. 73–84, 2013.

[8] X. J. Li and P. E. D. Love, "Employing land value capture in urban rail transit public private partnerships: retrospective analysis of Delhi's airport metro express," *Research in*

Transportation Business and Management, vol. 32, no. 2019, Article ID 100431, 2019.

[9] R. Cohen and T. Boast, "Governance of public-private partnerships and infrastructure delivery: case of the milan, Italy, metro line *M*4," *Transportation Research Record*, vol. 2597, no. 1, pp. 37–43, 2016.

[10] K. V. Gestel, T. Willems, K. Verhoest et al., "Public-private partnerships in Flemish schools: a complex governance structure in a complex context," *Public Money & Management*, vol. 34, no. 5, pp. 363–370, 2014.

[11] A. T. Zhang, "Research on charge pricing of urban rail transit PPP project," Master thesis, Beijing JiaoTong University, Beijing, China, 2019.

[12] M. D. Bas, J. Ortiz, L. Ballesteros et al., "Evaluation of a multiple linear regression model and SARIMA model in forecasting Be-7 air concentrations," *Chemosphere*, vol. 177, no. 2017, pp. 326–333, 2017.

[13] K. Nikolopoulos, P. Goodwin, A. Patelis et al., "Forecasting with cue information: a comparison of multiple regression with alternative forecasting approaches," *European Journal of Operational Research*, vol. 180, no. 1, pp. 354–368, 2007.

[14] C. T. L. Zhou, S. C. Gao, J. H. Wang et al., "Financial time series prediction using a dendritic neuron model," *Knowledge-Based Systems*, vol. 105, pp. 214–224, 2016.

[15] Y. M. Yang and G. Chen, "Artificial neural network forecasting method in monitoring technique by spectrometric oil analysis," *Spectroscopy and Spectral Analysis*, vol. 25, no. 8, pp. 1339–1343, 2005.

[16] M. Ray, K. N. Singh, and V. Ramasubramanian, "Integration of wavelet transform with ANN and WNN for time series forecasting: an application to Indian monsoon rainfall," *National Academy Science Letters-India*, vol. 43, no. 6, pp. 509–513, 2020.

[17] W. P. Cao, X. Z. Wang, Z. Ming et al., "A review on neural networks with random weights," *Neurocomputing*, vol. 275, no. 2018, pp. 278–287, 2018.

[18] Y. Y. Lv, W. J. Liu, Z. Wang et al., "WSN localization technology based on hybrid GA-PSO-BP algorithm for indoor three-dimensional space," *Wireless Personal Communications*, vol. 114, no. 1, pp. 167–184, 2020.

[19] C. Chen, N. An, J. Z. Wang et al., "Optimal parameters selection for BP neural network based on particle swarm optimization: a case study of wind speed forecasting," *Konwledge-Based Systems*, vol. 56, pp. 226–239, 2014.

[20] M. Zou, L. Xue, H. J. Gai et al., "Identification of the shear parameters for lunar regolith based on a GA-BP neural network," *Journal of Terramechanics*, vol. 89, no. 2020, pp. 21–29, 2020.

[21] H. Qu, K. Xing, and T. Alexander, "An improved genetic algorithm with co-evolutionary strategy for global path planning of multiple mobile robots," *Neurocomputing*, vol. 120, pp. 509–517, 2013.

[22] R. Nasimi, R. Irani, and R. Ashena, "Optimized scenario for bottomhole pressure prediction in underbalanced drilling based on neural networks coupled with particle swarm optimization," *Petroleum Science and Technology*, vol. 20, no. 21, pp. 1140–1150, 2012.

[23] G. Shaari, N. Tekbiyik-Ersoy, and M. Dagbasi, "The state of art in particle swarm optimization based unit commitment: a review," *Process*, vol. 7, no. 10, Article ID 733, 2019.

[24] J. K. Xue and B. Shen, "A novel swarm intelligence optimization approach: sparrow search algorithm," *Systems Science and Control Engineering*, vol. 8, no. 1, pp. 22–34, 2020.

[25] X. Lv, X. D. Mu, J. Zhang et al., "Chaos sparrow search optimization algorithm," *Journal of Beijing University of Aeronautics and Astronautics*, 2021.

[26] A. D. Tang, T. Han, D. W. Xu et al., "Path planning method of unmanned aerial vehicle based on chaos sparrow search algorithm," *Journal of Computer Applications*, vol. 41, no. 7, 2021.

[27] M. Koppen, D. H. Wolpert, and W. G. Macready, "Remarks on a recent paper on the "no free lunch" theorems," *IEEE Transactions on Evolutionary Computation*, vol. 5, no. 3, pp. 295-296, 2001.

[28] D. H. Li, Q. K. Li, W. C. Wang et al., "Prediction of coal calorific value based on MIV characteristic variable selection and PSO-BP neural network," *Coal Engineering*, vol. 52, no. 11, pp. 154–160, 2020.

[29] H. Ji, X. Chen, K. Zhang et al., "Construct drawing man-hour forecasting based on GA-BP in chemical equipment design process," in *Proceedings of the 22nd International Conference on Automation and Computing (ICAC)*, pp. 65–70, Colchester, UK, September 2016.

[30] Y. C. Mao, D. Xiao, J. F. Cheng et al., "Research in magnesite grade classification based on near infrared spectroscopy and ELM algorithm," *Spectroscopy and Spectral Analysis*, vol. 37, no. 1, pp. 89–94, 2017.

[31] Q. Xu, Z. H. Liu, and S. F. Fang, "Retrieval method for estimating snow depth using hyperspectral data in snowmelt period," *Spectroscopy and Spectral Analysis*, vol. 33, no. 7, pp. 1927–1931, 2013.

[32] M. Xu, G. M. Zeng, X. Y. Xu et al., "Application of Bayesian regularized BP neural network model for analysis of aquatic ecological data-A case study of chlorophyll-a prediction in Nanzui water area of Dongting lake," *Journal of Environmental Sciences*, vol. 17, no. 6, pp. 946–952, 2005.

[33] J. Y. Li, C. Men, J. F. Qi et al., "Impact factor analysis, prediction, and mapping of soil corrosion of carbon steel across China based on MIV-BP artificial neural network and GIS," *Journal of Soils and Sediments*, vol. 20, no. 8, pp. 3204–3216, 2020.

[34] L. Xu, X. L. Zhang, Q. Xiao et al., "Evaluation of pollutant exposure level at bus stop based on MIV-BP neural network," *Science Technology and Engineering*, vol. 20, no. 30, pp. 12664–12671, 2020.

[35] J. J. Dai, P. F. Shan, and Q. Zhou, "Study on intelligent identification method of coal pillar stability in fully mechanized caving face of thick coal seam," *Energies*, vol. 13, no. 2, Article ID 305, 2020.

[36] Q. Y. Xing and Y. H. Yuan, "Economic analysis of metro ticket system and political suggestions," *Urban Mass Transit*, vol. 19, no. 5, pp. 10–14, 2016.

[37] X. Y. Jiang, K. Lu, B. Xia et al., "Identifying significant risks and analyzing risk relationship for construction PPP projects in China using integrated FISM-MICMAC approach," *Sustainability*, vol. 11, no. 19, Article ID 5209, 2019.

[38] J. Y. Li, F. F. Song, and C. H. Zhao, "Financial compensation strategy of PPP project based on game theory and intelligent optimization," *Sustainability*, vol. 35, no. 3, pp. 2697–2702, 2018.

[39] Y. L. Wang, J. C. Liu, R. L. Gao et al., "Government subsidies in public-private partnership projects based on altruistic theory," *International Journal of Strategic Property Management*, vol. 24, no. 3, pp. 153–164, 2020.

[40] B. Wang, S. B. Zhang, X. Q. Wang et al., "The optimal capital structure of PPP projects: based on the real-option method,"

Journal of Management Sciences in China, vol. 22, no. 6, pp. 73–85, 2019.

[41] A. P. C. Chan, P. T. I. Lam, Y. Wen et al., "Cross-sectional analysis of critical risk factors for PPP water projects in China," *Journal of Infrastructure Systems*, vol. 21, no. 1, Article ID 04014031, 2015.

[42] G. W. Dombi, P. Nandi, J. M. Saxe et al., "Prediction of RIB fracture injury outcome by artificial neutral-network," *The Journal of Trauma*, vol. 39, no. 5, pp. 915–921, 1995.

[43] H. H. Xu and Y. Deng, "Dependent evidence combination based on Shearman coefficient and Pearson coefficient," *IEEE Access*, vol. 6, pp. 11634–11640, 2018.

[44] G. Q. Zhang, B. E. Patuwo, and M. Y. Hu, "Forecasting with artificial neural networks: the state of the art," *International Journal of Forecasting*, vol. 14, no. 1, pp. 35–62, 1998.

[45] X. Zhuang, X. L. Yu, Z. M. Zhao et al., "Application of laser ranging and grey neural network (GNN) for the structure optimization of radio frequency identification (RFID) tags," *Lasers in Engineering*, vol. 48, no. 1-3, pp. 43–62, 2021.

[46] A. E. Gurel, U. Agbulut, and Y. Bicen, "Assessment of machine learning, time series, response surface methodology and empirical models in prediction of global solar radiation," *Journal of Cleaner Production*, vol. 277, Article ID 122353, 2020.

[47] Y. B. Sun, L. Chen, B. S. Huang et al., "A rapid identification method for calamine using near-infrared spectroscopy based on multi-reference correlation coefficient method and back propagation artificial neural network," *Applied Spectroscopy*, vol. 71, no. 7, pp. 1447–1456, 2017.

[48] B. G. Francq and B. Govaerts, "How to regress and predict in a Bland-Altman plot? Review and contribution based on tolerance intervals and correlated-errors-in-variables models," *Statistics in Medicine*, vol. 35, no. 14, pp. 2328–2358, 2016.

[49] S. C. Gao, Y. Yu, Y. R. Wang et al., "Chaotic local search-based differential evolution algorithms for optimization," *IEEE Transactions on Systems, Man, and Cybernetics*, vol. 51, no. 6, pp. 3954–3967, 2021.

[50] J. J. Wang and T. Kumbasar, "Parameter optimization of interval type-2 fuzzy neural networks based on PSO and BBBC methods," *IEEE/CAA Journal of Automatica Sinica*, vol. 6, no. 1, pp. 247–257, 2019.

[51] S. C. Gao, M. C. Zhou, Y. R. Wang et al., "Dendritic neuron model with effective learning algorithms for classification, approximation and prediction," *IEEE Transactions on Neural Networks and Learning Systems*, vol. 30, no. 2, pp. 601–614, 2019.

[52] X. W. Yang, Q. Z. Yu, L. F. He et al., "The one-against-all partition based binary tree support vector machine algorithms for multi-class classification," *Neurocomputing*, vol. 113, pp. 1–7, 2013.

[53] H. Wu and J. W. Wang, "A method for prediction of waterlogging economic losses in a subway station project," *Mathematics*, vol. 9, no. 12, Article ID 1421, 2021.

WILEY | Hindawi

Research Article

On the Investigation of Monthly River Flow Generation Complexity Using the Applicability of Machine Learning Models

Ma Shaofu [ID],[1] **Anas Mahmood Al-Juboori** [ID],[2] **Asmaa Hussein Alwan** [ID],[3] **and Abdel-Salam G. Abdel-Salam** [ID][4]

[1]*College of Physical Education, Lanzhou City University, Lanzhou 730070, China*
[2]*Dams and Water Resources Research Center, University of Mosul, Mosul, Iraq*
[3]*College of Education for Human Science-Ibn Rushd, University of Baghdad, Baghdad, Iraq*
[4]*Department of Mathematics, Statistics and Physics, College of Arts and Sciences, Qatar University, Doha, Qatar*

Correspondence should be addressed to Asmaa Hussein Alwan; asmaahussienalwan@gmail.com and Abdel-Salam G. Abdel-Salam; abdo@qu.edu.qa

Streamflow is associated with several sources on nonstationaries and hence developing machine learning (ML) models is always the motive to provide a reliable methodology to understand the actual mechanism of streamflow. The current research was devoted to generating monthly streamflows from annual streamflow. In this study, three different ML models were applied for this purpose, including Multiple Additive Regression Trees (MART), Group Methods of Data Handling (GMDH), and Gene Expression Programming (GEP). The models were developed based on annual streamflow and monthly time index of three rivers (i.e., Upper Zab, Lower Zab, and Diyala) located in the north region of Iraq. The modeling results indicated an optimistic simulation for generating the monthly streamflow time series from annual streamflow time series. The potential of the MART model was superior to the GMDH and GEP models for Upper Zab River (R^2 0.84, 0.64, and 0.47), Lower Zab River (R^2 0.75, 0.46, and 0.40), and Diyala River (R^2 0.78, 0.42, and 0.5). The results of RMSE were 113, 169, and 208 for Upper Zab River, 95, 149, and 0.5 for Lower Zab River, and 73, 118, and 109 for Diyala River. The results have proved the possibility of changing the timescale in generating streamflow data.

1. Introduction

The hydrological processes are associated with several elements such as evaporation, evapotranspiration, precipitation, runoff, river flow, infiltration, and groundwater. In nature, the hydrological cycle is featured by high stochasticity, nonstationarity, and nonlinearity [1], and thus studying the hydrological process is one of the significant topics in the field of water resources engineering. Over the past literature, several models have been introduced for modeling hydrology cycle processes and evidently proofed their capacity [2–4]. Between several components of the hydrology cycle, streamflow is a very important process and has received major interest by the hydrologists and computer scientists [1]. The establishment of accurate and reliable models "forecasting, prediction, or optimization" for

the long scale, such as yearly, seasonally, or monthly, is very magnificent for reliable water resources management and planning [5]. In addition, for short scale like day, hour, and minutes, streamflow recording is very essential for flooding warning and monitoring in order to lessen and mitigate their effects on various structure and human well-being [6].

The data-driven streamflow models are regression-based where the relationships between model inputs and output are directly defined [7, 8]. With the advances of computer aided models, ML models such as fuzzy logic, neural network, nature-based algorithm, support vector machine, decision tree, and optimizers have been successfully implemented for modeling streamflow patterns. These models can help in detecting the nonlinear, dispensable, and dynamic pattern of the time series [9–12]. However, a number of problems are associated with most of the ML-based techniques due to their

inherent limitations [13]. The ML-based models need previous information of the stochastic behavior of the addressed research issue (i.e., hydrology or climatology processes or water quality data) [14, 15]. Hence, it is essential to configure reliably in terms of learning process to obtain the important information from the chronological data of streamflow. In addition, it is required to optimize a number of model internal parameters [16, 17]. Over the time, many hybrid models have been also implemented such as fractionally autoregressive integrated moving average (FARIMA) and self-exciting threshold autoregressive (SETAR) with GEP, MARS, and MLR [18]. Similarly, another authors used autoregressive conditional heteroscedasticity (ARCH) to hybridized GEP and MARS models [19]. In particular, the conventional ML-based models need numerous trial-and-error processes to determine the optimum architecture design. For example, hydrological models using neural network require optimization of the number of hidden layers, the type of the transfer function, and the number of neurons in a hidden layer's choices [20]. Hybrid models are one of the updated models that have started to be used extensively in hydrology science [21]. Correspondingly, fuzzy models are one of the traditional models that lack handling complex problems and too many rules [22] and same goes for MLR model when dealing with multiple output and complexity [23]. The highlighted limitations of the existing ML-based streamflow forecasting models have necessitated the search for more sophisticated ML-based modeling techniques.

Streamflow forecasting plays an essential role for the researchers and engineers to better understand the river pattern which in turn helps to design more sustainable and efficient infrastructure and management project. Streamflow data is important yet presents itself with various issues such as missing data, noncontinuous data, nonlinearity, and extreme events [24, 25]. Researchers have devised various techniques and tools to overcome them, yet to grasp the full scope of such data in terms of seasonality, point source pollution, and sudden changes due to event of heavy rain or other calamities, and more work is needed to be done. Disaggregating streamflow can sever an essential procedure for reservoir operation and river basin management in general [26, 27]. This topic has received an extensive capacity by several hydrology scholars. Stedinger and Vogel [28] developed a simple class of a disaggregation model that can reproduce a covariance matrix of streamflow and reasonable approximation to the lead times that should be imposed for the disaggregation approach. Of recent advanced computer models, the disaggregation procedure was investigated by several scholars. A stochastic model was proposed to disaggregate streamflow at multiple sites preserving their temporal and spatial dependencies [29]. An integrated nonparametric model with genetic algorithm was to simulate seasonal streamflow disaggregating [30]. Monthly streamflow scale was disaggregated into daily scale using simple stochastic, as conducted in [31]. Various other research studies were conducted on the streamflow disaggregation [32–35]. All the reported research over the literature evidenced the capacity of studying the streamflow disaggregation. However, the implementation of the ML models for the streamflow disaggregation is limited

and needs to be investigated. ML models such as Multiple Additive Regression Trees (MART), Group Methods of Data Handling (GMDH), and Gene Expression Programming (GEP) are yet to be explored for the generating monthly streamflow time series from annual streamflow time series. There was no established research over the literature using those models yet to be tested.

The main objective of the current research is to investigate the feasibility of MART, GMDH, and GEP models for generating monthly streamflow time series from annual streamflow time series. The proposed models represent three different types of ML models. The MART model is one of the most popular decision tree models that strengthen the weak learning, which results in strong learning process and better generalization [36], while the GMDH model is chosen to represent self-learning models. The GEP model was applied as revolutionary model. The proposed models were evaluated statistically among each other and analyzed based on their predictability capacity. The study aims to demonstrate the possibility of changing the timescale in generating streamflow. This is the first application of using the GMDH, GEP, and MART models to generate monthly streamflow data from annual monthly streamflow data without using method of fragments which is usually used to disaggregate the annual streamflow to monthly streamflow.

2. Materials and Models

2.1. Study Area and Data. Upper Zab, Lower Zab, and Diyala Rivers are the major tributaries of Tigris River in Iraq, which were selected for the case study in this research. The Tigris River is one of the largest rivers in the Middle East. The river is about 1718 km long that goes through Turkey then Syria then Iraq. However, the major percentage (253,000 km) of about 85% of the river travels through Iraq region. The Tigris River along with the Euphrates River contributes to the Iraqi region as the main natural resources of fresh water that is required for diverse necessity of water usages. The Upper Zab River headwaters are located in Turkey's territory, while the headwaters of the Lower Zab and Diyala rivers are located in Iran's territory [37]. Figure 1 shows the location of Upper Zab, Lower Zab, and Diyala Rivers in Iran. Table 1 summarizes the morphological and flow data characteristics for the Upper Zab, Lower Zab, and Diyala upstream Bekhme, Dokan, and Derbindi-Khan flow gauging stations, respectively. The climate of the basin is predominantly semiarid. The temperature in the basin varies from maximum 45°C during summer to minimum 10°C in winter. The mean monthly discharge and the standard deviation of Tigris River flow at Baghdad station are 411.35 m^3/s and 234.52 m^3/s, respectively. Monthly flow data for the period 1932–2004 were selected. This period was selected because there was no missing data during this period. The first 70% of data was selected for training the models, while the second 30% of data was selected to validate the models.

2.2. Introduction to the Gene Expression Programming (GEP) Model. GEP was invented by Ferreira as an extension of traditional genetic programming. The program is developed

(a)

(b)

(c)
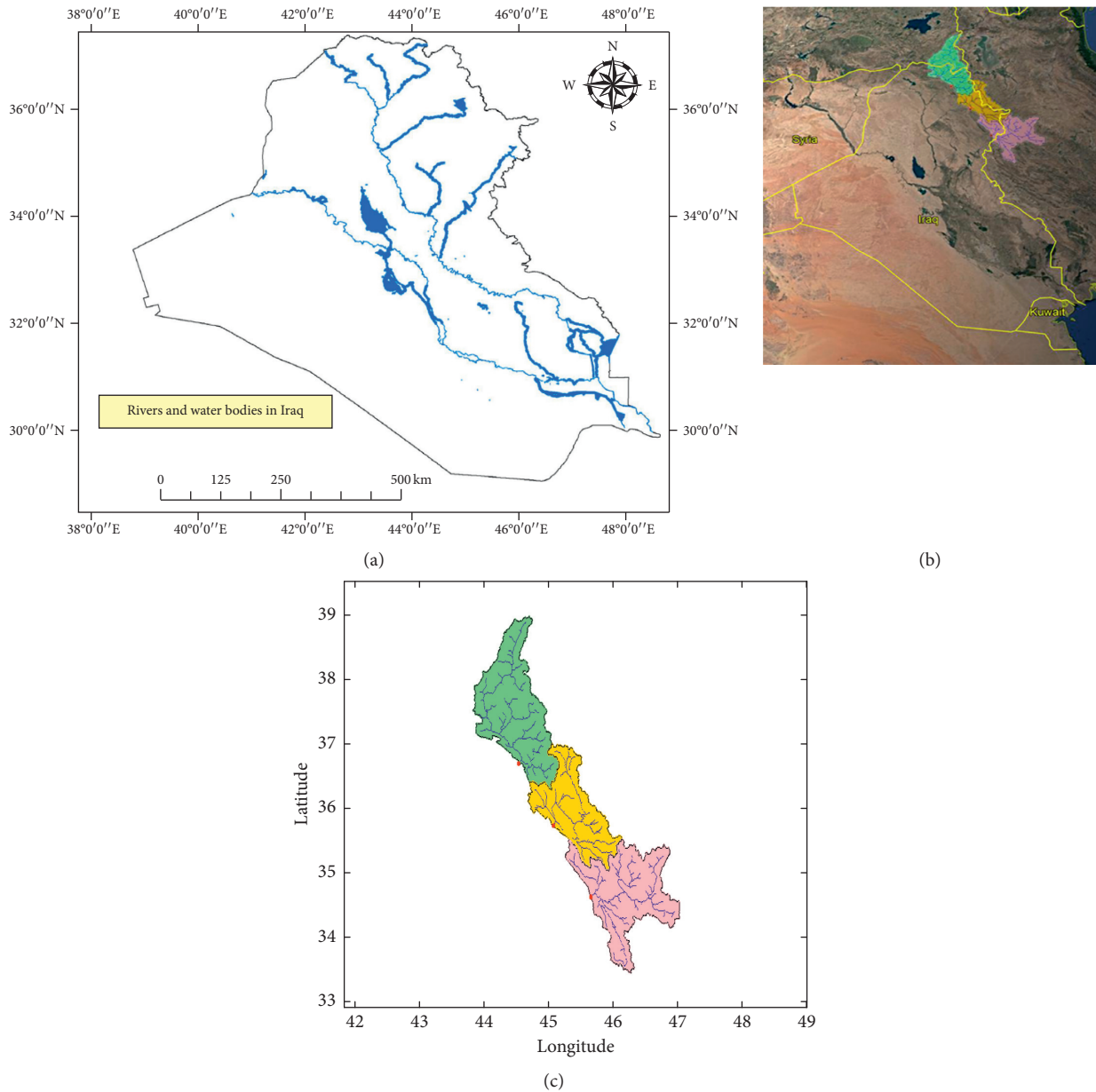
FIGURE 1: Upper Zab, Lower Zab, and Diyala Rivers' location.

as linear strings of fixed chromosome's length and then encoded as a nonlinear form with different dimensions [38]. In GEP, expressions are generated automatically by encoding the expression in the form of a tree consisting of nodes representing functions and leaves (terminal) representing constants and variables. The generated candidates were evaluated by a fitness function. The genes included two parts: tail that includes variables and head that includes variables and constants [39]. Five steps are used to develop the GEP model: (i) selecting a set of predictor variables, which can be used in discrete programs; (ii) selecting the specific functions and arithmetic operations; (iii) choosing the fitness measure; (iv) selecting the appropriate head length, quantity of genes, and the linking function; and (v)

selecting the genetic operators which include inversion rate and mutation rate [40]. More details for GEP are found in [41]. Figure 2 shows the flowchart of gene expression programming algorithm.

2.3. Introduction to the Multiple Additive Regression Trees (MART) Model. MART was developed by Derrig and Francis [42] to increase the accuracy of the traditional decision tree model result. The researchers found that the models developed using MART are more accurate models in comparison with any known modeling methodologies. The model can handle categorical and continuous inputs and target variables. The model is more stable due to the use of

TABLE 1: Morphological and flow data characteristics.

	Upper Zab	Lower Zab	Diyala
Basin area (km^2)	16863	11706	15765
Basin slope (m/m)	0.350	0.265	0.252
Average over land flow (m)	5.878	6.05	6.92
Perimeter (km)	1141.2	1053	1368.16
Basin length (km)	189.9	125	165.76
Mean basin elevation (m)	1870	1381.60	1551.15
Flow data record	1932–2004	1932–2004	1932–2004
Maximum flow (m^3/s)	1681	1135	947
Minimum flow (m^3/s)	32	9	3
Standard deviation (m^3/s)	277	180	148
Mean (m^3/s)	369	193	150
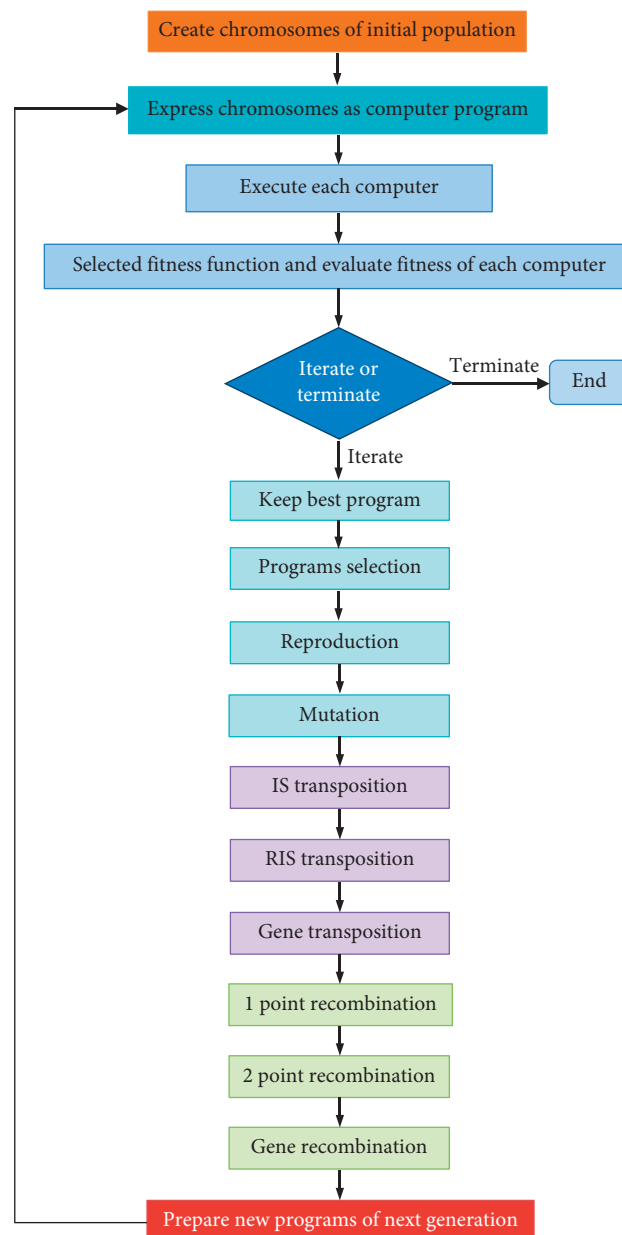
FIGURE 2: Flowchart of gene expression programming algorithm (Ferreira, 2001).

the Humber M-regression loss function in its algorithm. MART algorithm is started by fitting the inputs to first tree and then the biases from the first tree are inserted to the next tree to minimize the error [43]. This procedure is repeated through a series of following trees. The final results are adjusted by adding contribution weight of each tree. The MART algorithm can be expressed as [36]

$$\text{Target} = S + C_1 \times T_1(N) + C_2 \times T_2(N) + \cdots + C_n \times T_n(N), \tag{1}$$

where S is the mean value of the target variable; N is a pseudoresidual as set value's vector, $T_1(N), T_2(N), \ldots T_n(N)$ is tree fixed to the pseudoresiduals, and $C_1, C_2, \ldots, C_n$ are the tree node predicted coefficients. Figure 3 shows a simple MART structure and Figure 4 shows the flowchart of random trees algorithm.

2.4. Introduction to the Group Method of Data Handling (GMDH). GMDH was developed to solve the problems of predication, complex system, and optimization by using a nonlinear regression algorithm. GMDH structure is classified as a self-organizing polynomial neural network's method [44]. GMDH is a specific type of supervised artificial neural network. The algorithm of GMDH uses the concept of natural selection to control the network size, complexity, and accuracy [45]. The GMDH model starts by selecting a set of functions that showed highest prediction accuracy at previously unseen data. In GMDH model, layers of neurons are created using one or more inputs. The connections between neurons in the network are self-selected during training phase. The determination of number of layers and neurons in the network is automatic. The GMDH solutions are subsets of functions called partial models [46]. The best model is reached by gradually increasing the number of partial models. The GMDH algorithm uses the two variables' quadratic equation to develop the model.

$$y = a_1 + a_2 x_1 + a_3 x_2^1 + {} + a_4 x_2 + a_5 x_2^2 + a_6 x_1 x_2 ,$$
$$A = \left(X^T X \right)^{-1} X^T Y, \tag{2}$$

where $Y = [y_1, y_2, \ldots, y_n]^T$ and $A = [a_1, a_2, a_3, a_4, a_5]$.

$$X = \begin{bmatrix} 1 & x_{1I} & x_{1J} & x_{1I}x_{1J} & x_{1I}^2 & x_{1J}^2 \\ 1 & x_{2I} & x_{2J} & x_{2I}x_{2J} & x_{2I}^2 & x_{2J}^2 \\ \vdots & \vdots & \vdots & \vdots & \vdots & \vdots \\ \vdots & \vdots & \vdots & \vdots & \vdots & \vdots \\ 1 & x_{pI} & x_{pJ} & x_{pI}x_{pJ} & x_{PI}^2 & x_{PJ}^2 \end{bmatrix}, \tag{3}$$

where m presents the number of variables, (x_1, x_2, x_6) are vectors of input variables, and $(a_1, a_2, \ldots, a_6)$ are vectors of parameters. Figure 5 shows the structure of GMHD and Figure 6 shows the flowchart of GMDH algorithm. More details of GMHD are found in [44].

2.5. Performance Evaluation. In this research, two different performance metrics were selected to evaluate the proposed models: coefficient of determination (R^2) and root mean square error (RMSE) [47].
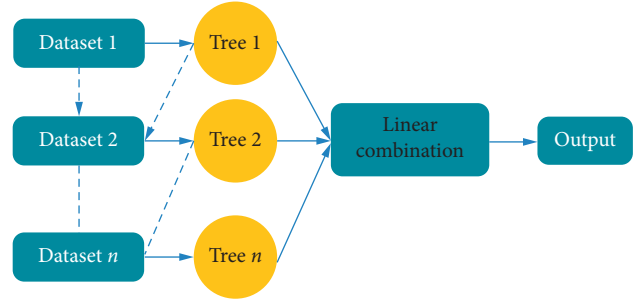
FIGURE 3: The structure of the MART model.

$$R^2 = \left[\frac{\sum_{i=1}^n \left(Q^\circ - \overline{Q}_o \right) \left(Q_p - \overline{Q}_p \right)_i}{\sqrt{\sum_{i=1}^n \left(Q^\circ - \overline{Q}_o \right)^2 \left(Q_p - \overline{Q}_p \right)_i^2}} \right]^2 ,$$

$$\text{RMSE} = \sqrt{\frac{1}{n} \sum_{i=1}^n \left(Q_o - Q_P \right)^2} , \tag{4}$$

where Q_{io} and Q_{ip} are the observed and generated streamflow values, respectively, $\overline{Q}_o$ is the observed streamflow mean value, and n is the data record number. The best models are those which showed low RMSE and are close to 1 value for R^2.

3. Modeling Results and Discussion

In this study, the three ML models were applied to develop the best models to generate monthly streamflow from annual streamflow. The models were developed using monthly streamflow as a target variable while the annual streamflow and monthly time index as predictor variables. The time index is an index that represents the monthly sequence within a year, and its values range from 1 (January) to 12 (December). Selecting the best model for predicting the monthly streamflow of the three proposed rivers requires choosing the best model settings for the MART, GMDH, and GEP models. The best MART model requires selecting the best settings for the three parameters in the model that includes the amount of trees in series, depth of discrete trees, and number of splits (least size). These values for the three rivers are 600, 5, and 10 for the Upper Zab River, 800, 5, and 10 for the Lower Zab River, and 300, 5, and 10 for Diyala River. The best GMDH model requires selecting the best settings for the four parameters in the model that include maximum network layers, maximum polynomial order, number of neurons per layer, and network layer connections type. The optimum parameter's settings of the GMDH model for the three rivers in this study are 20 for maximum network layers and 16 for maximum polynomial order, same number of neurons as inputs' option for the number of neurons per layer, and previous layer and original input variables for the network layer connections' type. There are five major steps for GEP modeling in this study: (1) selecting the set of functions to be used: 5 basic mathematical functions were used: +; −; ×; ÷; and power; (2) selecting the
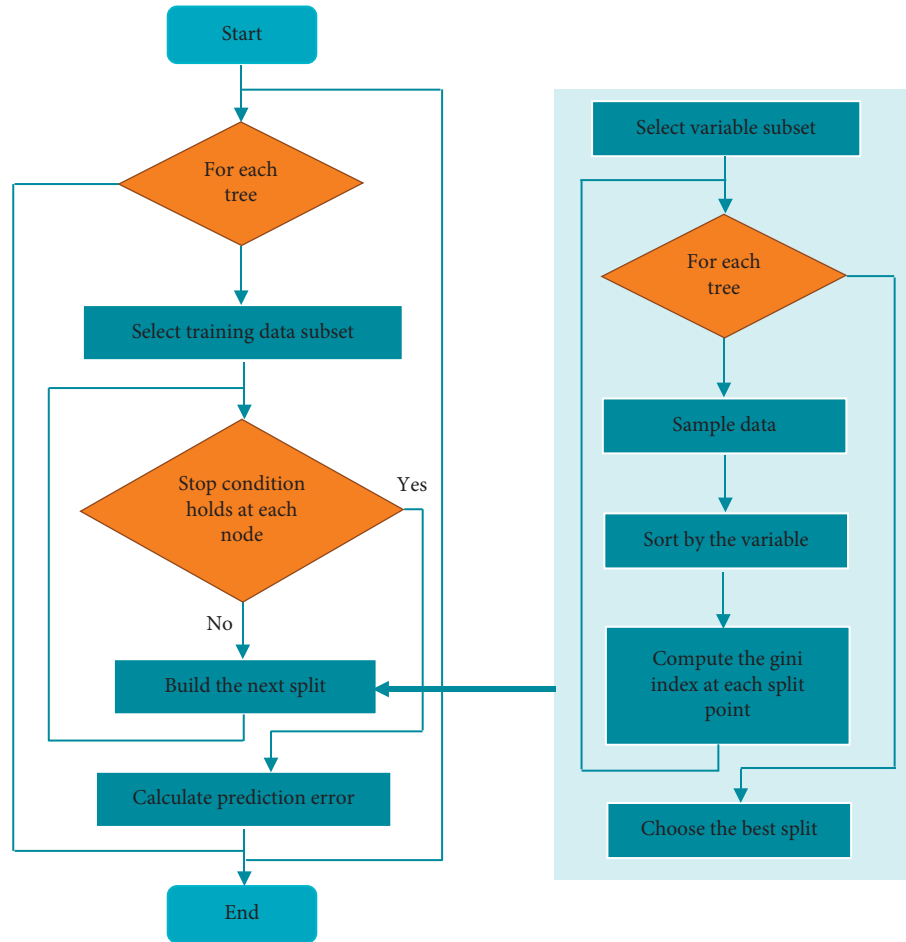
FIGURE 4: Flowchart of random trees algorithm.
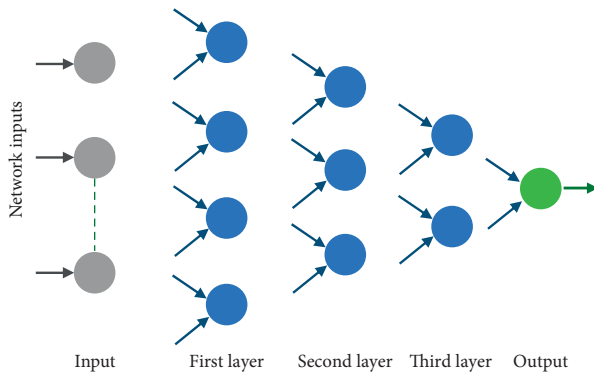
FIGURE 5: The structure of the GMDH model.

fitness function: the root relative square error (RRSE) was selected; (3) choosing the optimum general parameters: here, population size, genes per chromosomes, and gene head length were chosen; (4) choosing linking function: addition was chosen; and (5) we selected genetic operators, mutation rate of 0.044, and inversion rate of 0.1. Table 2 summarizes the best GEP model setting for the three rivers.

The results of the optimum symbolic fit regression functions from GEP model are explained in the following generated expressions for the Upper Zab, Lower Zab, and Diyala Rivers, respectively:

$$Q_m = \frac{-90151.84}{T} - 0.0012708T^2 + 80992.678$$

$$+ Q_a + \frac{89130.39}{T},$$

$$Q_m = 167.44 - T + Q_a - 16.4182T - T, \qquad (5)$$

$$Q_m = 262.276 - 22.8876T + Q_a$$

$$+ \sqrt{Q_a} + 383.9346 + \frac{64.230}{T - 2.6546},$$

where Q_m is a monthly flow, Q_a is an annual flow, and T is a time index (1, 2, 3, . . ., 12). The values of monthly streamflow change with the change in the value of the time index in the previous functions. The performance of the proposed models was evaluated utilizing the couple of statistical
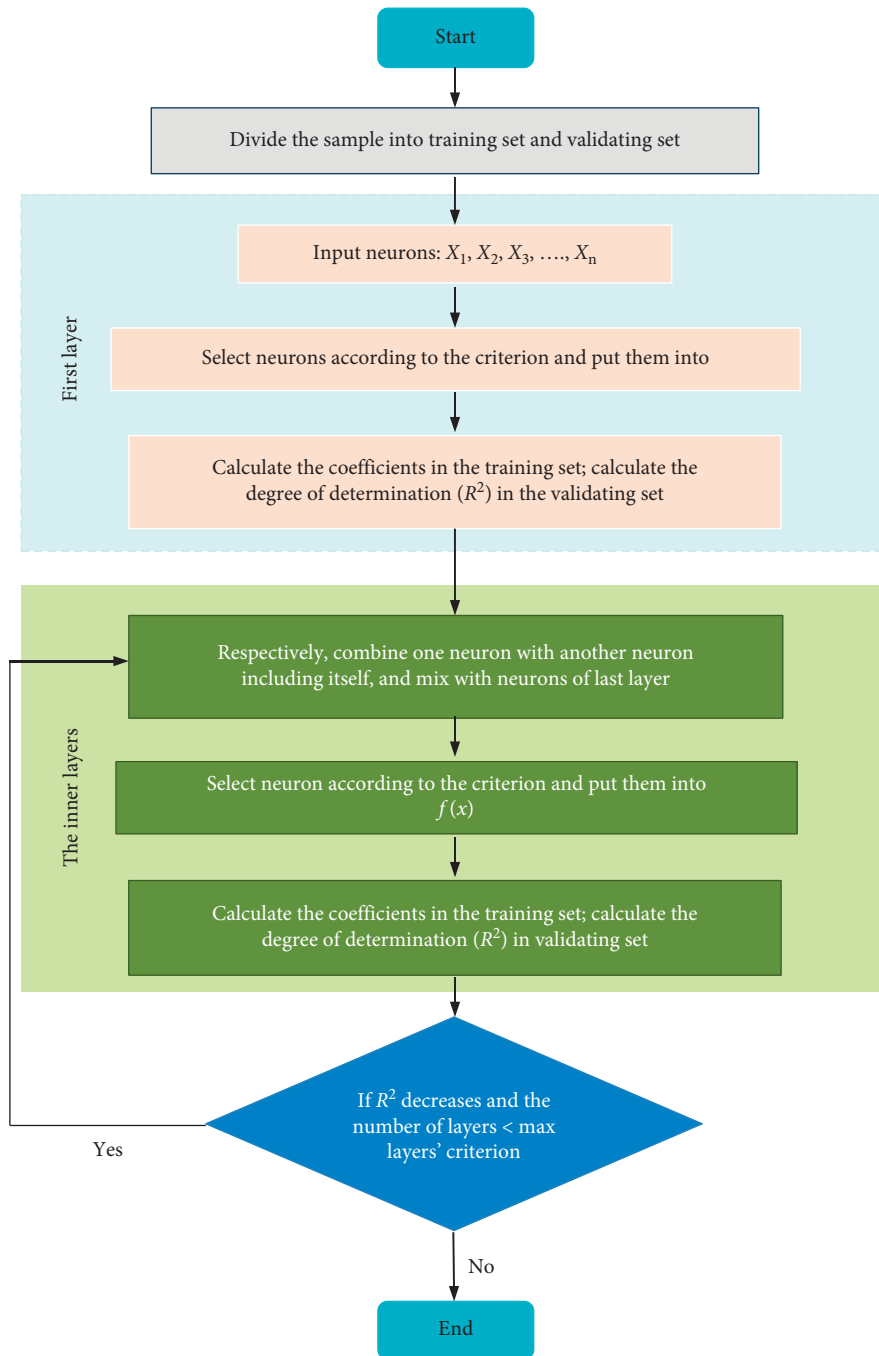
Figure 6: Flowchart of GMDH algorithm.

metrics and graphical visualization. Based on the reported statistical result in Table 3, the Upper Zab River simulation has shown that the performance of the MART model is superior over the performance of GMDH and GEP models. The R^2 values are 0.93, 0.81, and 0.53 for the training phase and 0.84, 0.64, and 0.47 in the validating phase for MART, GMDH, and GEP models, respectively. On the other hand, and using the absolute error measures, the results of RMSE have proved the accuracy of MART model in comparison with the other models, which can be due to the model of learning used by MART model where weak learning is boosted by regression learning leading to higher accuracy. The RMSE values are 85, 141, and 222 m³/s in training phase and 113, 169, and 208 m³/s in the validating phase for the MART, GMDH, and GEP models, respectively. For the Lower Zab River, R^2 values are 0.90, 0.47, and 0.41 in training phase and 0.75, 0.46, and with lowest of 0.40 through the validating phase for the MART, GMDH, and GEP models, respectively. The RMSE results have also proved the performance of MART model in comparison with the GMDH and GEP models. The RMSE values during the validating phase are 62, 144, and 151 m³/s, and during the training

TABLE 2: Model setting.

	Upper Zab	Lower Zab	Diyala
Function set			
Addition	+	+	+
Subtraction	−	−	−
Multiplication	×	×	×
Division	÷	÷	÷
Power	**	**	**
General parameters			
Population size	50	100	100
Genes per chromosomes	4	4	4
Gene head length	8	8	8
Fitness function	RRSE	RRSE	RRSE
Linking function	Addition	Addition	Addition
Genetic operators			
Mutation rate	0.044	0.044	0.044
Inversion rate	0.1	0.1	0.1

TABLE 3: The performance metrics of the applied ML predictive models through the training and validating phases when modeling the three investigated rivers.

Model	Upper Zab				Lower Zab				Diyala			
	Training		Validating		Training		Validating		Training		Validating	
	R^2	RMSE (m³/s)	R^2	RMSE (m³/s)	R^2	RMSE (m³/s)	R^2	RMSE (m³/s)	R^2	RMSE (m³/s)	R^2	RMSE (m³/s)
MART	0.93	85	0.84	113	0.90	62	0.75	95	0.85	66	0.78	73
GMDH	0.81	141	0.64	169	0.47	144	0.46	149	0.51	120	0.42	118
GEP	0.53	222	0.47	208	0.41	151	0.40	157	0.50	121	0.5	109

phase the errors produced are 95, 149, and 157 m³/s for the MART, GMDH, and GEP models, respectively. The R^2 values are 0.85, 0.51, and 0.50 in training phase and 0.78, 0.42, and 0.50 in the validating phase.

The RMSE values in the validating period are 66, 120, and 121 m³/s in the training phase and 73, 118, and 109 m³/s for the MART, GMDH, and GEP models, respectively, for the Diyala River. Both the R^2 and RMSE metrics results have proved the accuracy of the MART model to disaggregate annual flows to monthly streamflow in comparison with the GMDH and GEP models. The quality of the proposed models was measured by equating between the three statistical time series parameters which are maximum flow, standard deviation, and mean. Table 4 exhibits the results of these parameters. In accordance with the reported results in Table 4, it is apparent that the performance capacity of the MART model was superior to the performance of GMDH and GEP models. The observed data of the maximum monthly streamflow with the results of the applied models shows that the maximum monthly streamflow values in the validating phase were 1631, 1486, 1435, and 885 m³/s for the Upper Zab River, 1569, 1215, 769, and 588 m³/s for the Lower Zab River, and 864, 769, 626, and 570 m³/s for the Diyala River of the observed, MART, GMDH, and GEP models, respectively. Comparing the results of the statistical parameters, standard deviation, and the mean of the observed monthly streamflow with the results of the applied models as in Table 4 shows improved competence of the MART model compared to the GMDH and GEP models.

The predicted monthly streamflow over the validating period was assessed using the scatter plots variation as illustrated in Figures 7(a)–7(c). The plots in Figure 7 demonstrated a good relationship between the observed value and the generated monthly streamflow using the potential of the MART model in comparing to the other models. Also, the efficiency of the applied models was evaluated by comparing monthly statistical parameters for each month. The models' capability to handle streamflow data decreases with increased stochasticity of the data; however, the results depict that MART is more capable of predicting such data. The results of the maximum monthly flow, mean flow, and standard deviation for each month were compared with the results of observed monthly streamflow in the validating phase. The comparisons were made by plotting the maximum monthly flow, mean flow, and standard deviation against the months; see Figure 8. The results of Figure 8 also demonstrated that MART model is accurate and thus superior with respect to the GMDH and GEP models' performance to generate monthly streamflow from annual streamflow. As per the results of the statistical parameters, it is apparent that the MART model performance is accurate when compared to the observed data for the three studied rivers (Figure 8). It is apparent that rivers have diverging hydrological characteristics and model behavior and performance can change greatly according to that. As per the figure, it can be observed that each river presents different seasonality and deviation over the time period because of which models generate more error during modeling.

TABLE 4: Statistical analysis of observed and modeling results of the monthly streamflow values.

River name		Observed	MART	GMDH	GEP
		Training			
Upper Zab	Maximum flow (m³/s)	1681	1558	1897	993
	Standard deviation (m³/s)	326	303	293	229
	Mean (m³/s)	397	393	393	402
Lower Zab	Maximum flow (m³/s)	1406	1215	827	628
	Standard deviation (m³/s)	198	179	131	125
	Mean (m³/s)	198	196	199	203
Diyala	Maximum flow (m³/s)	1451	850	908	617
	Standard deviation (m³/s)	171	134	119	113
	Mean (m³/s)	156	150	154	160
		Validating			
Upper Zab	Maximum flow (m³/s)	1631	1486	1435	885
	Standard deviation (m³/s)	286	287	282	228
	Mean (m³/s)	353	364	388	370
Lower Zab	Maximum flow (m³/s)	1569	1215	769	588
	Standard deviation (m³/s)	205	201	149	129
	Mean (m³/s)	198	201	195	207
Diyala	Maximum flow (m³/s)	864	769	626	570
	Standard deviation (m³/s)	150	145	111	116
	Mean (m³/s)	150	148	157	160
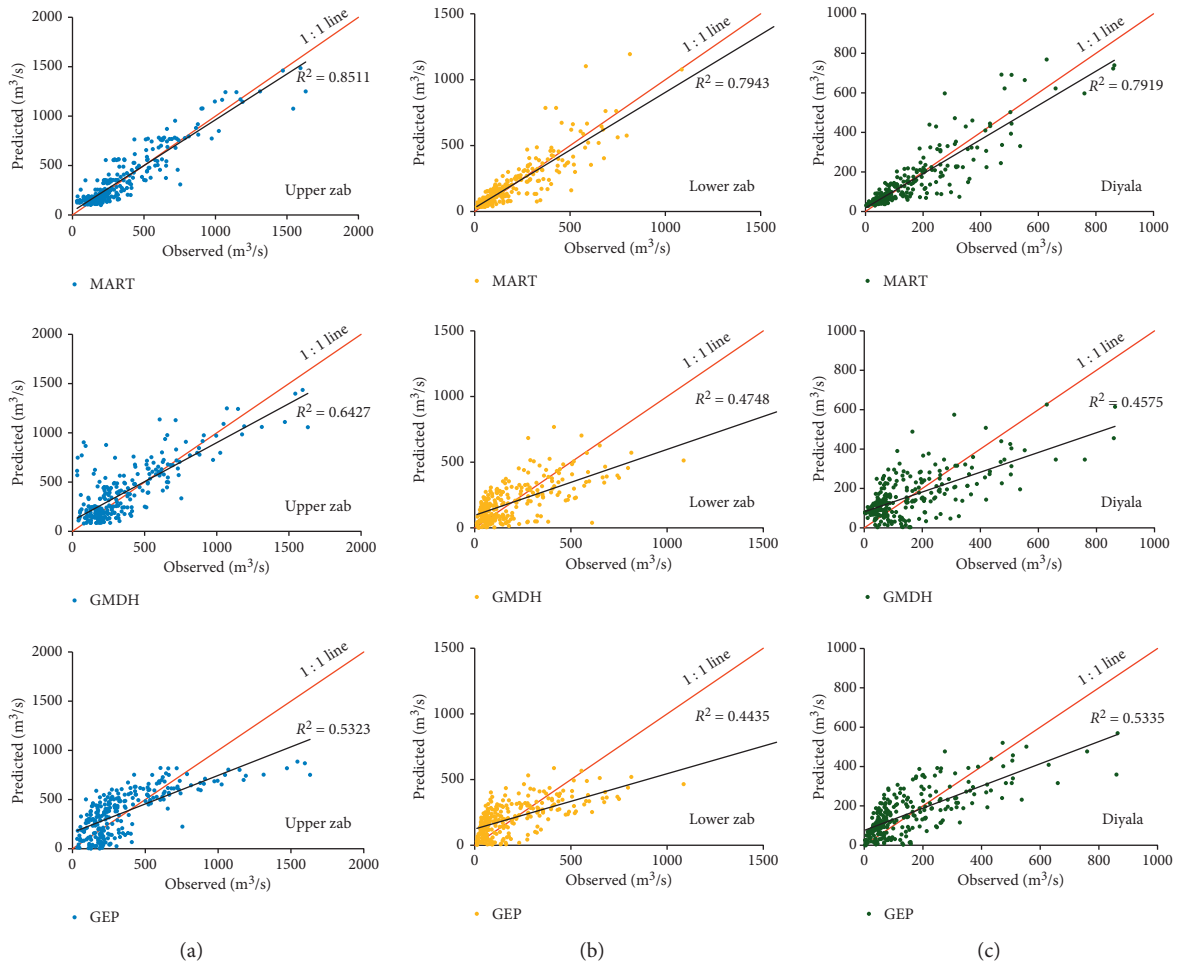
FIGURE 7: The scatter plots between the observed and predicted streamflow values for all applied predictive models. (a) Upper Zab River, (b) Lower Zab River, and (c) Diyala River.
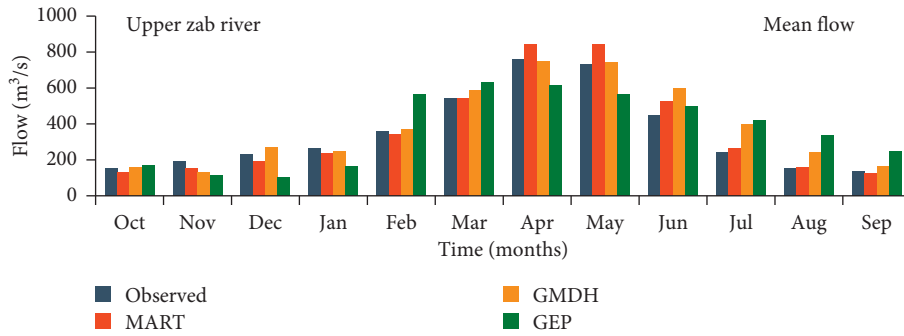
(a)
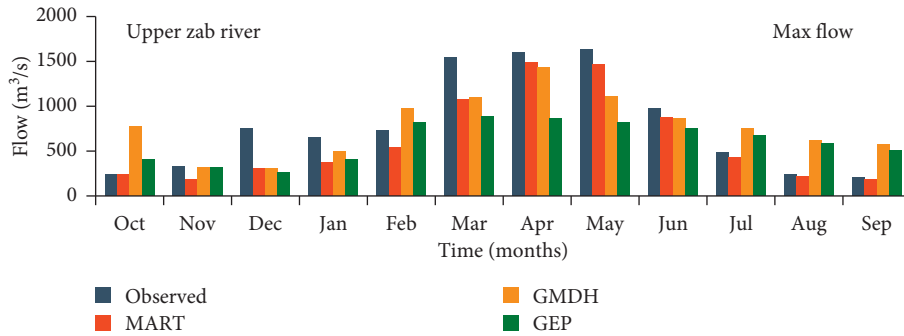
(b)
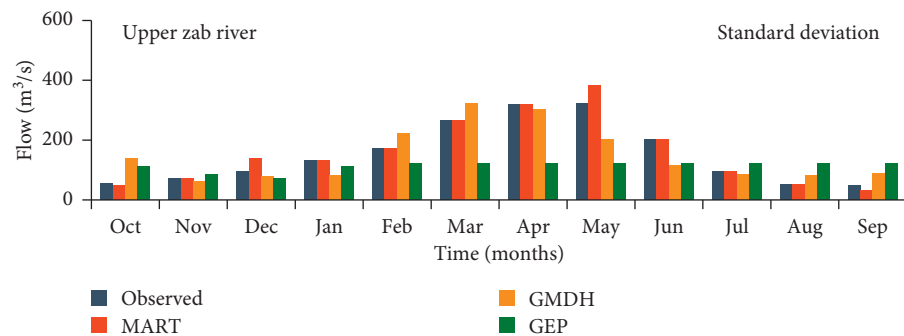
(c)
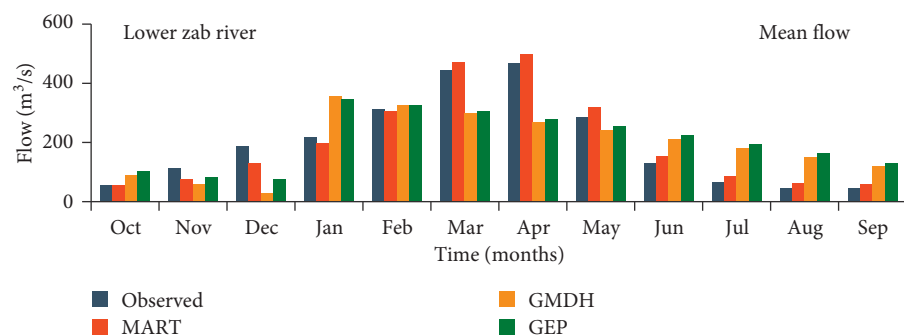
(d)

Figure 8: Continued.
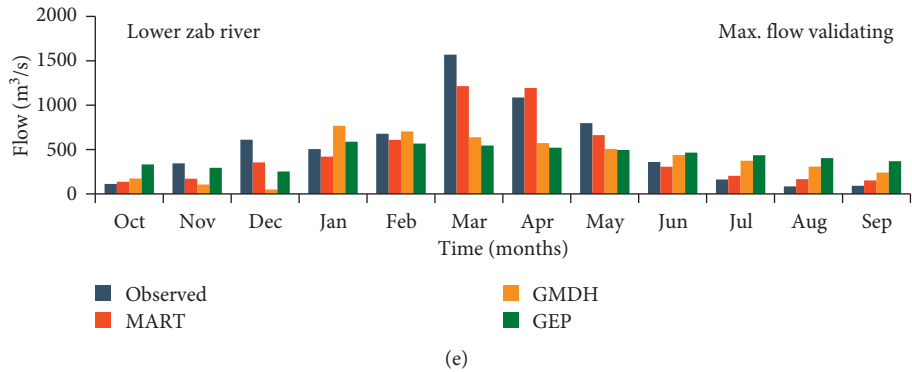
(e)
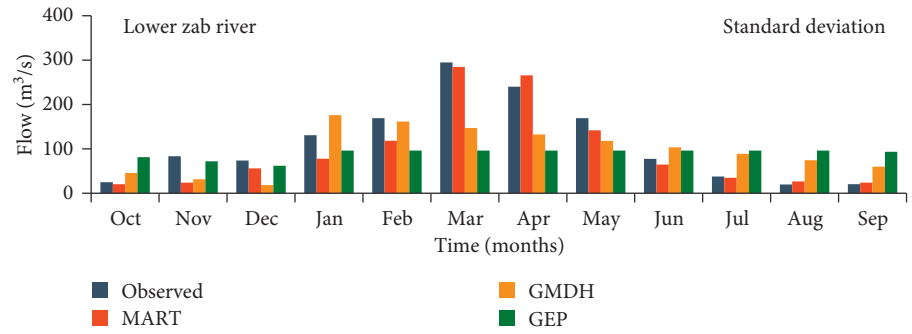
(f)
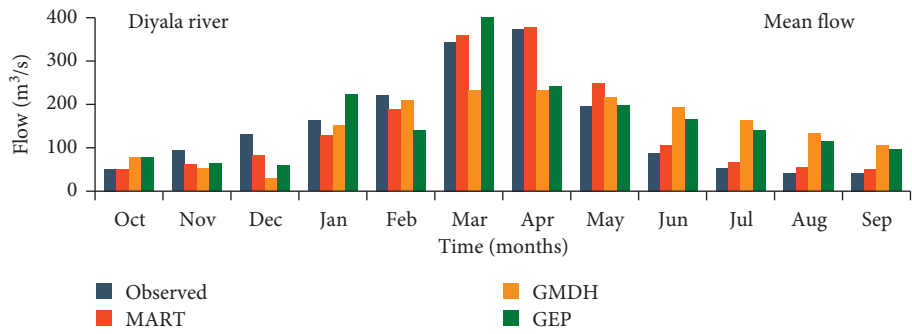
(g)
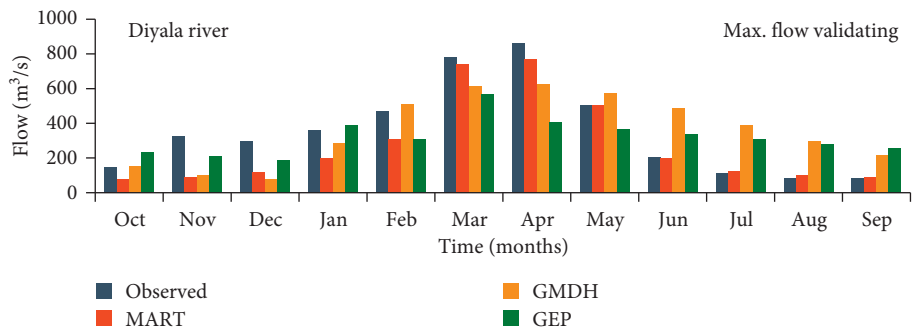
(h)

Figure 8: Continued.

(i)
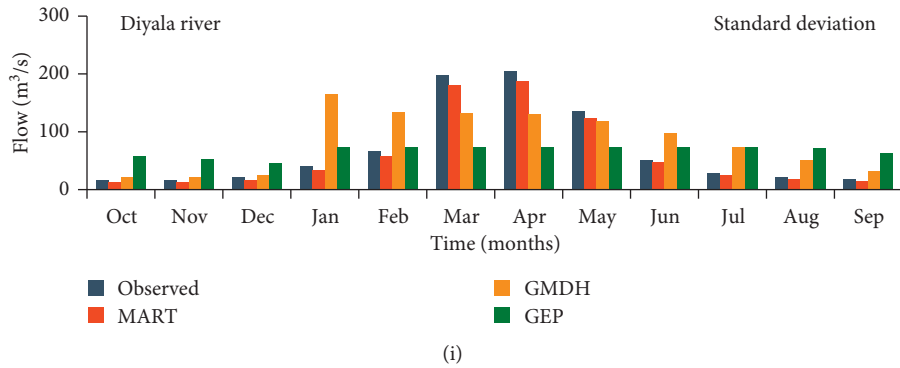
FIGURE 8: Results of the statistical parameters against the months.
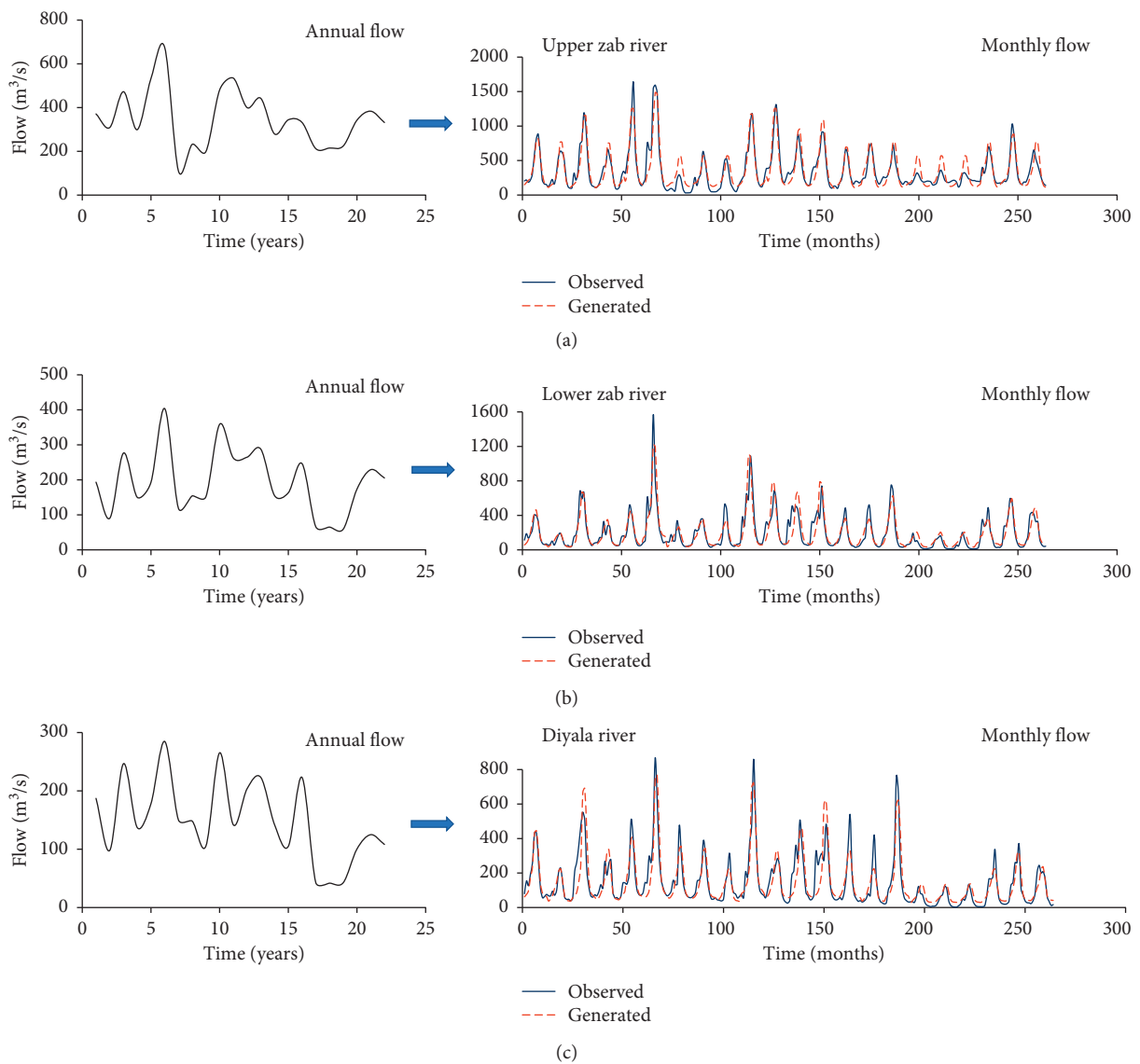
FIGURE 9: The graphs show the yearly time series flow of the three rivers and observed and generated monthly streamflow after application of MART model during the validating phase.

Figure 9 shows a comparison between the observed and generated monthly streamflow generated using MART model during the validation phase for the three rivers in this study and it also shows how the monthly flows were generated from the annual flows data. The results in Figure 9 show the proximity of the observed value and generated monthly streamflow which also evidenced that the MART model performance is able to produce monthly streamflow time series from annual monthly streamflow time series data.

The results indicated the efficiency of MART model in generating monthly flow data from annual flow data and this is due to MART model's structure, which enables the building of robust models with a limited number of inputs (the inputs included only the annual flow and time index). The results also showed the weakness of revolutionary and self-learning models in creating robust models with a limited number of inputs.

The results indicated the efficiency of using MART model to generate monthly streamflow from annual streamflow. This is the first application of using MART model to generate the monthly streamflow from annual streamflow. The results showed the importance of using time index to improve the accuracy of generating monthly streamflow from annual streamflow. The results of this paper are encouraging to develop new models for generating monthly streamflow data instead of the data of fragment method which is usually used for this purpose.

4. Conclusions

In this study, three different ML models were used to generate monthly streamflow time series from annual streamflow time series. The models included MART, GMDH, and GEP. The models input only included the annual streamflows and monthly time index. The results showed that the MART model is superior to the GMDH and GEP models in producing monthly streamflow time series by applying annual monthly streamflow time series data. The results indicated that the structure of MART model is better than the structure of polynomial neural networks or revolutionary models in generating modeling. The efficiency of MART model was better than the results of GMDH and GEP models for Upper Zab (R^2 0.84, 0.64, and 0.47), Lower Zab (R^2 0.75, 0.46, and 0.40), and Diyala (R^2 0.78, 0.42, and 0.5). The MART model accuracy is relating to its specific architecture, which may include number of trees growing in equivalence in addition to the use of boosting technique which helped to improve the prediction function. The results demonstrated the possibility of changing the timescale in generating streamflow. The application of MART model is easier than the method of data of fragment that is usually used to disaggregate the annual streamflow to monthly streamflow.

Data Availability

The data used to support the findings of this study are available from the corresponding author upon request.

Conflicts of Interest

The authors have no conflicts of interest to any party.

References

[1] M. Zounemat-Kermani, M. Elena, C. Andrea, X. Xia, Q. Liang, and R. Hinkelmann, "Neurocomputing in surface water hydrology and hydraulics: a review of two decades retrospective, current status and future prospects," *Journal of Hydrology*, vol. 588, 2020.

[2] N. Sujay Raghavendra and P. C. Deka, "Support vector machine applications in the field of hydrology: a review," *Applied Soft Computing*, vol. 19, pp. 372–386, 2014.

[3] A. Mosavi, P. Ozturk, and K. W. Chau, "Flood prediction using machine learning models: literature review," *Water*, vol. 10, no. 11, p. 1536, 2018.

[4] H. Lange and S. Sippel, "Machine learning applications in hydrology," in *Forest-Water Interactions*, pp. 233–257, Springer, Berlin, Germany, 2020.

[5] L. Diop, A. Bodian, K. Djaman et al., "The influence of climatic inputs on stream-flow pattern forecasting: case study of Upper Senegal river," *Environmental Earth Sciences*, vol. 77, no. 5, p. 182, 2018.

[6] P. A. Kagoda, J. Ndiritu, C. Ntuli, and B. Mwaka, "Application of radial basis function neural networks to short-term streamflow forecasting," *Physics and Chemistry of Earth*, vol. 35, no. 13-14, pp. 571–581, 2010.

[7] G. E. P. Box, G. M. Jenkins, G. C. Reinsel, and G. M. Ljung, *Times Series Analysis—Forecasting and Control*, Holden-Day Inc., San Francisco, CA, USA, 1976.

[8] J. D. Salas and J. T. B. Obeysekera, "ARMA model identification of hydrologic time series," *Water Resources Research*, vol. 18, no. 4, pp. 1011–1021, 1982.

[9] P. P. Balestrassi, E. Popova, A. P. Paiva, and J. W. Marangon Lima, "Design of experiments on neural network's training for nonlinear time series forecasting," *Neurocomputing*, vol. 72, no. 4–6, pp. 1160–1178, 2009.

[10] Q. Ju, Z. Yu, Z. Hao, G. Ou, J. Zhao, and D. Liu, "Division-based rainfall-runoff simulations with BP neural networks and Xinanjiang model," *Neurocomputing*, vol. 72, no. 13-15, pp. 2873–2883, 2009.

[11] S. Asadi, J. Shahrabi, P. Abbaszadeh, and S. Tabanmehr, "A new hybrid artificial neural networks for rainfall-runoff process modelling," *Neurocomputing*, vol. 121, pp. 470–480, 2013.

[12] H.-G. Han and J.-F. Qiao, "A structure optimisation algorithm for feedforward neural network construction," *Neurocomputing*, vol. 99, pp. 347–357, 2013.

[13] M. Sit, B. Z. Demiray, Z. Xiang, G. J. Ewing, Y. Sermet, and I. Demir, "A comprehensive review of deep learning applications in hydrology and water resources," 2020, https://arxiv.org/abs/2007.12269.

[14] P. A. Whigham and P. F. Crapper, "Modelling rainfall-runoff using genetic programming," *Mathematical and Computer Modelling*, vol. 33, no. 6-7, pp. 707–721, 2001.

[15] J. Guo, J. Zhou, H. Qin, Q. Zou, and Q. Li, "Monthly streamflow forecasting based on improved support vector machine model," *Expert Systems with Applications*, vol. 38, no. 10, pp. 13073–13081, 2011.

[16] D. Labat, "Recent advances in wavelet analyses: part 1. a review of concepts," *Journal of Hydrology*, vol. 314, no. 1–4, pp. 275–288, 2005.

[17] B. Keshtegar, M. F. Allawi, H. A. Afan, and A. El-Shafie, "Optimized river stream-flow forecasting model utilizing high-order response surface method," *Water Resources Management*, vol. 30, no. 11, pp. 3899–3914, 2016.

[18] S. Mehdizadeh, F. Fathian, and J. F. Adamowski, "Hybrid artificial intelligence-time series models for monthly streamflow modeling," *Applied Soft Computing*, vol. 80, pp. 873–887, 2019.

[19] S. Mehdizadeh, F. Fathian, M. J. S. Safari, and J. F. Adamowski, "Comparative assessment of time series and artificial intelligence models to estimate monthly streamflow: a local and external data analysis approach," *Journal of Hydrology*, vol. 579, Article ID 124225, 2019.

[20] E. S. Salami and M. Ehteshami, "Simulation, evaluation and prediction modeling of river water quality properties (case study: Ireland rivers)," *International Journal of Environmental Science and Technology*, vol. 12, no. 10, pp. 3235–3242, 2015.

[21] I. Ahmadianfar, M. Jamei, and X. Chu, "A novel hybrid wavelet-locally weighted linear regression (W-LWLR) model for electrical conductivity (EC) prediction in surface water," *Journal of Contaminant Hydrology*, vol. 232, Article ID 103641, 2020.

[22] A. P. Jacquin and A. Y. Shamseldin, "Review of the application of fuzzy inference systems in river flow forecasting," *Journal of Hydroinformatics*, vol. 11, no. 3, 2009.

[23] M. Fahmi, M. F. B. Mohd Nasir, M. S. Samsudin et al., "River water quality modeling using combined principle component analysis (PCA) and multiple linear regressions (MLR): a case study at klang river," *World Applied Sciences Journal*, vol. 14, no. 2002, pp. 73–82, 2011.

[24] A. J. Jakeman, I. G. Littlewood, and P. G. Whitehead, "An assessment of the dynamic response characteristics of streamflow in the Balquhidder catchments," *Journal of Hydrology*, vol. 145, no. 3-4, pp. 337–355, 1993.

[25] M. D. Dettinger and H. F. Diaz, "Global characteristics of stream flow seasonality and variability," *Journal of Hydrometeorology*, vol. 1, no. 4, pp. 289–310, 2000.

[26] R. DarioValencia and J. C. Schakke, "Disaggregation processes in stochastic hydrology," *Water Resources Research*, vol. 9, no. 3, pp. 580–585, 1973.

[27] D. N. Kumar, U. Lall, and M. R. Petersen, "Multisite disaggregation of monthly to daily streamflow," *Water Resources Research*, vol. 36, pp. 1823–1833, 2000.

[28] J. R. Stedinger and R. M. Vogel, "Disaggregation procedures for generating serially correlated flow vectors," *Water Resources Research*, vol. 20, no. 1, 1984.

[29] J. Prairie, B. Rajagopalan, U. Lall, and T. Fulp, "A stochastic nonparametric technique for space-time disaggregation of streamflows," *Water Resources Research*, vol. 43, no. 3, 2007.

[30] T. Lee, J. D. Salas, and J. Prairie, "An enhanced nonparametric streamflow disaggregation model with genetic algorithm," *Water Resources Research*, vol. 46, no. 8, 2010.

[31] A. Acharya and J. H. Ryu, "Simple method for streamflow disaggregation," *Journal of Hydrologic Engineering*, vol. 19, no. 3, pp. 509–519, 2014.

[32] A. T. Silva and M. M. Portela, "Disaggregation modelling of monthly streamflows using a new approach of the method of fragments," *Hydrological Sciences Journal*, vol. 57, no. 5, pp. 942–955, 2012.

[33] D. A. Hughes and A. Slaughter, "Daily disaggregation of simulated monthly flows using different rainfall datasets in southern Africa," *Journal of Hydrology: Regional Studies*, vol. 4, pp. 153–171, 2015.

[34] M. M. Portela and A. T. Silva, "Disaggregation modelling of annual flows into daily streamflows using a new approach of the method of fragments," *Water Resources Management*, vol. 30, no. 15, 2016.

[35] S. H. D. Al-Zakar, N. Şarlak, and O. M. A. M. Agha, "Disaggregation of annual to monthly streamflow: a case study of Kizilirmak Basin (Turkey)," *Advances in Meteorology*, vol. 2017, Article ID 3582826, 16 pages, 2017.

[36] T. A. Awchi, "River sischarges forecasting in Northern Iraq using different ANN techniques," *Water Resources Management*, vol. 28, no. 3, pp. 801–814, 2014.

[37] C. Ferreira, "Gene expression programming: a new adaptive algorithm for solving problems," *Complex System*, vol. 13, no. 2, pp. 87–129, 2001.

[38] C. Ferreira, *Gene Expression Programming: Mathematical Modeling by an Artificial Intelligence*, Springer, Berlin, Germany, 2006.

[39] T. Hong, K. Jeong, and C. Koo, "An optimized gene expression programming model for forecasting the national CO_2 emissions in 2030 using the metaheuristic algorithms," *Applied Energy*, vol. 228, pp. 808–820, 2018.

[40] C. Ferreira, "Gene expression programming in problem solving," in *Soft Computing and Industry*Springer, Berlin, Germany, 2011.

[41] J. H. Friedman, "Stochastic gradient boosting," *Computational Statistics & Data Analysis*, vol. 38, no. 4, pp. 367–378, 2002.

[42] R. Derrig and L. Francis, "Distinguishing the forest from the TREES: a comparison of tree based data mining methods," *Casualty Actuarial Society Forum*, 2006.

[43] A. G. Ivakhnenko, "The group method of data of handling; a rival of the method of stochastic approximation," *Soviet Automatic Control*, vol. 13, pp. 43–55, 1968.

[44] A. Sepahvand, B. Singh, P. Sihag, and A. N. Samani, "Assessment of the various soft computing techniques to predict sodium absorption ratio (SAR)," *Journal of Hydraulic Engineering*, vol. 5010, 2019.

[45] A. Ivakhnenko and G. Ivakhnenko, "The review of problems solvable by algorithms of the group method of data handling (GMDH)," *Pattern Recognition and Image Analysis*, vol. 5, no. 4, pp. 527–535, 1995.

[46] C. Willmott and K. Matsuura, "Advantages of the mean absolute error (MAE) over the root mean square error (RMSE) in assessing average model performance," *Climate Research*, vol. 30, no. 1, pp. 79–82, 2005.

[47] N. J. D. Nagelkerke, "A note on a general definition of the coefficient of determination," *Biometrika*, vol. 78, no. 3, pp. 691-692, 1991.

WILEY | Hindawi

Research Article

Random Forest versus Support Vector Machine Models' Applicability for Predicting Beam Shear Strength

Hayder Riyadh Mohammed Mohammed [ID] **and Sumarni Ismail** [ID]

Department of Architecture, Faculty of Design and Architecture, University Putra Malaysia, Serdang 43400, Malaysia

Correspondence should be addressed to Hayder Riyadh Mohammed Mohammed; upmhayder@gmail.com and Sumarni Ismail; sumarni@upm.edu.my

The shear and bending are the actions that are experienced in the beam owing to the fact that the beam is a flexural member due to the load in the transverse direction to their longitudinal axis. The shear strength (V_s) computation of reinforced concrete (RC) beams has been a major topic in the field of structural engineering. There have been several methodologies introduced for the V_s prediction; however, the modeling accuracy is relatively low owing to the complex characteristic of the resistance mechanism involving dowel effect of longitudinal reinforcement, concrete in the compression zone, contribution of the stirrups if existed, and the aggregate interlock. Hence, the current research proposed a new soft computing model called random forest (RF) to predict V_s. Experimental datasets were collected from the open-source literature including the related geometric properties and concrete characteristics of beam specimens. Nine input combinations were constructed based on the statistical correlation to be supplied for the proposed predictive model. The prediction accuracy of the RF model was validated against the Support Vector Machine (SVM), and several other empirical formulations have been adopted in the literature. The proposed RF model revealed better prediction accuracy in addition the model structure emphasis in the incorporation of seven predictors by excluding (beam flange thickness and coefficient). In the quantitative term, the minimal root mean square error value was attained (RMSE = 89.68 kN).

1. Introduction

During the design of reinforced concrete (RC) beams, one of the important parameters considered is the shear behaviour of the concrete structural members [1]. This is because shear failure normally occurs as a combined action of shearing forces and a bending moment; shear failure is mostly characterized by a lack of ductility and minor deflections and occurs suddenly without any notification [2, 3]. Shear failure is a complex process that involves several parameters whose impact makes the mechanism of shear failure a debatable matter. Until now, empirical methods are being used to derive the guidelines and design codes for the shear strength of RC beams [4]; such empirical methods are limited in physical simulation as practice, paving the way for the development of an effective mathematical technique that will provide better estimates of the accuracy of the shear strength of RC beams [5, 6].

Empirical-based prediction of the shear strength of RC beams has been the focus of various studies since the 1960s [7, 8]. When using the ACI code for the prediction of the shear capacity of RC beams with steel stirrups, the output is normally the sum of the concrete and stirrup contributions [4]; however, during this simple addition, the interaction between the stirrups is normally ignored [9]. Studies have reported the prediction of the shear strength of RC members without stirrups using a mechanics-based segmental approach [10, 11]. Various attempts have been made in this field towards the provision of simple predictive shear mechanism-based equations that will enable new ways of designing concrete structures [12]. Despite the convenience of these methods, there is still the issue of accuracy due to the shear action-induced masking of the sudden and brittle failure of RC beams; hence, most of the relevant building codes are devoid of rational design equations. It is important

to improve the predictive performance during the design of RC beams to enable the accurate prediction of the shear strength of different types of RC beams. Several proposals have been made in recent years regarding the use of advanced machine learning (ML) models for shear strength prediction [13, 14].

In the field of structural engineering, some of the nagging problems encountered are the analysis of beam behaviour, beam response to loading, and analysis of beam shear failure; these problems require the prediction of the behaviour of the system using few laboratory observations [15–17]. Most of the time, mathematical models are developed for the prediction and analysis of the performance of the system through scientific extrapolation of the laboratory test results on an undefined system [18]. These problems can be solved using artificial intelligence- (AI-) based machine learning algorithms which are mathematical tools that can detect patterns in a given dataset and extract such patterns for analysis purposes.

AI models have profound application in structural engineering owing to the ability to provide remarkable solutions [19–21]. AI models can provide solutions to problems associated with high stochasticity, nonlinearity, and nonstationarity. They can be used to map incomplete system data into a description state of the system [13]. In structural engineering, incomplete and unorganized datasets are interpreted and recognized for the formulation of problems. One common example is the detection of damage in a structure with numerous components via the collection of data at different locations on the structure [22, 23]. This is considered an inverse problem and requires that a state should be determined from the observed system behaviour [24]. The problems are first analyzed before finding the solution that will aid in achieving the desired system behavior, while those that will not improve performance are filtered out [21]. AI models can be used to map the behavior of a given system to a space of system attributes that can guarantee the expected behavior. Hence, it is required that system engineers be able to predict the behavior of the complex systems based on the known system configuration and the external loads that the system is subjected to. This implies a problem of mapping the cause to effect, and this is achievable using AI models.

One important area of AI model's application is the evaluation of the set of potential solutions to a given problem and the determination of the most appropriate solution from the pool of available alternatives via the estimation of the values of evaluation criteria from a known set of attributes. Beam shear strength was first investigated by Adhikary and Mutsuyoshi [25] using the artificial neural network (ANN). Adaptive neuro fuzzy inference system (ANFIS) model was developed for the wrapped shear deficient RC beams [26]. The development of hybridized response surface method (RSM) with support vector regression (SVR) model to predict shear strength of steel fiber-reinforced concrete beam (SFRCB) [27]. The integration of SVR model with firefly algorithm for the sake of prediction accuracy of SFRCB shear strength [28]. The hybrid least squares support vector regression-smart firefly

algorithm (LSSVR-SFA) model was established for shear strength prediction of RC beams [29]. A new novel AI model based on the hybridization of ANN model with atom search optimization (ASO) algorithm for SFRCB shear strength [30]. It can be observed that several versions of AI models for modeling beam shear strength. However, the introduced models have demonstrated limitations in the prediction performance.

To the best of the knowledge of the current study, the feasibility of the newly explored machine learning model called RF was tested to predict V_s of reinforced concrete beams. The validation of the proposed model was conducted in comparison with SVM and empirical formulations [31]. A deep analysis and prediction accuracy comparison were performed. The rest of the manuscript was structured, second section reports the methodology, third section presents the dataset, and fourth section exhibits the discussion and analysis of the studied predictive models. Section 5 explains the validation against the literature empirical; finally, Section 5 displays the research conclusion and recommended future research.

2. Methods and Materials

2.1. Random Forest. The random forest (RF) model was developed by Breiman [32] as a nonparametric ensemble classifier; the development of the RF was based on the flexible decision tree algorithm; hence, it is an extension of the classification and regression tree. The RF is comprised of a combination of different trees, with each tree being generated using bootstrap samples [33, 34]. For the model construction, the selected algorithm will perform auto-selection of the random parts of the training data, while the tree branch at each node will be determined from a subset of randomized variables during the training process. Classification error is minimized by expanding each individual tree, but the problem is that the result of this process is affected by the random selection step. The RF was mainly developed for the determination of the extent of increase in the prediction error upon the permutation of the data output for specific variables. Hence, the relevance of each variable can be determined with this approach as long as all the variables are adequate [35]. The training phase of RF generates loads of de-correlated regression trees, and each of these trees is grown in a randomly selected subset of the training set before combining them using a bagging method [36]. Bagging is used in this process to reduce the prediction-related variances and improve the prediction accuracy. To detail the process, assume n number of randomly selected samples from S_n, each having a selective probability of $1/n$. In this case, these n samples that are randomly selected are called a bootstrap sample S_n^θ, with θ being a vector distributed independently. Also, assume that the bagging algorithm has been used to select q number of bootstrap samples $(S_n^{\theta_1}, S_n^{\theta_2}, \ldots, S_n^{\theta_n})$, and q number of regression trees have been trained on these subsets $\widehat{h}(X, S_n^{\theta_1})$, $\widehat{h}(X, S_n^{\theta_2}), \ldots, \widehat{h}(X, S_n^{\theta_n})$. Then, the trained q number of regression trees generates q number of outputs $\widehat{Y}_1 = \widehat{h}(X, S_n^{\theta_1})$,

$\widehat{Y}_2 = \widehat{h}\ (X, S_n^{\theta_2}),\ldots, \widehat{Y}_q = \widehat{h}(X, S_n^{\theta_q})$; then, the values of the y outputs are averaged to obtain the final output of the system. Figure 1 presents the RF model structure.

2.2. Dataset Explanation and Modeling Development. In this study, the publicly available dataset on the experimental calculation of shear strength of the reinforced concrete beam was considered; this comprised of 349 samples collected from the open-source literature [37–56]. Among the considered dataset are b_w: beam width, d: effective depth, f_c': concrete compressive strength, h_f: thickness of the flange, b: flange width, a/d: wide range of shear span ratio to the effective depth, ρ_{sl}: flexural reinforcement ratio of the existing steel bar, ρ_{st}: transverse reinforcement ratio of the existing steel bar, $f_{st,y}$: the yield stress of steel stirrups, and K_f: flange coefficient. These parameters were engaged during the development of the predictive models for the determination of V_s. The statistical pattern of the input parameters and the predicted V_s is presented in Table 1. The observed maximum and minimum V_s values over the training dataset were 2237 kN and 22 kN, respectively. An instance of reinforced concrete beams under the condition of shear strength is presented in Figure 2. The correlation matrix between the predictors and predictand was presented in Figure 3. The modeling procedure was established based on the correlation statistic to identify the input combinations as reported in Table 1. Several performance metrics were calculated to evaluate the predictive models as reported in the appendix [24].

3. Models' Prediction Results and Analysis

Among several machine learning models that have been established for shear strength prediction, the SVM model was predominately adopted [57–61]. Hence, the current proposed model (i.e., RF) was validated against the SVM model. The evaluation of the statistical performance of the applied RF predictive model for shear strength prediction is presented in this section. The statistical performance was computed based on some performance metrics over the training and testing phases. These performance metrics were considered to achieve a better assessment and justification of the developed model in terms of the accuracy level since each of the statistical metrics is associated with certain limitations. The observed prediction accuracy for the training and testing phases of the RF model are shown in Tables 2 (RMSE for RF model = 77.13 kN, MAE = 26.17 kN, MAPE = 0.08, Nash = 0.94, and MD = 0.92); these metrics were computed using the nine input combination as all the input parameters were considered during the simulation step. For the testing phase, the RF model achieved the best results with the same ninth input combination (RMSE = 89.66 kN, MAE = 36.03 kN, MAPE = 0.17, Nash = 0.92, and MD = 0.88). Observably, the models achieved reasonable levels of learning accuracies. The predictive performance of the RF model was superior owing to its understanding of the internal relationship between the shear strength and the geometric/concrete properties of beams.

The prediction accuracies of the SVM during the training and testing phase are presented in Tables 3. The SVM model was attained during the training phase minimum RMSE value of 167.05 kN and MAE value of 43.83 kN using six input combinations after excluding a/d, h_f, and k_f parameters from the prediction matrix. On the contrary, the SVM model during the testing phase exhibited the minimum RMSE value of 163.06 kN, an MAE value of 50.03 kN, a MAPE value of 0.30, Nash value of 0.72, and MD value of 0.84. Based on the reported numerical results, it is essential to present the degree of prediction accuracy enhancement. The RMSE metric was selected to verify the degree of enhancement in which it obtained 82% accuracy improvement using the RF model over SVM during the test modeling phase.

Figure 4 shows the Taylor diagram of the comparison for the applied prediction models. This diagram eliminated the redundancy of the statistical indicators as it is generated using three statistical indicators which are correlation, RMSE, and standard deviation [62]. The figure shows that the RF model achieved the nearest value to the shear strength benchmark possibly due to the incorporation of all the predictors "for example M9." In other manner, the relative error of the first and the last input combination is drawn in Figure 5. It is clear that Model 9 reports the lower values of the relative error.

The scatter plot is one of the graphical forms of statistical visualization of the accuracy of machine learning models as it reveals the level of closeness of the observed and predicted values. The closeness of the observed and predicted shear strength of RC beams in this study is presented in Figures 6 and 7 for the training and testing phases, respectively. The figures indicate the regression equation and the determination coefficient (R^2) values for the model assessments. The scatter plots were generated for all input combinations. From the figures' presentation, the RF model achieved the closest level agreement between the observed and predicted shear strength values over the training and testing phases of the models. Based on the reported results explained in the scatter plots, the optimal prediction accuracy that has been attained using the proposed RF model are perfectly fitted for all the observations' magnitudes. It can be observed that Model 8 and Model 9 were reported identical prediction accuracy in which explained the unnecessary the of the flange coefficient information as predictor for the prediction matrix.

4. Validation against the Literature

Despite the ease of solving various structural engineering problems, their performance is yet to be validated against the available empirical formulations or the standard machine learning models available in the literature. The applied machine learning models for beam shear strength prediction in this study were validated using five empirical formulations pooled from the established dataset (served as the benchmark for the validation processes). The testing phase results were also considered for the comparison after conducting several reviews in this domain. Correlation was
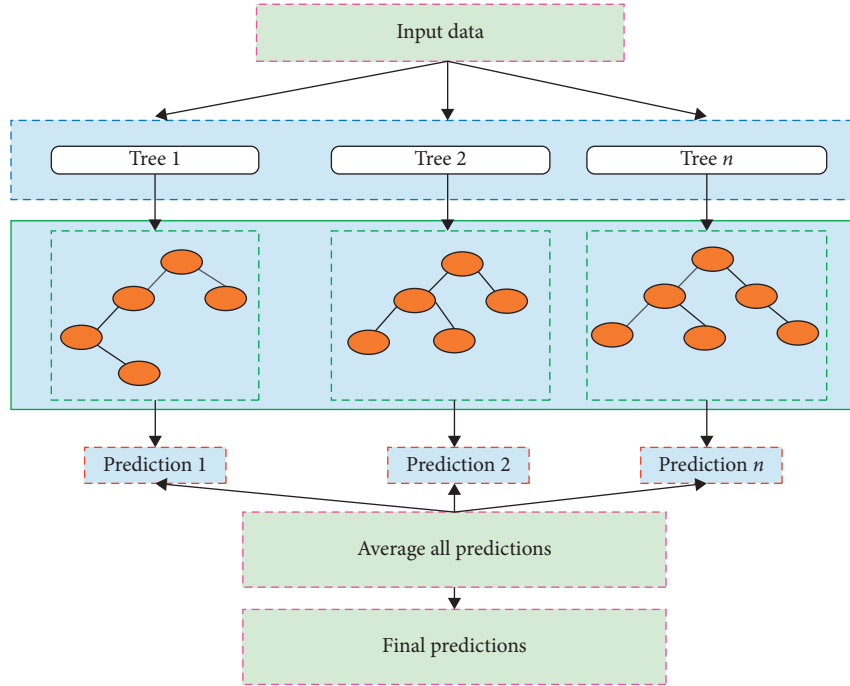
FIGURE 1: The random forest model structure.

TABLE 1: The initiated predictors' codes for the applied predictive models based on the statistical correlation.

Input codes	Associate parameters							
M1	$\rho_{st} \times f_{st,y}$							
M2	$\rho_{st} \times f_{st,y}$	d						
M3	$\rho_{st} \times f_{st,y}$	d	ρ_{sl}					
M4	$\rho_{st} \times f_{st,y}$	d	ρ_{sl}	f'_c				
M5	$\rho_{st} \times f_{st,y}$	d	ρ_{sl}	f'_c	b			
M6	$\rho_{st} \times f_{st,y}$	d	ρ_{sl}	f'_c	b	b_w		
M7	$\rho_{st} \times f_{st,y}$	d	ρ_{sl}	f'_c	b	b_w	a/d	
M8	$\rho_{st} \times f_{st,y}$	d	ρ_{sl}	f'_c	b	b_w	a/d	h_f
M9	$\rho_{st} \times f_{st,y}$	d	ρ_{sl}	f'_c	b	b_w	a/d	h_f	k_f
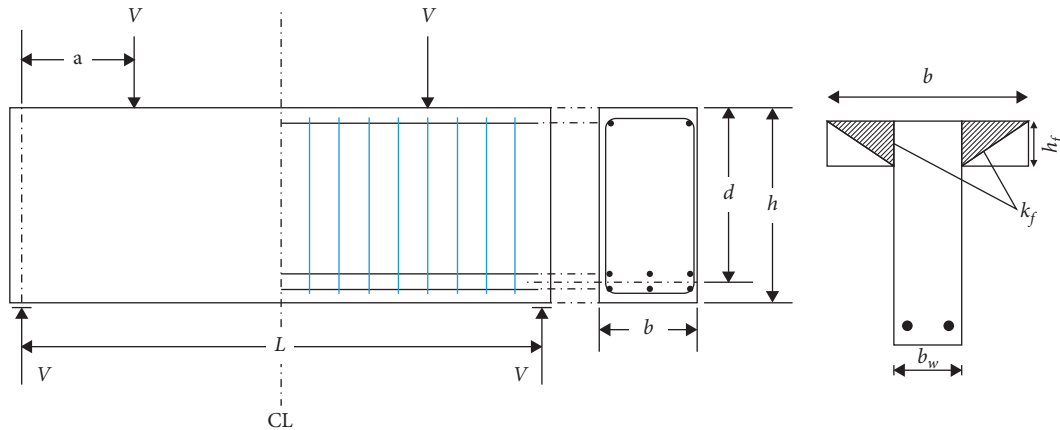
FIGURE 2: The studied reinforced concrete beam example experienced the shear strength case.
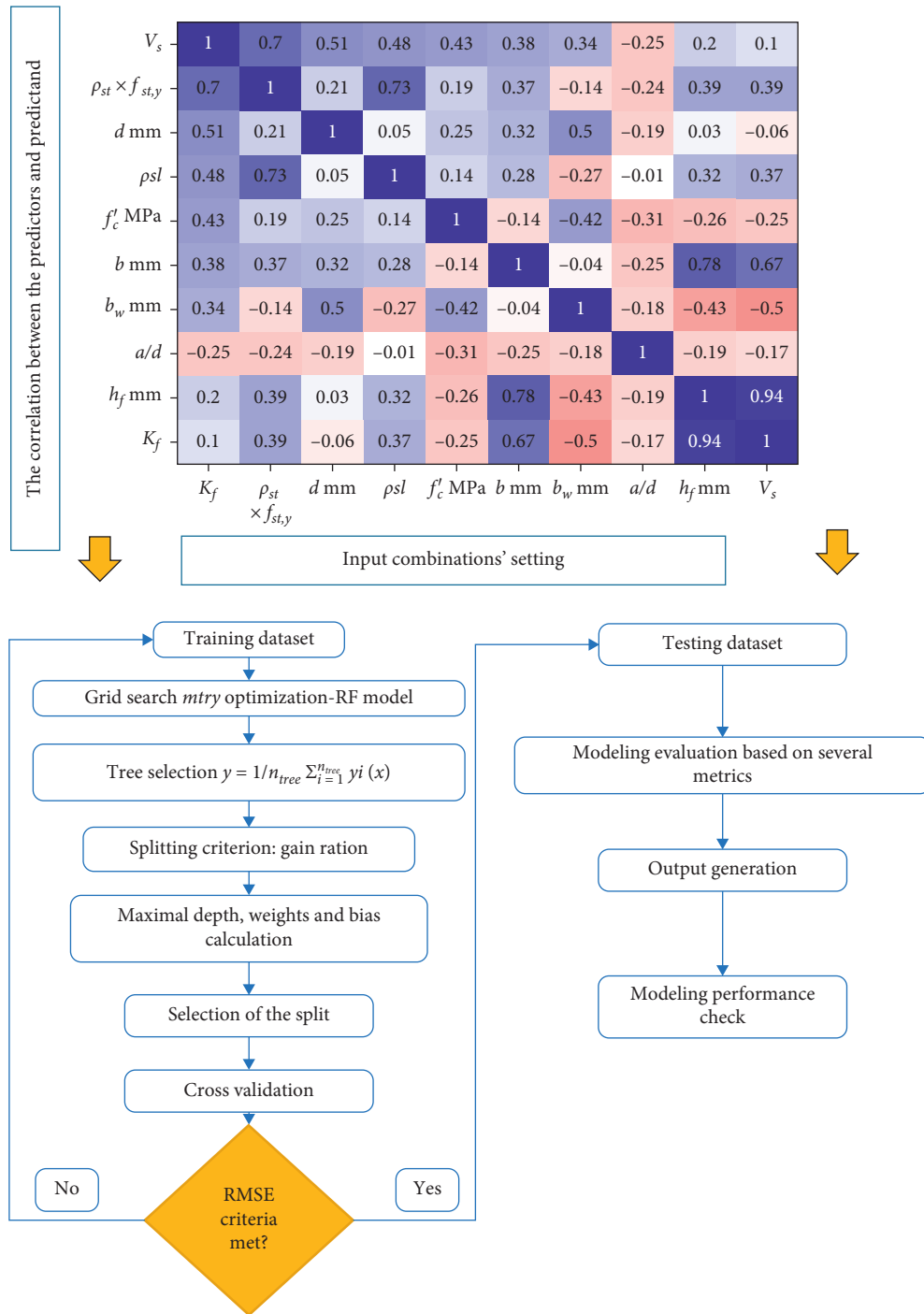
Figure 3: The modeling flowchart of the adopted AI model for the shear strength prediction.

TABLE 2: The prediction results for the investigated nine input combinations over the training and testing phases for the proposed RF model.

Models combinations	R^2	RMSE (kN)	MAE (kN)	MAPE	Nash	MD
Training phase						
M1	0.79	144.44	74.52	0.41	0.79	0.78
M2	0.94	85.88	35.73	0.12	0.93	0.90
M3	0.93	88.28	35.58	0.12	0.92	0.90
M4	0.95	80.34		0.09	0.93	0.92
M5	0.95	79.58		0.09	0.94	0.92
M6	0.95	74.69	28.89	0.08	0.94	0.93
M7	0.96	71.01	27.82	0.08	0.95	0.93
M8	0.96	74.81	25.67	0.08	0.94	0.93
M9	0.95	77.13	26.17	0.08	0.94	0.92
Testing phase						
M1	0.68	175.71	93.44	0.55	0.68	0.70
M2	0.83	129.69	59.14	0.27	0.83	0.82
M3	0.82	132.38	56.07	0.23	0.82	0.83
M4	0.92	103.61	43.98	0.23	0.89	0.86
M5	0.92	97.94	41.55	0.22	0.90	0.87
M6	0.93	92.57	35.60	0.16	0.91	0.89
M7	0.94	89.68	35.59	0.16	0.92	0.89
M8	0.95	89.66	36.03	0.17	0.92	0.88
M9	0.95	89.66	36.03	0.17	0.92	0.88

TABLE 3: The prediction results for the investigated nine input combinations over the training and testing phases for the proposed SVM model.

Input combinations	R^2	RMSE (kN)	MAE (kN)	MAPE	Nash	MD
Training phase						
M1	0.47	227.60	132.75	0.66	0.47	0.57
M2	0.63	209.86	75.61	0.27	0.55	0.76
M3	0.67	200.84	72.76	0.27	0.59	0.77
M4	0.77	174.56	60.52	0.28	0.68	0.80
M5	0.73	178.07	53.14	0.20	0.68	0.84
M6	0.76	167.05	43.83	0.18	0.72	0.87
M7	0.75	169.92	44.85	0.17	0.71	0.87
M8	0.74	170.11	45.06	0.18	0.71	0.87
M9	0.74	171.37	45.11	0.18	0.70	0.87
Testing phase						
M1	0.59	226.27	106.65	0.49	0.47	0.62
M2	0.64	197.63	78.41	0.36	0.59	0.74
M3	0.72	187.49	72.20	0.37	0.63	0.76
M4	0.75	177.63	68.11	0.37	0.67	0.77
M5	0.77	174.56	60.52	0.28	0.68	0.80
M6	0.77	167.65	50.01	0.25	0.71	0.83
M7	0.78	166.61	49.59	0.29	0.71	0.84
M8	0.79	163.06	50.03	0.30	0.72	0.84
M9	0.79	163.17	51.20	0.34	0.72	0.83
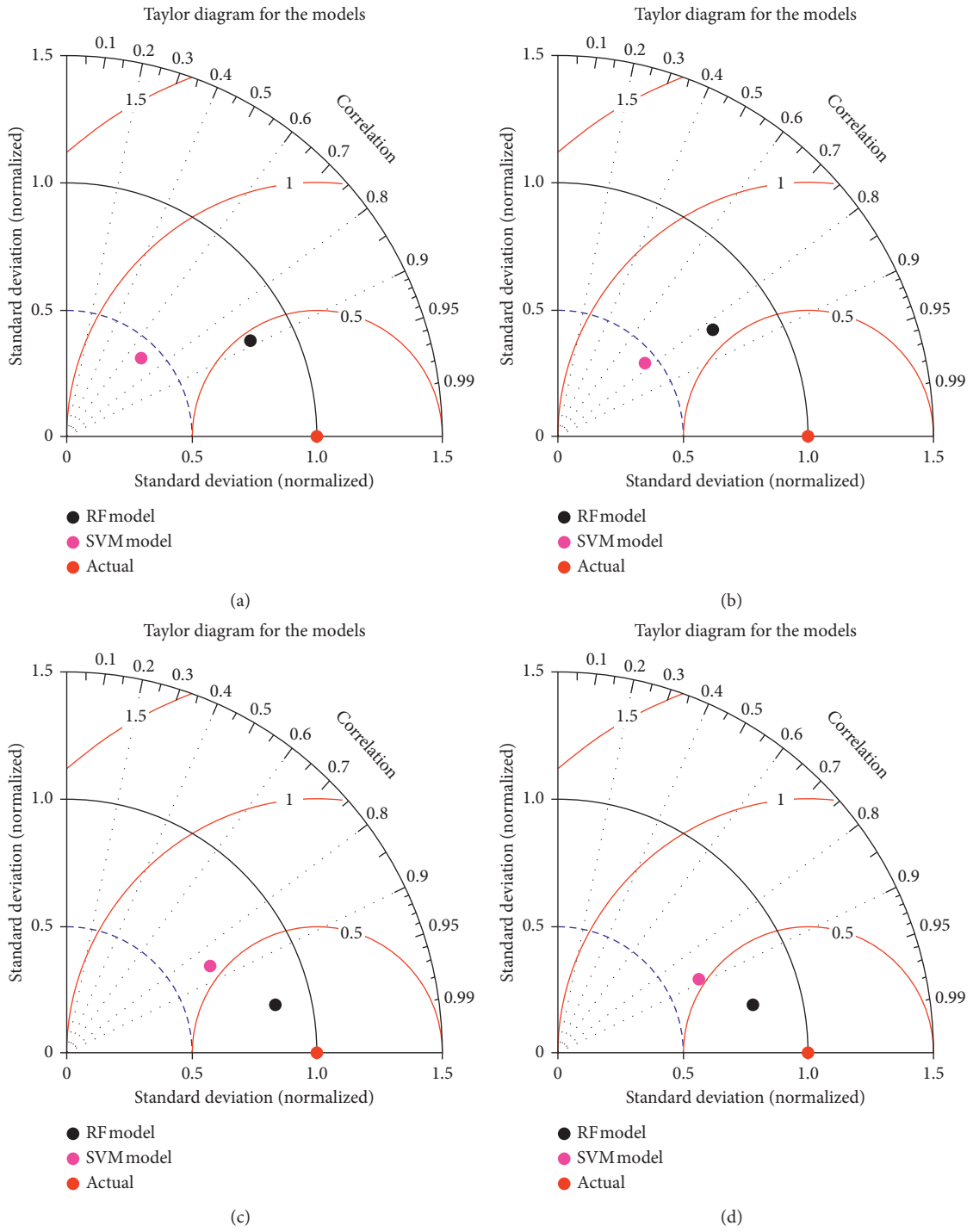
Figure 4: Taylor diagram presentation for the applied and comparable predictive models (RF and SVM). (a) Model 1 training. (b) Model 1 testing. (c) Model 9 training. (d) Model 9 testing.

(a)

(b)
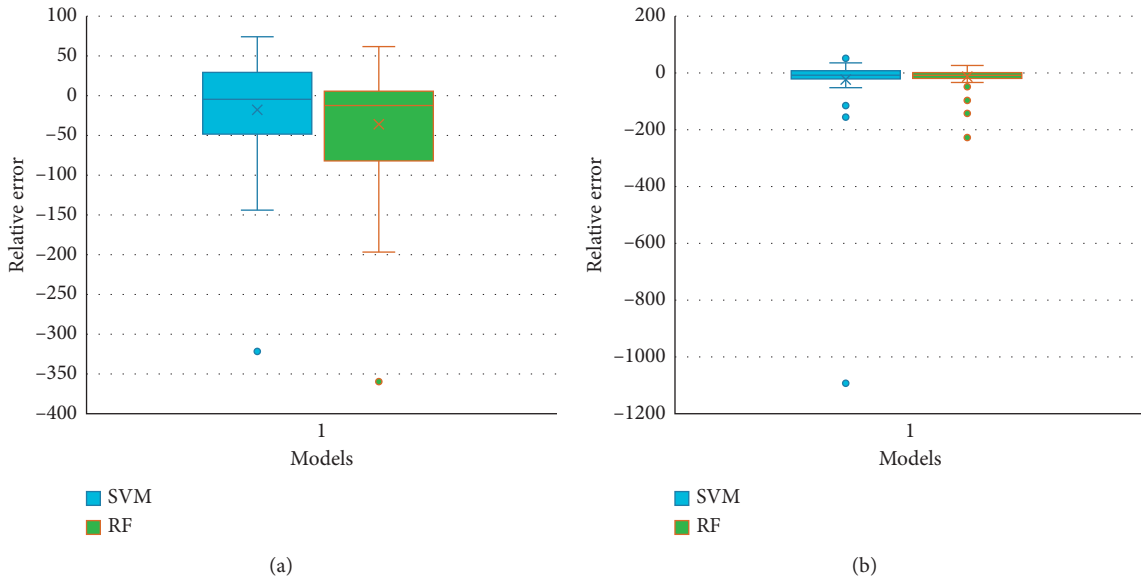
FIGURE 5: The relative error for the applied predictive models (RF and SVM) over the testing phase. (a) Model 1. (b) Model 9.

RF model 1

$y = 0.7363x + 69.321$
$R^2 = 0.7926$

SVM model 1

$y = 0.2978x + 116.93$
$R^2 = 0.4838$

(a)

(b)

RF model 2

$y = 0.8344x + 42.024$
$R^2 = 0.9364$

SVM model 2

$y = 0.4277x + 114.8$
$R^2 = 0.6307$

(c)

(d)

FIGURE 6: Continued.

(e)

(f)

(g)

(h)

(i)

(j)

FIGURE 6: Continued.

RF model 6

$y = 0.8506x + 38.943$
$R^2 = 0.9548$

(k)

SVM model 6

$y = 0.5888x + 92.732$
$R^2 = 0.7563$

(l)

RF model 7

$y = 0.8613x + 36.436$
$R^2 = 0.9588$

(m)

SVM model 7

$y = 0.581x + 91.982$
$R^2 = 0.7473$

(n)

RF model 8

$y = 0.8461x + 40.145$
$R^2 = 0.9559$

(o)

SVM model 8

$y = 0.5833x + 91.096$
$R^2 = 0.7448$

(p)

Figure 6: Continued.

(q)

(r)
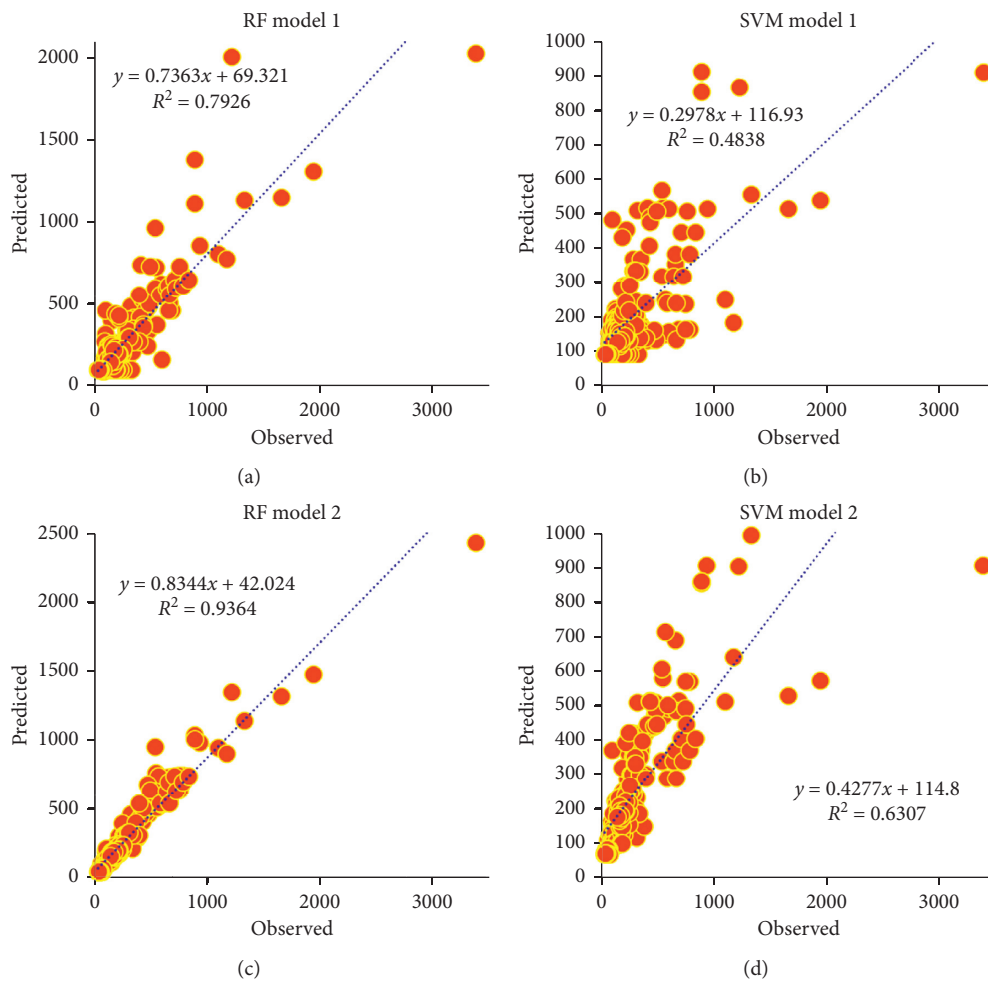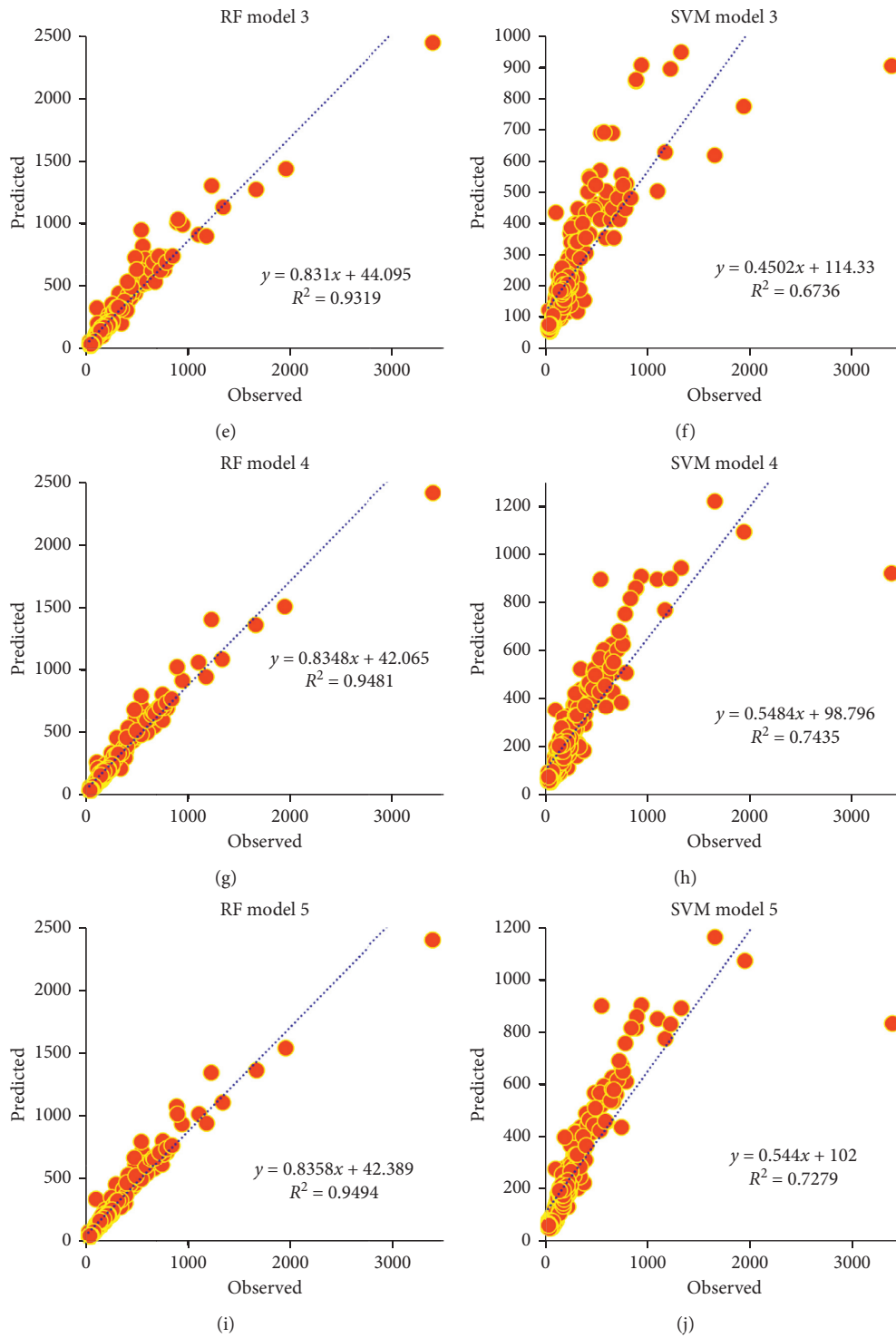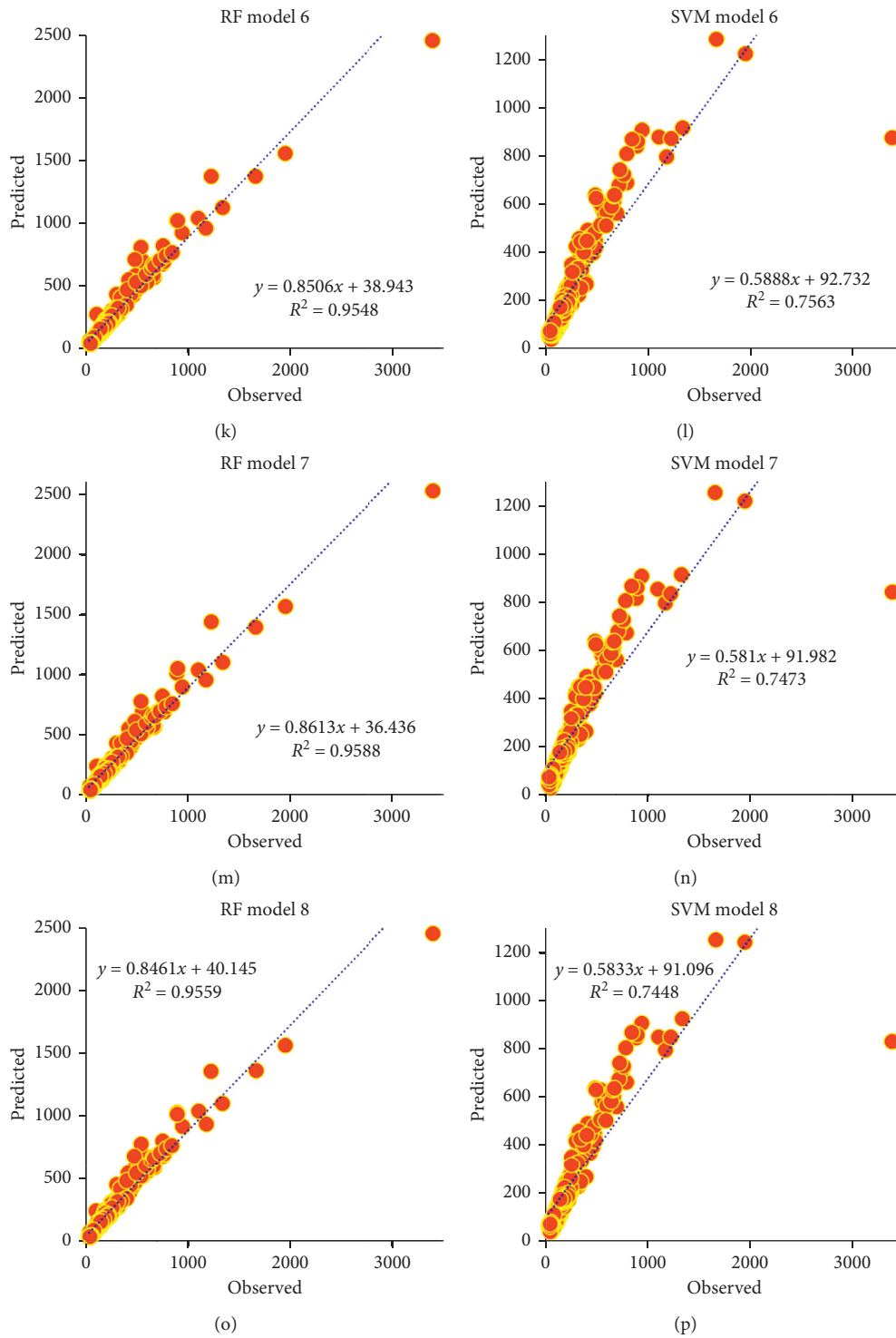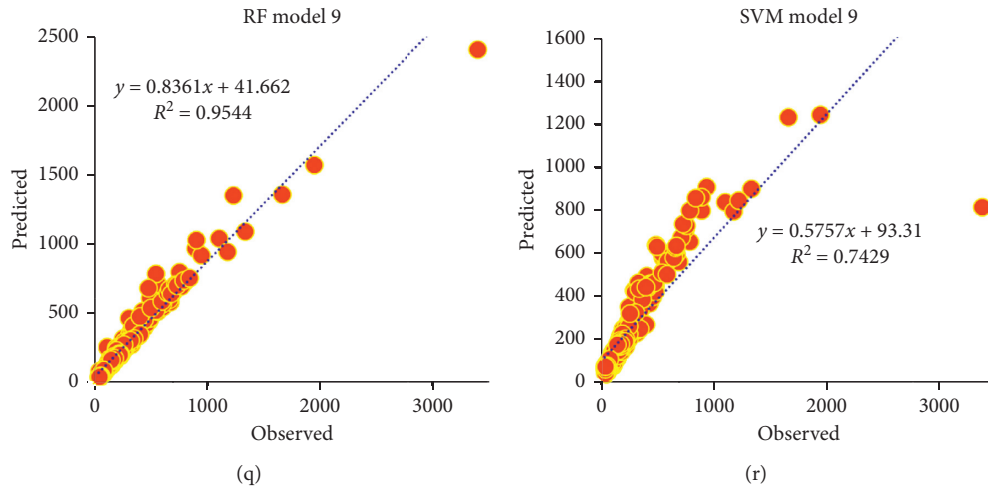
Figure 6: The scatter plots of the RF and SVM models over the training phase for all investigated input combinations.

(a)

(b)

(c)

(d)
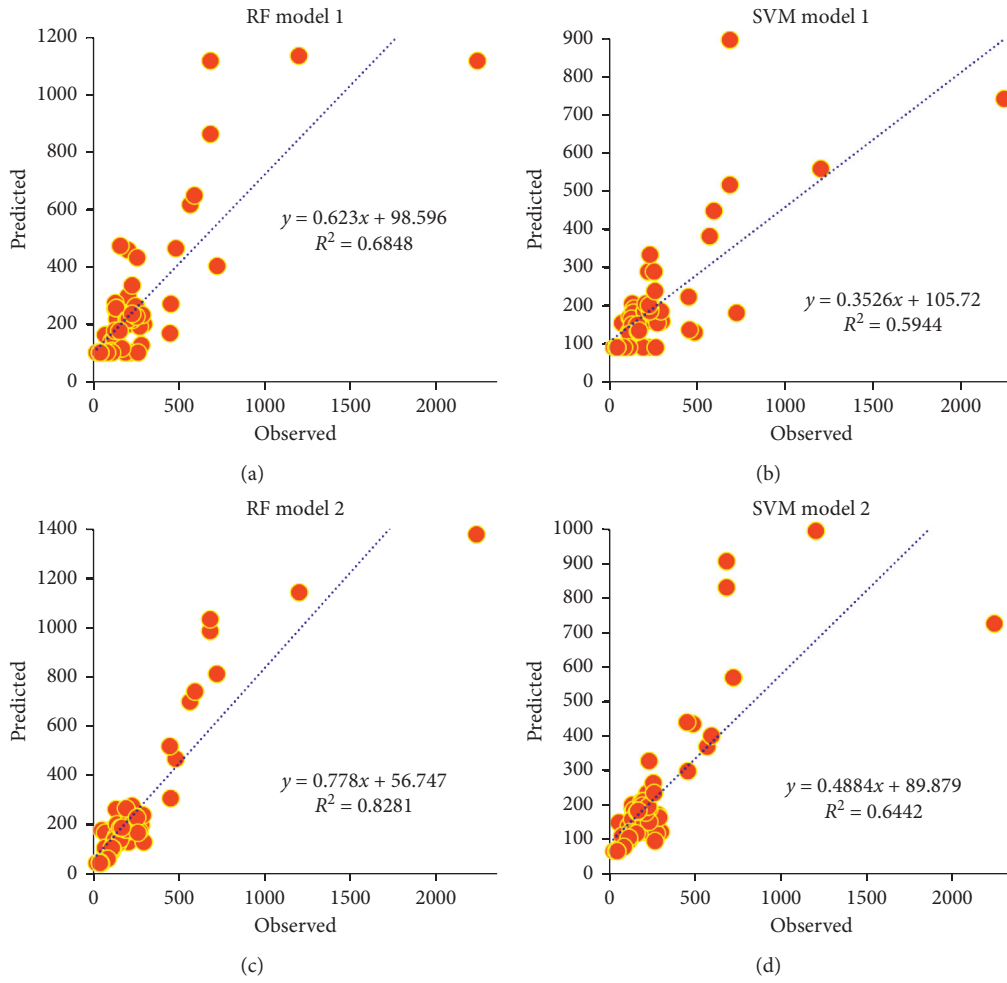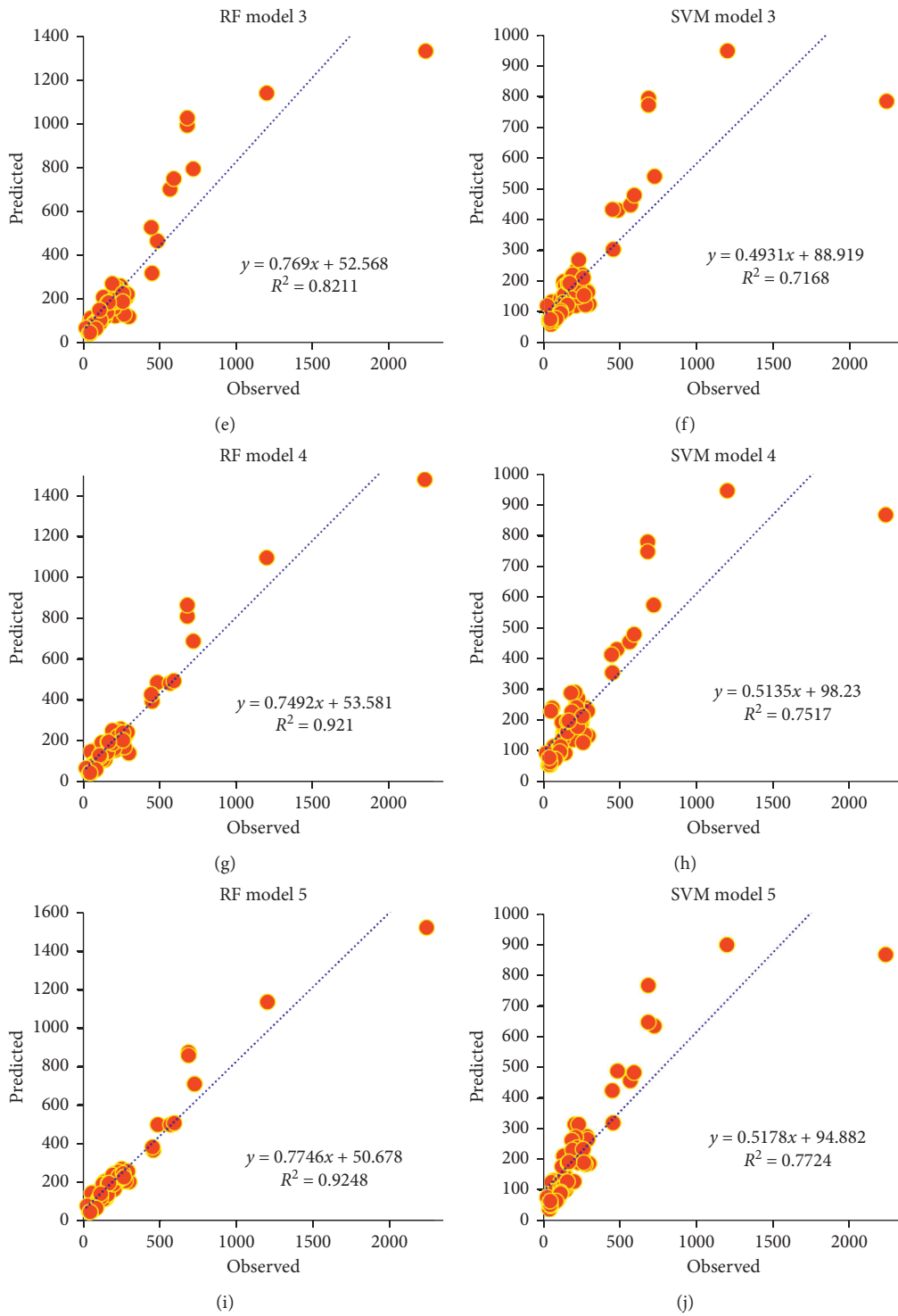
Figure 7: Continued.

FIGURE 7: Continued.

(k)

(l)

(m)

(n)

(o)

(p)
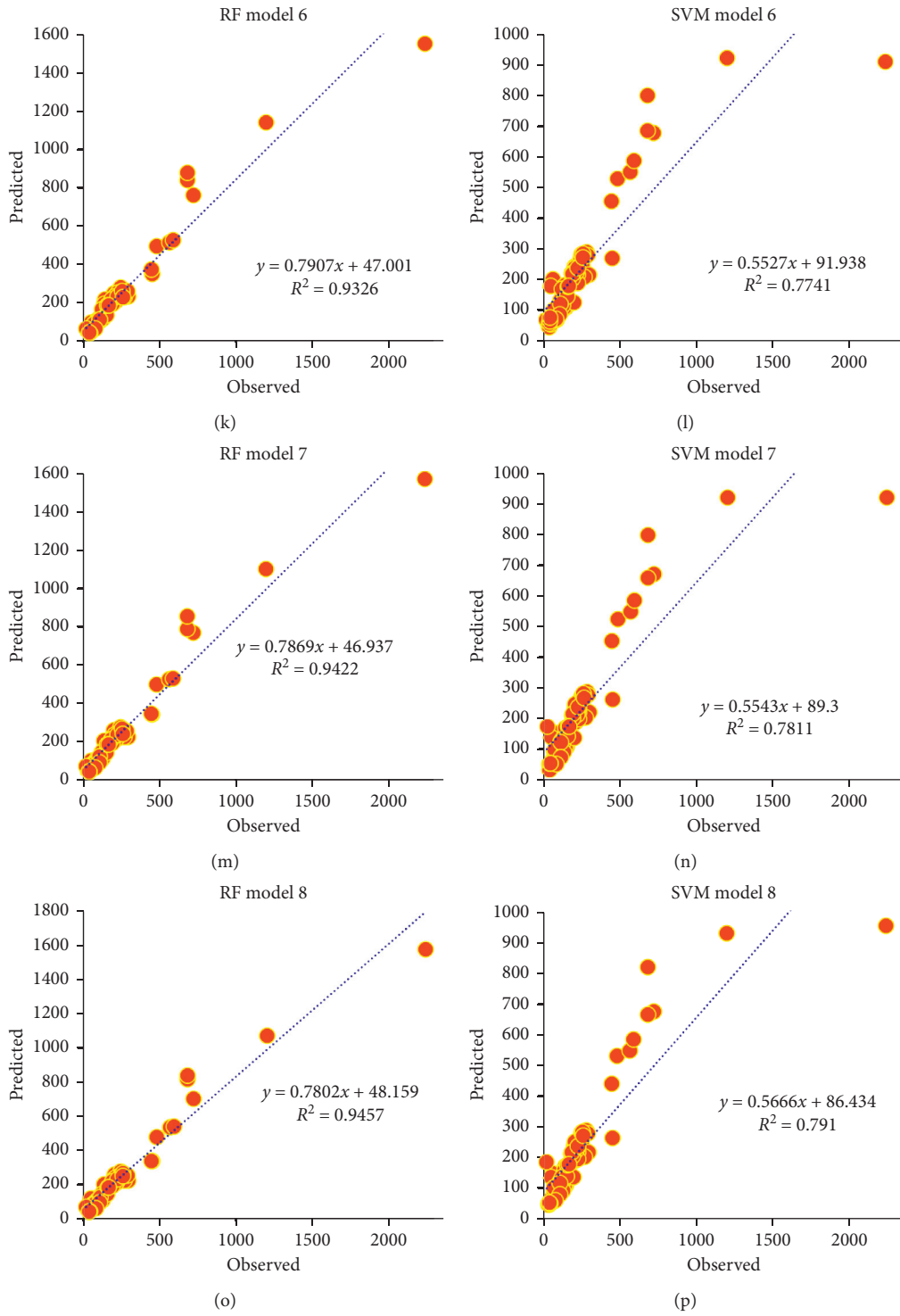
FIGURE 7: Continued.
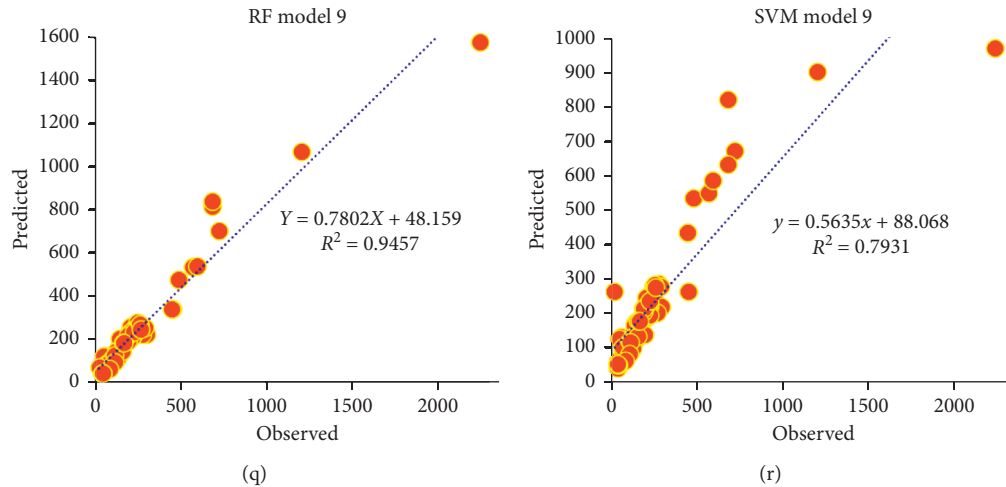
FIGURE 7: The scatter plots of the RF and SVM models over the testing phase for all investigated input combinations.

used as a statistical metric for the comparison. The correlation statistics were reported following standard codes and empirical formulations as follows: ACI 446 [63] ($R = 0.65$), ASCE-ACI 445 [64] ($R = 0.79$), CSA [65] ($R = 0.66$), NZS 3101 [66] ($R = 0.61$), and EC2 [67] ($R = 0.84$). Machine learning models have been noted to exhibit good performances in the previous studies; for example, the linear genetic programming (LGP) model has been used by Gandomi et al. [68] for shear strength prediction; the model achieved a maximum R value of 0.92. However, the proposed RF model in this study achieved better prediction performance ($R = 0.97$), meaning that the applied RF model can achieve better similarity between the experimental and predicted shear strength values. Furthermore, the proposed model can perform a better generalization of the internal mechanism between the physical properties of concrete and shear phenomenon.

5. Conclusion

Various limitations have been observed in the empirical formulation for the design of the shear strength of RC beams as evidenced in the literature; hence, efforts have been dedicated to the development of computer-aided models that can serve as alternatives. This work aims to develop the RF model as a robust machine learning approach to the prediction of the shear strength of RC beams. For this course, the parameters of the concrete and geometric properties of the beam were collected from previous studies and used for the model development. Nine input combinations of the "predictors for the models' matrix" were constructed, while the performance of the proposed model was validated against SVM and other empirical formulations. The modeling results showed that the proposed RF model is a robust approach to the modeling of V_s of RC beams. SVM achieved a comparable performance as well but not to the level of performance of the proposed RF model. The prediction results generally showed that the proposed

RF model achieved better performance accuracy than the empirical formulas. The model findings also suggested the relevance of the parameters of the geometric and concrete properties of beams on the learning process. Finally, a reliable and robust soft computing model has been developed in this study for the prediction of the V_s value of RC beams; hence, a significant contribution has been made to the basic knowledge of structural engineering design and sustainability. Future research direction is recommended to be devoted on the uncertainty analysis of model, data, and input parameters. In addition, there is a possibility to investigate the feature selection approach in which the redundant predictors can be eliminated.

Abbreviations

Vs: Shear strength
RC: Reinforced concrete
RF: Random forest
SVM: Support vector machine
R^2:   Determination coefficient
RMSE: Root mean square error
MAE: Mean absolute error
MAPE: Mean absolute percentage error
Nash: Nash–Sutcliffe efficiency
ML: Machine learning
MD: Modified index of agreement
LGP: Linear genetic programming.

Appendix

The mathematical expression of the computed performance metrics including determination coefficient (R^2), root mean square error (RMSE), mean absolute error (MAE), mean absolute percentage error (MAPE), Nash–Sutcliffe efficiency (NSE), and modified index of agreement (MD) is expressed as follows:

$$R^2 = \frac{\sum_{i=1}^{N} \left(y_0 - y_p\right)^2}{\sum_{i=1}^{N} \left(y_0 - y_p'\right)^2},$$

$$\text{RMSE} = \sqrt{(1/n) \sum_{i=1}^{N} \left(y_p - y_0\right)^2},$$

$$\text{MAE} = \frac{\sum_{i=1}^{N} \left|y_p - y_0\right|}{N},$$

$$\text{MAPE} = \frac{100}{n} \sum_{i=1}^{N} \left|\frac{y_0 - y_p}{y_0}\right|, \qquad \text{(A.1)}$$

$$\text{NSE} = \frac{\sum_{i=1}^{N} \left(y_p - y_0\right)^2}{\sum_{i=1}^{N} \left(y_p - y_p'\right)^2},$$

$$\text{MD} = \frac{\sum_{i=1}^{N} \left(y_0 - y_p\right)^j}{\sum_{i=1}^{N} \left(\left|y_p - y_0'\right| + \left|y_0 - y_0'\right|\right)^j}.$$

In the above equations, N is the number of the dataset, y_0 and y_p are the observed and predicted shear strength, y_o' and y_p' are the mean values of the observed and predicted shear strength, and j is the exponent term.

Data Availability

The data used to support the findings of the study are available from the corresponding author upon request.

Conflicts of Interest

The authors declare that they have no conflicts of interest.

References

[1] J. Wu, J. Xu, B. Diao, and D. K. Panesar, "Impacts of reinforcement ratio and fatigue load level on the chloride ingress and service life estimating of fatigue loaded reinforced concrete (RC) beams," *Construction and Building Materials*, vol. 266, p. 120999, 2021.

[2] V. T. Babar, P. K. Joshi, and D. N. Shinde, "Shear strength of steel fiber reinforced concrete beam without stirrups," *International Journal of Advanced Engineering and Technology*, vol. 15, no. II, p. 18, 2015.

[3] M. Jumaa'h, B. Kamil, and O. Baghabra, "Mechanical and structural properties of a lightweight concrete with different types of recycling coarse aggregate," *Tikrit Journal of Engineering Sciences*, vol. 26, no. 1, pp. 33–40, 2019.

[4] A. C. I. Committee and I. O. for Standardization, *Building Code Requirements for Structural Concrete (ACI 318-08) and Commentary*, American Concrete Institute, Indianapolis, IA, USA, 2008.

[5] F. Majdzadeh, S. M. Soleimani, and N. Banthia, "Shear strength of reinforced concrete beams with a fiber concrete matrix," *Canadian Journal of Civil Engineering*, vol. 33, no. 6, pp. 726–734, 2006.

[6] A. M. Ibrahim, W. D. Salman, and F. M. Bahlol, "Flexural behavior of concrete composite beams with new steel tube section and different shear connectors," *Tikrit Journal of Engineering Sciences*, vol. 26, no. 1, pp. 51–61, 2019.

[7] A. B. Matamoros and K. H. Wong, "Design of simply supported deep beams using strut-and-tie models," *ACI Structural Journal*, vol. 100, 2003.

[8] G. Russo, R. Venir, and M. Pauletta, "Reinforced concrete deep beams-shear strength model and design formula," *ACI Structural Journal*, vol. 102, no. 3, p. 429, 2005.

[9] H. E. Chabib, M. Nehdi, and A. Saïd, "Predicting the effect of stirrups on shear strength of reinforced normal-strength concrete (NSC) and high-strength concrete (HSC) slender beams using artificial intelligence," *Canadian Journal of Civil Engineering*, vol. 33, no. 8, pp. 933–944, 2006.

[10] T. Zhang, D. J. Oehlers, and P. Visintin, "Shear strength of FRP RC beams and one-way slabs without stirrups," *Journal of Composites for Construction*, vol. 18, no. 5, p. 04014007, 2014.

[11] T. Zhang, P. Visintin, D. J. Oehlers, and M. C. Griffith, "Presliding shear failure in prestressed RC beams. I: partial-interaction mechanism," *Journal of Structural Engineering*, vol. 104, 2014.

[12] M. Nehdi, H. El Chabib, and A. A. Saïd, "Proposed shear design equations for FRP-reinforced concrete beams based on genetic algorithms approach," *Journal of Materials in Civil Engineering*, vol. 19, no. 12, pp. 1033–1042, 2007.

[13] J. A. Khalaf, A. M. Abeer, S. A. Mohammed et al., "Hybridized deep learning model for perfobond rib shear strength connector prediction," *Complexity*, vol. 2021, Article ID 6611885, 21 pages, 2021.

[14] A. Sharafati, H. Masoud, S. Mohammad, and H. M. Mohamed, "Development of advanced computer aid model for shear strength of concrete slender beam prediction," *Applied Science*, vol. 10, no. 11, 2020.

[15] V. Birtel and P. Mark, "Parameterised finite element modelling of RC beam shear failure," in *Proceedings of the ABAQUS users' conference*, Providence, RI, USA, May 2006.

[16] M. A. Najafgholipour, S. M. Dehghan, A. Dooshabi, and A. Niroomandi, "Finite element analysis of reinforced concrete beam-column connections with governing joint shear failure mode," *Latin American Journal of Solids and Structures*, vol. 14, no. 7, pp. 1200–1225, 2017.

[17] B. A. Mahmood and K. I. Mohammad, "Finite element analysis of RC deep beams under eccentric load," *Tikrit Journal of Engineering Sciences*, vol. 26, no. 1, pp. 41–50, 2019.

[18] H. Shiohara, "New model for shear failure of RC interior beam-column connections," *Journal of Structural Engineering*, vol. 127, no. 2, pp. 152–160, 2001.

[19] I. Flood and N. Kartam, "Neural networks in civil engineering. I: principles and understanding," *Journal of Computing in Civil Engineering*, vol. 8, 1994.

[20] H.-B. Ly, T.-T. Le, H.-L. T. Vu, V. Q. Tran, L. M. Le, and B. T. Pham, "Computational hybrid machine learning based prediction of shear capacity for steel fiber reinforced concrete beams," *Sustainability*, vol. 12, no. 7, 2020.

[21] R. Solhmirzaei, H. Salehi, V. Kodur, and M. Z. Naser, "Machine learning framework for predicting failure mode and shear capacity of ultra high performance concrete beams," *Engineering Structures*, vol. 224, p. 111221, 2020.

[22] E. Figueiredo, G. Park, C. R. Farrar, K. Worden, and J. Figueiras, "Machine learning algorithms for damage detection under operational and environmental variability," *Structural Health Monitoring*, vol. 10, no. 6, pp. 559–572, 2011.

[23] O. Avci, O. Abdeljaber, S. Kiranyaz, M. Hussein, M. Gabbouj, and D. J. Inman, "A review of vibration-based damage

detection in civil structures: from traditional methods to Machine Learning and Deep Learning applications," *Mechanical Systems and Signal Processing*, vol. 147, p. 107077, 2021.

[24] W. Ben Chaabene, M. Flah, and M. L. Nehdi, "Machine learning prediction of mechanical properties of concrete: critical review," *Construction and Building Materials*, vol. 260, p. 119889, 2020.

[25] B. B. Adhikary and H. Mutsuyoshi, "Prediction of shear strength of steel fiber RC beams using neural networks," *Construction and Building Materials*, vol. 20, no. 9, pp. 801–811, 2006.

[26] S. Kar, A. R. Pandit, and K. C. Biswal, "Prediction of FRP shear contribution for wrapped shear deficient RC beams using adaptive neuro-fuzzy inference system (ANFIS)," *Structures*, vol. 23, no. 2019, 2020.

[27] B. Keshtegar, M. Bagheri, and Z. M. Yaseen, "Shear strength of steel fiber-unconfined reinforced concrete beam simulation: application of novel intelligent model," *Composite Structures*, vol. 212, 2019.

[28] A. A. Al-Musawi, A. A. H. Alwanas, S. Q. Salih, Z. H. Ali, M. T. Tran, and Z. M. Yaseen, "Shear strength of SFRCB without stirrups simulation: implementation of hybrid artificial intelligence model," *Engineering with Computers*, vol. 36, no. 1, pp. 1–11, 2020.

[29] J.-S. Chou, T.-P.-T. Pham, T.-K. Nguyen, A.-D. Pham, and N.-T. Ngo, "Shear strength prediction of reinforced concrete beams by baseline, ensemble, and hybrid machine learning models," *Soft Computing*, vol. 24, no. 5, pp. 3393–3411, 2020.

[30] W. B. Chaabene and M. L. Nehdi, "Novel soft computing hybrid model for predicting shear strength and failure mode of SFRC beams with superior accuracy," *Composites Part C: Open Access*, vol. 3, p. 100070, 2020.

[31] H. R. M. Mohammed and S. Ismail, "Proposition of new computer artificial intelligence models for shear strength prediction of reinforced concrete beams," *Engineering with Computers*, pp. 1–19, 2021.

[32] L. Breiman, "Random forests," *Machine Learning*, vol. 45, no. 1, pp. 5–32, 2001.

[33] L. Breiman, J. H. Friedman, R. A. Olshen, and C. J. Stone, *Classification and Regression Trees*, vol. 19, 1984.

[34] H. Hong, H. R. Pourghasemi, and Z. S. Pourtaghi, "Landslide susceptibility assessment in Lianhua County (China): a comparison between a random forest data mining technique and bivariate and multivariate statistical models," *Geomorphology*, vol. 259, pp. 105–118, 2016.

[35] A. Liaw and M. Wiener, "Classification and regression by randomForest," *R News*, vol. 2, no. 3, pp. 18–22, 2002.

[36] K. Fawagreh, M. M. Gaber, and E. Elyan, "Random forests: from early developments to recent advancements," *Systems Science & Control Engineering*, vol. 2, no. 1, pp. 602–609, 2014.

[37] H. Baghi and J. A. O. Barros, "Design approach to determine shear capacity of reinforced concrete beams shear strengthened with NSM systems," *Journal of Structural Engineering*, vol. 143, 2017.

[38] J. R. Gilman, R. T. Brickey, and M. M. Red, "Monte Carlo techniques for evaluating producing properties," in *Proceedings of the SPE Rocky Mountain Regional/Low-Permeability Reservoirs Symposium*, Denver, CO, USA, April 1998.

[39] R. Thamrin, J. Tanjung, R. Aryanti, O. F. Nur, and A. Devinus, "Shear strength of reinforced concrete T-beams without stirrups," *Journal of Engineering Science and Technology*, vol. 11, no. 4, pp. 548–562, 2016.

[40] S. J. E. Dias and J. A. O. Barros, "Shear strengthening of RC beams with NSM CFRP laminates: experimental research and analytical formulation," *Composite Structures*, vol. 99, pp. 477–490, 2013.

[41] O. Chaallal, A. Mofidi, B. Benmokrane, and K. Neale, "Embedded through-section FRP rod method for shear strengthening of RC beams: performance and comparison with existing techniques," *Journal of Composites for Construction*, vol. 15, no. 3, pp. 374–383, 2011.

[42] L. De Lorenzis and A. Nanni, "Shear strengthening of reinforced concrete beams with near-surface mounted fiber-reinforced polymer rods," *ACI Structure Journal*, vol. 98, no. 1, pp. 60–68, 2001.

[43] P. Y. L. Kong, *Shear Strength of High Performance Concrete Beams*, Curtin University, Perth, Australia, 1996.

[44] J. Sagaseta and R. L. Vollum, "Influence of beam cross-section, loading arrangement and aggregate type on shear strength," *Magazine of Concrete Research*, vol. 63, no. 2, pp. 139–155, 2011.

[45] J. A. Ramirez and J. E. Breen, "Discussion of "transverse stirrup spacing in R/C beams " by wayne hsiung and gregory C. Frantz (February, 1985, Vol. 111, No. 2)," *Journal of Structural Engineering*, vol. 113, no. 1, pp. 174-175, 1987.

[46] M. Khuntia, D. Angelakos, E. C. Bentz, and M. P. Collins, "Effect of concrete strength and minimum stirrups on shear strength of large members. Paper by Dino Angelakos, Evan C. Bentz, and Michael P. Collins," *ACI Structure Journal*, vol. 99, no. 2, pp. 224–226, 2002.

[47] A. Cladera and A. R. Marí, "Shear design procedure for reinforced normal and high-strength concrete beams using artificial neural networks. Part I: Beams without stirrups," *Engineering Structures*, vol. 26, 2004.

[48] R. J. Frosch, "Behavior of large-scale reinforced concrete beams with minimum shear reinforcement," *Structure Journal*, vol. 97, no. 6, pp. 814–820, 2000.

[49] Y. Yoon, W. Cook, and D. Mitchell, "Minimum shear reinforcement in normal, Medium, and high-strength concrete beams," *ACI Structure Journal*, vol. 93, no. 5, 1996.

[50] J. J. Roller and H. G. Russel, "Shear strength of high-strength concrete beams with web reinforcement," *Structures Journal*, vol. 87, no. 2, pp. 191–198, 1990.

[51] M. K. Johnson and J. A. Ramirez, "Minimum shear reinforcement in beams with higher strength concrete," *Structures Journal*, vol. 86, no. 4, pp. 376–382, 1989.

[52] K.-H. Reineck, E. Bentz, B. Fitik, D. A. Kuchma, and O. Bayrak, "ACI-DAfStb databases for shear tests on slender reinforced concrete beams with stirrups," *ACI Structure Journal*, vol. 111, no. 5, 2014.

[53] A. G. Mphonde, "Use of stirrup effectiveness in shear design of concrete beams," *Structures Journal*, vol. 86, no. 5, pp. 541–545, 1989.

[54] G. Ozcebe, U. Ersoy, and T. Tankut, "Evaluation of minimum shear reinforcement requirements for higher strength concrete," *Structures Journal*, vol. 96, no. 3, pp. 361–368, 1999.

[55] B. Bresler and A. C. Scordelis, "Shear strength of reinforced concrete beams," *Journal Proceedings*, vol. 60, no. 1, pp. 51–74, 1963.

[56] W. J. Krefeld and C. W. Thurston, "Studies of the shear and diagonal tension strength of simply supported reinforced concrete beams," *Journal Proceedings*, vol. 63, no. 4, pp. 451–476, 1966.

[57] M. Y. Cheng and M. T. Cao, "Evolutionary multivariate adaptive regression splines for estimating shear strength in

reinforced-concrete deep beams," *Engineering Applications of Artificial Intelligence*, vol. 28, 2014.

[58] S. Maryam, W. Karzan, S. Majid, and S. Mahdi, "Application of support vector machine with firefly algorithm for investigation of the factors affecting the shear strength of angle shear connectors," *Smart Materials and Structures*, vol. 22, 2018.

[59] G. Zhang, H. A. Zainab, S. Mohammed, and H. S. Mohammed, "Reinforced concrete deep beam shear strength capacity modelling using an integrative bio-inspired algorithm with an artificial intelligence model," *Engineering with Computers*, 2020.

[60] Z. M. Yaseen, M. T. Tran, S. Kim, T. Bakhshpoori, and R. C. Deo, "Shear strength prediction of steel fiber reinforced concrete beam using hybrid intelligence models: a new approach," *Engineering Structures*, vol. 177, pp. 244–255, 2018.

[61] D. Prayogo, M. Y. Cheng, Y. W. Wu, and D. H. Tran, "Combining machine learning models via adaptive ensemble weighting for prediction of shear capacity of reinforced-concrete deep beams," *Engineering with Computers*, vol. 36, 2020.

[62] K. E. Taylor, "Summarizing multiple aspects of model performance in a single diagram," *Journal of Geophysical Research: Atmospheres*, vol. 106, no. D7, pp. 7183–7192, 2001.

[63] Farmington Hills, *Subcommittee ACI-446B of ACI Committee 446 on FractureMechanics*, Farmington Hills, Oakland, CA, USA, 2005.

[64] A.-A. 445, "Summary of the evaluations of the proposals for the quick fix forreinforced concrete members without transverse reinforcement," in *Proceedings of the Sub-committee ACI-445F of ACI Committee 445 on Shear And Torsion*, 2003.

[65] C. Darwin, *On the Origin of Species by Means of Natural Selection or the Preservation of Favoured Races in the Struggle for Life*, International Book Company, New York, NY, USA, 1859.

[66] N 3101, *The Design of Concrete Structures*, New Zealand Standards, Wellington, New Zealand, 1995.

[67] R. P. Johnson and D. Anderson, *Designers' Guide to EN 1994-1-1: Eurocode 4: Design of Composite Steel and Concrete Structures. General Rules and Rules for Buildings. Thomas Telford*, London, UK, 2004.

[68] A. H. Gandomi, S. Mohammadzadeh, J. L. Pérez-Ordóñez, and A. H. Alavi, "Linear genetic programming for shear strength prediction of reinforced concrete beams without stirrups," *Applied Soft Computing*, vol. 19, pp. 112–120, 2014.

WILEY | Hindawi

Research Article

Investigation of ANN Architecture for Predicting Load-Carrying Capacity of Castellated Steel Beams

Thuy-Anh Nguyen ⃝, **Hai-Bang Ly** ⃝, **and Van Quan Tran** ⃝

University of Transport Technology, Hanoi 100000, Vietnam

Correspondence should be addressed to Hai-Bang Ly; banglh@utt.edu.vn

Castellated steel beams (CSB) are an attractive option for the steel construction industry thanks to outstanding advantages, such as the ability to exceed large span, lightweight, and allowing flexible arrangement of the technical pipes through beams. In addition, the complex localized and global failures characterizing these structural members have led researchers to focus on the development of efficient design guidelines. This paper aims to propose an artificial neural network (ANN) model with optimal architecture to predict the load-carrying capacity of CSB with a scheme of the simple beam bearing load located at the center of the beam. The ANN model is built with 9 input variables, which are essential parameters equivalent to the geometrical properties and mechanical properties of the material, such as the overall depth of the castellated beam, the vertical projection of the inclined side of the opening, the web thickness, the flange width, the flange thickness, the width of web post at middepth, the horizontal projection of inclined side of the opening, the minimum web yield stress, and the minimum flange yield stress. The output variable is the load-carrying capacity of the CSB. With the optimal ANN architecture [9-1-1] containing one hidden layer, the performance of the ANN model is evaluated based on statistical criteria such as R^2, RMSE, and MAE. The results show that the optimal ANN model is a highly effective predictor of the load-carrying capacity of the CSB with the best value of $R^2 = 0.989$, RMSE $= 3.328$, and MAE $= 2.620$ for the testing part. The ANN model seems to be the best algorithm of machine learning for predicting the CSB load-carrying capacity.

1. Introduction

In modern construction, steel structures are used for abundant structures, including heavy industrial buildings, high-rise buildings, equipment support systems, infrastructure, bridges, towers, and racking systems [1]. The steel structure has numerous advantages such as large bearing capacity thanks to the high strength steel material, high reliability thanks to the uniform material, and the elastic and ductile capacity of steel, making it easy to transport and assemble [2]. Due to the high cost of steel, many structural engineers have worked hard to find ways to reduce costs for steel structures [3, 4]. Therefore, several solutions have been proposed to increase the rigidity or load capacity of the structure without increasing the weight of steel. Castellated steel beams (CSB) with web openings are among the first

suggestions of these solutions [5]. This type of beam is made from wide flange I-beams, then cutting the belly plate in a zigzag line, welding the two halves on top of each other, and welding by vertical welding seams along the beam [3, 4, 6, 7]. This increases the section height but does not increase weight compared to the original solid beam; thus, bending resistance characteristics such as the moment of inertia, section modulus, and the radius of inertia are higher, and the beam stiffness and flexural resistance of sections are enhanced [3, 7, 8]. Therefore, the beam bearing capacity increases, the deflection is small, and the beam is able to exceed the large aperture [7].

However, the web openings will change the stress distribution on the bending sections [4]. Near the web openings, the stress distribution is quite complex, and stress concentration occurs. Moreover, due to the bending

moment effect, this area is also subjected to the torsion force [9]. Therefore, the critical loads of the structures are changed compared with the conventional beam [5]. So far, many experimental investigations, as well as numerical analyses, have been carried out to determine the behavior of the castellated beams under different loads. The beam failure is caused by numerous damage caused by overall bending, Vierendeel mechanism formation, welded joint rupture in the web, web post shear bucking, and web post-compression buckling [10–13]. The damage is affected by numerous factors, including geometrical dimensions of beams, loading type, and position, beam boundary conditions, material properties, as well as the distribution of residual stresses and geometric imperfections [14, 15]. Konstantinos and Mello [16] investigated the CSB behavior with close web openings by studying seven experimental samples and fourteen numerical simulation samples. The aim is to study the effects of different hole shapes and sizes on the bearing capacity and critical load of the CSB. The CSB finite element models with hexagonal and circular web openings are developed and analyzed using ANSYS. The results are compared with seven experiments test samples, thereby proposing an experimental formula to predict the load capacity of castellated beams. A numerical model studies the behavior of CSB with hexagonal and octagonal web openings up to failure developed by Soltani et al. [17]. The main purpose is to study and determine the instability in the position of web openings. In the work of Jamadar and Kumbhar [18], the authors used finite element models to determine the optimal hole size for CSB. In general, the numerical approach or laboratory experiments can only be applied to a limited number of cases, not enough to apply for general web openings beams. Furthermore, the cost of the experiment is high and requires a considerable amount of time [5]. Therefore, it is necessary to develop an efficient and universal model to study the behavior of CSB or estimate the load-carrying capacity of the CSB.

In recent years, with the rapid development of artificial intelligence technology, machine learning algorithms have been popularized in all areas of life [19–21]. Among AI algorithms, ANN is currently effective algorithms to simulate complex technical problems [22, 23]. ANN model is capable of solving complex, nonlinear problems, especially in problems where the relationship between the inputs and outputs cannot be established explicitly. An outstanding advantage of the neural network algorithm is the ability to self-study and adjust the weights. Thus, the calculation results are consistent without depending on mechanical equations, physical chemistry, or subjective opinion. Many complex problems related to structural engineering [24–26], geotechnical engineering [26–28], and materials science [29–31] have been successfully solved. In detail, Abdalla et al. [27] successfully predicted the minimum factor of safety against slope failure in clayey soils using the ANN model. The mechanical properties of FRP concrete are also predicted by the ANN model with high accuracy [32, 33]. In the field of calculating steel beams using neural networks, a number of studies have been published, such as

the study of Guzelbey et al. [34] and Fonseca et al. [35]. In these studies, a backpropagation (BP) neural network is used to predict the load-carrying capacity of steel beams. The results show that the BP network is more accurate than the numerical result, practical and fast, compared to the FE model. Recently, Amayreh and Saka [36] and Gholizadeh et al. [37] used ANN to predict load failure of the CSB. In the study of Amayreh and Saka, 47 experimental data are collected, the ANN model is built with 8 input parameters, the predicted results are compared with the Blodgett method, and BS Code shows the neural network provides an effective alternative to predicting the failure loads of CSB. In the investigation of Gholizadeh et al., 140 finite element models of the web post are analyzed with 7 input parameters related to geometry size. The BP networks and ANFIS are used to predict the load-carrying capacity of the CSB. The results show that the machine learning method provides better accuracy than the equations proposed in the document. Besides, methods such as genetic algorithm (GP) and an integrated search algorithm of genetic programming and simulated annealing (GSA) are also used to predict the load-carrying capacity of the CSB. The efficiency of the ANN model shows that it is an excellent choice to develop a numerical tool for engineers to predict the loading carrying capacity of CSB, which could help to reduce experimental time consumption and cost. Therefore, the main purpose of this investigation is to propose an efficient ANN model with a more general number of input parameters and to increase the accuracy in predicting the load-carrying capacity of the CSB.

In this work, the ANN model's performance will be studied to predict the load-carrying capacity of the CSB. One of the factors affecting the model performance is to finely determine the ANN architecture. Therefore, the first goal of this work is to identify and optimize the ANN architecture to predict the load-carrying capacity of CSB. To achieve this goal, 500 simulations taking into account a data random sampling effect are performed for each model to verify the convergence and feasibility of the proposed model by Monte Carlo simulation (MSC). Then, with the optimal ANN architecture, the performance evaluation of the model is performed based on three statistical criteria, including the Coefficient of Determination (R^2), Mean Absolute Error (MAE), and Root Mean Square Error (RMSE).

2. Significance of the Research Study

Accurately predicting the load-carrying capacity of the CSB is of crucial importance because of many possible advantages and contributions to construction design. Available numerical or experimental approaches in the literature still face several limitations, for instance, the limitation of data (Amayreh and Saka [36] with 47 samples; Gholizadeh et al. [37] with 140 samples; Gandomi et al. [38] with 47 samples; and Aminian et al. [39] with 142 samples), accuracy evaluation of the ANN model, or comparison with different prediction results in the literature. Thereby, the contribution of the present investigation could be highlighted via the following ideas:

(1) The largest dataset, to the best of the author's knowledge, is used for the construction of ANN models, including 150 experimental results

(2) The reliability of ANN models is evaluated by Monte Carlo simulations

(3) The best ANN architecture is determined by the performance evaluation of 240 ANN architectures, including 15 architectures using one hidden layer, and 225 architectures with two hidden layers

(4) The performance of the best ANN architecture is compared with four studies published in the literature and confirmed the highest accuracy of the proposed ANN model in the present study

3. Database Construction

To construct a model to predict the load capacity of the CSB, a database of 150 experimental data is collected, in which 140 beam samples are simulated from the validated finite element model introduced in document [37], and 10 beam samples are tested directly for bearing capacity published in document [13]. The beams are simulated and tested under concentrated loads placed in the center of the beam until failure. The basic parameters determining the beam failure load equivalent to the nine input variables and one output variable used in this study are as follows.

Seven parameters related to the size of the CSB are used: the overall depth of castellated beam (I_1, mm); the vertical projection of inclined side of opening (I_2, mm); the web thickness (I_3, mm); the flange width (I_4, mm); the flange thickness (I_5, mm); the width of web post at mi depth (I_6, mm); the horizontal projection of inclined side of the opening (I_7, mm), where I_1 varies from 180.00 mm to 550.00 mm (mean of 335.92 mm and standard deviation of 99.60 mm), I_2 ranges from 50.00 mm to 250.00 mm (mean of 103.36 mm and standard deviation of 40.15 mm), I_3 has values between 2.00 mm and 5.00 mm (mean value is 3.65 mm and standard deviation 0.88 mm), I_4 ranges from 58.42 mm to 78.49 mm (the mean value is 68.39 mm and standard deviation of 3.54 mm), the value of I_5 is between 3.99 mm and 6.90 mm (the mean is 5.34 mm and the standard deviation is 1.03 mm), I_6 ranges from 30.00 mm to 95.00 mm (mean 53.75 mm and standard deviation 19.26 mm), and I_7 ranges from 30.00 mm to 149.35 mm (mean value is 59.23 mm and the standard deviation is 22.75 mm). The remaining two parameters are related to the mechanical properties of the material, including the minimum web yield stress (I_8, MPa) and the minimum flange yield stress (I_9, MPa). For I_8, the value varies from 311.65 MPa to 374.40 MPa (mean is 351.36 mm and the standard deviation is 7.12 mm), and I_9 ranges from 307.52 MPa to 383.54 Mpa (mean is 350.97 mm and standard deviation is 8.25 mm). The detailed statistical information of these variables is shown in Table 1. The geometry and dimensions of the CSB are shown in Figure 1.

The dataset is randomly divided into two subsets using a uniform distribution, in which 70% of the data (corresponding to 105 data) is used to train ANN models, and 30% of the remaining data (corresponding to 45 data) is used for model verification. This means that the control data (30%) is entirely unknown to the ANN model. Therefore, the forecasting capacity of the ANN model can be assessed objectively and most accurately through the verification section. All data are normalized to the range of [0, 1] for reducing the number of errors in processing by ANN, according to the recommendations of [40]. This process ensures that the training phase of ANN models can be carried out with functional generalization capabilities. Such proportions are expressed using the following equation:

$$\chi_{\text{scaled}} = \frac{2(\chi - \lambda)}{\mu - \chi} - 1, \tag{1}$$

where λ and μ are the minimum and maximum values of given variables and χ is the value of the variable to be scaled.

In addition, a correlation analysis between the input and output parameters is performed and shown in Figure 2. Figure 2 is created to find a linear statistical correlation between parameters in the database. Therefore, a 10×10 matrix is established, where the upper triangle represents the values of the correlation coefficient, while the lower triangle shows a scatter plot between the two related variables. The diagonal of the matrix indicates the name of the parameter. The maximum value of the correlation coefficient (R) compared to Y is calculated by 0.52 (for variable I_3), followed by 0.39 (for variable I_2), 0.28 (for variable I_4), 0.24 (for variable I_7), 0.23 (for variable I_8), 0.21 (for variable I_9), 0.12 (for variable I_6), 0.09 (for variable I_5), and 0.04 (for variable I_1).

4. Methods

4.1. Artificial Neural Network. The ANN artificial neural network is a mathematical and statistical model based on the working mechanism of the biological nervous system [41]. ANN does not attempt to simulate the delicate workings of the brain, but they try to replicate the logical activity of the brain by gathering a lot of input in the form of neurons to perform computational or cognitive processes. The purpose of ANN is to define the relationship between the input parameters and the output parameters of the model. However, ANN only uses datasets without prespecifying the math functions that determine the relationship between the input and output parameters of the model. This is an effective soft computation method to solve too complex problems compared to classical mathematics and traditional methods [42].

In this study, a feedforward neural network trained by the backpropagation algorithm is used [43]. This neural network is made up of a series of processing elements, which can be called neurons or nodes. These neurons are partially or wholly connected through weights (w_{ji}) and are divided into 3 layers: input layer, output layer, and hidden layers.

During the learning process, the backpropagation algorithm uses the gradient descent search method to adjust the connection weight. The learning process starts from the input data (the input parameter vectors are entered into the

TABLE 1: Summary of the input and output variables of CSB beams used in this study.

	Symbol	Unit	Min	Median	Mean	Max	StD*	SK**
The overall depth of the castellated beam	I_1	mm	180.000	380.500	335.921	550.000	99.597	−0.244
The vertical projection of inclined side of opening	I_2	mm	50.000	110.000	103.358	250.000	40.154	0.389
The web thickness	I_3	mm	2.000	3.560	3.647	5.000	0.883	−0.576
The flange width	I_4	mm	58.420	66.900	68.386	78.486	3.538	0.590
The flange thickness	I_5	mm	3.988	4.590	5.344	6.900	1.032	0.666
The width of web post at middepth	I_6	mm	30.000	50.000	53.753	95.000	19.262	0.235
The horizontal projection of inclined side of opening	I_7	mm	30.000	55.000	59.230	149.352	22.754	1.128
The minimum web yield stress	I_8	MPa	311.654	352.000	351.360	374.400	7.123	−4.195
The minimum flange yield stress	I_9	MPa	307.517	352.000	350.968	383.540	8.251	−3.137
The load-carrying capacity	Y	kN	20.370	74.068	73.524	138.880	27.676	0.251

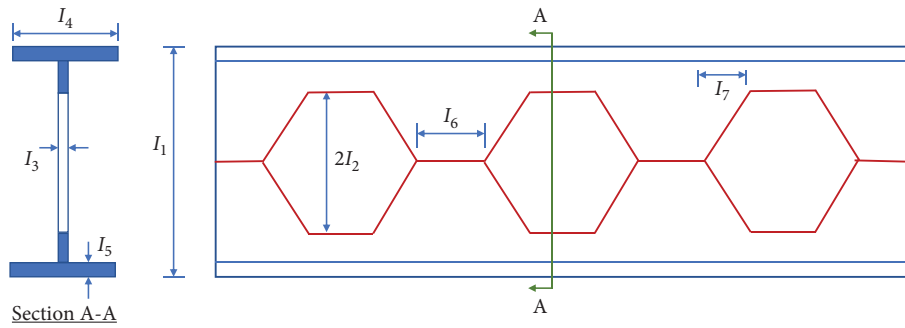*StD = standard deviation; **SK=skewness.

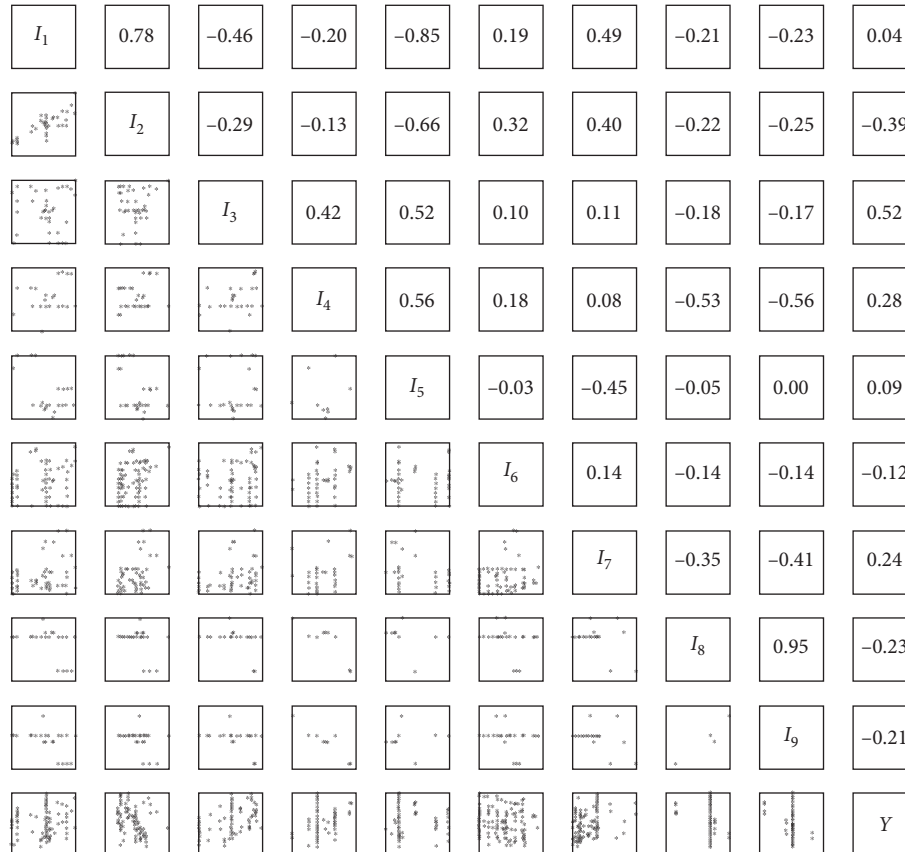FIGURE 1: Castellated steel beams and opening geometry.

FIGURE 2: Correlation graphs between input and output variables used in this study.

input layer's neurons). At the j hidden layer neuron, the signal value received from the input layer will be composed of a total input value according to the following formula:

$$I_j = \theta_j + \sum_{i=1}^{n} w_{ji} x_i, \tag{2}$$

in which x_i are the input parameters and weights (w_{ji}) and bias (θ_j) will be randomly generated.

The pass function will then be used to calculate the output value using the following formula:

$$y_j = f(I_j). \tag{3}$$

This output value again serves as the input to the next layer neuron. As it continues, this value is passed to the neuron in the output layer. For a hidden single-layer network, this step will move to reverse propagation. The difference between the output value (y_j) and the actual value (t_j) is called the cost function, calculated as follows:

$$J = t_j - y_j. \tag{4}$$

From the cost function, compute the weight derivative of the entered and hidden classes. From there, adjust the weights and bias variables to make the predicted output of the network closer to expected:

$$\Delta w_{ji} = \frac{\partial J}{\partial w_{ji}},$$

$$\Delta \theta_j = \frac{\partial J}{\partial \theta_j}, \tag{5}$$

$$w_{ji}(\text{new}) = w_{ji}(\text{old}) - \eta \Delta w_{ji},$$

$$\theta_j(\text{new}) = \theta_j(\text{old}) - \eta \Delta \theta_j,$$

where $w_{ji}(\text{new}), \theta_j(\text{new})$ are weight value and bias value after adjustment; $w_{ji}(\text{old}), \theta_j(\text{old})$ are weight value and previous bias values; and η is the learning rate.

Learning speed is the optimal algorithm parameter (gradient descent). If this parameter is small, it will take many iterations for the function to reach its minimum. Conversely, if this parameter is large, the algorithm will need fewer iterations, but then it is possible that the function will ignore the minima and cannot converge.

To overcome the weights (w_{ji}) and bias values (θ_j) of the next iteration step that do not fall into a local minimum point, the momentum algorithm is used [44]. This algorithm calculates the amount of change of the variables at time t (v_t) to update the new value:

$$w_{ji}(\text{new}) = w_{ji}(\text{old}) - \gamma v_{t-1}^w - \eta \Delta w_{ji},$$
$$\theta_j(\text{new}) = \theta_j(\text{old}) - \gamma v_{t-1}^w - \eta \Delta \theta_j, \tag{6}$$

where γ is the momentum term.

With multiple hidden layers, the algorithm formulas perform the same steps. After the learning process, the model will be verified by an independent testing database.

4.2. Performance Criteria. During the training of ANN models, it is necessary to quantify the performance of the model to be able to repeat the hyperparameter adjustment to choose the best model possible. Standard quantitative performance measures for a regression model include the Coefficient of Determination (R^2), Mean Absolute Error (MAE), and Root Mean Square Error (RMSE) [45, 46]. The R^2 criterion is widely used in regression problems to estimate the correlation between the actual value and the predicted results [47]. The value of R^2 is in the range [0; 1]. In addition, RMSE and MAE measure the mean error between actual and predicted outputs [48]. Quantitatively, RMSE and MAE values are closer to 0, and the closer the value of R^2 is to 1, the more accurate the machine learning model is. The following equations represent these values:

$$R^2 = 1 - \frac{\sum_{j=1}^{N} (P_j - \overline{P}_j)}{\sum_{j=1}^{N} (P_j - \overline{P})},$$

$$RMSE = \sqrt{\frac{\sum_{j=1}^{N} (P_j - \overline{P}_j)^2}{N}}, \tag{7}$$

$$MAE = \frac{\sum_{j=1}^{N} |P_j - \overline{P}_j|}{N},$$

in which P_j is the actual j_{th} output, $\overline{P}_j$ is the predicted j_{th} output, $\overline{P}$ is the average of the $\overline{P}_j$, and N is the number of the samples.

5. Methodology Flow Chart

The methodology of developing artificial neural networks to predict the load-carrying capacity of the CSB includes four primary steps as follows (as shown in Figure 3):

Step 1. Database preparation: in this step, a database of 140 finite element simulation beam samples and 10 direct test beam samples is collected to build the ANN model. The basic parameters to predict the load-carrying capacity of the CSB include 9 input variables divided into two groups of variables: the geometric size group and the physical properties of the material. The dataset is randomly divided into two parts, of which 70% of the data is used to train the ANN model and the remaining 30% is used to validate the built model.

Step 2. Determination of the optimum of ANN architecture: in this step, the construction of the optimum of ANN architecture based on the training dataset is carried out. The criteria used to validate the optimal ANN model include R^2, RMSE, and MAE.

Step 3. Training the optimal model: in this step, the ANN model with the optimum architecture is trained using the training dataset.

Step 4. Validating the model: in this step, the testing dataset is used to test and confirm the trained ANN model. The performance of the ANN model is evaluated by statistical criteria: R^2, RMSE, and MAE.
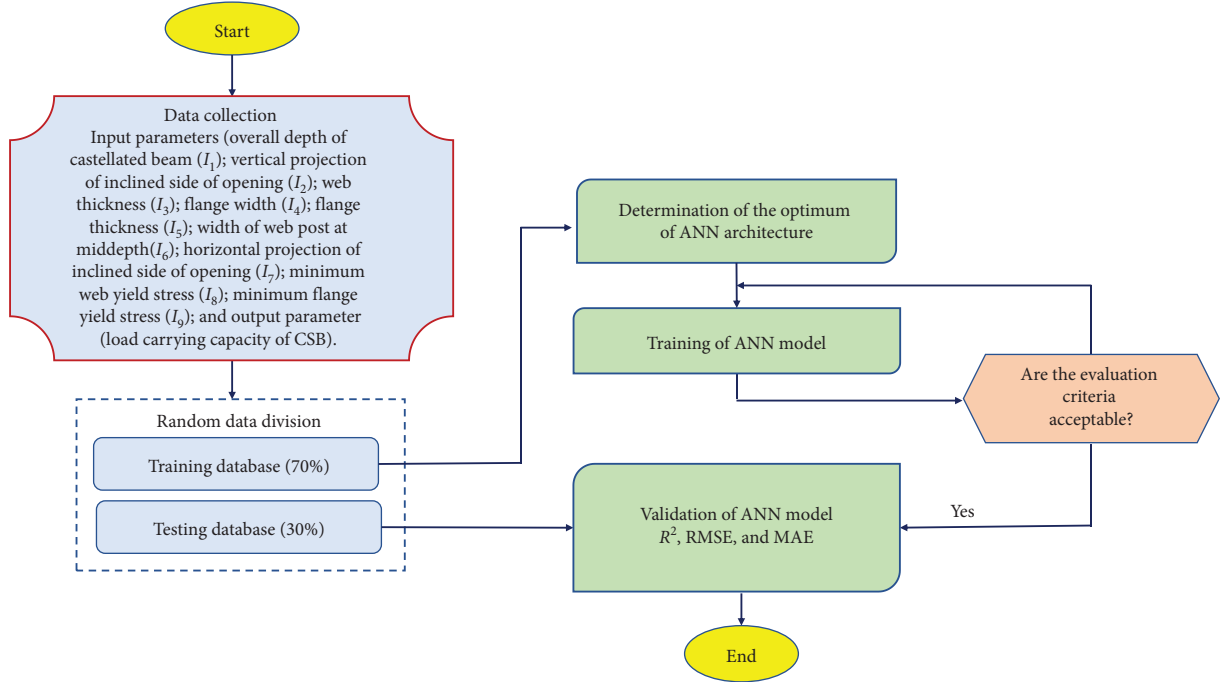
FIGURE 3: Methodology flowchart of the present study.

6. Results and Discussion

6.1. Investigation of Model Convergence. In this section, the determination of the ANN architecture and optimization of the ANN parameters are performed using the gradient descent algorithm. Parameters of the ANN model used in this study are given in Table 2, in which there are eight fixed parameters, and two parameters are subjected to a parametric study, namely, the number of hidden layers and the number of neurons in each hidden layer. In general, choosing the number of hidden layers and neurons in each layer is a trial-and-error test, needed to find the best configuration of the network [23]. In this study, ANN models containing one and two hidden layers are analyzed and tested. The number of neurons in each hidden layer is varied from 1 to 15. Regarding each network topology, the network training process is performed. In essence, network training is the process of adjusting the link weights and biases. These weight values are randomly taken initially, and then the network algorithm adjusts the values during the training phase. To build the network with the highest accuracy, optimization is performed with 1000 epochs to adjust the weights for each given ANN structure. In addition, in order to generalize the ANN model, 500 simulations are performed for each of the analyzed ANN structures. A total of 120,000 simulations are performed, corresponding to 15 architectures for one hidden layer and 225 architectures for two hidden layers.

    The optimization process for the training and testing parts is evaluated by three statistical criteria, namely, R^2, RMSE and MAE, presented above and shown in Figure 4. Specifically, Figures 4(a), 4(c), and 4(e) represent the values of the three criteria for the training part, while Figures 4(b), 4(d), and 4(f) represent the testing part. Thanks to MCS, Figure 4 shows that, with 100 simulations, the values of the three criteria converge in

TABLE 2: Summary of different ANN characteristics and investigation parameters in this study.

Parameter	Parameter	Description
Fix	Neurons in input layer	9
	Neurons in output layer	1
	Hidden layer activation function	Sigmoid
	Output layer activation function	Linear
	Cost function	Mean Square Error (MSE)
	Number of epochs	1000
	Number of simulations	500
	Training algorithm	Gradient descent
Varying	Number of hidden layers	Varying from 1 to 2
	Neurons in hidden layer	Varying from 1 to 15

about 10% of the corresponding average values. When the number of simulations increases to 400, the convergence of the ANN model improves (i.e., lower than 5% of the corresponding average values). Therefore, it could be stated that the simulations performed with 500 runs give reliable results. Overall, all investigations and results in the next sections are given by averaging the results of 500 simulations for each ANN structure.

6.2. Prediction Performance of Different ANN Architectures. In this section, the performance of different ANN architectures is presented to find the best ANN architecture. The performance evaluation is calculated for both the training and the testing parts by the mean and standard deviation values (StD) of the three statistical criteria (i.e., R^2, RMSE, and MAE). Figures 5(a), 5(b), and 5(c) depict the mean
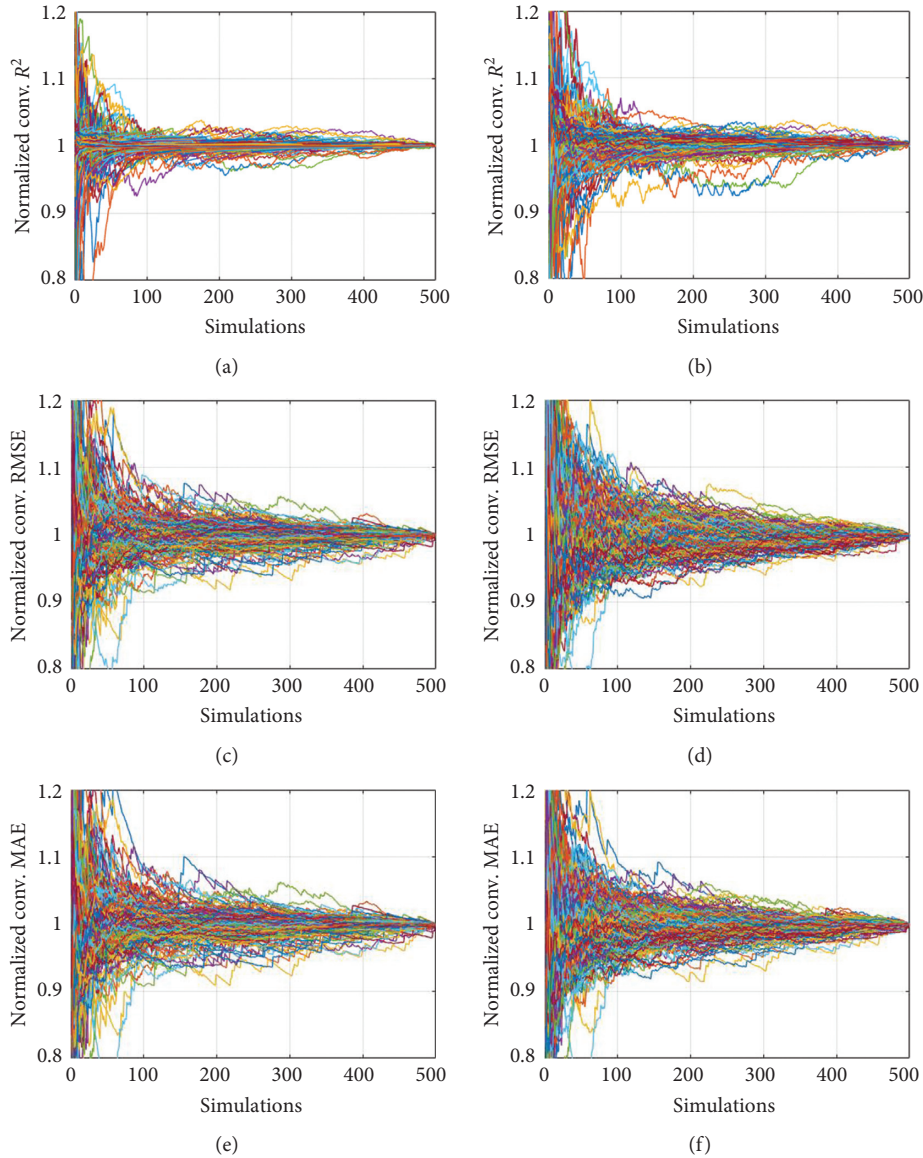
FIGURE 4: Convergence analysis for different ANN architecture with respect to (a) R^2 of the training parts; (b) R^2 of the testing part; (c) RMSE of the training part; (d) RMSE of the testing part; (e) MAE of the training part; and (f) MAE of the testing part.

values of R^2, RMSE, and MAE of all the analyzed ANN structures for both the training and testing parts.

In Figure 5, it worth noting that the first edge of R^2, RMSE, and MAE mean value curve is the performance of the ANN model containing 1 hidden layer, with the neuron number varying from 1 to 15. The second edge corresponds to the ANN architecture with 2 hidden layers. The first point of the second edge starts with the performance of the ANN model containing 1 neuron for the first hidden layer and 1 neuron for the second hidden layer or ANN architecture [9-1-1-1]. Each point of the remaining edges corresponds to the performance of ANN architecture containing 1 neuron in the first hidden layer, and the following points are results with 1 to 15 neurons in the second hidden layer. It means that the last point of the second edge corresponds to the performance of ANN architecture [9-1-15-1]. Overall, one edge is shown for ANN architecture containing 1 hidden layer, and 15 edges are shown for ANN

architecture containing 2 hidden layers (Figure 5). Precisely, the 225 performance values of different ANN architectures can also be shown by color-map in Figures 6 and 7 for the training part and testing part, respectively. Besides, Figures 6 and 7 also show the StD values of R^2, RMSE, and MAE. Figures 6(a) and 7(a) show that the value of R^2 is relatively greater than 0.9 and 0.8 for the training and testing dataset, respectively, for ANN architectures with more than 3 neurons in the first hidden layer. Similar observations are remarked with a specific zone with low values of RMSE and MAE for both the training and testing parts (Figures 6(c), 6(e), 7(c), and 7(e)).

The performance values presented in Figure 5 show that the highest mean value of $R^2 = 0.923$ and the lowest mean values of RMSE = 7.225, MAE = 5.047 for the testing part, correspond to the ANN architecture containing 1 hidden layer [9-1-1]. Therefore, this ANN architecture has the best performance.

(a)

(b)

(c)
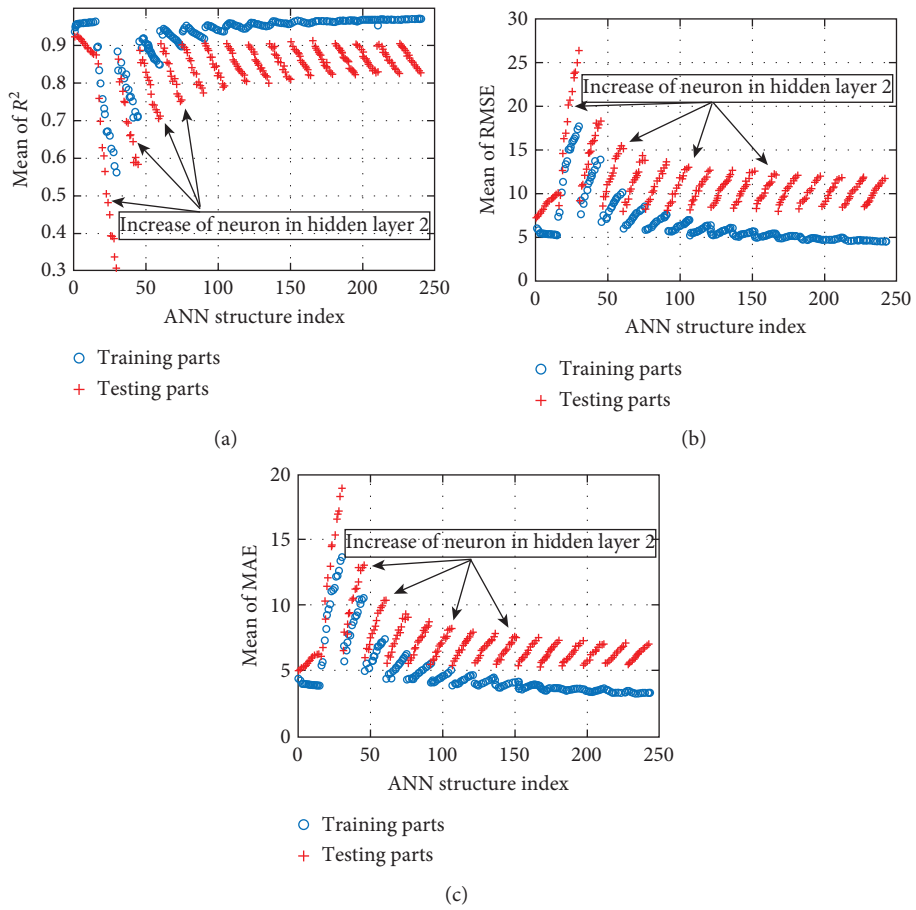
FIGURE 5: Performance of the ANN in the function of neuron number in 2 hidden layers, with respect to (a) mean value of R^2 for the training part, testing parts; (b) mean value of RMSE for the training part, testing parts; and (c) mean value of RMSE for the training part, testing parts.

(a)

(b)

FIGURE 6: Continued.

(c)

(d)

(e)

(f)
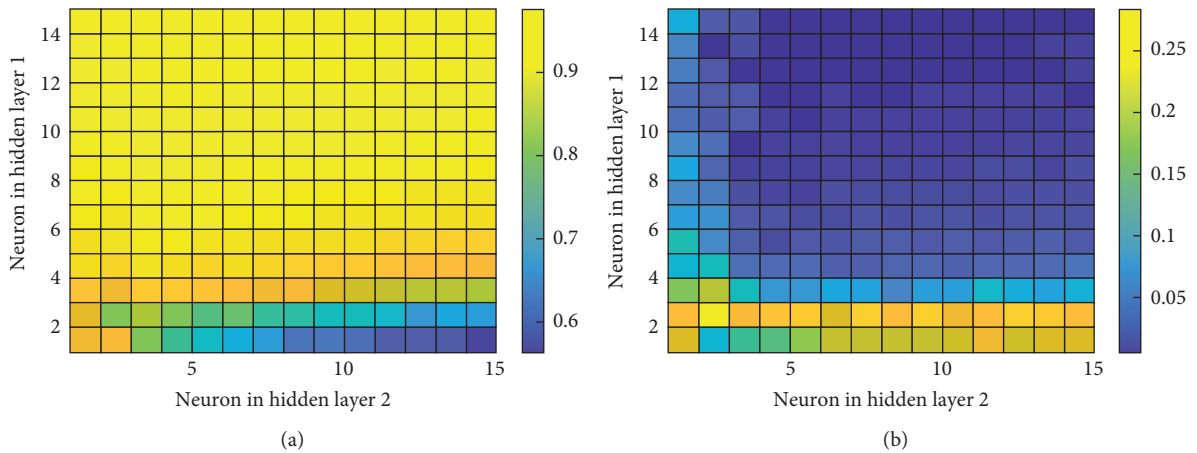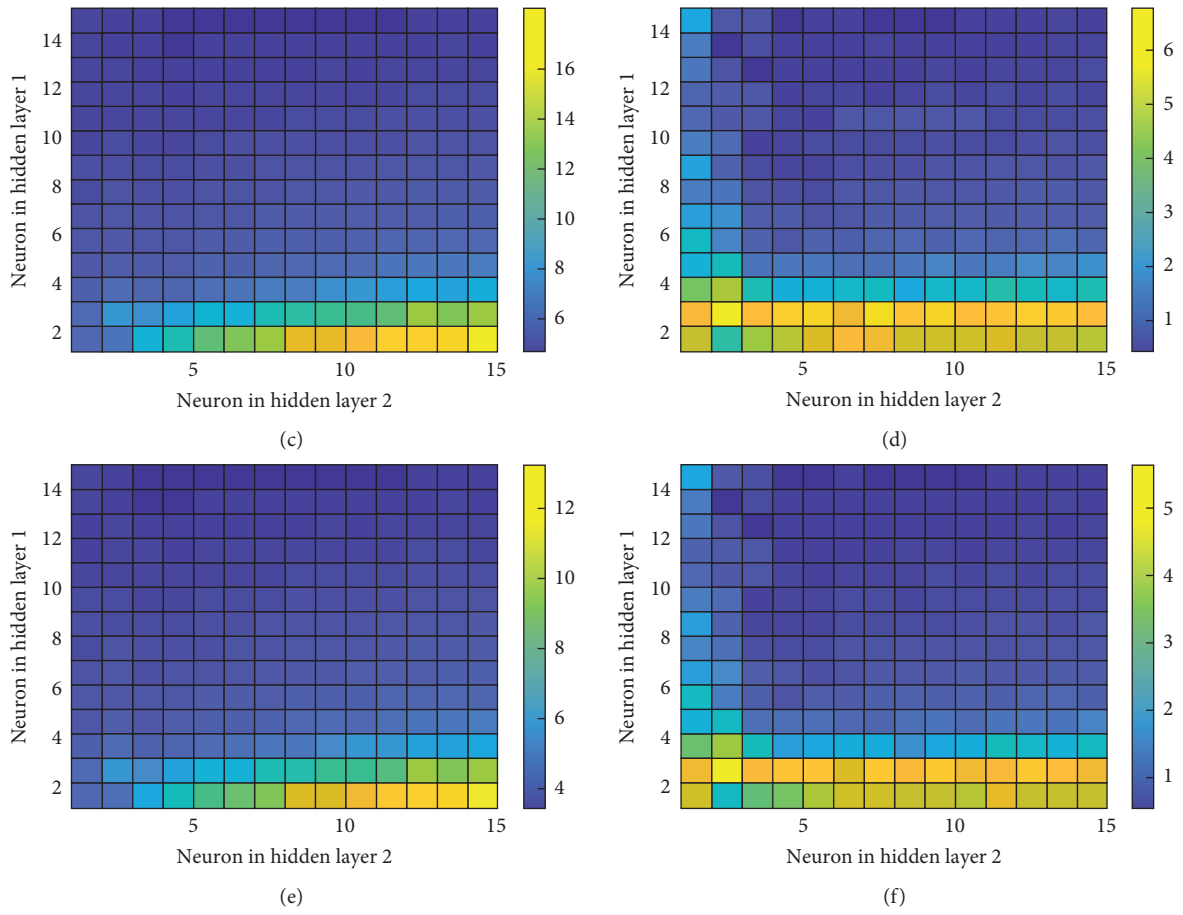
FIGURE 6: Color-map of ANN with 2 hidden layers in the function of the neuron of hidden layer for the training part with respect to (a) mean values of R^2; (b) StD of R^2; (c) mean of RMSE; (d) StD of RMSE; (e) mean of MAE; and (f) StD of MAE.

(a)

(b)

FIGURE 7: Continued.

(c)

(d)

(e)

(f)
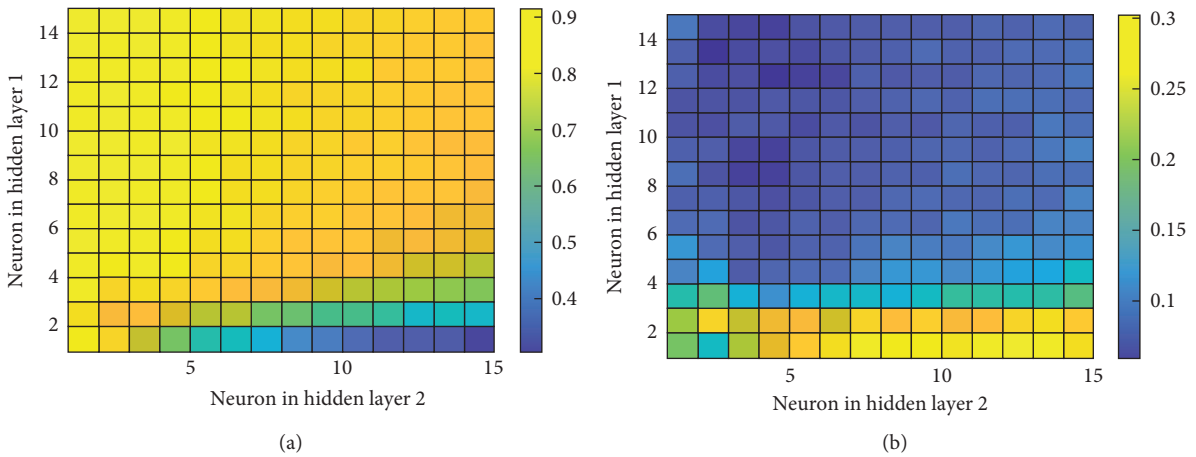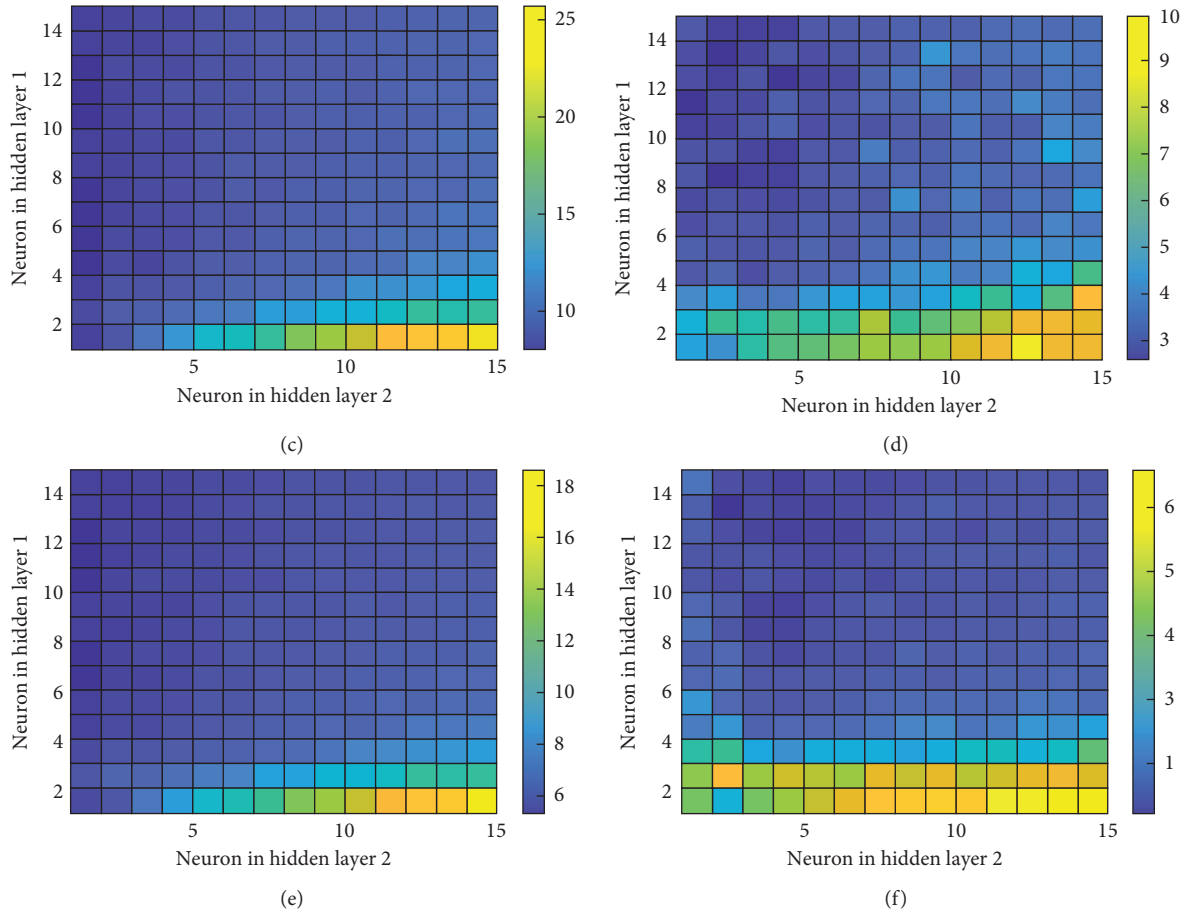
FIGURE 7: Color-map of ANN with 2 hidden layers in the function of neuron number of the hidden layer for the testing part with respect to (a) mean values of R^2; (b) StD of R^2; (c) mean of RMSE; (d) StD of RMSE; (e) mean of MAE; and (f) StD of MAE.

Furthermore, the results of Figures 5–7 also confirm that the ANN architecture [9-1-15-1] containing 2 hidden layers has the lowest performance, reflected by the lowest mean value of R^2, and the highest mean values of RMSE, MAE for the testing part. The lowest performance is also shown by the highest StD values of R^2, RMSE, and MAE, which means that the ANN architecture [9-1-15-1] is not stable to estimate a reliable result. Besides, with a higher neuron number of the second hidden layer, the performance of the ANN model decreases with decreasing R^2 values and increasing RMSE, MAE, and StD values. The best architecture of 2 hidden layers corresponds to the case [9-11-1-1] with performance through the mean value of R^2, RMSE, and MAE of 0.914, 7.883, and 5.233, respectively. However, these values are lower than those of the ANN architecture [9-1-1]. Therefore, such an architecture is used to predict the load-carrying capacity of CSB in the next section.

6.3. Load-Carrying Capacity Prediction of Best ANN Architecture.

The optimal architecture of the ANN model is [9-1-1] applied for this section. In this section, the predictive capacity of the best performance [9-1-1] of the ANN model is presented. Specifically, the ANN architecture's prediction results [9-1-1] with the highest predictive capacity among 500

simulations are presented. The comparison between experimental critical load and predicted value by the ANN model is shown in Figure 8 for the training and testing parts. The comparison shows that the predicted values are very close to the experimental ones. The model errors are plotted between the predicted and the experimental values for the training (Figure 9(a)) and the testing parts (Figure 9(b)). The error values corresponding to the training and testing databases are small. Based on the cumulative distribution (black line), the percentage error of samples within a range can be determined. For example, with the training database, the percentage of samples with errors in the range [−5; 5] kN is about 85%. Similarly, 90% of the error of the testing set are in the range of [−5; 5] kN.

Finally, a regression model in Figures 10(a) and 10(b) shows the correlation between the actual and predicted values for the training and testing datasets, respectively. A linear fit is also applied and plotted in each case. It is observed that the linear regression lines are very close to the diagonal lines, which confirms the close correlation between the actual and predicted load-carrying capacity. The calculated values of R^2 for the training dataset and the testing dataset are 0.959 and 0.989, respectively. The values of RMSE and MAE for the training dataset are 5.405 kN and 3.718 kN. For the testing dataset, these values are 3.328 kN and 2.622 kN, respectively.

FIGURE 8: Experimental and predicted load-carrying capacity in function of sample index for the training and testing datasets.

(a)

(b)
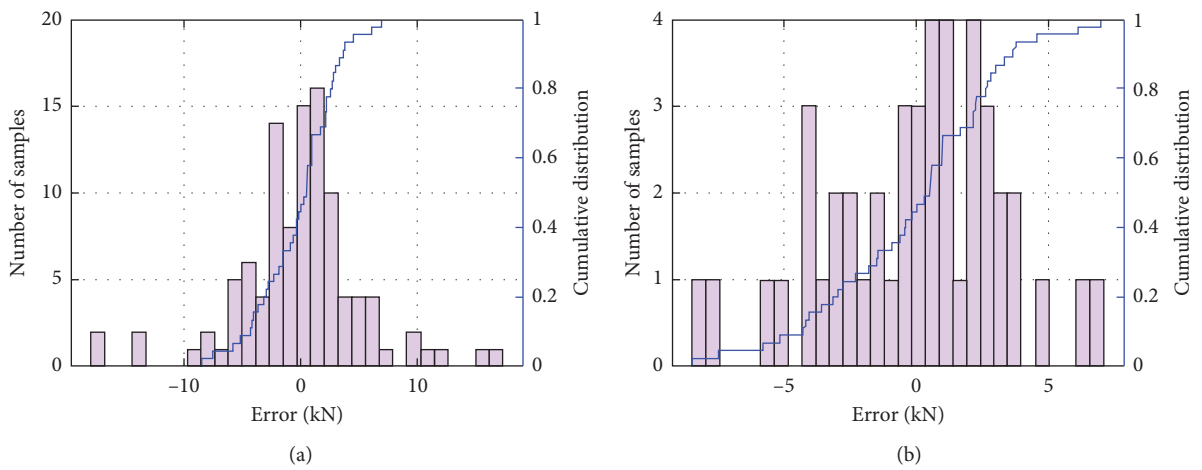
FIGURE 9: Experimental and predicted load-carrying capacity in function of the sample index for the training and testing datasets.

(a)

(b)
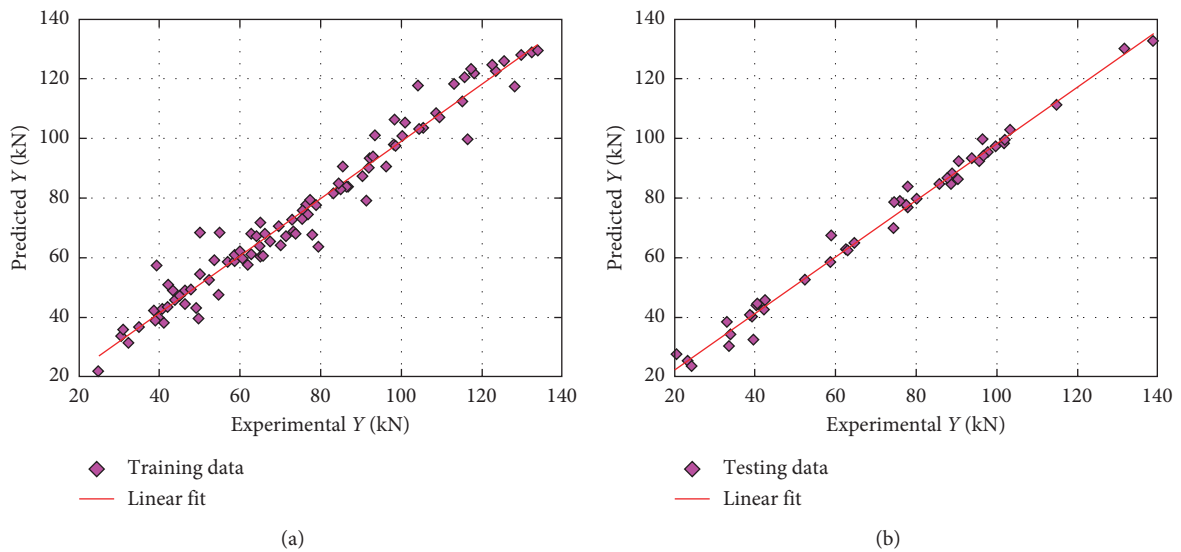
FIGURE 10: Regression graphs for the case of the best ANN architecture [9-1-1]: (a) training dataset and (b) testing dataset.

The results of the statistical criteria show that the ANN model with the [9-1-1] architecture can accurately predict the load-carrying capacity of the CSB.

For the sake of comparison, Table 3 shows the results of this investigation compared with different results available in the literature. For the database, the number of samples in

TABLE 3: Results comparison with currently popular AI techniques.

Reference	Number of data samples	Method and input	R^2	RMSE (kN)	MAE (kN)
Amayreh and Saka [36]	47	8 inputs (minimum web yield stress, span of the castellated beam, overall depth, minimum width of the web post, web thickness, flange thickness, width of flange, loading condition) Method: backpropagation network	0.995	Not provided	Not provided
Gholizadeh et al. [37]	140	Geometrical inputs only (the overall depth of castellated beam; the vertical projection of inclined side of opening; the web thickness; the flange width; the flange thickness; the width of web post at middepth; the horizontal projection of inclined side of opening) BP1 BP2 ANFIS1 ANFIS2		4.0625 3.5611 2.7276 2.0631	
Gandomi et al. [38]	47	8 inputs (minimum web yield stress, span of the castellated beam, overall depth, minimum width of the web post, web thickness, flange thickness, width of flange, loading condition) Methods Genetic programming Least-squares regression (LSR)	0.817 0.682		32.33 36.60
Aminian et al. [39]	142	5 inputs (the overall depth of castellated beam, the vertical projection of inclined side of opening, the web thickness, the minimum web yield stress, and the width of web post at middepth) Linear genetic programming GSA algorithm	0.960 0.952		4.62 4.95
This investigation	150	9 inputs (the overall depth of castellated beam, the vertical projection of inclined side of opening, the web thickness, the flange width, the flange thickness, the width of web post at middepth, the horizontal projection of inclined side of opening, the minimum web yield stress, the minimum flange yield stress)	0.989	3.328	2.622

this investigation is the highest with 150 samples. The number of inputs for the ANN model is 9 inputs. Overall, the best ANN architecture in the present study is able to predict the load-carrying capacity of CSB with the highest accuracy, comparing with the other investigations.

7. Conclusion

This investigation aims to develop a simple but effective ANN model to predict the load-carrying capacity of CSB. To achieve this purpose, the determination of optimal ANN architecture is carried out, with two cases of hidden layers number varying from 1 to 2. Regarding each case, the neuron number in each hidden layer is varied from 1 to 15. Overall, 240 cases of ANN architectures consisting of 15 cases of 1 hidden layer and 225 cases of 2 hidden layers are proposed. Based on 150 data collected from published studies, 70% of the data are randomly selected and used for the training dataset, whereas the remaining 30% are selected for the testing dataset. A number of 500 simulations are performed for each ANN architecture. The performance of each ANN architecture is evaluated by commonly used statistical criteria, such as Determination Coefficient (R^2), Root Mean Square Error (RMSE), and Mean Absolute Error (MAE). The

ANN architecture containing 1 hidden layer and 1 neuron is found as the best structure for predicting the load-carrying capacity of the CSB, with excellent agreement between model and experimental results (i.e., values of R^2, RMSE, and MAE are 0.989, 3.328, and 2.622, resp., for the testing dataset). The results of this investigation can help build a reliable soft computation tool to accurately and quickly predict the load-carrying capacity of CSB. It is important noticing that a parametric design-oriented study of CSB could be conducted in future works, thanks to the excellent accuracy of the proposed ANN model. In this case, Partial Dependence Plots analysis or parametric studies on the geometry parameters could be used to design CSB with targeted load-carrying capacity.

Data Availability

The data supporting this manuscript are from previously reported studies and datasets, which have been cited. The processed data are available from the corresponding author upon request.

Conflicts of Interest

The authors declare that they have no conflicts of interest.

References

[1] X. Zhou, Z. He, P. Chen, J. Li, and Z. Li, "Distortional buckling behavior and design consideration of castellated beams considering residual stresses," in *Proceedings of the 2019 Structural Stability Research Council Annual Stability Conference*, St Louis, MO, USA, April 2019.

[2] P. Ravi and S. Aiswarya, "Performance analysis of castellated beams with different web openings," *International Journal Of Engineering Research & Technology (IJERT)*, vol. 6, 2018.

[3] G. S. Nair and P. S. Pillai, "Review on characteristics of castellated beam," *International Research Journal of Engineering and Technology (IRJET)*, vol. 5, no. 4, pp. 3480–3484, 2018.

[4] H. W. A. Al-Thabhawee and M. A.-A. Al-Kannoon, "Improving behavior of castellated beam by adding spacer plat and steel rings," *Journal of University of Babylon for Engineering Sciences*, vol. 26, no. 4, pp. 331–344, 2018.

[5] D. K. Shendge and D. B. Shinde, "Castellated beam optimization by using finite element analysis: a review," *The International Journal of Engineering and Science*, vol. 4, pp. 12–14, 2015.

[6] B. K. Dougherty, "Castellated beams: a state of the art report," *Journal of the South African Institution of Civil Engineers*, vol. 35, no. 2, pp. 12–20, 1993.

[7] V. V. Kshirsagar and S. R. Parekar, "Behaviour of castellated beams with and without stiffeners-A review," *Behaviour*, vol. 54 pages, 2018.

[8] T. Zirakian and H. Showkati, "Distortional buckling of castellated beams," *Journal of Constructional Steel Research*, vol. 62, no. 9, pp. 863–871, 2006.

[9] S. Av and V. A. Auti, "Parametric study of castellated beam with varying depth of web opening," *International Journal of Scientific and Research Publications*, vol. 2, p. 287, 2012.

[10] A. A. Toprac and B. R. Cooke, *An Experimental Investigation of Open-Web Beams*, Welding Research Council, New York, NY, USA, 1959.

[11] M. D. Altifillisch, B. R. Cooke, and A. A. Toprac, "An investigation of open web expanded beams," *Welding Research*, vol. 22, no. 2, 1957.

[12] M. U. Hosain and W. G. Spiers, "Experiments on castellated steel beams," thesis, Department of Civil Engineering, University of Saskatchewan, Saskatoon, Canada, 1970.

[13] W. Zaarour and R. Redwood, "Web buckling in thin webbed castellated beams," *Journal of Structural Engineering*, vol. 122, no. 8, pp. 860–866, 1996.

[14] S. Elaiwi, B. Kim, and L.-Y. Li, "Bending analysis of castellated beams," *Athens Journal of Technology and Engineering*, 2018.

[15] C. H. Martins, F. P. V. Ferreira, A. Rossi, and E. V. W. Trentini, "Numerical analysis of physical and geometrical imperfections in cellular beams," *Open Journal of Civil Engineering*, vol. 7, no. 1, pp. 116–129, 2017.

[16] K. D. Tsavdaridis and C. D'Mello, "Web buckling study of the behaviour and strength of perforated steel beams with different novel web opening shapes," *Journal of Constructional Steel Research*, vol. 67, no. 10, pp. 1605–1620, 2011.

[17] M. R. Soltani, A. Bouchaïr, and M. Mimoune, "Nonlinear FE analysis of the ultimate behavior of steel castellated beams," *Journal of Constructional Steel Research*, vol. 70, pp. 101–114, 2012.

[18] A. M. Jamadar and P. D. Kumbhar, "Parametric study of castellated beam with circular and diamond shaped openings," *International Research Journal of Engineering and Technology*, vol. 2, no. 2, pp. 715–722, 2015.

[19] D. V. Dao, H. Adeli, H.-B. Ly et al., "A sensitivity and robustness analysis of GPR and ANN for high-performance concrete compressive strength prediction using a Monte Carlo simulation," *Sustainability*, vol. 12, no. 3, p. 830, 2020.

[20] H.-B. Ly, L. M. Le, H. T. Duong et al., "Hybrid artificial intelligence approaches for predicting critical buckling load of structural members under compression considering the influence of initial geometric imperfections," *Applied Sciences*, vol. 9, no. 11, p. 2258, 2019.

[21] T.-A. Nguyen, H.-B. Ly, H.-V. T. Mai, and V. Q. Tran, "Prediction of later-age concrete compressive strength using feedforward neural network," *Advances in Materials Science and Engineering*, vol. 2020, Article ID 9682740, 8 pages, 2020.

[22] M. Ahmadi, H. Naderpour, and A. Kheyroddin, "Utilization of artificial neural networks to prediction of the capacity of CCFT short columns subject to short term axial load," *Archives of Civil and Mechanical Engineering*, vol. 14, no. 3, pp. 510–517, 2014.

[23] P. B. Cachim, "Using artificial neural networks for calculation of temperatures in timber under fire loading," *Construction and Building Materials*, vol. 25, no. 11, pp. 4175–4180, 2011.

[24] Q. H. Nguyen, H.-B. Ly, V. Q. Tran et al., "A novel hybrid model based on a feedforward neural network and one step secant algorithm for prediction of load-bearing capacity of rectangular concrete-filled steel tube columns," *Molecules*, vol. 25, no. 15, p. 3486, 2020.

[25] H. Q. Nguyen, H.-B. Ly, V. Q. Tran, T.-A. Nguyen, T.-T. Le, and B. T. Pham, "Optimization of artificial intelligence system by evolutionary algorithm for prediction of axial capacity of rectangular concrete filled steel tubes under compression," *Materials*, vol. 13, no. 5, p. 1205, 2020.

[26] T. A. Pham, H.-B. Ly, V. Q. Tran, L. V. Giap, H.-L. T. Vu, and H.-A. T. Duong, "Prediction of pile axial bearing capacity using artificial neural network and random forest," *Applied Sciences*, vol. 10, no. 5, p. 1871, 2020.

[27] J. A. Abdalla, M. F. Attom, and R. Hawileh, "Prediction of minimum factor of safety against slope failure in clayey soils using artificial neural network," *Environmental Earth Sciences*, vol. 73, no. 9, pp. 5463–5477, 2015.

[28] T. A. Pham, V. Q. Tran, H.-L. T. Vu, and H.-B. Ly, "Design deep neural network architecture using a genetic algorithm for estimation of pile bearing capacity," *PLOS ONE*, vol. 15, no. 12, Article ID e0243030, 2020.

[29] D. Dao, H.-B. Ly, S. Trinh, T.-T. Le, and B. Pham, "Artificial intelligence approaches for prediction of compressive strength of geopolymer concrete," *Materials*, vol. 12, no. 6, p. 983, 2019.

[30] H.-B. Ly, B. T. Pham, D. V. Dao, V. M. Le, L. M. Le, and T.-T. Le, "Improvement of ANFIS model for prediction of compressive strength of manufactured sand concrete," *Applied Sciences*, vol. 9, no. 18, p. 3841, 2019.

[31] D. Dao, S. Trinh, H.-B. Ly, and B. Pham, "Prediction of compressive strength of geopolymer concrete using entirely steel slag aggregates: novel hybrid artificial intelligence approaches," *Applied Sciences*, vol. 9, no. 6, p. 1113, 2019.

[32] J. A. Abdalla, R. Hawileh, and A. Al-Tamimi, "Prediction of FRP-concrete ultimate bond strength using Artificial Neural Network," in *Proceedings of the 2011 Fourth International Conference on Modeling, Simulation and Applied Optimization*, pp. 1–4, Kuala Lumbur, Malaysia, April 2011.

[33] O. Abuodeh, J. A. Abdalla, and R. A. Hawileh, "Predicting the shear capacity of FRP in shear strengthened RC beams using ANN and NID," in *Proceedings of the 2019 8th International*

Conference on Modeling Simulation and Applied Optimization (ICMSAO), pp. 1–5, Manama, Bahrain, April 2019.

[34] I. H. Guzelbey, A. Cevik, and M. T. Gögüş, "Prediction of rotation capacity of wide flange beams using neural networks," *Journal of Constructional Steel Research*, vol. 62, no. 10, pp. 950–961, 2006.

[35] E. T. Fonseca, P. da S. Vellasco, S. A. L. De Andrade, and M. Vellasco, "Neural network evaluation of steel beam patch load capacity," *Advances in Engineering Software*, vol. 34, no. 11–12, pp. 763–772, 2003.

[36] L. Amayreh and M. P. Saka, "Failure load prediction of castellated beams using artificial neural networks," *Asian Journal of Civil Engineering*, vol. 6, no. 12, pp. 1-2, 2005.

[37] S. Gholizadeh, A. Pirmoz, and R. Attarnejad, "Assessment of load carrying capacity of castellated steel beams by neural networks," *Journal of Constructional Steel Research*, vol. 67, no. 5, pp. 770–779, 2011.

[38] A. H. Gandomi, S. M. Tabatabaei, M. H. Moradian, A. Radfar, and A. H. Alavi, "A new prediction model for the load capacity of castellated steel beams," *Journal of Constructional Steel Research*, vol. 67, no. 7, pp. 1096–1105, 2011.

[39] P. Aminian, H. Niroomand, A. H. Gandomi, A. H. Alavi, and M. Arab Esmaeili, "New design equations for assessment of load carrying capacity of castellated steel beams: a machine learning approach," *Neural Computing and Applications*, vol. 23, no. 1, pp. 119–131, 2013.

[40] I. H. Witten and E. Frank, "Data mining," *Acm Sigmod Record*, vol. 31, no. 1, pp. 76-77, 2002.

[41] Y. Du, Z. Chen, C. Zhang, and X. Cao, "Research on axial bearing capacity of rectangular concrete-filled steel tubular columns based on artificial neural networks," *Frontiers of Computer Science*, vol. 11, no. 5, pp. 863–873, 2017.

[42] S. Jegadesh and S. Jayalekshmi, "Application of artificial neural network for calculation of axial capacity of circular concrete filled steel tubular columns," *International Journal of Earth Sciences and Engineering*, vol. 8, pp. 35–42, 2015.

[43] D. E. Rumelhart, G. E. Hinton, and R. J. Williams, *Learning Internal Representations by Error Propagation*, Cognitive Science, California, CA, USA, 1985.

[44] A. Wanto, S. R. Andani, P. Poningsih, and R. Dewi, "Analysis of atandard gradient descent with GD momentum and adaptive LR for SPR prediction," 2018.

[45] T. Chai and R. R. Draxler, "Root mean square error (RMSE) or mean absolute error (MAE)? - arguments against avoiding RMSE in the literature," *Geoscientific Model Development*, vol. 7, no. 3, pp. 1247–1250, 2014.

[46] P. N. Chatur, A. R. Khobragade, and D. S. Asudani, "Effectiveness evaluation of regression models for predictive data-mining," *International Journal of Managment, IT and Engineering*, vol. 3, no. 3, pp. 465–483, 2013.

[47] S. Menard, "Coefficients of determination for multiple logistic regression analysis," *The American Statistician*, vol. 54, no. 1, pp. 17–24, 2000.

[48] C. Willmott and K. Matsuura, "Advantages of the mean absolute error (MAE) over the root mean square error (RMSE) in assessing average model performance," *Climate Research*, vol. 30, no. 1, pp. 79–82, 2005.

WILEY | Hindawi

Research Article

Optimization Scheme of Fine Toll and Bus Departure Quantity for Bottleneck Congestion Management

Jianhui Wu (ID),[1,2] **Yuanfa Ji,**[2] **Xiyan Sun** (ID),[2] **and Yan Xu**[1]

[1]*School of Information Science and Technology, Hunan Institute of Science and Technology, Yueyang 414006, China*
[2]*Guangxi Key Laboratory of Precision Navigation Technology and Application, Guilin University of Electronic Technology, Guilin 541004, China*

Correspondence should be addressed to Xiyan Sun; sunxiyan1@163.com

This paper chooses car travel and bus travel as the research objects, establishes a dual-mode equilibrium model based on the bottleneck model, and compares the travel characteristics of the no-toll and fine-toll schemes. We find that the fine-toll scheme can eliminate the queuing time at the bottleneck, but it also increases the congestion risk cost of bus travel. In order to eliminate the queuing time at the bottleneck and reduce the congestion risk cost of bus travel without increasing the car travel cost and bus travel cost, we propose an optimization scheme of fine toll and bus departure quantity and analyze its travel characteristics theoretically. Through the numerical example, we calculate and analyze the equilibrium results of no-toll scheme, fine-toll scheme, and optimization scheme of fine toll and bus departure quantity. The results indicate that the optimization scheme of fine toll and bus departure quantity can help travelers to choose a reasonable travel mode and travel time to travel in the rush hour.

1. Introduction

It is a worldwide management problem to change the phenomenon of traffic congestion in the rush hour. Especially in the central area of the city, a large number of commuting individuals gather together to form a commuting bottleneck. Vickrey [1] first proposed a bottleneck model to describe commuting behavior in the rush hour. According to the delay penalty and queuing time, travelers determine the departure time to minimize the travel cost in this model. Moreover, all individuals have the same travel cost in equilibrium. The bottleneck model can clearly reveal the formation and dissipation process of traffic congestion. On this basis, many researchers have carried out the research of commuting bottleneck management (e.g., Xiao et al. [2], Chen et al. [3], Khan and Amin [4], Guo and Sun [5], and Zhu et al. [6]). Li et al. [7] pointed out that the research on the bottleneck model in the past 50 years mainly focuses on travel behavior analysis, demand-side strategies, supply-side strategies, and joint strategies of demand and supply sides. The purpose of travel behavior analysis is to reveal the nature of congestion dynamics at the bottleneck. Relevant achievements include considerations of other travel choice dimensions (e.g., Kim [8] and Zhang et al. [9]), time-varying scheduling preferences (e.g., Abegaz et al. [10]), and vehicle physical length in queue and hypercongestion (e.g., Lamotte and Geroliminis [11]). The purpose of demand-side strategies is to reduce travel demand or redistribute the demand in space and time at the bottleneck. Relevant achievements include congestion pricing (e.g., Fosgerau and Van Dender [12]), emission pricing (e.g., Bulteau [13]), and public transit services (e.g., de Palma et al. [14]). The purpose of supply-side strategies is to determine the optimal capacity or service level of infrastructure elements. Relevant achievements include bottleneck capacity allocation (e.g., Lamotte et al. [15]) and capacity design (e.g., Qian et al. [16]). The joint strategies are the hybrid of demand-side and supply-side strategies.

From the perspective of the travel mode, the current research on commuting bottleneck management based on the bottleneck model mainly focuses on single-mode bottleneck management and multimode bottleneck management. We have summarized some research results of

commuting bottleneck management in Table 1. The single-mode bottleneck management based on the bottleneck model mostly regards car as the research object and guides some travelers to change their departure time by some strategies, so as to eliminate the queuing time at the commuting bottleneck. Xiao and Huang [27] pointed out that the single-step coarse toll can advance or postpone the earliest departure time and proved that their proposed piecewise time-varying toll can effectively reduce or eliminate the queues behind the bottleneck. Li et al. [28] presented the step tolling models with homogeneous and heterogeneous preferences and analyzed the optimal step toll schemes with constant and linear time-varying marginal activity utilities. Miralinaghi et al. [29] investigated the impact of a tradable credit scheme on managing morning commute congestion and proved that if commuters are equally sensitive to gain and loss, the credit allocation method does not affect the equilibrium departure rate and credit price. Wang et al. [30] proved that the total travel cost can be effectively reduced by properly allocating the capacity of high-occupancy vehicle lane and derived the optimal capacity of high-occupancy vehicle lane for minimizing the system total cost. Yu et al. [31] investigated the effect of carpooling with heterogeneous users in the bottleneck model and pointed out that if drivers choose carpooling, road capacity will be released, and this will reduce road congestion. Zhong et al. [32] believed that the high-occupancy vehicle lane can promote carpooling and the high-occupancy toll lane can bring additional welfare gains with a modest level of toll.

The multimode bottleneck management based on the bottleneck model generally takes car and public transport as the research object and guides some car travelers to take high-capacity public transport. Mirabel and Reymond [33] pointed out that the toll policy will be more efficient as long as the toll revenue is directed towards public transport when the railroad fare is equal to the average cost. Tian et al. [34] proposed a tradable credit scheme for managing bottleneck congestion and modal split and analyzed the efficiency of the tradable travel credit scheme in the highway and transit network. Li and Zhang [35] proved the critical condition for some passengers' transfer from one mode to another with congestion charging schemes and analyzed the impact of congestion charging schemes with or without internalizing the bus-related congestion externalities on the bottleneck system. At present, most of the research studies on the multimode bottleneck management based on the bottleneck model relax the interaction between car travel and public transport travel and the constraints of public transport capacity. In reality, some travelers may not be able to take the first public transport due to the difference between the limit of public transport capacity and the arrival rate of travelers, but can only wait for the next public transport. At this time, all waiting travelers need to bear the congestion risk cost of public transport.

Lin and Yang [36] assumed that the car and bus travel on the same bottleneck road and the transportation capacity of bus is limited, proposed a travel-mode equilibrium model under the condition of mixed traffic, and pointed out that the fine-toll scheme can eliminate the queuing time, but

greatly increase the congestion risk cost of bus travel. Aiming at this problem, we try to guide some car travelers to choose bus travel by the fine toll and reduce the congestion risk cost of bus travel by optimizing the bus departure quantity. However, the fine toll can eliminate the queuing time of car and bus travel and also can guide some car travelers to travel by bus, but it will increase the congestion risk cost of bus travel. Increasing the bus departure quantity may extend the length of the rush hour and increase the car travel cost on the bottleneck road. Therefore, the key to the optimization scheme design of fine toll and bus departure quantity is how to ensure that it cannot only eliminate the queuing time of car and bus travel but also reduce the congestion risk cost of bus travel without increasing the travel cost of travelers.

In order to design the optimization scheme of fine toll and bus departure quantity, we take car and bus travel as the research objects and establish a dual-mode equilibrium model based on the bottleneck model in Section 2. Section 3 analyzes the travel characteristics of the no-toll and fine-toll schemes. Section 4 designs and analyzes the optimization scheme of fine-toll and bus departure quantity. In Section 5, a numerical example is presented to validate the theoretical results. Finally, conclusions are given in Section 6.

2. Dual-Mode Equilibrium Model

To analyze the influence of fine toll and bus departure quantity on travelers' travel mode choice at the bottleneck, we suppose that there is a bottleneck road with limited capacity at the entrance of living area O to work area D, the maximum capacity of the bottleneck road is s, the bus departure quantity on the bottleneck road is f_0, the maximum passenger capacity of the unit bus is d, and travelers are completely rational, have complete traffic information, and can only choose to travel by car or bus on the bottleneck road. Suppose that the travel time for an individual who leaves living area O at time t is $T(t)$, the free-flow travel time from living area O to work area D is T_f, the queuing time from living area O to work area D at time t is $T_w(t)$, $T(t) = T_f + T_w(t)$, the departure time at which an individual arrives at work area D at time t^* is t_0, $t_0 + T_f + T_w(t_0) = t^*$, the car departure time at which the queue begins is t_{1e}, the car departure time at which the queue ends is t_{1l}, the bus departure time at which the queue begins is t_{2e}, the bus departure time at which the queue ends is t_{2l}, the congestion risk cost of bus travel at time t is $R(t)$, the bus ticket price is p, the unit cost of car travel time is α_1, the unit cost of bus travel time is α_2, the unit cost of an early arrival is β, the unit cost of a late arrival is γ, $\gamma > \alpha_1 > \alpha_2 > \beta$, ϕ and θ are the weight coefficient, the number of travelers departing from living area O to work area D every morning is N, the number of travelers who choose to go to work area D by car is N_1, the number of travelers who choose to go to work area D by bus is N_2, and all travelers expect to arrive at work area D at time t^*.

Considering that the fuel cost is related to travel time, we convert it into the travel time T. Based on this, we suppose that the car travel cost C_1 is the weighted sum of free-flow

TABLE 1: Some research results of commuting bottleneck management.

Literatures	Type of travel mode	Decision variable	Target
Ge et al. [17]	Single mode	Toll	Minimum generalized cost
Lindsey et al. [18]	Single mode	Step toll	Toll levels and tolling periods optimal
Laih [19]	Single mode	Step toll	Eliminate queuing time
Miralinaghi and Peeta [20]	Single mode	Tradable credit	Minimize emissions
Ma and Zhang [21]	Single mode	Ridesharing payment and parking charge	Eliminate queuing time
Liu and Li [22]	Single mode	Toll	System optimal
Xiao et al. [23]	Multimode	Tradable parking permit	System optimal
Chen et al. [24]	Multimode	Vehicle lane	Minimize social cost
Seilabi et al. [25]	Multimode	Tradable credit	Minimize total travel time
Holguín-Veras and Cetin [26]	Multimode	Toll	Maximize collective welfare
This paper	Multimode	Fine toll and bus departure quantity	Eliminate queuing time and reduce congestion risk cost without increasing travel cost

travel time, queuing time, and delay time of early or late arrival. This can be expressed as

$$
C_1(t) = \begin{cases} \alpha_1 T(t) + \beta(t^* - T(t) - t), & \forall t \in [t_{1e}, t_0], \\ \alpha_1 T(t) + \gamma(t - t^* + T(t)), & \forall t \in (t_0, t_{1l}]. \end{cases}
\tag{1}
$$

We define the bus travel cost C_2 as the weighted sum of walking time, waiting time, free-flow travel time, queuing time, delay time of early or late arrival, congestion risk cost, bus ticket price, and discomfort cost caused by physical contact. Assume that the walking time is constant, we convert it into the bus ticket price p. The waiting time is only the time to wait for the first bus to arrive. The waiting time for the next bus caused by the congestion in the first bus is represented by the congestion risk cost. As the bus timetable is known, travelers will reduce their waiting time as much as possible. For this reason, we assume that the waiting time is equal to zero. Meanwhile, if travelers choose to travel in the rush hour, they have fully considered that the bus is crowded with a large number of passengers. For this reason, we assume that the discomfort cost caused by physical contact is constant and convert it into the bus ticket price p. Based on these assumptions, the bus travel cost C_2 can be expressed as

$$
C_2(t) = \begin{cases} \alpha_2 T(t) + \beta(t^* - T(t) - t) + \phi R(t) + p, & \forall t \in [t_{2e}, t_0], \\ \alpha_2 T(t) + \gamma(t - t^* + T(t)) + \theta R(t) + p, & \forall t \in (t_0 t_{2l}]. \end{cases}
\tag{2}
$$

In order to reduce individual travel cost, travelers choose departure time by weighing travel time and delay cost. For car travelers, there are not queues at time t_{1e} and t_{1l}, and the queuing time $T_w(t_{1e}) = T_w(t_{1l}) = 0$. When no traveler can reduce the travel cost by changing the departure time, the traffic flow on the road reaches equilibrium. At equilibrium, all travelers have the same travel cost. It can be expressed as

$$
\begin{aligned}
C_1(t_{1e}) = C_1(t_{1l}) &= \alpha_1 T_f + \beta(t^* - T_f - t_{1e}) \\
&= \alpha_1 T_f + \gamma(t_{1l} - t^* + T_f).
\end{aligned}
\tag{3}
$$

Since cars and buses run on the same route, the length of the rush hour is affected by both individual car travelers and individual bus travelers. Hence, the length of the rush hour on the car travel route can be expressed as

$$
t_{1l} - t_{1e} = \frac{N_1 + \lambda(t_{1l} - t_{1e})f_0}{s}.
\tag{4}
$$

Evidently,

$$
t_{1l} - t_{1e} = \frac{N_1}{s - \lambda f_0},
\tag{5}
$$

where λ represents the conversion coefficient between a bus and an equivalent car.

When the car travel reaches equilibrium, we can obtain the car travel cost C_1, the car departure time t_{1e} at which the queue begins, and the car departure time t_{1l} at which the queue ends by formulas (1), (3), and (5). It can be expressed as

$$
C_1 = \alpha_1 T_f + \frac{\beta\gamma}{\beta + \gamma} \frac{N_1}{s - \lambda f_0},
\tag{6}
$$

$$
t_{1e} = t^* - T_f - \frac{\gamma}{\beta + \gamma} \frac{N_1}{s - \lambda f_0},
\tag{7}
$$

$$
t_{1l} = t^* - T_f + \frac{\beta}{\beta + \gamma} \frac{N_1}{s - \lambda f_0},
\tag{8}
$$

$$
t_0 = t^* - T_f - \frac{\beta\gamma}{\alpha_1(\beta + \gamma)} \frac{N_1}{s - \lambda f_0}.
\tag{9}
$$

For bus travelers at time t_{2e} and t_{2l}, they do not queue up, their queuing time $T_w(t_{2e}) = T_w(t_{2l}) = 0$, and the congestion risk cost $R(t_{2e}) = R(t_{2l}) = 0$, but the delay cost of early or late arrival is higher. For bus travelers between time t_{2e} and t_{2l}, their delay cost of early or late arrival is decreased, but their queuing time and congestion risk cost are increased as congestion. When the equilibrium is reached, the bus travel cost is equal at all times. It can be expressed as

$$C_2(t_{2e}) = C_2(t_{2l}) = \alpha_2 T_f + \beta(t^* - T_f - t_{2e}) + p \tag{10}$$
$$= \alpha_2 T_f + \gamma(t_{2l} - t^* + T_f) + p.$$

Since the bus passenger capacity is limited, we have

$$t_{2e} - t_{2l} = \frac{N_2}{f_0 d}. \tag{11}$$

When the bus travel reaches equilibrium, we can obtain the bus travel cost C_2, the bus departure time t_{2e} at which the queue begins, and the bus departure time t_{2l} at which the rush hour queue ends by formulas (10) and (11). It can be expressed as

$$C_2 = \alpha_2 T_f + p + \frac{\beta\gamma}{\beta + \gamma} \frac{N_2}{f_0 d}, \tag{12}$$

$$t_{2e} = t^* - T_f - \frac{\gamma}{\beta + \gamma} \frac{N_2}{f_0 d}, \tag{13}$$

$$t_{2l} = t^* - T_f + \frac{\beta}{\beta + \gamma} \frac{N_2}{f_0 d}. \tag{14}$$

3. Travel Characteristics under No Toll and Fine Toll

3.1. Travel Characteristics under No Toll.
If there is no one traveler who can change his travel mode or departure time to reduce travel cost, the road traffic flow reaches the equilibrium state. At this time, the car travel cost is equal to the bus travel cost, that is, $C_1 = C_2$. Hence, we can obtain the travel distribution of the car and bus by formulas (6) and (12) at equilibrium. It can be expressed as

$$\begin{cases} N_1 = \dfrac{s - \lambda f_0}{s + (d - \lambda)f_0}\left[N - \dfrac{f_0 d(\beta + \gamma)}{\beta\gamma}(\alpha_1 T_f - \alpha_2 T_f - p)\right], \\ \\ N_2 = N - N_1. \end{cases} \tag{15}$$

The system total travel cost SC can be expressed as

$$SC = \left(\alpha_1 T_f + \frac{\beta\gamma}{\beta + \gamma} \frac{N_1}{s - \lambda f_0}\right)N. \tag{16}$$

Since cars and buses share the same route at the bottleneck, they have to bear the same queuing time when they start at the same time. According to formulas (1), (6), and (7), the queuing time $T_w(t)$ can be written as

$$T_w(t) = \begin{cases} 0, & \forall t \in [t_{2e}, t_{1e}], \\ \\ \dfrac{\beta}{\alpha_1 - \beta}(t - t_{1e}), & \forall t \in (t_{1e}, t_0], \\ \\ \dfrac{\gamma}{\alpha_1 + \gamma}(t_{1l} - t), & \forall t \in (t_0, t_{1l}], \\ \\ 0, & \forall t \in (t_{1l}, t_{2l}]. \end{cases} \tag{17}$$

Using formulas (2), (12)–(14), and (17), the congestion risk cost $R(t)$ of bus travel can be expressed as

$$R(t) = \begin{cases} \dfrac{\beta}{\phi}(t - t_{2e}), & \forall t \in [t_{2e}, t_{1e}], \\ \\ \dfrac{\beta(\alpha_1 - \alpha_2)}{\phi(\alpha_1 - \beta)}t - \dfrac{\beta}{\phi}t_{2e} + \dfrac{\beta(\alpha_2 - \beta)}{\phi(\alpha_1 - \beta)}t_{1e}, & \forall t \in (t_{1e}, t_0], \\ \\ \dfrac{\gamma}{\theta}t_{2l} - \dfrac{\gamma(\alpha_2 + \gamma)}{\theta(\alpha_1 + \gamma)}t_{1l} - \dfrac{\gamma(\alpha_1 - \alpha_2)}{\theta(\alpha_1 + \gamma)}t, & \forall t \in (t_0, t_{1l}], \\ \\ \dfrac{\gamma}{\theta}(t_{2l} - t), & \forall t \in (t_{1l}, t_{2l}). \end{cases} \tag{18}$$

3.2. Travel Characteristics under Fine Toll.
The fine-toll scheme is a dynamic charging strategy, which is actually collecting the road usage toll converted by queuing time from car travelers and achieving the social optimal state by changing the time distribution of car travel. The fine toll π can be written as follows (Arnott et al. [37]):

$$\pi(t) = \begin{cases} \dfrac{\beta\gamma}{\beta + \gamma} \dfrac{N_1}{s - \lambda f_0} - \beta(t^* - T_f - t), & \forall t \in [t_{1e}, t^* - T_f], \\ \\ \dfrac{\beta\gamma}{\beta + \gamma} \dfrac{N_1}{s - \lambda f_0} - \gamma(t - t^* + T_f), & \forall t \in (t^* - T_f, t_{1l}]. \end{cases} \tag{19}$$

Since the fine-toll scheme does not increase the car travel cost, the demand distribution of car travel and bus travel under the fine-toll scheme is the same as that of the no-toll scheme. In addition, the system total travel cost SC under the fine-toll scheme can be written as

$$SC = \left(\alpha_1 T_f + \frac{\beta\gamma}{\beta + \gamma} \frac{N_1}{s - \lambda f_0}\right)N. \tag{20}$$

The fine-toll scheme eliminates the queuing time of car and bus travel on the road ($T_w(t) = 0$), but the congestion risk cost of bus travel is different from that of the no-toll scheme. According to formulas (2) and (12)–(14), the congestion risk cost $R(t)$ of bus travel can be expressed as

$$R(t) = \begin{cases} \dfrac{\beta}{\phi}(t - t_{2e}), & \forall t \in [t_{2e}, t^* - T_f], \\[12pt] \dfrac{\gamma}{\theta}(t_{2l} - t), & \forall t \in (t^* - T_f, t_{2l}]. \end{cases} \quad (21)$$

4. Optimization Scheme of Fine Toll and Bus Departure Quantity

Comparing formulas (18) and (21), it is not difficult to find that the fine-toll scheme increases the congestion risk cost of bus travel from t_{1e} to t_{1l}. To overcome this problem, this section attempts to find an optimization scheme of fine toll and bus departure quantity, which cannot only eliminate the queuing time of car and bus travel on the road but also reduce the congestion risk cost of bus travel without increasing the travel cost of travelers.

4.1. Scheme Formulation. In the whole rush hour, the bottleneck road is operating at full capacity; then, the total cost TC_1 of car travel can be expressed as

$$TC_1 = \int_{t_{1e}}^{t_{1l}} (s - \lambda f_0) C_1(t) dt. \quad (22)$$

By substituting formula (1) into formula (22), we can obtain the total cost TC_1 of car travel under the no-toll scheme when the queuing time $T_w(t) = 0$. It can be written as

$$\begin{aligned} TC_1 &= \int_{t_{1e}}^{t^* - T_f} (s - \lambda f_0)[\alpha_1 T_f + \beta(t^* - T_f - t)] dt \\ &\quad + \int_{t^* - T_f}^{t_{1l}} (s - \lambda f_0)[\alpha_1 T_f + \gamma(t - t^* + T_f)] dt \\ &= \alpha_1 T_f N_1 + \frac{\beta\gamma}{2(\beta + \gamma)} \frac{N_1^2}{s - \lambda f_0}. \end{aligned} \quad (23)$$

According to formula (23), we can obtain the average car travel cost $\overline{C}_1$ under the no-toll scheme when the queuing time $T_w(t) = 0$. It can be expressed as

$$\overline{C}_1 = \frac{TC_1}{N_1} = \alpha_1 T_f + \frac{\beta\gamma}{2(\beta + \gamma)} \frac{N_1}{s - \lambda f_0}. \quad (24)$$

Suppose that the bus departure quantity is f_0 ($f_b > f_0$) and the fine toll is $\pi'(t)$ under the optimization scheme of fine toll and bus departure quantity. Then, formula (1) can be rewritten as

$$C_1'(t) = \begin{cases} \alpha_1 T_f + \beta(t^* - T_f - t) + \pi'(t), & \forall t \in [t_{1e}', t^* - T_f], \\[6pt] \alpha_1 T_f + \gamma(t - t^* + T_f) + \pi'(t), & \forall t \in (t^* - T_f, t_{1l}']. \end{cases} \quad (25)$$

For car travelers at time t_{1e}' and t_{1l}', they do not have to pay a fine toll, that is, $\pi'(t_{1l}') = \pi'(t_{1l}') = 0$. Referring to the

solution steps under the no-toll scheme, it is not difficult to get the car travel cost C_1' and the bus travel cost C_2' at equilibrium. It can be expressed as

$$C_1' = \alpha_1 T_f + \frac{\beta\gamma}{\beta + \gamma} \frac{N_1'}{s - \lambda f_b}, \quad (26)$$

$$C_2' = \alpha_2 T_f + p + \frac{\beta\gamma}{\beta + \gamma} \frac{N_2'}{f_b d}, \quad (27)$$

where N_1' represents the number of travelers who choose to go to work area D by car and N_2' is the number of travelers who choose to go to work area D by bus. According to formulas (26) and (27), we have

$$\begin{cases} N_1' = \dfrac{s - \lambda f_b}{s + (d - \lambda) f_b} \left[N - \dfrac{f_b d(\beta + \gamma)}{\beta\gamma} (\alpha_1 T_f - \alpha_2 T_f - p) \right], \\[12pt] N_2' = N - N_1'. \end{cases} \quad (28)$$

In order to ensure that the optimization scheme of fine toll and bus departure quantity does not increase the travel cost of travelers, we suppose that $C_1' = \overline{C}_1$. According to formulas (24) and (26), we know

$$\frac{1}{2} \frac{N_1}{s - \lambda f_0} = \frac{N_1'}{s - \lambda f_b}. \quad (29)$$

According to formulas (15), (28), and (29), we have

$$f_b = \frac{[s + 2f_0(d - \lambda)]\beta\gamma N + sf_0 d(\beta + \gamma)(\alpha_1 T_f - \alpha_2 T_f - p)}{(d - \lambda)\beta\gamma N + d[2s + f_0(d - \lambda)](\beta + \gamma)(\alpha_1 T_f - \alpha_2 T_f - p)}. \quad (30)$$

According to formulas (25), (26), and (29), we have

$$\pi'(t) = \begin{cases} \dfrac{\beta\gamma}{2(\beta + \gamma)} \dfrac{N_1}{s - \lambda f_0} - \beta(t^* - T_f - t), & \forall t \in [t_{1e}', t^* - T_f], \\[12pt] \dfrac{\beta\gamma}{2(\beta + \gamma)} \dfrac{N_1}{s - \lambda f_0} - \gamma(t - t^* + T_f), & \forall t \in (t^* - T_f, t_{1l}']. \end{cases} \quad (31)$$

4.2. Travel Characteristics' Analysis. From the scheme formulation in the previous section, we can know that the optimization scheme of fine toll and bus departure quantity eliminates the queuing time of car and bus travel on the road and also changes the demand distribution of car and bus travel. Next, we will analyze these travel characteristics of this proposed scheme including the length of the rush hour, congestion risk cost, and system total travel cost.

4.2.1. The Length of the Rush Hour. Referring to the solution steps of the car departure time at which the queue begins and ends under the no-toll scheme, it is not difficult to get the car departure time t_{1e}' at which the queue begins, the car departure time t_{1l}' at which the queue ends, the bus departure

time t'_{2e} at which the queue begins, and the bus departure time t'_{2l} at which the queue ends. It can be expressed as

$$
\begin{aligned}
t'_{1e} &= t^* - T_f - \frac{\gamma}{\beta + \gamma} \frac{N'_1}{s - \lambda f_b}, \\
t'_{1l} &= t^* - T_f + \frac{\beta}{\beta + \gamma} \frac{N'_1}{s - \lambda f_b},
\end{aligned}
\tag{32}
$$

$$
\begin{aligned}
t'_{2e} &= t^* - T_f - \frac{\gamma}{\beta + \gamma} \frac{N'_2}{f_b d}, \\
t'_{2l} &= t^* - T_f + \frac{\beta}{\beta + \gamma} \frac{N'_2}{f_b d}.
\end{aligned}
\tag{33}
$$

According to formula (28), we can know that $N'_1 < N_1$. In addition, since $f_b > f_0$, then $N'_1/s - \lambda f_b < N_1/s - \lambda f_0$. Comparing formulas (7), (8), and (32), we can know that $t'_{1e} > t_{1e}$ and $t'_{1l} < t_{1l}$, that is, $t'_{1l} - t'_{1e} < t_{1l} - t_{1e}$.

Moreover, according to formulas (6), (12), (26), (27), and (29), we have

$$
\alpha_1 T_f + \frac{\beta\gamma}{\beta + \gamma} \frac{N_1}{s - \lambda f_0} = \alpha_2 T_f + p + \frac{\beta\gamma}{\beta + \gamma} \frac{N_2}{f_0 d},
\tag{34}
$$

$$
\alpha_1 T_f + \frac{\beta\gamma}{2(\beta + \gamma)} \frac{N_1}{s - \lambda f_0} = \alpha_2 T_f + p + \frac{\beta\gamma}{\beta + \gamma} \frac{N'_2}{f_b d}.
\tag{35}
$$

By substracting formula (35) from formula (34), we have

$$
\frac{N'_2}{f_b d} < \frac{N_2}{f_0 d}.
\tag{36}
$$

Comparing formulas (13), (14), and (33), we can know that $t'_{2e} > t_{2e}$ and $t'_{2l} < t_{2l}$, that is, $t'_{2l} - t'_{2e} < t_{2l} - t_{2e}$.

To sum up, it can be seen that the optimization scheme of fine toll and bus departure quantity reduces the length of the rush hour on the bottleneck road. This shows that the optimization scheme of fine toll and bus departure quantity can change the travel time distribution of car travelers and bus travelers.

4.2.2. Congestion Risk Cost.

Referring to the solution steps of the congestion risk cost under the no-toll scheme, the congestion risk cost R' of bus travel can be expressed as

$$
R'(t) = \begin{cases} \dfrac{\beta}{\phi}(t - t'_{2e}), & \forall t \in \left[t'_{2e}, t^* - T_f\right], \\[2ex] \dfrac{\gamma}{\theta}(t'_{2l} - t), & \forall t \in \left(t^* - T_f, t'_{2l}\right]. \end{cases}
\tag{37}
$$

Comparing formulas (21) and (37), we can know that the congestion risk cost of bus travel under the optimization scheme of fine toll and bus departure quantity is smaller than that of the fine-toll scheme. This also reflects that appropriately increasing the bus departure quantity in the rush hour can effectively reduce the congestion risk cost of bus travel.

4.2.3. System Total Travel Cost.

According to formulas (26) and (29), the system total travel cost SC' under the optimization scheme of fine toll and bus departure quantity can be written as

$$
SC' = \left(\alpha_1 T_f + \frac{\beta\gamma}{2(\beta + \gamma)} \frac{N_1}{s - \lambda f_0}\right) N.
\tag{38}
$$

Comparing formulas (16), (20), and (38), we can find that the system total travel cost under the optimization scheme of fine toll and bus departure quantity is smaller than that of the fine-toll scheme and the no-toll scheme. This also reflects that the optimization scheme of fine toll and bus departure quantity can help travelers to choose a reasonable travel mode and travel time to travel in the rush hour.

5. Numerical Experiments

To verify the validity of the proposed optimization scheme, we suppose that there is a bottleneck road with limited capacity at the entrance of living area O to work area D, the maximum bottleneck capacity $s = 2000$ vehicle/hour, 6000 ($N = 6000$) travelers departing from living area O to work area D every morning, and all travelers expect to arrive at work area D at 8 a.m. ($t^* = 8$). Meanwhile, we suppose that the free-flow travel time $T_f = 0.5$ hour from living area O to work area D, the maximum passenger capacity $d = 40$ of the unit bus, the bus departure quantity $f_0 = 50$, the bus ticket price $p = 1$, and the system parameter $\lambda = 2$, $\alpha_1 = 7$, $\alpha_2 = 4$, $\beta = 0.6$, $\gamma = 9$, $\phi = 1$, and $\theta = 1$, and the fine toll at the bottleneck road is realized by the electronic toll collection system.

Next, we will calculate and analyze these schemes including the no-toll scheme (NT), fine-toll scheme (FT), and optimization scheme of fine toll and bus departure quantity (FT-BDQ). For the ease of comparison, some formulas for NT, FT, and FT-BDQ schemes are listed in Table 2. The results of calculation are as follows.

In Table 3, we can observe that travel cost and system total travel cost under the optimization scheme of fine toll and bus departure quantity are smaller than that of the fine-toll scheme and the no-toll scheme. This reflects that the optimization scheme of fine toll and bus departure quantity can reduce travelers' travel cost. Comparing the equilibrium results of the 2nd column and 3rd column in Table 3, we can know that appropriately increasing the bus departure quantity in the rush hour can attract some travelers to travel by bus. This means that the optimization scheme of fine toll and bus departure quantity can effectively guide travelers to choose a reasonable travel mode to travel in the rush hour.

In Figure 1, we can observe that the congestion risk cost of bus travel under the optimization scheme of fine toll and bus departure quantity may be higher than that of the no-toll scheme in some times of the rush hour, but it is lower than that of the fine-toll scheme in the rush hour. This also reflects that appropriately increasing the bus departure quantity on the basis of the fine toll can effectively reduce the congestion risk cost of bus travel.

TABLE 2: Some formulas for NT, FT, and FT-BDQ schemes at equilibrium.

Variables	Schemes	Formulas
Car travel demand	NT	$N_1 = s - \lambda f_0/s + (d - \lambda)f_0[N - f_0 d(\beta + \gamma)/\beta\gamma(\alpha_1 T_f - \alpha_2 T_f - p)]$
	FT	$N_1 = s - \lambda f_0/s + (d - \lambda)f_0[N - f_0 d(\beta + \gamma)/\beta\gamma(\alpha_1 T_f - \alpha_2 T_f - p)]$
	FT-BDQ	$N_1' = s - \lambda f_b/s + (d - \lambda)f_b[N - f_b d(\beta + \gamma)/\beta\gamma(\alpha_1 T_f - \alpha_2 T_f - p)]$
Bus travel demand	NT	$N_2 = N - N_1$
	FT	$N_2 = N - N_1$
	FT-BDQ	$N_2' = N - N_1'$
Bus departure quantity	NT	f_0
	FT	f_0
	FT-BDQ	$f_b = [s + 2f_0(d - \lambda)]\beta\gamma N + sf_0 d(\beta + \gamma)(\alpha_1 T_f - \alpha_2 T_f - p)/(d - \lambda)\beta\gamma N + d[2s + f_0(d - \lambda)](\beta + \gamma)(\alpha_1 T_f - \alpha_2 T_f - p)$
Travel cost	NT	$C_1 = C_2 = \alpha_1 T_f + \beta\gamma/\beta + \gamma N_1/s - \lambda f_0$
	FT	$C_1 = C_2 = \alpha_1 T_f + \beta\gamma/\beta + \gamma N_1/s - \lambda f_0$
	FT-BDQ	$C_1' = C_2' = \alpha_1 T_f + \beta\gamma/\beta + \gamma N_1'/s - \lambda f_b$
System total travel cost	NT	$SC = (\alpha_1 T_f + \beta\gamma/\beta + \gamma N_1/s - \lambda f_0)N$
	FT	$SC = (\alpha_1 T_f + \beta\gamma/\beta + \gamma N_1/s - \lambda f_0)N$
	FT-BDQ	$SC' = (\alpha_1 T_f + \beta\gamma/2(\beta + \gamma)N_1/s - \lambda f_0)N$
Car departure time at which the queue begins	NT	$t_{1e} = t^* - T_f - \gamma/\beta + \gamma N_1/s - \lambda f_0$
	FT	$t_{1e} = t^* - T_f - \gamma/\beta + \gamma N_1/s - \lambda f_0$
	FT-BDQ	$t_{1e}' = t^* - T_f - \gamma/\beta + \gamma N_1'/s - \lambda f_b$
Car departure time at which the queue ends	NT	$t_{1l} = t^* - T_f + \beta/\beta + \gamma N_1/s - \lambda f_0$
	FT	$t_{1l} = t^* - T_f + \beta/\beta + \gamma N_1/s - \lambda f_0$
	FT-BDQ	$t_{1l}' = t^* - T_f + \beta/\beta + \gamma N_1'/s - \lambda f_b$
Bus departure time at which the queue begins	NT	$t_{2e} = t^* - T_f - \gamma/\beta + \gamma N_2/f_0 d$
	FT	$t_{2e} = t^* - T_f - \gamma/\beta + \gamma N_2/f_0 d$
	FT-BDQ	$t_{2e}' = t^* - T_f - \gamma/\beta + \gamma N_2'/f_b d$
Bus departure time at which the queue ends	NT	$t_{2l} = t^* - T_f + \beta/\beta + \gamma N_2/f_0 d$
	FT	$t_{2l} = t^* - T_f + \beta/\beta + \gamma N_2/f_0 d$
	FT-BDQ	$t_{2e}' = t^* - T_f + \beta/\beta + \gamma N_2'/f_b d$

Table 3: Equilibrium results under three schemes.

Schemes	Car travel demand	Bus travel demand	Bus departure quantity	Travel cost	System total travel cost
NT	2056.9800	3943.0199	50	4.1090	24653.8461
FT	2056.9800	3943.0199	50	4.1090	24653.8461
FT-BDQ	987.7681	5012.2319	87.6142	3.8045	22826.9230
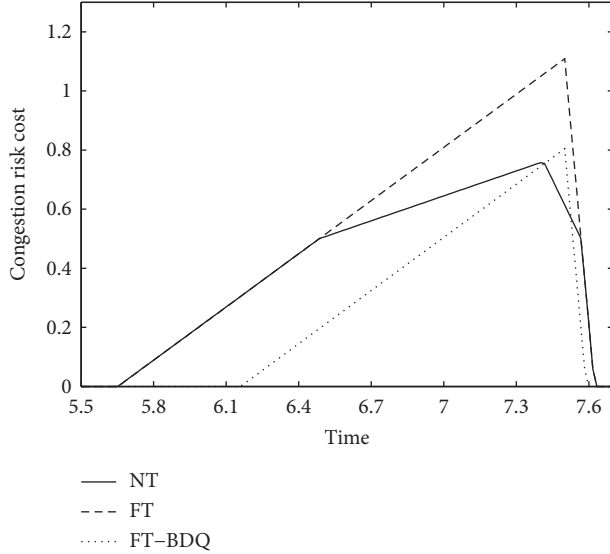
Figure 1: Congestion risk cost of bus travel under three schemes.

Table 4: Travel time distribution of car travelers and bus travelers under three schemes.

Schemes	t_{1e}(or t_{1e}')	t_{2e}(or t_{2e}')	t_{1l}(or t_{1l}')	t_{2l}(or t_{2l}')
NT	6:29	5:39	7:34	7:37
FT	6:29	5:39	7:34	7:37
FT-BDQ	6:59	6:09	7:32	7:35

In Table 4, we can observe that the car and bus departure time at which the queue begins under the optimization scheme of fine toll and bus departure quantity are later than that of the fine-toll scheme and the no-toll scheme; the car and bus departure time at which the queue ends under the optimization scheme of fine toll and bus departure quantity are earlier than that of the fine-toll scheme and the no-toll scheme. This also shows that the optimization scheme of fine toll and bus departure quantity cannot only help travelers to choose a reasonable travel time to travel in the rush hour but also shorten the rush hour of car and bus travel.

6. Conclusions

In this paper, we established a dual-mode equilibrium model based on the bottleneck model. In order to overcome the problem that the fine-toll scheme increases the congestion risk cost of bus travel, we proposed an optimization scheme of fine toll and bus departure quantity and demonstrated its travel characteristics from the perspective of theoretical analysis and numerical simulation. The findings from these experiments are summarized as follows:

(1) The optimization scheme of fine toll and bus departure quantity can reduce the system total travel cost and travelers' travel cost and help travelers to choose a reasonable travel mode to travel in the rush hour.

(2) The congestion risk cost of bus travel under the optimization scheme of fine toll and bus departure quantity is lower than that of the fine-toll scheme in the rush hour. Appropriately increasing the bus departure quantity can effectively reduce the congestion risk cost of bus travel.

(3) The optimization scheme of fine toll and bus departure quantity cannot only guide travelers to choose a reasonable travel time to travel in the rush hour but also shorten the rush hour of car and bus travel.

The bottleneck of road and public transportation is the key point to traffic congestion. Therefore, this study can help alleviate the urban traffic congestion and promote the development of urban traffic demand management methods.

With regard to the above finding, it is worth further looking at how to find the "best" simple scheme of fine toll and bus departure quantity under uncertain demand. Another interesting direction for further research is how to consider the influence of travel-mode choice behavior heterogeneity on the optimization scheme of fine toll and bus departure quantity. Additionally, the measurement of the congestion risk cost is also our future research direction.

Data Availability

The data used to support the findings of this study are available from the corresponding author upon request.

Conflicts of Interest

The authors declare that there are no conflicts of interest regarding the publication of this paper.

Acknowledgments

References

[1] W. Vickery, "Congestion theory and transport investment," *American Economic Review*, vol. 59, no. 2, pp. 251–260, 1969.

[2] L. Xiao, H. Huang, and L. Tian, "Stochastic bottleneck model with heterogeneous travelers," *Journal of Transportation Systems Engineering and Information Technology*, vol. 14, no. 4, pp. 93–98, 2014.

[3] D. Chen, N. Zhang, and L. J. Liu, "Bottleneck model for bi-arrival time: principle of staggered work hours," *Journal of Management Sciences in China*, vol. 18, no. 8, pp. 52–60, 2015.

[4] Z. Khan and S. Amin, "Bottleneck model with heterogeneous information," *Transportation Research Part B: Methodological*, vol. 112, pp. 157–190, 2018.

[5] X. Guo and H. J. Sun, "Modeling the morning commute problem in a bottleneck model based on personal perception," *Journal of Advanced Transportation*, vol. 2019, Article ID 6184827, 12 pages, 2019.

[6] Z. Zhu, X. Li, W. Liu, and H. Yang, "Day-to-day evolution of departure time choice in stochastic capacity bottleneck models with bounded rationality and various information perceptions," *Transportation Research Part E: Logistics and Transportation Review*, vol. 131, pp. 168–192, 2019.

[7] Z.-C. Li, H.-J. Huang, and H. Yang, "Fifty years of the bottleneck model: a bibliometric review and future research directions," *Transportation Research Part B: Methodological*, vol. 139, pp. 311–342, 2020.

[8] J. Kim, "Estimating the social cost of congestion using the bottleneck model," *Economics of Transportation*, vol. 19, pp. 1–19, 2019.

[9] X. Zhang, W. Liu, S. T. Waller, and Y. Yin, "Modelling and managing the integrated morning-evening commuting and parking patterns under the fully autonomous vehicle environment," *Transportation Research Part B: Methodological*, vol. 128, pp. 380–407, 2019.

[10] D. Abegaz, K. Hjorth, and J. Rich, "Testing the slope model of scheduling preferences on stated preference data," *Transportation Research Part B: Methodological*, vol. 128, pp. 380–407, 2019.

[11] R. Lamotte and N. Geroliminis, "The morning commute in urban areas with heterogeneous trip lengths," *Transportation Research Part B: Methodological*, vol. 117, pp. 794–810, 2018.

[12] M. Fosgerau and K. Van Dender, "Road pricing with complications," *Transportation*, vol. 40, no. 3, pp. 479–503, 2013.

[13] J. Bulteau, "Revisiting the bottleneck congestion model by considering environmental costs and a modal policy," *International Journal of Sustainable Transportation*, vol. 10, no. 3, pp. 180–192, 2016.

[14] A. de Palma, R. Lindsey, and G. Monchambert, "The economics of crowding in rail transit," *Journal of Urban Economics*, vol. 101, pp. 106–122, 2017.

[15] R. Lamotte, A. de Palma, and N. Geroliminis, "On the use of reservation-based autonomous vehicles for demand management," *Transportation Research Part B: Methodological*, vol. 99, pp. 205–227, 2017.

[16] Z. Qian, F. Xiao, and H. M. Zhang, "Managing morning commute traffic with parking," *Transportation Research Part B: Methodological*, vol. 46, no. 7, pp. 894–916, 2012.

[17] Y. E. Ge, K. Stewart, Y. D. Liu, C. Y. Tang, and B. Z. Liu, "Investigating boundary effects of congestion charging in a single bottleneck scenario," *Transport*, vol. 33, no. 1, pp. 77–91, 2018.

[18] C. R. Lindsey, V. A. C. V. D. Berg, and E. T. Verhoef, "Step tolling with bottleneck queuing congestion," *Journal of Urban Economics*, vol. 72, no. 1, pp. 46–59, 2012.

[19] C.-H. Laih, "Queueing at a bottleneck with single- and multi-step tolls," *Transportation Research Part A: Policy and Practice*, vol. 28, no. 3, pp. 197–208, 1994.

[20] M. Miralinaghi and S. Peeta, "Promoting zero-emissions vehicles using robust multi-period tradable credit scheme," *Transportation Research Part D: Transport and Environment*, vol. 75, pp. 265–285, 2019.

[21] R. Ma and H. M. Zhang, "The morning commute problem with ridesharing and dynamic parking charges," *Transportation Research Part B: Methodological*, vol. 106, pp. 345–374, 2017.

[22] Y. Liu and Y. Li, "Pricing scheme design of ridesharing program in morning commute problem," *Transportation Research Part C: Emerging Technologies*, vol. 79, pp. 156–177, 2017.

[23] L. L. Xiao, T. L. Liu, and H. J. Huang, "Tradable permit schemes for managing morning commute with carpool under parking space constraint," *Transportation*, vol. 1, pp. 1–24, 2019.

[24] Z. Chen, F. He, L. Zhang, and Y. Yin, "Optimal deployment of autonomous vehicle lanes with endogenous market penetration," *Transportation Research Part C: Emerging Technologies*, vol. 72, pp. 143–156, 2016.

[25] S. E. Seilabi, M. T. Tabesh, A. Davatgari, M. Miralinaghi, and S. Labi, "Promoting autonomous vehicles using travel demand and lane management strategies," *Frontiers in Built Environment*, vol. 6, no. 560116, pp. 1–20, 2020.

[26] J. Holguín-Veras and M. Cetin, "Optimal tolls for multi-class traffic: analytical formulations and policy implications," *Transportation Research Part A: Policy and Practice*, vol. 43, no. 4, pp. 445–467, 2009.

[27] L.-L. Xiao, H.-J. Huang, and R. Liu, "Congestion behavior and tolls in a bottleneck model with stochastic capacity," *Transportation Science*, vol. 49, no. 1, pp. 46–65, 2015.

[28] Z.-C. Li, W. H. K. Lam, and S. C. Wong, "Step tolling in an activity-based bottleneck model," *Transportation Research Part B: Methodological*, vol. 101, pp. 306–334, 2017.

[29] M. Miralinaghi, S. Peeta, X. He, and S. V. Ukkusuri, "Managing morning commute congestion with a tradable credit scheme under commuter heterogeneity and market loss aversion behavior," *Transportmetrica B: Transport Dynamics*, vol. 7, no. 1, pp. 1780–1808, 2019.

[30] J.-P. Wang, H.-J. Huang, and X. Ban, "Optimal capacity allocation for high occupancy vehicle (HOV) lane in morning commute," *Physica A: Statistical Mechanics and Its Applications*, vol. 524, pp. 354–361, 2019.

[31] X. Yu, V. A. C. van den Berg, and E. T. Verhoef, "Carpooling with heterogeneous users in the bottleneck model," *Transportation Research Part B: Methodological*, vol. 127, pp. 178–200, 2019.

[32] L. Zhong, K. Zhang, Y. Nie, and J. Xu, "Dynamic carpool in morning commute: role of high-occupancy-vehicle (HOV) and high-occupancy-toll (HOT) lanes," *Transportation Research Part B: Methodological*, vol. 135, pp. 98–119, 2020.

[33] F. Mirabel and M. Reymond, "Bottleneck congestion pricing and modal split: redistribution of toll revenue," *Transportation Research Part A: Policy and Practice*, vol. 45, no. 1, pp. 18–30, 2011.

[34] L.-J. Tian, H. Yang, and H.-J. Huang, "Tradable credit schemes for managing bottleneck congestion and modal split with heterogeneous users," *Transportation Research Part E: Logistics and Transportation Review*, vol. 54, pp. 1–13, 2013.

[35] Z.-C. Li and L. Zhang, "The two-mode problem with bottleneck queuing and transit crowding: how should congestion be priced using tolls and fares?" *Transportation Research Part B: Methodological*, vol. 138, pp. 46–76, 2020.

[36] Z. Lin and H. Yang, "Modal split based on bottleneck model of public transport," *China Civil Engineering Journal*, vol. 36, no. 7, pp. 1–6, 2003.

[37] R. Arnott, A. de Palma, and R. Lindsey, "Economics of a bottleneck," *Journal of Urban Economics*, vol. 27, no. 1, pp. 111–130, 1990.

WILEY | Hindawi

Research Article

Assessment of Artificial Intelligence Models for Estimating Lengths of Gradually Varied Flow Profiles

Majid Niazkar [ID],[1] **Farshad Hajizadeh mishi** [ID],[1] **and Gökçen Eryılmaz Türkkan** [ID][2]

[1]*Department of Civil and Environmental Engineering, School of Engineering, Shiraz University, Zand Blvd, Shiraz, Iran*
[2]*Department of Civil Engineering, Bayburt University, Bayburt, Turkey*

Correspondence should be addressed to Majid Niazkar; mniazkar@shirazu.ac.ir

The study of water surface profiles is beneficial to various applications in water resources management. In this study, two artificial intelligence (AI) models named the artificial neural network (ANN) and genetic programming (GP) were employed to estimate the length of six steady GVF profiles for the first time. The AI models were trained using a database consisting of 5154 dimensionless cases. A comparison was carried out to assess the performances of the AI techniques for estimating lengths of 330 GVF profiles in both mild and steep slopes in trapezoidal channels. The corresponding GVF lengths were also calculated by 1-step, 3-step, and 5-step direct step methods for comparison purposes. Based on six metrics used for the comparative analysis, GP and the ANN improve five out of six metrics computed by the 1-step direct step method for both mild and steep slopes. Moreover, GP enhanced GVF lengths estimated by the 3-step direct step method based on three out of six accuracy indices when the channel slope is higher and lower than the critical slope. Additionally, the performances of the AI techniques were also investigated depending on comparing the water depth of each case and the corresponding normal and critical grade lines. Furthermore, the results show that the more the number of subreaches considered in the direct method, the better the results will be achieved with the compensation of much more computational efforts. The achieved improvements can be used in further studies to improve modeling water surface profiles in channel networks and hydraulic structure designs.

1. Introduction

Gradually varied flow (GVF) is a nonuniform flow in natural and man-made canals. The study of GVF is crucial to water resources management as it may not only be categorized as one of the most common flow conditions in an open channel but also play a key role in various hydraulic projects. Some examples of the occurrence of GVF include flow through a change in channel bottom slope, canal constrictions and transitions, a variation of channel geometries, flow under the infection of hydraulic structures, and flow from a large reservoir to a canal. In such situations, flow variables, i.e., water depth and flow velocity, vary gradually in each cross-section along a channel.

The governing equation for computing GVF profiles in prismatic canals is shown in equation (1). It is basically a combination of energy (or momentum) equation and a resistance equation. The former presents the spatial variation of water depth in GVF profiles, while the latter relates friction slope (S_f) with flow and channel geometries of the canal under consideration:

$$\frac{dy}{dx} = S_0 \frac{1 - (y_n/y)^N}{1 - (y_c/y)^M},$$ (1)

where y is the water depth, x is the longitudinal distance along the channel, dy/dx is the water surface slope, y_n and y_c are the normal and critical water depths, respectively, S_0 is the channel bottom slope, and M and N are the hydraulic components for critical and uniform flows, respectively.

One of typical problem statements in GVF profiles is computation of the distance between two specific water depths. In other words, water depths at two cross-sections of the same profile are given while the distance between these

two sections (L) is unknown. According to the literature review, various attempts for solving this problem may be categorized into several groups based on their methods: (1) semianalytical methods [1, 2], (2) analytical solutions [3–7], (3) numerical schemes [8–11], (4) artificial intelligence (AI) models [12], and (5) optimization techniques [13–15].

The disadvantages of semianalytical and analytical solutions include (1) some of them are only applicable to specific conditions such as Bresse's analytical solution for wide rectangular channel and Chezy's equation and (2) the analytical solutions with a wide of range of applicability mostly have complex relations. On the other hand, the numerical schemes basically march on space between the two water depths are given. Additionally, they have been known to be susceptible to stability problems [16], while they may sometimes achieve different results [17]. Although analytical solutions are error-free, the accuracy of numerical solutions depends on several factors including the spatial interval (Δx) and the round-off characteristics of the method, which may lead to discretization and truncation errors, respectively [11]. Based on the current literature, application of AI models to GVF computation is limited. For instance, Sivapragasam et al. [12] utilized genetic programming (GP) and the artificial neural network (ANN) to predict water surface profile as a steady flow with different discharges passes over a rectangular notch. Although AI models have been successfully used for solving numerous problems in water resources management and hydraulic engineering [18–21], it has not been applied to estimate the length of GVF profiles.

In this study, two AI models were employed to predict the distance between two cross-sections with known water depths in the same GVF profile. A large database was provided for different flow conditions in rectangular and trapezoidal cross-sections. The performances of these models in estimating length of GVF profiles were also compared with those of the most common numerical method available in the literature.

2. Methods and Materials

2.1. Problem Statement of GVF Profile Length.
Steady GVF is one of the most common time-independent flow conditions occurred in open channels, while length of GVF profiles is necessary to channel design, design of hydraulic structures, and budget estimation of open-channel water conveyance projects [1, 22]. In the current literature, Swamee [1] presented empirical relations between the control section and the section with $0.99y_n$ or $1.01y_n$ for triangular, wide, and narrow rectangular. However, in this study, the distance between two arbitraries but known water depths (y_1 and y_2) within the same profile in trapezoidal sections is of interest.

In addition to equation (1), Manning's equation, which is the most widely used resistance equation in open-channel hydraulics [23], governs the flow filed in GVF profiles:

$$Q = \frac{1}{n} A R^{2/3} S^{1/2}, \tag{2}$$

where Q is the discharge, n is Manning's coefficient, A is the flow area, $R = A/P$ is the hydraulic radius, P is the wetter

perimeter, and S is the channel slope. When $S = S_0$, the water depth in equation (2) exclusively corresponds to y_n, while it can be any other water depth for $S = S_f$.

In the problem statement of computing the length of GVF profiles, Q channel geometries including canal bottom width (b), channel side slope (z), S_0, and n are the given information, while L is meant to be estimated.

The distance of varied flows is a determinant parameter in various water engineering problems, such as determining the location of hydraulic jump [13], predicting budget of channel design [24, 25], and estimating backwater impacts on hydraulic structures [26]. For instance, the influence length of GVF profiles propagating from a uniform or critical depth has been investigated in the literature [11, 27]. In modeling water surface of GVF profiles in real-life projects, the routine procedure in professional hydraulic software, such as HEC-RAS, is to divide the canal under consideration into several parts so called reaches so that each reach as similar flow conditions and channel geometries [28]. Due to spatial variation of channel geometries along natural streams, a reach-average value has been frequently designated to canal characteristics such as b, z, S_0, and n [28, 29]. As n is known to be a flow-dependent parameter and is not a measurable parameter [26, 30], a flow-independent bed roughness predictor may be utilized to estimate a reach-average value for steady GVF.

Steady GVF profiles is generally categorized based on the comparison between y_n and y_c: (1) when $y_n = y_c$, the channel slope is called critical slope ($S_0 = S_c$), (2) if $y_n > y_c$, the channel slope is mild slope ($S_0 < S_c$), and (3) steep channel occurs ($S_0 > S_c$) when $y_n < y_c$. In this classification, when water depth is higher than both y_n and y_c, it is located in M1 or S1 zone if the channel slope is mild or steep, respectively. Furthermore, when water depth is located between y_n and y_c, it may be called either M2 or S2 for mild or steep slope, respectively. Finally, M3 or S3 profile happens when the water depth is lower than both y_n and y_c in mild or steep slope, respectively.

2.2. Varied Flow Function.
In this method, it is commonly assumed that M and N that appeared in equation (1) are the flow invariants for simplicity. In other words, the variation of M and N with water depth can be neglected in engineering application [31]. Using the substitution of $u = y/y_n$, equation (1) is rewritten:

$$x = \frac{y_n}{S_0} \left[u - \int_0^u \frac{du}{1 - u^N} + \left(\frac{y_c}{y_n} \right)^M \int_0^u \frac{u^{N-M} du}{1 - u^N} \right] + c, \tag{3}$$

where x is the location of a specific cross-section along the channel, $M = 3[1 + 2z(y/b)]^2 - 2z(y/b)[1 + z(y/b)]/[1 + 2z(y/b)][1 + z(y/b)]$, $N = (10/3)(1 + 2z(y/b)/1 + z(y/b)) - (8/3)(\sqrt{1 + z^2}(y/b)/1 + 2\sqrt{1 + z^2}(y/b))$ for trapezoidal cross-sections, and c is a constant.

The first integral term in equation (3) is called varied flow function ($F(u, N) = \int_0^u du/1 - u^N$), which depends on two parameters u and N. The second integral in equation (3) can be turned into a varied flow function by setting $v = u^{N/J}$,

where $J = (N/N - M + 1)$. By further manipulating equation (3), the distance between two cross-sections 1 and 2

with known water depths is achieved by the following equation:

$$L = \frac{y_n}{S_0}\left\{u_2 - u_1 + F(u_1, N) - F(u_2, N) + \frac{J}{N}\left(\frac{y_c}{y_n}\right)^M [F(v_2, J) - F(v_1, J)]\right\}, \tag{4}$$

where 1 and 2 subscripts correspond to the first and second cross-sections in the channel reach.

Traditionally, magnitudes of the varied flow function are provided in tables covering numerous values of state variables [6]. Although this method has been introduced as a standard approach in hydraulic engineering texts [31, 32], its major drawback is determination of the varied flow function [6, 33]. The reasons for which this method is not suitable in practice may be as follows: (1) the varied flow function is relatively complicated to be solved by the hand, (2) according to equation (4), four integrals ($F(u_1, N)$, $F(u_2, N)$, $F(v_2, J)$, and $F(v_1, J)$) need to be computed to determine L, and (3) the tables provided for varied flow function can only be exploited for a set of discrete values of state variables. Consequently, an interpolation may be required for intermittent values, which produces inevitable errors. On the other hand, when varied flow function is calculated without interpolation, the obtained results may be used as benchmark since it considers no approximate assumption.

2.3. Simple Direct Method.
In this method, the distance between two cross-sections 1 and 2 is computed by using finite difference:

$$L = \frac{1}{S_0 - S_f}\left[\left(y_2 + \frac{Q^2}{2gA_2^2}\right) - \left(y_1 + \frac{Q^2}{2gA_1^2}\right)\right], \tag{5}$$

where g is the gravitational acceleration.

As shown equation (5), L can be computed directly when Q and channel properties are known, while S_f in equation (5) is substituted with the reach-average friction slopes using the first and second cross-sections. In this study, the direct method is utilized for calculating GVF profile length using (1) one-spatial step, (2) three-spatial steps, and (3) five-spatial steps. In the one-step version, equation (5) is exploited only one time to obtain L between the two water depths given in the problem statement, while the whole distance between sections 1 and 2 is divided into three and five subreaches in the three-step and five-step versions, respectively. For the better clarification, Figure 1 depicts schematic division of a channel reach into five subreaches in the five-step scenario. As shown, y_n and y_c are the same for all five subreaches in the five-step direct method. According to Figure 1, four additional water depths are required to be used between the first and second sections in the five-step direct method. For $y_1 > y_2$, the four additional water depths are $y_3 = y_1 - (y_1 - y_2/5)$, $y_4 = y_3 - (y_1 - y_2/5)$, $y_5 = y_4 - (y_1 - y_2/5)$, and $y_6 = y_5 - (y_1 - y_2/5)$. Therefore, when y_1

and y_2 are given, the additional water depths can be calculated one after another from y_3 to y_6. In the five-step direct method, the distance between two consecutive sections, such as L_{13} between sections 1 and 3, is computed using equation (5). Finally, the algebraic summation of the distances between the successive cross-sections is computed, which is equal to L as shown in Figure 1.

2.4. Artificial Neural Network.
Artificial neural network (ANN) is a well-documented AI model and has been successfully applied to various problems in water resources and hydraulic engineering [34, 35]. Basically, it consists of three layers, named as input, hidden, and output layers, while each layer includes some components called neurons. The number and objective of neurons are defined based on the layer to which they belong. For instance, the neurons of the input layer take the vector of input data. The structure of the ANN provides connections between neurons of two successive layers, while there is no connection between the neurons within a layer. Using these connections, the data flow through the network until an adequate relation between the input and output data is achieved [30].

Predicting the length of GVF profiles using the ANN is conducted for the first time in this study, based on authors' knowledge. The input data include the dimensionless u and N, while the output data are dimensionless $F(u, N)$. Furthermore, there is a trade-off between the number of neurons in the hidden layer in the ANN and the computational efforts. To be more specific, the more the number of neurons in the hidden layer is used, the more accurate results may be obtained. In this study, several hidden layers with four to ten neurons were tested, while a seven-neuron hidden layer was selected. After the ANN completed the prediction process, the estimated varied flow functions were substituted into equation (4) to compute the corresponding length of GVF profiles. As shown in equation (4), four $F(u, N)$ are required to determine the length between two specified water depths.

2.5. Genetic Programming.
Genetic programming (GP) is one of AI models that employs the genetic algorithm to create a powerful prediction tool. In essence, GP is an improved version of the genetic algorithm which is capable of finding a relation between two vectors of variables regardless of the physical background of those data. GP begins with creation of a random population comprising of random functions and coefficients [36]. It also uses the genetic algorithm features such as crossover and mutation to improve the fitness of new generations in light of minimizing an objective function. The objective function basically reflects
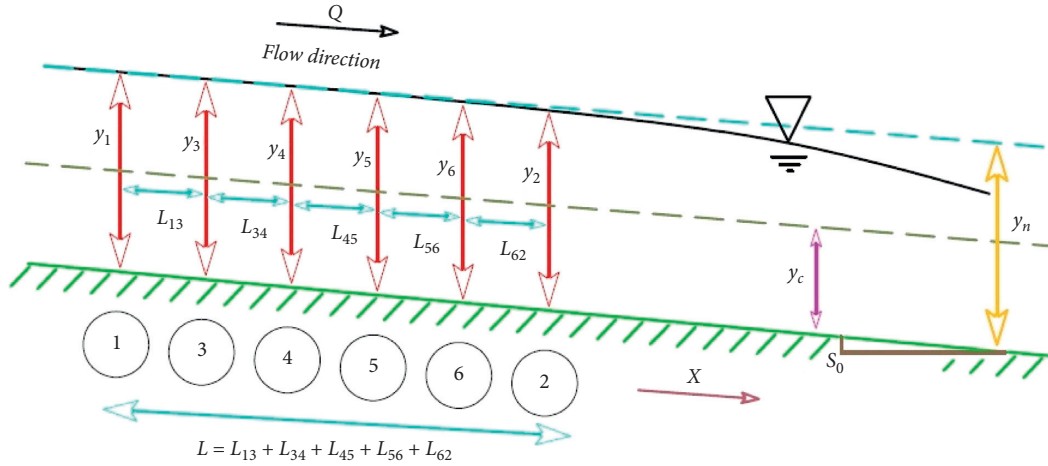
FIGURE 1: Schematic division of a channel reach into several subreaches.

the errors between the input and output data. This process continues until an expression with a desirable error is achieved. Such correlations may further be used for estimation purposes [25].

GP has a tree-like structure in which a variety of mathematical functions and variables may be adopted to seek for an appropriate relationship between the input and output data. As a result of these characteristics, Discipulus [37] software, which has been used for applying GP in the literature [35], was exploited to many problems in the fields' water resources and hydraulic engineering. The input data given to this program include u and N, while the output data were $F(u, N)$. The latter values were exploited to estimate L for each data point.

2.6. The Database.
The data considered in this study consist of two parts: (1) train data and (2) test data. The former includes 5154 rows of u, N (input data), and $F(u, N)$ (output data). They were basically gathered from the tables presented in engineering text books [31, 38]. These data were used for training the ANN and GP. On the other hand, the second part of data consists of 165 data for mild slope and 165 data for steep slope. To be more specific, the test data contain 70 data of M1, 54 data of M2, 41 data of M3, 48 data of S1, 51 data of S2, and 66 data of S3 profile. Furthermore, the values of Q, b, z, S_0, n, y_1, and y_2 of the test data were generated by the random function embedded in Excel [39]. Finally, y_n and y_c can be computed when Q and the reach-average values of n and S_0 are given.

Since the test data were developed randomly, they need to be checked. In this regard, three requirements were considered: (1) channel geometries and Q of each row should be practically feasible, (2) each row of data should only have one type of channel slope (i.e., mild or steep slope), and (3) each row of data should belong to one specific type of flow profile. For instance, the GVF profile is M1 or M2 or M3 when the channel slope is mild. In case a row of data did not satisfy the mentioned requirements, it was replaced with another randomly generated row of data to keep 330 rows of data, which correspond to 1320 pairs of u and N.

After checking each row of the developed data, u and N were determined for the specified water depths (y_1 and y_2). They were used to compute the corresponding $F(u, N)$ without interpolation. Table 1 presents the ranges of different parameters in the test data. As shown, the train data have a wider range of values than that of the test data. According to Table 1, the test data include a wide range of values for each parameter involved.

As previously mentioned, four $F(u, N)$ are required to calculate L for each row of data. Thus, the calculated values of $F(u, N)$ were substituted into equation (4) to give the benchmark distance between y_1 and y_2 for each row of the test data. Finally, the test data were also solved by other methods considered in this study for comparison purposes.

2.7. Performance Evaluation Criteria.
Six evaluation criteria were selected from the literature to compare the performances of different methods in estimation of the length of GVF profiles between two specified water depths [40, 41]. These indices are (1) root mean square error (RMSE), (2) mean absolute relative error (MARE), (3) mean absolute error (MAE), (4) relative absolute error (RAE), (5) relative squared error (RSE), and (6) coefficient of determination (R^2). These criteria are presented in equations (6)–(11), respectively:

$$\text{RMSE} = \sqrt{\frac{1}{N} \sum_{i=1}^{N} \left[L_{\text{estimated}} - L \right]^2}, \tag{6}$$

$$\text{MARE} = \frac{1}{N} \sum_{i=1}^{N} \left| \frac{L_{\text{estimated}} - L}{L} \right|, \tag{7}$$

$$\text{MAE} = \frac{1}{N} \sum_{i=1}^{N} \left| L_{\text{estimated}} - L \right|, \tag{8}$$

$$\text{RAE} = \frac{\sum_{i=1}^{N} \left| L_{\text{estimated}} - L \right|}{\sum_{i=1}^{N} \left| L - \left(\sum_{i=1}^{N} L/N \right) \right|}, \tag{9}$$

TABLE 1: Range of different parameters in the database.

Parameter	Mean	Maximum	Minimum	Standard deviation
Train data				
u	1.48	20.00	0.00	2.19
N	5.25	9.80	2.20	2.37
$F(u, N)$	0.49	3.52	0.00	0.50
Test data				
u	2.10	19.75	0.00	3.24
N	3.04	5.88	2.41	0.42
$F(u, N)$	0.42	2.98	0.00	0.42
Q	104.57	494.00	1.00	70.68
b	30.40	95.00	3.00	14.41
z	1.23	3.50	0.00	0.95
S	0.01	0.10	0.00	0.01
n	0.02	0.05	0.01	0.01
y_n	1.61	10.13	0.05	1.31
y_1	1.95	20.00	0.02	2.42
y_2	2.11	17.00	0.01	2.35
y_c	1.13	6.41	0.06	0.76

$$\text{RSE} = \frac{\sum_{i=1}^{N} \left(L_{\text{estimated}} - L \right)^2}{\sum_{i=1}^{N} \left(\left(\sum_{i=1}^{N} L/N \right) - L \right)^2}, \tag{10}$$

$$R^2 = \left(\frac{\sum_{i=1}^{N} \left[\left(L - \left(\sum_{i=1}^{N} L/N \right) \right) \left(L_{\text{estimated}} - \left(\sum_{i=1}^{N} L_{\text{estimated}}/N \right) \right) \right]}{\sqrt{\sum_{i=1}^{N} \left[\left(L - \left(\sum_{i=1}^{N} L/N \right) \right)^2 \left(L_{\text{estimated}} - \left(\sum_{i=1}^{N} L_{\text{estimated}}/N \right) \right)^2 \right]}} \right)^2. \tag{11}$$

where $L_{\text{estimated}}$ is the estimated length, i is a counter, and N is the number of data.

3. Results and Discussion

The ANN, GP, varied flow function, and 1-step direct method compute the length of GVF profile between y_1 and y_2 by considering one channel reach. However, 3-step and 5-step direct methods divided the channel reach into 3 and 5 subreaches, respectively. These methods were used for estimation of GVF profile length between two specified water depths. For comparison purposes, the test data consist of different GVF profiles to investigate performances of different methods in prediction of L between y_1 and y_2 of each row of the test data.

The performances of the methods described for calculating GVF profile lengths were compared for the test data with mild slopes shown in Table 2. As shown, the 5-step direct method achieved the closet results to the benchmark solutions in comparison with 1-step and 3-step direct methods. Thus, the accuracy of the direct step method enhances with the increase of the number of spatial intervals considered. Additionally, Table 2 depicts that the ANN obtained better RMSE, RAE, MAE, RSE, and R^2 than the 1-step direct method, while the latter achieved a better MARE than the former. Based on Table 2, GP performed better than 1-step and 3-step direct methods in terms of RMSE and RSE, while it yields to the same R^2 as the 3-step direct method. According to Table 2, the 5-step direct method outperformed others for estimating the length of GVF profiles

TABLE 2: Comparison of different methods for calculating distance of GVFs with mild slopes.

Method	RMSE	MARE	R^2	RAE	MAE	RSE
Direct method (1-step)	2068.69	0.25	0.89	0.18	735.29	0.12
Direct method (3-step)	799.92	0.07	0.99	0.06	242.64	0.02
Direct method (5-step)	429.3	0.04	1	0.03	132.61	0.01
ANN (this study)	1139.68	4.36	0.97	0.15	627.09	0.04
GP (this study)	710.16	1.21	0.99	0.08	321.89	0.01

having mild slopes, while GP performs similar to the 3-step direct method.

The improvement obtained by the AI techniques may be interpreted in the light of the connectivity topic. In a holistic point of view, a better understanding of connectivity may be beneficial to develop better schemes for modeling water resources. To be more specific, estimating the distance between two known water depths in a GVF profile may improve modeling of water movement through a man-made canal or a natural stream. This may help river engineering, which includes dam construction/removal, river restoration, and channel regulations. Since, river engineering is connected with channel processes and geomorphic channel response in small- to meso-scale fluvial systems [42]. Therefore, the improvement provided by the AI techniques in this specific application does not confine in design of open channels, particularly when catchment connectivity is assessed [43].

Table 3 compares different methods for calculating L for trapezoidal sections with steep slopes. As shown, the best RMSE, RSE, and R^2 were achieved by GP. Moreover, RMSE obtained by the ANN was lower than that of all direct step methods, while R^2 calculated by the ANN was equal to the best R^2 computed by the latter. According to Table 3, the 5-step direct method achieved better metrics than the 3-step direct method, while the latter reached better results than the 1-step direct method. Thus, Tables 2 and 3 imply that the fewer the spatial interval (Δx) is considered in a typical numerical scheme, the more accurate the results achieve and the more the computational efforts are required. Furthermore, the comparisons carried out in Tables 2 and 3 indicate that GP is an accurate method for computing the length of GVF profiles, particularly when channel has a mild slope.

Although Tables 2 and 3 compared the performances of different methods in estimation of L, they do not provide clearly how each considered method performs in each of GVF profiles. In this regard, six indices were separately calculated by each method for each GVF profiles. The obtained results are depicted in Figure 2, which provide a better detailed perspective required for comparison purposes. Figure 2 shows that RMSE values achieved for mild slopes, particularly M2 profile, are larger than that of steep slopes. This clearly addresses why RMSE values of mild slope shown in Tables 2 and 3 are relatively larger than that of steep slopes. According to Figures 2(a) and 2(b), RMSE values of M2 profile are relatively higher than RMSE of other mild and

TABLE 3: Comparison of different methods for calculating distance of GVFs with steep slopes.

Method	RMSE	MARE	R^2	RAE	MAE	RSE
Direct method (1-step)	191.75	0.26	0.96	0.18	735.29	0.12
Direct method (3-step)	142.51	0.1	0.97	0.06	242.64	0.02
Direct method (5-step)	135.56	0.07	0.98	0.03	132.61	0.01
ANN (this study)	110.17	0.73	0.98	0.15	627.09	0.04
GP (this study)	54.05	0.27	1	0.08	321.89	0.01

steep profiles. Also, RMSE values decrease with the increase of number of intervals in the step direct method for all GVF profiles, while this reduction is significant for M1, M2, S1, and S3 profiles. Based on Figures 2(a) and 2(b), the lowest RMSE was achieved by GP for S1 and S3 profiles and by the 5-step direct method for M1, M2, and M3 profiles. On the other hand, RMSE values computed by all methods for S2 profiles are close to one another. MARE values depicted in Figures 2(c) and 2(d) indicate that the ANN and GP achieved close values to different versions of direct step methods, whereas they obtained higher MARE values for M3 and S2 profiles. Moreover, MARE decreases with the increase of number of subreach considered in the direct method. According to Figures 2(c) and 2(d), the ANN and GP yield to better MARE than the 1-step direct method for M1 and S3 profiles, while they perform better than the 5-step direct method for S1 profile based on MARE criterion. The comparison of R^2 values shown in Figures 2(e) and 2(f) implies that the accuracy of estimation of L increases considering more intervals in direct step methods. Moreover, the 1-step direct method did not achieve acceptable R^2 for M2 and S1 profiles. Based on Figures 2(e) and 2(f), the ANN and GP resulted in promising R^2 values for M1, M2, S1, and S3 profiles, while their R^2 for M3 profile is lower than that of direct step methods. Finally, MARE values computed by all methods for S2 profile are comparable and relatively low.

Figure 3 depicts percentages of estimated L in error ranges for different GVF profiles. This figure provides a suitable opportunity for detailed accurate comparison so that a swift glance reveals which method performs well for each specific GVF profile. According to Figure 3, the percentages may increase with the increase of error ranges; while the more the percentage in one specific error range, the more precise the results are. For M1 profile, Figure 3(a) shows that all methods reach closer results to the benchmark solutions in comparison with the 1-step direct method. Based on Figure 3(b), estimated L by the 1-step method and the ANN for M2 profile contains significant errors, while GP results are relatively better. In addition, 3-step and 5-step direct methods reach more accurate solutions than the rest for M2 profile. Figures 3(c) and 3(e) depict the poor performance of the ANN and GP in predicting L of M3 and S2 profiles, while it also manifests inadequate performance of the 1-step direct method in comparison with 3-step and 5-step direct methods for M3 profile. On the contrary, Figure 3(d) clearly demonstrates the improvement achieved by both the ANN and GP in computation of L in S1 profile compared to all direct step methods. Figure 2(e) demonstrates the impact on considering more subreaches in direct

step methods since it shows that the 5-step direct method has better results than the 3-step direct method and 3-step better than the 1-step direct method, as well. Moreover, the error ranges shown in Figure 2(e) imply that ANN estimations are much closer to the benchmark solutions in each error range considered. Furthermore, Figure 2(e) indicates that GP is capable of accurate prediction of L in S3 profile, even better than direct step methods. In summary, GP was found to compute lengths of M1, S1, and S3 profiles with high accuracy, while the ANN performs well in prediction of L in M1 and S1 profiles.

Confidence limits of the lengths of GVF profiles using all considered methods are shown in Figure 4. It clearly shows that considering more intervals in the direct step method makes the estimated confidence limit closer to that of the benchmark solution for each and every GVF profile. According to Figure 4, all methods exploited for estimation of L yielded to close confidence limits as that of the benchmark solutions for M1 and S1 profiles. However, the confidence limits achieved for M2 and S3 profiles are different, while GP and the 5-step direct method reach to the closest confidence limits to that of the benchmark solutions. Figure 4(c) manifests the poor performance of the ANN in estimating L of M3 profile, while GP replicates the confidence limit of the benchmark solution with high accuracy for this GVF profile. Moreover, the comparison of the confidence limits shown in Figure 4(e) reveals that all methods failed to achieve the whole range of the confidence limit of the benchmark solution, while all confidence limits are within the minimum and maximum points of the benchmark confidence limit. In summary, Figures 2–4 indicate that GP computed the lengths of M1, S1, and S3 profiles with high accuracy compared, while the ANN was successful in estimation of M1 and S1 profile lengths.

According to the comparative analysis conducted in this study, the obtained results show that AI models can improve the prediction of the distance between two water depths specified when they both belong to M1, S1, and S3 profiles. Therefore, one of the main advantages of the AI techniques is that they can improve the accuracy of estimating lengths of gradually varied flow profiles, particularly when the common numerical modeling produces errors, e.g., when the water depth approaches either the normal or critical depth. Additionally, the AI methods, when they are trained, can give estimations with a less computational effort than the benchmark solution and numerical schemes. The two latter methods required integration calculations and marching on space to compute a length of a gradually varied flow profile. These benefits may attract attention toward using the AI techniques in this specific application. In conclusion, the AI
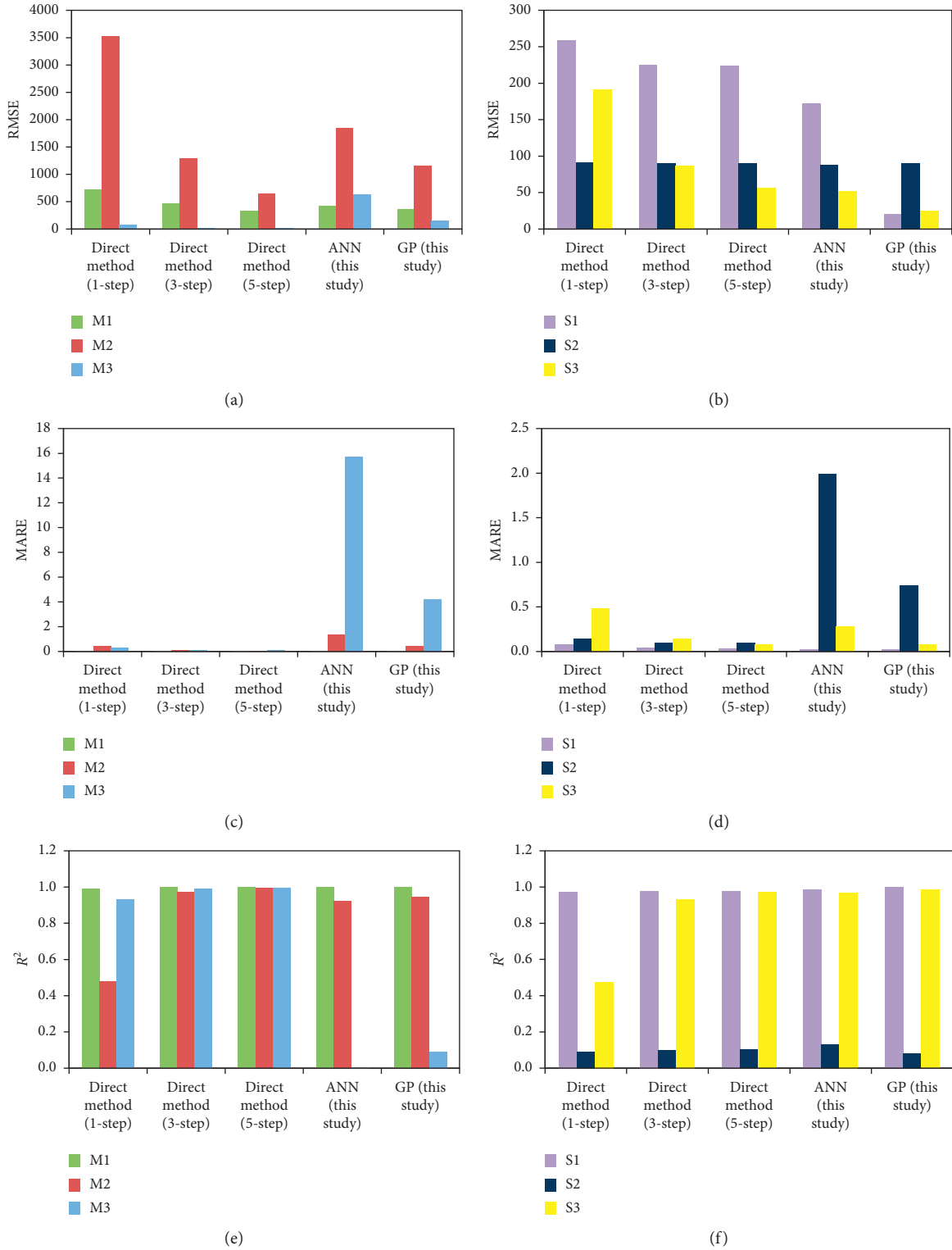
Figure 2: Performances of different methods for calculating distance of different GVF profiles: (a) RMSE for mild slopes, (b) RMSE for steep slopes, (c) MARE for mild slopes, (d) MARE for steep slopes, (e)R^2 for mild slopes, and (f)R^2 for steep slopes.

(a)

(b)

(c)

(d)

(e)

(f)
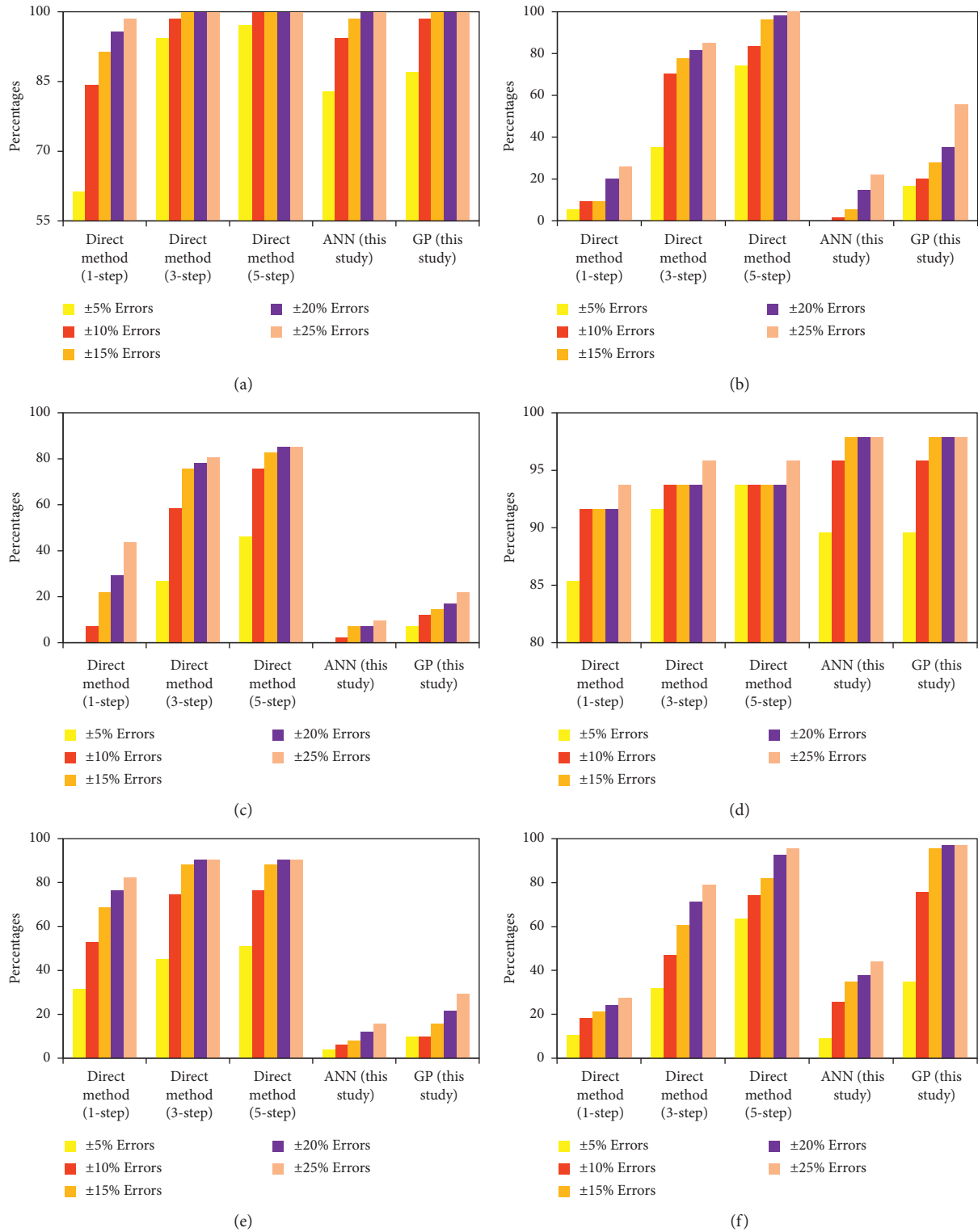
Figure 3: Percentages of estimated distance in error ranges for different GVF profiles: (a) M1, (b) M2, (c) M3, (d) S1, (e) S2, and (f) S3.
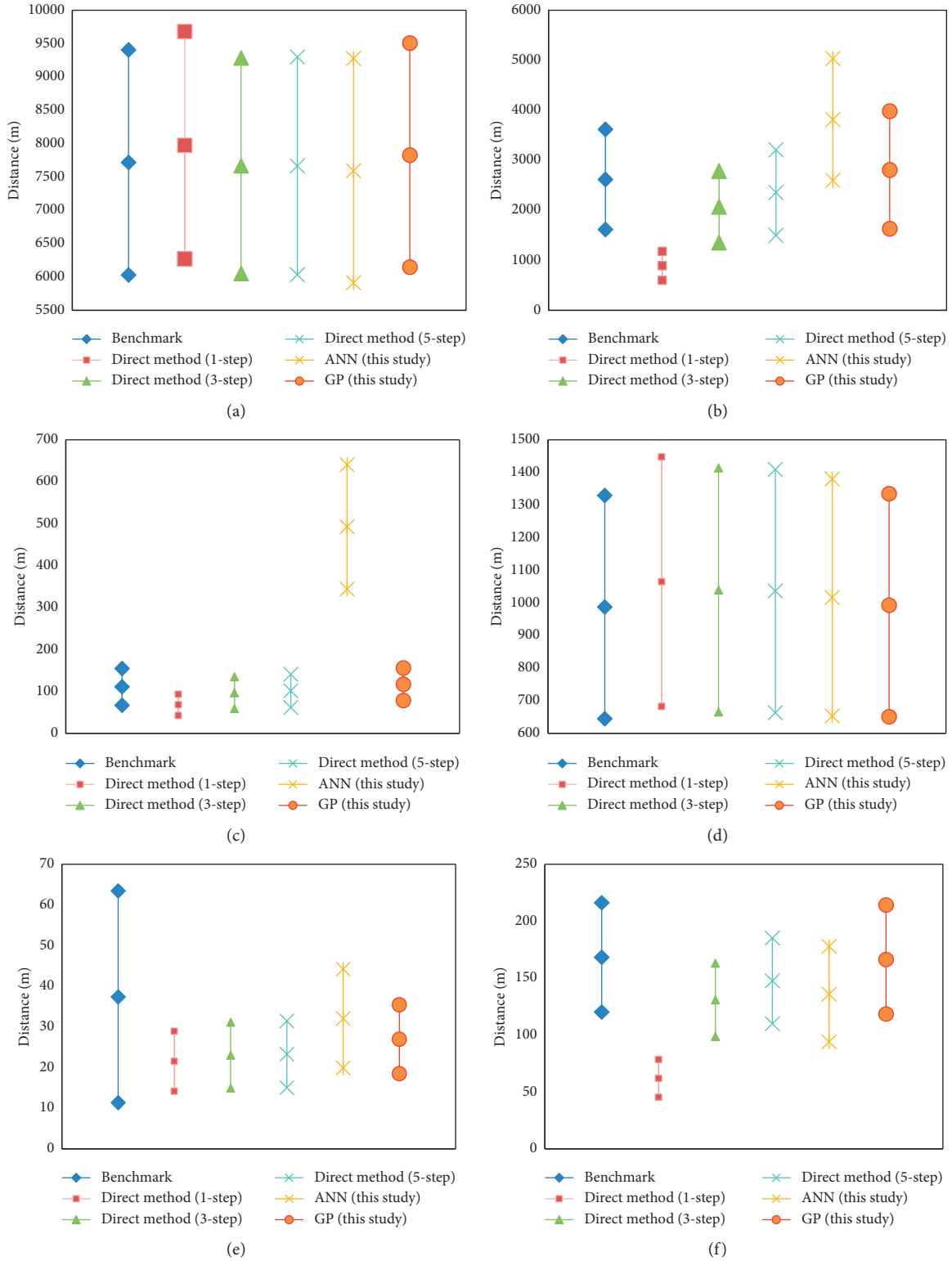
Figure 4: Confidence limits of estimated distances for different GVF profiles: (a) M1, (b) M2, (c) M3, (d) S1, (e) S2, and (f) S3.

models perform much better in many cases in comparison with other methods considered in this study.

4. Conclusions

Although varied flow function provides accurate estimation of the lengths between any pair of known water depths in steady GVF profiles, it requires four complicated integral forms to be calculated which makes it inadequate in practice in comparison to numerical methods such as the direct step method. In this regard, two AI models called the ANN and GP were trained with 5154 data that contained varied flow function. The performances of the ANN and GP in predicting the length between two specified water depths were compared with the direct method having one, three, and five steps, while the results of varied flow function were set as benchmark solutions. The test data consist of 165 data for mild slope and 165 data for steep slope. According to the results, the accuracy of the direct method increases considering more number of intervals considered by the compensation of increasing computational efforts. Also, the comparison clearly demonstrates that GP outperformed others for M1, S1, and S3 profiles. Furthermore, high accurate results were obtained by the ANN for M1 and S1 profiles. However, the results reveal better performance of 3-step and 5-step direct methods for M2, M3, and S2 profiles, while the 1-step direct method failed to estimate precise lengths for M2, M3, and S3 profiles. Finally, GP and the ANN are suggested for estimation of GVF lengths when water depth is larger than normal and critical depths in mild and steep slopes, respectively. The shortcomings and improvements of the AI models in estimating GVF lengths can be beneficial to water surface modeling in future studies.

Data Availability

The data used to support the findings of this study are available from the corresponding author upon request.

Conflicts of Interest

The authors declare that they have no conflicts of interest.

References

[1] P. K. Swamee, "Length of gradually varied flow profiles," *ISH Journal of Hydraulic Engineering*, vol. 9, no. 2, pp. 70–79, 2003.

[2] A. R. Vatankhah and S. M. Easa, "Accurate gradually varied flow model for water surface profile in circular channels," *Ain Shams Engineering Journal*, vol. 4, no. 4, pp. 625–632, 2013.

[3] A. S. Ramamurthy, S. F. Saghravani, and R. Balachandar, "A direct integration method for computation of gradually varied flow profiles," *Canadian Journal of Civil Engineering*, vol. 27, no. 6, pp. 1300–1305, 2000.

[4] R. G. Patil, V. N. Diwanji, and R. M. Khatsuria, "Integrating equation of gradually varied flow," *Journal of Hydraulic Engineering*, vol. 127, no. 7, pp. 624-625, 2001.

[5] M. Venutelli, "Direct integration of the equation of gradually varied flow," *Journal of Irrigation and Drainage Engineering*, vol. 130, no. 1, pp. 88–91, 2004.

[6] C.-D. Jan and C.-l. Chen, "Use of the Gaussian hypergeometric function to solve the equation of gradually-varied flow," *Journal of Hydrology*, vol. 456-457, pp. 139–145, 2012.

[7] A. R. Vatankhah, "Analytical solution of gradually varied flow equation in circular channels using variable Manning coefficient," *Flow Measurement and Instrumentation*, vol. 43, pp. 53–58, 2015.

[8] R. Szymkiewicz and A. Szymkiewicz, "Method to solve the non-linear systems of equations for steady gradually varied flow in open channel network," *Communications in Numerical Methods in Engineering*, vol. 20, no. 4, pp. 299–312, 2004.

[9] B. Kaya, "Investigation of gradually varied flows using differential quadrature method," *Scientific Research and Essays*, vol. 6, no. 13, pp. 2630–2638, 2011.

[10] W. Artichowicz and R. Szymkiewicz, "Computational issues of solving the 1D steady gradually varied flow equation," *Journal of Hydrology and Hydromechanics*, vol. 62, no. 3, pp. 226–233, 2014.

[11] S. Ghazizadeh and M. J. Abedini, "Gradually varied flow modeling: how to choose a reach with maximum information content?," *Flow Measurement and Instrumentation*, vol. 56, pp. 56–60, 2017.

[12] C. Sivapragasam, P. Saravanan, K. Ganeshmoorthy, A. Muhil, S. Dilip, and S. Saivishnu, "Mathematical modeling of gradually varied flow with genetic programming: a lab-scale application," in *Information and Communication Technology for Intelligent Systems*, pp. 409–416, Springer, Berlin, Germany, 2019.

[13] B. W. Karney, A. Malekpour, and H. Salehi, "An exploratory approach to teaching gradually varied flow," *Journal of Hydro-Environment Research*, vol. 4, no. 2, pp. 175–180, 2010.

[14] H. Damangir and M. J. Abedini, "System identification and subsequent discharge estimation based on level data alone-gradually varied flow condition," *Flow Measurement and Instrumentation*, vol. 36, pp. 24–31, 2014.

[15] E. Gadissa and A. Teshome, "Estimation of open channel flow parameters by using genetic algorithm," *Open Journal of Optimization*, vol. 7, no. 3, p. 51, 2018.

[16] F. Motaman, G. R. Rakhshandehroo, M. R. Hashemi, and M. Niazkar, "Application of RBF-DQ method to time-dependent analysis of unsaturated seepage," *Transport in Porous Media*, vol. 125, no. 3, pp. 543–564, 2018.

[17] M. Niazkar and N. Talebbeydokhti, "Comparison of explicit relations for calculating Colebrook friction factor in pipe network analysis using H-based methods," *Iranian Journal of Science and Technology, Transactions of Civil Engineering*, vol. 44, no. 1, p. 231, 2020.

[18] M. Najafzadeh, F. Saberi-Movahed, and S. Sarkamaryan, "NF-GMDH-based self-organized systems to predict bridge pier scour depth under debris flow effects," *Marine Georesources & Geotechnology*, vol. 36, no. 5, pp. 589–602, 2018.

[19] M. Najafzadeh, "Evaluation of conjugate depths of hydraulic jump in circular pipes using evolutionary computing," *Soft Computing*, vol. 23, no. 24, pp. 13375–13391, 2019.

[20] M. Najafzadeh and G. Oliveto, "Riprap incipient motion for overtopping flows with machine learning models," *Journal of Hydroinformatics*, vol. 22, no. 4, pp. 749–767, 2020.

[21] M. Niazkar and M. Zakwan, "Assessment of artificial intelligence models for developing single-value and loop rating curves," *Complexity*, vol. 2021, Article ID 6627011, 21 pages, 2021.

[22] M. Niazkar and S. H. Afzali, "Optimum design of lined channel sections," *Water Resources Management*, vol. 29, no. 6, pp. 1921–1932, 2015.

[23] M. Niazkar, "Revisiting the estimation of colebrook friction factor: a comparison between artificial intelligence models and C-W based explicit equations," *KSCE Journal of Civil Engineering*, vol. 23, no. 10, pp. 4311–4326, 2019.

[24] M. Niazkar, G. R. Rakhshandehroo, and S. H. Afzali, "Deriving explicit equations for optimum design of a circular channel incorporating a variable roughness," *Iranian Journal of Science and Technology, Transactions of Civil Engineering*, vol. 42, no. 2, pp. 133–142, 2018.

[25] M. Niazkar, "Assessment of artificial intelligence models for calculating optimum properties of lined channels," *Journal of Hydroinformatics*, vol. 22, no. 5, p. 1410, 2020.

[26] M. Niazkar, N. Talebbeydokhti, and S. H. Afzali, "Development of a new flow-dependent scheme for calculating grain and form roughness coefficients," *KSCE Journal of Civil Engineering*, vol. 23, no. 5, pp. 2108–2116, 2019a.

[27] A. R. Vatankhah, "Exact sensitivity equation for one-dimensional steady-state shallow water flow (application to model calibration)," *Journal of Hydrologic Engineering*, vol. 15, no. 11, pp. 939–945, 2010.

[28] L. Arneson, L. Zevenbergen, P. Lagasse, and P. Clopper, "Evaluating scour at bridges (HEC-18)," Technical Rep No HIF-12 3, Federal Highway Administration, Washington, DC, USA, 2012.

[29] M. Niazkar, N. Talebbeydokhti, and S. H. Afzali, "One dimensional hydraulic flow routing incorporating a variable grain roughness coefficient," *Water Resources Management*, vol. 33, no. 13, pp. 4599–4620, 2019c.

[30] M. Niazkar, N. Talebbeydokhti, and S. H. Afzali, "Novel grain and form roughness estimator scheme incorporating artificial intelligence models," *Water Resources Management*, vol. 33, no. 2, pp. 757–773, 2019b.

[31] V. T. Chow, *Open Channel Hydraulics*, McGraw-Hill, New York, NY, USA, l959.

[32] K. Subramanya, *Flow in Open Channels*, Tata McGraw-Hill Education, New York, NY, USA, Third edition, 1982.

[33] C.-D. Jan, *Gradually-varied Flow Profiles in Open Channels*, Springer, Berlin, Germany, 2014.

[34] M. Niazkar and S. H. Afzali, "Application of new hybrid method in developing a new semicircular-weir discharge model," *Alexandria Engineering Journal*, vol. 57, no. 3, pp. 1741–1747, 2018.

[35] M. Niazkar, N. Talebbeydokhti, and S.-H. Afzali, "Bridge backwater estimation: a comparison between artificial intelligence models and explicit equations," *Scientia Iranica*, 2020.

[36] H. R. Niazkar and M. Niazkar, "COVID-19 outbreak: application of multi-gene genetic programming to country-based prediction models," *Electronic Journal of General Medicine*, vol. 17, no. 5, p. em247, 2020.

[37] F. D. Francone, *Discipulus Owner's Manual*, Machine Learning Technologies, Inc, Littleton, CO, USA, 1998.

[38] F. M. Henderson, *Open Channel Flow*, Macmillan, New York, NY, USA, 1966.

[39] M. Niazkar and S. H. Afzali, "Streamline performance of excel in stepwise implementation of numerical solutions," *Computer Applications in Engineering Education*, vol. 24, no. 4, pp. 555–566, 2016.

[40] M. Niazkar and S. H. Afzali, "New nonlinear variable-parameter muskingum models," *KSCE Journal of Civil Engineering*, vol. 21, no. 7, pp. 2958–2967, 2017.

[41] M. Najafzadeh and S. Sarkamaryan, "Extraction of optimal equations for evaluation of pipeline scour depth due to currents," in *Proceedings of the Institution of Civil Engineers-Maritime Engineering*, vol. 171, no. 1, pp. 1–10, 2018.

[42] S. Keesstra, J. P. Nunes, P. Saco et al., "The way forward: can connectivity be useful to design better measuring and modelling schemes for water and sediment dynamics?" *Science of the Total Environment*, vol. 644, pp. 1557–1572, 2018.

[43] S. D. Keesstra, J. Davis, R. H. Masselink, J. Casalí, E. T. H. M. Peeters, and R. Dijksma, "Coupling hysteresis analysis with sediment and hydrological connectivity in three agricultural catchments in Navarre, Spain," *Journal of Soils and Sediments*, vol. 19, no. 3, pp. 1598–1612, 2019.

WILEY | Hindawi

Research Article

Hybridized Deep Learning Model for Perfobond Rib Shear Strength Connector Prediction

Jamal Abdulrazzaq Khalaf [ID],[1] Abeer A. Majeed [ID],[2] Mohammed Suleman Aldlemy [ID],[3] Zainab Hasan Ali [ID],[4] Ahmed W. Al Zand [ID],[5] S. Adarsh,[6] Aissa Bouaissi [ID],[7,8] Mohammed Majeed Hameed [ID],[9] and Zaher Mundher Yaseen [ID][10]

[1]*Civil Engineering Department, Collage of Engineering, University of Anbar, Ramadi, Iraq*
[2]*Reconstruction and Projects Department, University of Baghdad, Baghdad, Iraq*
[3]*Department of Mechanical Engineering, Collage of Mechanical Engineering Technology, Benghazi, Libya*
[4]*College of Engineering, Civil Engineering Department, University of Diyala, Baquba, Iraq*
[5]*Department of Civil Engineering, Faculty of Engineering and Built Environment, Universiti Kebangsaan Malaysia (UKM), UKM Bangi 43600, Selangor, Malaysia*
[6]*Department of Civil Engineering, TKM College of Engineering Kollam, Kollam, India*
[7]*School of Engineering, University of Plymouth, Plymouth PL4 8AA, UK*
[8]*UNA Developments Ltd., Airport Business Center, Plymouth Devon PL6 7PP, UK*
[9]*Department of Civil Engineering, Al-Maaref University College, Ramadi, Iraq*
[10]*Faculty of Civil Engineering, Ton Duc Thang University, Ho Chi Minh City, Vietnam*

Correspondence should be addressed to Zaher Mundher Yaseen; zaheryaseen88@gmail.com

Received 30 November 2020; Revised 11 February 2021; Accepted 20 February 2021; Published 8 March 2021

Academic Editor: Mostafa Al-Emran

Accurate and reliable prediction of Perfobond Rib Shear Strength Connector (PRSC) is considered as a major issue in the structural engineering sector. Besides, selecting the most significant variables that have a major influence on PRSC in every important step for attaining economic and more accurate predictive models, this study investigates the capacity of deep learning neural network (DLNN) for shear strength prediction of PRSC. The proposed DLNN model is validated against support vector regression (SVR), artificial neural network (ANN), and M5 tree model. In the second scenario, a comparable AI model hybridized with genetic algorithm (GA) as a robust bioinspired optimization approach for optimizing the related predictors for the PRSC is proposed. Hybridizing AI models with GA as a selector tool is an attempt to acquire the best accuracy of predictions with the fewest possible related parameters. In accordance with quantitative analysis, it can be observed that the GA-DLNN models required only 7 input parameters and yielded the best prediction accuracy with highest correlation coefficient ($R = 0.96$) and lowest value root mean square error (RMSE = 0.03936 KN). However, the other comparable models such as GA-M5Tree, GA-ANN, and GA-SVR required 10 input parameters to obtain a relatively acceptable level of accuracy. Employing GA as a feature parameter selection technique improves the precision of almost all hybrid models by optimally removing redundant variables which decrease the efficiency of the model.

1. Introduction

Steel-concrete composite/hybrid systems have found wide application in several engineering works, due to the recent advancements in structural engineering. In this regard, the shear connector serves as an important component that ensures the development of composite actions by facilitating the shear transfer between the concrete slab and the steel profile [1–3]. At the site, conventional shear connectors (i.e., Nelson stud) are beneficial owing to their high level of automation; meanwhile, they are prone to certain problems, especially, in structures that are subjected to stress [3–5]. When compared with other connectors, Nelson stud somehow exhibits low resistance which can lead to the

design of girders with partial interaction. Considering this fact, many research studies have focused on how to improve the shear connector for hybrid composite systems [6, 7], with the first work dated back to the 1980s. The development of Perfobond, another form of a connector with higher resistance, was reported by Leonhardt, Andra, and Partners in 1987, when working on the third bridge that crossed the Caroni River in Venezuela [3, 6, 8]. A study by Vianna et al. [9] compared the economic costs of steel girders manufacturing using different types of connectors. From the outcome of the study, it was observed that Perfobond connectors are more cost-efficient to be used in the steel-concrete composite. Later, Vianna et al. reported another study on Perfobond and T-Perfobond rib shear connectors in terms of their ductility, resistance, and collapse modes [3]. The results showed that PRSC is both structurally efficient and economical in terms of shear transfer in hybrid and composite structures. Other research studies focused on the numerical and parametric evaluation of PRSC on 40 pushout samples [2, 10]. The study of a simple perforated plate PRSC contains several holes and transverse rebars; the sample also exhibited varying concrete compressive strengths. The study reported two major findings as it involved finite element (FE) method and regression analysis during the prediction of the PRSC shear capacity [11, 12]. Another experimental study on the structural response of PRSC was performed by [4]. The study reported an increase in the resistance of PRSC with increases in the number of holes, and based on this outcome, it was submitted that the resistance and ductility of PRSC can be increased by passing the reinforcement bars through the holes while reducing the upward displacement. Rodrigues and Laím focused on the influence of the holes number, rib holes, and transverse reinforcement, as well as the doubled PRSC at both ambient and high temperatures [6]. From the outcomes, higher temperatures significantly impacted PRSC in terms of its load-carrying capacity, especially the doubled PRSC. The study further showed that transverse reinforcement bars, when present in rib holes, cause a reduction in the capacity of PRSC to carry a load, especially at high temperatures. A parametric study on PRSC shear strength based on the FE method has been reported [13]. The developed model in this study was verified using experimental pushout tests, and from the results, a mathematical model was developed for the estimation of the shear capacity of PRSC. The shear behavior of PRSC has been investigated by [14], under both cyclic and static loadings. Based on the static tests, the results showed the shear capacity of pure concrete-based specimens to be about 65% of that of specimens with both concrete end-bearing zone and concrete dowels. Specimens with transverse rebars in holes exhibited shear capacity of about two times that of specimens with transverse rebars. From the cyclic tests, samples without transverse rebars showed a significant decrease in residual shear capacity compared to that of static shear capacity. Hence, specimens with transverse rebars exhibited residual shear capacity that was almost similar to their static shear capacity.

A parametric study has been reported on the circular-hole and long-hole PRSC [15]. From the outcome of the study, a relationship was established between the failure mode of both long-hole and circular-hole PRSC and the concrete failure. It was also reported that the increase in both height and diameter increases the shear stiffness of PRSC. Steel-concrete decks with PRSC have been investigated for dynamic characteristics in [16, 17]. The study considered PRSC with both normal-weight high-strength concrete and lightweight high-strength concrete. The considered characteristics include the natural frequencies, frequency response functions, and damping ratio; these were evaluated using a nondestructive approach. The experimental outcomes of natural frequencies were also compared using the FE model. From the results, the first mode with a damping ratio of almost 0.5% was found to be the most effective mode for both concrete types. Relying on these studies, it is evident that several factors influence the structural behavior of PRSC. Such factors include end-bearing force, rib spacing, rib arrangement, and concrete compressive strength, as well as the yield and area strength of the transverse rebars [18]. Having identified these factors that govern the behavior of PRSC, it becomes necessary that the resistance of PRSC should be predicted for proper implementation by the decision makers [19, 20]. The quantification of the PRSC resistance based on analytical methodologies has been introduced; however, there are certain limitations of such methods [21].

According to several studies published in the literature, their behavior of PRSC is affected by various contributing factors, including the area and the yield strength of transverse rears, the end-bearing force, the concrete compressive strength, the rib spacing, and the rib arrangement. In addition, several analytical and empirical models were developed to predict the resistance of PRSC; however, it provided undesirable predictions with an increase in calculated errors as well.

The advancements in technology have made computer-aid methods some of the optimistic alternatives for modelling several structural engineering-related problems, and the most famous among them is the artificial intelligence models which are easy, applicable, convenient, and strong predictive models [22–25]. AI models are beneficial as they can solve nonlinear, stochastic, and nonstationary problems that may not be addressed when the classical regression models are used [26–29]. Several AI models have been developed to determine the actual relationship between the predictors and perfobond rib shear strength. For instance, Köroğlu et al. [30] investigated the genetic programming (GP) model for ultimate shear capacity prediction in composite beams with profiled steel sheeting. The study compared the model's accuracy in an ultimate shear capacity prediction of the composite beams to that of the proposed GP model based on the employed test data. From the results, it was submitted that the new GP performed more accurate ultimate shear capacity prediction of the composite beams compared to the building codes. Another study by Ali [31] focused on the prediction of the shear strength of channel shear connectors in a composite beam that consists of concrete and steel sections based on adaptive neuro-fuzzy inference system (ANFIS) and linear regression (LR) which are nonlinear and linear modelling tools, respectively. From the results, ANFIS performed more accurate and precise predictions than LR. Although, there have been several

explorations of AI models for modelling shear strength-related structure and material problems [32, 33]. It can be observed for the existing approaches that the capacity of the used model is mainly influenced by the structure of the used approach and the selection of input parameters. Based on that, introducing a novel approach has capabilities to discover the complex relationship between predictors and target which is very important to increase the prediction precession [34]. Moreover, incorporating that approach with a novel algorithm to select the most important input parameters and accurately predict the Perfobond Rib Shear Strength Connector with high accuracy is very significant for structural engineering.

The research scope of computer aid is still limited, and the exploration of newly developed AI models is still ongoing research motivation. The DLNN model is a newly explored AI version that demonstrates a reliable machine learning model for solving nonlinear regression problems [35–39] and yet to be developed for the PRSC shear strength prediction. The current research is conducted based on the implementation of the deep learning model for predicting PRSC shear strength modelling. Prior to the step, to predict the PRSC shear strength, genetic algorithm is used with the DNN model to select the most important input parameters and then introduce these factors to the adopted approach. The proposed DLNN model is validated against several well-established machine learning models including M5Tree, ANN, and SVR. The investigation is extended with the integration of the genetic algorithm as a robust nature-inspired optimization algorithm for input parameters' selection. The obtained results are assessed and discussed comprehensively.

2. Experimental Dataset Description

To evaluate the shear strength capacity of a Perfobond connector (see Figure 1), data included 90 records related to the shear connector of steel-concrete structures. These records were collected from eight databases published in literature studies. These studies comprised data was collected from [1–5, 10, 40]. The input variables included concrete compressive strength (f_c), area of concrete dowels (A_D), rib holes number (n), area of cross reinforcement bars and yield stress of reinforcement bars ($A_{tr,r}f_{y,r}$), area of cross reinforcement bars and the tensile strength of cross rebar ($A_{tr}f_y$), area of the connector at the end-bearing zone (Ab), the ratio between the thickness of the concrete slab to connector height (b/h_{sc}), connector height (h_{sc}), the contact area between the connector and concrete (A_F), and coefficient of end-bearing force (α). These parameters were entered to the hybrid model to predict shear of Perfobond connector Q_{exp}. The description statistics of the experimental dataset are shown in Table 1. The data were separated into groups: training dataset 85% and testing dataset 15%.

3. Methodology Overview

3.1. Artificial Neural Network (ANN).
In the last few decades, artificial networks, such as neural networks, social networks,
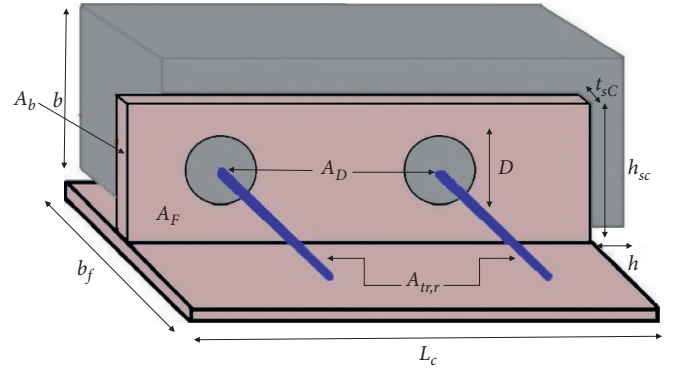
FIGURE 1: The systematic framework of the Perfobond rib shear strength connector.

and other algorithms, have established. The main merit of these technologies is their abilities to predict data and deal with complex systems. Neural network is a mathematical model applied to make the decision in the right way by mimicking the neurons in the biological brain [41]. The construction of a neural network is depending on the connection of several layers called neurons. Feedforward neural network with backpropagation learning algorithm is widely used by researchers. Backpropagation is a common algorithm in neural network applications due to its ability in training the network based on the supervised learning method [42]. In this algorithm, the predicted value is compared with the original variable to compute the error between them. The algorithm modified the weights in the neural network to decrease the error value to a small amount. The structure of the algorithm is explained as follows:

$$N - H_1 - H_2 - \cdots - H_{\text{NHL}} - M, \tag{1}$$

where N represents the input neuron, H is the number of hidden layers in the neural network, and M is the output variable. The construction of a feedforward neural network contains at least an input variable, output, and hidden layer. In this network, the information is transferred in one direction from input to hidden and output layer without loops in the network. The number of input variables and predicted labels are corresponded to the number of neurons in the input and output layer, respectively. Neurons in hidden layers are used for nonlinear transformation of the input variables. Hidden layers in the neural network are calculated by

$$v_i = \left(1 + \exp\left(-1 \times \sum_{i=1}^{1} x_i w_{ij}\right)\right)^{-1}, \tag{2}$$

where v_i refers to the hidden layer, x_i is the input variable, and w_{ij} represents the weight between the layers. The value of the output layer can be computed as below:

$$y = \left(1 + \exp\left(-1 \times \sum_{j=1}^{1} v_j w_{ij}\right)\right)^{-1}. \tag{3}$$

To design the network, a number of nodes and hidden layers are required. Various studies stated that one or two

TABLE 1: Descriptive statistics of experimental data.

	fc	AD	n	$A_{tr,r}f_{y,r}$	$A_{tr}f_y$	$Ab = t_{SC}h_{SC}$	b/h_{SC}	h_{SC}	A_F	α	q_{exp}
Training phase QUOTE hsc											
Max	52.6	9817.48	5	281486.7	876251.51	1950	3.6	150	112993.4	1	774.2
Min	20.91	0	0	0	0	137.5	1.2	25	8831.77	0	13.14
Mean	30.60	3601.63	2.2	33955.61	417272.072	1325.95	1.65	107.16	69384	0.85	387.15
SD	8.84	3100.35	1.37	74153.85	328887.75	566.76	0.84	38.06	31925.45	0.35	181.96
CV	0.28	0.86	0.62	2.18	0.79	0.42	0.51	0.36	0.46	0.42	0.47
Testing phase											
Max	52.6	9817.48	5	281486.7	876251.51	1950	3.6	150	112993.4	1	774.2
Min	26.6	0	0	0	302378.29	612	1.2	102	45500	1	282
Mean	30.07	5628.68	2.86	60056.78	799735.0807	1068.4	1.67	115.06	74868.07	1	505.94
SD	8.84	3646.44	1.85	103972.06	195079.3831	454.23	0.76	17.41	18781.76	0	174.36
CV	0.29	0.65	0.64	1.731	0.243930006	0.43	0.45	0.15	0.25	0	0.34

layers are enough to achieve better prediction performance [43, 44]. The best performance of the training process is based on the good selection of inputs' network. During this process, the relations between inputs and outputs are designed by the neural network. In every iteration phase, the modification of weights and biases is done by decreasing the error measure between actual and predicted outcomes. The error between actual and predicted values is presented below:

$$Error = 0.5 (d - y)^2, \quad (4)$$

where d represents the real value and y is the estimated value obtained from the algorithm. In this study, one hidden layer was used with sigmoid activation function due to its validity in the regression process. Figure 2 shows the structure of the neural network.

3.2. Deep Learning Neural Networks (DLNN).

Recently, the study of neural network application is based on the concept of deep learning technique. The structure of deep neural network is an extension of classical neural network with the addition of extra hidden layer(s) to the network. Deep learning was introduced by Hinton et al. through proposing the layerwise greedy-learning method. By this method, the neural network is pretrained by unsupervised learning technique before the training process layer by layer. Deep learning technique is popular due to two reasons: (i) developing of huge technical data, which can solve the problem of overfitting and (ii) assigning of nonrandom value to the neural network before the unsupervised learning process [45]. Thus, better performance can be reached after the training phase. There are various types of deep learning tools, and in this study, the backpropagation neural network was used.

This approach is used in many types of application, the same multihidden layers' approach, and trained via backpropagation with gradient descent algorithm. The network contains input, output, and large numbers of neurons and hidden layers. The algorithm is worked based on the connection between the first layer and hidden layers which leads to yielding of a new variable that is transferred to the output layer. Then, the output layer predicts the result of the process. The specific thing in deep learning is the nonlinear
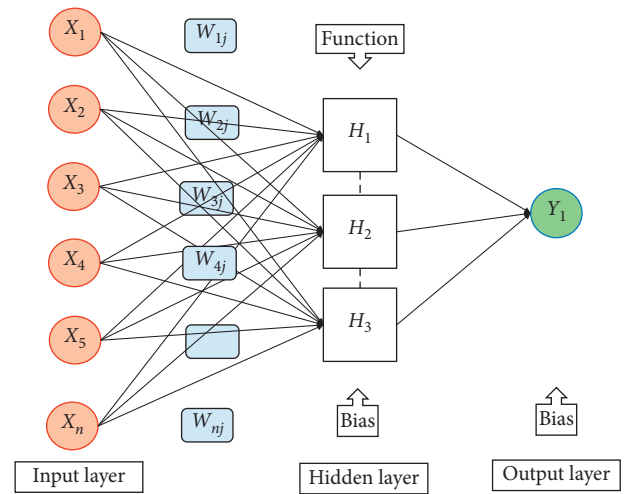
FIGURE 2: The schematic structure of the applied ANN predictive model.

relations between the multiple layers in the network that gave them the ability to deal with different nonlinear functions. This deep network can recognize complex patterns used in a complicated process. Figure 3 describes the general structure of a deep neural network with input, output, and multiple hidden layers. The mathematical process can be discussed as follows:

$$M^I = f\left(w^I \varphi^{I-1} + b^I\right), \quad \text{for } 0 < I < L, \quad (5)$$

where f represents the activation function, w is the weight matrix and, b is the bias. The input variable is denoted by 0 layer and L represents the output layer. In this research, hyperbolic tangent function is utilized as an activation function due to its ability to obtain better performance in the study problem.

3.3. M5 Rule Model.

M5 rule algorithm was developed by Holmes et al. [35] to forecast the numeric and nominal data. Building of the M5 rule is based on M5 tree by using the trees to build the model. The popular technique of M5 Model Tree (MT) works with classification cum regression principle. MT propounded by Quinlan [46] divides the complete domain
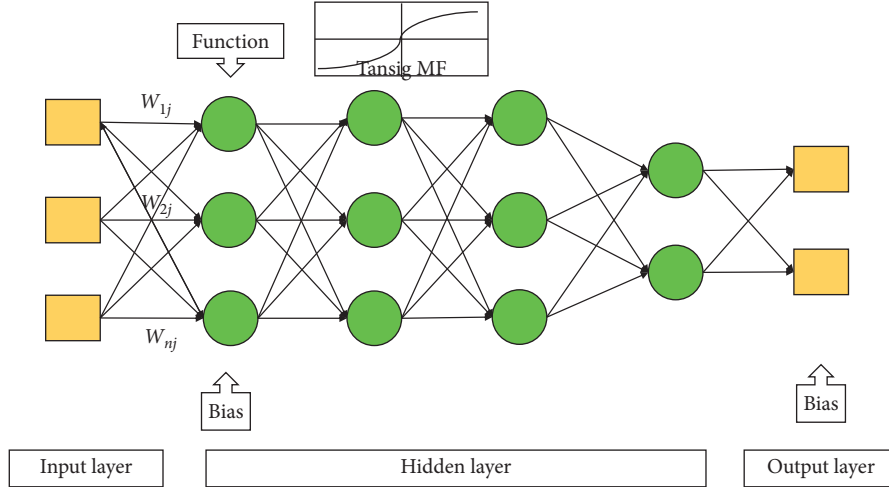
FIGURE 3: The systematic structure of the developed DLNN model.

into many subdomains, and multiple linear regression models are developed for each of them. In this case, nonlinear input-output relationships are approximated by a number of linear models.

Rule generation depended on the partial and regression tree (PART) model developed by [47]. The work of the algorithm depends on iterating model constructing and choosing the rule which has a good result at each iteration. In the training phase, the M5 model is applied, and then, the best leaf is chosen as a rule. The process continues until all instances are tested and utilized by the rules. The main merit in this approach is that the algorithm builds full trees and develops a small amount of dataset at the testing phase [48, 49]. In the first stage, in the development of the MT model, a decision tree is developed following a division criterion. Based on the criterion used for dividing the domain, a number of variants of model trees are available, and the one which follows standard deviation reduction (SDR) as the criterion is known as an M5 Model Tree [42, 43]. The SDR quantifies the reduction in error at each node while testing of attributes, and its computation can be made as follows:

$$\sigma^R = \sigma(N) - \sum \frac{|T_i|}{|N|} \sigma(T_i),\qquad(6)$$

where σ^R = standard deviation reduction, N is the number of training samples, T_i is the training samples of ith subdomain, and = $\sigma(N)$ and $\sigma(T_i)$ are the SDs of total samples and ith subdomain sample. The resulting model for the subdomain can be represented as $O = a_0 + a_1 x_1 + a_2 x_2 + \cdots$, where O is the output, $a_1, a_2 \ldots$ are the coefficients of linear regression, and $x_1, x_2 \ldots$ are the inputs. The procedure of computation is illustrated in Figure 4, which shows the division to the number of subdomains followed by development of different models considering x_1 and x_2 as inputs.

The partitioning process should be continued till the variation in the class values of all the instances that are associated with a node becomes negligible. Then, the models are refined by the "pruning" and "smoothing" processes, which may help to alleviate the "overfitting" and abrupt

changes between individual subclasses [50]. The complete theoretical description of M5 model trees is available in literature [43, 51]. This method does not demand any control parameter settings, while on the contrary, its application results in more user friendly linear models [45, 48].

3.4. Support Vector Regression (SVR).
Support vector regression has been developed by [52] as an algorithm based on using a hyperplane to separate a dataset and calculate the distance from the hyperplane and the nearest variable. In recent year, SVR algorithm has been intensively used by many researchers for solving different engineering problems and shown better prediction than other machine learning algorithms [53, 54]. SVR estimates the error between the input and output variable in the regression process by computing the distance from SVR margin. The mathematical expression of the SVR model is shown as follows:

$$M = \{x_1, y_1), x_2, y_2), \ldots, x_n y_n),\qquad(7)$$

where M denotes the dataset training and x and y represent the input and output variables. The SVR function that applied to the training dataset is

$$f(x) = w \cdot \varphi(x) + b,\qquad(8)$$

where w represents the weight vector and $\varphi(x)$ refers to the high dimension of input space, whereas b represents the scalar vector. In the regression problem, error deviation can be calculated by the following optimization algorithm:

$$\min \varphi(w, \xi) = 0.5w^2 + C\left(\sum_{i=1}^{n} \xi_i\right)\varphi(x_i) + b \qquad(9)$$

$$\text{subjected to} \quad M_i\left(w^M x_i + b\right) \geq 1 - \xi_i,\ \xi \geq 0,$$

where ξ represents the slag variable and C is equal to the error between regularization and empirical error. To optimize the SVR model, Lagrange multipliers and sequential minimal optimization were used. Figure 5 illustrates SVR regression with ε-insensitive loss function. In this study, the predicted
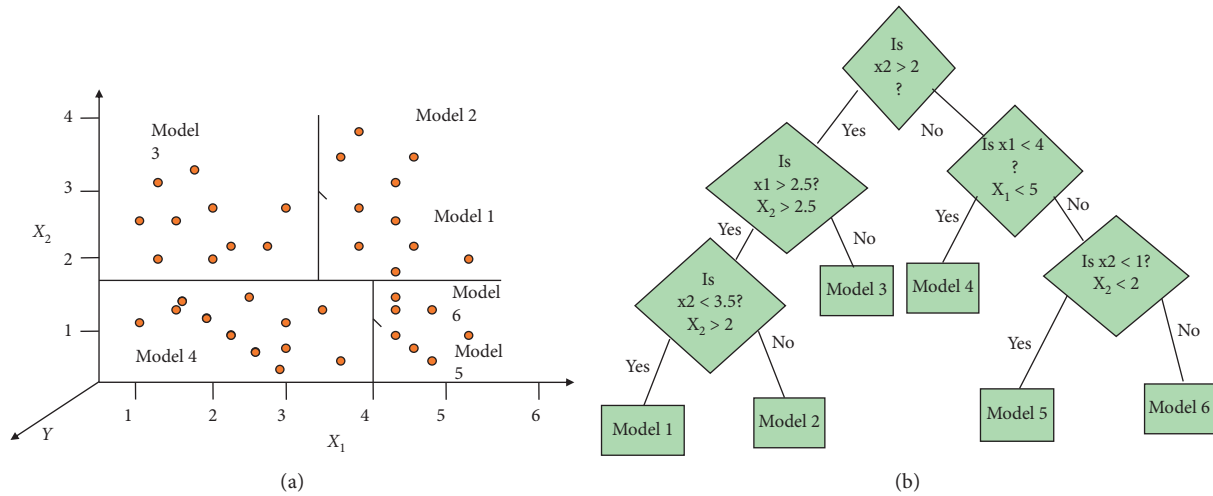
FIGURE 4: The systematic structure of M5 Tree modelling approach.
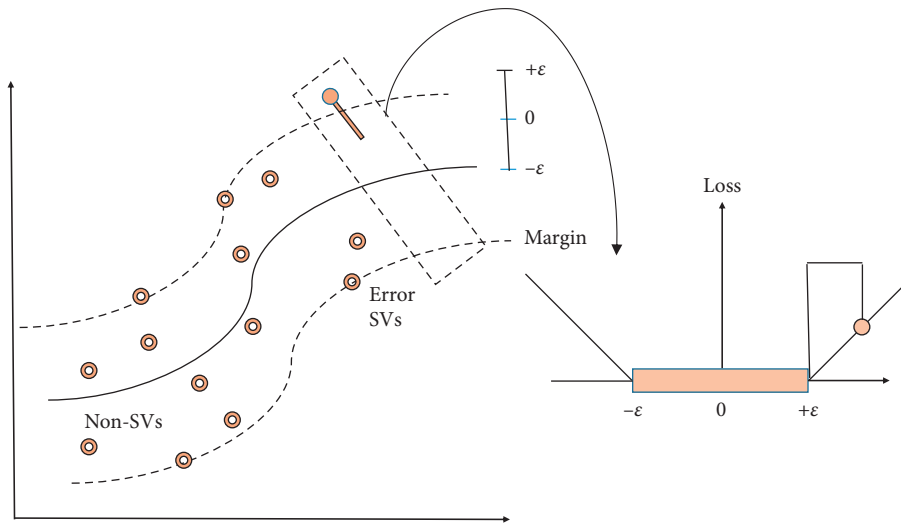
FIGURE 5: A basic structure of the SVR model and calibrating data points with ε-insensitive loss function.

problem is characterized by a nonlinear relationship between input and output variables, in which the nonlinear mapping of SVR can be suitable to calculate the data correlation. In the SVR model, 4 kernel functions can be used for nonlinear mapping during the training phase. These kernels include linear, sigmoid, polynomial, and radial basis functions [53]. Radial basis function is applied due to its efficiency and ability to deal with complex regression problems [55].

3.5. Hybridized Genetic Algorithm (GA) with AI Models. Genetic algorithm is an evolutionary algorithm used to optimize solutions in complicated systems by finding on biological selections [56]. GA has been employed in various research areas such as pattern recognition, image processing, and control system [57]. In several research studies in engineering and science applications, GA demonstrated a reliable method in feature selection than other selection tools [58, 59]. The efficiency of GA can be

discussed by its ability to explore the search space and concentration on the global optimization which led to a better investigation, utilizing the search space. The main idea included the application of natural selection, such as the creation of chromosomes, crossover, and mutation in solving complex processes. These processes are employed to reduce the features which are transferred to binary string [60, 61].

There are three main phases at natural selection (see Figure 6). Firstly, use crossover to produce offspring, then mutation may occur to the generated individuals and, finally, the fittest individual is selected. The first step in genetic programming is the population initialization. In this step, many individuals are generated randomly. Then, the fittest individual is chosen to produce the offspring. This phenomenon can be applied for search space. We produce many solutions to the study problem and the best solution is selected from them. In this study, a genetic algorithm is employed to choose the highly correlated
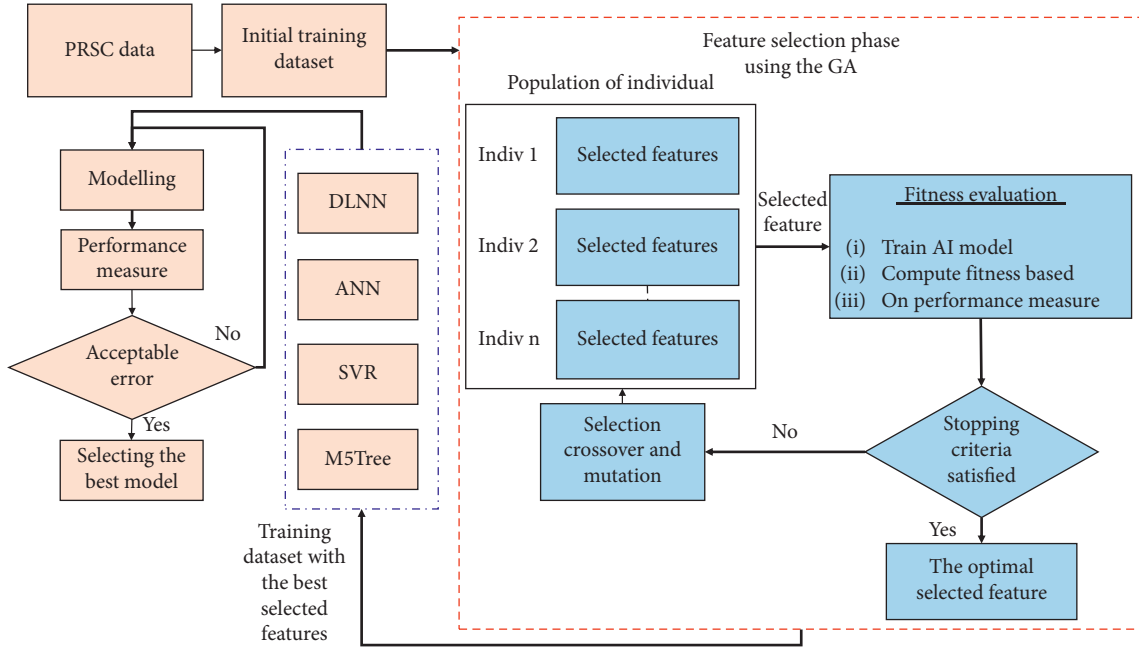
FIGURE 6: Process of selecting best input variables of each AI modelling using GA algorithm.

variables and the process is begun from two variables. Then, the models ANN, DLNN, SVR, and M5 rule are applied [62, 63].

3.6. Performance Metrics. In order to select the best predictive modelling approaches, five statistical indicators are used in this study which are root mean square error (RMSE), mean absolute (MAE), mean absolute percentage error (MAPE), relative root mean squared error (RRMSE), relative error (RE), mean relative error (MRE), Nash–Sutcliffe efficiency (NSE), and BIAS. The mathematical expressions of these measures can be seen below [64–66]:

$$RMSE = \sqrt{\frac{1}{N} \sum_{i=1}^{N} \left(Q_{i\,exp} - Q_{ipre} \right)^2},$$

$$MAE = \frac{1}{N} \sum_{i=1}^{n} \left| \left(Q_{i\,exp} - Q_{ipre} \right) \right|,$$

$$MAPE\% = \frac{1}{N} \sum_{i=1}^{n} \left| \frac{\left(Q_{i\,exp} - Q_{ipre} \right)}{Q_{i\,exp}} \right| * 100,$$

$$RRMSE = \frac{\sqrt{(1/N) \sum_{i=1}^{n} \left(Q_{i\,exp} - Q_{ipre} \right)^2}}{\sum_{I=1}^{N} Q_{i\,exp}},$$

$$BIAS = \frac{1}{N} \sum_{i=1}^{N} \left| \left(Q_{i\,exp} - Q_{ipre} \right) \right| * 100,$$

$$NSE = 1 - \left[\frac{\sum_{i=1}^{n} \left(Q_{i\,exp} - Q_{ipre} \right)^2}{\sum_{i=1}^{n} \left(Q_{i\,exp} - \overline{Q_{exp}} \right)^2} \right],$$

$$RE\% = 100 * \frac{Q_{i\,exp} - Q_{ipre}}{Q_{i\,exp}},$$

$$MRE\% = \frac{100}{N} \sum_{i=1}^{N} \left| \frac{Q_{i\,exp} - Q_{ipre}}{Q_{i\,exp}} \right|,$$

(10)

where $Q_{i\,exp}$ and Q_{ipre} are the observed and predicted ith values of PRSC capacity, $\overline{Q_{exp}}$ represents the average values of PRSC, and N is the total number of experimental samples. In this regard, eight statistical measures have been used to assess the performances of the adopted models. The mentioned measures are commonly used to assess the efficiency of AI models, including statistical parameter (i.e., RMSE and MAE) used for evaluating the forecasted error between actual and predictive values. Besides, the other measures such as NSE are employed to compute the degree of correlation between the predictive and actual points.

4. Results and Discussion

This section describes the results obtained from standard AI models according to all available data. The other scenario of this part of the study shows the incorporation of genetic algorithm as a tool used for selecting the most significant input parameters for adopted AI models. In both scenarios, the performance of each model is assessed based on quantitative assessment, using different statistical criteria, and visualized assessments, using different plots and figures.

4.1. First Scenario: Applying the Standard Models. The motivation of this current study is to accurately predict the shear strength of PRSC using different AI modelling approaches, including DLNN, SVR, ANN, and M5 Tree. In this

scenario, all mentioned predictive models have been established based on ten predictors (f_c, A_Dn, $A_{tr,r}f_{y,r}$, $A_{tr}f_y$, Ab, b/h_{sc}, connector height h_{sc}, A_F, and α). The collected experimental samples were divided into two sets, during the stage of developed standalone AI models. The majority of samples (85%) were used for modelling construction, whereas the rest was used for validation purposes. In order, to evaluate the performance accuracy of each modelling technique separately, ten statistical metrics were used, including correlation measures and error measures. Simulated results obtained by four predictive models for both training and testing stages were illustrated in Table 2. It can be clearly seen that all models during the training stage yielded unpromising accuracy except DLNN models which provided the best accuracy of predictions and produced the highest values of NSE (0.957) and the lowest values of RMSE (0.047 KN), MAE (0.033 KN), and RMSRE (0.914). However, the testing phase is the most important stage in the evaluation of the accuracy of the predictive models. According to Table 2, the superiority of DLNN over other AI models can be easily observed during the testing phase. Moreover, DLNN models generated the highest accuracy of predicted shear strength values with the shortest magnitudes of RMSE (0.045 KN), MAE (0.020 KN), RRMSE (0.092), and the highest values of NSE (0.888).

To evaluate the performance of each developed model during the testing phase in a more rigorous way, several graphical visualizations were established including scatter plots, relative error plots, and Taylor diagram. The scatter plot is considered a very important figure in the evaluation of the variance between the predicted and the actual shear strength values. Based on Figure 7, DLNN modes presented less scatter and recorded a higher value of correlation coefficient ($R = 0.96$) than the other comparable models (R of 0.95, 0.95, and 0.94, respectively, for M5Tree, ANN, and SVR). Besides, among all AI models, the DLNN modelling approaches produced fewer relative error percentages (see Figure 8). Figure 8 clearly indicates that except for one sample (sample 12), the relative error of predictions by DLNN is ±20% indicating a success rate of 92%, while by other AI methods, multiple samples surpass the relative error limits of even 40%.

For better visual comparison, the Taylor diagram was established because it can summarize different statistical measures (correlation coefficient and standard deviation) in one figure thereby, facilitating the process of selecting the best model accuracy.

Taylor diagrams are polar plots that present the similarity between observed and predicted data based on the correlation coefficient and standard deviation in a 2D plane. From Figure 9, it is evident that the point corresponding to DLNN predictions is the closest to the point corresponding to the observed dataset, indicating the best performance by the standalone DNN model, i.e., DLNN generated more accurate predicted values and closer to the actual ones. Based on the mentioned result, DLNN models showed better generalization capabilities in comparison with the other AI models during training and testing phases. Conversely, SVR modelling approach exhibited the lowest level of prediction accuracy in comparison with all AI predictive models.

4.2. Second Scenario: Applying the Hybrid Models.
This section of the paper investigates the capability of using GA as a bioinspired algorithm for assisting the four AI models in selecting the best combination of input parameters, which importantly affects the PRSC. As the AI models can efficiently learn from the behavior of the datasets, it is very essential to minimize the model complexity. Thus, any improvement in the model performance with the use of minimal input parameters can be considered as economical in the modelling process. With this objective, the potential of GA was used for developing hybrid models with different AI methods in this study. Accordingly, eight different combination models were developed by hybridizing different AI methods with GA (GA-ANN, GA-SVR, GA-DLNN, and GA-M5Tree. The model combinations for different hybrid methods were designated as M1 to M8 in this paper, whereas the number of input parameters varied from 2 to 9 as presented in Tables 3–6.

The performance of prediction abilities over the training and the testing phases for the hybrid models are summarized in Tables 7–10. The most remarkable note can be observed that the GA improved the performance of the most predictive models in comparison with pure AI models, which have been carried out in the first scenario of this paper. For instance, the hybrid (GA-M5Tree-M8) recorded good accuracy of predictions compared with standard (M5Tree) model and the statistical measures, such as RMSE and MAE reduced by 8.55% and 3.77%, respectively, during the testing phase. The robustness of GA in properly selecting the optimal input parameters can be clearly seen when GA-M5Tree-M6 (with seven parameters) model generated slightly higher predicting accuracy than standard M5Tree model (with ten input variables). For more comparative analysis, GA-ANN-M6 (with 7 input variables) performed better than the best standalone DLNN and GA-M5Tree-M6, respectively. With respect to SVR-GA models, they were slightly improved in comparison with standard SVR. Moreover, all these GA-SVR models (8 models) showed the lowest accuracy and none of them could outperform the standard DLNN. On top of that, GA-SVR models scored the highest values of relative error (ranging from 20.25 to 25.44%) in comparison with other modelling approaches. Although all GA-SVR models performed the lowest accuracy of performances in comparison with other hybrid models in this scenario, they also showed lower prediction accuracy than standard SVR models which have been carried out in the first scenario. Therefore, it can be concluded that there was no specific advantage in the hybridization of SVR with GA for this problem and dataset. On the contrary, the hybridization of GA with DLNN provided more excellent predicted results than all standalone models which performed in the first scenario.

Among the different hybrid DLNN models, the hybrid GA-DLNN- M6 model performed very well (with NSE of 0.914, RMSE of 0.039 KN, MAPE of 0.052, and MAE of 0.021 KN). Furthermore, it was noted that very fewer bias indicators were generated in GA-DLNN-M6, GA-DLNN-M7, and GA-DLNN-M8 (−0.0004, -0.0004, and -0.01) than standalone DLNN model (-0.011). It was evident that GA-based hybrid models can improve the performance when

TABLE 2: The performance prediction skills for the standalone predictive models over the training and testing phase.

AI model	MAPE	RMSE (KN)	MAE (KN)	RRMSE (KN)	MRE	BIAS	NSE
Training phase							
DLNN	0.173	0.047	0.033	0.914	0.163	−0.026	0.957
M5Tree	0.636	0.089	0.064	4.176	0.528	0.000	0.848
ANN	0.283	0.090	0.065	1.312	0.178	0.000	0.845
SVR	1.235	0.108	0.086	8.377	1.120	0.000	0.776
Testing phase							
DLNN	0.047	0.045	0.020	0.093	0.027	−0.011	0.888
M5Tree	0.062	0.047	0.023	0.129	0.041	−0.005	0.880
ANN	0.064	0.047	0.023	0.130	−0.009	−0.003	0.878
SVR	0.096	0.052	0.023	0.252	0.096	−0.007	0.853
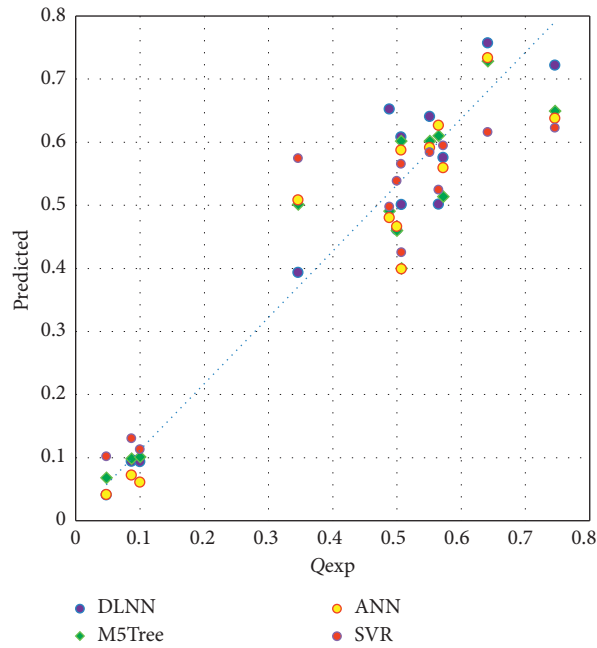
FIGURE 7: The scatter plots graphical presentation over the testing modelling phase: classical AI models.
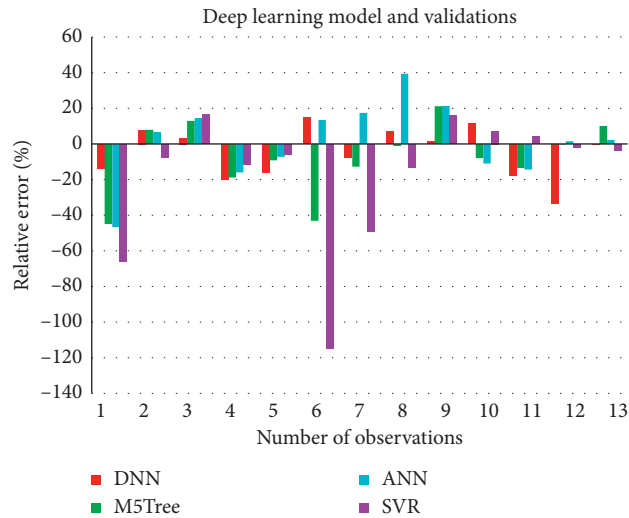
FIGURE 8: Relative error distribution for each AI approach: testing phase.

0.1 0.2 0.3 0.4 0.5 0.6 0.7 0.8 0.9 0.95 0.99

1.5 1.0 0.5 0.0

1.5 1 0.5

Correlation

Standard deviation (normalized)

0.0 0.5 1.0 1.5

Standard deviation (normalized)

- DLNN
- M5TRree
- ANN
- SVR
- Actual
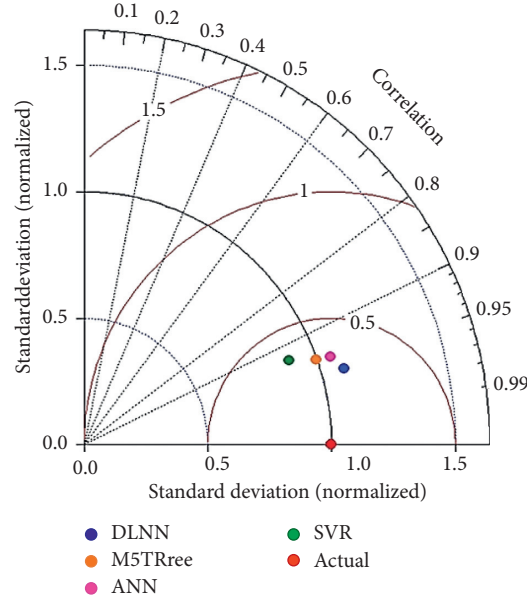
FIGURE 9: Taylor diagram graphical presentation over the testing modelling phases: classical AI models.

TABLE 3: The abstraction of the influential input parameters using GA-DLNN for building the prediction process for the shear strength.

Inputs	Models
2	M_1: $Q_{exp} = f(A_D, \alpha)$
3	M_2: $Q_{exp} = f(A_D, A_F, \alpha)$
4	M_3: $Q_{exp} = f(A_D, n, A_{tr,r} f_{y,r}, \mathbf{h}_{SC})$
5	M_4: $Q_{exp} = f(A_D, n, A_{tr,r} f_{y,r}, \mathbf{h}_{SC}, \alpha)$
6	M_5: $Q_{exp} = f(A_D, n, A_{tr,r} f_{y,r}, A_{tr} f_y, Ab = t_{SC}\mathbf{h}_{SC}, A_F)$
7	M_6: $Q_{exp} = f(f_c, n, A_{tr,r} f_{y,r}, A_{tr} f_y, b/h_{SC}, h_{SC}, \alpha)$
8	M_7: $Q_{exp} = f(f_c, A_D, A_{tr,r} f_{y,r}, A_{tr} f_y, b/h_{SC}, h_{SC}, A_F, \alpha)$
9	M_8: $Q_{exp} = f(f_c, n, A_{tr,r} f_{y,r}, A_{tr} f_y, Ab = t_{SC}\mathbf{h}_{SC}, b/h_{SC}, h_{SC}, A_F, \alpha)$

TABLE 4: The abstraction of the influential input parameters using GA-M5tree for building the prediction process for the shear strength.

Inputs	Combinations
2	M_1: $Q_{exp} = f(A_D, \alpha)$
3	M_2: $Q_{exp} = f(A_D, A_F, \alpha)$
4	M_3: $Q_{exp} = f(f_C, n, A_{tr} f_y, A_F)$
5	M_4: $Q_{exp} = f(A_D, n, A_{tr,r} f_{y,r}, \mathbf{h}_{SC}, \alpha)$
6	M_5: $Q_{exp} = f(A_D, n, A_{tr,r} f_{y,r}, b/\mathbf{h}_{SC}, A_F, \alpha)$
7	M_6: $Q_{exp} = f(f_c, A_D, A_{tr,r} f_{y,r}, A_{tr} f_y, Ab = t_{SC}\mathbf{h}_{SC}, \mathbf{b}/h_{SC}, h_{SC})$
8	M_7: $Q_{exp} = f(f_c, n, A_{tr,r} f_{y,r}, A_{tr} f_y, b/h_{SC}, h_{SC}, A_F, \alpha)$
9	M_8: $Q_{exp} = f(f_c, n, A_{tr,r} f_{y,r}, A_{tr} f_y, Ab = t_{SC}\mathbf{h}_{SC}, b/h_{SC}, h_{SC}, A_F, \alpha)$

TABLE 5: The abstraction of the influential input parameters using GA-ANN for building the prediction process for the shear strength.

Inputs	Combinations
2	M_1: $Q_{exp} = f(A_D, \mathbf{Ab} = t_{sc} h_{sc})$
3	M_2: $Q_{exp} = f(A_D, A_{tr,r}, f_{y,r}, \alpha)$
4	M_3: $Q_{exp} = f(n, A_{tr,r} f_{y,r}, \mathbf{Ab} = t_{sc} h_{sc}, h_{sc})$
5	M_4: $Q_{exp} = f(f_c, A_D, n, A_{tr,r} f_{y,r}, \mathbf{h}_{sc})$
6	M_5: $Q_{exp} = f(f_C, n, A_{tr,r} f_{y,r}, A_{tr} f_y, \mathbf{Ab} = t_{SC} h_{SC}, h_{SC})$
7	M_6: $Q_{exp} = f(f_C, n, A_{tr,r} f_{y,r}, A_{tr} f_y, Ab = t_{SC}\mathbf{h}_{SC}, A_F, \alpha)$
8	M_7: $Q_{exp} = f(f_c, A_D, n, A_{tr,r} f_{y,r}, A_{tr} f_y, b/h_{SC}, A_F, \alpha)$
9	M_8: $Q_{exp} = f(f_c, A_D, n, A_{tr,r} f_{y,r}, A_{tr} f_y, Ab = t_{SC}\mathbf{h}_{SC}, b/h_{SC}, h_{SC}, \alpha)$

Table 6: The abstraction of the influential input parameters using GA-SVR for building the prediction process for the shear strength.

Inputs	Combinations
2	M_1: $Q_{\exp} = f(A_D, \alpha)$
3	M_2: $Q_{\exp} = f(f_c, A_D, A_F)$
4	M_3: $Q_{\exp} = f(A_{tr,r}f_{y,r}, A_{tr}f_y, b/h_{SC}, h_{sc})$
5	M_4: $Q_{\exp} = f(f_c, A_D, n, A_{tr}f_y, Ab = t_{SC}\mathbf{h}_{SC}, \alpha)$
6	M_5: $Q_{\exp} = f(f_c, A_D, A_{tr,r}f_{y,r}, A_{tr}f_y, A_F, \alpha)$
7	M_6: $Q_{\exp} = f(f_c, n, A_{tr,r}f_{y,r}, A_{tr}f_y, Ab = t_{SC}\mathbf{h}_{SC}, b/h_{SC}, \alpha)$
8	M_7: $Q_{\exp} = f(f_c, A_D, A_{tr,r}f_{y,r}, A_{tr}f_y, Ab = t_{SC}\mathbf{h}_{SC}, \mathbf{h}_{SC}, A_F, \alpha)$
9	M_8: $Q_{\exp} = f(f_c, n, A_{tr,r}f_{y,r}, A_{tr}f_y, Ab = t_{SC}\mathbf{h}_{SC}, b/h_{SC}, h_{SC}, A_F, \alpha)$

Table 7: The performance prediction skills for the hybrid GA-DLNN predictive model over the training and testing phases.

	MAPE	RMSE (kN)	MAE (kN)	RRMSE (kN)	MRE	BIAS	NSE
Training phase							
GA-DLNN-M1	0.675	0.123	0.094	4.025	0.506	−0.006	0.710
GA-DLNN-M2	1.099	0.122	0.097	7.470	0.955	−0.001	0.714
GA-DLNN-M3	0.823	0.115	0.089	5.415	0.693	−0.002	0.746
GA-DLNN-M4	0.414	0.110	0.086	2.100	0.275	0.005	0.766
GA-DLNN-M5	0.862	0.102	0.074	6.117	0.734	0.002	0.800
GA-DLNN-M6	0.519	0.086	0.064	3.388	0.407	0.001	0.859
GA-DLNN-M7	0.501	0.086	0.064	3.079	0.374	−0.001	0.859
GA-DLNN-M8	0.239	0.046	0.030	1.462	0.228	−0.022	0.959
Testing phase							
GA-DLNN-M1	0.117	0.084	0.039	0.256	−0.018	−0.004	0.611
GA-DLNN-M2	0.097	0.078	0.034	0.222	0.037	−0.005	0.663
GA-DLNN-M3	0.081	0.071	0.032	0.187	0.051	−0.006	0.718
GA-DLNN-M4	0.059	0.064	0.027	0.160	0.028	−0.005	0.776
GA-DLNN-M5	0.054	0.051	0.024	0.121	0.021	−0.003	0.858
GA-DLNN-M6	0.052	0.039	0.021	0.087	−0.013	0.000	0.914
GA-DLNN-M7	0.044	0.042	0.020	0.090	0.010	0.000	0.903
GA-DLNN-M8	0.042	0.040	0.019	0.082	0.011	−0.007	0.912

Table 8: The performance prediction skills for the hybrid GA-M5Tree predictive model over the training and testing phases.

	MAPE	RMSE (kN)	MAE (kN)	RRMSE (kN)	MRE	BIAS	NSE
Training phase							
GA-M5Tree-M1	0.674	0.121	0.095	4.023	0.522	0.000	0.718
GA-M5Tree-M2	0.319	0.123	0.095	0.978	0.153	0.006	0.706
GA-M5Tree-M3	0.409	0.111	0.086	1.350	0.275	0.000	0.762
GA-M5Tree-M4	1.365	0.123	0.096	9.442	1.221	0.000	0.710
GA-M5Tree-M5	0.465	0.115	0.090	2.353	0.323	0.000	0.743
GA-M5Tree-M6	0.636	0.089	0.064	4.176	0.528	0.000	0.848
GA-M5Tree-M7	1.178	0.110	0.087	8.547	1.018	−0.002	0.765
GA-M5Tree-M8	0.769	0.094	0.069	5.262	0.637	−0.001	0.830
Testing phase							
GA-M5Tree-M1	0.097	0.079	0.035	0.227	−0.006	−0.002	0.653
GA-M5Tree-M2	0.114	0.085	0.039	0.246	−0.031	0.003	0.605
GA-M5Tree-M3	0.107	0.080	0.041	0.208	0.004	−0.003	0.650
GA-M5Tree-M4	0.134	0.083	0.039	0.306	0.104	−0.006	0.616
GA-M5Tree-M5	0.072	0.073	0.030	0.188	0.044	−0.006	0.705
GA-M5Tree-M6	0.062	0.047	0.023	0.129	0.041	−0.005	0.880
GA-M5Tree-M7	0.096	0.063	0.028	0.236	−0.027	−0.005	0.781
GA-M5Tree-M8	0.071	0.043	0.024	0.129	−0.005	−0.004	0.900

hybridized with DLNN, NN, and M5 Model Tree with a fewer number of input parameters for this dataset. Moreover, the GA-DLNN-M6 was considered very simply when compared to the other models because fewer input parameters are needed, and it can achieve a significant improvement compared to the standard DLNN, in which the RMSE and the RMSRE reduced by 12.62% and 6.06%, respectively, whereas the NSE was increased by 2.98%. The superiority of this model (GA-DLNN) did not only appear in comparison to simple models, but also appeared when compared to hybrid models

TABLE 9: The performance prediction skills for the hybrid GA-ANN predictive model over the training and testing phases.

	MAPE	RMSE (kN)	MAE (kN)	RRMSE (kN)	MRE	BIAS	NSE
Training phase							
GA-ANN-M1	1.895	0.127	0.098	13.468	1.733	0.000	0.687
GA-ANN-M2	0.622	0.117	0.096	3.617	0.469	0.000	0.734
GA-ANN-M3	0.529	0.124	0.098	2.162	0.378	0.000	0.705
GA-ANN-M4	1.218	0.112	0.085	8.436	1.089	0.000	0.758
GA-ANN-M5	0.311	0.095	0.069	1.374	−0.105	0.000	0.826
GA-ANN-M6	0.701	0.093	0.070	4.675	−0.518	0.000	0.833
GA-ANN-M7	0.204	0.099	0.079	0.454	0.078	0.000	0.811
GA-ANN-M8	0.209	0.091	0.066	0.690	0.102	0.000	0.842
Testing phase							
GA-ANN-M1	0.167	0.094	0.045	0.400	0.137	−0.007	0.514
GA-ANN-M2	0.077	0.073	0.030	0.190	0.016	−0.003	0.706
GA-ANN-M3	0.106	0.076	0.033	0.247	0.088	−0.008	0.685
GA-ANN-M4	0.104	0.074	0.034	0.241	0.066	−0.005	0.696
GA-ANN-M5	0.066	0.051	0.026	0.125	0.001	−0.005	0.857
GA-ANN-M6	0.083	0.044	0.024	0.181	−0.035	−0.003	0.893
GA-ANN-M7	0.072	0.049	0.024	0.149	−0.018	−0.002	0.867
GA-NN-M8	0.065	0.048	0.023	0.133	−0.008	−0.004	0.874

TABLE 10: The performance prediction skills for the hybrid GA-SVR predictive model over the training and testing phases.

	MAPE	RMSE (kN)	MAE (kN)	RRMSE (kN)	MRE	BIAS	NSE
Training phase							
GA-SVR-M1	4.123	0.154	0.132	30.498	3.949	−0.002	0.544
GA-SVR-M2	5.964	0.169	0.135	44.736	5.805	−0.016	0.447
GA-SVR-M3	3.415	0.159	0.134	25.019	3.225	0.010	0.513
GA-SVR-M4	2.398	0.122	0.102	17.574	2.250	0.008	0.713
GA-SVR-M5	2.621	0.122	0.103	19.240	2.487	−0.003	0.713
GA-SVR-M6	1.689	0.121	0.100	11.560	1.551	0.005	0.715
GA-SVR-M7	1.691	0.111	0.087	12.229	1.575	0.000	0.760
GA-SVR-M8	1.483	0.122	0.099	9.990	1.349	0.003	0.712
Testing phase							
GA-SVR-M1	0.312	0.086	0.041	0.972	0.379	−0.018	0.589
GA-SVR-M2	0.465	0.112	0.049	1.525	0.593	−0.028	0.306
GA-SVR-M3	0.269	0.071	0.038	0.822	0.320	−0.014	0.719
GA-SVR-M4	0.157	0.054	0.026	0.471	0.176	−0.008	0.841
GA-SVR-M5	0.185	0.057	0.029	0.558	0.217	−0.011	0.822
GA-SVR-M6	0.148	0.050	0.026	0.413	0.164	−0.008	0.859
GA-SVR-M7	0.115	0.051	0.025	0.310	0.118	−0.007	0.854
GA-SVR-M8	0.124	0.050	0.024	0.340	0.138	−0.009	0.863

(GA-SVR, GA-ANN, and GA-M5Tree). Generally, the best input parameters improved the models comprising f_c, n, $A_{tr,r} f_{y,r}$, $A_{tr} f_y$, b/h_{sc}, h_{sc}, and α. These input combinations are considered the most efficient parameters which significantly affect the PRSC.

For visualization assessment, scatter plots for each hybrid model were shown in Figures 10–13. These figures are very important in evaluating the performance of each predictive model. Besides, the best model should be established based on fewer input variables as well as generating predicted values with less diversion from the actual ones. It can be seen from these figures that GA-DLNN-M6 produced the highest accuracy performance with R of 0.96 with respect to other hybrid models, they generated lower accuracy of performances, and, in most cases, they required many input parameters to gain slight improvements.

Figure 14 portrays more concrete and convincing statistical relationship between the forecasted and the actual shear strength, using the Taylor diagram. A visual comparison of the four plots shows that the points corresponding to the high-end hybrid models M6–M8 resulted in points closer to the point corresponding to the actual data. Among these models, M6 (7 input model) lies much closer except for the SVR-based hybrid model. Also, it is clearly evident that the GA-DLNN-M6 hybrid model recorded the closer predicted values to the actual ones. This also supported the selection of the adopted model (GA-DLNN-M6), which has been considered in this study, and its assessment was very consistent with other quantitative and visualized assessments which performed previously. Furthermore, it can be noted that the GA-DLNN-M6 model presented fewer input parameters with the best
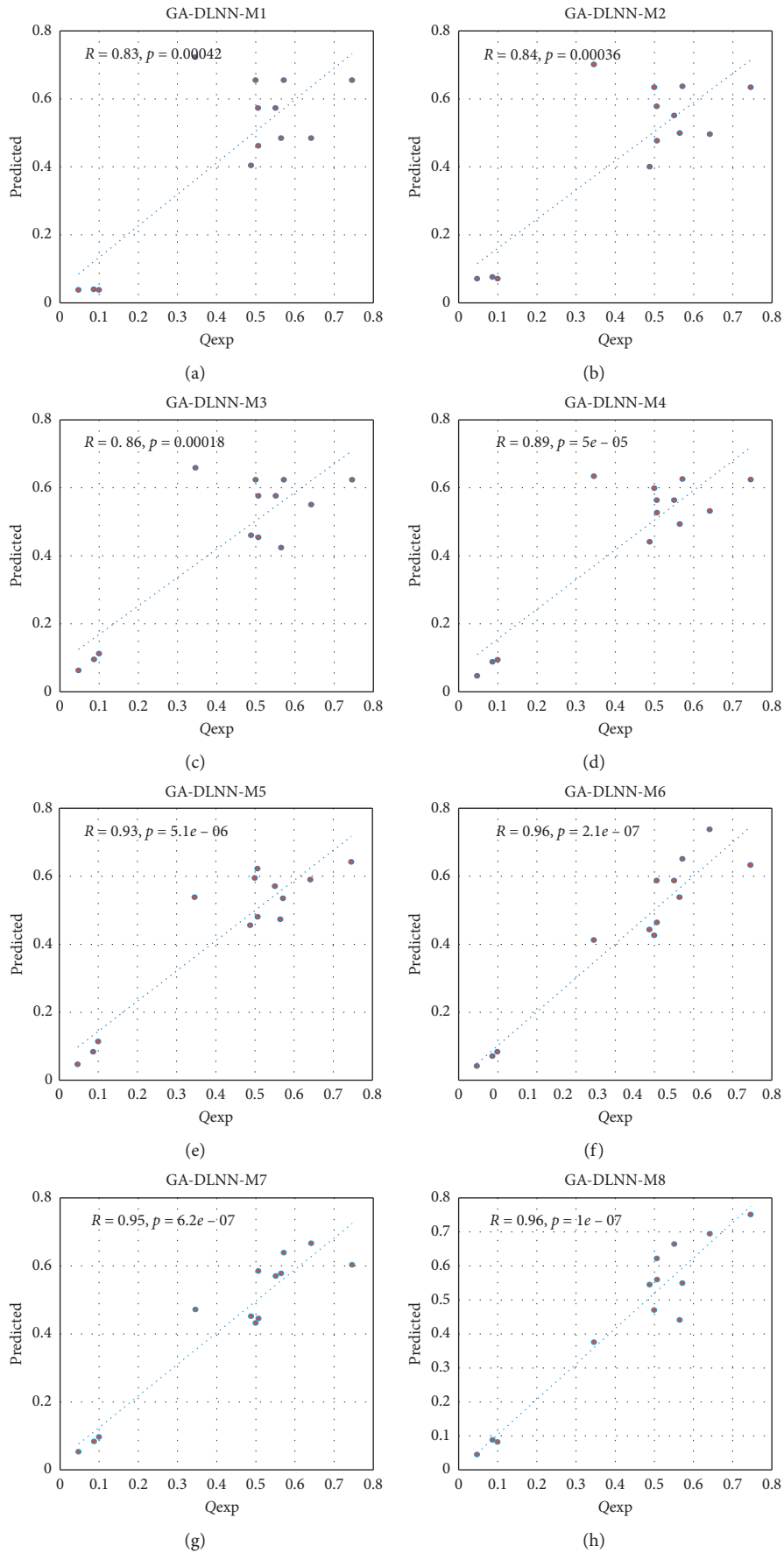
Figure 10: The scatter plots graphical presentation over the testing modelling phase: hybrid GA-DLNN models.
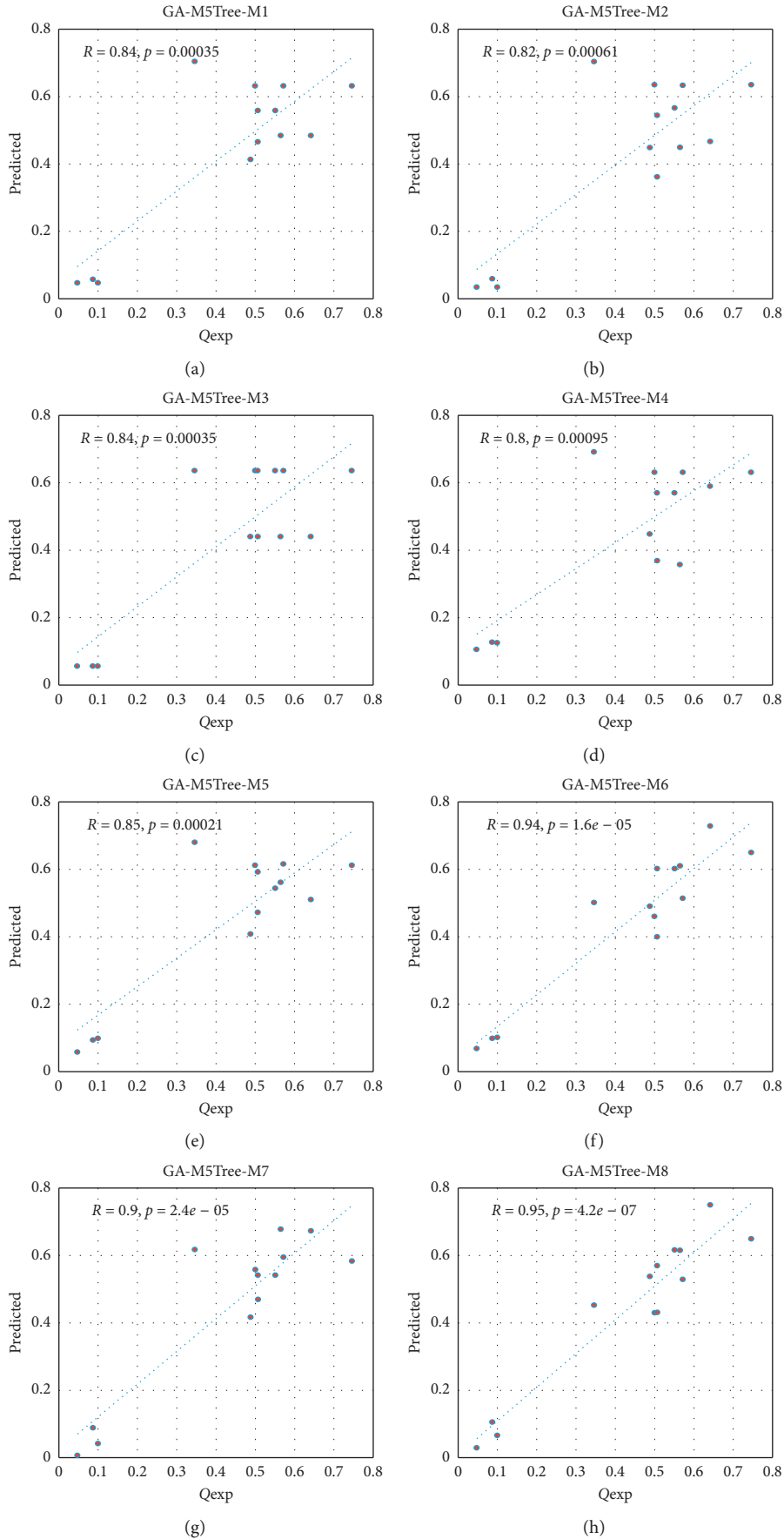
Figure 11: The scatter plots graphical presentation over the testing modelling phase: hybrid GA-M5Tree models.
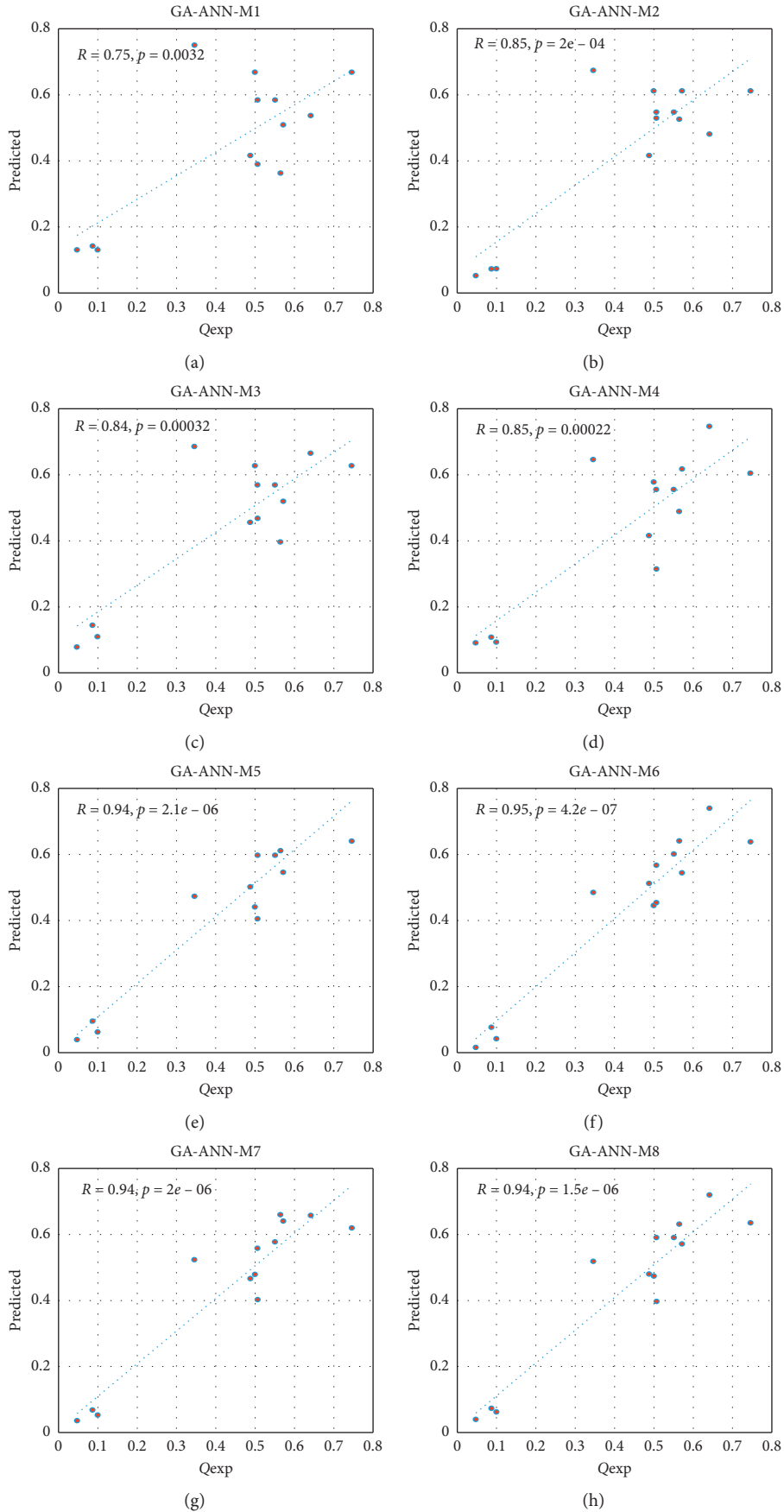
FIGURE 12: The scatter plots graphical presentation over the testing modelling phase: hybrid GA-ANN models.
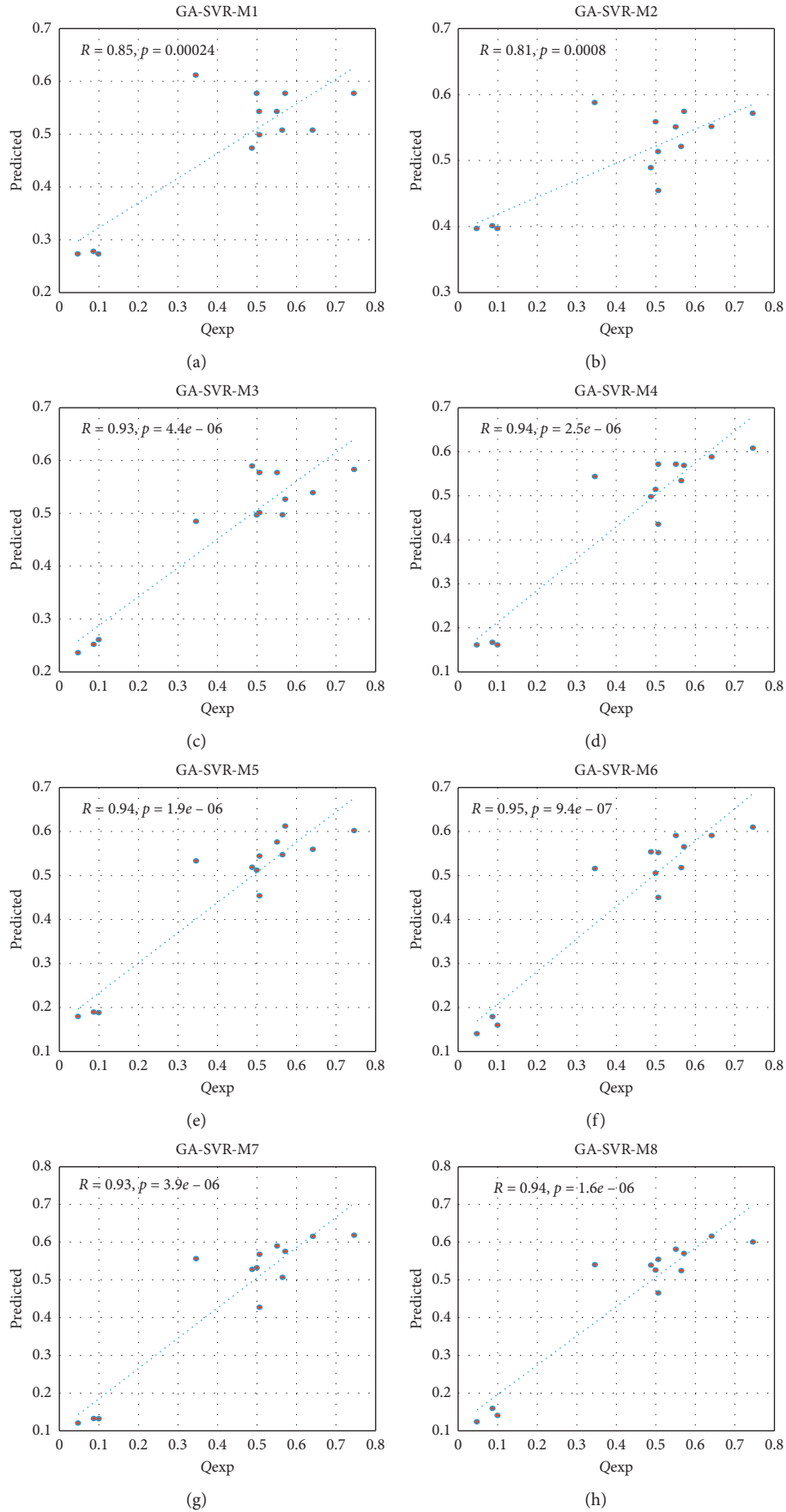
FIGURE 13: The scatter plots graphical presentation over the testing modelling phase: hybrid GA-SVR models.
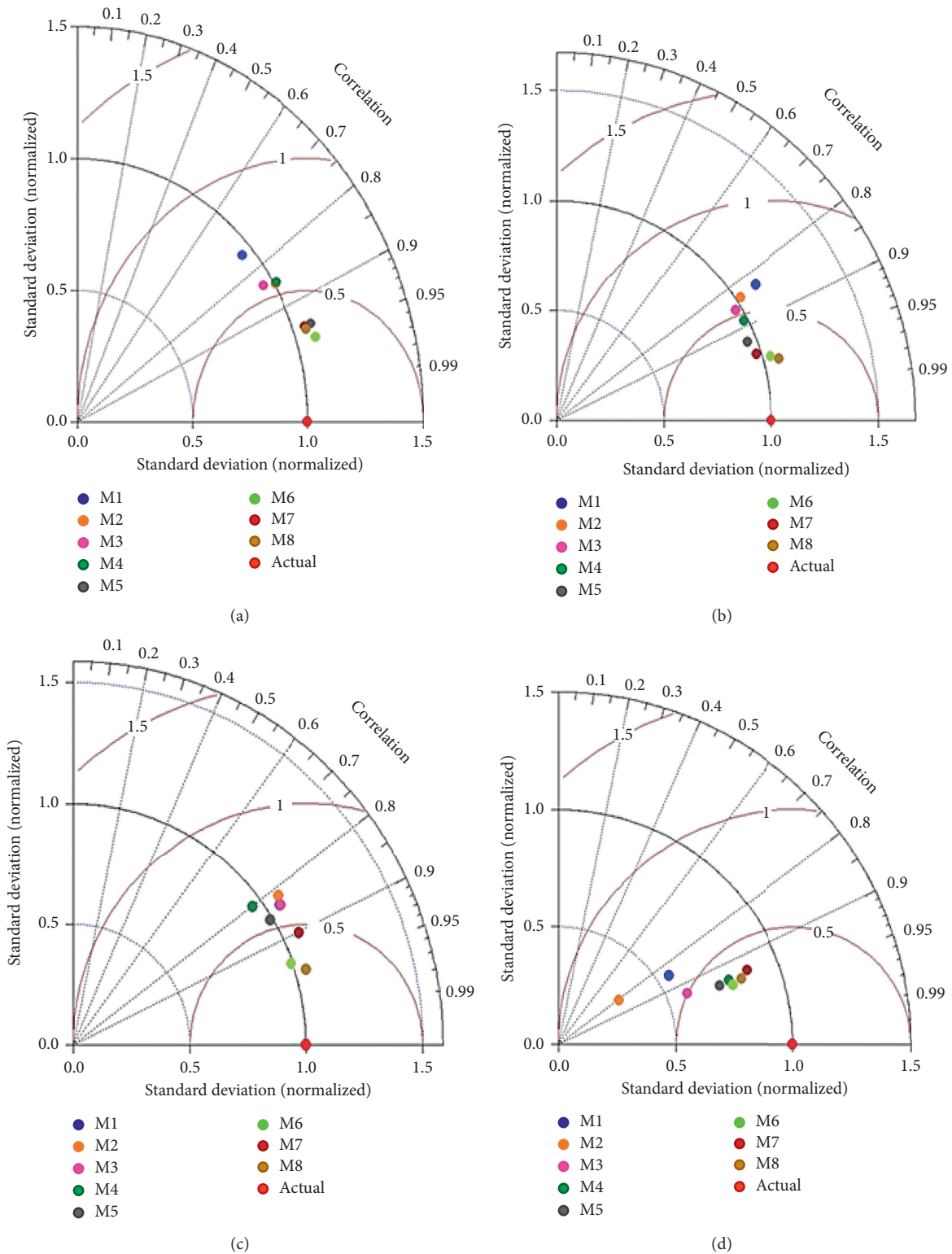
Figure 14: Taylor diagram graphical presentations over the testing phase by different hybrid models. (a) GA-ANN models. (b) GA-DLNN models. (c) GA-M5Tree models. (d) GA-SVR models.

accuracy in comparison with other comparable AI models and yielded more accurate predictions of PRSC values based on all quantitative and visualized assessments. The adopted technique for the selection of the best and most

suitable input parameters for suggested approaches has in general a significant influence on the predictive models' performances by removing the redundant information and hence producing sufficient and clean data to the
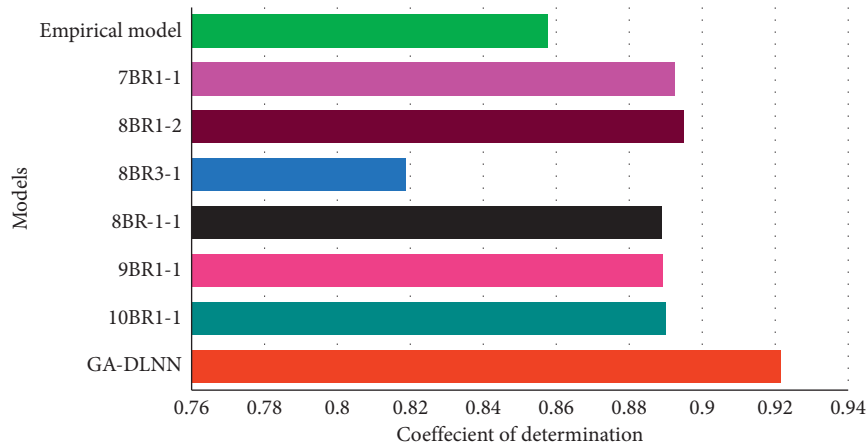
FIGURE 15: Validating the proposed GA-DLNN model against several models developed in the previous studies.

predictive models [67]. Finally, the integration of GA with a deep learning model was found to produce the best model in terms of minimizing the forecasted errors according to assessments carried out using different statistical measures.

In this study, a novel hybrid modelling framework for the Perfobond rib connectors based on several AI methods has been presented. This study performed rigorous sensitivity by considering eight different combination models, in which the input parameter is optimally selected by the effective utilization of GA and the following four AI methods (DLNN, M5Tree, ANN, and SVR) as prediction tools. The use of GA was very successful in selecting the optimal number and combination of the predictor dataset, which considerably reduced the model complexity. Increasing the number of input parameters alone will not help in improving the predictive power of AI models; instead a recognition of appropriate predictor dataset is very important. The DLNN displayed excellent generalization capabilities in understanding the nonlinear relationships between the candidate variables and PRSC. Hybridizing DLNN with GA successful in identifying the 7-input model (M6) was found to be the best for shear strength predictions, i.e., it was found to be successful in identifying the best model with the least number of input parameters with excellent prediction skill for the shear strength predictions of PRSCs. A multitude of statistical performance evaluation measures and graphical representations confirmed the robustness of the DLNN-GA hybrid model for prediction of shear strength of Perfobond rib connectors. This could solve many complexities and problems in structural engineering.

4.3. Validating the Proposed Model against Several Models Conducted in the Previous Research Studies. It is an important aspect to validate the reliability and accuracy of the suggested GA-DLNN model in predicting the PRSC capacity against the recognized researches over the literature studies. Herein, the results obtained by the GA-DLNN model over the testing phase are validated against some predictive models which were described in the literature.

Allahyari et al. [16] developed several models based on ANN approaches trained by Bayesian Regularization (BR) backpropagation algorithm to predict the capacity of PRSC. The main challenge was to probably select the best input combinations; therefore, they adopted classical and statistical methods. The adopted approaches may lead to select redundant information and decrease the efficiency of the predictive models. Subsequently, this study revealed that the best models were GA-DLNN based on 7 input parameters; therefore, we compared the proposed model (GA-DLNN) with several models established in [16] depending on 7 to 10 parameters (i.e., 7-BR1 and 8-BR1). The comparison assessment, as shown in Figure 15, reveals that the proposed model in this study outperformed the comparable models. Moreover, Oguejiofort and Hosaint [2] utilized empirical models to predict the shear strength capacity and yielded good accuracy of prediction with R^2 of 0.8577, as shown in Figure 15. In accordance with these comparative analyses, it can be observed that the adopted models of this study shows better performance prediction and yielded a higher value of R^2 than the comparable models.

5. Conclusions

Accurate prediction of Perfobond Rib Shear Strength is very important in structural engineering sectors. In this investigation, four AI approaches comprising ANN, SVR, DLNN, and M5Tree were developed using 90 experimental samples collected from previous studies. Ten input parameters were used in this current study including concrete compressive strength (f_c), area of concrete dowels (A_D), rib holes number (n), area of cross reinforcement bars and yield stress of reinforcement bars ($A_{tr,r} f_{y,r}$), area of cross reinforcement bars and the tensile strength of cross rebar ($A_{tr} f_y$), area of the connector at the end-bearing zone (Ab), the ratio between the thickness of the concrete slab to connector height (b/h_{sc}), connector height (h_{sc}), the contact area between the connector and the concrete (A_F), and coefficient of end-bearing force (α). The simulated result revealed that the DLNN model achieved a high prediction accuracy and outperformed the comparable

models based on ten input variables. Moreover, the SVR models were the worst predicted models during the training and the testing phases. In order to reduce the number of input parameters, we hybridized the AI models with a bioinspired natural optimization approach called a genetic algorithm (GA) for properly selecting the best input parameters for each AI model separately. Optimal selection of input combinations can effectively reduce the complexity of the model, thereby, obtaining better generalization capabilities, decreasing the computational cost, and increasing the quality of predictions, as well as removing the redundant information. The obtained results showed that the hybridization of AI models with GA importantly improved the prediction accuracy for all predicted models (GA-ANN, GA-M5Tree, and GA-DLNN) except the GA-SVR model. Moreover, the GA-DLNN produced a higher accuracy of performance than other hybrid modelling approaches. The obtained result revealed that the GA-DLNN models required only 7 input parameters to generate the best result accuracy in comparing other hybrid models and classical AI models (DLNN, ANN, SVR, and M5Tree) which were developed based on ten input parameters. Additionally, the outcomes of this study illustrated that removing three input parameters (area of the connector at the end-bearing zone, connector height, and concrete slab thickness) efficiently improved the prediction accuracy of GA-DLNN. The remarkable observation in this study is that is possible to accurately predict the Perfobond rib shear strength with fewer input parameters. This study found that the proper selection of input parameters has a great influence on the performances of AI models. Accordingly, the recommendations for future studies are to intensify the use of GA as a feature selection and combine that algorithm with different AI models to address the most difficult issues related to structural and material engineering.

Abbreviations

PRSC: Perfobond rib shear strength connector
DLNN: Deep learning neural network
SVR: Support vector regression
ANN: Artificial neural network
GA: Genetic algorithm
FE: Finite element method
GP: Genetic programming
ANFIS: Adaptive neuro-fuzzy inference system
LR: Linear regression
(f_c): Concrete compressive strength
(A_D): Area of concrete dowels
(n): Rib holes number
$(A_{tr,r} f_{y,r})$: Area of cross reinforcement bars and yield stress of reinforcement bars
$(A_{tr} f_y)$: Area of cross reinforcement bars and the tensile strength of cross rebar
(Ab): Area of the connector at the end-bearing zone
(b/h_{sc}): The ratio between the thickness of the concrete slab to connector height
(h_{sc}): Connector height
(A_F): The contact area between the connector and concrete
(α): Coefficient of end-bearing force
(MT): Model tree
PART: Partial and regression tree
SDR: Standard deviation reduction
RMSE: Root mean square error
MAE: Mean absolute
MAPE: Mean absolute percentage error
RRMSE: Relative root mean squared error
RE: Relative error
MRE: Mean relative error
NSE: Nash–Sutcliffe efficiency.

Data Availability

The data used to support the findings of the study are available from the corresponding author upon request.

Conflicts of Interest

The authors declare no conflicts of interest.

References

[1] S.-H. Kim and J.-H. Choi, "Experimental study on shear connection in unfilled composite steel grid bridge deck," *Journal of Constructional Steel Research*, vol. 66, no. 11, pp. 1339–1344, 2010.

[2] E. C. Oguejiofor and M. U. Hosain, "Numerical analysis of push-out specimens with perfobond rib connectors," *Computers & Structures*, vol. 62, no. 4, pp. 617–624, 1997.

[3] J. D. C. Vianna, L. F. Costa-Neves, P. C. G. Da S. Vellasco, and S. A. L. De Andrade, "Experimental assessment of Perfobond and T-Perfobond shear connectors' structural response," *Journal of Constructional Steel Research*, vol. 65, no. 2, pp. 408–421, 2009.

[4] J. P. S. Cândido-Martins, L. F. Costa-Neves, and P. C. G. Da Vellasco, "Experimental evaluation of the structural response of Perfobond shear connectors," *Engineering Structures*, vol. 32, no. 8, p. 1976, 1985.

[5] L. F. Costa-Neves, J. P. Figueiredo, P. C. G. D. S. Vellasco, and J. D. C. Vianna, "Perforated shear connectors on composite girders under monotonic loading: an experimental approach," *Engineering Structures*, vol. 56, pp. 721–737, 2013.

[6] J. P. C. Rodrigues and L. Laím, "Behaviour of perfobond shear connectors at high temperatures," *Engineering Structures*, vol. 33, no. 10, pp. 2744–2753, 2011.

[7] A. M. Ibrahim, W. D. Salman, and F. M. Bahlol, "Flexural behavior of concrete composite beams with new steel tube section and different shear connectors," *Tribunal de Justiça do Espírito Santo*, vol. 26, no. 1, pp. 51–61, 2019.

[8] W. Zellner, "Recent designs of composite bridges and a new type of shear connectors," *Composite Construction in Steel and Concrete*, vol. 34, pp. 52–240, 1988.

[9] J. C. Vianna, L. F. Costa Neves, P. Vellasco, and S. A. L. Andrade, "Estudo Comparativo de Conectores de Corte para Estruturas Mistas de Aço e Betão," *Construção Magazine*, vol. 23, pp. 23–30, 2008.

[10] E. C. Oguejiofor and M. U. Hosain, "A parametric study of perfobond rib shear connectors," *Canadian Journal of Civil Engineering*, vol. 21, no. 4, pp. 614–625, 1994.

[11] M. M. Jumaa'h, B. T. Kamil, and O. S. Baghabra, "Mechanical and structural properties of a lightweight concrete with different types of recycling coarse aggregate," *Tikrit Journal of Engineering Sciences*, vol. 26, no. 1, pp. 33–40, 2019.

[12] A. A. Shubbar, Z. S. Al-khafaji, M. S. Nasr, and M. W. Falah, "Using non-destructive tests for evaluating flyover footbridge: case study," *Knowledge-Based Engineering and Sciences*, vol. 1, no. 1, pp. 23–39, 2020.

[13] S. Y. K. Al-Darzi, A. R. Chen, and Y. Q. Liu, "Finite element simulation and parametric studies of perfobond rib connector," *American Journal of Applied Sciences*, vol. 4, no. 3, pp. 122–127, 2007.

[14] J.-H. Ahn, S.-H. Kim, and Y.-J. Jeong, "Shear behaviour of perfobond rib shear connector under static and cyclic loadings," *Magazine of Concrete Research*, vol. 60, no. 5, pp. 347–357, 2008.

[15] S. Zheng, Y. Liu, T. Yoda, and W. Lin, "Parametric study on shear capacity of circular-hole and long-hole perfobond shear connector," *Journal of Constructional Steel Research*, vol. 117, pp. 64–80, 2016.

[16] H. Allahyari, I. M. Nikbin, S. Rahimi, and A. Heidarpour, "A new approach to determine strength of Perfobond rib shear connector in steel-concrete composite structures by employing neural network," *Engineering Structures*, vol. 157, pp. 235–249, 2018.

[17] N. S. Radhi, K. F. Morad, M. H. Hafiz, A. A. Atiyah, and A. Bouaissi, "Optimization of nickel content on some properties of (niti) shape memory alloy," *Knowledge-Based Engineering and Sciences*, vol. 1, no. 1, pp. 40–47, 2020.

[18] Q. Zhang, S. Pei, Z. Cheng, Y. Bao, and Q. Li, "Theoretical and experimental studies of the internal force transfer mechanism of perfobond rib shear connector group," *Journal of Bridge Engineering*, vol. 22, no. 2, 2017.

[19] S.-H. Kim, S. Park, K.-S. Kim, and C.-Y. Jung, "Generalized formulation for shear resistance on Y-type perfobond rib shear connectors," *Journal of Constructional Steel Research*, vol. 128, pp. 245–260, 2017.

[20] M. Abdulrahman and S. Mahmood, "Strength of reinforced reactive powder concrete hollow beams," *Tikrit Journal of Engineering Sciences*, vol. 26, no. 2, pp. 15–22, 2019.

[21] S.-H. Kim, K.-S. Kim, D.-H. Lee, J.-S. Park, and O. Han, "Analysis of the shear behavior of stubby Y-type perfobond rib shear connectors for a composite frame structure," *Materials*, vol. 10, no. 11, p. 1340, 2017.

[22] H. Q. Nguyen, H.-B. Ly, V. Q. Tran, T.-A. Nguyen, T.-T. Le, and B. T. Pham, "Optimization of artificial intelligence system by evolutionary algorithm for prediction of axial capacity of rectangular concrete filled steel tubes under compression," *Materials*, vol. 13, no. 5, p. 1205, 2020.

[23] E. Miranda and J. Suñé, "Memristors for neuromorphic circuits and artificial intelligence applications," *Materials*, vol. 13, no. 4, p. 938, 2020.

[24] B. Savkovic, P. Kovac, B. Dudic et al., "Comparative characterisics of ductile iron and austempered ductile iron modeled by neural network," *Materials*, vol. 12, no. 18, p. 2864, 2019.

[25] A. A. Al-Musawi, "Determination of shear strength of steel fiber RC beams: application of data-intelligence models," *Frontiers of Structural and Civil Engineering*, vol. 11, 2019.

[26] B. Keshtegar, M. Bagheri, and Z. M. Yaseen, "Shear strength of steel fiber-unconfined reinforced concrete beam simulation: application of novel intelligent model," *Composite Structures*, vol. 212, 2019.

[27] A. A. Al-Musawi, A. A. H. Alwanas, S. Q. Salih, Z. H. Ali, M. T. Tran, and Z. M. Yaseen, "Shear strength of SFRCB without stirrups simulation: implementation of hybrid artificial intelligence model," *Engineering with Computers*, vol. 36, no. 1, 2020.

[28] Z. M. Yaseen, R. C. Deo, A. Hilal et al., "Predicting compressive strength of lightweight foamed concrete using extreme learning machine model," *Advances in Engineering Software*, vol. 115, pp. 112–125, 2018.

[29] Z. M. Yaseen, M. T. Tran, S. Kim, T. Bakhshpoori, and R. C. Deo, "Shear strength prediction of steel fiber reinforced concrete beam using hybrid intelligence models: a new approach," *Engineering Structures*, vol. 177, pp. 244–255, 2018.

[30] M. A. Köroğlu, A. Köken, M. H. Arslan, and A. Çevik, "Genetic programming based modeling of shear capacity of composite beams with profiled steel sheeting," *Adv Steel Constr*, vol. 7, no. 2, pp. 157–172, 2011.

[31] T. Ali, *Applications of the ANFIS and LR Models in the Prediction of Shear Connection in Composite beams/Ali Toghroli*, University of Malaya, Kuala Lumpur, Malaysia, 2015.

[32] M.-Y. Cheng and M.-T. Cao, "Evolutionary multivariate adaptive regression splines for estimating shear strength in reinforced-concrete deep beams," *Engineering Applications of Artificial Intelligence*, vol. 28, pp. 86–96, 2014.

[33] V. Le and L. Caracoglia, "A neural network surrogate model for the performance assessment of a vertical structure subjected to non-stationary, tornadic wind loads," *Computers & Structures*, vol. 231, Article ID 106208, 2020.

[34] A. Ashrafian, F. Shokri, M. J. Taheri Amiri, Z. M. Yaseen, and M. Rezaie-Balf, "Compressive strength of Foamed Cellular Lightweight Concrete simulation: new development of hybrid artificial intelligence model," *Construction and Building Materials*, vol. 230, 2020.

[35] C. Wang, D. Shi, and S. Li, "A study on establishing a microstructure-related hardness model with precipitate segmentation using deep learning method materials," 2020.

[36] C. Jaremenko, N. Ravikumar, E. Affronti, M. Merklein, and A. Maier, "Determination of forming limits in sheet metal forming using deep learning materials," 2019.

[37] Z. M. Yaseen, H. A. Afan, and M.-T. Tran, "Beam-column joint shear prediction using hybridized deep learning neural network with genetic algorithm," *In IOP Conference Series: Earth and Environmental Science*, vol. 143, p. 1, 2018.

[38] A. A. H. Alwanas, A. A. Al-Musawi, S. Q. Salih, H. Tao, M. Ali, and Z. M. Yaseen, "Load-carrying capacity and mode failure simulation of beam-column joint connection: application of self-tuning machine learning model," *Engineering Structures*, vol. 194, 2019.

[39] C. A. Jeyasehar and K. Sumangala, "Nondestructive evaluation of prestressed concrete beams using an artificial neural network (ANN) approach," *Structural Health Monitoring*, vol. 5, no. 4, pp. 313–323, 2006.

[40] J.-H. Ahn, C.-G. Lee, J.-H. Won, and S.-H. Kim, "Shear resistance of the perfobond-rib shear connector depending on concrete strength and rib arrangement," *Journal of Constructional Steel Research*, vol. 66, no. 10, pp. 1295–1307, 2010.

[41] A. De Fenza, A. Sorrentino, and P. Vitiello, "Application of artificial neural networks and probability ellipse methods for damage detection using lamb waves," *Composite Structures*, vol. 133, pp. 390–403, 2015.

[42] J. J. Hopfield, "Neural networks and physical systems with emergent collective computational abilities," *Proceedings of*

the *National Academy of Sciences*, vol. 79, no. 8, pp. 2554–2558, 1982.

[43] R. Lippmann, "An introduction to computing with neural nets," *IEEE Assp Magazine*, vol. 4, no. 2, pp. 4–22, 1987.

[44] D. E. Rumelhart, G. E. Hinton, and R. J. Williams, *Learning Internal Representations by Error Propagation*, California Univ San Diego La Jolla Inst for Cognitive Science, San Diego, CL, USA, 1985.

[45] M. Fu, T. Fan, Z. Ding, S. Q. Salih, N. Al-ansari, and Z. M. Yaseen, "Deep learning data-intelligence model based on adjusted forecasting window scale," *Application in Daily Streamflow Simulation*, vol. 8, 2020.

[46] J. R. Quinlan, "Learning with continuous classes," *Machine Learning*, vol. 92, pp. 343–348, 1992.

[47] E. Frank and I. H. Witten, "Generating accurate rule sets without global optimization," 1998.

[48] G. Holmes, M. Hall, and E. Prank, "Generating rule sets from model trees," in *Lecture Notes in Computer Science (Including Subseries Lecture Notes in Artificial Intelligence and Lecture Notes in Bioinformatics)*Springer, Berlin, Germany, 1999.

[49] Y. Ayaz, A. F. Kocamaz, and M. B. Karakoç, "Modeling of compressive strength and UPV of high-volume mineral-admixtured concrete using rule-based M5 rule and tree model M5P classifiers," *Construction and Building Materials*, vol. 21, 2015.

[50] V. Jothiprakash and A. S. Kote, "Effect of pruning and smoothing while using M5 model tree technique for reservoir inflow prediction," *Journal of Hydrologic Engineering*, vol. 16, no. 7, pp. 563–574, 2011.

[51] G. E. Hinton, S. Osindero, and Y.-W. Teh, "A fast learning algorithm for deep belief nets," *Neural Computation*, vol. 18, no. 7, pp. 1527–1554, 2006.

[52] V. N. Vapnik, *The Nature of Statistical Learning Theory*, Springer, Berlin, Germany, 2000.

[53] S. Raghavendra and P. C. Deka, "Support vector machine applications in the field of hydrology: a review," *Applied Soft Computing*, vol. 19, pp. 372–386, 2014.

[54] G. Zhang, "Reinforced concrete deep beam shear strength capacity modelling using an integrative bio-inspired algorithm with an artificial intelligence model," *Engineering with Computers*, vol. 28, 2020.

[55] M. K. AlOmar, M. M. Hameed, N. Al-Ansari, and M. A. AlSaadi, "Data-driven model for the prediction of total dissolved gas: robust artificial intelligence approach," *Advances in Civil Engineering*, vol. 2020, Article ID 6618842, 2020.

[56] J. H. Holland, *Adaptation in Natural and Artificial Systems: An Introductory Analysis with Applications to Biology, Control, and Artificial Intelligence*, MIT press, Cambridge, MA, USA, 1992.

[57] A. T. Azar and S. Vaidyanathan, *Computational Intelligence Applications in Modeling and Control*, Springer, Berlin, Germany, 2015.

[58] P. L. Braga, A. L. I. Oliveira, and S. R. L. Meira, "A GA-based feature selection and parameters optimization for support vector regression applied to software effort estimation," *Proceedings of the 2008 ACM Symposium on Applied Computing*, vol. 8, pp. 1788–1792, 2008.

[59] G. Stein, B. Chen, A. S. Wu, and K. A. Hua, "Decision tree classifier for network intrusion detection with GA-based feature selection," *Proceedings of the 43rd Annual Southeast Regional Conference on - ACM-SE*, vol. 43, 2005.

[60] E. Bruderer and J. V. Singh, "Organizational evolution, learning, and selection: a genetic-algorithm-based model,"

[61] J. Yang and V. Honavar, "Feature subset selection using a genetic algorithm," in *Feature Extraction, Construction and Selection*, pp. 117–136, Springer, Berlin, Germany, 1998.

[62] R. K. Yin and G. B. Moore, "The use of advanced technologies in special education," *Journal of Learning Disabilities*, vol. 20, no. 1, pp. 60–63, 1987.

[63] M. S. Podder and C. B. Majumder, "The use of artificial neural network for modelling of phycoremediation of toxic elements As(III) and As(V) from wastewater using Botryococcus braunii," *Spectrochimica Acta Part A: Molecular and Biomolecular Spectroscopy*, vol. 155, pp. 130–145, 2016.

[64] M. M. Hameed and M. K. AlOmar, "Prediction of compressive strength of high-performance concrete: hybrid artificial intelligence technique bt - applied computing to support industry," *Innovation and Technology*, vol. 35, pp. 323–335, 2020.

[65] B. Badarloo, A. Kari, and F. Jafari, "Experimental and numerical study to determine the relationship between tensile strength and compressive strength of concrete," *Civil Engineering Journal*, vol. 4, no. 11, pp. 2787–2800, 2018.

[66] H. Tao, A. A. Ewees, A. O. Al-Sulttani et al., "Global solar radiation prediction over North Dakota using air temperature: development of novel hybrid intelligence model," *Energy Reports*, vol. 7, pp. 136–157, 2021.

[67] M. K. Alomar, M. M. Hameed, and M. A. AlSaadi, "Multi hours ahead prediction of surface ozone gas concentration: robust artificial intelligence approach," *Atmospheric Pollution Research*, vol. 11, no. 9, 2020.

Academy of Management Journal, vol. 39, no. 5, pp. 1322–1349, 1996.

WILEY | Hindawi

Research Article

Estimation of Daily Suspended Sediment Load Using a Novel Hybrid Support Vector Regression Model Incorporated with Observer-Teacher-Learner-Based Optimization Method

Siyamak Doroudi [iD],[1] **Ahmad Sharafati** [iD],[1] **and Seyed Hossein Mohajeri** [iD][2]

[1]*Department of Civil Engineering, Science and Research Branch, Islamic Azad University, Tehran, Iran*
[2]*Department of Civil Engineering, Faculty of Engineering, Kharazmi University, Tehran, Iran*

Correspondence should be addressed to Ahmad Sharafati; asharafati@srbiau.ac.ir

Predicting suspended sediment load (SSL) in water resource management requires efficient and reliable predicted models. This study considers the support vector regression (SVR) method to predict daily suspended sediment load. Since the SVR has unknown parameters, the observer-teacher-learner-based Optimization (OTLBO) method is integrated with the SVR model to provide a novel hybrid predictive model. The SVR combined with the genetic algorithm (SVR-GA) is used as an alternative model. To explore the performance and application of the proposed models, five input combinations of rainfall and discharge data of Cham Siah River catchment are provided. The predictive models are assessed using various numerical and visual indicators. The results indicate that the SVR-OTLBO model offers a higher prediction performance than other models employed in the current study. Specifically, SVR-OTLBO model offers highest Pearson correlation coefficient ($R = 0.9768$), Willmott's Index ($WI = 0.9812$), ratio of performance to IQ ($RPIQ = 0.9201$), and modified index of agreement ($md = 0.7411$) and the lowest relative root mean square error ($RRMSE = 0.5371$) in comparison with SVR-GA ($R = 0.9704$, $WI = 0.9794$, $RPIQ = 0.8521$, and $md = 0.7323$, 0.5617) and SVR ($R = 0.9501$, $WI = 0.9734$, $RPIQ = 0.3229$, $md = 0.4338$, and $RRMSE = 1.0829$) models, respectively.

1. Introduction

Proper estimate of sediment transport load is highly essential in water engineering purposes such as the design and operation of dams, flood control structures, water conveyance channels, and other hydraulic structures [1]. In this context, forecasting and evaluating the suspended sediment load (SSL) in the catchment scale is a vital hydroenvironmental issue [2, 3]. Despite the importance of SSL, due to the dependency of the multiple hydrological, metrological, and hydraulic variables, the evaluation process is too complicated [4–6].

So far, various SSL prediction models such as physical, numerical, and empirical models are applied. Physical models are formed based on the theoretical governing equations of sediment transport composed of the partial differential equation of mass and flow transport. Although the physical models are the most accurate prediction models, the complexity in governing equations solution and incorporation and dependency on the various simplifying assumptions confines their application to practical engineering problems [7]. The numerical models, which are almost the most widespread approach in recent years, are built on solving the mass and flow transport using numerical calculus approaches and computer programming [8, 9]. Despite the popularity of this approach, especially in recent years, these models' main drawback is the demand for knowledge in the application, limitations, and abilities of various numerical schemes and techniques. Furthermore, the numerical models require high intelligence in complicated computer programming and high computing speed [10].

Another class of SSL prediction approach depends on the experimental measurement and is known as empirical methods. In the middle of this approach, the most popular one is sediment rating curves. In this approach, a regression model is usually employed to develop a relationship between discharge and SSL [11, 12]. However, the sediment rating curves method has some methodological constraints. Also, an essential requirement for this approach is the availability of high-quality experimental data used in the curve fitting process [13].

Data-driven models are also efficient tools for predicting the SSL. This approach could draw on the causal factors and consequences of an event without any necessity of a deep understanding of a complex phenomenon process [14]. Data-driven models, which simulate a system using observed data in real life of the system, include a broad range of models such as regression-based models, time series models, and artificial intelligence (AI) models. The regression-based models evaluate the relationship of a dependent variable and several independent variables. In previous water resource engineering studies, the regression-based models have been applied to explore different sediment load, water level, energy dissipation, and similar essential hydrological parameters [15–17]. Demirci and Baltaci [18] assessed three models based on the fuzzy logic approach (FL), sediment rating curves (SRC), and multilinear regression models. The models' performance is investigated, and the FL model provided better performance in calculating the SSL than the other models. Singh et al. [19] evaluated different heuristic methods for predicting the SSL. The results show that multilayer perceptron (MLP) offered the best performance. The time series models, which are based on processing sequence inputs data, consist of statistical methods such as autoregressive (AR) and autoregressive moving average (ARMA) models, autoregressive integrated moving average (ARIMA) model, and autoregressive moving average with exogenous (ARMAX) data [20]. However, Moeeni and Bonakdari [21] indicated that the time series models are inadequate for nonlinear hydrological problems such as suspended sediment load modeling.

The AI models are a fast, cost-effective, and appropriate predicting approach that does not require detailed physical information. Their process for obtaining and loading the data is partly simple with high predicting accuracy [22]. In recent years, artificial neural networks (ANNs), fuzzy-based models, support vector machine (SVM), and support vector regression (SVR) have been employed for predicting the SSL [23–25]. Mustafa et al. [26] used a multilayer perceptron (MLP) with four different training algorithms to forecast the suspended sediment discharge. Results showed that the Levenberg–Marquardt (LM) indicated a better performance than other training algorithms.

Despite such broad usage of ANN models, the models provided unsatisfactory results in some engineering problems. In previous studies, the combined form of AANs, known as hybrid ANNs, has been extensively employed to solve such problems. ARMAX-ANN was used to estimate SSL. The proposed model provided better accuracy in comparison with the ARMAX and ANN models [27]. Adib

and Mahmodi [28] predicted SSL by incorporating the ANN and genetic algorithm (GA). They found that the hybrid model is more effective than the ANN.

In the case of the predicting SSL models, it has been observed that a sort of models such as fuzzy logic [29–31] or linear genetic programming (LPG) [32, 33] can solely predict the SSL with high accuracy. Despite applying these models in the SSL prediction, to improve the prediction accuracy and quality, similar to the artificial neural networks, the other AI methods can be employed in the hybrid form. Generally, the hybrid models based on the fuzzy logic and ANNs could be trained faster and adaptive than the solo application of the ANNs or fuzzy logic. Samet et al. [34] investigated the prediction performance of the ANN, adaptive neuro-fuzzy inference system (ANFIS), and AAN-GA in forecasting SSL. Results indicated that the ANFIS model indicated the best prediction performance compared to other models.

In addition to the hybrid fuzzy logic and ANN model, it is common to use support vector machine (SVM). The SVR method structure is more straightforward than fuzzy and ANN models that enhance the predicting model [35, 36]. As a result, the SVR method can solve problems across hydrological datasets such as small sample sizes, nonlinearity, and high dimensionality [37, 38]. These profits of SVR make the method a popular option for simulating and predicting the SSL in river and sediment transport studies. The summary of studies that used the support vector machine model to predict suspended sediment load is given in Table 1.

Although the SVR application has various advantages, it has some unknown parameters in its structure, which drastically affect SSL prediction accuracy. To solve this fundamental limitation of SVR, a method is required to apply the optimization algorithm [50, 51]. Due to this fact, researchers are still looking for a robust, reliable model that can solve the complex problem of suspended sediment transport using AI models. In this way, this study enhances the SVR model's performance by combining the SVR and observer-teacher-learner-based optimization (OTLBO). The optimization algorithm (OTLBO) is employed to determine the optimal parameters of the support vector machine. OTBLO is a heuristic algorithm introduced by Shahrouzi et al. [52]. Furthermore, the second model based on genetic algorithm and SVR is developed and named SVR-GA. Finally, the models are employed to evaluate the SSL of at Cham Siah River catchment in Iran.

Although an increasing trend is observed in applying artificial intelligence models in the literature to estimate the SSL, as far as authors know, the model developed in the present study, SVR-OTLBO, has not been used in water engineering concerns and estimation of SSL in particular.

Due to the lack of information on suspended sediment load data in watersheds of Iran, continuous sediment data are not available. However, the rainfall and river discharge data are available in the form of time series. Hence, a dataset of rainfall and river discharge with different lead times is employed as predictors to simulate SSLs selected based on available observed events. Hence, the model, which is developed based on available observed SSL events, simulates the daily sediment.

TABLE 1: The summary of support vector machine models for predicting suspended sediment load.

Scholars	Predictive model	Input variables	Study area	Time scale
Kisi [7]	LSSVM	Discharge, SL	USA	Daily
He et al. [35]	SVR	Discharge	China	Daily
Sadeghpourhaji et al. [39]	WSVM	Discharge	UAS	Daily
Nourani and Andalib [40]	WLSSVM	Discharge, SL	USA	Daily, monthly
Kumar et al. [41]	LSSVM	Discharge, rainfall	India	Daily
Nourani et al. [42]	SVM	Discharge, SL	Iran	Monthly
Rashidi et al. [43]	GT-SVM	Discharge, SL	Iran	Monthly
Buyukyildiz and Kumcu [23]	SVR	Discharge, SL	Turkey	Daily
Himanshu et al. [44]	WLSSVM	Discharge, rainfall, SL	India	Daily
Himanshu et al. [45]	WLSSVM	Discharge, rainfall, SL	India	Daily, monthly
Hssanpour et al. [46]	FCM-SVR	Discharge, SL	Iran	Daily
Malik et al. [47]	LSSVR	Discharge, SL	India	Daily
Rahgoshay et al. [48]	SVR-GA	Discharge, SL	Iran	Daily
Al-Mukhtar [49]	SVM	Discharge	Iraq	Daily

LSSVM: least square support vector machine; SVR: support vector regression; WSVM: wavelet support vector machine; WLSSVM: wavelet least square support vector machine; SVM: support vector machine; GT-SVM: gamma test support vector machine; FCM-SVR: fuzzy C-mean clustering-support vector regression.

The main objectives of this study are as follows: (i) considering a new hybrid intelligence model (SVR-OTLBO model) for the suspended sediment load estimation, (ii) evaluation of the predictability of the developed model in one of the Iranian rivers (i.e., Cham Siah River) despite the lack of the sediment information, and (iii) developing a predictive model using river discharge and rainfall as the main factors in the sediment suspension load.

2. Case Study and Data Collection

To examine the proposed models' performance, the Cham Siah River catchment in Kohgiluyeh and Boyer-Ahmad Province, southwest of Iran, is used as a case study area. Cham Siah River catchment, which is shown in Figure 1, covers an area of 793 km^2. The average annual rainfall and river discharge of the catchment are 623.5 mm and 8.02 m^3/s. Its minimum and maximum heights are 600 to 1500 meters; the average slope of the subbasin is 26.9%, and the annual sediment volume is 328711 tons/year.

The daily hydrological data of the catchment, including the discharge, rainfall, and SSL recorded from 1986 to 2015, are used for prediction modeling. The daily rainfall data are obtained from two rain gauges, namely, Saeed Abad, which is located at 50°43′05″E, 30°41′ 34″N with an altitude of 690 m, and Dehdasht, which is located at 50°34′27″E, 30°47′24″N with an altitude of 840 m. Besides, the daily river discharge and event-based sediment data are provided from the Saeed Abad station, which is located at 50°43′37″E, 30°43′21″N with an altitude of 663 m.

To provide the predictive models, observational data are divided into training dataset (68%) and testing dataset (32%). In this study, to ensure that all variables receive equal consideration during the training of the models, all the variables are rescaled from $x\varepsilon[a\,b]$ to $x'\varepsilon[-1\,1]$ and their dimensions are removed [14] using the following equation:

$$x' = 2 \times \frac{x-a}{b-a} - 1. \tag{1}$$

3. Methods

3.1. Support Vector Regression. Support vector regression (SVR) can be used for classification and regression problems [53]. SVR can perform a linear classification for two-dimensional space. Moreover, the data with higher SVR variables can be implicitly mapped into higher-dimensional space using a nonlinear map function. In this context, the main equation of the method is as follows:

$$f(x) = W^T \varphi(x) + b, \tag{2}$$

where $f(x)$ indicates the function between target and input variables, W^T is the m-dimensional weight vector, $\varphi(.)$ is the mapping function that maps x into the m-dimensional feature vector, and b is the bias term.

SVR investigates a hard margin for a classifier. Using the following equation (i.e., equation (2), which is called primal problem), the hard margin can be converted to a soft margin. The objective function of SVR converts to a minimizing problem.

$$\text{minimize: } \frac{1}{2}W^2 + C\sum_{i=1}^{m}\left(\xi_i^- + \xi_i^+\right)$$

$$\text{subject to}\left(w_i.\varphi(x_i) + b_{y_i}\right) - y_i \leq \varepsilon + \xi_i^+, \quad i = 1, 2, ..., m$$

$$y_i - \left(w_i.\varphi(x_i) + b_{y_i}\right) \leq \varepsilon + \xi_i^-, \quad i = 1, 2, ..., m$$

$$\xi_i^-, \xi_i^+ \geq 0, \quad i = 1, 2, ..., m. \tag{3}$$

where C is the penalty, ξ_i^+ and ξ_i^- are slack variables, W is the weight of vector, m is the number of inputs, x is the input variables, y_i is the observational target variable, and ε is the insensitive loss function.

As the results show a rational value, avoiding inappropriate results, some constraints could be inserted into the above equation's objective function. To consider the constraints, the primal problem alters to the following equation:
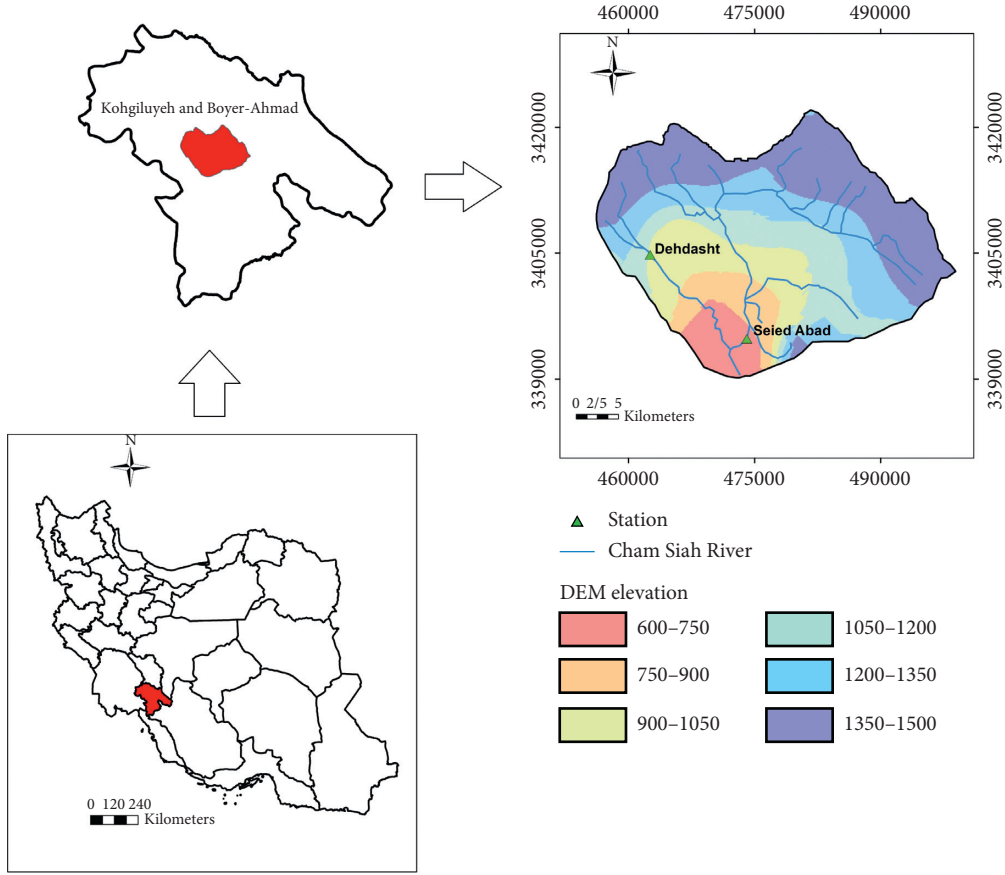
FIGURE 1: Schematic of the catchment of Cham Siah in Iran.

minimize: $L\left(w, b, \propto_i^+, \propto_i^-\right) = \dfrac{1}{2}W^2 + C\sum_{i=1}^{m}\left(\xi_i^- + \xi_i^+\right)$

$-\sum_{i=1}^{m} \propto_i^+ \left(w_i.\varphi\left(x_i\right) + b_{y_i} - y_i + \varepsilon + \xi_i^+\right)$

$-\sum_{i=1}^{m} \propto_i^- \left(y_i - w_i.\varphi\left(x_i\right) - b_{y_i} + \varepsilon + \xi_i^-\right) - \sum_{i=1}^{m}\left(\eta_i\xi_i^+ + \eta_i^*\xi_i^-\right),$

$$\tag{4}$$

where $\propto^+$, $\propto^-$, η_i, and η_i^* are Lagrange coefficients, which are multiplied by the constraints. Through applying the Lagrange function and KKT condition, equation (3) can be converted to the dual problem as equation (5) where the terms b, w, $\propto^-$, and $\propto^+$ are neglected:

maximize $L_D = -\dfrac{1}{2}\sum_{i}\sum_{j}\left(\alpha_i - \alpha_i^-\right)\left(\alpha_j - \alpha_j^-\right).k\left(x_i, x_j\right)$

$-\sum_{i=1}^{m}y_i\left(\alpha_i - \alpha_i^-\right) + \sum_{i=1}^{m}\varepsilon\left(\alpha_i + \alpha_i^-\right),$

$$\tag{5}$$

subject to $\sum_{i=1}^{m}\left(\alpha_i - \alpha_i^-\right) = 0,$

$$\tag{6}$$

$k\left(x_i, x_j\right) = \varphi\left(x_i\right).\varphi\left(x_j\right),$

In equation (4), $k\left(x_i, x_j\right)$ is the kernel function. Thus, equation (1) can be rewritten as follows:

$$f\left(x\right) = \sum_{i=1}^{m}\left(\alpha_i - \alpha_i^-\right)k\left(x_i, x_j\right) + b. \tag{7}$$

The output values are computed based on the values of the obtained parameters, i.e., b, w, α, C, and the kernel function parameters. In this study, a radial basis function (RBF) in the form of equation (8) has been chosen as the kernel function:

$$k\left(x_i, x_j\right) = \exp\left(\dfrac{-x - x_i}{2\sigma^2}\right), \tag{8}$$

where σ is the kernel parameter.

3.2. Description of Optimization Methods.
To obtain the optimistic values of the SVR parameters (e.g., ε, σ, and C), the observer-teacher-learner-based optimization (OTLBO) and genetic algorithm (GA) methods are used. OTLBO is a powerful metaheuristic optimization method that was firstly introduced by Shahrouzi et al. [52]. The OTLBO is worked based on the impact of teacher and observer on the learners in a class. Precisely, the method consists of the three primary phases of the education: (i) via teacher (known as teacher stage), (ii) via interplay with observer (known as observer stage), and (iii) via interplay with the other learners (known

as learner stage) [54]. In OTLBO, a set of learners is considered as population. This means that all comparatively designed variables are supposed to class members in this optimization algorithm. Furthered details of OTLBO were given by Shahrouzi et al. [52].

The GA, which is employed in this study, is a popular method in evolutionary computation studies to solve optimization problems. The GA has an initial population that is randomly generated, and each population member includes chromosome. The chromosome represents a possible solution, including genes. Also, the method has a step, which is known as the iteration loop. In the iteration loop, a new population is generated using selection, crossover, and mutation operations. At each stage, the new and old populations are selected based on the objective function's value [55].

3.3. Description of Hybrid SVR Models.
As mentioned above, the SVR parameters, including the value of ε, σ, and C, are considered decision variables, which require to be optimized through OTLBO or GA in an objective function. In the case of SVR-OTLBO, the development of the process is composed of the following steps:

(i) The initial values of the decision variables (e.g., ε, σ, and C) are randomly determined.

(ii) The SVR model predicts the initial target values based on the training data. The value of the objective function, which is the correlation coefficient between observed and predicted target values in this study, is computed.

(iii) The teacher or observer phase is randomly selected to determine the SVR parameters: ε, σ, and C. Consequently, the objective function is calculated and learner phase is started, and the objective function is evaluated as the same as the previous randomly selected phase.

(iv) The best solution is updated.

(v) The steps mentioned above are repeated to satisfy the termination criterion.

The above step-by-step algorithm of the SVR-OTLBO model for predicting the SSL is presented in Figure 2.

The second hybrid model is based on the SVR-GA method. The following steps are used to develop the model:

(i) The initial decision variables (first population) are randomly determined.

(ii) The SVR model computes the initial target variable; consequently, the initial value of the objective function is calculated.

(iii) The crossover operator is used to generate the offspring and new parameters of SVR. Later, the SVR model is employed to predict the target variable and evaluate the offspring according to objective function values.

(iv) The mutation operator is applied to generate the mutant population. The SVR model is then used to simulate the target variable and assess the mutant population based on objective function values.

(v) The population is sorted, and the repository of the member is updated.

(vi) The steps mentioned above are repeated to satisfy the termination criterion.

The SVR-GA modeling to predict the SSL is shown in Figure 3.

3.4. Assessing the Prediction Performance.
Five indices are used to evaluate the prediction performance of the SVR, GA-SVR, and OTLBO-SVR models. These indices are composed of Pearson correlation coefficient (R) [56], relative root mean squared error (RRMSE) [57, 58], Willmott's Index (WI) [59], ratio of performance to IQ (RPIQ) [60], and modified index of agreement (md) [61] as follows:

$$R = \left[\frac{\sum_{i=1}^{m} (O_i - \overline{O})(X_i - \overline{X})}{\sqrt{\sum_{i=1}^{m} (O_i - \overline{O})^2 \sum_{i=1}^{m} (X_i - \overline{X})^2}} \right],$$

$$\text{RRMSE} = \sqrt{\frac{1}{m} \sum_{i=1}^{m} \left(\frac{O_i - X_i}{X_i} \right)^2},$$

$$\text{WI} = 1 - \left[\frac{\sum_{i=1}^{m} (O_i - X_i)^2}{\sqrt{\sum_{i=1}^{m} (|X_i - \overline{O}| + |O_i - \overline{O}|)^2}} \right], \quad (9)$$

$$\text{RPIQ} = \frac{Q_3 - Q_1}{\sum_{i=1}^{m} \sqrt{(O_i - X_i)/m}},$$

$$\text{md} = 1 - \frac{\sum_{i=1}^{m} (O_i - X_i)^2}{\sum_{i=1}^{N} (|X_i - \overline{O}| - |O_i - \overline{O}|)},$$

where the O_i and X_i are the observed SSL and predicted SSL, $\overline{O}$ is the average of the observed SSL and $\overline{X}$ is the average of the predicted SSL, Q_1 and Q_3 are the first (25%) and third (75%) values of the samples, and m is the number of samples.

3.5. Uncertainty Analysis.
To evaluate the uncertainty of the models (SVR, SVR-GA, and SVR-OTLBO), the confidence limits of prediction errors ($CL_e^{\pm}$) are described as follows [62]:

$$CL_e^{\pm} = \mu_e \pm Z_\alpha \times S_e, \quad (10)$$

where μ_e and S_e are the mean and standard deviation of prediction errors, respectively. Z_α is the standard normal variable at the $\alpha\%$ of significant level. A predictive model with a positive value of μ_e provides overestimated prediction while a negative value of μ_e indicates the underestimated result.
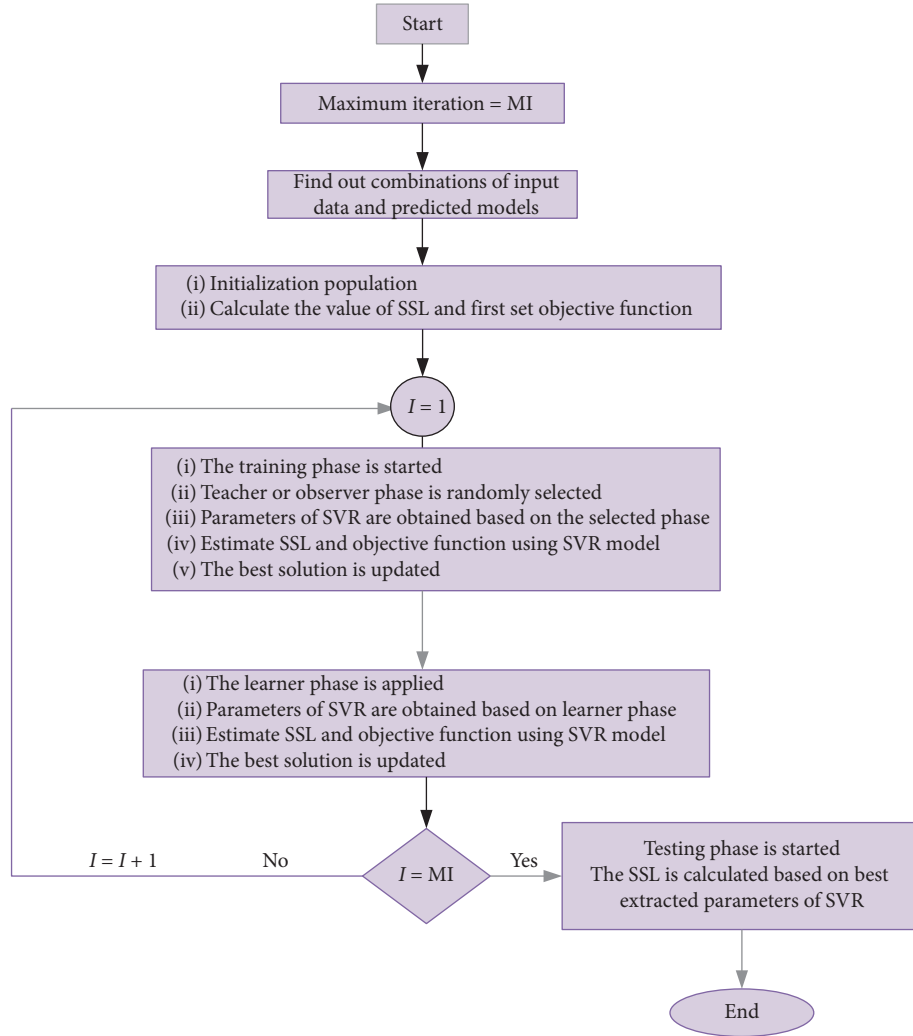
FIGURE 2: Algorithm of the SVR-OTLBO model.

4. Results and Discussion

4.1. Description of the Input Combinations. It is essential to explore the best input combinations for predicting the target variable as a first step. A number of feature selection methods including Pearson correlation, autocorrelation function (ACF), partial autocorrelation function (PACF), and cross-correlation function (CCF) can be used to obtain the optimal predictive variables [23, 63]. However, the Pearson correlation is a simple and effective method to estimate appropriate input variables [64–66]. Herein, the input combinations are identified by calculating the correlation between the SSL on the origin day (t) and inputs variables, including the river discharge (Q_s) from origin day to four days earlier ($t-4$) and the rainfall depth (R_s and R_d) from origin day to six days earlier ($t-6$).

Table 2 presents the correlation coefficients obtained between the $SSL_{(t)}$ and the input variables.

As shown in the table, the highest correlation between the $SSL_{(t)}$ and input variables are found in five variables including $R_{s(t)}$, $R_{d(t)}$, $Q_{s(t)}$, $R_{d(t-1)}$, and $R_{s(t-1)}$. Moreover, a decreasing trend is observed between the lag time of

predictive variables and correlation coefficients. For instance, the correlation coefficients obtained by $R_s(t)$ and $R_s(t-4)$ are 0.59 and 0.01, respectively.

Several input combinations are adopted using the variables nominated by correlation analysis, namely, M1 to M5 (Table 3). The river discharge is ignored through two combinations (M1 and M2) to assess the impact of the other predictive variables on prediction performance. It should be highlighted that, as explained in the methodology, the input combinations and output data are normalized using equation (1).

4.2. Assessment of the Models' Performance. To compare the prediction performance of the models used in this study (e.g., SVR, SVR-OTLBO, and SVR-GA), their metric indices obtained for different input combinations over the testing phase are presented in Table 4. From the table, it is evident that, for the SVR models, SVR-M4 provides better performance (RRMSE: 1.08, R: 0.95, RPIQ: 0.3229, md: 0.4338, and WI: 0.97). In the case of SVR-OTLBO models, the lowest RRMSE (0.537) is observed in the SVR-OTLBO-M4. The
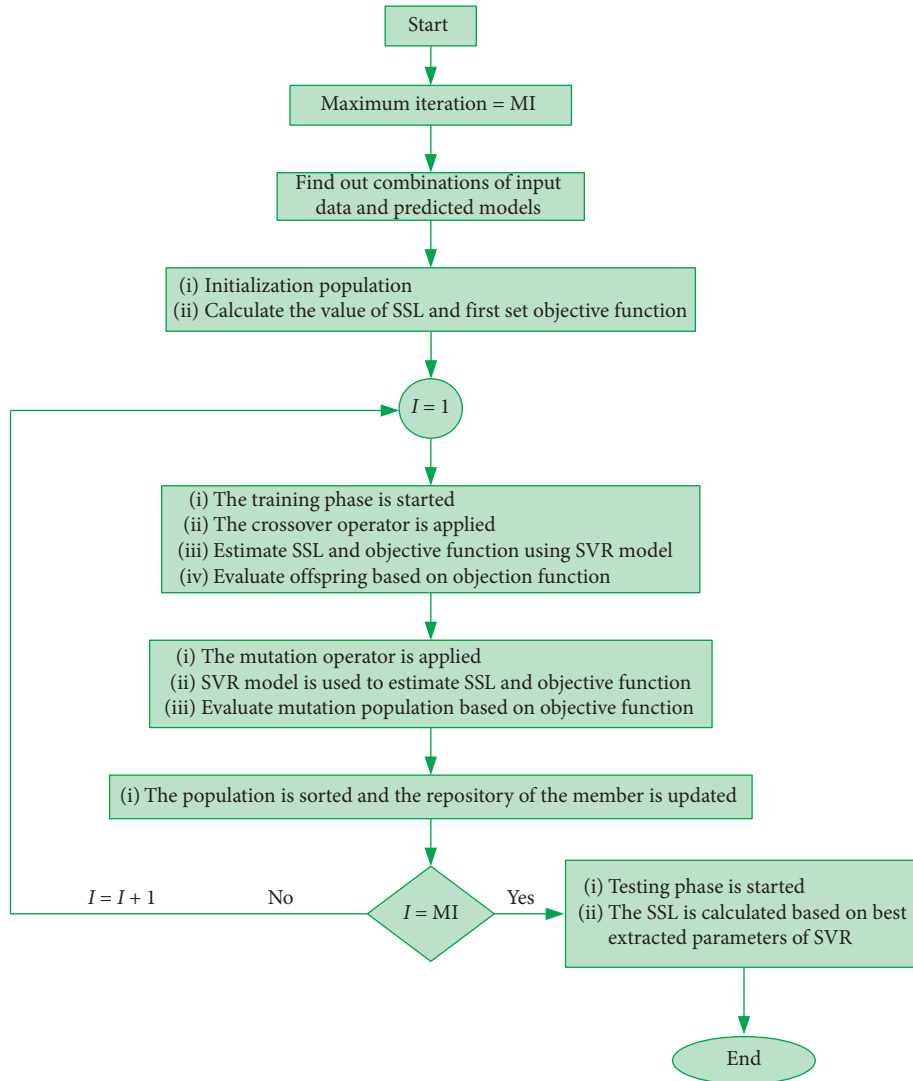
FIGURE 3: Algorithm of the SVR-GA model.

highest value of R (0.9769) is found in the SVR-OTLBO-M3, while the SVR-OTLBO-M4 provides the highest WI (0.9812), RPIQ (0.9201), and md (0.7411). In general, the SVR-OTLBO-M4 offers better prediction performance compared to other SVR-OTOBO models. Regarding the SVR-GA, values reported in Table 4 indicate that the lowest RRMSE (0.562) is seen in the SVR-GA-M4 model while the highest R (0.97) and WI (0.979), RPIQ (0.8521), and md (0.7323) are observed, respectively, in the SVR-GA-M5 and SVR-GA-M4 models.

The metrics obtained from different predictive models (e.g., SVR, SVR-OTLBO, and SVR-GA models) confirm that the M4 input combination, which comprises the $R_{s(t)}$, $R_{d(t)}$, $Q_{s(t)}$, and $R_{d(t-1)}$, is the best combination for predicting the $SSL_{(t)}$. Hence, the predictive models, including SVR-M4, SVR-OTLBO-M4, and SVR-GA-M4, are nominated for further assessment.

To find out the best-fit model among all the models nominated in the present study, the heat map diagram (Figure 4) is used as a visual comparing tool. The diagram

employed the different normalized metrics to compare the cells with one and zero values, respectively, indicating the highest and lowest performance. Figure 4 demonstrates that the SVR-OTLBO-M4 has the best performance in both training and testing phases.

To further explore the performance of the models, the scatter plots of the estimated SSL using the models and the measured SSL are shown in Figure 5 for both training and testing phases. Also, the values of R^2 for the selected models have been reported. Based on Figure 5, it is clear that the proposed hybrid models are generally closer to the best line than the SVR model. Furthermore, the SVR-OTLBO-M4 provides the highest values of the R^2 in both training ($R^2 = 0.958$) and testing ($R^2 = 0.953$) phases.

To investigate the simulated data changes, the box plot is employed. The box plot of the simulated SSL for the selected models is shown in Figure 6. As some can see, the minimum and maximum of the SSL_{50} are, respectively, in the observed data ($SSL_{50\%} = 91 mg/l$) and SVR – M4 model ($SSL_{50\%} = 287 mg/l$). The relative difference between the

TABLE 2: The correlation obtained between the input variables and SSL.

Input variable	R
$Q_{s(t)}$	0.53
$Q_{s(t-1)}$	0.28
$Q_{s(t-2)}$	0.21
$Q_{s(t-3)}$	0.07
$Q_{s(t-4)}$	0.07
$R_{d(t)}$	0.58
$R_{d(t-1)}$	0.37
$R_{d(t-2)}$	0.14
$R_{d(t-3)}$	0.11
$R_{d(t-4)}$	0.06
$R_{d(t-5)}$	0.01
$R_{d(t-6)}$	0.02
$R_{s(t)}$	0.59
$R_{s(t-1)}$	0.34
$R_{s(t-2)}$	0.24
$R_{s(t-3)}$	0.08
$R_{s(t-4)}$	0.01
$R_{s(t-5)}$	−0.03
$R_{s(t-6)}$	0.04

R_d refers to Dehdasht rain gauge station and R_s refers to Saeed Abad rain gauge station.

TABLE 3: The input combinations used for the development of prediction models.

Input combination	Input variables				
M1	$R_{s(t)}$	—	—	—	—
M2	$R_{s(t)}$	$R_{d(t)}$	—	—	—
M3	$R_{s(t)}$	$R_{d(t)}$	$Q_{s(t)}$	—	—
M4	$R_{s(t)}$	$R_{d(t)}$	$Q_{s(t)}$	$R_{d(t-1)}$	—
M5	$R_{s(t)}$	$R_{d(t)}$	$Q_{s(t)}$	$R_{d(t-1)}$	$R_{s(t-1)}$

TABLE 4: The performance indices of the predictive models obtained in the testing phase.

Model	RRMSE	CC	WI	RPIQ	md
SVR-M1	6.550506	0.8115	0.232189	0.0	0.1051
SVR-M2	2.233665	0.9455	0.719599	0.0	0.2645
SVR-M3	1.122063	0.9321	0.963375	0.2599	0.426
SVR-M4	**1.082923**	**0.9502**	**0.973483**	**0.3229**	**0.4338**
SVR-M5	2.244611	0.9482	0.719599	0.0763	0.2616
SVR-OTLBO-M1	0.683569	0.9716	0.967713	0.0	0.5776
SVR-OTLBO-M2	0.741011	0.9729	0.963401	0.0	0.5382
SVR-OTLBO-M3	0.542558	**0.9769**	0.980796	0.7656	0.7208
SVR-OTLBO-M4	**0.537165**	0.9761	**0.981207**	**0.9201**	**0.7411**
SVR-OTLBO-M5	0.539417	0.9741	0.981165	0.8753	0.7379
SVR-GA-M1	0.722344	0.9674	0.964097	0.0	0.5694
SVR-GA-M2	1.146802	0.9684	0.912041	0.0	0.4142
SVR-GA-M3	0.689017	0.9649	0.969368	0.5517	0.64
SVR-GA-M4	**0.561758**	0.96961	**0.979467**	**0.8521**	**0.7323**
SVR-GA-M5	1.025376	**0.9704**	0.930302	0.2313	0.4493

observed data and the selected models is 215%, 56%, and 47%, respectively, associated with the SVR-M4, SVR-OTLBO-M4, and SVR-GA-M4 models. These values demonstrate that the hybrid models are closer to the observed data compared to the SVR model. Moreover, Figure 6 shows

that the minimum and maximum IQR measurements are referred to the observed data (81.5 mg/l) and SVR-GA-M4 model (112.95 mg/l). The relative difference in the observed data and the SVR-M4, SVR-OTLBO-M4, and SVR-GA-M4 models is, respectively, 13.8%, 12.5%, and 38.5%. This
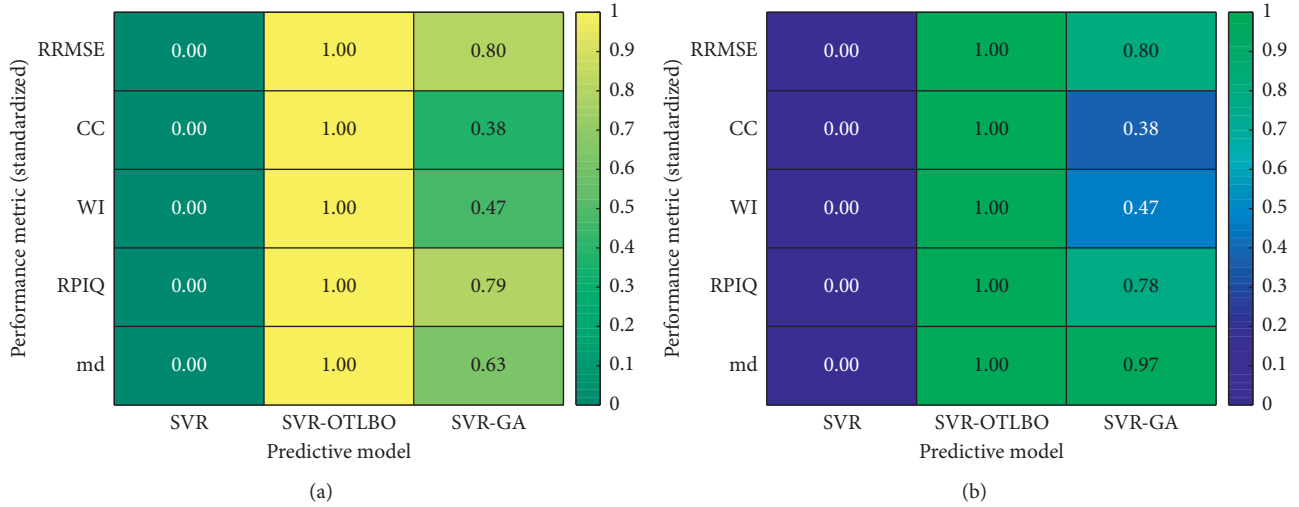
FIGURE 4: The performance of the selected models: (a) training phase and (b) testing phase.
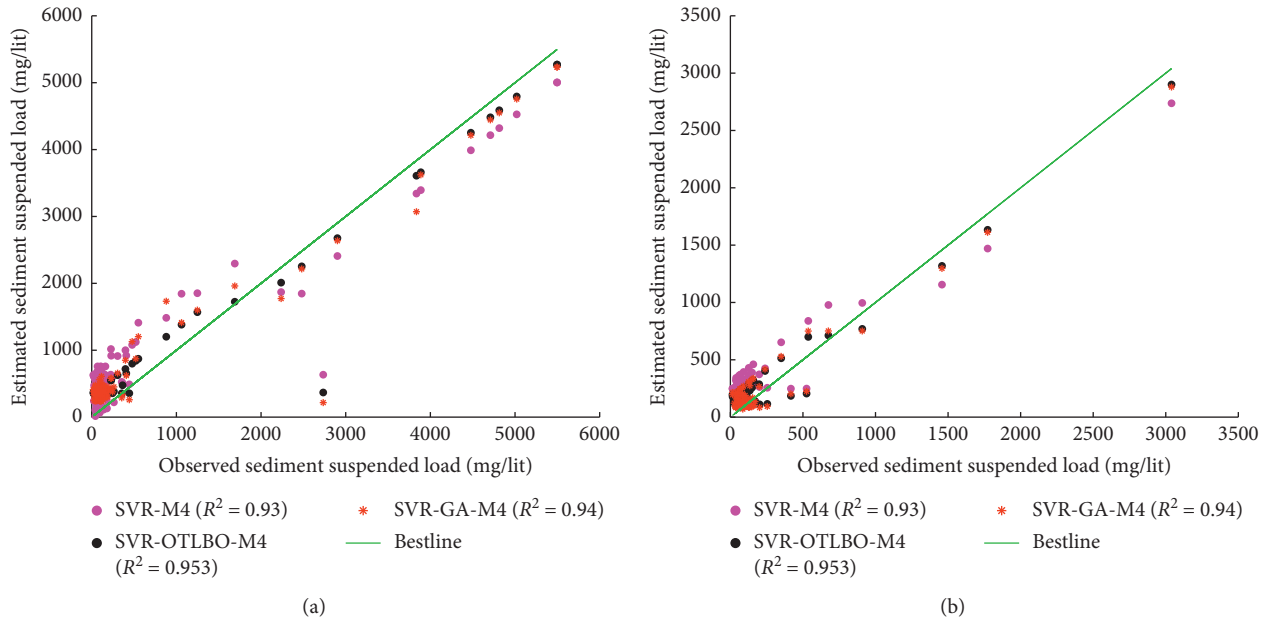
FIGURE 5: Scatter plots of observed and estimated suspended sediment load (mg/lit): (a) training phase and (b) testing phase.

observation depicts that the SVR-OTLBO has minimum changes compared to the other models.

In this study, the Taylor diagram is applied to combine several statistical criteria, including the standard deviation, correlation coefficient, and RSME [67]. Indeed, the main aim of the Taylor diagram is to discover the nearest predictive model with benchmark record data (in the present study, the observed SSL). The Taylor diagrams of the selected models are shown in Figure 7. Figure 7 shows that the simulated data by the SVR-OTLOB-M4 model is nearer to the observed data compared to the SVR-M4 or SVR-GA model in both the training and testing phases. Hence, the performance of the SVR-OTLBO model is higher compared to the other predictive models.

Previous studies have been widely used the SSL with different lags as input features to predict the SSL. However, providing a predictive model based on the other hydrological variables such as discharge or rainfall depth is more efficient due to the simplicity in measuring discharge and rainfall. To confirm this fact, the hybrid model proposed in the current study effectively estimates the suspended sediment load based on the rainfall and discharge data as input features.

4.3. Assessment of the Models' Uncertainty.
To measure the uncertainty of selected models in the present study, $CL_e^{\pm}$ values at the 5% of significant level over the testing phase are presented in Table 5.
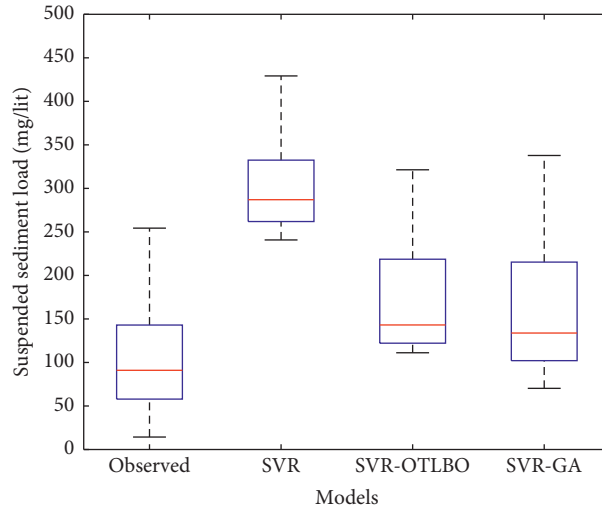
FIGURE 6: Boxplot of observed and estimated suspended sediment load.

(a)

(b)
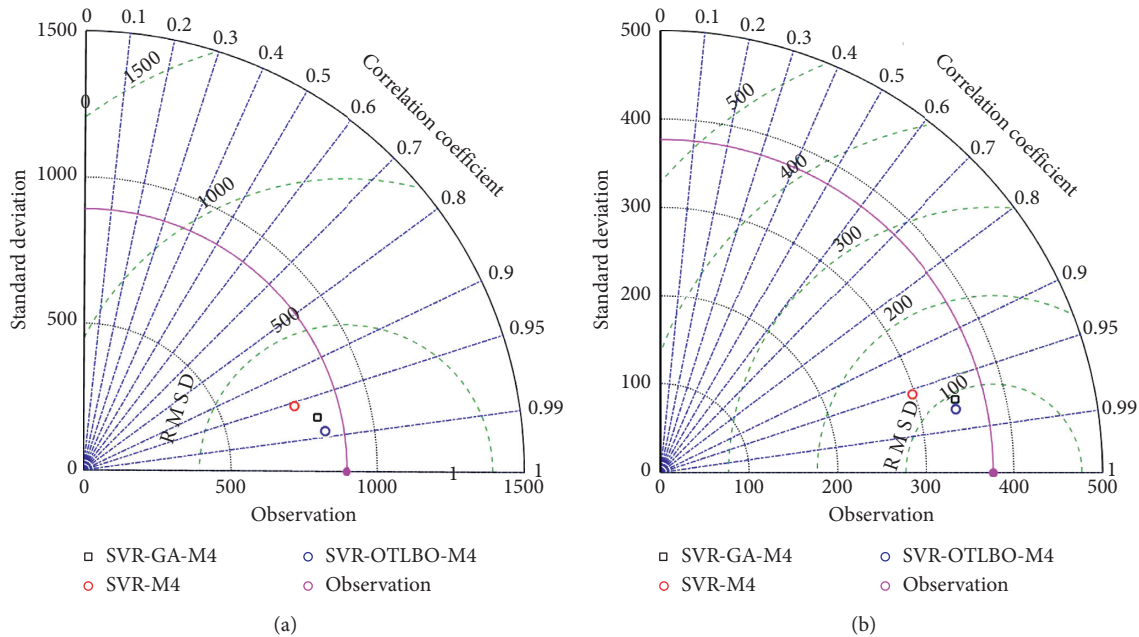
FIGURE 7: Taylor diagram of the observed and the predicted SSL (mg/lit) for the SVR, SVR-OTLBO, and SVR-GA models in (a) training phase and (b) testing phase.

Table 5 shows that the models provide the underestimated prediction values of suspended sediment load. Further, the lowest uncertainty band (312.0) is detected in the results gained by the SVR-OTLBO model. Mutually, the SVR model offers the highest uncertainty (369.2). This finding is consistent with the results attained from the performance metric that the SVR-OTLBO model has the highest advantage compared to other models used in the present study.

4.4. Assessment of the Proposed Models against Literature Models. Although the newly developed hybrid model in the current study, SVR-OTLBO, successfully predicts SSL, it is

interesting to compare its performance with those obtained in the other studies. Sadeghpourhaji et al. [39] investigated WSVM and SVM models for forecasting SSL, obtaining $R^2 = 0.838$ and 0.327, respectively. Rashidi et al. [43] developed two predictive models GT-SVM and SVM (RBF kernel), gaining $R^2 = 0.88$ and 0.79, respectively. Nourani et al. [42] executed SVM for forecasting SSL, gaining $R^2 = 0.91$. Kumar et al. [41] applied ANN, LASVR, multilinear regression (MLR), classification and regression tree (CART), and M5 to predict SSL, obtaining $R^2 = 0.919, 0.923, 0.91, 0.91$, and 0.92, respectively. Buyukyildiz and Kumcu [23] predicted daily SSL using scaled conjugate gradient (SCG) algorithm, radial basis neural

TABLE 5: Statistical characteristics of the prediction errors obtained by models proposed in the present study.

Predictive model	μ_e	S_e	CL_e^+	CL_e^-	Uncertainty band $CL_e^+ - CL_e^-$
SVR-M4	175.5	129.1	388.6	19.4	369.2
SVR-OTLBO-M4	52.9	94.5	208.9	−103.1	312.0
SVR-GA-M4	44.4	104.3	216.5	−127.7	344.2

network (RBNN), generalized regression neural network (GRNN), ANFIS-GP, ANFIS-GC, and SVR, obtaining $R^2 = 0.879, 0.864, 0.862, 0.861, 0.847$, and 0.868, respectively. Hssanpour et al. [46] developed a hybrid model based on FCM-SVR for predicting SSL, achieving $R^2 = 0.91$. Therefore, it can be found that the hybrid models reported in this research have better predictive performance compared to the SVR-based models in the literature.

5. Summary and Conclusions

The present study focused on the development of a hybrid model to estimate the suspended sediment load. For this purpose, the hydrometry and hydroclimatology data of the Cham Siah basin composed of river discharge, SSL, and rainfall depth data are employed. The support vector regression method is used to predict the SSL. As a number of parameters in the SVR are unknown, two hybrid models are developed. These hybrid models are composed of SVR-GA and SVR-OTLBO. In this study, five input variables are investigated. Also, five predictive models are designed for each SVR, SVR-GA, and SVR-OTLBO model. The correlation of SSL and the inputs variable is evaluated to identify the most significant input variables. Furthermore, five indices of RRMSE, R, WI, RPIQ, and md are employed to determine the best performance of models.

In general, the following findings are obtained in this study:

(i) Among all the SVR models, the performance of SVR-M4 is the highest. The SVR-OTLBO-M4 has the best performance compared with the other SVR-OTLBO models, and SVR-GA-M4 is the best-fit model among all the SVR-GA models.

(ii) Among those models with the highest performance, the SVR-OTLBO-M4 has the highest performance in both testing and training phases.

(iii) The hybrid models' predicted data are closer to observational data compared with the SVR model's output data. Besides, the SVR-OTLBO-M4 is the nearest predicted model with observational data.

(iv) Feature selection based on correlation methods is an inadequate approach due to the complexity of hydrological phenomena such as sediment. Using metaheuristic algorithms is an appropriate method in selecting features and finding the best input combinations. This limitation can be solved in the future by developing a multiobjective optimization model based on the OTLBO algorithm.

Data Availability

The data used to support the findings of this study are available from the corresponding author upon request.

Conflicts of Interest

The authors declare that they have no conflicts of interest.

References

[1] B. Choubin, H. Darabi, O. Rahmati, F. Sajedi-Hosseini, and B. Kløve, "River suspended sediment modelling using the CART model: a comparative study of machine learning techniques," *Science of The Total Environment*, vol. 615, pp. 272–281, 2018.

[2] J. M. Martinez, J. L. Guyot, N. Filizola, and F. Sondag, "Increase in suspended sediment discharge of the Amazon River assessed by monitoring network and satellite data," *Catena*, vol. 79, no. 3, pp. 257–264, 2009.

[3] V. Gholami, M. J. Booij, E. Nikzad Tehrani, and M. A. Hadian, "Spatial soil erosion estimation using an artificial neural network (ANN) and field plot data," *Catena*, vol. 163, pp. 210–218, 2018.

[4] R. M. Frings and M. G. Kleinhans, "Complex variations in sediment transport at three large river bifurcations during discharge waves in the river Rhine," *Sedimentology*, vol. 55, no. 5, pp. 1145–1171, 2008.

[5] M. Y. A. Khan, F. Tian, F. Hasan, and G. J. Chakrapani, "Artificial neural network simulation for prediction of suspended sediment concentration in the River Ramganga, Ganges Basin, India," *International Journal of Sediment Research*, vol. 34, no. 2, pp. 95–107, 2019.

[6] L. Wu, M. Peng, S. Qiao, and X.-y. Ma, "Effects of rainfall intensity and slope gradient on runoff and sediment yield characteristics of bare loess soil," *Environmental Science and Pollution Research*, vol. 25, no. 4, pp. 3480–3487, 2018.

[7] O. Kisi, "Modeling discharge-suspended sediment relationship using least square support vector machine," *Journal of Hydrology*, vol. 456-457, pp. 110–120, 2012.

[8] H.-W. Fang and G.-Q. Wang, "Three-dimensional mathematical model of suspended-sediment transport," *Journal of Hydraulic Engineering*, vol. 126, no. 8, pp. 578–592, 2000.

[9] B. Greimann, Y. Lai, and J. Huang, "Two-dimensional total sediment load model equations," *Journal of Hydraulic Engineering*, vol. 134, no. 8, pp. 1142–1146, 2008.

[10] M. H. Garcia, "Sedimentation engineering: processes, measurements, modeling and practice," *ASCE Manuals and Reports on Engineering Practice*, no. 110, American Society Civil Engineering Publications, 9780784408148, , p. 1150, 2008 .

[11] A. J. Horowitz, "An evaluation of sediment rating curves for estimating suspended sediment concentrations for subsequent flux calculations," *Hydrological Processes*, vol. 17, no. 17, pp. 3387–3409, 2003.

[12] N. E. M. Asselman, "Fitting and interpretation of sediment rating curves," *Journal of Hydrology*, vol. 234, no. 3-4, pp. 228–248, 2000.

[13] K. Vercruysse, R. C. Grabowski, and R. J. Rickson, "Suspended sediment transport dynamics in rivers: multi-scale drivers of temporal variation," *Earth-Science Reviews*, Elsevier, vol. 166, pp. 38–52, , Amsterdam, Netherlands, 2017.

[14] S. Araghinejad, *Data-Driven Modeling: Using MATLAB® in Water Resources and Environmental Engineering*, Vol. 67, Springer, Berlin, Germany, 2014.

[15] A. Parsaie, A. H. Haghiabi, M. Saneie, and H. Torabi, "Prediction of energy dissipation on the stepped spillway using the multivariate adaptive regression splines," *ISH Journal of Hydraulic Engineering*, vol. 22, no. 3, pp. 281–292, 2016.

[16] M. A. Shamim, M. Hassan, S. Ahmad, and M. Zeeshan, "A comparison of Artificial Neural Networks (ANN) and Local Linear Regression (LLR) techniques for predicting monthly reservoir levels," *KSCE Journal of Civil Engineering*, vol. 20, no. 2, pp. 971–977, 2016.

[17] P. Wang and L. C. Linker, "Improvement of regression simulation in fluvial sediment loads," *Journal of Hydraulic Engineering*, vol. 134, no. 10, pp. 1527–1531, 2008.

[18] M. Demirci and A. Baltaci, "Prediction of suspended sediment in river using fuzzy logic and multilinear regression approaches," *Neural Computing & Applications*, vol. 23, no. 1, pp. 145–151, 2013.

[19] V. K. Singh, D. Kumar, P. S. Kashyap, and O. Kisi, "Simulation of suspended sediment based on gamma test, heuristic, and regression-based techniques," *Environmental Earth Sciences*, vol. 77, no. 19, 2018.

[20] J. D. Salas, *Applied Modeling of Hydrologic Time Series*, Water Resources Publications, 1980.

[21] H. Moeeni and H. Bonakdari, "Forecasting monthly inflow with extreme seasonal variation using the hybrid SARIMA-ANN model," *Stochastic Environmental Research and Risk Assessment*, vol. 31, no. 8, p. 1997, 2017.

[22] S. Russell and P. Norvig, *Artificial Intelligence: A Modern Approach*, Pearson Education Limited, Upper Saddle River, NJ, USA, 3rd edition, 2016.

[23] M. Buyukyildiz and S. Y. Kumcu, "An estimation of the suspended sediment load using adaptive network based fuzzy inference system, support vector machine and artificial neural network models," *Water Resources Management*, vol. 31, no. 4, pp. 1343–1359, 2017.

[24] M. Haghbin, A. Sharafati, D. Motta, N. Al-Ansari, and M. H. M. Noghani, "Applications of soft computing models for predicting sea surface temperature: a comprehensive review and assessment," *Progress in Earth and Planetary Sciences*, vol. 8, no. 1, pp. 1–19, 2021.

[25] M. Haghbin, A. Sharafati, B. Dixon, and V. Kumar, "Application of soft computing models for simulating nitrate contamination in groundwater: comprehensive review, assessment and future opportunities," *Archives of Computational Methods in Engineering*, 2020.

[26] M. R. Mustafa, R. B. Rezaur, S. Saiedi, and M. H. Isa, "River suspended sediment prediction using various multilayer perceptron neural network training algorithms-a case study in Malaysia," *Water Resources Management*, vol. 26, no. 7, pp. 1879–1897, 2012.

[27] H. Moeeni and H. Bonakdari, "Impact of normalization and input on ARMAX-ANN model performance in suspended sediment load prediction," *Water Resources Management*, vol. 32, no. 3, pp. 845–863, 2018.

[28] A. Adib and A. Mahmoodi, "Prediction of suspended sediment load using ANN GA conjunction model with Markov chain approach at flood conditions," *KSCE Journal of Civil Engineering*, vol. 21, no. 1, pp. 447–457, 2017.

[29] R. Bakhtyar, A. Ghaheri, A. Yeganeh-Bakhtiary, and T. E. Baldock, "Longshore sediment transport estimation using a fuzzy inference system," *Applied Ocean Research*, vol. 30, no. 4, pp. 273–286, 2008.

[30] A. K. Lohani, N. K. Goel, and K. K. S. Bhatia, "Deriving stage-discharge-sediment concentration relationships using fuzzy logic," *Hydrological Sciences Journal*, vol. 52, no. 4, pp. 793–807, 2007.

[31] S. J. Mianaei and A. R. Keshavarzi, "Prediction of riverine suspended sediment discharge using fuzzy logic algorithms, and some implications for estuarine settings," *Geo-Marine Letters*, vol. 30, no. 1, pp. 35–45, 2010.

[32] A. Guven and Ö. Kişi, "Estimation of suspended sediment yield in natural rivers using machine-coded linear genetic programming," *Water Resources Management*, vol. 25, no. 2, pp. 691–704, 2011.

[33] E. Shamaei and M. Kaedi, "Suspended sediment concentration estimation by stacking the genetic programming and neuro-fuzzy predictions," *Applied Soft Computing*, vol. 45, pp. 187–196, 2016.

[34] K. Samet, K. Hoseini, H. Karami, and M. Mohammadi, "Comparison between soft computing methods for prediction of sediment load in rivers: maku dam case study," *Iranian Journal of Science and Technology, Transactions of Civil Engineering*, vol. 43, no. 1, pp. 93–103, 2019.

[35] Z. He, X. Wen, H. Liu, and J. Du, "A comparative study of artificial neural network, adaptive neuro fuzzy inference system and support vector machine for forecasting river flow in the semiarid mountain region," *Journal of Hydrology*, vol. 509, pp. 379–386, 2014.

[36] Z. Liang, Y. Li, Y. Hu, B. Li, and J. Wang, "A data-driven SVR model for long-term runoff prediction and uncertainty analysis based on the Bayesian framework," *Theoretical and Applied Climatology*, vol. 133, no. 1-2, pp. 137–149, 2018.

[37] M. Karamouz, A. Ahmadi, and A. Moridi, "Probabilistic reservoir operation using Bayesian stochastic model and support vector machine," *Advances in Water Resources*, vol. 32, no. 11, pp. 1588–1600, 2009.

[38] G.-F. Lin, Y.-C. Chou, and M.-C. Wu, "Typhoon flood forecasting using integrated two-stage support vector machine approach," *Journal of Hydrology*, vol. 486, pp. 334–342, 2013.

[39] M. Sadeghpourhaji, S. A. Mirbagheri, A. H. Javid, M. Khezri, and G. D. Najafpour, "A wavelet support vector machine combination model for daily suspended sediment forecasting," *International Journal of Engineering*, vol. 27, no. 6, pp. 855–864, 2014.

[40] V. Nourani and G. Andalib, "Daily and monthly suspended sediment load predictions using wavelet based artificial intelligence approaches," *Journal of Mountain Science*, vol. 12, no. 1, pp. 85–100, 2015.

[41] D. Kumar, A. Pandey, N. Sharma, and W.-A. Flügel, "Daily suspended sediment simulation using machine learning approach," *Catena*, vol. 138, pp. 77–90, 2016.

[42] V. Nourani, F. Alizadeh, and K. Roushangar, "Evaluation of a two-stage SVM and spatial statistics methods for modeling monthly river suspended sediment load," *Water Resources Management*, vol. 30, no. 1, pp. 393–407, 2016.

[43] S. Rashidi, M. Vafakhah, E. K. Lafdani, and M. R. Javadi, "Evaluating the support vector machine for suspended sediment load forecasting based on gamma test," *Arabian Journal of Geosciences*, vol. 9, no. 11, 2016.

[44] S. K. Himanshu, A. Pandey, and B. Yadav, "Ensemble wavelet-support vector machine approach for prediction of suspended sediment load using hydrometeorological data," *Journal of Hydrologic Engineering*, vol. 22, no. 7, 2017.

[45] S. K. Himanshu, A. Pandey, and B. Yadav, "Assessing the applicability of TMPA-3B42V7 precipitation dataset in wavelet-support vector machine approach for suspended

sediment load prediction," *Journal of Hydrology*, vol. 550, pp. 103–117, 2017.

[46] F. Hassanpour, S. Sharifazari, K. Ahmadaali, S. Mohammadi, and Z. Sheikhalipour, "Development of the FCM-SVR hybrid model for estimating the suspended sediment load," *KSCE Journal of Civil Engineering*, vol. 23, no. 6, pp. 2514–2523, 2019.

[47] A. Malik, A. Kumar, O. Kisi, and J. Shiri, "Evaluating the performance of four different heuristic approaches with Gamma test for daily suspended sediment concentration modeling," *Environmental Science and Pollution Research*, vol. 26, no. 22, pp. 22670–22687, 2019.

[48] M. Rahgoshay, S. Feiznia, M. Arian, and S. A. A. Hashemi, "Simulation of daily suspended sediment load using an improved model of support vector machine and genetic algorithms and particle swarm," *Arabian Journal of Geosciences*, vol. 12, no. 9, 2019.

[49] M. Al-Mukhtar, "Random forest, support vector machine, and neural networks to modelling suspended sediment in Tigris River-Baghdad," *Environmental Monitoring and Assessment*, vol. 191, no. 11, pp. 1–12, 2019.

[50] M. Rahgoshay, S. Feiznia, M. Arian, and S. A. A. Hashemi, "Modeling daily suspended sediment load using improved support vector machine model and genetic algorithm," *Environmental Science and Pollution Research*, vol. 25, no. 35, pp. 35693–35706, 2018.

[51] E. Kakaei Lafdani, A. Moghaddam Nia, and A. Ahmadi, "Daily suspended sediment load prediction using artificial neural networks and support vector machines," *Journal of Hydrology*, vol. 478, p. 50, 2013.

[52] M. Shahrouzi, M. Aghabagloua, and F. Rafiee, "Observer-teacher-learner-based optimization: an enhanced meta-heuristic for structural sizing design," *Structural Engineering and Mechanics*, vol. 62, no. 5, pp. 537–550, 2017.

[53] V. N. Vapnik, *The Nature of Statistical Learning Theory*, Springer, Berlin, Germany, 2000.

[54] S. H. H. Lavasani and R. Doroudi, "Meta heuristic active and semi-active control systems of high-rise building," *International Journal of Structural Engineering*, vol. 10, no. 3, pp. 232–253, 2020.

[55] J. Holland, *Adaptation in Natural and Artificial Systems*, University Michigan Press, Ann Arbor, MI, USA, 1975.

[56] A. Malik, A. Kumar, and J. Piri, "Daily suspended sediment concentration simulation using hydrological data of Pranhita River Basin, India," *Computers and Electronics in Agriculture*, vol. 138, pp. 20–28, 2017.

[57] D. Mouillot and A. Leprêtre, "A comparison of species diversity estimators," *Researches on Population Ecology*, vol. 41, no. 2, pp. 203–215, 1999.

[58] G.-F. Lin and L.-H. Chen, "A non-linear rainfall-runoff model using radial basis function network," *Journal of Hydrology*, vol. 289, no. 1-4, pp. 1–8, 2004.

[59] C. J. Willmott, "On the validation of models," *Physical Geography*, vol. 2, no. 2, pp. 184–194, 1981.

[60] V. Bellon-Maurel, E. Fernandez-Ahumada, B. Palagos, J.-M. Roger, and A. McBratney, "Critical review of chemometric indicators commonly used for assessing the quality of the prediction of soil attributes by NIR spectroscopy," *TrAC Trends in Analytical Chemistry*, vol. 29, no. 9, pp. 1073–1081, 2010.

[61] D. R. Legates and G. J. McCabe, "Evaluating the use of "goodness-of-fit" Measures in hydrologic and hydroclimatic model validation," *Water Resources Research*, vol. 35, no. 1, pp. 233–241, 1999.

[62] M. Najafzadeh, M. Rezaie Balf, and E. Rashedi, "Prediction of maximum scour depth around piers with debris accumulation using EPR, MT, and GEP models," *Journal of Hydroinformatics*, vol. 18, no. 5, pp. 867–884, 2016.

[63] V. Nourani, A. Molajou, A. D. Tajbakhsh, and H. Najafi, "A wavelet based data mining technique for suspended sediment load modeling," *Water Resources Management*, vol. 33, no. 5, pp. 1769–1784, 2019.

[64] A. Tafarojnoruz and A. Sharafati, "New formulations for prediction of velocity at limit of deposition in storm sewers based on a stochastic technique," *Water Science and Technology*, vol. 81, no. 12, pp. 2634–2649, 2020.

[65] A. Sharafati, S. B. H. S. Asadollah, and A. Neshat, "A new artificial intelligence strategy for predicting the groundwater level over the Rafsanjan aquifer in Iran," *Journal of Hydrology*, vol. 591, p. 125468, 2020.

[66] A. Sharafati, S. B. H. S. Asadollah, and M. Hosseinzadeh, "The potential of new ensemble machine learning models for effluent quality parameters prediction and related uncertainty," *Process Safety and Environmental Protection*, vol. 140, 2020.

[67] K. E. Taylor, "Summarizing multiple aspects of model performance in a single diagram," *Journal of Geophysical Research: Atmospheres*, vol. 106, no. D7, pp. 7183–7192, 2001.

Research Article

Estimation of Suspended Sediment Load Using Artificial Intelligence-Based Ensemble Model

Vahid Nourani [ID],[1] **Huseyin Gokcekus** [ID],[2] **and Gebre Gelete** [ID][2,3]

[1]*Center of Excellence in Hydroinformatics and Faculty of Civil Engineering, University of Tabriz, Tabriz, Iran*
[2]*Faculty of Civil and Environmental Engineering, Near East University, Northern Cyprus, Mersin 10, Turkey*
[3]*College of Agriculture and Environmental Science, Arsi University, 193, Asela, Ethiopia*

Correspondence should be addressed to Vahid Nourani; vnourani@yahoo.com

Suspended sediment modeling is an important subject for decision-makers at the catchment level. Accurate and reliable modeling of suspended sediment load (SSL) is important for planning, managing, and designing of water resource structures and river systems. The objective of this study was to develop artificial intelligence- (AI-) based ensemble methods for modeling SSL in Katar catchment, Ethiopia. In this paper, three single AI-based models, that is, support vector machine (SVM), adaptive neurofuzzy inference system (ANFIS), feed-forward neural network (FFNN), and one conventional multilinear regression (MLR) modes, were used for SSL modeling. Besides, four different ensemble methods, neural network ensemble (NNE), ANFIS ensemble (AE), weighted average ensemble (WAE), and simple average ensemble (SAE), were developed by combining the outputs of the four single models to improve their predictive performance. The study used two-year (2016-2017) discharge and SSL data for training and verification of the applied models. Determination coefficient (DC) and root mean square error (RMSE) were used to evaluate the performances of the developed models. Based on the performance measure results, the ANFIS model provides higher efficiency than the other developed single models. Out of all developed ensemble models, the nonlinear ANFIS model combination method was found to be the most accurate method and could increase the efficiency of SVM, MLR, ANFIS, and FFNN models by 19.02%, 37%, 9.73%, and 16.3%, respectively, at the verification stage. Overall, the proposed ensemble models in general and the AI-based ensemble in particular provide excellent performance in SSL estimation.

1. Introduction

Accurate modeling of the suspended sediment transported by a river is of great importance in environmental and water resources engineering, as it directly affects the design, planning, operation, and management of water resources [1]. Moreover, modeling of suspended sediment is crucial because it has a major effect on the reservoir capacity and dam operation [2], water quality, and contaminant transport [3, 4]. However, suspended sediment estimation is a challenging task for hydrologists as its interaction with geomorphological characteristics of the catchment and the streamflow is highly complex and nonlinear. Suspended sediment transport in the river is a function of meteorological and hydrological parameters as a complicated process [5].

For the last decades, several studies were conducted to model the relationship between river flow and suspend sediment amount [1]. However, none of the developed models has gotten universal acceptance for application in all cases. So far, several researchers have proposed many models to estimate this complex process ranging from simple statistical, physical, and black-box models. In earlier decades, modeling suspended sediment load using mathematical models was a common task. However, their application was limited because of the significant time required to set up the model [6] and the large number of variables involved in the equations [7].

The physically based models are reliable methods for assessing the actual physics of a phenomenon. Physically based models for suspended sediment load (SSL) modeling

are usually based on the simplified equitation of sediment and discharge as well as on the relationship between the erosive effect of flow and rainfall (e.g., [8–10]). Such physical and conceptual models can take into account the effect of catchment property and uneven distribution evapotranspiration and rainfall on the catchment [1]. However, using physically based models for hydrological modeling is rather complex as they require detailed temporal and spatial data, which are not easily available. Estimating suspended sediment load using a physically based model is a very difficult task due to its requirement of high-resolution sediment and discharge data which are not often available [11]. Moreover, direct measurement of high-resolution sediment concentration and discharge is expensive and any error in measurement of these variables also influences the modeling of suspended sediment load. When accurate estimation is more important than the physical understanding of the phenomenon, the application of black-box modeling is helpful.

To overcome the limitation of the physical-based models, black-box artificial intelligence- (AI-) based approaches which are reliable methods in dealing with nonlinear and complex phenomena have been employed in different fields of water resources engineering. Examples of this include modeling suspended sediment load of the rivers (e.g., see [12, 13]), rainfall-runoff process (e.g., see [14, 15]), longitudinal dispersion coefficient of water pipeline (e.g., see [16]), and estimation of overtopping flow the incipient motion of riprap stones (e.g., see, [17]). The AI methods applied for the modeling of SSL include artificial neural network (ANN), adaptive neurofuzzy inference system (ANFIS), and support vector machine (SVM). ANFIS model is an AI-based model appropriate for modeling nonlinear and complex processes like suspended sediment load (e.g., [1, 12–18]). So far, different works have been reported in the literature on the application of ANN in SSL modeling (e.g., [19–21]). SVM is another AI-based model capable of giving a reliable estimation of suspended sediment load (e.g., [1, 4, 22]). In addition to AI-based models, conventional multilinear regression (MLR) was used in this study. Because of some difficulties in working with AI-based models, some researchers applied straightforward, simple, and fast modeling tools such as MLR to describe the linear relationship between the response and one or more independent variables [23]. MLR has been successfully applied in modeling different hydrological problems like evapotranspiration [23], rainfall-runoff process [14], and suspended sediment load [20, 24].

Although the abovementioned AI-based models can give reasonable results, it is clear that one model may show higher performance than the others for a given data set and when different data sets are used, the results may entirely be different [25]. No single model is superior in providing a hydrological process forecast for any kind of watershed in all conditions compared to those of other competing models [26]. Therefore, combining the outputs of different models using different ensemble techniques was believed to give high predictive performance results and low error by taking the advantages of different models. In this regard, Bates and Granger [27] approved that combining the

outputs from several models using ensemble techniques would lead to results that outperform the individual forecasts. The thought behind the model combination is to make use of the exclusive characteristics of the single models in a unique framework that would improve the modeling accuracy [28]. The combination of different model outputs using several ensemble techniques has become a common practice for the improvement of prediction accuracy in different fields [29–31]. In the field of hydrology, the first ensemble method was examined by Cavadias and Morin [32]. Since then, the advantages of ensemble techniques for improving modeling efficiency have been proven in modeling several hydrological processes (e.g., see [26, 33, 34]). However, to date and based on our knowledge, there is no study done so far showing the application of AI-based model combination methods for suspended sediment load simulation. The main objective of this work was to develop AI-based ensemble methods for daily suspended sediment load estimation in Katar catchment, Ethiopia. Three steps were followed to achieve this objective. Sensitivity analysis was made to select significant and relevant inputs in the first step. Secondly, four black-box models, namely, ANFIS, ANN, SVM, and MLR models, were developed to estimate suspended sediment load. These AI-based (ANFIS, FFNN, and SVM) models are chosen in this study because of their fast convergence time, simplicity, and reliable estimation performance for complex hydrological processes like SSL. Finally, the four ensemble models (ANFIS ensemble (AE), neural network ensemble (NNE), simple average ensemble (SAE), and weighted average ensemble (WAE)) were created to increase the predicting performance of the single black-box models in forecasting suspended sediment. AE and NNE were chosen as the nonlinear ensemble method over the other AI-based models because of their compatibility, popularity, and also their high performance reported in model combination studies in other different fields [25, 35]. Moreover, the AE was introduced in this study due to the robustness of the model observed in the single models. These ensemble techniques have the potential to provide researchers, decision-makers, and river and watershed managers with accurate and fast methods for SSL estimation.

The models were examined for modeling SSL of Katar catchment containing Katar River that drains into Lake Ziway which supports the lives of millions of people. The catchment is characterized by intensive agriculture where both rainfed and irrigated crops are grown. Because of sediment deposition attributed to periodic flooding together with improper agriculture, floodplains are formed along the bank of the lake and the river. Moreover, this sediment transported through the river causes siltation of irrigation canals and Lake Ziway. Thus, in this study, the Katar catchment is chosen as the case study due to the availability of discharge and SSL data (even though it is only two years) and also for challenging problems associated with sedimentation. Therefore, the Katar catchment represents a good case study to assess the SSL estimation accuracy of the proposed single and ensemble models.

2. Materials and Methods

2.1. Study Area Description.
The study area, the Katar River catchment, is a subcatchment of the Ethiopian central rift valley basin. This watershed is located in the Oromia Regional State of Ethiopia and the northern part of the central rift valley basin as part of the Ziway-Shala basin. Geographically, the catchment lies between 7°21'34" and 8°9'55" north latitudes and 38°53'57" and 39°24'46" east longitude (see Figure 1). The topography of the Katar catchment is complex, with elevations ranging from 1673 m (Abura) to 4181 m above sea level. The total area of the watershed, upstream, of the Abura gauging station is estimated to be 3350 km^2. The climate of the catchment is characterized by a semiarid to subhumid climate with minimum and maximum annual precipitation values of 731.8 mm and 1229.7 mm, respectively. The mean annual temperature ranges between 16°C and 20°C. The dry season occurs from October to May, and more than 70% of the rain falls during the summer season. The catchment attained a maximum discharge of 116.32 m^3/s in August and a minimum discharge of 0.115 m^3/s in January. Runoff from Katar catchment drains into the Lake Ziway. The land use of the study area is characterized dominantly by intensive agriculture where both rainfed and irrigated crops are grown.

Regarding soil type, Katar catchment consists of six major soil types as vertisols, andosols, leptosols, fluvisols, cambisols, and luvisols (see Figure 2).

2.1.1. Sedimentation Problem in the Study Area.
Katar catchment is one of the data-scarce areas of the country where there is very limited historical measured suspended sediment data. Therefore, studying suspended sediment of the catchment is important to obtain accurate information about the siltation rate and the resulted reservoir storage loss over time. The catchment attains a maximum SSL of 57335.524 ton/day in August and a minimum SSL of 0 ton/day in January. The catchment is one of the degraded areas with intensive agriculture and farming on steep slopes. Furthermore, the dense population together with improper agricultural activity and rolling topography makes the catchment susceptible to soil erosion. The Katar River joins Lake Ziway and according to Aga et al. [36], there is a proposed dam on this river for multiple uses. Soil erosion due to poor management and heavy rainfall is common phenomena occurring upstream. The sediment is transported and deposited at the mouth of the stream channel (see Figure 3). Despite the aforementioned problems, little attention was given to the catchment in the field of suspended sediment load modeling and management. Therefore, it is necessary to study the SSL of the catchment using an effective technique to obtain better information about the sediment condition of the area to have reliable management projects.

2.2. Data Used in the Study.
In this study, the daily SSL and discharge data of Katar River catchment at Abura station for two years (2016-2017) were used for training and verification of the developed models. The data were divided into two subsets: the first 70% were used for training and 30% of the data were used for verification purposes. Table 1 presents the descriptive statistics (minimum, average, maximum, and standard deviation) of the used data.

The time series plot of daily SSL and discharge values of Katar catchment at Abura station throughout the study period is shown in Figure 4. The data from 1 January 2016 to 25 May 2017 were used for training and the remaining data (from 26 May to 31 December 2017) served for verification of the applied models.

2.3. Proposed Methodology.
In this paper, three AI (SVM, ANFIS, and FFNN) and one MLR were used for modeling suspended sediment load in the Katar catchment. The input data used were normalized and classified into training and verification sets. The study was conducted via three stages (see Figure 5). In the first stage, the selection of the most relevant and dominant inputs for suspended sediment load estimation was conducted through nonlinear sensitivity analysis. Secondly, four black-box models, namely, FFNN, SVM, NFIS, and MLR, models were applied for the estimation of suspended sediment. Finally, four ensemble techniques, namely, AE, NNE, SAE, and WAE, were developed. In this stage, the outputs from single black-box models were used as the inputs for the ensemble process. The obtained suspended sediment load from the last stage was compared with the results obtained from individual models in the second step.

2.3.1. Feed-Forward Neural Network (FFNN).
ANN is among the extensively applied AI techniques in hydrological modeling which works based on simulation of the structure and operational performance of a biological neural network. In recent years, ANN as a self-adaptive and self-learning simulation function has shown great ability in forecasting and modeling complex hydrological processes. Its ability to learn from example makes ANN more efficient and applicable in many fields of science, economics, engineering, etc. [35]. According to [37], the advantage of the ANN model is that it establishes a relationship between the dependent and predicted variables by training the neural network without detailed knowledge of the characteristics of the catchment. Among different ANN forms, FFNN with a backpropagation algorithm was used for this study because of its simplicity and extraordinary preferred position of giving exceptional answers for different problems without prior knowledge of the process.

The FFNN consists of interconnected processing elements known as nodes with unique characteristics of information processing such as learning, nonlinearity, noise tolerance, and generalization capability.

FFNN structure contains three layers, namely, the input, hidden, and output layer (see Figure 6). In the FFNN, the inputs presented to the input layers' neuron are propagated in a forward direction and a nonlinear function known as activation function is used to compute the output vector.
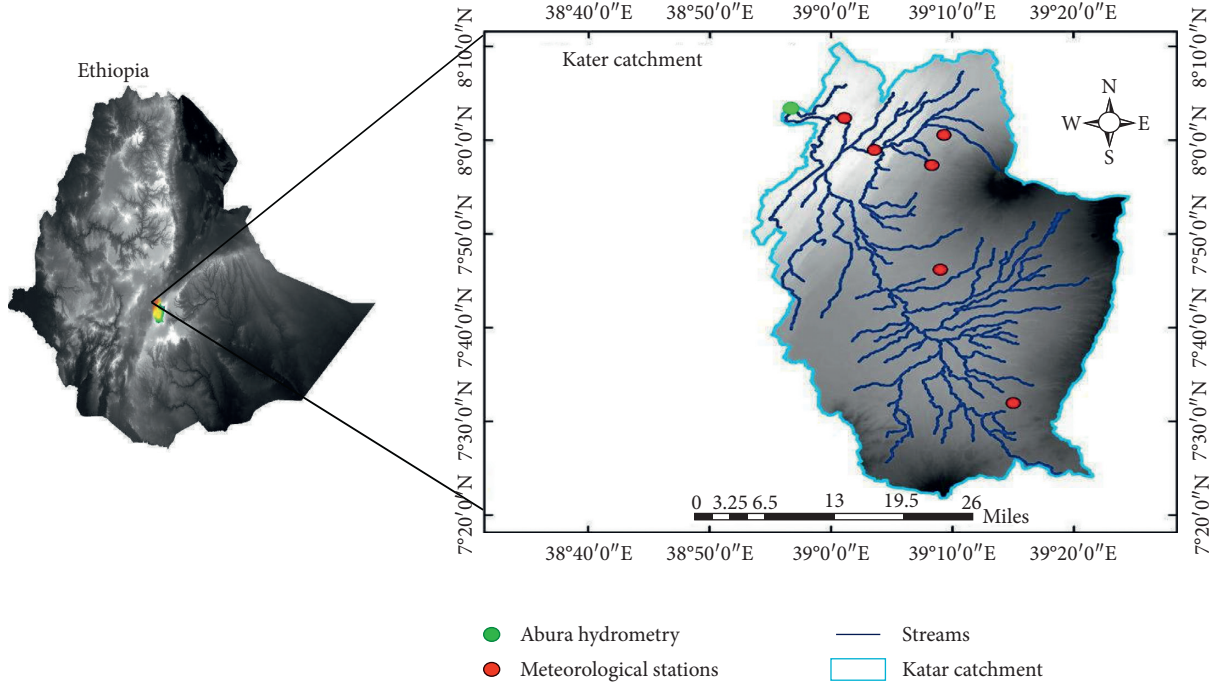
FIGURE 1: Study area map.

2.3.2. Adaptive Neurofuzzy Inference System (ANFIS). ANFIS developed by Jang [38] is a universal approximator to overcome the limitations of both ANN and fuzzy inference system. ANFIS is an amalgamation of both ANN and fuzzy inference systems (FIS) that has a strong capability to handle the uncertainty of dynamic and complex interactions that exist between the input and output variables.

Every fuzzy system has three different parts, namely, defuzzifier, fuzzifier, and fuzzy database. The fuzzy rule base consists of rules which are fuzzy proposition related as is demonstrated by Jang et al. [39]. As a result, the fuzzy inference is applied in the operational analysis. This goal can be achieved by employing different fuzzy inference engine. The most famous FIS are Tsukamoto's system [40], Sugeno's system [41], and Mamdani's system [42]. These three types are different from each other. Sugeno's approach uses constant functions, whereas fuzzy membership functions (MFs) are used in Mamdani's approach.

The ANFIS model architecture consists of five layers with layer 1 representing the input layer; layer 2 representing the input membership function; layer 3 representing rules; layer 4 representing the output MFs; and layer 5 representing the output configured as illustrated in Figure 7.

Once the fuzzy system has been built, the relation between fuzzy variables is specified using if-then fuzzy rules. Assuming that FIS contains two inputs (x and y) and output (f), a first-order Sugeno fuzzy has the following rules:

$$\text{Rule (1): if } \mu(x) \text{ is } A_1 \text{ and } \mu(y) \text{ is } B_1 \text{: then } f_1 = p_1 x + q_1 y + r_1,$$

$$\text{Rule (2): if } \mu(x) \text{ is } A_2 \text{ and } \mu(y) \text{ is } B_2 \text{: then } f_2 = p_2 x + q_2 y + r_2,$$

$$\tag{1}$$

where A_1 and A_2 are MF parameters for input x and B_1 and B_2 are MFs for the inputs y, respectively, whereas p_1, q_1, r_1, p_2, q_2, and r_2 are outlet functions' parameters. The arrangement and structural formula of ANFIS layers are as follows:

Layer 1: every node i is an adaptive node in this layer, which has a node function as equation (2).

$$Q_i^1 = \mu Ai(x), \quad \text{for } i = 1, 2$$
$$\text{or } Q_i^1 = \mu Bi(x), \quad \text{for } i = 3, 4, \tag{2}$$

where Q_i^1 represents the membership grade for inputs x and y. Gaussian MF was chosen due to its lowest prediction error.

Layer 2: every rule between inputs in this layer is connected by the T-Norm operator which is performed with "and" operator as in equation (3).

$$Q_i^2 = wi = \mu Ai(x) \cdot \mu Bi(y), \quad \text{for } i = 1, 2. \tag{3}$$

Layer 3: the output in this layer is normalized firing strength and calculated as

$$Q_i^3 = \overline{w} = \frac{w_i}{w_1 + w_2}, \quad i = 1, 2. \tag{4}$$

Layer 4: each node i in this layer calculates the consequence of the rules on the output of the model:

$$Q_i^4 = \overline{w}(p_i x + q_i y + r_i) = \overline{w} f_i. \tag{5}$$
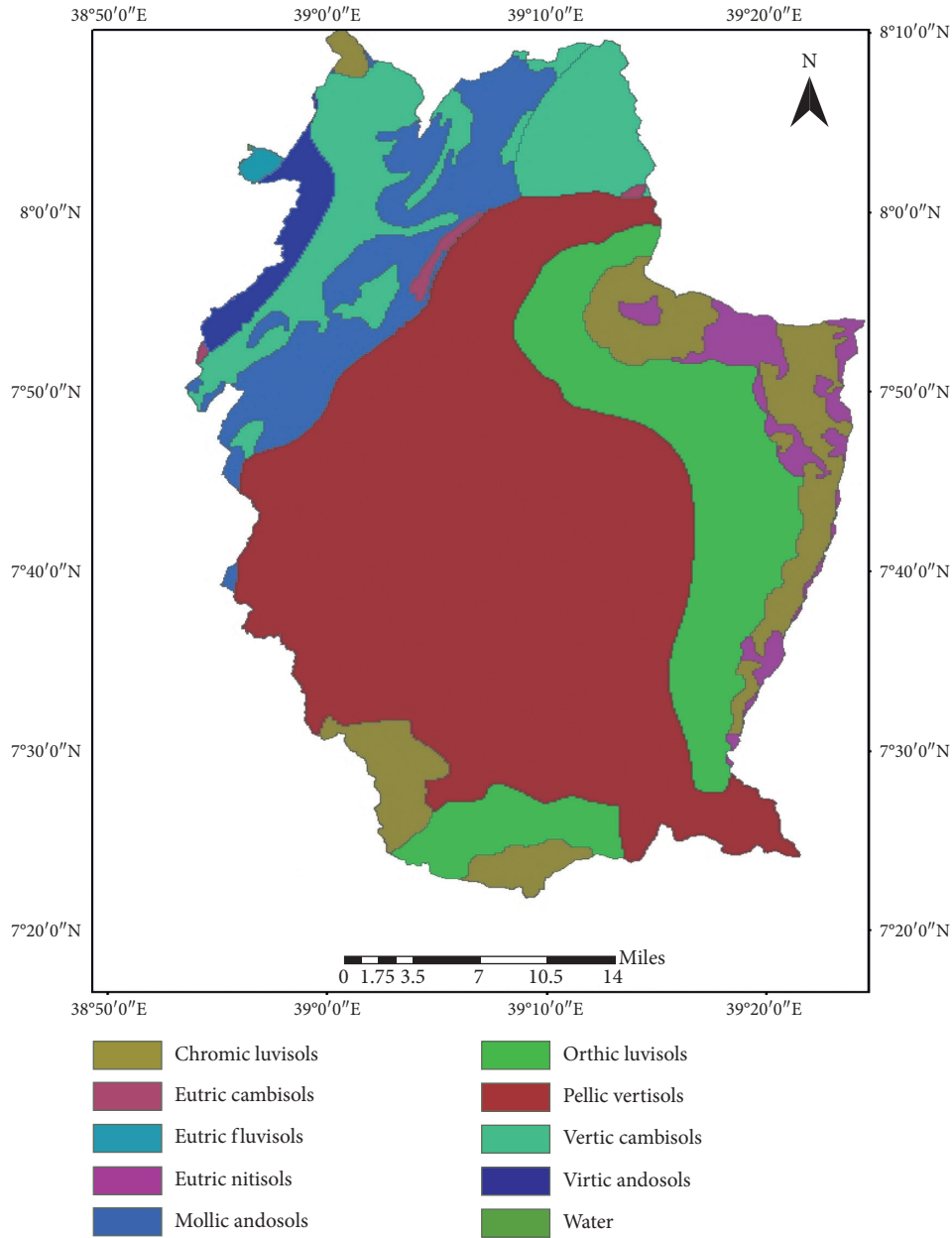
Figure 2: Soil map of the study area.

Figure 3: Siltation along the riverbank [36].

$\overline{w}$ is the layer 3 output and p_1, q_1, and r_1 are consequent parameters.

Layer 5: the overall ANFIS output is calculated by adding all of the incoming signals to this layer as

$$Q_i^5 = \overline{w}\left(p_i x + q_i y + r_i\right) \sum w_i f_i = \frac{\sum w_i f_i}{\sum w_i}. \qquad (6)$$

2.3.3. Support Vector Machine (SVM). It is an artificial intelligence model that can be used for both regression and classification tasks [43]. SVM is a relatively new approach that can successfully be applied in the modeling of nonlinear

TABLE 1: Descriptive statistics of daily runoff and sediment data.

Data set	Period	Statistical parameters				
		Min	Mean	Max	Standard deviation	Coefficient of variation
Discharge (m^3/s)	Training	0.115	8.862	116.32	15.3016	1.727
	Verification	0.8	17.338	111.32	20.062	1.157
	Whole	0.115	11.401	116.32	17.31	1.518
SSL (ton/day)	Training	0	1760.29	57335.524	5102.626	2.899
	Verification	0	3391.356	52947.35	5850.01	1.725
	Whole	0	2248.94	57335.52	5389.566	2.397

FIGURE 4: Time series of suspended sediment load and river discharge observed at Katar catchment (Abura station) for a period of two years (2016-2017).
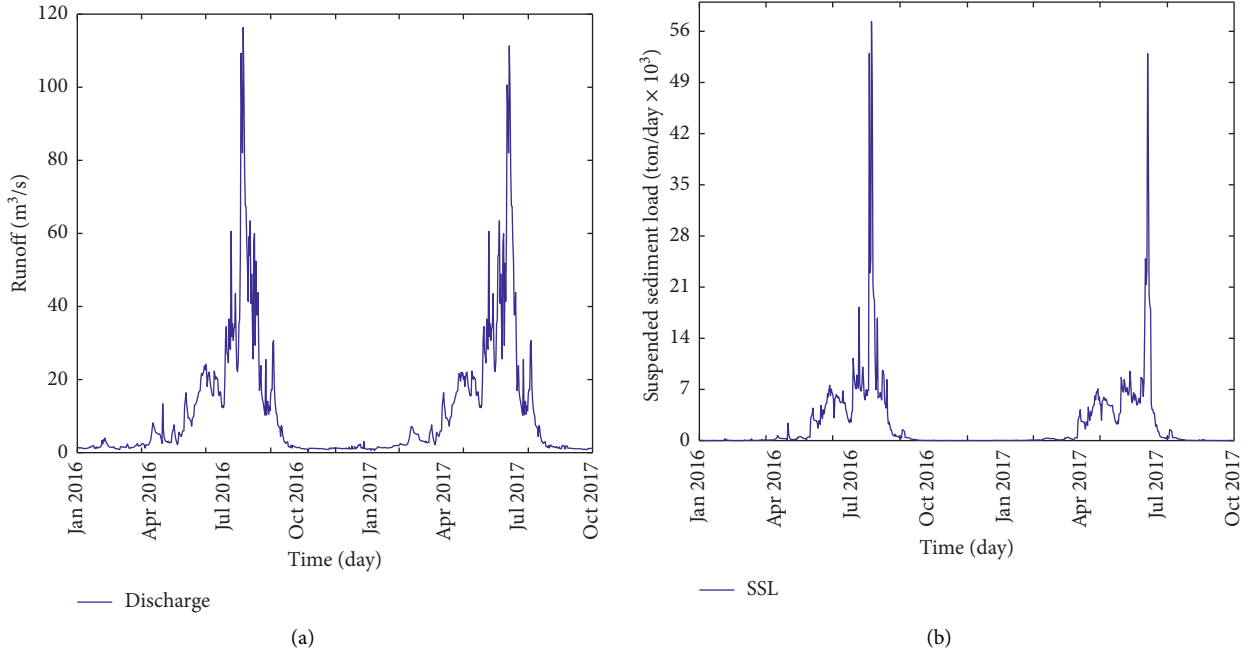
and complex real-world problems. The regression estimation with SVM is to estimate a function according to a given data set, $\{(x_i, d_i)\}_i^n$ where x_i denotes the input vector, d_i denotes the actual value, and n is the total number of data sets. The general SVM regression function is formulated as

$$y = f(x) = \omega\varphi(x_i) + b, \qquad (7)$$

where φ is nonlinear mapping function and ω and b are regression function parameters and determined by assigning positive values for the slack parameters of ξ and $\xi*$ and minimization of the objective function as shown in

$$\text{Minimize} \frac{1}{2}\|w\|^2 + c\left(\sum_{i}^{n}(\xi_i + \xi_i^*) \right)$$

$$\text{Subjected to} \quad \begin{cases} w_i\phi(x_i) + b_i - d_i \leq \varepsilon + \xi_i^* \\ d_i - w_i\phi(x_i) + b_i \leq \varepsilon + \xi_i^*, \quad i = 1, 2, \ldots n, \\ \xi_i\xi_i^* \end{cases}$$

$$(8)$$

where $(1/2)\|w\|^2$ is the weights vector norm and C is the regularized constant; the general conceptual model structure of SVM is illustrated in Figure 8.

By defining Lagrange multipliers α_i and α_i^*, the optimization problem shown above can be changed to a dual quadratic optimization problem. The vector w can be determined after finding the problem solution of optimization [44].

$$w^* = \sum_{i}^{n}(\alpha_i - \alpha_i^*)\varphi(x_i). \qquad (9)$$

Therefore, the general form of SVM can be in the form as

$$f(x, \alpha_i, \alpha_i^*) = \sum_{i=1}^{n}(\alpha_i - \alpha_i^*)K(x, x_i) + b, \qquad (10)$$

where $k(x_i, x_j)$ is the kernel function and b is the bias term. The radial basis function (Gaussian) is the most common kernel function [45] and is expressed as

$$k(x_1, x_2) = \exp\left(-\gamma\|x_1 - x_2\|^2\right), \qquad (11)$$

FIGURE 5: Schematic of the proposed methodology.

FIGURE 6: The structure of the FFNN model.

where γ is the kernel parameter.

2.3.4. Multilinear Regression (MLR). MLR is one of the most commonly used mathematical modeling techniques to analyze the linear relationship that exists between the

dependent and one or more independent variables. This method is based on the assumption that the dependent variable Y is affected by predictor variables $X_1, X_2, \ldots, X_n$ and then a linear equation is selected for the relationship between the dependent and independent variables [14].
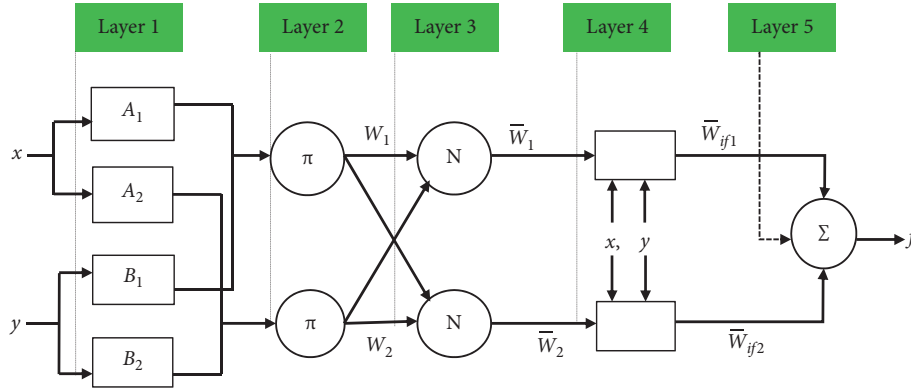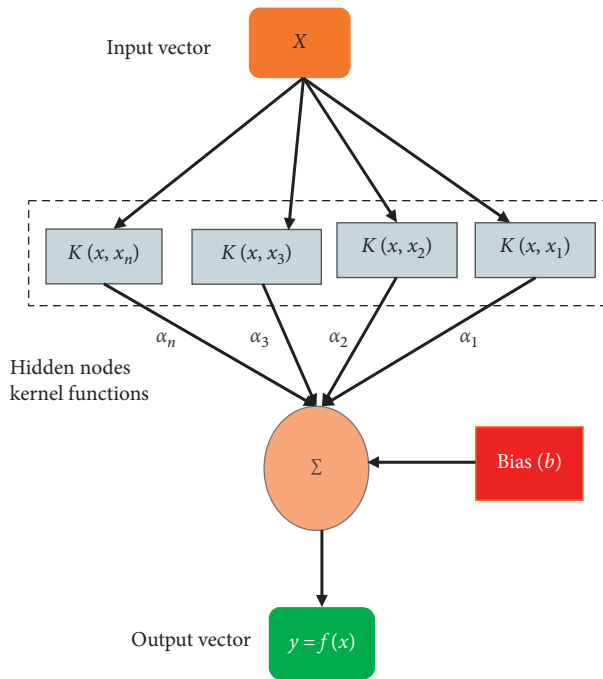
FIGURE 7: Structure of equivalent ANFIS.

FIGURE 8: The architecture of SVM algorithms.

Generally, the regression equation for the dependent variable (Y) can be written as

$$Y = b_0 + b_1 x_1 + b_2 x_2 + \cdots b_n x_n, \tag{12}$$

where x_n is the value of the nth predictor, b_0 is the regression constant, and b_n is the coefficient of the nth predictor.

2.4. Ensemble Techniques.
Ensemble modeling is a type of machine learning in which the outputs of different models are combined to improve the final model performance [46]. Even though it is a complex process and consumes a long time for designing and computation, an amalgamation of the outputs of several models produces results that are more accurate than the individual models [47]. This is because one of the used techniques for a given data set may perform better than the others and when different data sets are used, the result may become the opposite. Therefore, an ensemble technique may be developed to get benefit from the advantages of all single models. Ensemble method utilizes output from every single method with a certain priority level assigned to each with the help of arbitrator, providing the output [28]. For this study, two nonlinear (AE and NNE) and two linear (WAE and SAE) ensemble models were used for enhancing the performance of the single models.

Multimodel combination methods have already been applied in various forecasting applications such as clustering, classification, time series, regression and web ranking [48], weather and economic forecasting in the early 1960s [49], rainfall-runoff [26], dissolved oxygen concentration modeling [50], groundwater level prediction [34], river water quality index prediction [30], and wastewater effluent quality modeling [31]. However, no study is reported on the applicability of ensemble modeling in suspended sediment load modeling to the best of our knowledge. Thus, this study employed four ensemble methods (two nonlinear and two linear) to enhance the accuracy of the single models in the estimation of SSL.

2.4.1. Linear Ensemble Methods. Simple average ensemble (SAM): in this ensemble technique, the arithmetic average of outputs (suspended sediment load) of SVM, ANFIS, FFNN, and MLR models was calculated as the final computed suspended sediment load value as

$$SS = \frac{1}{N} \sum_{i=1}^{N} SS_i, \tag{13}$$

where SS is the output of the SAM model, SS_i is the output of the ith single model (i.e., ANFIS, FFNN, SVM, and MLR), and N is the number of single models (here, $N = 4$).

Weighted average ensemble (WAE): in this method, the prediction is made by assigning different weight to each output based on the relative importance of the outputs as

$$SS = \sum_{i=1}^{N} w_i SS_i, \tag{14}$$

where w_i stands for weight on the output of the ith method and it is computed based on the performance measure of the ith method as

$$w_i = \frac{DC_i}{\sum_{i=1}^{N} DC_i}, \tag{15}$$

where DC_i represents the determination coefficient of the ith model.

2.4.2. Nonlinear Ensemble Methods. In the nonlinear ensemble methods, the nonlinear averaging is performed by training an AI nonlinear model such as ANFIS and FFNN using suspended sediment values obtained from the single models. In the nonlinear ensemble modeling, the outputs of individual ANFIS, SVM, MLR, and FFNN models are combined and used as new inputs for the nonlinear ensemble models (AE and NNE) to get the overall ensemble output.

Neural network ensemble (NNE): in this technique, a nonlinear ensemble is made by training another FFNN by feeding the outputs of single models as inputs. Then, the maximum number of epochs and hidden layers' neurons is determined by trial and error.

ANFIS ensemble (AE): in this method, the suspended sediment load values obtained from single SVM, FFNN, MLR, and ANFIS models are fed to train a new ANFIS model using various numbers of epochs and membership functions. The general procedure used in the ensemble process is presented in Figure 9.

2.5. Data Normalization and Model Evaluation Criteria. The input and output data should be first normalized before the model is trained to remove their dimensions and to ensure that equal attention is given to all variables [25, 47]. Data normalization helps to avoid numerical calculation difficulty. To bring the data in a range of [0, 1], the dataset should be normalized as

$$SS_n = \frac{SS_i - SS_{min}}{SS_{max} - SS_{min}}, \tag{16}$$

where SS_n, SS_{max}, SS_{min}, and SS_i represent the normalized, maximum, minimum, and actual suspended sediment load values, respectively.

In forecasting hydrological parameters, Dawson et al. [51] discussed and explained 20 frequently used model performance indicators. As indicated in the previous parts, three AI-based models (ANFIS, ANN, and SVM) and a commonly used linear model (MLR) were used in this study. The performance of hydrological and climatological time series forecasting models must be evaluated in both training and verification phases. The model that yields the best modeling result on the training and verification steps is determined by trial and error. For better evaluation of model performance, at least one absolute error measure and one good of fit should be used [47]. For this study, Root Mean Square Error (RMSE) and Nash-Sutcliffe Efficiency (NSE) or Determination Coefficient (DC) were used to evaluate the performance and efficiency of the developed models. DC has values between $-\infty$ and 1 and measures how well the predicted value fits with the observed data. Higher model performance is obtained when the DC value is closed to 1, and vice versa [52]. The other performance measure used in this study is RMSE. It measures the deviation of the computed from the observed values. The best model is the model that gives the least RMSE and the highest DC values, as calculated by equations (17) and (18), respectively.

$$RMSE = \sqrt{\frac{1}{N} \sum_{i=1}^{N} \left(SS_{obsi} - SS_{prei}\right)^2}, \tag{17}$$

$$DC = 1 - \frac{\sum_{i=1}^{N} \left(SS_{obsi} - SS_{prei}\right)^2}{\sum_{i=1}^{N} \left(SS_{obsi} - S_{\bar{S}obs}\right)^2}, \tag{18}$$

where SS_{obsi}, SS_{prei}, $S_{\bar{S}obs}$, and N are observed, predicted, and average of the observed SSL values and number of observations, respectively.

3. Results and Discussion

All of the used models, namely, SVM, FFNN, ANFIS, and MLR, were trained and tested for modeling suspended sediment load in Katar catchment. The results of sensitivity analysis to select dominant inputs, single black-box modeling, and ensemble models for suspended sediment load are presented in the following subsections.

3.1. Results of Inputs Selection. The effect of several factors, for example, runoff, precipitation, and catchment characteristics, are involved in the suspended sediment load modeling [5]. Therefore, careful selection of the most relevant and significant factors as inputs in any AI-based modeling is an important step to obtain the optimum result. Previous studies indicated that there exists the highest correlation between the present value of suspended sediment load and its previous values. The influence of different factors can indirectly be considered by the antecedent SSL values [53]. To estimate the current SSL (SS_t), different lag time series of discharge (Q) and SSL were used in previous researches [4, 18]. Thus, the value of suspended sediment load at the current time step (SS_t) would be the function of
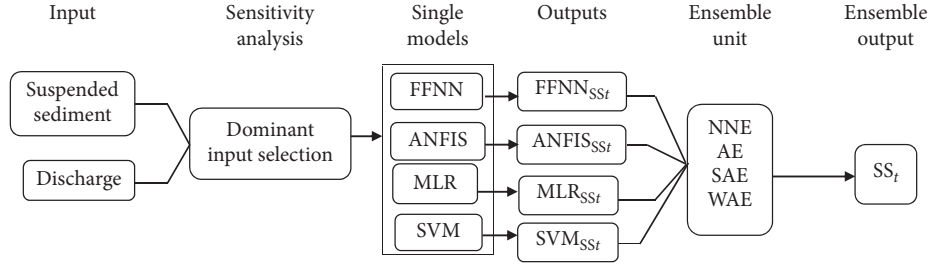
Figure 9: Schematic view of the ensemble process.

the sediment values up to time step n and also runoff (Q) values at present and up to time step m as

$$SS_t = f\left(Q_t, Q_{t-1}, Q_{t-2}, \ldots, Q_m, SS_{t-1}, SS_{t-2}, \ldots, SS_n\right). \tag{19}$$

Selection of the most relevant input variables and correct network parameter adjustment (e.g., number of training iterations, hidden neurons, and transfer function) in any AI-based modeling is a crucial step in attaining the most optimal result [35, 54]. Linear sensitivity analysis methods (e.g., Pearson correlation) have previously been used for the selection of the dominant input variable in suspended sediment modeling (e.g., see [6, 21, 22, 55]). However, the application of linear Pearson correlation analysis for selecting the dominant input variables has been criticized by previous works (e.g., [35, 56]) since, for a complex nonlinear hydrological process like SSL, there may exist a stronger nonlinear relationship between the predictor and predicted variables than a weak linear relationship. Because of this, sensitivity analysis of input variables for suspended sediment load estimation using nonlinear FFNN was conducted in this work to determine the most relevant inputs. To predict current-day suspended sediment load (SS_t), different lags (up to 5 past days) of suspended sediment and discharge data were evaluated as sole input and ranked based on the verification phase DC values of the modeling. The ranking results based on sensitivity analysis of input variables to predict SS_t are presented in Table 2.

In Table 2, t stands for the present time step and the corresponding output is the current suspended sediment load (SS_t). In the table, the highest DC value implies the most dominant input variable. Thus, Q_t is the first most dominant and SS_{t-1} is the second, and Q_{t-1} is the third dominant input parameter. Insufficient input variables cannot give accurate results whereas including too many input variables makes the modeling process complex and may cause overfitting issues [35]. Thus, after ranking the input variables based on their verification DC value, the Student t-test was performed to identify the dominant inputs and remove those which do not have a significant impact on the estimation results. Based on the result of the Student t-test, Q_{t-4}, Q_{t-5}, SS_{t-4}, and SS_{t-5} were found less relevant and not included in the inputs combination set. After the selection of the dominant inputs and removal of less relevant inputs, different input combinations using the remaining parameters, that is, SS_{t-1}, SS_{t-2}, SS_{t-3}, Q_t, Q_{t-1}, Q_{t-2}, and Q_{t-3}, were examined to predict the SSL by the proposed models.

Table 2: Sensitivity analysis results.

Inputs	Verification DC	Rank
Q_t	0.8208	1
SS_{t-1}	0.7964	2
Q_{t-1}	0.7605	3
SS_{t-2}	0.6338	4
Q_{t-2}	0.60438	5
Q_{t-3}	0.5188	6
SS_{t-3}	0.4966	7
Q_{t-4}	0.3594	8
SS_{t-4}	0.3027	9
Q_{t-5}	0.2934	10
SS_{t-5}	0.2134	11

3.2. Results of SS Modeling Using Single Models. For each input combination, the ANFIS, SVM, FFNN, and MLR models were trained and tested where the best results of each model are presented in Table 3. The FFNN model with five inputs and one hidden layer trained by the Levenberg-Marquardt algorithm was developed for suspended sediment load estimation in the Katar catchment. Determination of the optimal model structure (e.g., number of the hidden neurons) is an important step in FFNN modeling to obtain the best result. This is because too small neurons may capture unacceptable information while too many neurons may cause overfitting A trial and error method by assessing the accuracy of different models trained with varying hidden neuron number was used to determine the best structure of the model. For the best input combination, 8 hidden neurons were found as the optimum structure of the hidden layer.

The second AI applied in this study was SVM. Radial basis function (RBF) kernel was used to create the SVM model for all input combinations. This kernel was selected because it provides better performance and contains fewer tuning parameters than polynomial and sigmoidal kernels [44].

The third AI-based model used was the ANFIS model that is known for its ability to handle the uncertainty of complex and nonlinear processes via a fuzzy concept. In this way for the ANFIS model, Sugeno fuzzy inference system using a hybrid algorithm was used to calibrate the MF parameters. The study also used a trial and error approach by changing the types of MFs to obtain the best result. Trapezoidal, triangular, and Gaussian-shaped MFs were examined because of their suitability in modeling the hydroclimatic process [25]. As well, the trial and error

TABLE 3: Results of single black-box models for SSL modeling by the best input combination.

Model	Input combination	Best structure	Training		Verification	
			DC	RMSE	DC	RMSE
FFNN	Q_t, Q_{t-1}, Q_{t-2}, SS_{t-1}, SS_{t-2}	5-8-1	0.876	0.03134	0.834	0.04155
ANFIS	Q_t, Q_{t-1}, Q_{t-2}, SS_{t-1}, SS_{t-2}	Gaussian	0.918	0.0255	0.884	0.0339
SVM	Q_t, Q_{t-1}, Q_{t-2}, SS_{t-1}, SS_{t-2}	RBF	0.867	0.0324	0.815	0.0439
MLR	Q_t, Q_{t-1}, Q_{t-2}, SS_{t-1}, SS_{t-2}	5-1	0.755	0.0441	0.708	0.0553

RMSE has no unit as the data are normalized.

method was used to determine the number of membership functions and to determine the best ANFIS construction. ANFIS model with Gaussian MFs trained by 55 epochs gave the best result among the others. Lastly, MLR that expresses the linear relationship between the predictor (independent) and output (dependent) variables was also applied for SSL modeling. The obtained results of the developed AI-based and MLR models to predicted suspended sediment load in Katar catchment for the best input combination are presented in Table 3. The numbering of a-b-c in the FFNN (Table 3) stands for the number of input, hidden, and output neuron layers. Similarly, the numbering y-z in the structure of MLR in Table 3 represents the number of inputs and output parameters.

Table 3 shows that the ANFIS model having the highest DC and lowest RMSE outperformed all developed AI and MLR models in suspended sediment load estimation followed by FFNN, SVM, and MLR. The result is confirmed by previous studies about the performance of ANFIS and ANN models in suspended sediment load estimation [12, 13]. The MLR which measures the linear relationship between the inputs and output led to less accurate results than the AI-based models. This is because the suspended sediment load is a dynamic, nonlinear, and complex process and hence a nonlinear model may be used to accurately model it instead of a linear technique.

From the results of single models shown in Table 4, the application of the best model (ANFIS) could increase the performances (based on DC value) of FNNN, SVM, and MLR by 6%, 8.47%, and 24.86%, respectively. In addition to statistical performance measures, different visual indicators like scatter plots, boxplot, and Taylor diagram were used in this study to obtain a better view of the estimation performances of the employed models. The scatter plots of single AI-based and MLR model result against the observed value in the verification phase are presented in Figure 10.

According to Sharafati et al. [31], a scatter plot shows the possible pattern similarity between the observed and estimated data. Figure 10 compares the estimation performance of FFNN, MLR, SVM, and ANFIS models in the estimation of SSL on scatter plots. The figure reveals less spread of points for predicted and observed SSL in the ANFIS model than other computing single models. This could be due to the ability of the ANFIS model to handle the uncertainties of the SSL process.

In Figure 11, the median ($Q_{50\%}$) value for ANFIS model = 1,497.3 ton/day, MLR = 2014.4 ton/day, SVM = 1,672.7, FFNN = 1,562.8 ton/day, and observed = 1,482 ton/day. This indicates the ANFIS model performs better than

the other models with FFNN being the second while MLR provides the worst estimation. The reasonable performance of the ANFIS model is because of its ability to handle the uncertainty of complex SSL process. Kumar et al. [12] applied ANFIS and ANN to model the current-day suspended sediment and runoff in the Godavari basin using the previous period discharge and SSL data as input. They found that the ANFIS model gave a better performance than ANN in suspended sediment prediction. Nourani and Andalib [4] employed the least squares support vector regression (LSSVR) and ANN for monthly and daily SSL prediction. The result showed that LSSVR has a better predictive performance than ANN. Buyukyildiz and Kumcu [18] applied SVM, ANFIS, and SVM to estimate the current-day SSL of Coruh River using a different combination of lag time series of Q and SSL as input. They found that ANN performed better than the other models. From the comparison with the reported studies in the literature, it can be observed that the estimation accuracy of AI-based models varies for different case studies. According to Salih et al. [2], it is because of SSL data stochasticity of each considered catchment and also the capacity of the constructed AI-based models to handle the nonstationarity and nonlinearity in the data set.

Figure 12(a) shows the time series plot of observed versus computed suspended sediment load in the verification phase of Abura station for the applied MLR, SVM, FFNN, and ANFIS models. Figure 12(b) shows a section of modeling of SSL time series by MLR, SVM, FFNN, and ANFIS models. For better visibility of predicted values of SSL by each model, only a 51-day period (from July 26 to September 14, 2017) has been focused on in Figure 12(b).

As shown in Figure 12(b), the date of July 29, August 08, August 24, and August 31 are marked as points 1, 2, 3, and 4, respectively. With regard to point 1, ANFIS = 5752.136 ton/day, MLR = 3857.018 ton/day, FFNN = 4620.326 ton/day, SVM = 6573.967 ton/day, and observed = 3831.348 ton/day. This indicates that the MLR value is more close to the actual value than the other models. This, in turn, shows that even the least accurate model at a certain point in the time series could give the best result. With regard to point 2, ANFIS = 6313.366 ton/day, MLR = 4563.506 ton/day, SVM = 8595.878 ton/day, FFNN = 6695.642 ton/day, and observed = 6245.252 ton/day. This implies that the ANFIS model performs better than other models. At point 3, ANFIS = 6181.81 ton/day, MLR = 4190.825 ton/day, SVM = 6270.75 ton/day, FFNN = 5424.629 ton/day, and observed = 5249.579 ton/day. This indicates that the FFNN value has less deviation from the observed SSL value than the other competing models. At the final point (point 4), SVM

TABLE 4: Results of the proposed ensemble methods for SSL modeling.

Ensemble method	Best structure	Calibration		Verification	
		DC	RMSE	DC	RMSE
SAE	4-1	0.922	0.0249	0.8793	0.0349
WAE	0.257, 0.274, 0.251, 0.218	0.9257	0.0243	0.888	0.0327
AE	Gausian-3	0.9804	0.0125	0.97	0.0176
NNE	4-7-1	0.953	0.0193	0.924	0.0281

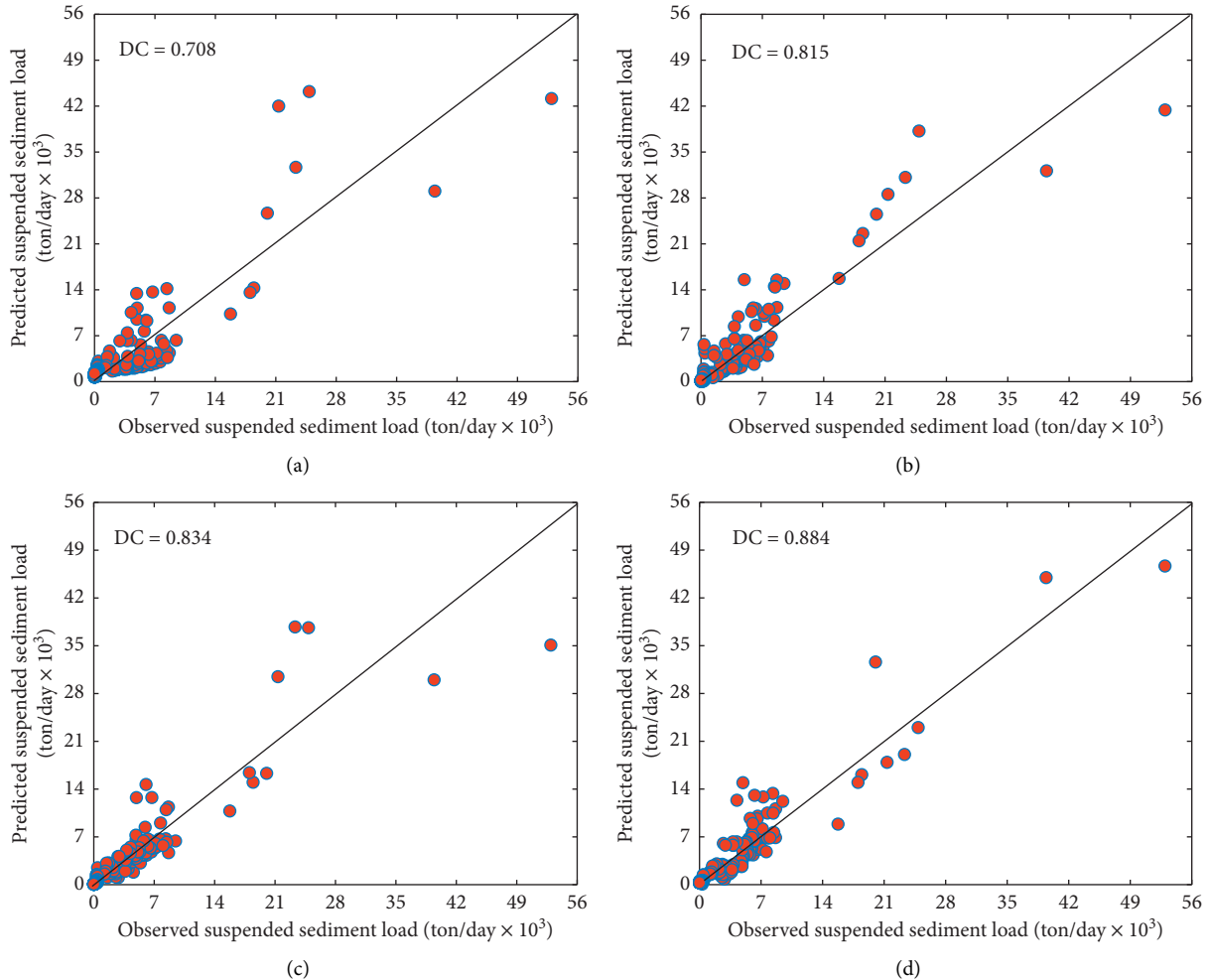RMSE has no unit as the data used is normalized.

FIGURE 10: Scatter plots showing the actual and predicted SSL, at verification phase by (a) MLR, (b) SVM, (c) FFNN, and (d) ANFIS.

performs better than the other models. From the results of the selected points, it is clear that different models at different time points could lead to different performances (from different data aspects). Thus, the objective of more accurate SSL estimation can be better achieved through an ensemble method. In this regard, WAE, SAE, NNE, and AE ensemble methods were developed for SSL modeling to improve the overall performance of the modeling.

3.3. Results of Ensemble Techniques.

In order to increase the estimation efficiency of single AI-based and MLR models, the outputs of ANFIS, SVM, MLR, and FFNN models were used as inputs for the four ensemble techniques as a novel ensemble method for SSL modeling. The results of linear and nonlinear ensemble models for suspended sediment estimation are presented in Table 4.

Table 4 shows the performances of WAE, SAE, AE, and NNE for the estimation of SSL. In the SAE structure, a-b is used to show the number of inputs and outputs (SSt). In WAE structure, w, x, y, and z denote the weights of FFNN, ANFIS, SVM, and MLR models, respectively. In Table 4, it can be seen that AE outperformed all the competing model combination techniques because of its robustness by combining the advantages of both ANN and fuzzy concepts via the ANFIS framework.
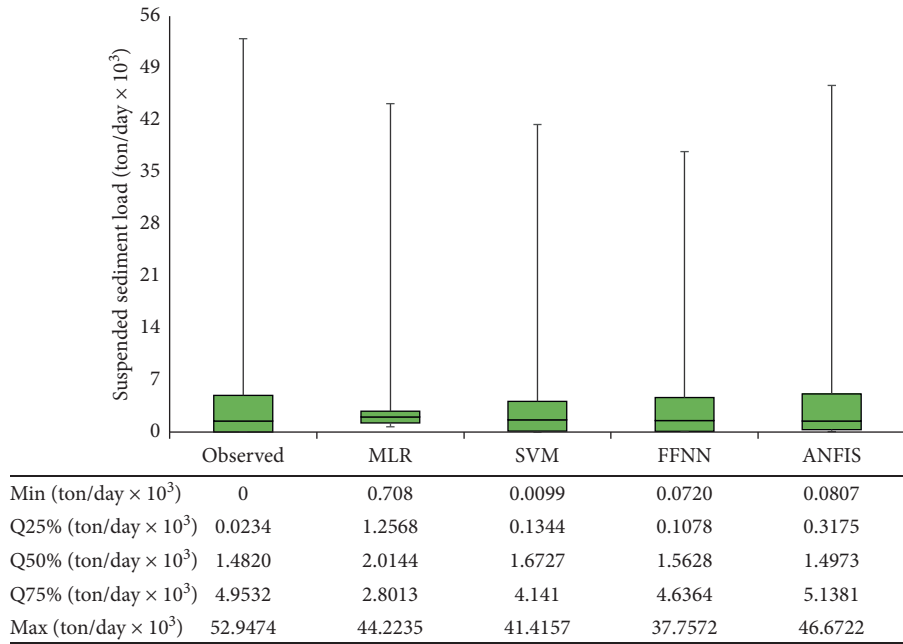
Figure 11: Boxplot of observed versus computed SSL in the verification phase.

The table below the boxplot:

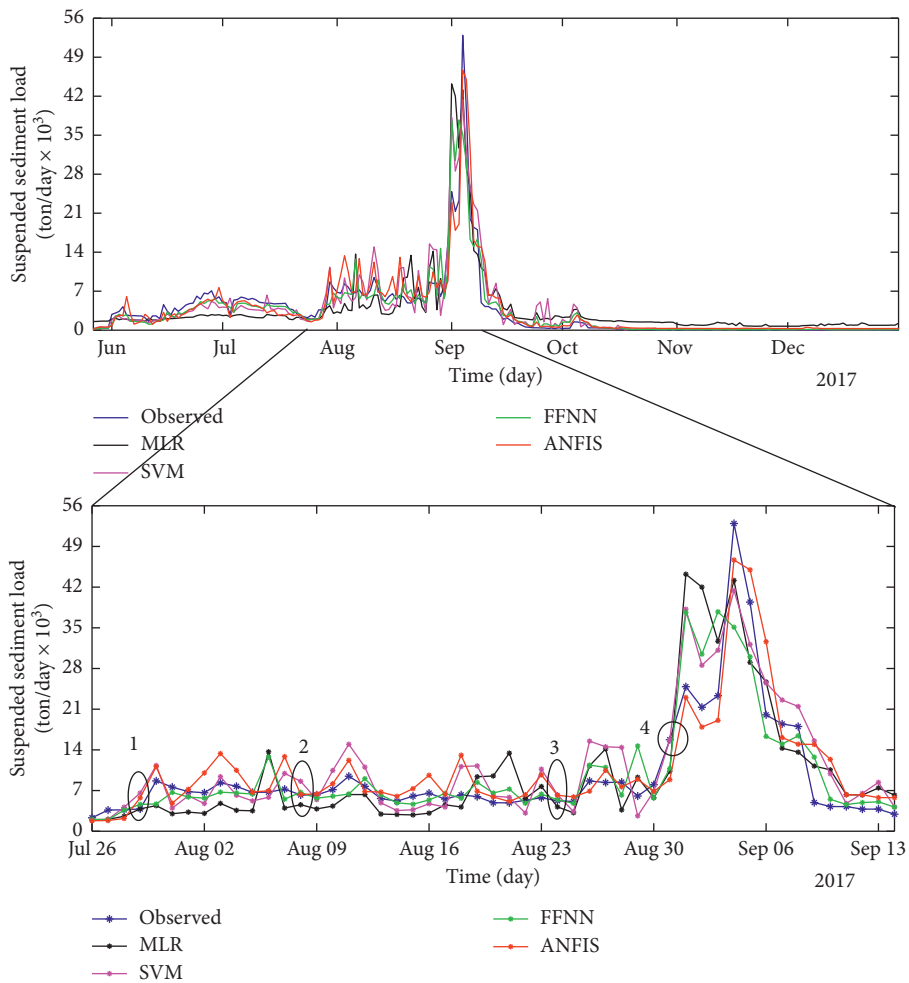|	Observed	MLR	SVM	FFNN	ANFIS
Min (ton/day × 10³)	0	0.708	0.0099	0.0720	0.0807
Q25% (ton/day × 10³)	0.0234	1.2568	0.1344	0.1078	0.3175
Q50% (ton/day × 10³)	1.4820	2.0144	1.6727	1.5628	1.4973
Q75% (ton/day × 10³)	4.9532	2.8013	4.141	4.6364	5.1381
Max (ton/day × 10³)	52.9474	44.2235	41.4157	37.7572	46.6722

Figure 12: Observed versus predicted suspended sediment load value in the verification stage of Abura station in (a) January 2016–December 2019 and (b) July 26 up to September 14, 2017.

The linear ensemble (SAE) performed better than all the single models except the ANFIS model. It is known that linear averaging usually gives values higher than the minimum value and lesser than the highest value in the data set [35]. Even from the nonlinear ensemble methods, WAE gives a slightly better performance than SAE. This could be due to the assigned weights on the parameter based on their relative importance.

NNE model was trained by the Levenberg-Marquardt algorithm similar to the single FFNN model and the tangent sigmoid activation function was utilized for both output and hidden layers. In this study, the Levenberg-Marquardt algorithm was selected among different ANN training algorithms because of its fastest convergence ability as reported by Sahoo et al [57]. A trial and error process was used to determine the best epoch number and the appropriate number of hidden neurons. NNE has been successfully used as multimodel combination techniques in hydrological modeling (e.g., [25, 46, 52]). Similar to the ANFIS single model, Sugeno fuzzy inference system using a hybrid training algorithm was used to calibrate the MFs parameters in AE. The AE model has greatly enhanced the accuracy of single models in previous studies in another field [35].

The result in Table 5 shows the capability of ensemble techniques to improve the prediction performance of single AI and MLR models based on their DC values. The results in Table 5 show that all used ensemble methods can be applied to improve single model performance in SSL modeling. However, nonlinear ensemble techniques show superiority over the linear ensemble models. This could be because of the incapability of linear ensemble methods to undergo another black-box learning process unlike the nonlinear ensemble methods (AE and NNE). The NNE increased the performance of SVM, FFNN, ANFIS, and MLR models by 12%, 12.8%, 6.6%, and 28.4%, respectively in the verification stage. In the AE model, the performance of SVM, FFNN, ANFIS, and MLR models was increased by 16.4%, 17.3%, 10.9%, and 33.5%, respectively, in the verification stage. Also, from the obtained results shown in Table 4, the AE performed better than the other three ensemble methods because of its robustness to handle the complex nonlinear process between outputs and inputs. The performance accuracy of the ANFIS model over AI-based and MLR single models applied in modeling suspended sediment load was also confirmed by the AE model.

The scatter plots of the ensemble methods result and the observed suspended sediment load values in the verification phase are presented in Figure 13.

In Figure 13, the scatter plots of the developed ensemble models for SSL estimation in the verification are compared. As indicated in the figure, the AE is seen to have less spread estimation and the points were closer to the best line compared to the other ensemble models, while the linear ensemble methods (SAE and WAE) show the most scattered estimation.

TABLE 5: The comparison of the nonlinear ensemble models using single AI and MLR models.

Model	Training (%)	Verification (%)
AE vs MLR	29.85	37
AE vs FFNN	11.9	16.3
AE vs SVM	13.08	19.02
AE vs ANFIS	6.8	9.73
NNE vs MLR	26.22	30.5
NNE vs SVM	9.92	13.37
NNE vs FFNN	8.8	10.79
NNE vs ANFIS	3.8	4.5

The boxplot is also another graph commonly used to make a comparison between the observed value and estimated outputs obtain by different models [6, 31]. The variability of observed SSL values versus those obtained by the developed ensemble models was compared using different quartiles and interquartile range (IQR) through boxplots in Figure 14. In this figure, the median (Q_{50}%) value for SAE = 1,681.1 ton/day, WAE = 1, 678 ton/day, NNE = 1,212.4 ton/day, AE = 1,636.4 ton/day, and observed = 1, 482 ton/day. This shows that AE outperforms the other ensemble techniques. Moreover, Figure 14 depicts that the most consistency is found between the output obtained by AE (IQR = 4,968.3 ton/day) and observed value (IQR = 4,929.8 ton/day).

Figure 15 shows the time series of observed versus predicted SSL in the verification phase of Abura station SSL modeling for the applied ensemble methods (SAE, WAE, NNE, and AE). From Figure 15, it is clear that the WAE and SAE methods were less accurate than AE and NNE. The values of AE were more fitted with the observed data, whereas there is a wider fluctuation between observed data and the values obtained by WAE and SAM ensembles.

Alternatively, four ensemble methods (SAE, WAE, AE, and NNE) were also assessed using the Taylor diagram (two-dimensional diagram), which shows the predicted and observed values. Taylor's diagram could be used as a successful diagram for comparison of model performances in different fields [2, 6, 58–60]. Taylor's diagram was used to construct and graphically visualize the combination of two performance indicators, namely, correlation (r) and standard deviation (SD) [61] (Figure 16). The key objective of using this diagram is to combine different models performances indicators in one graph and it can also statistically quantify the level of resemblance between the predicted and observed values. From Figure 16, it is seen that the best ensemble method is AE ($r = 0.985$) and SAE is the least with the r-value of 0.927. From the ensemble result comparisons, the mentioned performance metrics indicate the degree of prediction accuracy of AE. The AE outperformed the other ensemble methods as the predicted values are more close to the observed values. This can be additionally confirmed by considering the high SD value which could be credited to the AE.
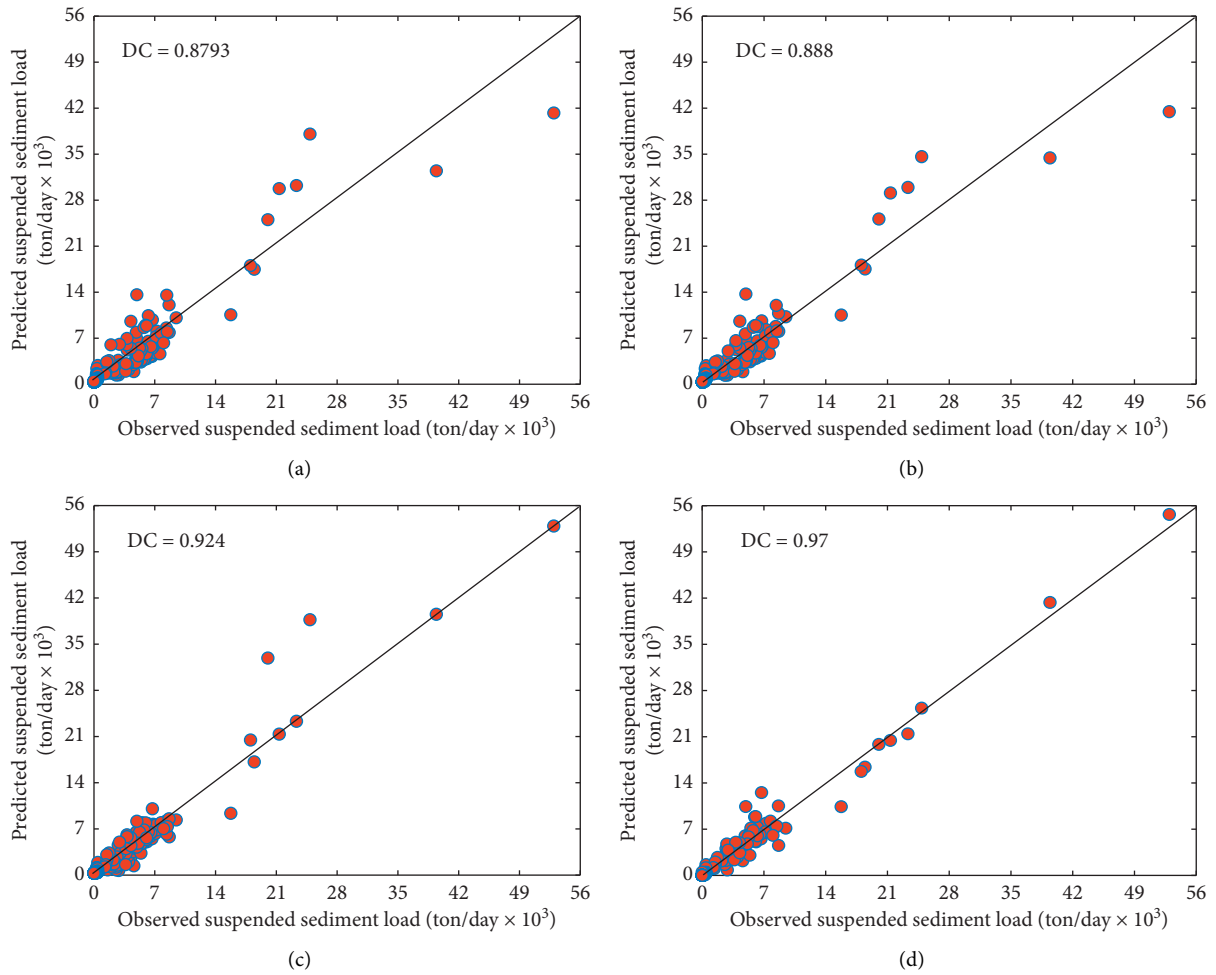
FIGURE 13: Scatter plots showing observed versus predicted suspended sediment load by (a) SAE, (b) WAE, (c) NNE, and (d) AE, in the verification phase.

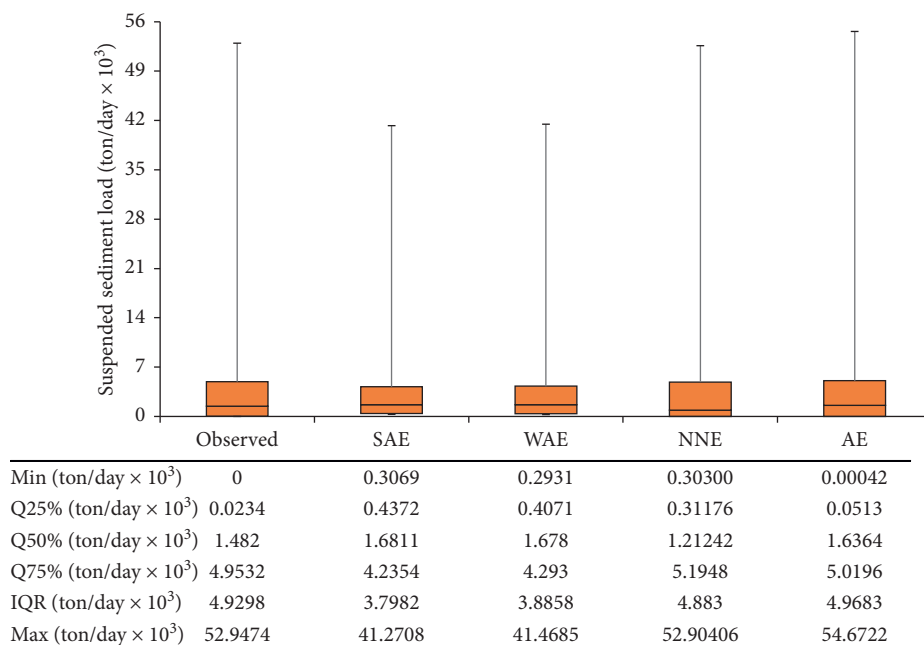|	Observed	SAE	WAE	NNE	AE
Min (ton/day $\times 10^3$)	0	0.3069	0.2931	0.30300	0.00042
Q25% (ton/day $\times 10^3$)	0.0234	0.4372	0.4071	0.31176	0.0513
Q50% (ton/day $\times 10^3$)	1.482	1.6811	1.678	1.21242	1.6364
Q75% (ton/day $\times 10^3$)	4.9532	4.2354	4.293	5.1948	5.0196
IQR (ton/day $\times 10^3$)	4.9298	3.7982	3.8858	4.883	4.9683
Max (ton/day $\times 10^3$)	52.9474	41.2708	41.4685	52.90406	54.6722

FIGURE 14: Boxplot of observed versus predicted values by ensemble models in the verification phase.
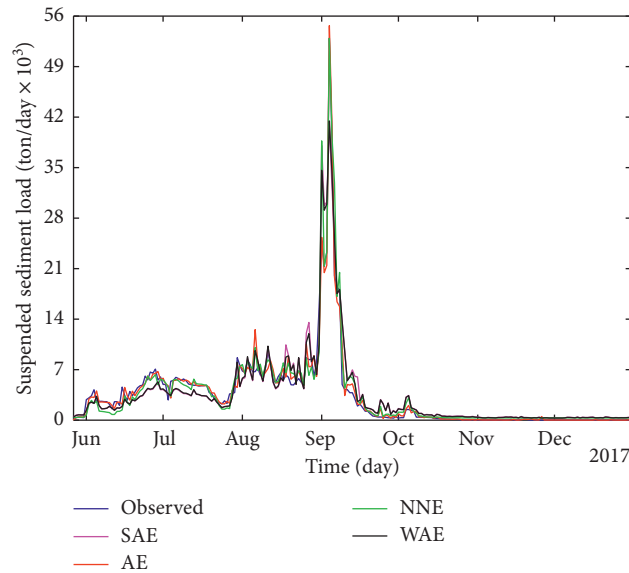
Figure 15: Time series of the observed versus ensemble models value in the verification phase.
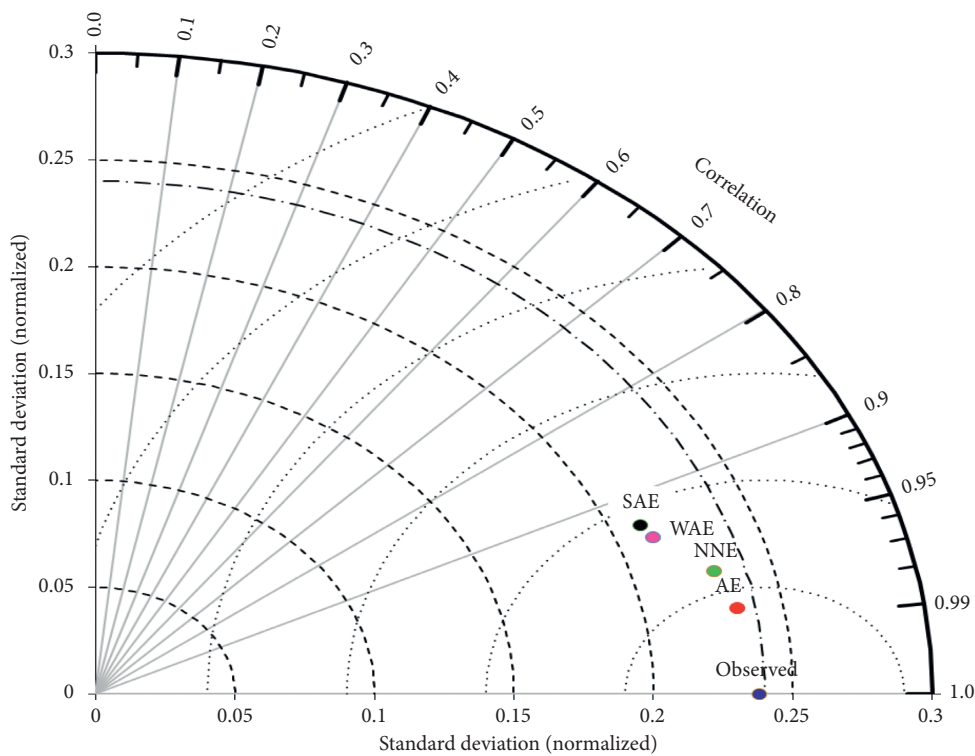

Figure 16: Normalized Taylor diagram showing the performance of ensemble models.

4. Conclusions

In this study, the capability of ANFIS, SVR, FFNN, and MLR models was examined for modeling daily SSL of Katar catchment, Ethiopia. Before the development of suspended sediment load estimation using single AI and MLR models, a nonlinear sensitivity analysis was conducted for selecting the relevant inputs. After conducting the Student t-test, some irrelevant and less significant input variables were removed

and only the dominant inputs were used in different combinations to predict SSL.

By comparing the results obtained from the single models, it was demonstrated that the ANFIS model could lead to the highest prediction performance over the other competing models because of its strength in dealing with the dynamic, nonlinear, and complex process via fuzzy concept. After developing single AI and conventional MLR models, four ensemble methods that combine the outputs from every

single back box models were created to improve the performances of the individual models. Combining the results of individual models enhanced the accuracy of single models in the estimation of suspended sediment. Nonlinear ensemble techniques (AE and NNE) showed the highest performance because of their capability of handling the uncertainty of complex and nonstationary processes such as the suspended sediment process. AE method showed superiority over the other ensemble methods by increasing the predictive performance of FFNN, ANFIS, MLR, and SVM models in the testing phase by 16.3%, 9.73%, 37%, and 19.02%, respectively. The performance of the nonlinear ensemble (SAE) showed higher efficiency compared to the single black-box models except the ANFIS model. This is because linear averaging always gives a result that is higher than the minimum value and lesser than the maximum value in the set. In this study, the linear ensemble provides less performance than the ANFIS model because of the lower performance of the conventional MLR. Therefore, the limitation of the linear ensemble method is that the least performed single models may lead to performance lower than that of the most accurate model.

The result of this study generally revealed the promising power of ensemble methods in SSL modeling. The ensemble outputs obtained specifically by the AE technique revealed that better SSL forecasting accuracy could be achieved via a combination of individual model outputs rather than the use of single models. This study is limited to the application of black-box models for ensemble SSL modeling. Hence, the inclusion of physically based models in the ensemble unit should be tested for future study. Moreover, this study used only two years of daily SSL and discharge data for suspended sediment load estimation due to the data limitation. Thus, more data and input parameters can be tested for future studies.

Data Availability

Data are available from the corresponding author upon request.

Conflicts of Interest

The authors declare no conflicts of interest.

References

[1] O. Kisi, A. H. Dailr, M. Cimen, and J. Shiri, "Suspended sediment modeling using genetic programming and soft computing techniques," *Journal of Hydrology*, vol. 450-451, pp. 48–58, 2012.

[2] S. Q. Salih, A. Sharafati, K. Khosravi et al., "River suspended sediment load prediction based on river discharge information: application of newly developed data mining models," *Hydrological Sciences Journal*, vol. 65, no. 4, pp. 624–637, 2020.

[3] C. G. Liu, Z. Y. Li, Y. Hao, J. Xia, F. W. Bai, and M. A. Mehmood, "Computer simulation elucidates yeast flocculation and sedimentation for efficient industrial fermentation," *Biotechnology Journal*, vol. 13, no. 5, pp. 1–7, 2018.

[4] V. Nourani and G. Andalib, "Daily and monthly suspended sediment load predictions using wavelet based artificial intelligence approaches," *Journal of Mountain Science*, vol. 12, no. 1, pp. 85–100, 2015.

[5] V. Nourani, A. Molajou, A. D. Tajbakhsh, and H. Najafi, "A wavelet based data mining technique for suspended sediment load modeling," *Water Resources Management*, vol. 33, no. 5, pp. 1769–1784, 2019.

[6] A. Sharafati, S. B. Haji Seyed Asadollah, D. Motta, and Z. M. Yaseen, "Application of newly developed ensemble machine learning models for daily suspended sediment load prediction and related uncertainty analysis," *Hydrological Sciences Journal*, vol. 65, no. 12, pp. 1–21, 2020.

[7] M. J. Alizadeh, E. Jafari Nodoushan, N. Kalarestaghi, and K. W. Chau, "Toward multi-day-ahead forecasting of suspended sediment concentration using ensemble models," *Environmental Science and Pollution Research*, vol. 24, no. 36, pp. 28017–28025, 2017.

[8] T. Abebe and B. Gebremariam, "Modeling runoff and sediment yield of kesem dam watershed, awash basin, Ethiopia," *SN Applied Sciences*, vol. 1, no. 5, pp. 1–13, 2019.

[9] G. D. Betrie, Y. A. Mohamed, A. Van Griensven, and R. Srinivasan, "Sediment management modelling in the blue nile basin using SWAT model," *Hydrology and Earth System Sciences*, vol. 15, no. 3, pp. 807–818, 2011.

[10] A. Martínez-Salvador and C. Conesa-García, "Suitability of the SWAT model for simulating water discharge and sediment load in a karst watershed of the semiarid mediterranean basin," *Water Resources Management*, vol. 34, pp. 85–802, 2020.

[11] B. Sivakumar, "Suspended sediment load estimation and the problem of inadequate data sampling: a fractal view," *Earth Surface Processes and Landforms*, vol. 31, no. 4, pp. 414–427, 2006.

[12] A. Kumar, P. Kumar, and V. K. Singh, "Evaluating different machine learning models for runoff and suspended sediment simulation," *Water Resources Management*, vol. 33, no. 3, pp. 1217–1231, 2019.

[13] E. Olyaie, H. Banejad, K. W. Chau, and A. M. Melesse, "A comparison of various artificial intelligence approaches performance for estimating suspended sediment load of river systems: a case study in the United States," *Environmental Monitoring and Assessment*, vol. 187, no. 4, 2015.

[14] O. Kisi, J. Shiri, and M. Tombul, "Modeling rainfall-runoff process using soft computing techniques," *Computers & Geosciences*, vol. 51, pp. 108–117, 2013.

[15] R. M. Adnan, A. Petroselli, S. Heddam, C. A. G. Santos, and O. Kisi, "Short term rainfall-runoff modeling using several machine learning methods and a conceptual event-based model," *Stochastic Environmental Research and Risk Assessment*, pp. 1–20, 2020.

[16] F. Saberi-Movahed, M. Najafzadeh, and A. Mehrpooya, "Receiving more accurate predictions for longitudinal dispersion coefficients in water pipelines: training group method of data handling using extreme learning machine conceptions," *Water Resources Management*, vol. 34, no. 2, pp. 529–561, 2020.

[17] M. Najafzadeh and G. Oliveto, "Riprap incipient motion for overtopping flows with machine learning models," *Journal of Hydroinformatics*, vol. 22, no. 4, pp. 749–767, 2020.

[18] M. Buyukyildiz and S. Y. Kumcu, "An estimation of the suspended sediment load using adaptive network based fuzzy inference system, support vector machine and artificial neural

network models," *Water Resources Management*, vol. 31, no. 4, pp. 1343–1359, 2017.

[19] H. A. Afan, A. El-Shafie, Z. M. Yaseen, M. M. Hameed, W. H. M. Wan Mohtar, and A. Hussain, "ANN based sediment prediction model utilizing different input scenarios," *Water Resources Management*, vol. 29, no. 4, pp. 1231–1245, 2014.

[20] A. M. Melesse, S. Ahmad, M. E. McClain, X. Wang, and Y. H. Lim, "Suspended sediment load prediction of river systems: an artificial neural network approach," *Agricultural Water Management*, vol. 98, no. 5, pp. 855–866, 2011.

[21] T. Rajaee, V. Nourani, M. Zounemat-Kermani, and O. Kisi, "River suspended sediment load prediction: application of ANN and wavelet conjunction model," *Journal of Hydrologic Engineering*, vol. 17, no. 5, pp. 604–614, 2011.

[22] E. K. Lafdani, A. M. Nia, and A. Ahmadi, "Daily suspended sediment load prediction using artificial neural networks and support vector machines," *Journal of Hydrology*, vol. 478, pp. 50–62, 2013.

[23] H. Tabari, O. Kisi, A. Ezani, and P. Hosseinzadeh Talaee, "SVM, ANFIS, regression and climate based models for reference evapotranspiration modeling using limited climatic data in a semi-arid highland environment," *Journal of Hydrology*, vol. 444, no. 445, pp. 78–89, 2012.

[24] R. Ampomah, H. Hosseiny, L. Zhang, V. Smith, and K. Sample-Lord, "A regression-based prediction model of suspended sediment yield in the cuyahoga river in Ohio using historical satellite images and precipitation data," *Water (Switzerland)*, vol. 12, no. 3, 2020.

[25] V. Nourani, G. Elkiran, and J. Abdullahi, "Multi-step ahead modeling of reference evapotranspiration using a multi-model approach," *Journal of Hydrology*, vol. 581, Article ID 124434, 2020.

[26] A. Y. Shamseldin, K. M. O'Connor, and G. C. Liang, "Methods for combining the outputs of different rainfall-runoff models," *Journal of Hydrology*, vol. 197, no. 1–4, pp. 203–229, 1997.

[27] J. M. Bates and C. W. J. Granger, "The combination of forecasts," *Journal of the Operational Research Society*, vol. 20, no. 4, pp. 451–468, 1969.

[28] R. N. Kiran and V. Ravi, "Software reliability prediction by soft computing techniques," *Journal of Systems and Software*, vol. 81, no. 4, pp. 576–583, 2008.

[29] S. Makridakis, A. Andersen, R. Carbone et al., "The accuracy of extrapolation (time series) methods: results of a forecasting competition," *Journal of Forecasting*, vol. 1, no. 2, pp. 111–153, 1982.

[30] S. B. H. S. Asadollah, A. Sharafati, D. Motta, and Z. M. Yaseen, "river water quality index prediction and uncertainty analysis: a comparative study of machine learning models," *Journal of Environmental Chemical Engineering*, vol. 9, no. 1, Article ID 104599, 2020.

[31] A. Sharafati, S. B. H. S. Asadollah, and M. Hosseinzadeh, "The potential of new ensemble machine learning models for effluent quality parameters prediction and related uncertainty," *Process Safety and Environmental Protection*, vol. 140, pp. 68–78, 2020.

[32] G. Cavadias and G. Morin, "The combination of simulated discharges of hydrological models," *Hydrology Research*, vol. 17, no. 1, pp. 21–32, 1986.

[33] V. Nourani, G. Elkiran, and J. Abdullahi, "Multi-station artificial intelligence based ensemble modeling of reference evapotranspiration using Pan evaporation measurements," *Journal of Hydrology*, vol. 577, Article ID 123958, 2019.

[34] A. Sharafati, S. B. H. S. Asadollah, and A. Neshat, "A new artificial intelligence strategy for predicting the groundwater level over the Rafsanjan aquifer in Iran," *Journal of Hydrology*, vol. 591, Article ID 125468, 2020.

[35] V. Nourani, H. Gökçekuş, and I. K. Umar, "Artificial intelligence based ensemble model for prediction of vehicular traffic noise," *Environmental Research*, vol. 180, Article ID 108852, 2020.

[36] A. Aga, A. Melesse, and B. Chane, "Estimating the sediment flux and budget for a data limited rift valley lake in Ethiopia," *Hydrology*, vol. 6, no. 1, p. 1, 2018.

[37] R. Tanty and T. S. Desmukh, "Application of artificial neural network in hydrology—a review," *International Journal of Engineering and Technical Research*, vol. 4, no. 6, 2015.

[38] J.-S. R. Jang, "ANFIS: adaptive-network-based fuzzy inference system," *IEEE Transactions on Systems, Man, and Cybernetics*, vol. 23, no. 3, pp. 665–685, 1993.

[39] J. S. R. Jang, C. T. Sun, and E. Mizutani, *Neuro-Fuzzy and Soft Computing—A Computational Approach to Learning and Machine Intelligence*, Prentice Hall, Trenton, NJ, USA, 1997.

[40] Y. Tsukamoto, "An approach to fuzzy reasoning method," *Advances in Fuzzy Set Theory and Applications*, vol. 137, no. 149, 1979.

[41] T. Takagi and M. Sugeno, "Fuzzy identification of systems and its applications to modeling and control," *IEEE Transactions on Systems, Man, and Cybernetics*, vol. SMC-15, no. 1, pp. 116–132, 1985.

[42] E. H. Mamdani and S. Assilian, "An experiment in linguistic synthesis with a fuzzy logic controller," *International Journal of Man-Machine Studies*, vol. 7, no. 11, pp. 1–13, 1975.

[43] A. M. Kalteh, "Monthly river flow forecasting using artificial neural network and support vector regression models coupled with wavelet transform," *Computers & Geosciences*, vol. 54, pp. 1–8, 2013.

[44] W.-C. Wang, D.-M. Xu, K.-W. Chau, and S. Chen, "Improved annual rainfall-runoff forecasting using PSO-SVM model based on EEMD," *Journal of Hydroinformatics*, vol. 15, no. 4, pp. 1377–1390, 2013.

[45] A. H. Haghiabi, H. M. Azamathulla, and A. Parsaie, "Prediction of head loss on cascade weir using ANN and SVM," *ISH Journal of Hydraulic Engineering*, vol. 23, no. 1, pp. 102–110, 2017.

[46] E. Sharghi, V. Nourani, and N. Behfar, "Earthfill dam seepage analysis using ensemble artificial intelligence based modeling," *Journal of Hydroinformatics*, vol. 20, no. 5, pp. 1071–1084, 2018.

[47] V. Nourani, G. Elkiran, and S. I. Abba, "Wastewater treatment plant performance analysis using artificial intelligence—an ensemble approach," *Water Science and Technology*, vol. 78, no. 10, 2018.

[48] P. Kazienko, E. Lughofer, and B. Trawiński, "Hybrid and ensemble methods in machine learning J.UCS special issue," *Journal of Universal Computer Science*, vol. 19, no. 4, pp. 457–461, 2013.

[49] N. K. Ajami, Q. Duan, X. Gao, and S. Sorooshian, "Multi-model combination techniques for analysis of hydrological simulations: application to distributed model intercomparison project results," *Journal of Hydrometeorology*, vol. 7, no. 4, pp. 755–768, 2006.

[50] S. I. Abba, N. T. T. Linh, J. Abdullahi et al., "Hybrid machine learning ensemble techniques for modeling dissolved oxygen concentration," *IEEE Access*, vol. 8, pp. 157218–157237, 2020.

[51] C. W. Dawson, R. J. Abrahart, and L. M. See, "HydroTest: a web-based toolbox of evaluation metrics for the standardised

assessment of hydrological forecasts," *Environmental Modelling & Software*, vol. 22, no. 7, pp. 1034–1052, 2007.

[52] G. Elkiran, V. Nourani, S. I. Abba, and J. Abdullahi, "Artificial intelligence-based approaches for multi-station modelling of dissolve oxygen in river," *Global Journal of Environtal Scince and Management*, vol. 4, no. 4, pp. 439–450, 2018.

[53] T. Partal and H. K. Cigizoglu, "Estimation and forecasting of daily suspended sediment data using wavelet-neural networks," *Journal of Hydrology*, vol. 358, no. 3-4, pp. 317–331, 2008.

[54] E. Sharghi, V. Nourani, H. Najafi, and H. Gokcekus, "Conjunction of a newly proposed emotional ANN (EANN) and wavelet transform for suspended sediment load modeling," *Water Supply*, vol. 19, no. 6, pp. 1726–1734, 2019.

[55] S. K. Himanshu, A. Pandey, and B. Yadav, "Ensemble wavelet-support vector machine approach for prediction of suspended sediment load using hydrometeorological data," *Journal of Hydrologic Engineering*, vol. 22, no. 7, Article ID 05017006, 2017.

[56] V. Nourani, K. T. Rezapour, and H. Baghanam, "Case studies in intelligent computing," in *Case Studies in Intelligent Computing*, N. Issac and B. Israr, Eds., Taylor and Francis Group, New York, NY, USA, 2014.

[57] G. B. Sahoo, C. Ray, and H. F. Wade, "Pesticide prediction in ground water in North Carolina domestic wells using artificial neural networks," *Ecological Modelling*, vol. 183, no. 1, pp. 29–46, 2005.

[58] G. Elkiran, V. Nourani, and S. I. Abba, "Multi-step ahead modelling of river water quality parameters using ensemble artificial intelligence-based approach," *Journal of Hydrology*, vol. 577, Article ID 123962, 2019.

[59] S. J. Hadi, S. I. Abba, S. S. Sammen, S. Q. Salih, N. Al-Ansari, and Z. M. Yaseen, "Non-linear input variable selection approach integrated with non-tuned data intelligence model for streamflow pattern simulation," *IEEE Access*, vol. 7, pp. 141533–141548, 2019.

[60] V. Nourani, H. Gökçekuş, I. K. Umar, and H. Najafi, "An emotional artificial neural network for prediction of vehicular traffic noise," *Science of the Total Environment*, vol. 707, 2020.

[61] K. E. Taylor, "Summarizing multiple aspects of model performance in a single diagram," *Journal of Geophysical Research: Atmospheres*, vol. 106, pp. 7183–7192, 2001.